INFORMATION TO USERS

This manuscript has been reproduced from the microfilm master. UMI films the text directly from the original or copy submitted. Thus, some thesis and dissertation copies are in typewriter face, while others may be from any type of computer printer.

The quality of this reproduction is dependent upon the quality of the copy submitted. Broken or indistinct print, colored or poor quality illustrations and photographs, print bleedthrough, substandard margins, and improper alignment can adversely affect reproduction.

In the unlikely event that the author did not send UMI a complete manuscript and there are missing pages, these will be noted. Also, if unauthorized copyright material had to be removed, a note will indicate the deletion.

Oversize materials (e.g., maps, drawings, charts) are reproduced by sectioning the original, beginning at the upper left-hand corner and continuing from left to right in equal sections with small overlaps.

Photographs included in the original manuscript have been reproduced xerographically in this copy. Higher quality 6" x 9" black and white photographic prints are available for any photographs or illustrations appearing in this copy for an additional charge. Contact UMI directly to order.

ProQuest Information and Learning
300 North Zeeb Road, Ann Arbor, MI 48106-1346 USA
800-521-0600

Université d'Ottawa · University of Ottawa

Resolving the Magnetic and Structural Anomalies in Face Centred Cubic Fe-Ni Alloys

A Solution to the Invar and Anti-Invar Problems

by

Ken Lagarec

A thesis submitted to
the Faculty of Graduate and Postdoctoral Studies
in partial fulfilment of the requirements
for the degree of Doctor of Philosophy

Department of Physics
University of Ottawa
Ottawa, Ontario, Canada

Abstract

We have studied the magnetic and structural properties of synthetic and meteoritic face centred cubic (FCC) Fe-Ni alloys in an effort to understand the underlying mechanisms responsible for the Invar and anti-Invar effects.

We have performed a detailed ^{57}Fe Mössbauer spectroscopic and electronic imaging study of the Santa Catharina meteorite, an FCC Fe-Ni meteorite with a bulk composition close to that of Invar ($Fe_{65}Ni_{35}$). Its microstructure consists of islands of tetrataenite in a matrix of Fe-rich antitaenite. Using Mössbauer spectroscopy (MS) and electron probe microanalysis (EPMA), we have determined that antitaenite is a low moment alloy with an Fe content of 88 ± 2 at. %. Antitaenite appears to be stabilized in the FCC phase by its epitaxial relation with tetrataenite. Its Néel temperature is ~60 K and its isomer shift (*IS*) is close to that of γ-Fe. The effect of the magnetic interaction with tetrataenite has been studied by Monte Carlo (MC) simulations and have been shown to be consistent with the anomalous temperature dependence of the width of the antitaenite's Mössbauer spectrum.

Using electronic structure calculations (ESCs), we have studied the T = 0 K properties of chemically ordered and disordered FCC Fe-Ni alloys in the ferromagnetic (FM), non-magnetic (NM) and disordered local moment (DLM) states. A significant drop in the *IS* and in the atomic volume are shown to occur at the transition from the high moment (HM) FM phase to the NM phase which occurs, according to our calculations, at 74.5 at. % Fe. Our calculations of the DLM and FM states show that in Fe-rich Invar alloys, the FM order contributes to stabilizing large moment magnitudes. Our systematic study of the hyperfine fields (HF) by ESCs supports the phenomenological model of Dang and Rancourt (1996a). Calculations on a supercell of $Fe_{11}Ni_5$ show the effects of nearest neighbour (NN) chemical and magnetic environments on the local magnetic moment magnitude and the HF distribution, thereby explaining the main observed features in Fe-rich alloys.

Using the *IS* as a direct probe of the electronic structure, a HM/LM (low moment) transition has been unambiguously observed to occur at ~70 at. % Fe. This is the first experimental evidence of the HM/NM transition in FCC Fe-Ni which had been predicted by ESCs. The presence of this transition explains the anomalous decrease of the atomic volume observed at these compositions. High temperature Mössbauer measurements have revealed a

thermal stabilization of the HM phase in anti-Invar alloys, the most Fe-rich FCC Fe-Ni alloys that are in a LM phase at low temperatures. We have argued that the anti-Invar effect is due to the entropic drive to increase the moment magnitude in systems which exhibit a magneto-volume instability. Contrary to the present dominant view, our results have allowed us to conclude that the Invar effect in Fe-Ni is not directly caused by HM/LM admixture or so-called 2-γ-state like excitations.

MC calculations using a local moment model with a large volume dependence of the Fe-Fe magnetic exchange parameter [Rancourt, 1996a] adequately reproduce the temperature and composition dependence of the magnetic and structural anomalies in Invar alloys. The large interatomic distance dependence of the NN Fe-Fe magnetic exchange parameter has been shown to be corroborated by ESCs. The Invar effect in Fe-Ni must therefore be understood as a volume expansion mediated by magnetic order in a predominantly HM local moment system having a large Fe-Fe magneto-volume coupling.

Statement of Originality

The work performed in this thesis has resulted in many original measurements, calculations and observations that have been reported in many journal's and at several international scientific conferences. The following is a list of articles and presentations at conferences based on the work found in the various chapters:

Meteorites (chapter 3)

Presentation at the *1996 Congress of the Canadian Association of Physicists* (Ottawa, Canada):
Investigation of Fe-Ni Alloys in Meteorites using Mössbauer Spectroscopy
K. Lagarec, D. G. Rancourt, R. B. Scorzelli and I. de Souza Azevedo

Experimental proof of the distinct electronic structure of a new meteoritic Fe-Ni alloy phase
D. G. Rancourt, K. Lagarec, A. Densmore, R. A. Dunlap, J. I. Goldstein, R. J. Reisener, R. B. Scorzelli, *Journal of Magnetism and Magnetic Materials.* **191** (1999) L255-L260.

ESCs and HM/LM transition (chapters 5 and 6)

Invited speaker at the *1999 International Conference on the Application of the Mössbauer Effect* (Aug. 29-Sep. 3 1999, Garmisch-Partenkirchen, Germany):
A high-moment/low-moment transition does occur in Fe-Ni alloys but thermal excitation of the low-moment phase does not cause the Invar effect
K. Lagarec and D. G. Rancourt

Observation of a composition-controlled high-moment/low-moment transition in the face centered cubic Fe-Ni system: Invar effect is an expansion, not a contraction
K. Lagarec, D. G. Rancourt, S. K. Bose, B. Sanyal, and R. A. Dunlap, accepted for publication in *Journal of Magnetism and Magnetic Materials* pending minor corrections.

Speaker at the *International Symposium on Dynamics of Heterogeneous Systems II* (28-29 August 2000, Duisburg, Germany) and the *41th UK Mössbauer Discussion Group* (4-5 September 2000, Greenwich, England)
Observation of a composition-controlled high-moment/low-moment transition in the face centered cubic Fe-Ni system: Invar effect is an expansion, not a contraction

K. Lagarec, D. G. Rancourt, S. K. Bose, B. Sanyal, and R. A. Dunlap
(proceedings are in press in *Phase Transitions*)

MC Simulation of the Invar effect (chapter 7)

Fe_3Ni-type chemical order in $Fe_{65}Ni_{35}$ films grown by evaporation: Implications regarding the Invar problem
K. Lagarec and D. G. Rancourt, *Physical Review B* **62** (2000) 978-985.

Mössbauer Spectral Analysis (appendices A and B)

Extended Voigt-based analytic lineshape method for determining N-dimensional correlated hyperfine parameter distributions in Mössbauer spectroscopy
K. Lagarec and D. G. Rancourt, *Nuclear Instruments and Methods in Physics Research B* **129** (1997) 266-280.

Spectral analysis in Mössbauer spectroscopy (abstract)
K. Lagarec and D. G. Rancourt, proceedings of the 11th International Clay Conference (Ottawa, Canada, 1997)

Poster presentation at the *1999 International Conference on the Application of the Mössbauer Invar Effect* (Aug. 29-Sep. 3 1999, Garmisch-Partenkirchen, Germany):
Correcting for Non-Uniform Thickness Effects in Mössbauer Spectra
K. Lagarec and D. G. Rancourt

During the course of my research, I have also developed the advanced spectral analysis software that I have used to do all the analysis and named Recoil. Recoil has also been presented at several conferences as a poster presentation and is available commercially. More information regarding the capabilities of the software can be found at http://www.physics.uottawa.ca/~recoil.

Acknowledgments

When I started working for Denis G. Rancourt, I did not know exactly what I was getting into but I quickly realized I had found an impressive supervisor that would lead me to complete this research as a final step in his own career in Fe-Ni alloys. Denis is always directly involved in his students' research and takes pride of our work. This leads to a working environment to which I have had the pleasure of contributing. Denis, thank you for trusting me with this work, for sometimes letting me do things my way and sometimes guiding me through tougher times.

On a personal note, I really have to thank Isabelle Tremblay who has supported and encouraged me through three years of this work. Isabelle, I hope by reading this you will finally realize how much this meant to me. Thanks for being there. Now, I can finally tell you it's done. I most definitely also owe this thesis to my parents and my family who have always believed in me and stood behind me throughout my life. You have waited a long time for this and here it is.

There are several very important people who have collaborated on several aspects of this research and without which most of this work would not have come to fruition. Drs. Scorzelli, de Souza Azevedo and Rechenberg have provided us with the sample of the Santa Catharina meteorite as well as data from experiments on this meteorite. When it came to imaging the intergrowth in the Santa Catharina, the work was carried out by Drs. Goldstein and Reisener. Dr. Dunlap has kindly and most efficiently provided us with the synthetic Fe-Ni samples, as he had previously in the work carried out by Dr. Dang. Finally, last but certainly not least, Drs. Bose and Sanyal have helped me with the electronic structure calculations by performing some of the calculations and showing me how to do the rest myself. All of the work regarding ESCs has been made possible thanks to our collaboration with Dr. Bose. Thank you to all the people mentioned here and to all those not explicitly mentioned but who have played a part in this accomplishment.

Of the graduate students I have met in Dr. Rancourt's group, there are two who have really contributed to my work. Dr. Mei-Zhen Dang, who was the last student of Dr. Rancourt to work on Fe-Ni alloys, was an essential source of information and inspiration. This work is in large part an extension of her own Ph. D. thesis and she followed it and discovered it with me with the same fascination as if it was her own work. We have had too many important

discussions to even remember but I will not forget her friendliness and generosity. Patrick Mercier is another student who, even though he does not work in the field of Fe-Ni alloys, has had to sustain my barrage of arguments and explanations about my work. If I needed to clear something up in my mind, I would often explain it to Patrick. In order to verbalize my thoughts, I had to make them clear and coherent and this helped me a great deal. Thank you Patrick for dealing with my sometimes lengthy tirades about this work. To all the other people in the department, thank you for always making me feel welcome and appreciated.

Table of Content

Abstract ii
Acknowledgments vi
Table of Content viii
List of Figures xv
List of Tables xxviii
List of Abbreviations xxxi
List of Symbols xxxiii

Chapter 1. Introduction 1
1.1 Anomalous Properties of FCC Fe-Ni Alloys 1
1.2 Models of the Invar Effect in Fe-Ni Alloys 3
1.3 Choice of Experimental and Theoretical Tools 6
1.4 Organization of the Thesis 6

Chapter 2. Experimental Methods: Mössbauer Spectroscopy 9
2.1 Introduction to Mössbauer Spectroscopy 9
2.1.1 Transmission Mössbauer Spectroscopy 10
2.1.2 Conversion Electron Mössbauer Spectroscopy 11
2.2 Hyperfine Interactions and Their Effect on the Mössbauer Spectrum 12
2.2.1 Electric Monopole Interaction and Second-Order Doppler Shift 12
2.2.1.1 The Isomer Shift 12
2.2.1.2 Second-Order Doppler Shift 14
2.2.2 Electric Quadrupole Interaction 15
2.2.3 Magnetic Dipole Interaction 16
2.2.4 Calculating and Fitting the Mössbauer Spectrum 17
2.2.4.1 Distributions of Hyperfine Parameters 20
2.2.4.2 Complexities Involved in Getting Accurate Hyperfine Parameters (*CS* in Particular) 21
2.2.4.2.1 Correlation Between the *CS* and the HF 21

2.2.4.2.2 Dynamic Effects Near 22
2.2.4.2.3 Average Quadrupole Shift 23
2.3 Experimental Mössbauer Setup 25
2.3.1 Physical Layout and Electronics for Data Acquisition 25
2.3.2 Oven for Mössbauer Spectroscopy 28
2.3.2.1 Design and Construction 28
2.3.2.2 Temperature Control 31
2.3.2.3 Vacuum System 31
2.3.2.4 Testing and Temperature Calibration 32
2.3.3 Cryogenic Setups for Mössbauer Spectroscopy 34

Chapter 3. Fe-Ni Alloys in Meteorites 36
3.1 Overview of Meteorites 36
3.1.1 Introduction 36
3.1.2 Origin and Classification of Meteorites 37
3.1.3 Fe-Ni Phases in Meteorites 38
3.1.3.1 Kamacite and Taenite 38
3.1.3.2 Tetrataenite 38
3.2 The Santa Catharina Meteorite: Epitaxially Stabilized Tetrataenite and Antitaenite .. 39
3.2.1 Introduction 39
3.2.2 Sample Preparation 39
3.2.3 Characterization Using MS and Electron Microscopy Methods 40
3.2.3.1 Mössbauer Spectroscopy 40
3.2.3.1.1 Interpretation of the Mössbauer Spectrum 40
3.2.3.1.2 Extracting the Debye Temperatures of the Phases ... 46
3.2.3.2 Imaging of the Tetrataenite/Antitaenite Intergrowth 55
3.2.3.3 Electron Probe Micro-Analysis 55
3.2.4 Composition of Antitaenite 56
3.2.5 Saturation Magnetization of Antitaenite 59
3.2.6 Temperature Dependence of the Mössbauer Parameters 60
3.3 Effect of the Epitaxial Relation Between Tetrataenite and Antitaenite on the Magnetism

of Antitaenite 66
3.3.1 Anomalous Temperature Dependence of the FWHM of Antitaenite 66
3.3.2 Simulated Effect of Epitaxial Interaction of Antitaenite with Tetrataenite ... 67
3.4 Antitaenite as a New Mineral 75

Chapter 4. Overview of Fe-Ni Alloys as Collinear Ferromagnets 76
4.1 Bulk Magnetic Moment: The Slater-Pauling Relation 76
4.2 Atomic Volume: Deviation from Vegard's law 78
4.3 Hyperfine Parameters: Analysis of Mössbauer Spectra 80
4.3.1 Analysis Methodology 80
4.3.2 Results and Discussion 81
4.3.2.1 Modelling the Hyperfine Field Distribution Using a Binomial Distribution of Nearest Neighbours 94
4.3.2.2 The Isomer Shift 95

Chapter 5. Electronic Structure Calculations of Fe-Ni Alloys 99
5.1 Introduction 99
5.2 ESCs Using the LMTO Method 99
5.2.1 Calculating $T = 0$ K Equilibrium Properties 100
5.2.1.1 The Lattice Parameter and Volume 100
5.2.1.2 The Bulk Modulus 101
5.2.1.3 The Magnetic Moment 101
5.2.1.4 The Contact Hyperfine Field 101
5.2.1.5 The Isomer Shift 102
5.3 ESC of Chemically Ordered Phases 103
5.3.1 Description of the Crystallographic Structure 103
5.3.2 Calculated ESC in Ferromagnetic and Non-Magnetic Configurations 105
5.3.2.1 Ground States and Magnetic Moments 106
5.3.2.2 Systematics of the Charge Density at the Nucleus 112
5.3.2.3 Systematics of the Hyperfine Field 115
5.3.2.4 Site to Site Variations in Fe-Rich Alloys 121

5.3.2.5 Composition Dependence of the Ground State Properties 129
5.4 ESC of Chemically Disordered Phases Using the CPA 133
5.4.1 Constrained Collinear Magnetic Structure Calculations 133
5.4.2 Disordered Local Moment Calculations 134
5.4.3 CPA Calculations of $Fe_{65}Ni_{35}$ 135
5.4.4 Composition Dependence of the CPA FM, DLM and NM Equilibrium Properties 141
5.5 Magnetism of γ-Fe: FM, AF and DLM Calculations 148
5.6 Conclusion 151

Chapter 6. Experimental Observation of a HM/LM Transition in Fe-Rich FCC Fe-Ni Alloys. Implications Regarding the Invar and Anti-Invar Effects 152
6.1 Introduction 152
6.2 Experimental Procedures 153
6.2.1 Sample Preparation 153
6.2.2 X-ray Diffraction 153
6.2.3 Mössbauer Spectroscopy 154
6.3 Description of the RT Mössbauer Spectra 155
6.4 Observation of a HM/LM Transition Occurring Around 70 at. % Fe 159
6.4.1 The Hyperfine Field 159
6.4.2 The Isomer Shift 163
6.4.3 The Lattice Parameter 168
6.4.3.1 Identifying the HM/LM Transition 168
6.4.3.2 Distinction Between the HM/LM Transition and the Invar Effect .. 170
6.4.4 Differentiating the Observation of the HM/LM Transition from the Normal *IS* and Volume Correlation 174
6.5 High-Temperature Measurements 187
6.5.1 Analysis Method 187
6.5.2 Observation of a Correlation Between the *IS* and *z* in Invar Alloys 187
6.5.3 Thermal Stabilization of a HM Phase in Anti-Invar Alloys 189
6.5.3.1 Description of the Experimental Data 189

6.5.3.2 Entropic Drive Towards a Larger Moment Magnitude and the Anti-Invar Effect 193
6.5.3.3 Analysis of Peak Widths for Evidence of Thermal Excitations 197
6.5.4 Austenitic Transformation 199
6.6 Conclusion 200

Chapter 7. Monte Carlo Simulation of Magneto-Volume Effects in Fe-Ni Alloys 203
7.1 Model Hamiltonian of the System 203
7.2 Simulation Method 205
7.3 Details of the Simulations 208
7.3.1 Sample Averages Calculated in the Simulation 208
7.3.2 Avoiding Sampling Autocorrelation Effects 210
7.4 Choice of the Fe-Fe Magnetic Exchange Parameter 211
7.4.1 Theoretical Calculations of 211
7.4.2 Model Used in the Simulations 215
7.4.2.1 Interatomic Distance and Composition dependence of 215
7.4.2.2 Choice of and 217
7.5 Simulation Results 218
7.5.1 Simulated Properties as a Function of Composition 218
7.5.1.1 Pure Ni 218
7.5.1.2 Alloy Properties in the Absence of Magneto-Volume Coupling 225
7.5.2 Properties with Magneto-Volume Coupling 231
7.5.2.1 Simulating the Invar Effect in $Fe_{65}Ni_{35}$ 231
7.5.2.2 Invar Effect at Other Compositions 240
7.5.3 Effect of the choice of 247
7.6 Conclusion 248

Chapter 8. Conclusion 249
8.1 Summary of Results 249
8.2 What Causes the Invar Effect? 251

8.3 What Causes the Anti-Invar Effect? 252
8.4 What Can We Learn From This Work? 252

Appendix A. The Extended Voigt-Based Fitting Method 254
A.1 Introduction 254
A.2 Mathematical Description 256
A.2.1 Paramagnetic Case 256
A.2.2 Magnetic Case 258
A.3 Application to a Synthetic Taenite 259
A.4 Conclusion 260

Appendix B. A General Method for Removing Non-Uniform Thickness Effects in Mössbauer Spectra 268
B.1 The Transmission Integral Formulation 268
B.2 Assumptions and Limitations 269
B.3 Dealing with Non-Uniform Thickness 269
B.3.1 Some Physical Examples 271
B.3.2 General Method to Correct for Non-Uniform Thickness Effects 272
B.3.2.1 Prior Knowledge About the Absorber 272
B.3.2.2 Pattern Smoothing using the Voigt Lineshape 272
B.3.2.3 Self-Consistent Solution to the Problem 272
B.3.2.4 Generating a Thickness-Effect Free Spectrum 273

Appendix C. Correcting for Geometrical Artifacts in Mössbauer Spectra 275
C.1 Introduction 275
C.2 Geometrical Effects on a Folded Spectrum 277
C.2.1 Effect on the Background 280
C.2.2 Effect on the Peak Shape 281
C.3 Correcting for Geometrical Artifacts 284

Appendix D. Tables of Results of Analyses of High Temperature MS Spectra . 286

Appendix E. Source Code for MC Simulations 301

References 346

List of Figures

Chapter 2

Figure 1 Diagram of the decay of ^{57}Co into ^{57}Fe. The 14.4 keV transition used in ^{57}Fe MS. 9

Figure 2 Conventional transmission MS setup. 10

Figure 3 Surface sensitive CEMS setup. 11

Figure 4 Effect of the electric monopole (H_δ), electric quadrupole (H_Q) and magnetic dipole (H_M) interactions on the nuclear levels and on the transmission Mössbauer spectrum. The relation between the relevant hyperfine parameters and the energy levels are also given. 19

Figure 5 Transmission Mössbauer spectrum of $Fe_{30}Ni_{70}$ illustrating the line depth asymmetry due to correlations between hyperfine parameters (in this case it is mainly due to a ε-z correlation). 24

Figure 6 Transmission Mössbauer spectrum of $Fe_{65}Ni_{35}$ showing signs of δ-z correlations (left) and the extracted and strongly skew HFD (right). 24

Figure 7 Diagram of the experimental setup for Mössbauer spectroscopy. Solid lines represent a signal, dashed lines represent an applied voltage and the arrows indicate where the signal is sent (or where the voltage is applied) 27

Figure 8 Schematic view of the oven used for Mössbauer spectroscopy. 28

Figure 9 Schematic view of the vacuum system and its vibration reduction components 30

Figure 10 α-Fe Mössbauer data [Kobeissi81] used for the calibration of the oven temperature. (■) relative Zeeman splitting (relative to value at T = 0 K) and (◆) centre shift (relative to value at RT). The lines represent the calibration curves obtained from the data points, in the range of interest. 33

Figure 11 Schematic representation of the cryostat for variable temperature measurements from 4.2 K to RT. 35

Chapter 3

Figure 12 Absorption Mössbauer spectrum of the thick (100 μm) slices of the Santa Catharina meteorite. Three separate phases are noticeable: tetrataenite which is magnetic and characterized by a substantial asymmetry, ordinary taenite which is also magnetic and

has broad lines and antitaenite which is seen as a paramagnetic singlet. 41

Figure 13 Mössbauer spectrum of the powder produced during the cutting of the SC meteorite slices. The sextet has parameters consistent with a BCC Fe-Ni alloy, indicating that most of the microstructure has been destroyed. 43

Figure 14 CEMS spectrum of a slice of the SC meteorite after etching with an acid solution (5 % vol. HCl, 5 % vol. H_2SO_4 in water). The asymmetry of the lines of tetrataenite and the paramagnetic line of antitaenite show that this surface is similar to the bulk. Cosine smearing due to the closeness of the source and the sample and the low signal-to-noise ratio preclude us from getting much more information from this spectrum. 44

Figure 15 Mössbauer spectra of the SC meteorite at 80 K and 295 K. The top two spectra are taken with the roughing pump turned off, while the bottom two have the pump activated which results in noticeable broadening. Notice also the broadening of the antitaenite's signal at 80 K. 47

Figure 16 Temperature dependence of the centre shifts of the tetrataenite (◆) and antitaenite (■) phases of the Santa Catharina meteorite, as measured by De Grave *et al.* [DeGrave92]. The solid lines represent the best fit to a model where the *IS* does not change with temperature. 50

Figure 17 Residuals of the fit of the *CS* of antitaenite assuming a constant *IS*. In addition to yielding an unrealistic value of Θ_D = 595 K, the regularity of the deviations indicates the fitting model is incorrect. [data from DeGrave92] 51

Figure 18 Difference between the measured *CS* of tetrataenite (tt) and antitaenite (nt). The solid line represents what the difference would be, assuming there *IS*s are independent of temperature and there is a difference of 130 K in their Debye temperatures ($\Theta_{D,tt}$ = 380 K and $\Theta_{D,nt}$ = 510 K chosen such that the highest and lowest temperature data match). [data from DeGrave92] 51

Figure 19 SEM secondary electron image of the SC meteorite, showing the dominant CZ as well as some iron phosphide and oxide. Based on other images, the presence of phosphides is not characteristic of the sample, but is showed here as an illustration of the technique. 52

Figure 20 HRSEM secondary electron image of the CZ microstructure which shows the tetrataenite islands (light) in an antitaenite honeycomb matrix (dark). 53

Figure 21 HRSEM secondary electron imaging of the CZ microstructure taken at an angle. In this image, it is clear that the etching has preferentially removed the antitaenite phase, as tetrataenite globules can be seen extruding from the surface. 54

Figure 22 Mössbauer spectra of the SC meteorite from LN_2T to RT, as indicated. 61

Figure 23 Mössbauer spectra of the SC meteorite from LHeT to 50 K, as indicated. 62

Figure 24 Temperature variation of the Zeeman splittings in tetrataenite (a, ◆) and ordinary taenite (b, ●), as well as the average quadrupole shift in tetrataenite (c, ■) (1-σ fitting uncertainties are illustrated). The line in (c) corresponds to the average value of $\varepsilon = 0.19$ mm/s. 65

Figure 25 Temperature variation of the FWHM of the antitaenite peak (1-σ fitting uncertainties are displayed). The inset shows the data from 75 to 300 K on a different scale. The solid line in the inset corresponds to a slope of -0.00035 mm/s/K. 66

Figure 26 Effect of the tetrataenite/antitaenite interface on the normalized staggered magnetization (long-range order parameter) in antitaenite. ■ antitaenite epitaxially linked to tetrataenite, ● bulk antitaenite. 71

Figure 27 Effect of the tt/nt interface on the average moment magnitude. Same symbols as above. The line at $y = 0.013$ represents the theoretical result for randomly distributed moments (non-zero because of finite sampling time). 71

Figure 28 Average moment magnitude in the atomic layers in the [001] direction as a function of temperature. Line symbols represent different temperatures: (solid) $T = 50$ K, (dash) $T = 70$ K, (dot) $T = 100$ K, (dash-dot) $T = 150$ K, (dash-dot-dot) $T = 200$ K, (short dash) $T = 250$ K and (short dot) $T = 300$ K ((b) is a blow -up for small magnitudes of (a)) 72

Figure 29 Average moment per layer at $T = 100$ K in constrained antitaenite. The bottom plot shows a rescaled version (is displayed to show the spatial variation of both the large and small moments) which illustrates how the antiferromagnetic structure is preserved well into the bulk of the antitaenite, even far above 73

Figure 30 Penetration depth of the tt/nt interaction as a function of temperature. The average moment magnitude is reduced to half of its saturation value at the given depth (layer in [001] direction). 74

Figure 31 Simulated distribution of moment magnitudes in antitaenite at $T = 100$ K, after $N = 3900$ time samples. The moment magnitude with maximum probability eventually

converges to 0, but the tail at higher values remains even for large N. 74

Chapter 4

Figure 32 Experimental determinations of the average saturation magnetic moment in Fe-Ni alloys at 4.2 K and the Slater-Pauling relation. Filled symbols represent the FCC phase, whereas open symbols are for the BCC phase. Similar symbols (open and filled) correspond to the same reference: ■ Kondorskii and Fedotov [Kondorskii52], ◆ Crangle and Hallam [Crangle63], ▲ Cochrane and Graham [Cochrane70], ▼ Peschard [Peschard25], ● Brando [Brando64], ★ Asano [Asano69]. The solid line represents the Slater-Pauling relation, the dashed line represents a situation where the Fe moment is assumed to decrease linearly with the composition, as calculated in chapter 5. 77

Figure 33 Composition dependence of the atomic volume in Fe-Ni alloys at RT. Solid symbols represent measurements of the FCC phase, open symbols are for the BCC phase. The straight line corresponds to Vegard's law, extrapolated from the Ni-rich (< 20 at. % Fe) data. Symbols are: ■ Bradley *et al.* [Bradley37], ◆ Phragmén [Phragmen31], ● Owen *et al.* [Owen37d], ▲ Newkirk [Newkirk57], ★ Dang [Dang96a] and Lagarec [see chapter 6]. 79

Figure 34 Properties of the HFD for RT SQ and RQ samples (the inset in (a) shows an expanded version). The solid line corresponds to the model described in the text. The deviation from the model line becomes apparent above ~50 at. % Fe and is at first mainly due to a deviation from collinear ferromagnetism. Symbols are for different series of synthetic alloys: ● SQ series #1, ■ SQ series #2, ◆ SQ series #3, ▲ RQ series #1. 97

Figure 35 Calculated IS and Θ_D in FCC Fe-Ni alloys, assuming IS and Θ_D are temperature independent. The solid and dashed lines in (b) corresponds to Θ_D = 380 ± 20 K. 98

Chapter 5

Figure 36 Chemically ordered structures in FCC Fe-Ni alloys with simple stoichiometries. The black and white atoms represent the two different species. 105

Figure 37 ESC results for γ-Fe. The solid line represents the HM FM state, the dash-doted line the IM FM state, the dashed line the NM state, the sort-dash-dotted line is the AF state and the dotted line the extrapolated HM FM state. 107

Figure 38 ESC results for Fe_3Ni. The solid line represents the FM state, the dashed line the NM state and the dotted line the extrapolated HM FM state. 108

Figure 39 ESC results for cubic FeNi. The line styles represent the same states as in fig. 37. . 109

Figure 40 ESC results for $FeNi_3$. The line styles are the same as in fig. 37. 110

Figure 41 ESC results for Ni. The line styles represent the same states as in fig. 37. 111

Figure 42 Valence ($\rho_v(0)$) and core ($\rho_c(0)$) charge densities at the Fe nucleus in NM (dotted line) and HM FM (solid line) γ-Fe. 112

Figure 43 Valence ($\rho_v(0)$) and core ($\rho_c(0)$) charge densities at the Fe nucleus in NM (dotted line) and HM FM (solid line) FeNi. 114

Figure 44 Calculated total hyperfine field at the Fe (a) and Ni (b) nuclei, as a function of the average magnetic moment per atom in the structure. ■ FM γ-Fe, ▲ Fe_3Ni, ◆ FeNi, ▼ $FeNi_3$, ● Ni. The solid line is H = -15.5 μ. 118

Figure 45 Calculated core (a, H_c) and valence (b, H_v) hyperfine fields at the nuclei as a function of the moment on the Fe atoms. ■ FM γ-Fe, □ AF γ-Fe, ▲ Fe_3Ni, ◆ FeNi, ▼ $FeNi_3$. The solid line in (a) is H_c = -11 μ. 119

Figure 46 Calculated core (a, H_c) and valence (b, H_v) hyperfine fields at the Ni nuclei as a function of the moment on the Ni atoms. ● Ni, ▼ $FeNi_3$, ◆ FeNi, ▲ Fe_3Ni. The solid line in a. is H_c = -11 μ.
..... 120

Figure 47 Effect of the local chemical environment on (a) the number of valence electrons, (b) the Fe moment and (c) the isomer shift. The open symbol represents the atom whose moment is aligned opposite to the others. 126

Figure 48 Effect of the local number of valence electrons on the moment of the Fe atoms. . 127

Figure 49 Correlation between the valence contribution to the charge density at the nucleus and the total number of valence electrons at the Fe atoms. 127

Figure 50 Hyperfine field distribution on the Fe atoms in $Fe_{11}Ni_5$. The low field component is due to the atom whose moment is aligned opposite to the others. 128

Figure 51 Correlation between the hyperfine field and the isomer shift of Fe atoms in $Fe_{11}Ni_5$.
..... 128

Figure 52 Calculated composition dependencies of the energy (a), atomic volume (b) and bulk modulus (c) of the ordered phases. ■ FM HM, □ NM, ★ equilibrium. In (a), at each

composition, E_0 is the linear interpolation between the energies of pure Ni and pure Fe. 131

Figure 53 Calculated composition dependencies of (a) the isomer shifts, (b) the hyperfine fields and (c) the magnetic moments of the ordered phases. In (a) ■ HM FM, □ NM, ★ equilibrium. In (b) and (c) ■/□ HM FM, ★/☆ equilibrium. Filled symbols are for Fe atoms, open symbols for Ni atoms and half filled for the average. 132

Figure 54 CPA results for $Fe_{65}Ni_{35}$ in the FM (solid line), DLM (dashed line) and NM (dotted line) phases. The arrows indicate the equilibrium volumes for each phase (a). In (b) the Ni moment in the DLM phase is 0. 138

Figure 55 Calculated composition dependence of the energy (a), the atomic volume (b) and the bulk modulus (c) of the chemically disordered phases (■ FM, □ NM, ◆ DLM) and the chemically ordered phases (★ HM FM, ☆ NM). 139

Figure 56 Calculated composition dependence of the isomer shift (a), hyperfine field (b) and magnetic moment (c). In (a), ■ FM, □ NM, ◆ DLM, ★ HM FM-ordered, ☆ NM-ordered. In (b) and (c), ■ FM Fe, □ FM Ni, ◆ DLM Fe (in the DLM case, Ni is non-magnetic), ★ Fe HM FM-ordered, ☆ Ni HM FM-ordered. Half-filled symbols represent the averages. 140

Figure 57 Calculated Θ_D for Fe-Ni alloys based on the CPA calculations in the FM (■) and NM (□) phases. 144

Figure 58 Relation between the DLM moment squared and the relative volume between the DLM and NM phases in Fe-Ni alloys. 146

Figure 59 Calculated moments in γ-Fe for different magnetic structures: — DLM phase, - - HM FM phase, ··· IM FM phase, - ·- AF-1 phase, - ··- AF-2 phase. The DLM calculation was non-relativistic, with some relativistic corrections while the other calculations were fully scalar-relativistic. The phase which is most stable at the given lattice parameter is indicated at the top (this excludes the DLM phase because the energies cannot be directly compared). 148

Figure 60 Illustrations of (a) NM and (b) HM states. - - internal energy (of formation of the moment), ··· magnetic ordering energy (in a NN Heisenberg model), — total energy. In the HM case, the moments in the DLM case (μ_{DLM}) and with magnetic order (μ_{MO}) are indicated. 149

Chapter 6

Figure 61 RT Mössbauer spectra of RQ Fe-Ni alloys with compositions from 67 to 72 at. % Fe. 157

Figure 62 RT Mössbauer spectra of RQ Fe-Ni alloys with compositions from 73 to 78 at. % Fe. 158

Figure 63 Range of values of the average Zeeman splitting as a function of composition, for different analysis models. The dark symbols represent data presented in the previous chapter, whereas the light columns represent data for Fe-rich alloys presented in this chapter. 160

Figure 64 Variation of the Curie temperature of Fe-Ni alloys as a function of composition. The data are from [Wassermann90]. The horizontal dashed line represents RT. Alloys with compositions below 70.5 at. % Fe are magnetic at RT, while alloys with an Fe content above this composition are paramagnetic. 161

Figure 65 Variation of the FWHM of the FCC signal as a function of composition. In the absence of thickness effects in the absorber or the source and hyperfine parameter distributions, the theoretical FWHM would be 0.2 mm/s. 162

Figure 66 Average RT *IS* of FCC Fe-Ni alloys as a function of composition. The column represents the range of possible values obtained from satisfactory fits using different models, and the error bars represent the 1-σ statistical uncertainty due to the fitting. Again, the dark columns represents previously reported data, and the light columns the results of analysis of new Fe-rich alloys. 166

Figure 67 Experimental and calculated *IS* in various HM and LM Fe-Ni alloys. Vertical columns with error bars represent the synthetic FCC Fe-Ni alloys described in this chapter. Other symbols for experimental RT data are: (●) BCC Fe-Ni alloys [Dang96a and this work], (▽) LM γ-Fe [Keune77, Halbauer83], (◇) meteoritic antitaenite [chapter 3], (□) nanophase FCC material [Rancourt99]. Theoretical results based on ESCs using the CPA are represented by solid lines, ESC results on ordered structures are given by (★) and (☆), where the solid symbols represent the HM solution, and the open symbol the NM solution. 167

Figure 68 Composition dependence of the RT volume in FCC (solid symbols) and BCC (open symbols) Fe-Ni alloys. The straight line represents Vegard's law, as obtained by

extrapolating from volumes of alloys with compositions less than 20 at. % Fe. See chapter 4 for the references regarding all the data points. 169

Figure 69 Spontaneous volume expansion ω_{s0} at T = 0 K (solid line) and RT thermal expansion coefficient α_{RT} (dotted line) of FCC Fe-Ni alloys (data taken from [Wassermann90]). 170

Figure 70 T = 0 deviation from Vegard's law and comparison with ω_{s0} 171

Figure 71 Illustration of the difference between the Invar expansion and HM/LM transition contraction of the atomic volume in FCC Fe-Ni alloys, relative to Vegard's law. Symbols are the same as used in fig. 68. Solid Symbols represent RT measurements, and open symbols represent extrapolation to T = 0 K based on thermal expansion curves between 0 K and RT (from [Hayase73]). As seen, the HM/LM contraction (left scale), which has a midpoint around 70 at. % Fe is an order of magnitude larger than the Invar expansion seen in alloys of lower Fe content (right scale). 173

Figure 72 High-temperature Mössbauer spectra of $Fe_{30}Ni_{70}$ (T_C ≈ 860 K). 183

Figure 73 High-temperature Mössbauer spectra of $Fe_{50}Ni_{50}$ (T_C ≈ 790 K). 183

Figure 74 High-temperature Mössbauer spectra of $Fe_{60}Ni_{40}$ (T_C ≈ 665 K). 184

Figure 75 High-temperature Mössbauer spectra of $Fe_{67}Ni_{33}$ (T_C ≈ 460 K). 184

Figure 76 High-temperature Mössbauer spectra of $Fe_{69}Ni_{31}$ (T_C ≈ 370 K). The cooled RT spectrum (top) shows that the sample has undergone a spinodal decomposition into phases of slightly different compositions, as is evidenced by the increase in the Zeeman splitting 185

Figure 77 High-temperature Mössbauer spectra of $Fe_{71}Ni_{29}$ (T_C ≈ 270 K). The high temperature and cooled RT (top) spectra show important signs of oxidation (this was the first series taken, before the leak in the oven was discovered and fixed). 185

Figure 78 High-temperature Mössbauer spectra of $Fe_{73}Ni_{27}$ (T_C < RT). The BCC phase disappears at the austenitic end temperature (~800 K). The cooled sample is nearly pure FCC. 186

Figure 79 High-temperature Mössbauer spectra of $Fe_{75}Ni_{25}$ (T_C < RT). Again we see a disappearance of the BCC phase above 800 K, and a recovered sample which has a higher proportion of the FCC phase. 186

Figure 80 Illustration of the correlation between the *IS* (columns) and $< |z| >$ (solid lines) in Invar alloys. The given scale is for the *IS* and is the same for all alloys. The *IS* of each

alloy is vertically offset for more clarity. The $< |z| >$ data is rescaled for each alloy to match the range of the *IS* and is displayed as a continuous curve for comparative purposes. The arrows indicate T_C for each of the alloys. 188

Figure 81 Thermal evolution of the *IS* in anti-Invar alloys (from top to bottom at RT: 69 - dark and solid, 71 - ///, 73 - light and solid and 75 at. % Fe - \\\\). 191

Figure 82 *IS* in the various phases of pure Fe. The Curie point of α-Fe is shown by an arrow. The equilibrium α (BCC), γ (FCC), and δ (reentrant BCC) phase regions are separated by vertical dotted lines. The original *CS* data is from Kobeissi [Kobeissi81] (filled circles), Kovats *et al.* [Kovats69] (filled squares), and Keune *et al.* [Keune77] and Halbauer *et al.* [Halbauer83] (half-filled squares). The solid lines are guides to the eye. 192

Figure 83 Calculated magnetic moment in the DLM state in γ-Fe as a function of volume [see chapter 5 for details]. 196

Figure 84 Thermal evolution of the FCC signal's FWHM in paramagnetic alloys. (■) 69 at. % Fe, (●) 71 at. % Fe, (▲) 73 at. % Fe, (▼) 75 at. % Fe. The hollow symbols at RT correspond to measurements taken on the sample after cooling from the highest temperature. The theoretical FWHM in the absence of thickness effects, hyperfine parameter distributions or thermal gradients is 0.2 mm/s. 198

Figure 85 Increased linewidth (ΔFWHM) of a peak resulting from the superposition of two overlapping peaks of a given FWHM and separated by an *IS* of 0.1 mm/s. 198

Figure 86 Variation of the normalized areas of the FCC (■) and BCC (◆) phases of $Fe_{73}Ni_{27}$. The lines are fits to a Debye model. The arrows indicate how the proportions of the phases at high temperature evolved as they were cooled back to RT. 201

Figure 87 Variation of the normalized areas of the FCC (■) and BCC (◆) phases of $Fe_{75}Ni_{25}$. The lines are fits to a Debye model. The arrows indicate how the proportions of the phases at high-temperature evolved as they were cooled back to RT. 201

Figure 88 High-temperature phase diagram of the Fe-Ni systems. The ranges of stability of the γ (FCC) and α (BCC) phase are indicated, as well as the martensitic start temperature (M_S, dotted line) [data from Reuter88]. The diamonds indicate the approximate temperatures at which the austenitic transition was half complete. 202

Chapter 7

Figure 89 Autocorrelation functions of V (solid line), E (dashed line), $E \times V$ (dotted line), (dash-dotted line) and (dash-double dotted line). 210

Figure 90 Effective Fe-Fe NN magnetic exchange parameter, based on the calculation by Sabiryanov *et al.* [Sabiryanov95]. 212

Figure 91 Calculated magnetic moment and magnetic exchange parameters in Fe_3Ni. In (c), the symbols are: ■ J_{FeFe}, ▲ $J^{(2)}_{FeFe}$ and ◆ J_{FeNi}. 214

Figure 92 Renormalized (see text) magnetic exchange parameters in Fe_3Ni. ■ J_{FeFe}, ◆ $J^{(2)}_{FeFe}$, ▲ J_{FeNi} and ● $J_{0,Ni}/12$. 215

Figure 93 Effect of the NN distance on J_{FeFe} as used in the simulation. 216

Figure 94 Simulated reduced magnetization (relative to the Slater-Pauling value, solid line) and linear thermal expansion coefficient ($\times 10^{-6}$ K^{-1}, dashed line) at T = 300 K in $Fe_{65}Ni_{35}$ as a function of J'_{FeFe} and d_0. 218

Figure 95 Simulated atomic volume (a, V) and linear thermal expansion (b, α_T) of Ni as a function of temperature. In (a), the volume at T = 0 K is the volume calculated from r^0_{NiNi}. In (b), ◆ are calculated by numerically differentiating data in (a) and ▲ are calculated in the simulation at each temperature. 221

Figure 96 Simulated bulk modulus (a, B) and specific heat (b, c_p lattice contribution only) of pure Ni as a function of temperature. Again ◆ are calculated by differentiation whereas ▲ are obtained directly from the simulation. 222

Figure 97 Simulated average moment per atom (a, M) and magnetic susceptibility (b, χ_M) of pure Ni. In (b), the inverse susceptibility (▲, χ_M^{-1}) shows a standard Curie-Weiss law above T_C, with a Curie-Weiss temperature just below 650 K. 223

Figure 98 Simulated magnetic contribution to the specific heat (c_p^{mag}) which shows a standard "lambda" divergence at the critical temperature that is estimated to be between 600 K and 650 K. 224

Figure 99 Simulated atomic volume (a) and deviation from Vegard's law (b) at T = 300 K in the absence of magneto-volume effects. In (b), we see that the deviation is at most ±0.015 % throughout the composition range. 227

Figure 100 Average chemical potential energy per atom relative to E_0 (see text) (a) and bulk

modulus (b) at T = 300 K in the absence of magneto-volume effects. 228

Figure 101 Composition dependence of the linear thermal expansion (a) and specific heat (b, lattice only) at T = 300 K in the absence of magneto-volume effects. 229

Figure 102 Composition dependence of the average interatomic distance at T = 300 K, separated by the type of bond (◆ d_{FeFe}, ▲ d_{FeNi} and ■ d_{NiNi}). The equilibrium positions for the pair-wise interactions are 2.561 Å, 2.519 Å and 2.482 Å respectively. 230

Figure 103 Difference between the average interatomic distances illustrated in fig. 102 and the average interatomic distance (◆ d_{FeFe}, ▲ d_{FeNi} and ■ d_{NiNi}). 230

Figure 104 Simulated linear thermal expansion in $Fe_{65}Ni_{35}$ in the presence (a, ◆) and in the absence (a, ▲) of magneto-volume coupling. In (b), the difference is shown (◆), as well as the experimentally observed difference (dashed line) [after data from Hayase73]. ... 234

Figure 105 Simulated atomic volume in $Fe_{65}Ni_{35}$ in the presence (a, ◆) and in the absence (a, ▲) of magneto-volume coupling. In (b), the difference between the two volumes (◆) is shown to disappear at T_C, as is observed experimentally (dashed line) [data from Hayase73]. 235

Figure 106 Simulated specific heat per atom in $Fe_{65}Ni_{35}$ in the presence (a, ◆) and in the absence (b, ▲) of magneto-volume coupling. In (b), the difference is shown (◆), as well as the experimentally determined difference (dashed line) [data from Wassermann90]. 236

Figure 107 Simulated bulk modulus in $Fe_{65}Ni_{35}$ in the presence (a, ◆) and in the absence (a, ▲) of magneto-volume coupling. In (b), the difference is shown (◆), as well as the experimentally determined difference (dashed line) [data from Wassermann90]. 237

Figure 108 Simulated average magnetization in $Fe_{65}Ni_{35}$ in the presence of magneto-volume coupling. The experimental data for $Fe_{65.8}Ni_{34.2}$ are shown as a dotted line [Crangle63]. T_C is found to be ~700 K. The slight increase at very low temperature is due to the mixed interactions (some positive and some negative exchange constants) and the use of the Ising model. It does not occur in the measured data. 238

Figure 109 Simulated average interatomic distances in $Fe_{65}Ni_{35}$ grouped by the type of bond (◆ Fe-Fe, ● Fe-Ni and ▲ Ni-Ni, the solid line is the average bond length). In addition, the Fe-Fe bonds are distinguished based on the average spin pair orientations (half-filled symbols, solid on the right for parallel bonds, solid on the left for anti-parallel bonds). 239

Figure 110 Average energy per atom (potential + magnetic) at T = 300 K in the presence (a, ◆) and in the absence (a, ▲) of magnetism and magneto-volume coupling. Average moment per atom at T = 300 K (b, ◆) with the Slater-Pauling relation (dashed line) and the T = 4.2 K measured magnetic moments (b, dotted line [Crangle63, Brando64]). 243

Figure 111 Simulated atomic volume at T = 300 K in the presence (a, ◆) and in the absence (a, ▲) of magneto-volume coupling. The relative difference between the two is plotted in (b), as well as the experimental deviation from the linear composition dependence of the volume which occurs below 20 at. % Fe (dashed line, data from [Bradley37]) and the T = 0 K volume enhancement relative to the volume extrapolated from high temperatures (dotted line, data from [Wassermann90]). 244

Figure 112 Simulated linear thermal expansion coefficient at T = 300 K in the presence (◆) and in the absence (▲) of magneto-volume coupling. The dashed line represents experimental results at RT (295 K) [Wassermann90]. 245

Figure 113 Simulated bulk modulus at T = 300 K in the presence (◆) and in the absence (▲) of magneto-volume coupling. The dashed line represents the experimental results at RT [Tanji83]. 246

Appendix A

Figure 114 Effect of the δ-Δ correlation on the Mössbauer spectrum. All spectra use a single Gaussian distribution for the quadrupole splitting ($<\Delta>$ = 3 mm/s, σ_Δ = 0.8 mm/s) and the centre shift ($<\delta>$ = 0 mm/s, σ_δ = 0.2 mm/s). 262

Figure 115 xVBF probability density contour plots corresponding to the spectra in fig. . (a) $\rho_{\delta\Delta}$ = 0, (b) $\rho_{\delta\Delta}$ = 0.5 and (c) $\rho_{\delta\Delta}$=0.9 (instead of 1). In the case where $\rho_{\delta\Delta}$=1, the contour plot would simply yield a straight line. 263

Figure 116 Effect of the various correlations on magnetically split Mössbauer spectra, compared to the spectra in the absence of correlations (ρ = 0). All spectra were generated using PIPDs with only a single Gaussian component for the Zeeman splitting ($<\delta>$ =0 mm/s and σ_δ=0.05 mm/s), the quadrupole shift ($<\varepsilon>$ =0 mm/s and σ_ε=0.05 mm/s) and the centre shift ($<\delta>$ =0 mm/s and σ_δ=0.05 mm/s) with the following correlation parameters: (a) $\rho_{\delta\varepsilon}$=0 and 1, (b) $\rho_{\delta z}$=0 and 1 and (c) $\rho_{\varepsilon z}$=0 and 1. The difference spectra between the spectra with uncorrelated and correlated distributions are also plotted on

the same scale. 264

Figure 117 Thickness corrected Mössbauer spectrum of $Fe_{65}Ni_{35}$ at 77 K. The residuals spectra correspond to the best fits of the xVBF and VBF models, as explained in the text. Notice how the VBF model, which uses linear coupling, cannot correctly model all the peaks' widths, whereas the xVBF model does so correctly. 265

Figure 118 Partially integrated probability density (PIPD) of the Zeeman splitting z of the spectrum in fig. , as obtained by the xVBF (solid line) and VBF (dashed line) models. 266

Figure 119 Partially integrated probability density (PIPD) of the quadrupole shift ε of the spectrum in fig. , as obtained by the xVBF (solid line) and VBF (dashed line) models. Notice the artificial "tail" in the distribution obtained by the VBF model, which is due to the coupling with the Zeeman splitting distribution. 266

Figure 120 Contour plot of the total probability density distribution (PDD) of Zeeman splitting and quadrupole shift, obtained by the xVBF method. 267

Appendix C

Figure 121 Schematic drawing of the MS geometrical specifications. 275

Figure 122 Illustration of the time dependence of the acceleration, velocity and source position in a "constant acceleration" mode. 279

Figure 123 Effect of source motion on the background in a folded spectrum. The solid and dashed lines represent cases where $z_{max}/(D+l) = 1/20$ and $z_{max}/(D+l) = 1/10$, respectively, for a constant acceleration waveform with a frequency of 1 Hz, and a range of ± 10 mm/s. 281

Figure 124 Effect of cosine smearing at different peak positions. All peaks are calculated with $R_a/D = 1/2$. 283

Figure 125 Effect of R_a/D on the position of the maximum (—) and on the FWHM (···) of a peak located at $v_0 = 5$ mm/s. 283

Figure 126 Effect of R_a/D on a peak located at $v_0 = 5$ mm/s. ratios are (—) 1/100, (– –) 1/10, (– ·–) 1/4, (···) 1/2. 284

List of Tables

Chapter 2

Table 1 Nuclear transitions in ^{57}Fe, the energy of the emitted γ-rays and their relative intensity 9

Table 2 Calibration of the sample temperature based on the thermocouple readings 32

Chapter 3

Table 3 Parameters of the xVBF fit of the RT spectrum of the SC meteorite (fig. 12). Antitaenite is analysed as having a broad tail in its HFD. 45

Table 4 Parameters of the xVBF fits to the spectra of the SC meteorite shown in fig. 4. 2-σ (95 %) fitting uncertainties are given in the second column of each parameter. Unless specified, the correlations parameters were 0. 48

Table 5 Extracted Debye temperature and isomer shift for the various phases of the SC meteorite, based on the analyses in table 4. 2-σ (95 %) uncertainties are given in the second column of the parameters. 49

Table 6 Extracted Debye temperature and isomer shift for tetrataenite and antitaenite based on the data from De Grave [DeGrave92] shown in fig. 16. 2-σ (95 %) uncertainties are given in the second column of the parameters. 50

Table 7 Fitted phase fractions (Fe content) of the various phases of the SC meteorite based on ^{57}Fe MS. The spectra were corrected for thickness effects using the method of Rancourt [Rancourt89]. 57

Table 8 Parameters of the xVBF fits of the low temperature MS spectra of the SC meteorite. 2-σ (95 %) fitting uncertainties are given in the second column for each parameter. 63

Chapter 4

Table 9 Parameters of the xVBF fit of the RT Mössbauer spectra of a series of splat quenched alloys (SQ #1). 2-σ (95 %) fitting uncertainties are given in the second column of the parameter. Parameters with an uncertainty of 0 were not refined during the fit. 82

Table 10 Compiled parameters of the fits of SQ #1. 83

Table 11 Parameters of the xVBF fit of a second series of SQ alloys (SQ #2). 84

Table 12 Compiled parameters of the fits of SQ #2. 86

Table 13 Parameters of the xVBF fit of a third SQ series (SQ #3) and a series of three roller quenched alloys (RQ #1 – 50, 55 and 60 at. % Fe). 87

Table 14 Compiled parameters for the fits of SQ #3 and RQ #1. 88

Table 15 Parameters of the VBF fits to the RT Mössbauer spectra of alloys from the SQ #1, #2, #3 and RQ #1 series. 2-σ (95 %) fitting uncertainties are given in the second column of the parameter. Parameters with an uncertainty of 0 were kept fixed during the fit. . . . 89

Table 16 Compiled parameters of the VBF fits of SQ #1, #2, #3 and RQ #1 series. 91

Table 17 Parameters of the xVBF fits of the LN_2T Mössbauer spectra of the alloys of the SQ #1 series. 2-σ (95 %) fitting uncertainties are given in the second column of each parameter. Parameters with 0 uncertainty were kept fixed during the fit. 92

Chapter 5

Table 18 Atomic positions (in units of $a = 6.66$) of the Fe and Ni atoms in the $Fe_{11}Ni_5$ supercell. The NNs are also given, as well as the total number of Fe NNs. 124

Table 19 Calculated properties of the Fe and Ni atoms in an $Fe_{11}Ni_5$ supercell with $a = 6.66$ 124

Table 20 Core and valence hyperfine fields on local sites in $Fe_{11}Ni_5$. The model of Dang and Rancourt is used to calculate the HF contributions based on the local and NN moments, according to where the A and B best fit parameters are listed at the bottom. 125

Table 21 Calculated equilibrium properties of $Fe_{65}Ni_{35}$ in various phases 134

Table 22 Effective Heisenberg magnetic exchange interactions with the first 3 NN shells, for the various magnetic structures considered (the total exchange interaction should be maximum when the structure is stable) 150

Chapter 6

Table 23 Parameters of the magnetic phase of the xVBF fits of RT Mössbauer spectra of Fe-rich RQ Fe-Ni alloys. 2-σ (95 %) fitting uncertainties are given in the second column for each parameter. For alloys with $c > 73$ at. %, the parameters of the BCC phase are given. 175

Table 24 Parameters of the VBF fits to the RT Mössbauer spectra of Fe-rich RQ Fe-Ni alloys. 2-

σ (95 %) fitting uncertainties are given in the second column of each parameter. 178
Table 25 Parameters of the DLS fit of the RT spectra of Fe-rich RQ Fe-Ni alloys with close to RT. 180
Table 26 Parameters of the xVBF fit of the paramagnetic FCC phase of the RT spectra of Fe-rich RQ Fe-Ni alloys. 180
Table 27 Compiled results (FCC phase) of the xVBF fits of the RT spectra of Fe-rich RQ Fe-Ni alloys. 181
Table 28 Compiled results of the VBF fits of the RT spectra of Fe-rich RQ Fe-Ni alloys. 182
Table 29 Evolution of the fit quality with the complexity of the xVBF and VBF models. 261
Table 30 Comparison of the fitted parameters from the best fits using the xVBF and VBF models. 261

List of Abbreviations

AF	antiferromagnetic
ASA	atomic sphere approximation
BCC	body-centred cubic
CPA	coherent potential approximation
CSD	centre shift distribution
DFT	density functional theory
DLM	disordered local moment
EFG	electric field gradient
ESC	electronic structure calculation
FCC	face-centred cubic
FM	ferromagnetic
FWHM	full-width at half-maximum
HF	hyperfine field
HFD	hyperfine field distribution
HM	high-moment
HWHM	half-width at half-maximum
KKR	Korringa-Kohn-Rostoker
L(S)DA	local (spin) density approximation
LHeT	liquid helium temperature (= 4.2 K)
LM	low-moment
LMTO	linear muffin-tin orbitals
LN2T	liquid nitrogen temperature (= 77 K)
MC	Monte Carlo
MS	Mössbauer spectroscopy
NM	non-magnetic
NN	nearest neighbour
QSD	quadrupole splitting (or shift) distribution
RQ	roller quenched
RT	room temperature (= 295 K)

SQ	splat quenched
VBF	Voigt-based fitting
WSR	Wigner-Seitz radius
XRD	X-ray diffraction
xVBF	Extended Voigt-based fitting

List of Symbols

CS, δ	centre shift
IS	isomer shift
SOD	second-order Doppler shift
ε	quadrupole shift
z	Zeeman splitting
Q	excited state nuclear electric quadrupole moment
eq, V_{zz}	principal axis component of the EFG
η	EFG asymmetry parameter
I , I_z	nuclear angular momentum and magnetic component
$g_{1/2}$, $g_{3/2}$	ground state (I = 1/2) and excited state (I = 3/2) nuclear g-factors
B_m	bulk modulus
α_T	linear thermal expansion coefficient
J_{ij}	magnetic exchange parameter between atoms i and j
V	atomic volume
H	hyperfine field
H_c, H_v	core and valence contributions to H
$\rho(0)$	electronic charge density at the nucleus
$\rho_c(0)$, $\rho_v(0)$	core and valence contribution to $\rho(0)$
n_v	number of valence electrons
T	temperature
e^-	electrons
a_0	Bohr radius
μ_i	magnetic moment of atom i
μ_B	Bohr magneton
μ_N	nuclear magneton
γ (Γ)	HWHM (FWHM) of a Lorentzian function
c or x	concentration (usually of Fe)

1. Introduction

1.1 Anomalous Properties of FCC Fe-Ni Alloys

Ever since the discovery of the Invar effect in the $Fe_{65}Ni_{35}$ alloy by Guillaume in 1897 [Guillaume97], the experimental quest for characterising and the theoretical quest for understanding anomalies in Fe-Ni alloys has been a significant research topic in many fields related to materials science. In 1920, Guillaume was awarded the Nobel Prize in Physics for his discovery of the Invar effect. Guillaume's work has since inspired many physicists, material scientists and metallurgists to understand and exploit this discovery. Though much work has been done to explain the effect, most of the early outcome of the discovery has been purely experimental, as many other similar effects and anomalous properties of Fe-Ni alloys were being examined.

The Invar effect, as characterized by Guillaume, occurs in FCC Fe-Ni alloys with a composition of ~65 at. % Fe and is characterized by an unusually low linear thermal expansion coefficient of $\alpha_T \leq 2 \times 10^{-6}\ K^{-1}$ over a broad range of temperatures around RT, as opposed to 13.4 $\times 10^{-6}\ K^{-1}$ for Ni and 11.8 $\times 10^{-6}\ K^{-1}$ for Fe, for example. In addition to the Invar effect, systematic investigations of Fe-Ni alloys have resulted in the discovery of other similarly anomalous effects: Elinvar is a material that has a very low thermoelastic coefficient (i.e., Young's modulus is temperature independent) and permalloys (e.g., Permalloy 45: $Fe_{54.7}Ni_{45}Mn_{0.3}$) are materials that have a high magnetic permeability. When alloyed with other elements (Mn, Al, Cu, *etc.*) a great number of different alloys with unique and technologically appealing properties can be manufactured. As in the case of steels, several derivatives have been developed for technological purposes, such as stainless Invar, and are now of wide-spread use. Apart from increasing at least ten-fold the precision of mechanical watches (which was one of Guillaume's motivations, being the son of watchmakers [Guillaume20]), Invar has found its place

in many common-place and high-tech technologies such as in thermostats, shadow-masks in televisions and computer screens, high-precision optical measuring devices and glass-to-metal seals used in electronics packaging, to name a few [Wittenauer96]

Since the discovery of Invar alloys, apart from metallurgists and materials scientists who were busy developing new exotic Fe-Ni based alloys through trial and error, many researchers have also been looking for the physical explanation, at the microscopic level, for the anomalies found in Fe-Ni alloys. The search for what was known as the Invar effect had begun and would occupy the minds of many scientists throughout the 20th century. Now, a century after the discovery, the Invar effect still receives much attention and, throughout the last decades, a number of good reviews have been written of the experimental and theoretical progresses to understand the anomalies [Sato78, Wassermann87, 90, Rancourt89, Russel90, Shiga93, Witteauer96]. The first important observation about the Invar property is that it was directly related to the magnetism of the alloy: the anomalous thermal expansion disappeared as the material was heated above its Curie point [Guillaume20]. Apart from this assertion, it is still not possible to get a consensus among researchers on what constitutes the cause of the Invar effect.

In addition to exhibiting the Invar effect at concentrations around 65 at. % Fe, Fe-Ni alloys also exhibit magnetic anomalies as the Fe-content exceeds ~50 at. %, such as deviation from the Slater-Pauling curve [see chapter 4], a structural instability with respect to a martensitic transition to the BCC phase [see for example Wassermann90] above ~70 at. % Fe and deviation from Vegard's law [see chapter 4] around ~60 at. % Fe. Though none of these anomalies were directly related to the Invar effect, it seemed clear that most of the unusual properties in Fe-Ni alloys were related to the properties of Fe in an FCC phase. Most of the theories to describe the Invar effect are related to effects due to the occurrence of Fe in an FCC lattice. Several theories have come and gone through time, as they failed to be compatible with the mass of experimental data which was accumulated over time: Theories involving the importance of magnetic or chemical inhomogeneities, "pre-martensitic effects" or the role of the martensitic transition have been put aside.

To complicate things even further, an additional effect, the anti-Invar effect, was observed in Fe-rich FCC Fe-Ni alloys above ~65 at. % [Acet94a, 94b, 97a, 97b]. Contrary to the Invar effect, the anti-Invar effect is an anomalously high thermal expansion ($\alpha_T \approx 20 - 30 \times 10^{-6}$ K^{-1}) which occurs in the paramagnetic phase at high temperature. Its name comes from the fact

that the anti-Invar effect is opposite to the Invar effect, even though there was no evidence that the two are directly related by the same microscopic processes. It has nonetheless become yet another important property of the FCC Fe-Ni alloys which must be understood before we can claim to fully comprehend FCC Fe-Ni alloys.

Since the discovery of the Invar effect in Fe-Ni alloys, the term "Invar effect" has now often become synonymous with "low thermal expansion", which is now observed in a wide range of materials. In some cases, such as Fe-Pt or Fe-Pd alloys, the similarities with Fe-Ni alloys are striking and we can expect that the same microscopic processes are at play in all these alloys. However, in other classes of materials such as laves and intermetallics [Wassermann90], it is not as clear cut whether or not the low thermal expansion is due to the same processes. Throughout this thesis, when we refer to the Invar effect, we are referring specifically to the effect in ferromagnetic FCC Fe-Ni alloys. Extensions of our ideas to similar effects in other alloys will be discussed when appropriate.

1.2 Models of the Invar Effect in Fe-Ni Alloys

In order to explain the deviation from the Slater-Pauling curve in Fe-Ni alloys, Carr Jr. *et al.* [Carr52, 79, Colling70] and Kondorskii *et al.* [Kondorskii59, 60a, 60b] developed the theory of latent antiferromagnetism (LAF) which was a local-moment model based on having an antiferromagnetic Fe-Fe magnetic exchange coupling ($J_{\mathrm{FeFe}} < 0$), as opposed to the ferromagnetic exchange couplings of Fe-Ni ($J_{\mathrm{FeNi}} > 0$) and Ni-Ni bonds ($J_{\mathrm{NiNi}} > 0$). This model was used to explain why deviation from the Slater-Pauling curve occurs as Fe content was increased, since antiparallel Fe spins would occur because of the antiferromagnetic Fe-Fe interactions in an otherwise ferromagnetic Fe-Ni matrix. In order to explain the Invar effect, a large dependence of the Fe-Fe exchange parameter with interatomic distance ($J'_{\mathrm{FeFe}} = \partial J_{\mathrm{FeFe}} / \partial r$) was assumed [Menshikov77, 79], thereby providing a link between the magnetism of the alloy and its structural properties and possibly explaining the Invar effect. Unfortunately, there was no justification for the large J'_{FeFe} required, so many researchers put aside this model in favour of other options. Recently however, Rancourt and Dang [Rancourt96a] re-examined local moment models and showed that such a local moment model can reproduce all the $T = 0$ K properties if there is a large and positive J'_{FeFe}. In particular, they recognized the importance of magnetic

frustration of Fe-Fe bonds and their role in reproducing the volume increase seen in Invar alloys relative to the volume extrapolated from high temperatures where the effect has disappeared.

Another dominant model related to the occurrence of Fe in an FCC phase was put forth by Weiss [Weiss63] and further refined by Chikazumi *et al.* [Chikazumi68, 79, 80] and Matsui *et al.* [Matsui78, 79, 80]. Known as the 2-γ-state model, it assumes that Fe atoms in an FCC lattice (the γ phase, as opposed to the α or BCC phase) can be in either of two ionic states which are associated with different magnetic moments and different atomic volumes (the LM state has a smaller volume than the HM state). At the Invar composition, it is assumed that the energy difference between the two states is only ~300 K (~25 meV) and that the HM state would be the ground state. As temperature is increased (around RT), thermal excitation would occur such that the LM state would be populated, thereby reducing the average volume in such a way that it counters normal thermal expansion. This model provides a nice explanation for the Invar effect, but the link between the effect and the magnetism of the alloy is less clear, in particular, why the effect disappears around T_C.

This model has been further developed with the advent, in the mid-70's, of ESCs of γ-Fe. Early calculations of γ-Fe which included constrained collinear magnetism showed that γ-Fe could occur as a HM or NM phase. Similar calculations for Fe$_3$Ni also showed an instability in the moment: as the volume was reduced the HM phase was destabilized in favour of a NM or LM phase. The prediction of two distinct phases at $T = 0$ K calculations was taken as providing the theoretical grounds for accepting the Weiss 2-γ-state model as valid [Williams82, 83, Moruzzi86, 88, 89a, 89b, 90, 92, 93, Mohn89, 91, Entel93, Hoffmann95, Wassermann87, 90, 91], even though these calculations are for extended phases (where all atoms are in HM or LM states) while the Weiss model deals with "independent" atomic states. For example, even the stability of a single LM atom in a HM phase has not been ascertained by ESCs.

More recent and elaborate calculations show that if the constraint of collinear magnetism is lifted, or if more complicated magnetic structures are allowed in the calculation, then the two minimum structure of the γ-Fe energy curve disappears and instead there is only a single true minimum [Schröter95, James99]. In light of the disappearance of the two minimum structure, the 2-γ-state picture is invalidated. Proponents of the 2-γ-state model now appeal to fluctuations between bonding and anti-bonding states, even though no physical information regarding the types of fluctuations is given [Acet2000]. Even in this more modern version of the 2-γ-state

model, an *ad nihilo* link with the magnetism is required to explain why the Invar effect disappears at T_C. It is important to note the difference between this view and the local moment model of Rancourt and Dang [Rancourt96] is that in the 2-γ-state model, the Invar effect is seen as a contraction relative to the normal behaviour of the $T = 0$ K HM alloy, whereas the model of Rancourt and Dang views the effect as an expansion, at low temperature relative to the normal HM behaviour which occurs above T_C. These views are thus fundamentally different in how they describe the final high-temperature phase.

Another important model that was developed in the 70's is the theory of weak itinerant ferromagnetism (WIF) of Wohlfarth [Wohlfarth75, 79, 80]. In this model, Invar is assumed to be a weak itinerant ferromagnet according to the classification of Stoner and Wohlfarth, in which the moment disappears at T_C through Stoner-type excitations. Because of the difference in the kinetic energy of electrons in the various states, this could result in an Invar-like behaviour which disappears at T_C. This theory predicts that the magnetic moment should disappear above T_C, which is incompatible with many measurements which indicate that the moment magnitudes remain large at high temperatures [e.g., Tajima87, Acet00].

The most recent attempt at explaining the Invar effect came in the form of sophisticated ESCs which allowed for non-collinear magnetic moments in a 32-atom supercell of the Invar composition [vanSchlifgaarde99]. As in the case of γ-Fe, the calculation showed that the 2-state (HM and LM) picture is invalid and instead a single minimum exists, with a continuing variation from a HM phase at large volumes to a LM phase at lower volumes. In addition, as the volume was decreased, some Fe moments started to align opposite to the bulk magnetization and if the volume was further reduced, the Fe moments would have nearly random orientations, while the Ni moments would remain fairly ferromagnetically ordered. The properties of the energy *vs.* volume curve were such that one can calculate a very low thermal expansion coefficient at $T = 0$ K. Unfortunately, as precise as this calculation is, it remains a calculation valid only at $T = 0$ K and not an explanation of the processes that cause the Invar effect at and around RT. Extrapolation to finite temperatures is still done by hand-waving arguments, without the solid foundations required by an acceptable theory. Several other statements by the authors are also unfounded, such as non-collinearity being the source of the Invar effect, contrary to what is observed in Fe_3Pt [Wassermann90] or in films of $Fe_{65}Ni_{35}$ [Lagarec00, Dumpich87, 88, 92, Wassermann92] where no deviation from the Slater-Pauling curve is seen.

Throughout this thesis, we will investigate, on new and existing theoretical and experimental grounds the implications regarding these models and show how a global understanding of the intrinsic properties of FCC Fe-Ni alloys leads to a clear and simple explanation of the Invar and anti-Invar effects. As we shall see, it is using a combination of tools that a clear picture of Fe-Ni alloys can emerge.

1.3 Choice of Experimental and Theoretical Tools

Mössbauer spectroscopy (MS) has often been used in the study of Fe-Ni alloys because of its sensitivity to changes in the magnetic or electronic environments of the probe atoms. For example, MS has been used to study order-disorder transitions in Fe-Ni alloys [Larsen82], the effect of substitution of Fe and Ni atoms in chemically ordered $FeNi_3$ [Cranshaw87] and the distribution of local hyperfine fields in Invar [Window73, 74, Rancourt91]. It has also been used to prove the existence of chemically ordered FeNi in synthetic samples [Gros64, 68, 70a, 70b] as well as meteorites [Petersen77, Albertsen78a, 78b], the low-temperature antiferromagnetic state of γ-Fe [Gonser63, Keune77] and many other peculiarities of the Fe-Ni system. In this work, we have found the *IS*, one of the parameters obtained from the analysis of Mössbauer spectra, to be an invaluable tool to differentiate between HM and LM alloys and thus explore an entire field of Fe-Ni alloys which had previously been unattainable by other experimental methods. In addition to MS, we have also used theoretical methods such as ESCs and MC simulations. The possibility of rapidly calculating the electronic structure of materials has proven invaluable and such $T = 0$ K calculations are now part of the modern tools used to further our understanding of materials. As previously stated, ESCs have already played an important role in the Invar problem. MC simulations, on the other hand, remain one of the most powerful ways of exploring finite temperature properties of systems and have also been extensively used to study Fe-Ni alloys [e.g., Dang96a].

1.4 Organization of the Thesis

With all these theories and a century of experimental data, how can we improve and refine the understanding of FCC Fe-Ni alloys? We have decided to combine many different and

complimentary techniques for studying the properties of these alloys: Experimental characterization of temperature dependent properties using MS combined with state-of-the-art spectral analysis techniques, a systematic study of Fe-Ni alloy properties using ESCs, Monte Carlo simulation of magnetic and structural properties as a function of temperature. Also, we have analysed both synthetic Fe-Ni samples produced by rapid quenching techniques (cooling rates of ~10^5-10^6 K/s) as well as meteoritic material which cooled at rates of ~10 K per million years.

This thesis has been organized as a logical progression leading to a comprehensive understanding of the properties and microscopic processes involved in FCC Fe-Ni alloys. After this introduction, we present the basis of the experimental work using MS, covering the necessary theoretical background as well as the details of the experiments. The next chapter deals with the study of the Santa Catharina meteorite, which is nearly a pure Fe-Ni meteorite with a bulk composition which is the same as that of the Invar alloy. With time, it has decomposed from a chemically uniform alloy to a two phase alloy of tetrataenite and antitaenite. The study deals mainly with characterizing the antitaenite phase as it is a very Fe-rich LM phase that cannot be duplicated in synthetic alloys. Chapter 4 proposes a review of Fe-Ni alloys in the Ni-rich range where their magnetic and structural properties can be understood based on simple models related to binary alloys. Chapter 5 is a detailed ESC study of chemically ordered and disordered Fe-Ni alloys in collinear magnetic order or complete magnetic disorder. We have pushed the limits of the ESCs to link the calculated electronic structure to physically measurable quantities such as the *IS* and the HF. A detailed analysis of the differences between the HM and NM phases in these alloys is put to the test in chapter 6 where MS is used to study Fe-rich alloys to show for the first time that a HM/LM transition occurs in FCC Fe-Ni alloys as Fe content is increased above ~70 at. %. Temperature dependent measurements show how one can further identify anti-Invar behaviour based on the *IS* and conclusively show that the anti-Invar and Invar effects are two phenomena which have physically different origins. Finally, in chapter 7, MC simulations of Fe-Ni alloys based on a simple local moment model with a distance dependent Fe-Fe magnetic exchange coupling illustrate how the Invar effect occurs throughout the HM Fe-Ni alloys, culminating at 65 at. % and leading to the known properties.

The combination and cooperation between these various experimental and theoretical techniques allows us to develop a complete picture and understanding of the behaviour of FCC

Fe-Ni alloys and the microscopic processes that lead to it and, in particular, give a clear answer to what causes the Invar and anti-Invar effects.

2. Experimental Methods: Mössbauer Spectroscopy

2.1 Introduction to Mössbauer Spectroscopy

Mössbauer spectroscopy is the main experimental tool used in this research. It is a nuclear fluorescence technique which can be used to detect changes in the electronic environment around the nucleus by measuring their effect on a specific nuclear transition. Thanks to the Mössbauer effect, it is possible to have recoilless emission and recoilless absorption of a nuclear gamma-ray. By Doppler-shifting the energy of the source, we can scan a small range of energies around the source transition energy and resolve nuclear energy shifts caused by hyperfine interactions with the electrons or magnetic fields in the sample.

Since the absorption energy must be the same as the emission energy (plus or minus a

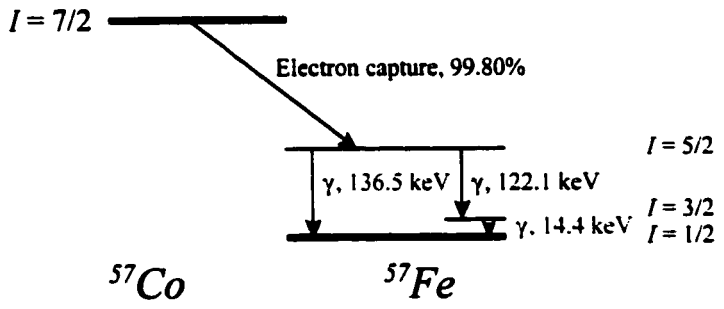

Figure 1 Diagram of the decay of ^{57}Co into ^{57}Fe. The 14.4 keV transition used in ^{57}Fe MS.

Table 1 Nuclear transitions in ^{57}Fe, the energy of the emitted γ-rays and their relative intensity

3/2 → 1/2	14.413	9.16(15)
5/2 → 3/2	122.061	85.60(17)
5/2 → 1/2	136.473	10.68(8)

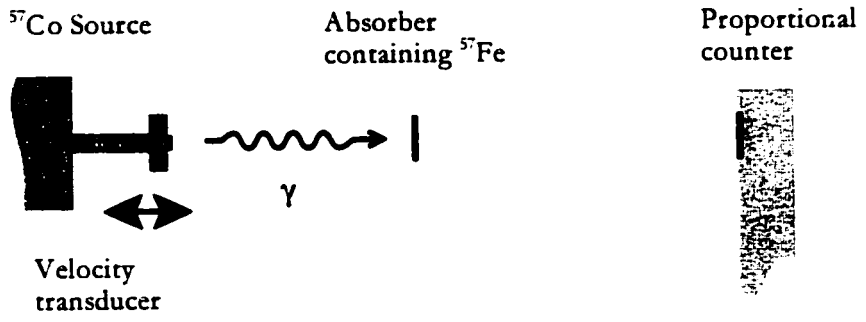

Figure 2 Conventional transmission MS setup.

small Doppler shift), only one isotope of one element can be probed using a specific source. The most commonly studied isotope is ^{57}Fe. As a source, we use a material in which ^{57}Co atoms are embedded in a rigid lattice (in our case Rh). ^{57}Co decays to ^{57}Fe with a half-life of 271.8 days [Lide93]. The resulting ^{57}Fe nucleus appears in an excited state (I = 5/2 with 99.80% probability), from which it can decay to the I = 3/2 state which then decays to the I = 1/2 ground state by emitting a gamma-ray of 14.4129 keV. The transition diagram of the complete transitions to the ground state is shown in fig. 1. The $I = 3/2 \rightarrow 1/2$ transition is Mössbauer active, which means absorption or emission of a γ-ray with the right energy can occur without recoil of the nucleus. It is this transition that is used in ^{57}Fe Mössbauer spectroscopy.

2.1.1 Transmission Mössbauer Spectroscopy

There are different methods for performing absorption or emission MS. In the course of this research, we have used the transmission and conversion electron methods. In a transmission geometry (fig. 2), the sample is placed between the oscillating source and a γ-ray detector (in our case a 1 atm. Kr-4% CO_2 sealed proportional counter). γ-rays from the source are absorbed by the sample's ^{57}Fe nuclei which are in their ground state (I = 1/2) and which can then decay, emitting a γ-ray in any direction. With a small sample/detector solid angle, we obtain a transmission spectrum, where absorption peaks occur at the energies where the γ-rays are resonantly absorbed by the sample (very few reemitted γ-rays are detected because of the small solid angle of the detector). Non-resonant electronic absorption also occurs but it has no energy dependence in the energy range we measure, so it does not interfere with the resonant absorption signal because it simply uniformly attenuates the signal.

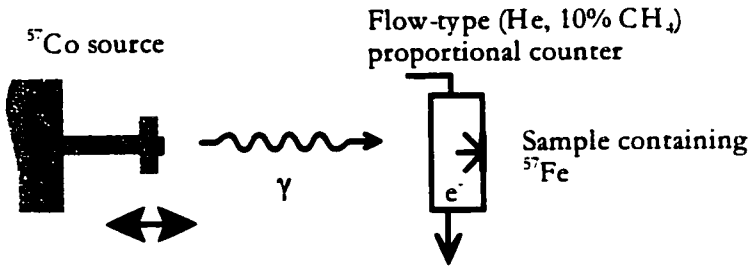

Figure 3 Surface sensitive CEMS setup.

2.1.2 Conversion Electron Mössbauer Spectroscopy

Contrarily to conventional transmission MS, conversion electron Mössbauer spectroscopy (CEMS) is an emission spectroscopy, which means we are detecting a signal produced by the sample after the absorption of the source γ-ray. There are at least two ways in which the ^{57}Fe nucleus can decay back to its ground state after having absorbed a γ-ray:

① It can simply emit a γ-ray with the same energy (14.4 keV). This process is used in conventional emission MS where the emitted γ-rays are detected. Nine percent of all excited ^{57}Fe nuclei decay through this process;

② It can transfer its energy to the electrons in the Fe atom. If the energy is transferred to a core 1*s* electron (the most common conversion process), the electron will be ejected from the atom and possibly from the sample. This electron can also produce secondary electrons with lower energy through collisions in the sample. Detection of the resulting emitted electrons is the basis of CEMS (fig. 3). Since the atom has been ionized, it will also revert to its ground state through x-ray fluorescence. In particular, a 5.6 keV K_α x-ray will also be emitted when the ^{57}Fe nucleus decays. Detection of such secondary x-rays is the basis of conversion x-ray Mössbauer spectroscopy.

Because the escape depth of low-energy electrons (≤10 keV) is small in most materials, only electrons emitted close to the surface (within ~100 nm) can be detected. For this reason, CEMS is a surface-sensitive method. For example, we used CEMS to determine if our meteoritic sample preparation techniques produced a surface that was the same as the bulk.

2.2 Hyperfine Interactions and Their Effect on the Mössbauer Spectrum

2.2.1 Electric Monopole Interaction and Second-Order Doppler Shift

2.2.1.1 The Isomer Shift

The isomer shift is due to the electric monopole interaction which results from the finite volume of the nucleus and the different nuclear volumes of the excited and ground states of the Mössbauer transition. The treatment of the finite size of the volume can be carried out using a perturbation approach, as is elaborated by Shirley [Shirley64] and reproduced here. We first assume that the nuclear charge Ze is uniformly distributed in a sphere of radius R. In such a case, the electric potential inside the nucleus is

$$V(r < R) = \frac{Ze^2}{R}\left[-\frac{3}{2} + \frac{1}{2}\left(\frac{r}{R}\right)^2\right], \tag{1}$$

and we recover the normal Coulomb potential outside the nucleus:

$$V(r > R) = -\frac{Ze^2}{r}. \tag{2}$$

The energy shift caused by this potential, as opposed to using only the Coulomb potential is given, to first-order perturbation, as the average of the difference between the two potentials weighted by the electron density.

In the non-relativistic treatment, only the s electrons contribute significantly to the density inside the nucleus and it is nearly constant ($|\psi(r < R)|^2 \approx |\psi_s(0)|^2$), we obtain a shift

$$\Delta E = \frac{2}{5}\pi Ze^2R^2 |\psi_s(0)|^2. \tag{3}$$

The difference in the shift between the excited nuclear state and the ground state is thus

$$\delta\Delta E = \frac{4\pi Ze^2R^2}{5}\frac{\delta R}{R}|\psi_s(0)|^2, \tag{4}$$

where $\delta R = R_{excited} - R_{ground}$. The Doppler shift, which must be applied to the source's radiation in order to get resonant absorption (or emission) in a Mössbauer experiment, is

$\Delta v = c(\delta\Delta E_{absorber} - \delta\Delta E_{source})/E_\gamma$, or

$$\Delta\nu = \frac{4\pi Z e^2 R^2 c}{5E_\gamma}\left[\frac{\delta R}{R}\right](|\psi_{absorber}(0)|^2 - |\psi_{source}(0)|^2). \quad (5)$$

The first two terms of the right-hand-side form a constant which depends only on the isotope and the nuclear transition used in the experiment, through Z, R, E_γ and $\delta R/R$. By comparing calculated non-relativistic densities and experimentally observed shifts, these terms, which are commonly grouped and denoted as α, give -0.24 a_0^3 mm/s [Akai86] for the 14.4 keV transition in ^{57}Fe. The last term, the difference between the densities at the nucleus in the source and in the absorber, constitute all the chemical information contained in the isomer shift.

When a full relativistic treatment is used, one can show that there is a simple correction factor compared to the isomer shift obtained in the non-relativistic case. Since the electronic structure calculations performed in this work were performed using the scalar relativistic approximation, it is useful to show how the correction factor arises. We once again follow the derivation by Shirley [Shirley64].

In the relativistic case, when a point nucleus is used, the electron density at the nucleus is found to diverge as $r \to 0$. Close to $r = 0$, the density can be expressed as the product of the non-relativistic density at the nucleus $|\psi(0)|^2$ with a divergent factor:

$$\rho(r) = |\psi(0)|^2 \frac{2(1+\lambda)}{\Gamma^2(2\lambda+1)}\left(\frac{2Zr}{a_0}\right)^{2\lambda-2}, \quad (6)$$

where $\lambda = \sqrt{1-\alpha^2 Z^2}$ (with α being the fine structure constant) and a_0 is the Bohr radius, or 1 atomic unit of length. Relativistic effects increase as Z increases and λ deviates from 1. In the perturbation approximation, as in the previous section, we must integrate the perturbing potential weighted by this density over the nuclear volume to obtain the atomic energy shift:

$$\Delta E = |\psi(0)|^2 \frac{6\pi R_\infty a_0^3 (1+\lambda)}{Z\lambda(2\lambda+1)(2\lambda+3)\Gamma^2(2\lambda+1)}\left(\frac{2ZR}{a_0}\right)^{2\lambda}. \quad (7)$$

R_∞ is the Rydberg constant. Differentiation with respect to R and conversion to a Doppler shift result in the final expression for the fully relativistic isomer shift:

$$\Delta\nu = \frac{4\pi Z e^2 R^2 c}{5E_\gamma}\left[\frac{\delta R}{R}\right] S(Z)\,(|\psi_{absorber}(0)|^2 - |\psi_{source}(0)|^2), \quad (8)$$

where

$$S(Z) = \frac{30(1+\lambda)}{(2\lambda+1)(2\lambda+3)\Gamma^2(2\lambda+1)}\left(\frac{2ZR}{a_0}\right)^{2\lambda-2} \quad (9)$$

is the relativistic correction factor. In the case of Fe, $S(Z) = 1.32$. A more detailed treatment which takes into account the distortion of the electron wavefunctions by the finite volume of the nucleus add another corrective factor of 0.98 in the case of Fe and Ni. As is the case in the non-relativistic case, the only chemical information contained in the isomer shift is the difference in (non divergent or Schrödinger) electron densities at the nucleus. The relativistic correction factors only come into play when comparing calculated densities with experimental isomer shifts.

The *IS* is independent of the azimuthal angular momentum I_z of the nucleus and thus shifts the energies of all transitions from the excited state to the ground state by the same amount (fig. 4). In metals, at temperatures far below the Fermi temperature, the *IS* is not expected to be temperature dependent since there is usually no significant change in the electronic structure of the material with temperature. This thesis is in part concerned with an important exception to this rule, when the *IS* is found to be temperature dependent, indicating a change in electronic structure.

2.2.1.2 Second-Order Doppler Shift

In addition to the *IS*, thermal motion of the absorber atoms also contribute to a global shift of the transition energies from one sample to another because of Doppler shifting. At any temperature, the vibration of the Fe atoms result in an average Doppler shift of the transition energies. Because the atomic vibration period is much shorter than the lifetime of the excited state, first-order terms (and indeed all odd-order terms) in the atom velocities average to 0. However, second order-terms of the velocity are also present in the relativistic expression for the Doppler shifting of the radiation:

$$\frac{\Delta E}{E} = 1 - \left(1 - \frac{v}{c}\right)\Big/\left(1 - \frac{v^2}{c^2}\right) = \frac{v}{c} - \frac{v^2}{c^2} + O\left(\left(\frac{v}{c}\right)^3\right). \quad (10)$$

Because the frequency of atomic oscillations is typically 10^{13}-10^{14} Hz and the lifetime of the excited state is ~10^{-9} s, the average shift ΔE over the lifetime of the excited state is thus

$$\left\langle \frac{\Delta E}{E} \right\rangle = -\frac{\langle v^2 \rangle}{c^2} + O\left(\left\langle \frac{v}{c} \right\rangle^4 \right). \tag{11}$$

This shift, which is named the second-order Doppler shift (*SOD*), also changes the energies of all transitions by the same amount. The *SOD* is dependent on the material and the temperature since it depends on $\langle v^2 \rangle$. Within the Debye approximation of solids, the *SOD* can be calculated:

$$SOD(T) = -\frac{3}{2}\frac{k}{Mc}\Theta_D\left[\frac{3}{8} + 3\left(\frac{T}{\Theta_D}\right)^4 \int_0^{\Theta_D/T} dx \frac{x^3}{e^x - 1}\right]. \tag{12}$$

The measured centre shift (*CS* or δ) is the total shift of all the transition energies relative to some standard material (a standard calibration material is used to calibrate the source velocity in order to provide a measured *CS* that is independent of the source used):

$$CS = IS + SOD. \tag{13}$$

Since the resulting *CS* is also temperature dependent, it must be given relative to a standard material at a given temperature. The *CS* is an experimental parameter that is directly obtained from the Mössbauer spectrum (fig 4). Without any assumptions about the absorber or measurements at different temperatures, it is not possible to differentiate the *IS* from the *SOD*. For this thesis, resolution of the *IS* and *SOD* was required.

2.2.2 Electric Quadrupole Interaction

Because the first excited state of the ^{57}Fe nucleus has a quadrupole moment *Q*, it interacts with an electric field gradient (EFG) according to the following Hamiltonian:

$$\begin{aligned} H_Q &= \frac{eQ}{2I(2I-1)}\left(V_{xx}I_x^2 + V_{yy}I_y^2 + V_{zz}I_z^2\right) \\ &= \frac{e^2qQ}{4I(2I-1)}\left(3I_z^2 - I(I+1) + \eta(I_x^2 - I_y^2)\right), \end{aligned} \tag{14}$$

where V_{xx} (= *eq*), V_{yy} and V_{zz} are the principal components of the EFG tensor. By convention, the directions are chosen such that $|V_{zz}| > |V_{xx}| \geq |V_{yy}|$. The asymmetry parameter, defined as $\eta = (V_{xx} - V_{yy}) / V_{zz}$, is then between 0 and 1. The ground state has no quadrupole moment and is thus unaffected by an EFG. When the ^{57}Fe nucleus is placed in an EFG, the 4-fold degeneracy of its excited state will be partially lifted since the ($I = 3/2, I_z = 3/2$) and ($I = 3/2, I_z$

= 1/2) have different energies:

$$E_Q = \frac{e^2qQ}{4I(2I-1)}\left[3I_z^2 - I(I+1)\right]\left(1+\frac{\eta^2}{3}\right)^{1/2}. \quad (15)$$

There will then be two possible transition energies between the first excited state and the ground state, resulting in a two-line spectrum known as a doublet (fig 4). The energy difference between the two possible transitions is known as the quadrupole splitting (QS or Δ) which is related to V_{zz} and η:

$$QS = \frac{e^2qQ}{6}\left(1+\frac{\eta^2}{3}\right)^{1/2}. \quad (16)$$

2.2.3 Magnetic Dipole Interaction

All degeneracies of the $I = 1/2$ and $I = 3/2$ states can be lifted if the nucleus is subjected to a magnetic field. In such a case, the Hamiltonian of the magnetic dipole interaction is:

$$H_M = -g\mu_N \vec{H}\cdot\vec{I}, \quad (17)$$

which splits the $I = 1/2$ into two sublevels ($I_z = \pm 1/2$, $E = E_{1/2} - g_{1/2}\mu_N H I_z$) and the $I = 3/2$ into 4 sublevels, ($I_z = \pm 3/2, \pm 1/2$, $E = E_{3/2} - g_{3/2}\mu_N H I_z$). Since electric dipole transitions (emission or absorption of a photon) can only occur between levels with $\Delta I_z = \pm 1, 0$ (to first order), this results in a six line pattern known as a sextet (fig. 4), since the $I_z = 3/2 \rightarrow -1/2$ and $I_z = -3/2 \rightarrow 1/2$ transitions are forbidden. The sextet is usually characterized by the hyperfine magnetic field H or the Zeeman splitting of the excited state $z = g_{3/2}\mu_N H$.

When a magnetic field and an EFG are present simultaneously, the spectrum can comprise up to eight lines but calculating the line positions and their intensities becomes a non-trivial task. However, in our situation, we are dealing with materials with cubic symmetry where the EFG is usually small enough so H_Q can be treated as a perturbation of H_M. In that case, the spectrum is composed of 6 lines which are shifted relative to the EFG=0 case. The relevant hyperfine parameters to describe that situation are the Zeeman splitting of the excited state z (or the hyperfine magnetic field H) and the quadrupole shift ε,

$$\varepsilon = \frac{e^2qQ}{4}\left[1+\frac{(\eta\cos 2\phi - 3)}{2}\sin^2\theta\right], \quad (18)$$

where ϕ and θ are the azimuthal and polar angles describing H in the EFG principal axes reference frame.

2.2.4 Calculating and Fitting the Mössbauer Spectrum

In either transmission or emission experiments, the magnitude of the observed Mössbauer signal is related to the cross-section of the $I = 1/2 \rightarrow 3/2$ transition and this cross-section is simply the sum of the cross-sections for each of the ^{57}Fe atoms present in the sample. In the absence of an EFG or hyperfine field, the cross-section for the transition has a Lorentzian dependence on the energy, with a half-width related to the life-time of the excited state according to Heisenberg's uncertainty principle. For ^{57}Fe, the maximum cross-section is $\sigma_0 = 2.56$ barn and the FWHM $\Gamma = 0.097$ mm/s [Mössbauer Effect Data Center89]. If all ^{57}Fe nuclei are in identical environments (subjected to the same hyperfine interactions), their cross-sections are identical and will simply be a sum or Lorentzians centred on the energies of all possible transitions ($I = 1/2, I_z$) $\rightarrow$ ($I^* = 3/2, I_z^*$). In the absence of a hyperfine field H, the two transition energies are

$$\nu_{\pm} = \delta \pm \frac{\Delta}{2}, \tag{19}$$

whereas in the presence of a hyperfine field and within the first-order perturbation approximation ($\varepsilon < \zeta$), the six possible transition energies are:

$$\nu_l = \delta + \beta_l \varepsilon + \alpha_l \zeta, \tag{20}$$

where $\beta_l = \{-1, 1, 1, 1, 1, -1\}$ and $\alpha_l = \{-(Z+3)/2, -(Z+1)/2, -(Z-1)/2, (Z-1)/2, (Z+1)/2, (Z+3)/2\}$, with $Z = |g_{3/2} / g_{1/2}| = 1.7509$ in the case of ^{57}Fe [Mössbauer Effect Data Center89]. The Zeeman splitting z is related to H as

$$\zeta = g_{3/2} \mu_N H, \tag{21}$$

where $g_{3/2}$ is the gyromagnetic ratio of the excited state, μ_N is the nuclear magneton. The Zeeman splitting z is usually expressed in mm/s, with $\zeta(\text{mm/s}) = 0.0679\, H(\text{T})$ in the case of ^{57}Fe spectroscopy.

When fluctuations of the hyperfine parameters are either much slower or much faster than the lifetime of the excited state it is said that we are dealing with a "static" or "effectively static" case, and a peak corresponding to each possible transition is observed. Whenever the hyperfine parameters fluctuate at a rate where they vary over the lifetime of the excited state,

dynamic effects are present in the spectrum and the analysis of the hyperfine parameters requires more complex analysis methods which take these fluctuations into account and which result in unusual lineshapes.

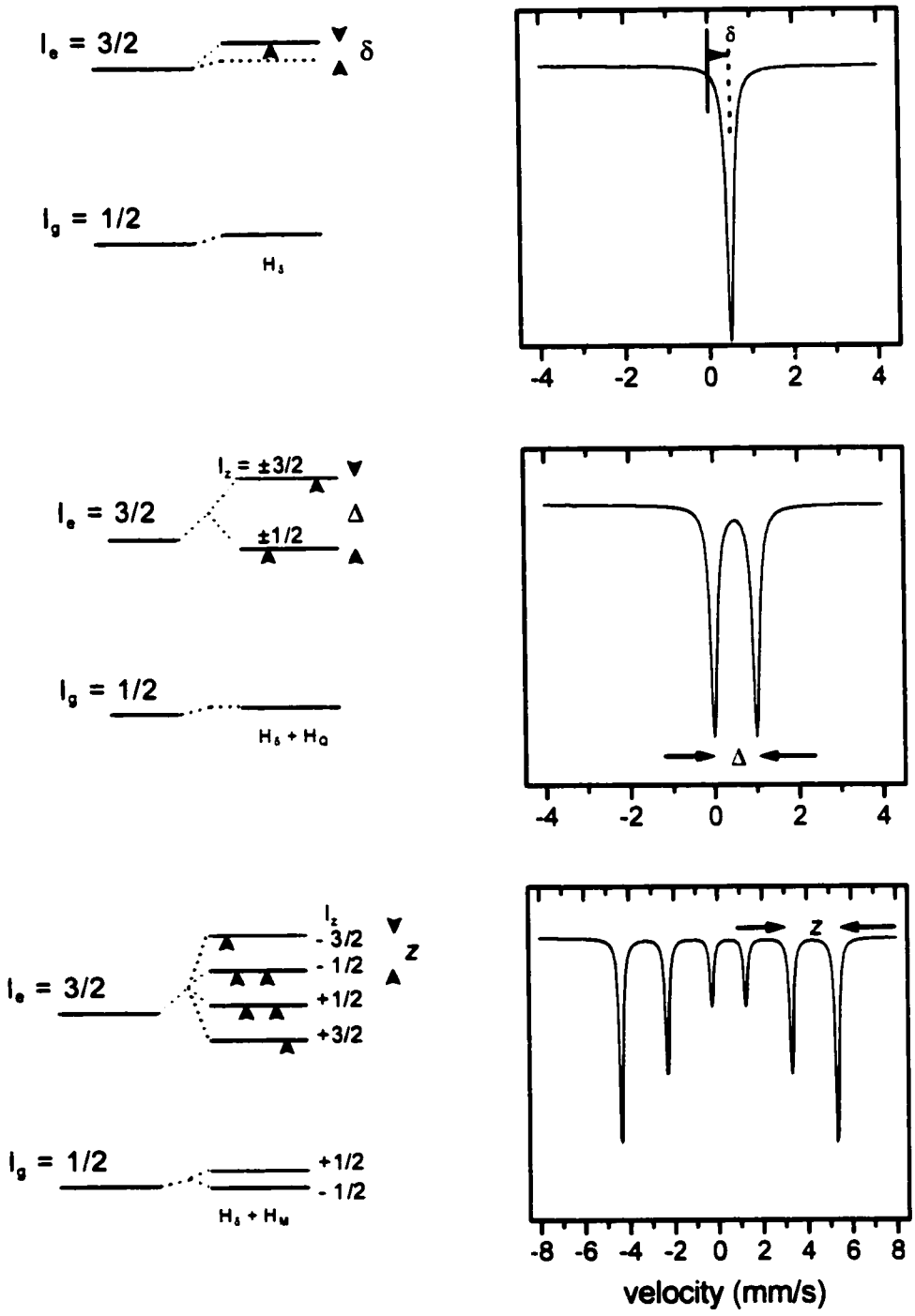

Figure 4 Effect of the electric monopole (H_δ), electric quadrupole (H_Q) and magnetic dipole (H_M) interactions on the nuclear levels and on the transmission Mössbauer spectrum. The relation between the relevant hyperfine parameters and the energy levels are also given.

2.2.4.1 Distributions of Hyperfine Parameters

By their nature, the hyperfine parameters are sensitive to local chemical and magnetic environments. In an alloy, all sites have different local environments so the bulk Mössbauer measurement will actually result from a distribution of hyperfine parameters corresponding to each individual site. If all sites are considered to be equivalent in terms of their average orientation with respect to the incident γ-ray radiation, then we can characterize all the individual sites as a generalized site with an associated distribution of hyperfine parameters. For a site which exhibits magnetic splitting, the general distribution would be given by a probability density distribution (PDD) of the form $P(\delta, \varepsilon, z)$. Because of the arbitrary shape and complexity of this distribution, it is difficult to extract it from the Mössbauer spectrum, so simplified models are used.

When predominantly concerned with HFs, the simplest analysis is to consider that only the Zeeman splitting z is distributed and that δ and ε are the same for all sites, which means

$$P(\delta, \varepsilon, z) = P(z)\, \delta(\delta - \delta_0)\, \delta(\varepsilon - \varepsilon_0)\,, \tag{22}$$

where $\delta(x)$ is the Dirac delta-function. In this case, only $P(z)$ needs to be extracted, along with the values δ_0 and ε_0. In many cases though, it is found that this is insufficient and it is necessary to include distributions of the other parameters as well. The second approach and the most common one, is to assume that at each site, δ and ε are linearly coupled to z, as $\delta = \delta_0 + \delta_1 z$ and $\varepsilon = \varepsilon_0 + \varepsilon_1 z$, which means the distributions of δ and ε are also coupled to $P(z)$:

$$P(\delta, \varepsilon, z) = P(z)\, \delta(\delta - (\delta_0 + \delta_1 z))\, \delta(\varepsilon - (\varepsilon_0 + \varepsilon_1 z))\,. \tag{23}$$

This model is implemented in the Voigt-based fitting (VBF) method of Rancourt and Ping [Rancourt91a], where $P(z)$ is modelled as an arbitrary sum of Gaussian components.

A more general but still tractable approach has been developed to allow for simultaneously independent distributions of the three parameters, where correlations between parameters are allowed. This is implemented as the extended Voigt-based fitting (xVBF) method of Lagarec and Rancourt [Lagarec97, see appendix A]. Because there is no inherent reason for the various parameters to be strictly linearly coupled together, this allows for more physically realistic distributions of hyperfine parameters and usually provides better fits than the VBF method.

When analysing the spectra of Fe-Ni alloys, it was always necessary to use distributions

of parameters. Because both methods (VBF and xVBF) could produce slightly different results, we have generally used them both to get a feel for the "true" range of the parameters.

2.2.4.2 Complexities Involved in Getting Accurate Hyperfine Parameters (*CS* in Particular)

It is very important to realize that getting accurate and precise parameters from the Mössbauer spectra of Fe-Ni alloys isn't a simple task. One of the main reasons is that these are alloys and, as such, are not characterized by a discrete set of hyperfine parameters but rather by a distribution of each of the parameters. Among other things, the existence of such distributions makes an exact and unique fit impossible. The reason for this is that the amount of information one might want to extract (shapes of the distributions of the HF, *CS* and *QS* and how they are correlated together, relative spectral areas of each line, etc...) is usually greater than the amount of information contained in a spectrum (typically 512 data points of velocity and intensity) and is made even less tractable because of the noise in the spectrum. Without getting into to much detail, it is easy to see that one must make assumptions on the shapes of the distributions and how they are correlated to each other in order to simplify and solve the problem. The VBF and xVBF models do just that by defining a generalized site which establishes rules on building the distributions. The two methods provide different methods of building the distributions and these methods may or may not be well suited to describe the "true" distributions that characterise the sample. Because of the inherent lack of information contained in the spectrum and the ever present statistical noise, the problem of uncovering the true parameters is usually ill-defined (there is no single solution) and these methods provide the best way of getting a solution which is reliable (albeit constrained to the specific model).

2.2.4.2.1 Correlation Between the *CS* and the HF

In the case of Fe-Ni alloys, it is generally admitted that the observed line broadening is due mainly to a distribution of hyperfine field magnitudes on the various probe nuclei sites. However, it is clear from the line asymmetries seen in figs. 5 and 6 that either (or both) the *CS* or the *QS* must also be distributed and correlated to the HFD because the observed asymmetries can

only arise because of such correlations. This implies that the method used to describe the joint distribution of hyperfine parameters is critical in obtaining reliable averages of the parameters. Consider a spectrum (such as the one of 65 at.% Fe at RT, shown in fig. 6) which yields a strongly skewed HFD and requires a CS-HF correlation. The VBF model assumes a linear coupling between the CSD and the HFD, which means that the CSD is forced to have the exact same shape as the HFD (but on a different scale and offset to some different value). In such a case, because of the skewness of the distribution, the average *CS* will be different from the most probable *CS*. In the xVBF model, the distributions are built independently and then a correlation is added. A good fit can be obtained by assuming the CSD is described by a Gaussian distribution which is correlated to the skewed and more complicated HFD. In such a case, the average *CS* and the most probable *CS* are the same and they will usually be very close to the most probable *CS* obtained from the VBF fit. The two fits result in the same (or very similar) HFD, have essentially the same statistical significance (χ^2 value) yet give significantly different average *CS*s (the discrepancy between the values is significantly larger than the precision of each value as obtained from the fit). There is generally no way of favouring one value over another, so both must be accepted as possible. One could say that the "true" joint CSD and HFD does lie in between these two models and so the "true" average *CS* could lie anywhere between the two values obtained.

2.2.4.2.2 Dynamic Effects Near T_C

The determination of hyperfine parameter distributions can also be complicated by the existence of dynamic effects near T_C (in the case of these alloys). Such effects must be expected to occur near T_C [Rancourt96b]. These complicate the extraction of hyperfine parameters since there effect (homogeneous broadening) is nearly impossible to distinguish from inhomogeneous broadening. Also, a complete fitting model that admits distributions and dynamic effects is not available. The simplifications used in the analysis also affect the accuracy of the extracted parameters.

2.2.4.2.3 Average Quadrupole Shift

The EFG in a cubic environment is normally nil. However, because of the alloying, none of the sites truly have a cubic symmetry and it is possible to have non-vanishing local EFG. In the presence of an HF, the EFG contributes to the quadrupole shift ε, which depends on the angles between the local HF and EFG principal axes. Because of the alloying, the local chemical environment (which results in the direction of the EFG principal axes) may be uncorrelated with the magnetic domains (which is related to the direction of the HF), so the average ε can be expected to be 0, since

$$\int_0^{2\pi} d\phi \int_0^{\pi} \sin\theta \, d\theta \, \varepsilon(\phi,\theta) = 0 . \qquad (24)$$

In most cases, when the sextet pattern is clearly resolved, a fit does produce a value of $\varepsilon \leq 0.008$ mm/s. In such cases, the *CS* is not much affected by forcing ε to be 0. When the sextet pattern started to collapse (near but below T_C), a free fit often produces values of ε ≈0.01-0.02 mm/s. These values are suspect and give corresponding values for the *CS* which are significantly different from the ones obtained by forcing ε = 0. In order to fit all spectra in the same fashion and with the same reproducibility, the average value of ε was always forced to be 0 mm/s. When using the VBF model with a ε-z coupling, the parameters ε_0 and ε_1 were first free, then ε_0 was manually adjusted such that $\langle\varepsilon\rangle < 0.0001$ mm/s: both ε_0 and ε_1 were frozen and the other parameters were fit again.

All these factors (and more) are the reason for some of the large ranges of hyperfine parameter values that are reported in this work and because so much of this work relies on accurate measurements of the *CS*, we have had to be very careful in gauging the accuracy of the *CS* obtained from fitting a spectrum to any specific model.

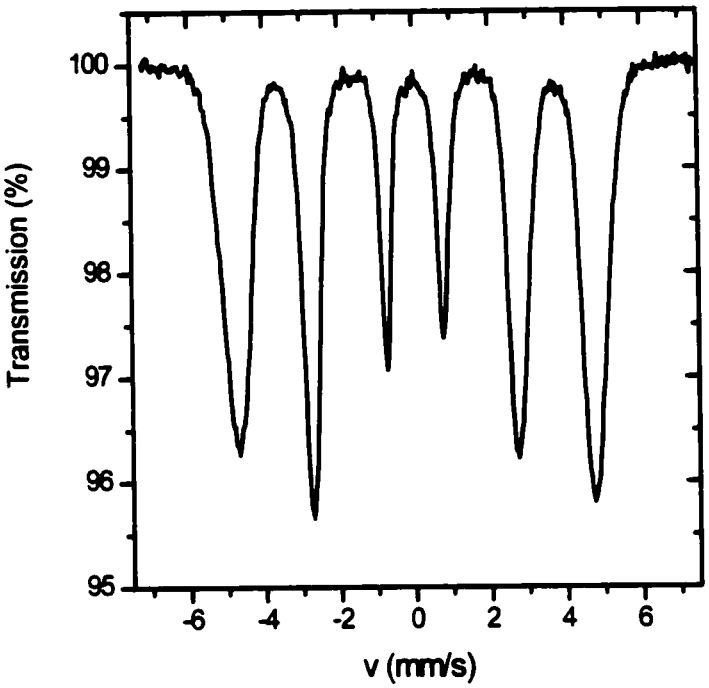

Figure 5 Transmission Mössbauer spectrum of $Fe_{30}Ni_{70}$ illustrating the line depth asymmetry due to correlations between hyperfine parameters (in this case it is mainly due to a ε-z correlation).

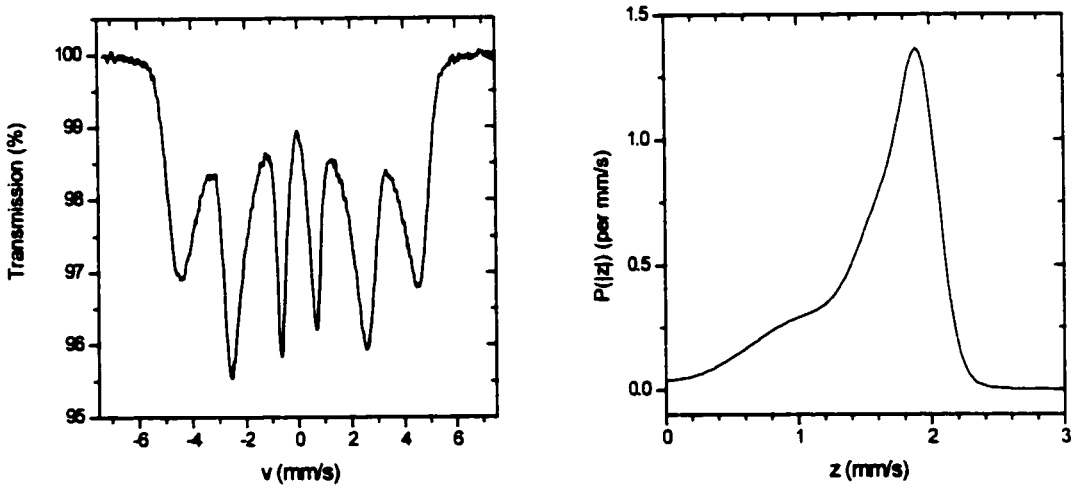

Figure 6 Transmission Mössbauer spectrum of $Fe_{65}Ni_{35}$ showing signs of δ-z correlations (left) and the extracted and strongly skew HFD (right).

2.3 Experimental Mössbauer Setup

2.3.1 Physical Layout and Electronics for Data Acquisition

Most ^{57}Fe Mössbauer spectroscopy measurements were performed in transmission geometry with 40 to 50 mCi ^{57}Co source in a Rh matrix. A diagram of the complete experimental setup for RT measurements is shown in fig. 7. The source-to-sample and sample-to-detector distances are chosen to virtually eliminate geometrical effects such as cosine-smearing, by taking into account the source size (~30 mm^2 active area), the absorber area (maximum of 1.27 cm^2) and the detector window (~7 cm^2). The source velocity, driven in constant acceleration mode followed a triangular waveform which was calibrated using the spectrum of 95% ^{57}Fe enriched α-Fe taken in the same conditions. All CSs and ISs reported in this chapter are thus relative to the CS of α-Fe at RT. A calibration spectrum was taken before and after each spectrum, or series of spectra when the same absorber was used and only the temperature was varied.

Fig. 7 distinguishes the three parts of the setup: the instruments, the electronics and the computer hook-up for data acquisition and analysis. The instruments include the transducer (T) which drives the source (S) in its oscillatory motion, according to a waveform provided by the transducer driving unit (TDU). For radiation safety reasons, the source is encased in a lead box, to which is affixed the absorber (A). In the RT setup, the TDU frequency is approximately 2 Hz, which leads to a source displacement of ±0.8 mm (assuming a velocity range of ±8 mm/s). The absorber, which is contained in a cylindrical holder that fits into a pre-aligned socket, is placed at least 10 cm from the source to avoid cosine smearing and other similar geometrical artifacts (see Appendix C for a description of the artefacts). The radiation which is transmitted through the absorber is detected by a sealed 1 atm Kr(2% CO_2) gas filled proportional counter (PC). The high-voltage bias (~1700 V) necessary to detect the γ-rays is supplied to the PC, through the pre-amplifier (pA), by an external high voltage power supply (HV). The charge sensitive pA, which is powered by a 12V supply from the spectroscopy amplifier (SA), accumulates the charge produced by the detection of a γ-ray, converts it to a voltage pulse, amplifies it (~×10) and relays it to the SA. The SA further amplifies (~×500) and shapes the pulse before feeding it to the single channel analyser (SCA). The SCA is setup to output a fast TTL pulse only when it receives the

pulse corresponding to a γ-ray with an energy of 14.4 keV. By this filtering, we eliminate all other detected radiation which cannot be resonantly absorbed and which would simply contribute to the background and hence reduce the signal-to-noise ratio of the Mössbauer spectrum. The settings of the SCA window are determined by performing a pulse height analysis (PHA) of the SA output on a computer. Because the amplified pulse voltage is proportional to the energy of the detected γ-ray, the PHA system allows us to view the energy spectrum of the detected radiation and set the SCA window to discriminate the 14.4 keV radiation. The other undesired radiation detected by the proportional counter include the 6.4 keV conversion X-rays (Fe K_α) from the source and inelastically scattered radiation from the 122 and 136.5 keV transitions. The acquisition of the Mössbauer spectrum is performed using a multichannel scaler (MCS) in a computer. The MCS channels, which accumulate a count for each TTL pulse from the SCA, are synchronized with the source drive by a signal from the TDU, such that the channels correspond to time and thus source velocity. All the electronics are high-quality research grade devices and their settings and cables are optimized to reduce the electrical noise in the system and produce the best possible Mössbauer spectrum. Spectral calibration, folding and analysis is performed using the Recoil software we have developed in house and which is available commercially [http://www.physics.uottawa.ca/~recoil/].

In addition to the standard setup shown in fig. 7, we have the possibility to put the sample in an oven in order to acquire Mössbauer spectra from RT to ~900 K, or in a liquid N_2 cryostat to perform measurements from ~80 K to RT. In both cases, the sample, in the oven or the cryostat, is directly inserted between the source and detector which remain at RT. A third possibility is to use a completely different setup for cryogenic measurements down to 4.2 K. We now give a detailed description of the oven and cryostats, in addition to the calibration and technical characteristics of the oven.

Figure 7 Diagram of the experimental setup for Mössbauer spectroscopy. Solid lines represent a signal, dashed lines represent an applied voltage and the arrows indicate where the signal is sent (or where the voltage is applied)

2.3.2 Oven for Mössbauer Spectroscopy

2.3.2.1 Design and Construction

In order to perform Mössbauer measurements at temperatures up to ~900 K, it was necessary to construct an oven suitable for such measurements. As shown in fig. 8, the oven consists of a ceramic core in which the sample is inserted and which is enclosed in a vacuum-tight water cooled stainless steel cylindrical shell with γ-ray transparent Be windows. This shell is clamped onto a solid base which contains the connections for the thermocouples and the heating elements.

The core is made of Macor® machinable glass ceramic (code 9658) manufactured by Corning Glass Works (rated for continuous operating temperature up to 1270 K) and is wound with 25 gauge (0.020" diameter) Nichrome (80 % Ni, 20 % Cr) heating wire. The heating wire is wound twice in opposite directions in order to cancel the magnetic field caused by the large current in the wire. The sample, which is seated into a ring-shaped insert, is positioned in the middle of the oven where the temperature is expected to be uniform. To minimize thermal gradients, pure Al radiation shields are used on either side of the sample insert. To approximately determine the temperature of the sample, two K-type thermocouples (Chromel-Alumel in a 304 stainless steel sheath, rated for temperatures between 4 K and 1150 K) are inserted in fine holes drilled directly into the core, with the tip located close to the sample. A further calibration of the temperature using measurements of a material with a known thermal behaviour is required to get an accurate temperature and a measurement of thermal gradients. As the thermocouple hole and the Be windows are simply glued in place, the external case must be water cooled to avoid a deterioration of the vacuum-tight seals.

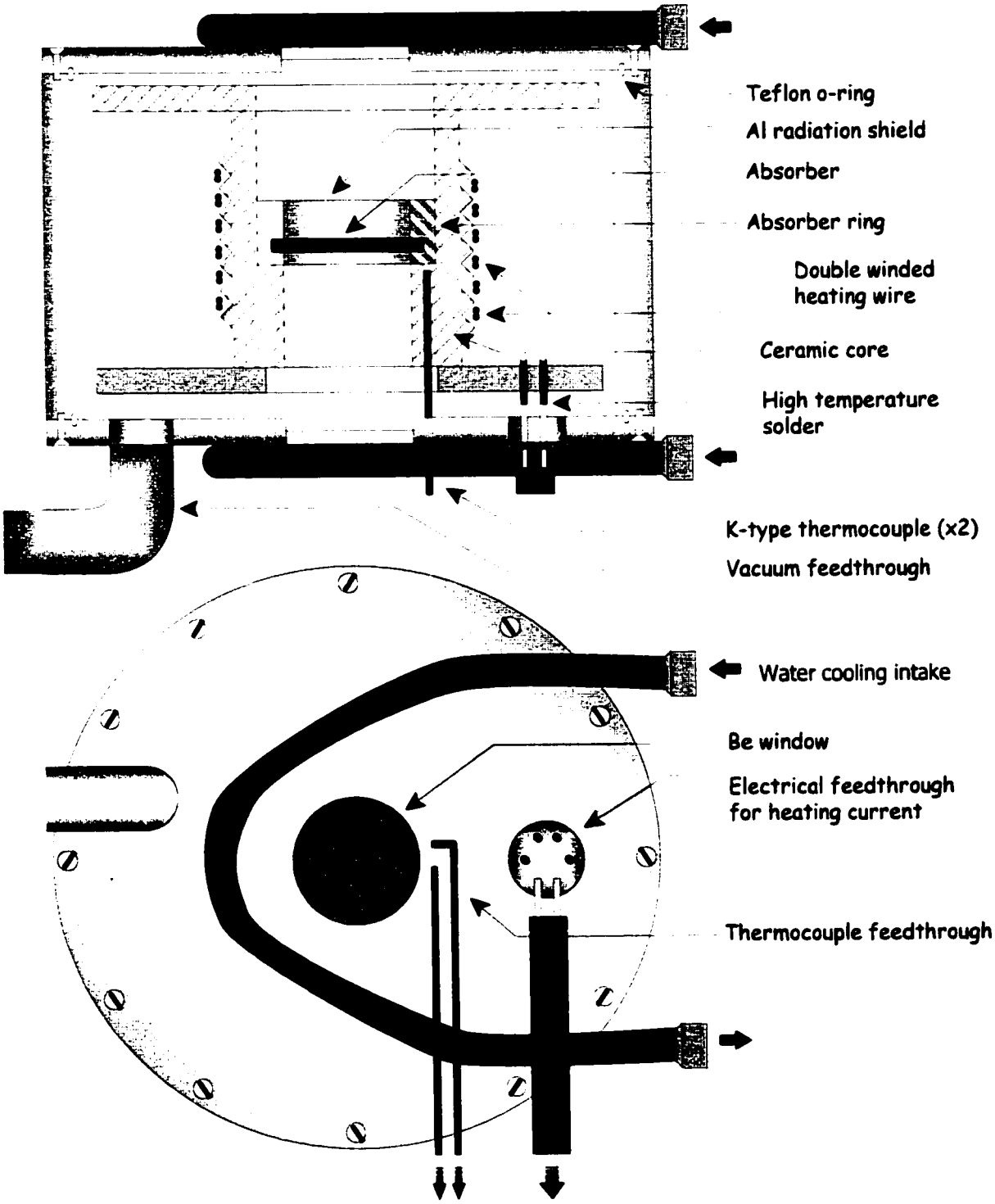

Figure 8 Schematic view of the oven used for Mössbauer spectroscopy.

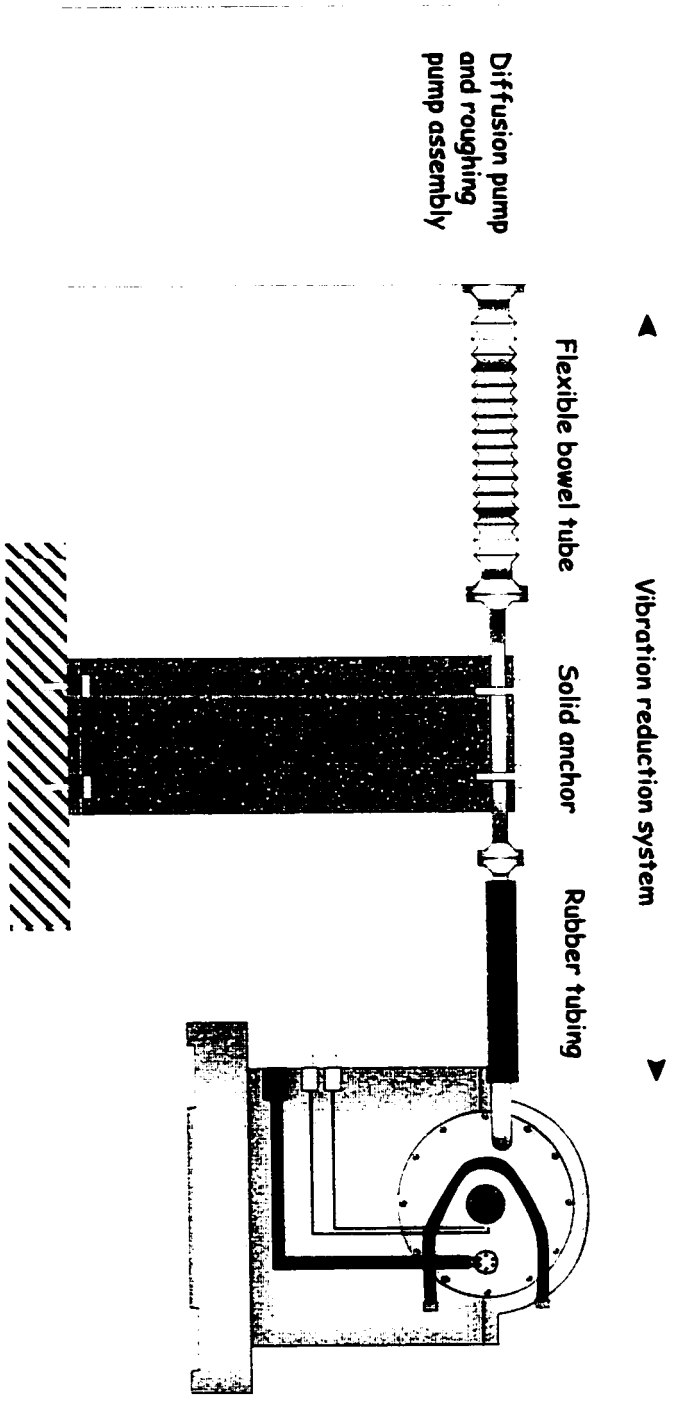

Figure 9 Schematic view of the vacuum system and its vibration reduction components

2.3.2.2 Temperature Control

One thermocouple and the heating wires are connected to a temperature controller (Eurotherm 840P) and thyristor (Eurotherm 425A) which produces the heating current. This pair of instruments can generate and maintain a sample temperature which is stable to within 1 K over the entire measurement time (usually 1 day). The second thermocouple is connected to a secondary temperature controller which cuts the power to the main temperature controller in case of failure of the primary thermocouple. Though the thyristor is rated to output up to 15 A, its maximum current was set to ~2 A, which yielded a maximum oven temperature of ~900 K and prevented the Nichrome heating wires to melt when instantaneously subjected to the maximum load. Because the melting point of the Al radiation shields is 933 K, this was chosen to be a suitable maximum operating temperature. All other materials used in the construction of the oven are rated for temperatures up to at least 1150 K. This simple oven design, however, is not convenient for work at higher temperatures.

2.3.2.3 Vacuum System

In order to avoid oxidation of the sample and to reduce thermal conductivity with the external case, the oven was operated at a pressure of less than 10^{-3} mbar, by using a diffusion pump. Since line broadening in Mössbauer measurements is extremely sensitive to vibrations, we have performed many tests to determine the best pumping mechanism. The turbo molecular pump was found to produce high-frequency vibrations which we could not attenuate to reasonable limits. We thus chose an oil diffusion pump coupled to a primary roughing pump. As shown in fig. 9, this assembly was connected to a large boweled tube to remove high and medium frequency vibrations. The next section was clamped to a heavy anchor to remove low and medium frequency vibrations. A rubber tubing was finally used to connect to the oven inlet. A section with a Piranni and a high-vacuum gauge could be inserted next to the oven to determine the pressure in the oven. Under these conditions, it was determined that the broadening caused by mechanical vibrations would be within the usual experimental uncertainty of a linewidth (less than 5% of the intrinsic linewidth of the source).

Table 2 Calibration of the sample temperature based on the thermocouple readings

17	18	17	40	23	0.002	0.969
100	101	93	105	97	-0.050	0.955
200	206	202	204	203	-0.125	0.928
300	313	312	306	308	-0.201	0.895
400	422	423	414	417	-0.279	0.848
500	526	523	519	520	-0.350	0.785
550	578	569	571	571	-0.382	0.741
17	18	20	17	19	0.000	0.973

2.3.2.4 Testing and Temperature Calibration

In order to calibrate the sample temperature relative to the thermocouple temperature, we performed a test run using a 20 μm natural α-Fe foil. The thermal behaviour of α-Fe hyperfine parameters is well-known and documented. We have used the *CS* and normalized Zeeman splitting (z/z_0) data reported by Kobeissi [Kobeissi81] and shown in fig. 10 to compare the thermocouple reading to a calibrated temperature. The calibrated temperature we used was the average of the calibrated temperatures based on the *CS* and z/z_0, weighted by their relative precisions.

$$T^{cal} = w_{CS} T_{CS} + w_{z/z_0} T_{z/z_0}, \tag{25}$$

with $w_{CS} = \sigma_T^{-2}(CS) / (\sigma_T^{-2}(CS) + \sigma_T^{-2}(z/z_0))$ and $w_{z/z_0} = \sigma_T^{-2}(z/z_0) / (\sigma_T^{-2}(CS) + \sigma_T^{-2}(z/z_0))$ and $\sigma_T(CS)$ and $\sigma_T(z/z_0)$ are the relative uncertainties on the temperatures calculated from *CS* and z/z_0. For temperatures above RT, the main temperature dependence of the *CS* is from the *SOD* and it is approximately linear, such that

$$\sigma_T(CS) = \sigma_{CS} \left(\frac{\partial CS}{\partial T} \right)^{-1} = \sigma_{CS} / 7 \cdot 10^{-4}. \tag{26}$$

In the case of z/z_0, the temperature dependence is non-linear but we can simply calculate $\sigma_T(z/z_0)$ for any temperature, using

$$\sigma_T(z/z_0) = \sigma_{z/z_0} \left(\frac{\partial z/z_0}{\partial T} \right)^{-1}. \tag{27}$$

Because σ_{CS} and σ_{z/z_0} are essentially equal to 0.005 mm/s and 0.005 respectively, we can calculate

the weights for T_{CS} and T_{z/z_0} and thus calculate T^{cal}. Table 2 gives the values of the thermocouple readings (T_1 and T_2), the measured CS and z/z_0, the calculated temperatures T_{CS} and T_{z/z_0} and the calibrated temperature T^{cal}.

As one can see, the calibrated temperature is systematically between T_1 and T_2. Based on these results, we have calculated the following calibration equation for the sample temperature T (in °C), given T_1 (in °C)

$$T = T_1 + 10(\tanh[0.009\,(T_1 - 320)] + 1), \tag{28}$$

and we have established that a conservative estimate of the uncertainty is ~ ± 10°C at the highest attainable temperature (the uncertainty increases with temperature). This uncertainty comes

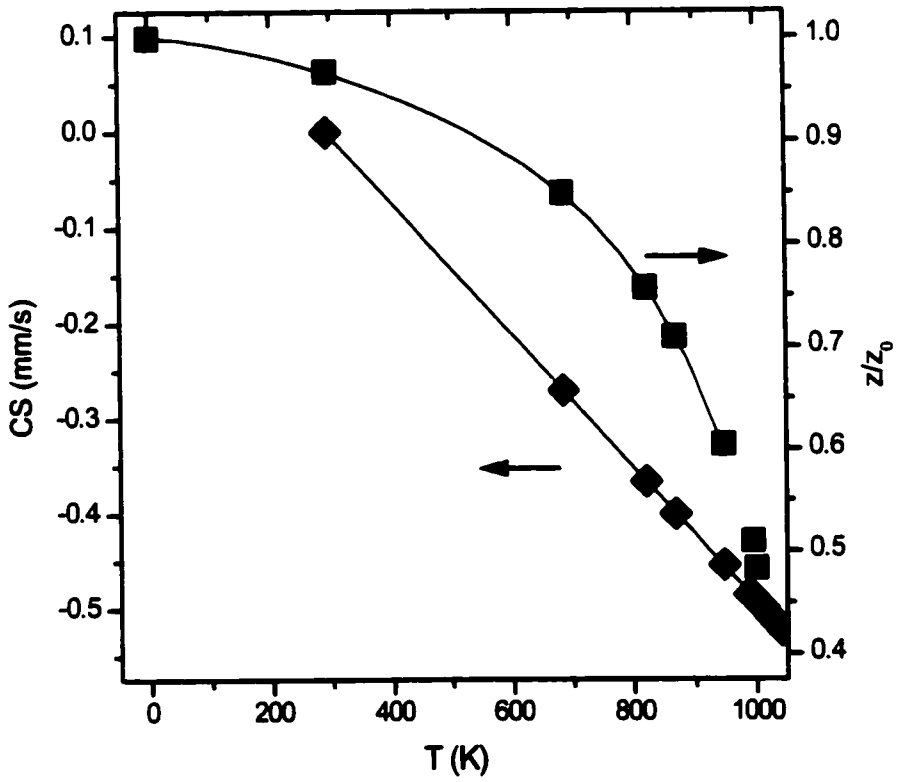

Figure 10 α-Fe Mössbauer data [Kobeissi81] used for the calibration of the oven temperature. (■) relative Zeeman splitting (relative to value at T = 0 K) and (◆) centre shift (relative to value at RT). The lines represent the calibration curves obtained from the data points, in the range of interest.

entirely from the calibration, as the thermocouple temperatures are reliable and repeatable to less than 1°C. By analysing the widths of the peaks as a function of temperature, we have determined that the total temperature gradient on the sample varies approximately linearly with temperature, going from 0°C at RT to ≤10°C at 550°C. This is also probably an overestimation since the sample is metallic and has very good thermal conductivity. The estimated gradient also justifies that the uncertainty on the temperature should be ~10°C, though this might be a slight underestimate for the highest temperatures reached (typically 600°C). Whenever the *IS* is calculated by correcting the *CS* for the *SOD*, an uncertainty of 5°C in the temperature results in an uncertainty of 0.0035 mm/s in the *IS*, which is close to the experimental uncertainty on the *CS* obtained by fitting the spectrum.

2.3.3 Cryogenic Setups for Mössbauer Spectroscopy

Two different cryostats were used for low temperature MS measurements. The simplest is a cold-finger liquid N_2 cryostat which enables us to make measurements at 82 K. In this setup, the cold sample, which is in the cryostat, is inserted between the source and detector which are kept at RT. The sample is cooled by contact using a cold-finger which is also in contact with the liquid N_2 chamber.

The other cryostat is made for measurements down to liquid He temperature (LHeT = 4.2 K) and is an exchange gas chamber type cryostat. In this case, a completely different setup than previously described is used. The source and sample are both refrigerated inside the cryostat. The transducer, located on top of the cryostat drives the source in a vertical motion and the detector is placed below the cryostat, as illustrated in fig. 11. The sample, sandwiched by heat shields, is fixed to a brass block which houses two diodes (used to measure the temperature) and is laced with heating wire. In this configuration, the sample's temperature can be maintained anywhere between RT and LHeT. The source's temperature, while it is expected to be similar to the measured sample temperature, is not directly measured and hence not known. It is only known precisely at 4.2 K and 77 K where the entire system is in equilibrium at the boiling temperatures of the liquid coolants. Because of the unknown source temperature, it is not possible to relate the *CS*s measured at different temperatures as the source's temperature is changing. Because the source temperature changes (and is unknown) the *SOD* contribution to

the source energy is unknown. As the source energy is changing, the measured *CS*s of the sample at different temperatures cannot be compared or used to get an *IS*.

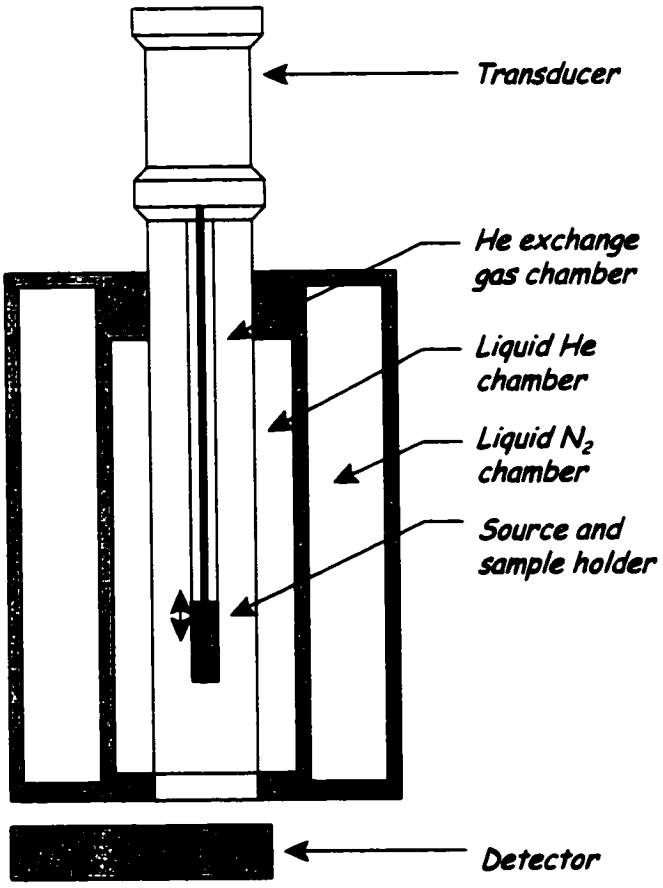

Figure 11 Schematic representation of the cryostat for variable temperature measurements from 4.2 K to RT.

3. Fe-Ni Alloys in Meteorites

3.1 Overview of Meteorites

3.1.1 Introduction

Meteorites are extraterrestrial objects that, after having travelled and cooled down in space for millions of years or more, have fallen onto Earth. Technically speaking, the meteorite is the object recovered on Earth. The original or parent object is named an asteroid as long as it travels in space but becomes a meteor when it darts through the Earth's atmosphere in a fiery blaze. Asteroids come in all sizes, from several kilometres in diameter which could wreak havoc if they collided with Earth (e.g. K/T mass extinction [Melosh97]) to very fine particles, space dust, which deposit themselves uneventfully on Earth.

Because of the extreme heat generated upon their entry in the Earth's atmosphere, not all asteroids result in appreciably sized meteorites. The larger ones typically break up into smaller pieces which can be scattered over great distances before they reach the ground. The much smaller ones, because of their very large surface to volume ratio dissipate the heat very quickly and as such are practically unaffected by their entry in the atmosphere, except for slowing down considerably. Finally, medium-sized asteroids heat up, causing them to have an outer-shell which is changed compared to the original asteroid, but the bulk of it is left in pristine condition until it actually hits the ground. Even after impact, most of the meteorites show little signs of their spectacular fall to Earth and are found in the same condition as the asteroid was. Once on Earth, the meteorites will start to be weathered, that is they will show signs of oxidation and other reactions to the Earth's atmosphere.

3.1.2 Origin and Classification of Meteorites

Most asteroids come from larger parent bodies that were either destroyed and scattered into pieces by the collision with another large body, or simply had their surface chipped away by a smaller collision. The second option is how, for instance, we can recover on Earth meteoritic material which comes from the planet Mars or from our Moon. The typical geological evolution of a small planetoid results in a structure similar to that of the Earth. A core, constituted primarily of Fe is surrounded by an outer layer of rocky minerals such as silicates. When such a planetoid is destroyed and scattered into asteroids, one usually obtains three types of asteroids which we recover as meteorites. Iron meteorites, which come directly from the core of the planetoid, are primarily a pure metal meteorite containing predominantly Fe and Ni. They represent ~6 % of all meteorites found on Earth. Stony meteorites (~93 %) are rocky and contain many of the minerals found in the Earth's crust, as well as some inclusions of metals particles (Fe-Ni). Stony meteorites are also sub-categorized as chondrites and achondrites depending on whether or not they contain chondrules, millimetre-sized spheres of rocks formed during intense heat. These meteorites come from the rocky crust of the parent body or from simple accretion of space dust. A third, mixed category, called stony-iron (~1 %) meteorites comes from the region between the core and the crust where separation of the iron and the rocky material is incomplete.

Iron meteorites are made up of Fe-Ni alloys and contain from 5 to 60 at. % Ni (though such high concentrations of Ni are extremely rare) and trace amounts of Co, P, S, C. As the core of the parent body, they are isolated by the crust and thus cool very slowly, at rates between 5 and 500 K per million years [Goldstein90]. The vast majority of iron meteorites were single crystal FCC (γ) Fe-Ni at high temperature. As the parent body cools below 750 °C, the BCC (α) phase nucleates and a Widmanstatten pattern starts developing [Goldstein90]. As cooling continues, the Ni-poor BCC phase grows at the expense of the FCC phase in which the Ni accumulates until the temperature becomes so low that diffusion is effectively stopped. In meteoritic materials, the mineral name for BCC Fe-Ni is kamacite and that for FCC Fe-Ni is taenite. In some unusual cases, there is no Widmanstatten pattern, but a very small-scale microstructure of various phases which cannot be resolved by optical microscopy. Such meteorites are called ataxites because they have no visible microstructure.

3.1.3 Fe-Ni Phases in Meteorites

3.1.3.1 Kamacite and Taenite

When the Fe is found in its metallic form, it is nearly always alloyed with Ni. In any type of meteorite the Fe-Ni alloy can be found in the form of various phases. Kamacite is the chemically disordered BCC Fe-Ni alloy which can contain up to 6 or 7 at. % Ni. When found as a chemically disordered FCC phase, Fe-Ni is called taenite. The composition of taenite is found to range from ~30 at. % Ni to 60 at. % Ni. The synthetic counterpart (disordered FCC Fe-Ni) can be produced with concentrations up to 100 % Ni.

3.1.3.2 Tetrataenite

Tetrataenite was discovered in synthetic samples under special growth conditions (irradiation, in a high magnetic field, of disordered $Fe_{50}Ni_{50}$ by electrons or neutrons) [Paulevé62a, 62b, Gros64, 68, 70, Laugier65] but later found to occur naturally in meteorites with the use of ^{57}Fe Mössbauer spectroscopy [Petersen77, Albertsen78a, 78b, 80, 81, Danon78, 79a, 79b, 80b, Clarke80]. It is a chemically ordered alloy with an FeNi stoichiometry in which the Fe and Ni occur as layers in the (001) direction (fig. 36, chapter 5) which, being magnetic at RT, results in a quadrupole shift ε of ~0.2 mm/s [Albertsen80]. Because the chemical ordering temperature of tetrataenite is ~320 °C [Paulevé62b], it only starts ordering when the diffusion of Ni is already quite low, so very long cooling times, as found in meteorites, are required. Tetrataenite is typically found in meteorites in a two-phase structure called a cloudy zone which is made up of small islands of tetrataenite within a matrix of Ni-poor taenite [Goldstein80, Albertsen78, 80b, 83, Danon83, Larsen84, Christiansen84]. Observations in meteorites indicate that tetrataenite can occur within a composition range of 46 to 52 at. % Ni [Albertsen83] and has lattice parameters $a = 3.5761 \pm 0.0005$ Å and $c = 3.5890 \pm 0.0005$ Å, resulting in a slight tetragonal distortion ($c/a = 1.0036 \pm 0.0002$) [Albertsen80, Albertsen81].

3.2 The Santa Catharina Meteorite: Epitaxially Stabilized Tetrataenite and Antitaenite

3.2.1 Introduction

The Santa Catharina meteorite, which originates from the island of Santa Catharina in Brazil and is classified as an anomalous ataxite, is composed primarily of Fe and Ni and has a bulk composition very close to the bulk composition of synthetic Invar alloys, 65 at. % Fe. Most known samples have been severely weathered, resulting in controversies regarding the original microstructure of the meteorite. The sample we have obtained from our collaborator Dr. Rosa Scorzelli of the Centro Brasileiro de Pesquisas Físicas (Rio de Janeiro, Brazil) is from the collection of the Musée d'Histoire Naturelle (Paris, France). Unlike other samples of the meteorite, this one is in pristine condition which enabled us to perform detailed measurement to elucidate its microstructure and characterize the phases present.

Much work has already been done on the Santa Catharina meteorite and it is known to be composed of a cloudy zone (CZ) where there is tetrataenite and disordered taenite [Danon78, 79a, 79b, 80a, Schroscher80, Jago82, Scorzelli82, 90, Goldstein90, 98, Miller89]. The microstructure of the CZ in the meteorite had not yet been clearly seen. In order to better characterize this meteorite, we have established a collaboration with Dr. Joseph Goldstein at the University of Massachusetts to do some high resolution scanning electron microscopy (HRSEM) and electron probe microanalysis (EPMA). In our own lab, we have performed transmission CEMS, MS at temperatures between 4.2 K and RT and XRD characterization. As we will show in this chapter, these analyses have revealed some very important insights on the properties of the Ni-rich phase which have important implications regarding the understanding of all FCC Fe-Ni alloys [Rancourt99].

3.2.2 Sample Preparation

The original sample we received from Dr. Scorzelli was shaped like a parallelepiped, with dimensions of 3 mm × 4 mm ×10 mm. In order to make an absorber for transmission MS experiments, four slices of ~100-120 μm × 3 mm × 4 mm were cut using a low-speed precision saw equipped with a thin diamond coated blade. The saw dust was also recovered for analysis.

The slices were arranged to form a rectangular absorber which was used to a take preliminary spectrum. To obtain an absorber with a more optimal thickness for low-temperature measurements, the slices were then sanded to a thickness of 52 ± 5 μm using 400 grit SiC powder and 600 grit alumina powder. Most Mössbauer measurements were performed on an absorber made with these ~50 μm slices.

After preliminary work on an SEM done with Dr. Shehata at CANMET, we found that the grounded surfaces of the slices were completely covered with embedded SiC and alumina crystallites, so the true thickness of the meteoritic material was close but less than 50 μm. Before pursuing more detailed microscopy studies, the samples were sanded again on 1200 grit paper and then etched using a mild solution of 5% hydrochloric acid (HCl) and 5% sulfuric acid (H_2SO_4) in water. This solution removed the SiC and alumina layer and exposed fresh meteoritic material free of defects induced by the mechanical stress of the polishing. We confirmed that the surface was representative of the bulk by performing CEMS measurements (see fig. 14). These slices were then used for more studies at CANMET and were then sent to Dr. Goldstein for HRSEM and EPMA measurements.

3.2.3 Characterization Using MS and Electron Microscopy Methods

3.2.3.1 Mössbauer Spectroscopy

3.2.3.1.1 Interpretation of the Mössbauer Spectrum

Fig. 12 shows the Mössbauer spectrum of the thick slice of the meteorite, untreated after they were cut. One can clearly distinguish three phases. Of the two magnetic phases, tetrataenite is most noticeable by its sharp lines and significant quadrupole shift, both indicative of the chemical order. The second magnetic phase corresponds to ordinary taenite which is chemically disordered, has broad lines and a mean quadrupole shift of zero. Finally, the dominant singlet, indicative of a paramagnetic phase is also attributed to antitaenite [Rancourt95b]. This name is used to distinguish it from ordinary taenite, as it has significantly different properties. Based on this spectrum, the meteorite appears to be free of oxides (in a measurable amount), even though the original sample had some apparent magnetite on the surface.

We have also recovered the powder which resulted from the sawing process ("saw-dust") and its spectrum is shown in fig. 13. The meteoritic phases have obviously been significantly transformed, and based on the large hyperfine field of the dominant sextet (z = 2.22 mm/s), it appears to be a BCC phase. As we shall see later, based on the known compositions of the phases, it is expected that the antitaenite would transform to the BCC phase when it is not epitaxially stabilized in an FCC structure by the tetrataenite. As had been found by Danon *et al.*, the meteorite microstructure is extremely sensitive to mechanical stress [Danon79]. Since the chemical ordering temperature of tetrataenite is only ~320 °C, the microstructure is also destroyed by heating the sample at, for example 800 °C for 24 h. [Danon80].

Because these samples are all considered thick in the Mössbauer sense, it is not possible to determine phase fractions without performing thickness corrections. To determine the composition of each phase, it is also necessary to know the bulk composition of the meteorite, obtained using EPMA. The following paragraphs detail some analyses that were conducted by electron microscopy methods.

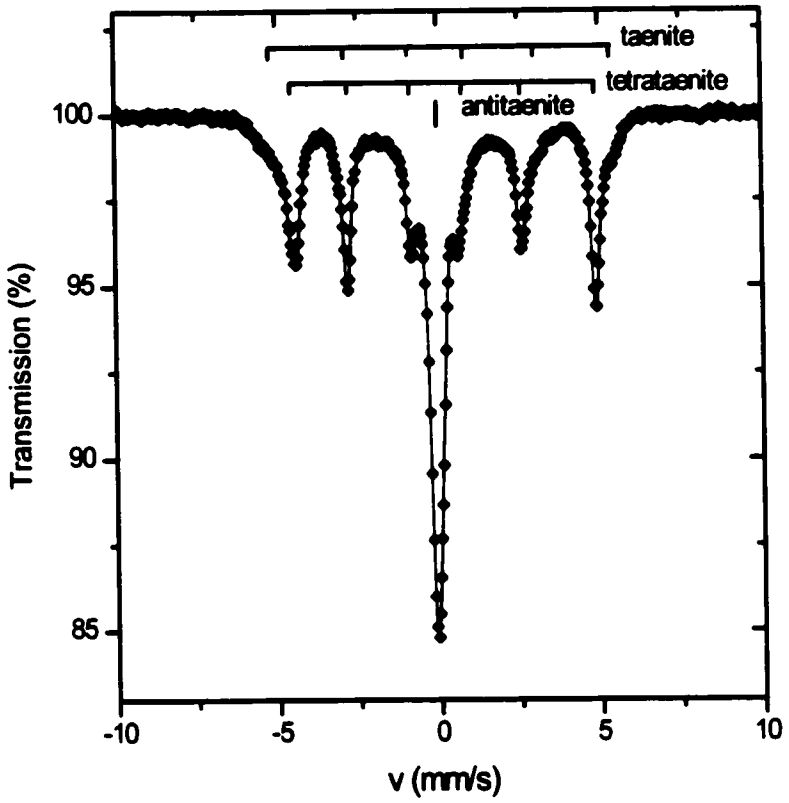

Figure 12 Absorption Mössbauer spectrum of the thick (100 μm) slices of the Santa Catharina meteorite. Three separate phases are noticeable: tetrataenite which is magnetic and characterized by a substantial asymmetry, ordinary taenite which is also magnetic and has broad lines and antitaenite which is seen as a paramagnetic singlet.

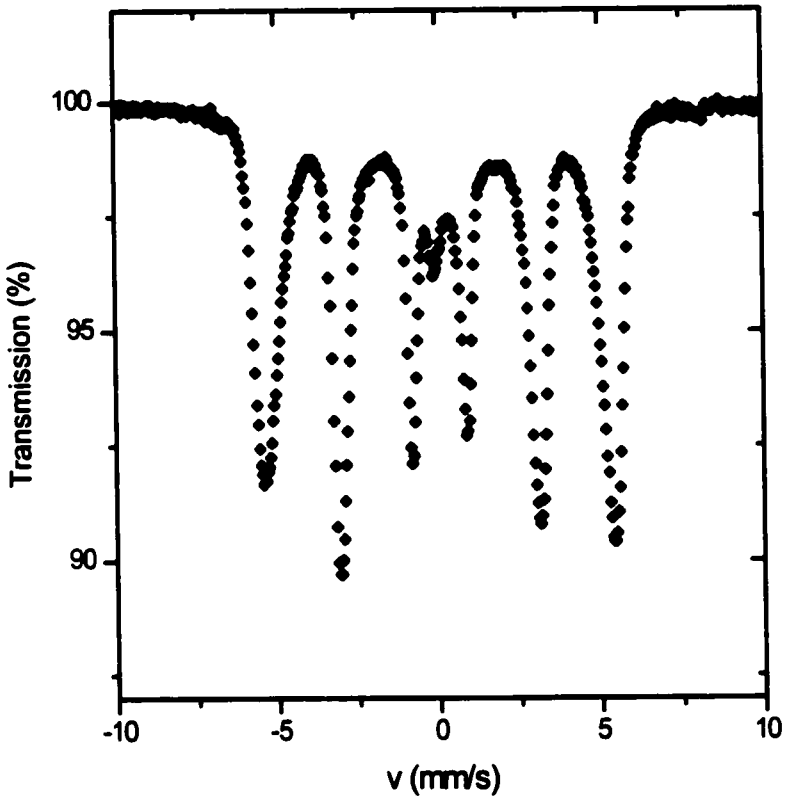

Figure 13 Mössbauer spectrum of the powder produced during the cutting of the SC meteorite slices. The sextet has parameters consistent with a BCC Fe-Ni alloy, indicating that most of the microstructure has been destroyed. The small paramagnetic peak is probably due to residual antitaenite which has not been transformed.

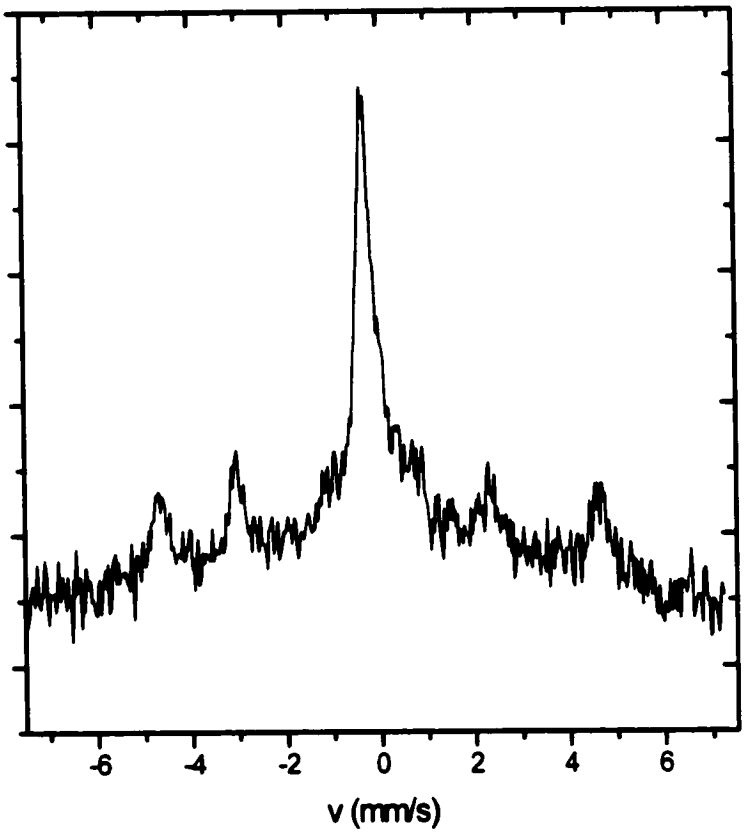

Figure 14 CEMS spectrum of a slice of the SC meteorite after etching with an acid solution (5 % vol. HCl, 5 % vol. H_2SO_4 in water). The asymmetry of the lines of tetrataenite and the paramagnetic line of antitaenite show that this surface is similar to the bulk. Cosine smearing due to the closeness of the source and the sample and the low signal-to-noise ratio preclude us from getting much more information from this spectrum.

Table 3 Parameters of the xVBF fit of the RT spectrum of the SC meteorite (fig. 12). Antitaenite is analysed as having a broad tail in its HFD.

χ^2	2.03					
bkg (counts)	2189050	166				
γ (mm/s)	0.1347	0.0038				
A (counts mm/s)	215705	7107	93903	6482	302318	2760
A_1/A_3	2.45	0.10	3	0	3	0
A_2/A_3	1.75	0.07	2	0	2	0
$\rho_{\delta\varepsilon}$	0	0	0	0	0	0
$\rho_{\delta z}$	0	0	0	0	1.00	0.08
$\rho_{\varepsilon z}$	-1.00	0.08	0	0	0	0
$<\delta>$(mm/s)	0.0480	0.0024	0.0568	0.0126	-0.0591	0.0029
σ_δ (mm/s)	0	0	0	0	0.0186	0.0047
$<\varepsilon>$(mm/s)	0.1678	0.0032	0	0	0	0
σ_ε (mm/s)	0.0296	0.0053	0	0	0	0
p_1	1	0	1	0	0.625	0
z_1	1.959	0.001	2.157	0.015	0.059	0.002
σ_{z1}	0.037	0.003	0.148	0.012	0.031	0.006
p_2					0.375	0.010
z_2					0.351	0.296
σ_{z2}					1.394	0.091

3.2.3.1.2 Extracting the Debye Temperatures of the Phases

Knowing the Debye temperatures of each of the phases of the meteorite is important for several reasons. First, the spectral area of the phases is related to the recoilless fraction of the phase, which can be calculated from the Debye temperature. Next, the thermal evolution of the *CS* is due solely to the *SOD*, as long as the *IS* is temperature independent. The *SOD* can also be calculated from the Debye temperature. It is possible to use either of these measurements (spectral areas or *CS*) to determine the Debye temperature by taking measurements at various temperatures. We have decided to use the *CS* since thickness corrections are needed to get spectral areas which are proportional to the recoilless fractions.

We have thus taken several measurements at RT and 80 K (fig. 15) of an absorber placed in a cold-finger liquid nitrogen cryostat (see chapter 2 for details). With this cryostat, the source is kept at RT, so the *CS*s can be compared directly. The measurements were taken in the exact same geometry to avoid geometrical artifacts. For measurements at 80 K, the sample was subjected to external vibrations due to the roughing pump (in one case) and due to the boiling of the liquid nitrogen in the cryostat. This causes broadening of the Mössbauer signal which inhibits detailed analysis of the peak widths and (possibly) areas. The spectra are shown in fig. 15 and the resulting parameters are given in table 4. Assuming that the *IS* does not change between these two measurements, we can calculate the Debye temperatures of each phase. These are listed in table 5. The value of 388 ± 12 K for tetrataenite is consistent with the known values of chemically disordered FCC Fe-Ni alloys (see chapter 4, fig. 35), while the value for antitaenite is somewhat larger than expected. The uncertainty on the Debye temperature of the ordinary taenite phase is much too large for it to be really meaningful, even though it close to the range of expected values [chapter 4]. Once the Debye temperature is known, we can also extract the *IS* from the *CS*. Again, the values for tetrataenite and taenite are consistent with the measured *IS*s in synthetic FCC Fe-Ni alloys [chapter 4]. The value for antitaenite is, however, very different and can only be explained by antitaenite having a different electronic structure than ordinary taenites [Rancourt99]. This will be discussed later as a proof that antitaenite is a new meteoritic mineral that is different from taenite at the electronic structure level.

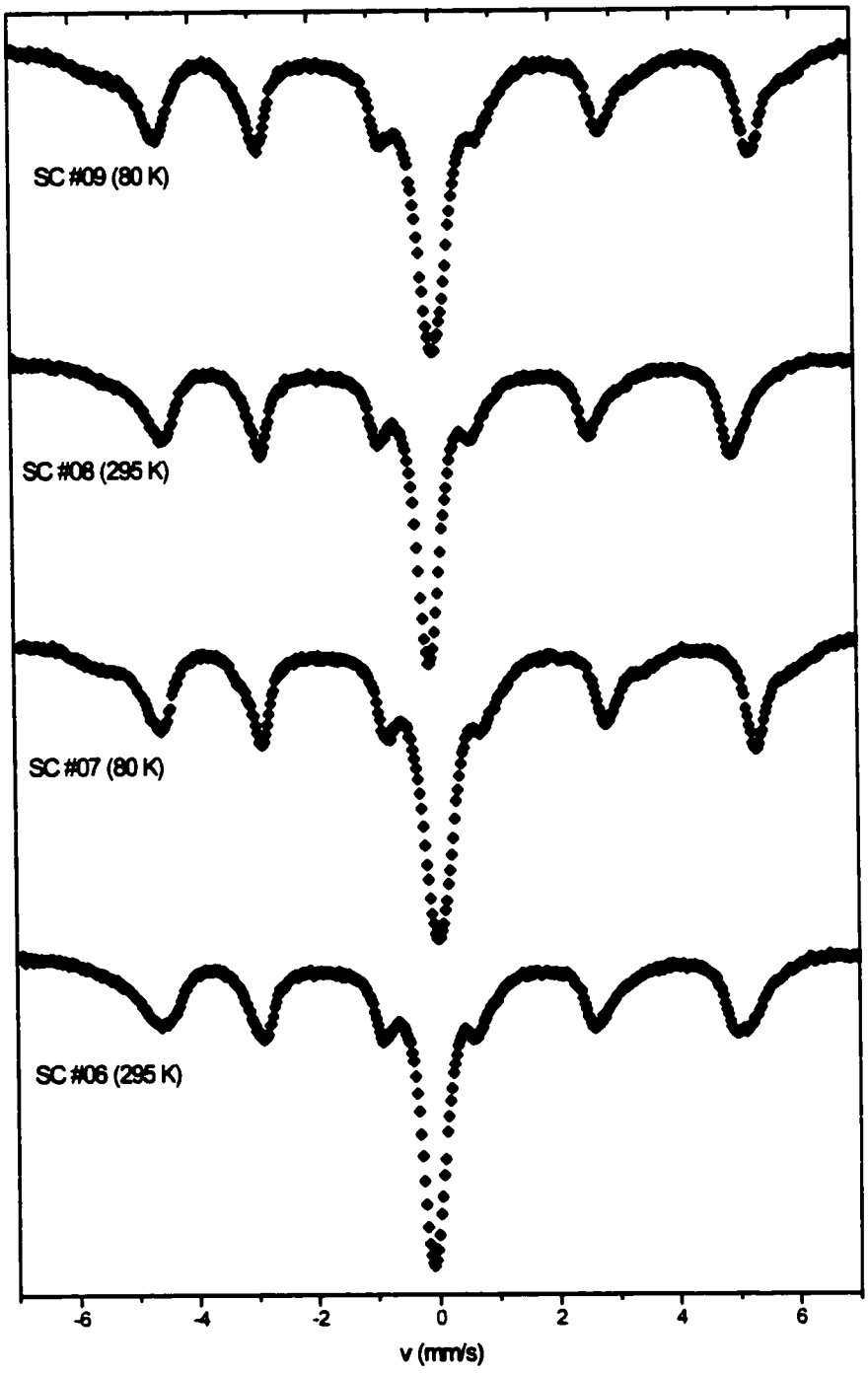

Figure 15 Mössbauer spectra of the SC meteorite at 80 K and 295 K. The top two spectra are taken with the roughing pump turned off, while the bottom two have the pump activated which results in noticeable broadening. Notice also the broadening of the antitaenite's signal at 80 K.

Table 4 Parameters of the xVBF fits to the spectra of the SC meteorite shown in fig. 4. 2-σ (95 %) fitting uncertainties are given in the second column of each parameter. Unless specified, the correlations parameters were 0.

Sckl006	295	2.60	1840570	364	0.147	0.011
Sckl007	80	2.12	1607220	347	0.170	0.004
Sckl008	295	2.70	1981460	298	0.147	0.006
Sckl009	80	1.41	1310870	279	0.191	0.005

Sckl006	206223	8119	2.43	0.12	1.73	0.06	-0.57	0.64	0.0357	0.0037	0.1854	0.0042
Sckl007	186292	3494	2.06	0.07	1.57	0.06	-1.00	0.10	0.1576	0.0032	0.1885	0.0040
Sckl008	192042	4539	2.31	0.11	1.66	0.08	-0.87	0.39	0.0379	0.0033	0.1875	0.0040
Sckl009	147996	4499	2.10	0.09	1.61	0.08	-1.00	0.18	0.1564	0.0033	0.1903	0.0040
taenite												
Sckl006	83418	7323	3	0	2	0	0	0	0.0468	0.0143	0	0
Sckl007	86729	4489	3	0	2	0	0	0	0.1744	0.0107	0	0
Sckl008	82900	5061	3	0	2	0	0	0	0.0444	0.0143	0	0
Sckl009	65023	5196	3	0	2	0	0	0	0.1708	0.0134	0	0
antitaenite												
Sckl006	255772	8890	3	0	2	0	0	0	-0.0904	0.0023	0	0
Sckl007	210405	3489	3	0	2	0	0	0	0.0246	0.0017	0	0
Sckl008	244828	5684	3	0	2	0	0	0	-0.0921	0.0021	0	0
Sckl009	152818	2774	3	0	2	0	0	0	0.0199	0.0015	0	0

Sckl006	0.017	0.023	1	0	2.023	0.003	0.086	0.004
Sckl007	0.027	0.008	1	0	2.088	0.002	0.040	0.004
Sckl008	0.021	0.014	1	0	1.996	0.002	0.055	0.004
Sckl009	0.026	0.010	1	0	2.079	0.002	0.043	0.004
taenite								
Sckl006	0	0	1	0	2.233	0.016	0.160	0.014
Sckl007	0	0	1	0	2.377	0.010	0.161	0.011
Sckl008	0	0	1	0	2.189	0.011	0.145	0.010
Sckl009	0	0	1	0	2.356	0.016	0.163	0.014
antitaenite								
Sckl006	0	0	0.644	0	0.052	0.003	0.032	0.010
Sckl007	0	0	0.726	0	0.069	0.001	0.039	0.003
Sckl008	0	0	0.647	0	0.049	0.002	0.031	0.008
Sckl009	0	0	0.767	0	0.065	0.002	0.029	0.005

Sckl006	0.356	0.031	0.223	0.443	1.222	0.187
Sckl007	0.274	0.014	0.082	0.283	1.141	0.089
Sckl008	0.353	0.018	0.045	0.312	1.338	0.113
Sckl009	0.233	0.016	0.224	0.288	0.933	0.101

Table 5 Extracted Debye temperature and isomer shift for the various phases of the SC meteorite, based on the analyses in table 4. 2-σ (95 %) uncertainties are given in the second column of the parameters.

tetrataenite	388	24	0.2706	0.0034
taenite	340	94	0.2753	0.0133
antitaenite	435	14	0.1472	0.0020

In order to better understand the differences between the Debye temperatures of tetrataenite and antitaenite, we have reanalysed the *CS* data published by De Grave *et al.* [DeGrave92] which is reproduced in fig. 16. If the *CS* data is fit assuming the *IS* is temperature independent,

$$CS(T) = IS + SOD(\Theta_D, T) \tag{29}$$

with *IS* and Θ_D as the only adjustable parameters, we get the results shown in table 6. The value for tetrataenite is quite high, but the uncertainty in this calculation is most likely larger than what is obtained from the fit. We will thus use the value of Θ_D = 388 ± 12 K (1-σ) for tetrataenite, as found by our own measurement and as is consistent with the Debye temperatures of synthetic FCC Fe-Ni alloys [chapter 4]. On the other hand, the extracted Θ_D for antitaenite is again unrealistically high considering it is an FCC Fe-Ni alloy and so it cannot be much different from other alloys. When investigating the residuals of the fit (fig. 17), we see systematic deviations, which indicate that the fitting model (constant *IS*) is incorrect. We can also see in fig. 18 that the difference between the *CS* of tetrataenite, which does behave as expected, and the *CS* of antitaenite is unusual and cannot be explained, even by a very large difference in Debye temperatures of the two phases. In fact, as shown in fig. 18, a difference in Debye temperature would be mostly noticeable at low temperature (below 200 K), whereas the difference between the two CSs is practically constant up to 300 K. Based on this analysis, we thus estimate that the Debye temperature of antitaenite is the same (or similar) as the Debye temperature of tetrataenite and that the thermal evolution of the difference between the measured CSs of tetrataenite and antitaenite (fig. 18) is actually due to a change in the *IS* of antitaenite with temperature. This hypothesis is corroborated by measurements of the *IS* at high temperature in synthetic Fe-rich FCC Fe-Ni alloys, as presented in chapter 6. We shall thus also use a value of Θ_D = 388 K for

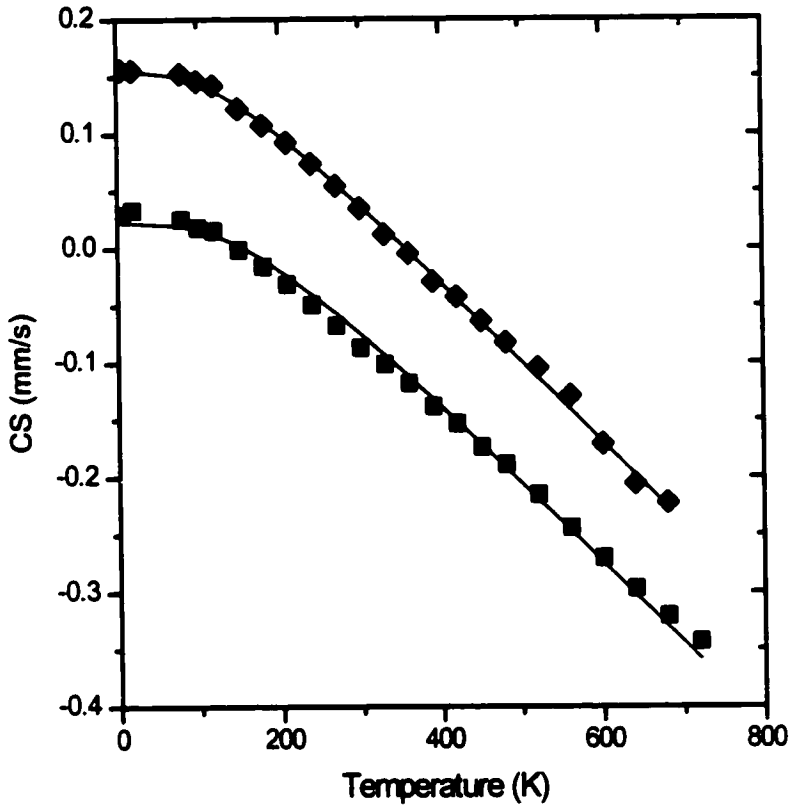

Figure 16 Temperature dependence of the centre shifts of the tetrataenite (◆) and antitaenite (■) phases of the Santa Catharina meteorite, as measured by De Grave *et al.* [DeGrave92]. The solid lines represent the best fit to a model where the *IS* does not change with temperature.

antitaenite.

Table 6 Extracted Debye temperature and isomer shift for tetrataenite and antitaenite based on the data from De Grave [DeGrave92] shown in fig. 16. 2-σ (95 %) uncertainties are given in the second column of the parameters.

tetrataenite	465	10	0.282	0.005
antitaenite	595	10	0.186	0.005

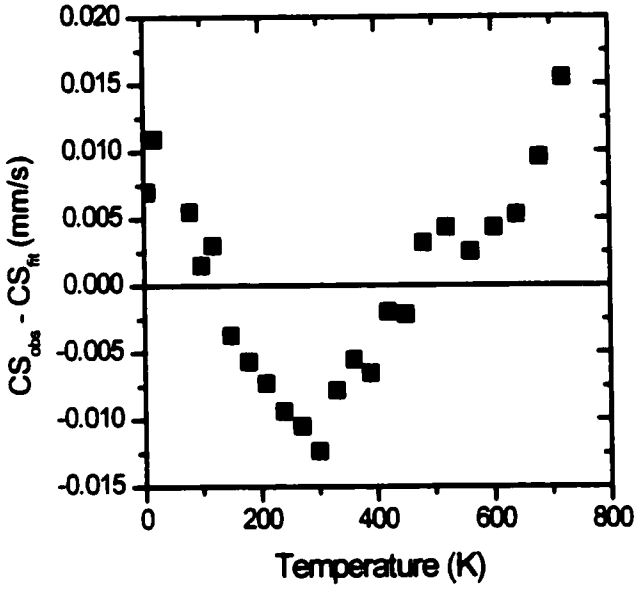

Figure 17 Residuals of the fit of the *CS* of antitaenite assuming a constant *IS*. In addition to yielding an unrealistic value of Θ_D = 595 K, the regularity of the deviations indicates the fitting model is incorrect. [data from DeGrave92]

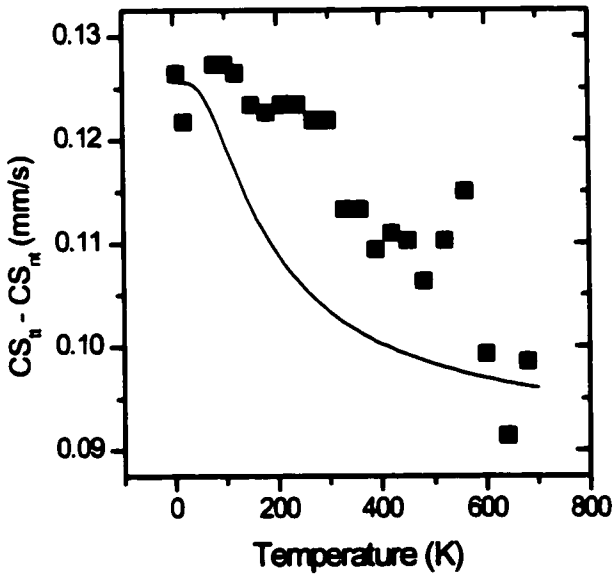

Figure 18 Difference between the measured *CS* of tetrataenite (tt) and antitaenite (nt). The solid line represents what the difference would be, assuming there *IS*s are independent of temperature and there is a difference of 130 K in their Debye temperatures ($\Theta_{D,tt}$ = 380 K and $\Theta_{D,nt}$ = 510 K chosen such that the highest and lowest temperature data match). [data from DeGrave92]

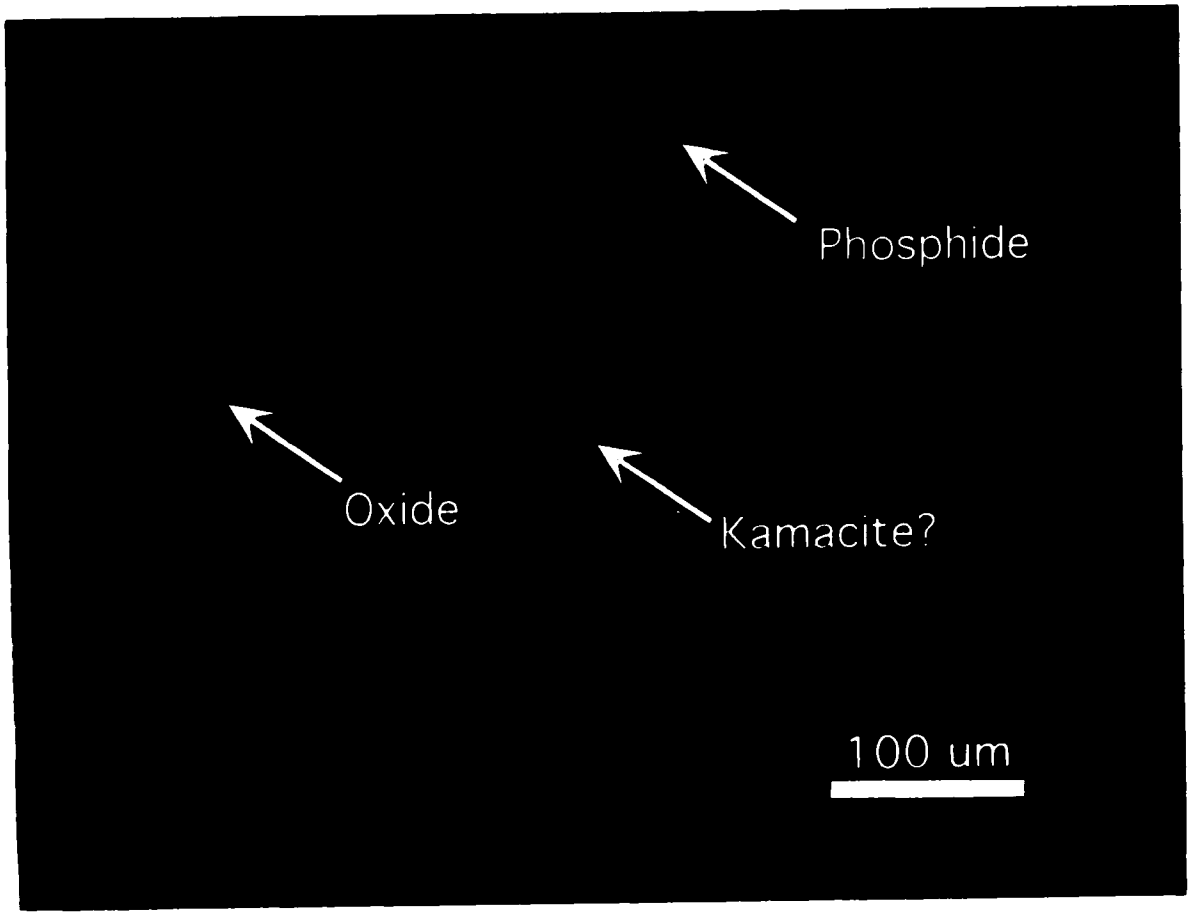

Figure 19 SEM secondary electron image of the SC meteorite, showing the dominant CZ as well as some iron phosphide and oxide. Based on other images, the presence of phosphides is not characteristic of the sample, but is showed here as an illustration of the technique.

Figure 20 HRSEM secondary electron image of the CZ microstructure which shows the tetrataenite islands (light) in an antitaenite honeycomb matrix (dark).

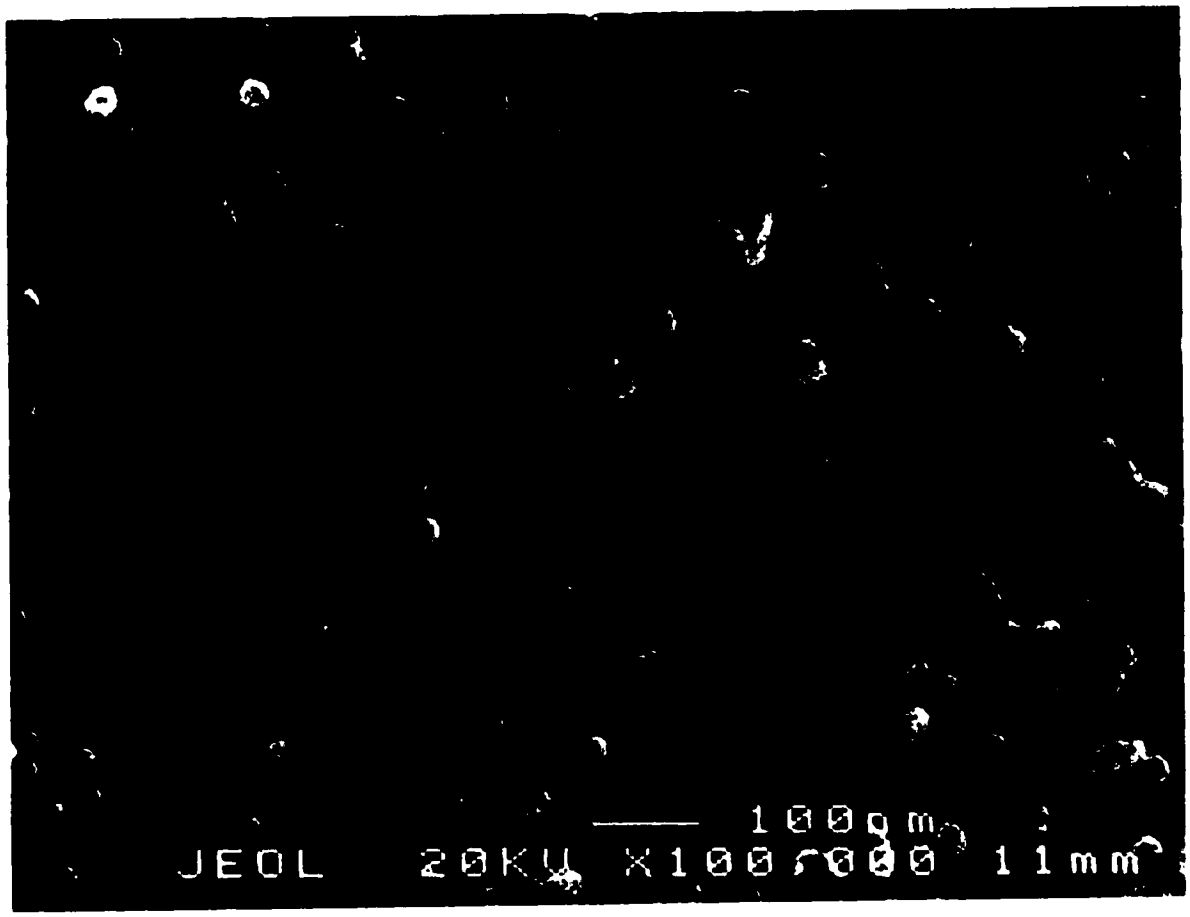

Figure 21 HRSEM secondary electron imaging of the CZ microstructure. In this image, it is clear that the etching has preferentially removed the antitaenite phase, as tetrataenite globules can be seen extruding from the surface.

3.2.3.2 Imaging of the Tetrataenite/Antitaenite Intergrowth

Figures 19, 20 and 21 show three images at different magnifications which were taken by Rob J. Reisner (under the direction of Dr. J. I. Goldstein) using secondary electron imaging in an HRSEM with a field emission electron gun. In Fig. 19, which is taken near the side of one of the slices, one can see that the meteorite is entirely composed of a cloudy zone (CZ) microstructure but also indicates the presence of iron phosphides and iron (with Ni substitution) oxides. As stated earlier, the oxides are not clearly noticeable in the Mössbauer spectrum, indicating that they are not as abundant as it may seem based on this image. The second image (fig. 20) is a high magnification image of the CZ. In this image one can clearly see two distinct phases: tetrataenite appears as islands of 30-50 nm in diameters and antitaenite serves as a honeycomb matrix in which the tetrataenite has grown. The typical thickness of this matrix is ~10 nm between the tetrataenite grains. It is possible to identify the tetrataenite and the antitaenite based on their compositions. Tetrataenite is roughly 50 at. % Ni, whereas the composition of antitaenite is known to be at least more than 71 at. % Fe (otherwise it would be magnetic at RT, see chapters 4 and 6). Because of the greater average Z value (number of electrons per atom, $Z_{Fe} = 26$ and $Z_{Ni} = 28$) in tetrataenite, it appears slightly lighter in a secondary electron image. Fig. 21, taken with the sample surface off-perpendicular also shows a similar magnification image of the CZ. When comparing figs. 20 and 21, it is possible to see from fig. 21 that the acid etching used to prepare the sample preferentially etched away the antitaenite, leaving mounds of tetrataenite protruding from the surface. These images provide clear observation of the microstructure of the CZ in the Santa Catharina meteorite [Rancourt99] and show how intricately linked the two phases are. As will be explained later, the ordinary taenite phase is associated with chemically disordered $Fe_{50}Ni_{50}$ which most likely is found within the tetrataenite islands (which would thus be constituted of partially ordered tetrataenite) or on the edges of the tetrataenite islands as slow diffusion prevented sufficient chemical ordering to occur.

3.2.3.3 Electron Probe Micro-Analysis

The bulk composition of the non-oxidized CZ in the SC meteorite was determined by electron probe microanalysis (EPMA). The average of ten spot measurements yields a

composition of 33.0 ± 0.3 wt. % Ni, 66.2 ± 0.5 wt. % Fe, 0.54 ± 0.03 wt. % Co and 0.01 to 0.43 wt. % P [Goldstein98, Rancourt99], which converts to 31.9 ± 0.3 at. % Ni, 67.2 ± 0.5 at. % Fe, 0.52 ± 0.03 at. % Co and 0.48 ± 0.5 at. % P. Because of the small scale of the microstructure, it is not possible to obtain EPMA measurements of the individual tetrataenite or antitaenite phases. With a thick slice such as the ones used here, the interaction volume in which x-rays are produced is much larger than the size of each phase (and indeed much larger than the spot size of the electron beam). Such a measurement would be possible with a sample prepared for TEM use, as it would have a very fine thickness and the EPMA spatial resolution would be the same as the electron beam size. Unfortunately, the sample preparation for such a measurement is difficult and we could not arrange for these measurements to be performed.

3.2.4 Composition of Antitaenite

One of the strengths of Mössbauer spectroscopy is that the spectral areas can directly be related to the proportions of the phases in a sample. Knowing the bulk composition of the meteorite and the composition of tetrataenite, it is thus possible to determine the composition of the antitaenite phase.

In the case of a thin absorber (in the Mössbauer sense), the spectral area A_i of a phase is directly proportional to the product of the recoilless fraction $f_{a,i}$ and the number of ^{57}Fe atoms $n_{a,i}$ present in the phase:

$$A_i \propto f_{a,i}\, n_{a,i}. \tag{30}$$

If two phases i and j have the same recoilless fractions, then

$$A_i / A_j = n_{a,i} / n_{a,j}, \tag{31}$$

and it is sufficient to know their relative spectral areas to compare the amount of Fe in each of them. In order to determine the composition of antitaenite, it is thus necessary to determine the recoilless fractions (which can be calculated based on the Debye model) and the spectral areas of each phase present in the spectrum, in the thin absorber limit. Because the 50 μm slices are thick ($t_a \approx 11$), it is necessary to perform thickness corrections on the spectrum, before determining relative spectral areas. In particular, because the antitaenite phase is a sharp singlet, its area is underestimated (because it saturates more than the other phases) in the measured spectrum. Since we already determined that all phases have essentially the same Debye temperature ($\Theta_D \approx 380$

Table 7 Fitted phase fractions (Fe content) of the various phases of the SC meteorite based on ^{57}Fe MS. The spectra were corrected for thickness effects using the method of Rancourt [Rancourt89].

Sckl016 *	295	25.0	15.7	59.4
Sckl010 *	77	27.9	17.0	55.0
Sckl017 *	4.2	30.4	17.5	52.2
average		*27.8*	*16.7*	*55.5*

K), their relative spectral areas will be directly proportional to their relative Fe contents.

To perform thickness corrections, it is necessary to know the number of ^{57}Fe atoms per area in the absorber. Based on XRD measurements, the atomic volume of the tetrataenite and antitaenite phases is the same, V = 11.475 Å^3/atom. The measured average thickness of the slices is 52 ± 5 μm. Knowing that the atomic fraction of Fe is 67.2 % and the natural isotopic fraction of ^{57}Fe is 2.1 % [Mössbauer Effect Data Center89], this leads to n_a = 6.5 × 10^{18} ^{57}Fe atoms/cm^2. Because these slices were found to be embedded with SiC and alumina particles, it is fair to estimate the true number to be between 5.5 and 6.0 × 10^{18} ^{57}Fe atoms/cm^2. Table 7 shows the results of the analyses of three thickness corrected spectra, taken at RT (295 K), LN_2T (77 K) and LHeT (4.2 K) but in otherwise identical conditions in an exchange-gas type cryostat [chapter 2]. Thickness corrections were performed using n_a = 5.5 × 10^{18} ^{57}Fe atoms/cm^2. Using n_a = 6.0 × 10^{18} ^{57}Fe atoms/cm^2 results in the antitaenite phase proportion to be at most 1% larger. Complete details regarding these spectra will be given in section 3.2.6 which deals specifically with low-temperature measurements.

Based on these results, we attribute the phase fraction (of Fe content) of antitaenite to be 55.5 ± 2 %. The Zeeman splitting (z = 2.12 mm/s at RT) and extrapolated T_C (data from [DeGrave92]) of the ordinary taenite phase indicate that it has a Fe content of approximately 55 at. %. Since we know the total Fe content of the meteorite, we can determine the Fe content of antitaenite, the only phase with an unknown composition. Let N_{Fe} be the total number of Fe atoms in the meteorite sample and c_0 be the bulk atomic fraction of Fe. Let c_{at}, c_{tt} and c_t be the Fe content of antitaenite, tetrataenite and the ordinary taenite phases, respectively. Let N_{at}, N_{tt} and N_t be the numbers of atoms in the three phases. Then the measured thin limit relative ^{57}Fe Mössbauer phase fractions are:

$$p_{at} = \frac{c_{at} N_{at}}{N_{Fe}}, \; p_{tt} = \frac{c_{tt} N_{tt}}{N_{Fe}} \quad \text{and} \quad p_t = \frac{c_t N_t}{N_{Fe}}. \tag{32}$$

We also have

$$N_{at} + N_{tt} + N_t = \frac{N_{Fe}}{c_0}. \tag{33}$$

These two equations lead to

$$\frac{p_{at}}{c_{at}} + \frac{p_{tt}}{c_{tt}} + \frac{p_t}{c_t} = \frac{1}{c_0}, \tag{34}$$

or

$$c_{at} = p_{at}\left[\frac{1}{c_0} - \frac{p_{tt}}{c_{tt}} - \frac{p_t}{c_t}\right]^{-1}. \tag{35}$$

Using c_0 = 67.2 %, c_{tt} = 50 %, c_t = 55 %, p_{at} = 55.5 %, p_{tt} = 27.8 % and p_t = 16.7 %, we find that the atomic fraction of Fe in antitaenite is 88 %. Without more knowledge, we must assume that the balance is Ni, Co and P in the same relative amounts as in the bulk. The phosphorus likely only occurs as phosphides, so the metal fraction would only contain Fe and Ni with trace amounts of Co. The uncertainty on this calculation is ~5 % and is primarily due to the uncertainty on the compositions of tetrataenite, which can occur with concentrations between 48 and 54 at. % Fe [Albertsen83], and of the ordinary taenite (the uncertainty on c_t is most likely 3 %), as well as the uncertainty in the Fe phase fractions based on the three spectra which were analysed. The variability between the various measurements of the Fe phase fractions shown in table 7 is most likely due to inaccurate thickness correction because of various artifacts such as inhomogeneous thickness and crystallographic texture. Even with such problems, it is possible to get reasonably precise phase fractions. We also calculate that antitaenite represents 43 % of the total atomic fraction of the meteorite ($N_{at}/N = c_0 p_{at}/c_{at}$), which is reasonable based on the SEM image in fig. 20.

It is quite extraordinary that antitaenite, being so Fe rich can exist in the FCC phase, as it is known that Fe-Ni alloys with compositions above ~70 at. % Fe usually undergo a martensitic transition at or below RT. Is is quite remarkable also that it does not undergo the martensitic transition, even after cycling down to 4.2 K. The extremely small scaled intergrowth between tetrataenite and antitaenite, as seen in fig. 20, provides an explanation. Just as γ-Fe can be stabilized as a precipitate in an FCC Cu matrix [Newkirk57] or as a thin film [Keune77], the

epitaxial intergrowth with FCC tetrataenite keeps the antitaenite in the FCC phase. However, as stated previously, mechanical stress can destroy the microstructure, which results in most of the meteorite undergoing the martensitic transition. We should also mention that antitaenite is most likely not a uniform phase (composition-wise), but might exhibits a composition gradient as is often found in the CZ of meteorites [Goldstein90].

As previously stated, tetrataenite is often found in combination with Ni-poor taenite [Albertsen83, Rancourt95b], which we call antitaenite. The actual composition of the antitaenite phase will probably vary from meteorite to meteorite and also within each meteorite, but antitaenite is always characterized by having the same lattice parameter as tetrataenite and being paramagnetic at RT. As will be explained in chapter 6, these Fe-rich (Ni-poor) FCC Fe-Ni alloys are found to be low moment alloys (the moment magnitude on the Fe and Ni atoms is significantly smaller than in ordinary taenite) which exhibit antiferromagnetic order at low temperatures. This is the reason for giving these alloys a different name than ordinary taenite [Rancourt95b].

3.2.5 Saturation Magnetization of Antitaenite

Dr. Scorzelli, the collaborator who provided us with the meteorite samples, also did, with the help of Dr. Rechenberg, some interesting measurements on SC samples when subjected to an external magnetic field. We present here the measurement of the saturation magnetization of the sample, which will enable us to determine the saturation magnetization of antitaenite.

Using the data measured by Dr. Rechenberg, we have determined the saturation magnetization to be 112 emu/g or 1.14 μ_B/atom (calculated using the measured bulk composition of our sample). Based on ESCs, the saturation magnetization in tetrataenite is roughly 5 % larger than in disordered $Fe_{50}Ni_{50}$ for which μ_{sat} = 1.69 μ_B/atom (see fig. 32, chapter 4). We thus estimate the saturation magnetization in tetrataenite to be μ_{sat}(tt) = 1.77 μ_B/atom. The saturation magnetization of the ordinary taenite phase ($Fe_{55}Ni_{45}$) is also μ_{sat}(t) = 1.77 μ_B. Since we have determined the atomic phase fractions of each phase, we can calculate the saturation magnetization of antitaenite as being μ_{sat}(nt) = 0.30 ± 0.05 μ_B/atom, which is consistent with reported values of Fe-rich LM alloys. Keep in mind that we have not taken into account iron oxides or phosphides which are present in the meteorite and which can carry a large

magnetic moment. The indicated value is thus an upper range for the saturation moment of antitaenite.

3.2.6 Temperature Dependence of the Mössbauer Parameters

We have performed Mössbauer measurements on the SC meteorite at temperatures between 4.2 K (LHeT) and 295 K (RT) in order to determine if and at what temperature antitaenite would exhibit magnetic order. The measurements were performed using the same sample as previously (using four 50 μm slices) in the helium cryostat described in chapter 2. In this cryostat, the source is also refrigerated, but is most likely at a slightly different temperature than the sample. Because only the sample temperature is known, it is not possible to use the measured *CS*s to determine the *IS*, since the *SOD* correction is unknown. The spectra are shown in figs. 22 and 23. Because of the relatively low signal-to-noise ratio, only a simple analysis model was used. The xVBF model was used with HFD for all three phases, with area ratios 3:2:1 fixed except for tetrataenite (A_2/A_3 was free). Also, only tetrataenite was allowed a quadrupole shift.

Tables 8 list the results of the analyses. These results show that the only phase which shows any significant change with temperature is the antitaenite phase. The Zeeman splittings in both tetrataenite and ordinary taenite increase slightly with temperature, as expected and shown in fig. 24a and b, and the quadrupole shift of tetrataenite seems to remain constant throughout the temperature range (fig. 24c). The important change evident from these measurements is the onset of magnetic order in the antitaenite phase, as manifested by an increased width below ~60 K. In fig. 25, we have plotted the FWHM of the antitaenite peak as a function of temperature. As in γ-Fe, even at 4.2 K, the Zeeman splitting is insufficient to produce a well resolved sextet [Keune77], thereby showing that like γ-Fe, antitaenite is a low-moment phase which exhibits a reduced Fe magnetic moment ($\mu_{Fe} \approx 0.5\ \mu_B$) compared to the ordinary taenites which have large Fe moment magnitudes ($\mu_{Fe} \approx 2.8\ \mu_B$).

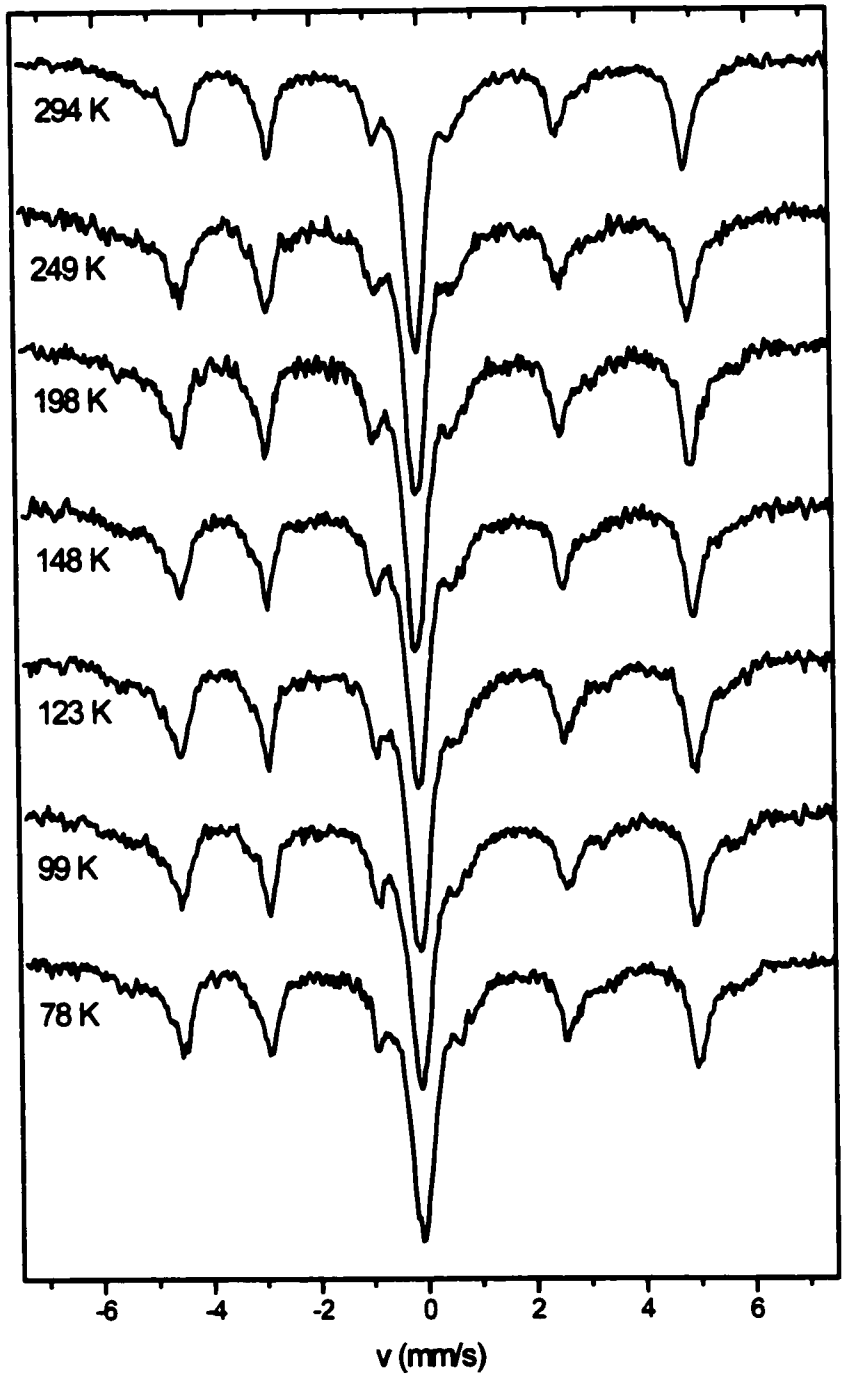

Figure 22 Mössbauer spectra of the SC meteorite from LN_2T to RT, as indicated.

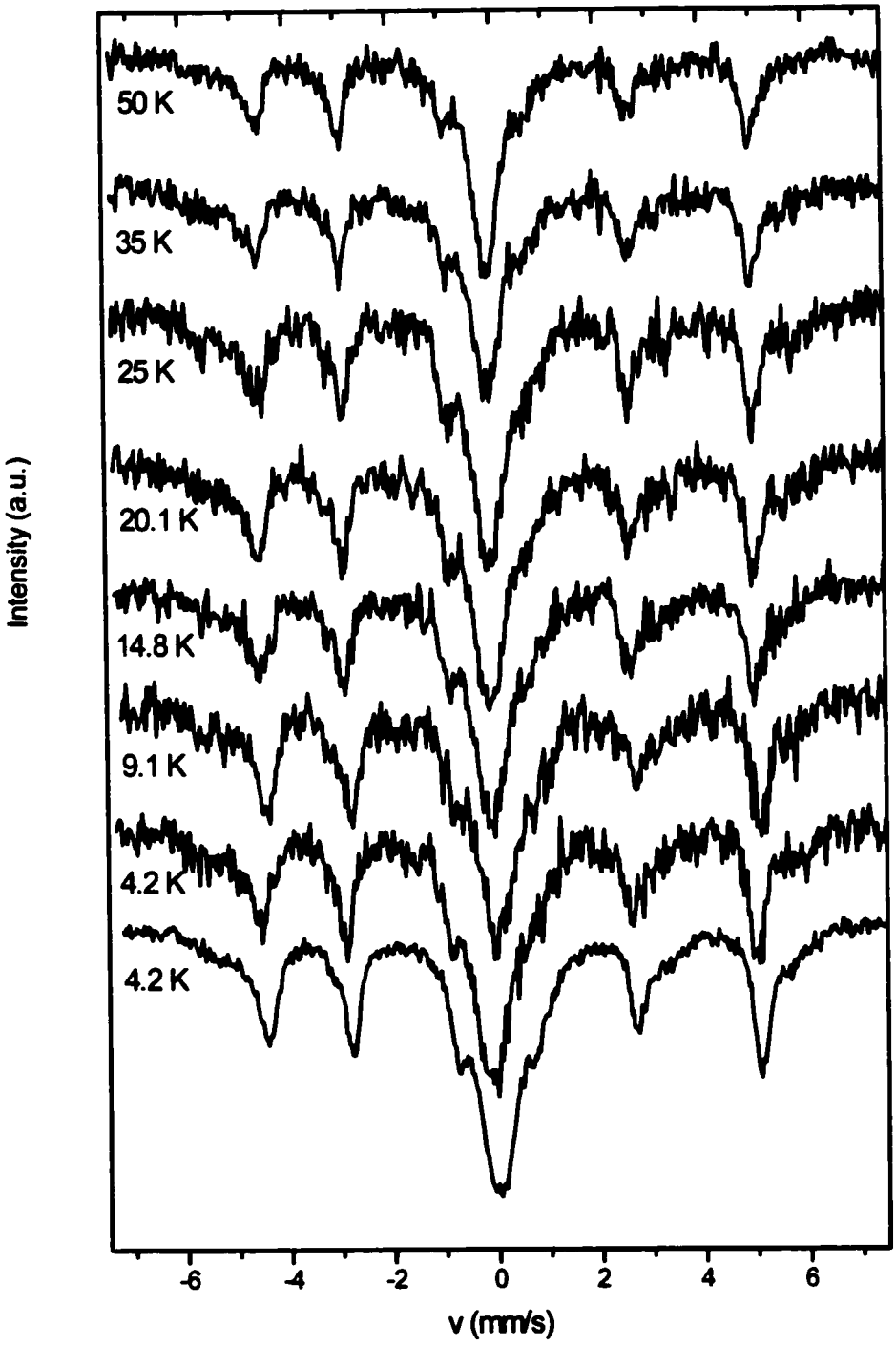

Figure 23 Mössbauer spectra of the SC meteorite from LHeT to 50 K, as indicated.

Table 8 Parameters of the xVBF fits of the low temperature MS spectra of the SC meteorite. 2-σ (95 %) fitting uncertainties are given in the second column for each parameter.

Sckl016	294	0.73	704703	183	0.129	0.009
Sckl015	249	0.65	246038	83	0.148	0.012
Sckl014	198	0.62	227504	97	0.153	0.016
Sckl013	148	0.68	236146	58	0.129	0.006
Sckl012	123	0.79	287905	38	0.139	0.005
Sckl011	98.7	0.85	264708	65	0.142	0.010
Sckl010	78	0.62	252793	68	0.144	0.014
Sckl025	50	0.85	52875	55	0.123	0.019
Sckl024	35	0.93	42928	19	0.125	0.018
Sckl023	25	0.93	37384	49	0.108	0.021
Sckl022	20.1	0.82	38493	75	0.141	0.018
Sckl021	14.8	0.81	38009	57	0.119	0.016
Sckl018	9.1	0.79	38445	42	0.130	0.032
Sckl017	4.2	1.22	480508	174	0.148	0.013
Sckl020	4.2	0.85	39624	33	0.140	0.029

Sckl016	32290	1778	2.02	0.12	0.0423	0.0045	0.1873	0.0050	1.9490	0.0020	0.0328	0.0081
Sckl015	12906	1213	2.07	0.16	0.0290	0.0050	0.1890	0.0081	1.9693	0.0035	0.0333	0.0087
Sckl014	13369	1000	2.11	0.12	0.0112	0.0061	0.1988	0.0072	1.9861	0.0033	0.0251	0.0126
Sckl013	14189	787	2.05	0.08	0.0228	0.0047	0.1940	0.0065	1.9916	0.0035	0.0388	0.0067
Sckl012	18807	600	1.96	0.07	0.0176	0.0029	0.1867	0.0022	2.0012	0.0014	0.0428	0.0028
Sckl011	16959	1012	2.08	0.09	0.0267	0.0044	0.1892	0.0055	2.0015	0.0032	0.0303	0.0088
Sckl010	15854	1305	2.12	0.13	0.0336	0.0050	0.1921	0.0062	2.0028	0.0028	0.0317	0.0077
Sckl025	3607	295	2.18	0.27	0.0293	0.0069	0.1901	0.0112	2.0078	0.0054	0.0431	0.0091
Sckl024	2918	218	2.13	0.19	0.0309	0.0067	0.1851	0.0077	2.0091	0.0045	0.0359	0.0183
Sckl023	2343	326	2.21	0.33	0.0361	0.0109	0.1928	0.0141	2.0052	0.0065	0.0416	0.0139
Sckl022	3018	328	2.10	0.18	0.0286	0.0082	0.1873	0.0098	2.0106	0.0042	0.0306	0.0110
Sckl021	2766	383	2.12	0.22	0.0392	0.0108	0.1993	0.0109	2.0067	0.0066	0.0527	0.0126
Sckl018	2680	436	1.83	0.23	0.1390	0.0107	0.1859	0.0156	2.0038	0.0073	0.0385	0.0124
Sckl017	35989	2437	2.20	0.12	0.1377	0.0045	0.1877	0.0056	2.0014	0.0029	0.0331	0.0073
Sckl020	2988	519	2.26	0.28	0.0340	0.0104	0.1881	0.0128	2.0093	0.0062	0.0309	0.0152

Sckl016	19804	1881	0.019	0.014	2.119	0.017	0.144	0.019
Sckl015	8920	1456	0.010	0.025	2.175	0.030	0.188	0.030
Sckl014	9971	959	-0.022	0.023	2.209	0.022	0.196	0.017
Sckl013	9629	1146	-0.017	0.014	2.223	0.022	0.184	0.018
Sckl012	11526	713	0.028	0.011	2.247	0.012	0.179	0.009
Sckl011	12013	938	0.006	0.019	2.257	0.022	0.190	0.015
Sckl010	11616	1320	0.021	0.022	2.258	0.028	0.192	0.023
Sckl025	2188	450	-0.021	0.049	2.235	0.037	0.178	0.031
Sckl024	2360	309	-0.016	0.021	2.240	0.034	0.190	0.021
Sckl023	2715	881	0.024	0.047	2.244	0.054	0.265	0.065
Sckl022	2631	576	0.019	0.031	2.283	0.044	0.207	0.042
Sckl021	2373	516	0.007	0.037	2.256	0.038	0.210	0.052
Sckl018	1870	518	0.129	0.030	2.280	0.034	0.171	0.050
Sckl017	26261	2682	0.121	0.015	2.246	0.018	0.193	0.021
Sckl020	2392	460	0.028	0.034	2.257	0.047	0.192	0.035

Sckl016	50617	3712	-0.0729	0.0019	0.589	0	0.0508	0.0026	0.0303	0.0062
Sckl015	18917	1199	-0.0895	0.0025	0.614	0	0.0521	0.0029	0.0132	0.0112
Sckl014	18671	2266	-0.1124	0.0044	0.625	0	0.0528	0.0185	0.0244	0.0228
Sckl013	19461	455	-0.1040	0.0017	0.659	0	0.0018	0.0175	0.0837	0.0037
Sckl012	28676	515	-0.1048	0.0013	0.554	0	0.0602	0.0015	0.0410	0.0079
Sckl011	23871	618	-0.0978	0.0029	0.644	0	0.0009	0.0291	0.0862	0.0098
Sckl010	22937	990	-0.0890	0.0033	0.656	0	0.0340	0.0332	0.0841	0.0286
Sckl025	5184	548	-0.0944	0.0076	0.590	0	0.0781	0.0096	0.0622	0.0135
Sckl024	4509	273	-0.1099	0.0061	0.594	0	0.0969	0.0090	0.0758	0.0228
Sckl023	3828	688	-0.0881	0.0114	0.632	0	0.1201	0.0156	0.0885	0.0335
Sckl022	4488	1620	-0.0989	0.0084	0.593	0	0.1096	0.0082	0.0745	0.0148
Sckl021	4189	1074	-0.0887	0.0101	0.598	0	0.1194	0.0076	0.0749	0.0136
Sckl018	4494	741	0.0007	0.0119	0.546	0	0.1296	0.0108	0.0863	0.0305
Sckl017	50236	1362	0.0051	0.0048	0.492	0	0.1272	0.0059	0.0756	0.0101
Sckl020	4586	214	-0.1027	0.0118	0.520	0	0.1265	0.0139	0.0761	0.0284

Sckl016	0.411	0.039	0.09	0.36	1.04	0.21	
Sckl015	0.386	0.045	0.67	0.45	0.89	0.39	
Sckl014	0.375	0.063	0.15	0.63	1.03	0.29	
Sckl013	0.341	0.018	0.21	0.25	0.99	0.12	
Sckl012	0.446	0.015	0.00	0.17	1.32	0.07	
Sckl011	0.356	0.031	0.48	0.24	0.86	0.18	
Sckl010	0.344	0.034	0.35	0.39	0.93	0.20	
Sckl025	0.410	0.051	0.04	0.26	0.61	0.36	
Sckl024	0.406	0.097	0.00	0.32	0.61	0.28	
Sckl023	0.368	0.184	0.28	0.70	0.42	0.66	
Sckl022	0.407	0.089	0.02	0.69	0.67	0.29	
Sckl021	0.402	0.084	0.05	0.61	0.62	0.32	
Sckl018	0.454	0.166	0.84	0.44	0.86	0.61	
Sckl017	0.508	0.043	0.18	0.09	0.49	0.09	
Sckl020	0.480	0.161	0.22	0.40	0.49	0.21	

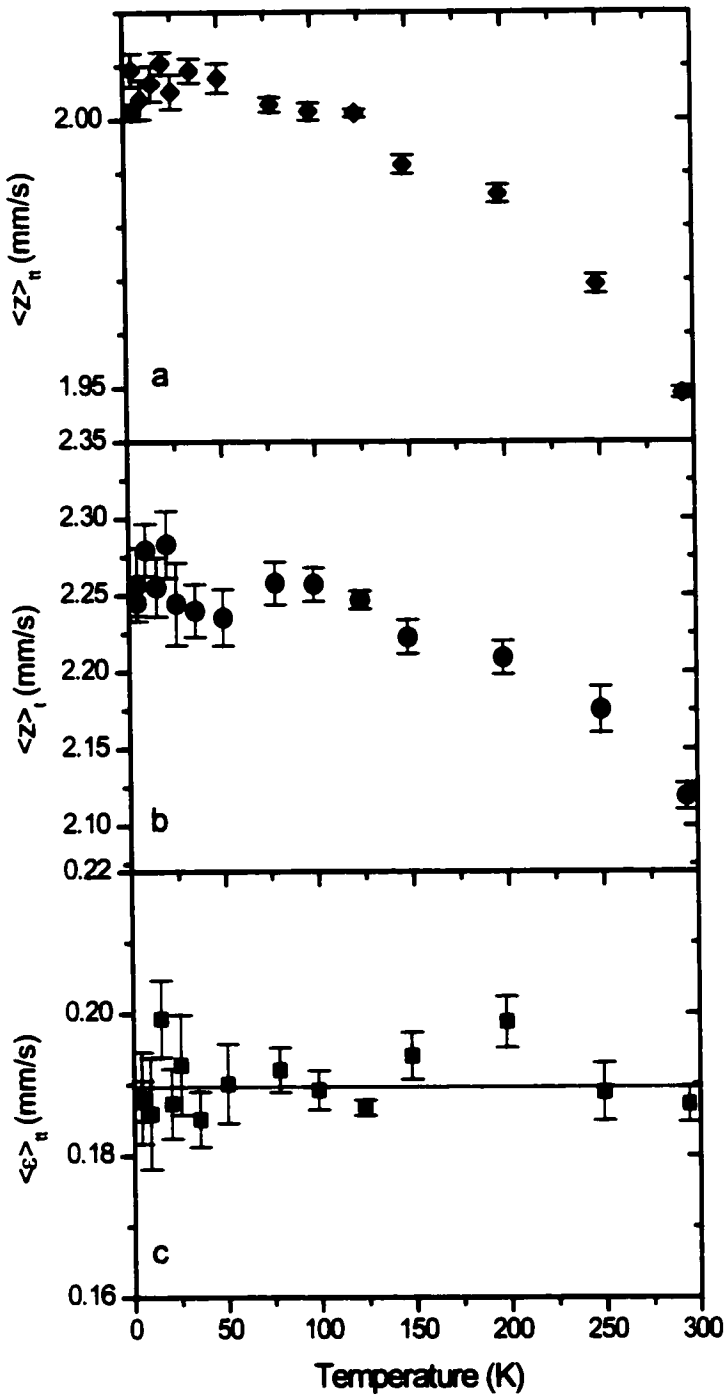

Figure 24 Temperature variation of the Zeeman splittings in tetrataenite (a, ◆) and ordinary taenite (b, ●), as well as the average quadrupole shift in tetrataenite (c, ■) (1-σ fitting uncertainties are illustrated). The line in (c) corresponds to the average value of $\varepsilon = 0.19$ mm/s.

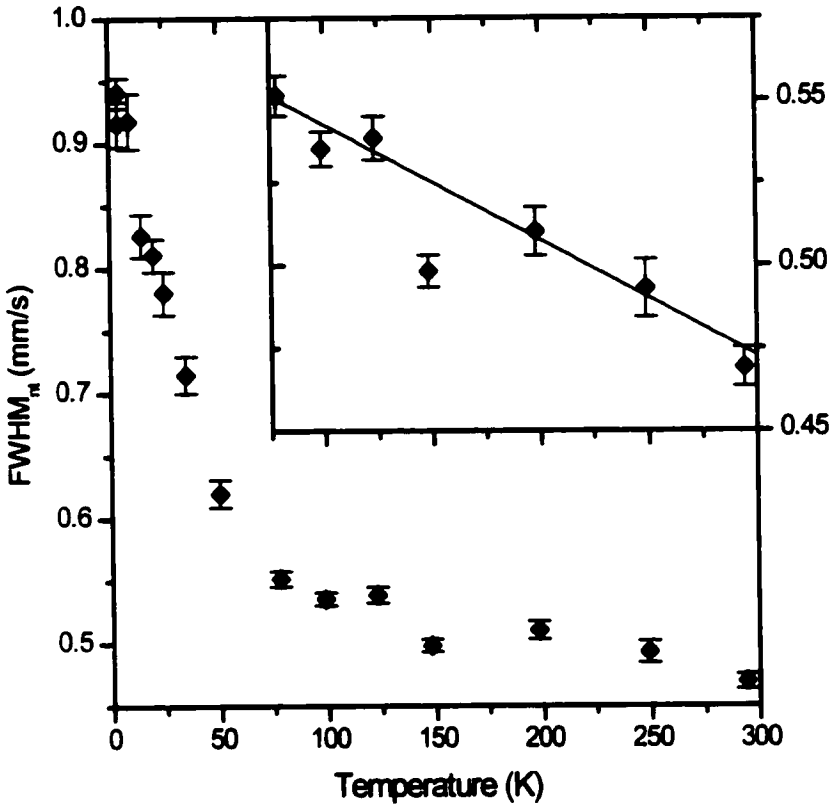

Figure 25 Temperature variation of the FWHM of the antitaenite peak (1-σ fitting uncertainties are displayed). The inset shows the data from 75 to 300 K on a different scale. The solid line in the inset corresponds to a slope of -0.00035 mm/s/K.

3.3 Effect of the Epitaxial Relation Between Tetrataenite and Antitaenite on the Magnetism of Antitaenite

3.3.1 Anomalous Temperature Dependence of the FWHM of Antitaenite

The inset in fig. 25 also shows an interesting feature. Even before the onset of magnetic ordering, from T = 300 K down to 75 K, the FWHM of antitaenite increases regularly with decreasing temperature at a rate of ~3.5 × 10^{-4} mm/s/K. At first, we thought this might be due to thickness effects: As the temperature was reduced, the recoilless fraction increased and caused

an increase in thickness broadening. If the cross-section is a single Lorentzian line with the intrinsic width (γ = 0.0485 mm/s), this would produce the maximum thickness effects. Even in these conditions, the FWHM of the thickness broadened peak would only change by ~10^{-4} mm/s/K, three times less than what is observed. In our case, the whole signal is much less affected by thickness because the cross-section is distributed over a broad range of peaks and velocities, not just in one narrow Lorentzian peak. It is thus impossible that the increase arises from thermal changes in thickness broadening.

A more natural explanation is provided by the nature of the tetrataenite/antitaenite intergrowth. From the SEM photograph of the intergrowth, we know that the antitaenite matrix walls are roughly 10 nm wide, which corresponds to ~50 interatomic layers in the (001) direction (c = 3.6 Å, [Albertsen80]). Because antitaenite is surrounded by magnetic material (tetrataenite and the ordinary taenite), we can consider that either

1) there is an effective field in antitaenite due to long-range dipolar interactions with the magnetic taenite, or

2) the magnetic inter-atomic exchange interaction at the interface between antitaenite and the magnetic taenites results in partial magnetic order in the antitaenite, even above its Néel point.

The first point could be seen as simply applying an external magnetic field, and the result, in both the case of a ferromagnet above T_C or an antiferromagnet above T_N is to produce a residual magnetization which decreases asymptotically to 0 as the temperature increases.

The second point produces a different result but which could also explain the temperature dependence of the FWHM of antitaenite. We have simulated the effect of the interaction with tetrataenite by freezing the end-points of a slab of antitaenite, as if they were constrained by their interaction with tetrataenite. Because we don't know much about the interface (composition gradient, etc), we don't presume that we are truly simulating the magnetism of the intergrowth, but we simply want to examine the effect of a magnetic interaction with at the interface on the magnetism of the antitaenite phase.

3.3.2 Simulated Effect of Epitaxial Interaction of Antitaenite with Tetrataenite

We have modeled antitaenite as a slab of 50 atomic layers in the [001] direction, with

periodic boundary conditions in the [100] and [010] directions (10×10×25 unit cells, or 10000 atoms). An FCC structure was imposed with NN Ising interactions only. We fixed the Fe-Fe exchange parameter (J_{FeFe} = -40 K) corresponding to a value of T_N = 67 K (the experimental value for γ-Fe, [Johanson70]) in pure γ-Fe and we assumed that the Ni atoms did not interact with each other or with the Fe atoms. Since the Fe content composition of antitaenite is very high, the Ni should have very little effect on the magnetism. The same Monte Carlo code as described in chapter 7 (listed in Appendix E) was used.

The effect of tetrataenite is simulated by forcing the end moments along the [001] direction to remain fixed, as if they were polarized by a direct interaction with tetrataenite. We have chosen this method because we have no real knowledge regarding the interface or the magnetic interactions between the two phases.

The simulation was started at T = 10 K in the antiferromagnetic configuration along the [001] direction (the ground state for NN antiferromagnetic interactions in an FCC lattice), and temperature was increased up to 300 K. At each temperature, the average staggered magnetization and thermal average moment magnitudes were calculated. As a comparison, the same calculation was done for a system where the end moments are not fixed, simulating bulk antitaenite. Based on the model proposed by Dang and Rancourt to describe the hyperfine fields in Fe-Ni alloys (see chapter 4), the hyperfine field at a given site will be directly related to the average local moment and the average NN moments. Because we do not know precisely how the local and NN moments combine to produce the hyperfine field in the low moment phase (in the HM phase, $H_i = A<\mu_i> + B\sum_{NN}<\mu_j>$, with A = 20 mm/s/μ_B and B = 0.3 mm/s/μ_B), we can't directly generate the HFD. However, we can simply look at the average moment magnitudes to see if the modelled interaction with tetrataenite has an effect above T_C.

The site-specific average moment is calculated by averaging the moment over several MC steps (for each sampling step, 5 MC steps are dropped to avoid correlations between measurements):

$$<\mu_i>_t = \frac{1}{N\mu_0}\sum_{t=1}^{N}\mu_i(t), \qquad (36)$$

where μ_0 is 0.88 (we assume the Ni moment is 0, the Fe moment 1 μ_B, and we use a composition of 88 at. % Fe) and N is the number of samples used. The average staggered magnetization, m, which serves as a long-range order parameter for this system is

$$m = \frac{1}{M\mu_0} \sum_{i=1}^{M} (-1)^l < \mu_i >_t , \tag{37}$$

where M is the number of sites in the lattice and l is the number of the atomic layer in the [001] direction (l = 0..49). We are also using the local moment magnitude instead of the sample magnetization to eliminate the effect of the magnetic structure by only focussing on the time averaged moment magnitude and not its direction. The sample average of the magnetic moment magnitude is the average over all the sites in the sample (or in a specific layer):

$$< |\mu| >_t = \frac{1}{M\mu_0} \sum_{i=1}^{M} |< \mu_i >_t| . \tag{38}$$

Figs. 26 and 27 show the temperature variation of the average staggered magnetization and the average Fe moment magnitude in the slab and in the bulk (unconstrained) antitaenite. Below T_N = 60 K, the epitaxial interaction doesn't change much. However, above T_N, it is clear that the interaction stabilizes the antiferromagnetic structure which also leads to finite moment magnitudes up to 300 K. In the case of bulk antitaenite, above T_N, the moments are randomly oriented in space (m = 0) and time (MC steps, $< |\mu| >_t \to 0$). Because we are looking only at the magnitude (and not the orientation), the average value will be non-zero because of the finite sampling in time. The time averages of a set of moments which are randomly distributed between +1 and -1 and which are sampled N times (N > 1) are normally distributed with a width $\sigma = 1/\sqrt{N}$. The average moment magnitudes are then distributed as a half-Gaussian (from 0 to ∞). The spatial average of the time averaged moment magnitudes will thus be $< |\mu| >_t = \sqrt{2/\pi}/\sqrt{N}$ (which goes to 0 as N, the sampling time, increases). This is in fact the case for the unconstrained antitaenite, as shown for N = 3900. The slight deviation below 100 K is due to finite size effects. Notwithstanding the effect of finite time sampling, we clearly see that in the constrained case, the average moment is systematically higher than the unconstrained average moment magnitude, and that the difference decreases slowly with temperature. Because the local hyperfine field is related to the average local moment, this shows that a direct exchange mechanism at the tetrataenite/antitaenite interface is capable of causing a significant change in the width of the antitaenite peak as seen from 75 K to 300 K.

To better understand the effect of the interface, we also show in figs. 28 and 29 the average moment per [001] layer as well as the average moment magnitude per [001] layer. We see clearly that even above T_N, the effect of the interface is to stabilize the moments in their low-

temperature (below T_N) antiferromagnetic arrangement. The average moment magnitudes are found to drop to 0 exponentially as the distance from the interface increases. As temperature increases, the drop is more sudden, as the interface only has an effect on near-interfacial moments. This is illustrated in fig. 30 which shows the penetration depth at which the average moment magnitude is half of its saturation value. As temperature increases above 150 K, the depth is significantly reduced (less than 1 atomic layer), illustrating that any stabilization of the moment only happens in the first few layers next to the interface. Because the interface effects is reduced with increasing temperature, the average bulk moment also shows a systematic decrease as the temperature increases. We can also guess what the HFD would look like, since it should resemble the distribution of moment magnitudes which is shown in fig. 31. The tail of the high-field side of the distribution comes from moments located close to the interface.

Based on these calculations, it is entirely possible that the change in the width of the peak of antitaenite is mainly due to a direct exchange mechanism between tetrataenite and antitaenite at the interface between the two phases. If the antitaenite occurred as a thicker matrix, such an effect would not necessarily be visible as it primarily occurs at the interface rather than in the bulk. The visibility of the effect is thus related to the ratio between the surface (interface) and the volume (bulk) of the antitaenite phase.

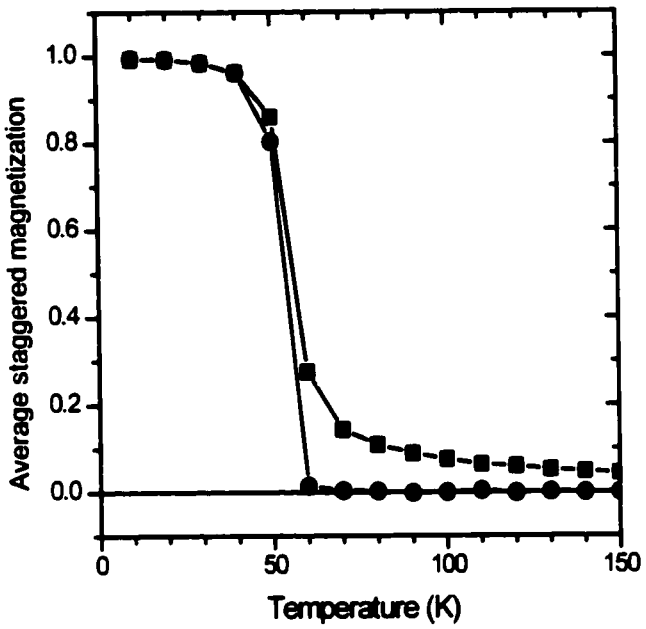

Figure 26 Effect of the tetrataenite/antitaenite interface on the normalized staggered magnetization (long-range order parameter) in antitaenite. ■ antitaenite epitaxially linked to tetrataenite, ● bulk antitaenite.

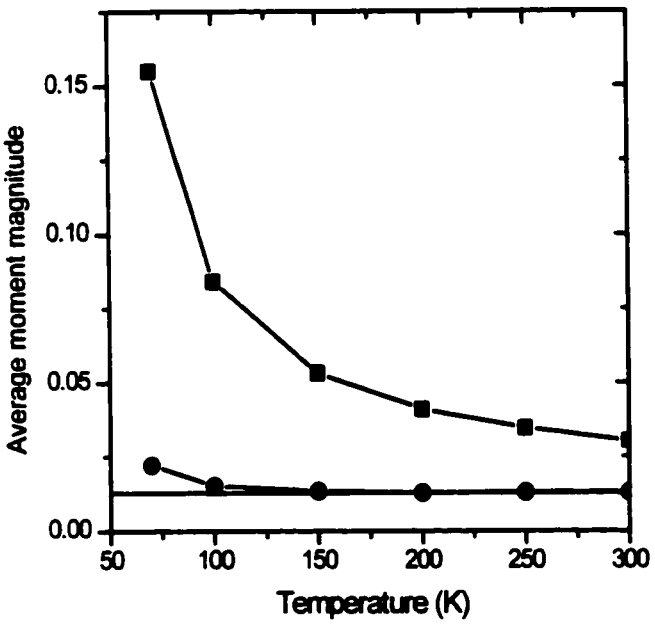

Figure 27 Effect of the tt/nt interface on the average moment magnitude. Same symbols as above. The line at $y = 0.013$ represents the theoretical result for randomly distributed moments (non-zero because of finite sampling time).

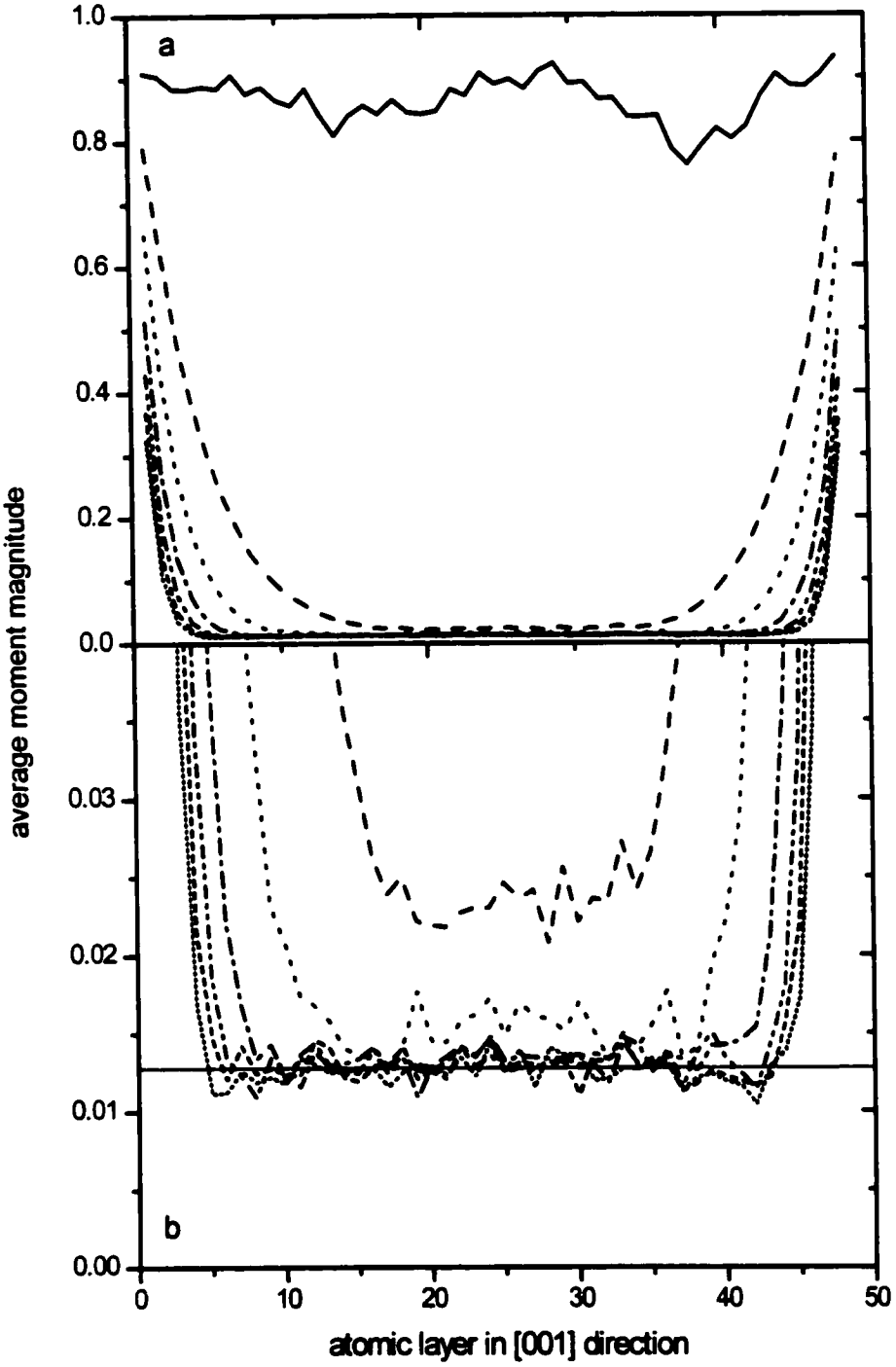

Figure 28 Average moment magnitude in the atomic layers in the [001] direction as a function of temperature. Line symbols represent different temperatures: (solid) T = 50 K, (dash) T = 70 K, (dot) T = 100 K, (dash-dot) T = 150 K, (dash-dot-dot) T = 200 K, (short dash) T = 250 K and (short dot) T = 300 K ((b) is a blow -up for small magnitudes of (a))

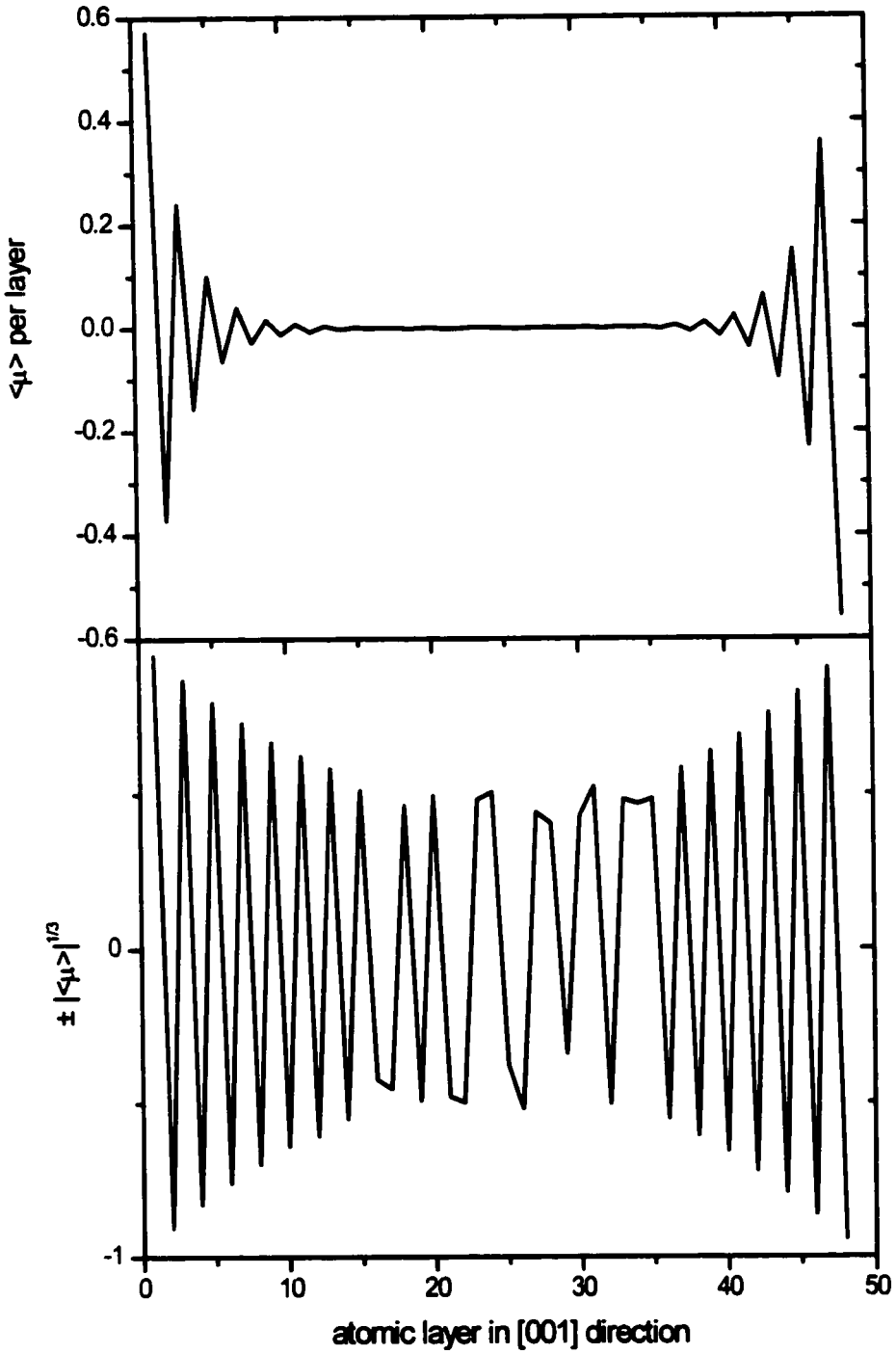

Figure 29 Average moment per layer at T = 100 K in constrained antitaenite. The bottom plot shows a rescaled version ($\pm |<\mu>|^{1/3}$ is displayed to show the spatial variation of both the large and small moments) which illustrates how the antiferromagnetic structure is preserved well into the bulk of the antitaenite, even far above T_N.

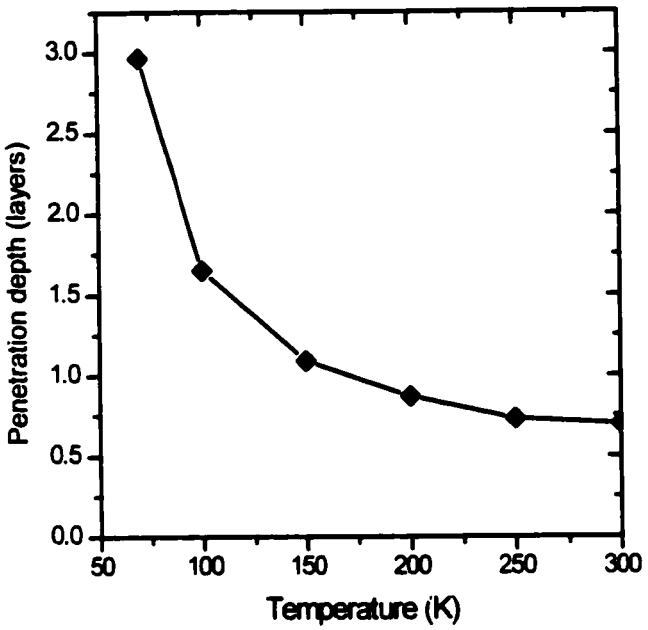

Figure 30 Penetration depth of the tt/nt interaction as a function of temperature. The average moment magnitude is reduced to half of its saturation value at the given depth (layer in [001] direction).

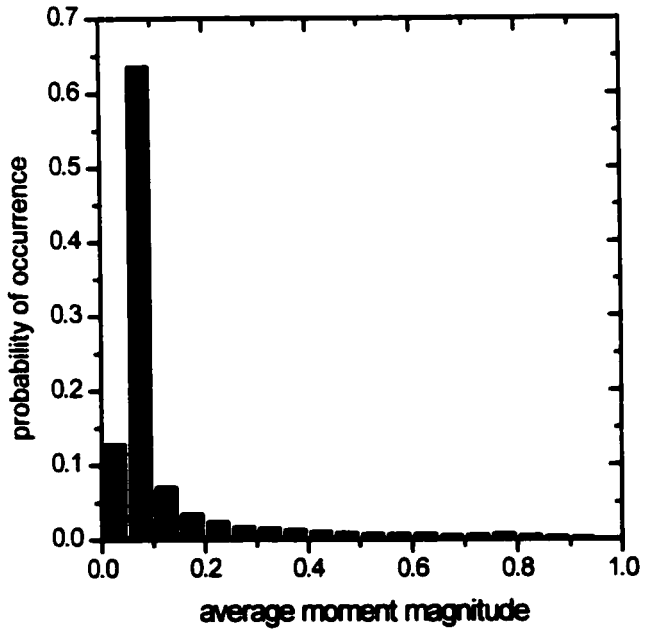

Figure 31 Simulated distribution of moment magnitudes in antitaenite at T = 100 K, after N = 3900 time samples. The moment magnitude with maximum probability eventually converges to 0, but the tail at higher values remains even for large N.

3.4 Antitaenite as a New Mineral

The presence of a tetrataenite/antitaenite intergrowth is relatively common in iron meteorites [Goldstein80, Albertsen78, 80b, 83, Danon83], yet very little is known about the nature of antitaenite [Rancourt95, 97]. Most people simply assume it is an Fe-rich alloy which is like ordinary taenites found with lower Fe content. There are however important differences between ordinary taenite and antitaenite and in fact, antitaenite resembles more LM γ-Fe than it does the HM taenites. Its lattice parameter is very similar to that of γ-Fe. Though there is no evidence regarding the nature of the magnetic ordering, it orders magnetically at temperatures below ~60 K (T_N = 67 K in γ-Fe [Gonser63, Johanson70]). Measurements of the Néel temperature of various LM Fe-rich FCC Fe-Ni alloys show it to vary linearly with composition, rising from 0 K at 52. at % Fe to 67 K in γ-Fe [Rancourt89]. Based on the calculated composition of antitaenite (88 at. % Fe), the interpolated Néel temperature would be 50 K, similar to what is experimentally observed. Finally, the measured RT ^{57}Fe *CS* of antitaenite (-0.090 mm/s) and γ-Fe (-0.088 mm/s [Keune77]) are nearly identical, indicating that the electronic structure is most likely very similar. In fact, the very large difference between the *CS* in antitaenite and ordinary taenites (*CS* ≈ 0.12-0.15 mm/s [see chapter 4]) is the definitive argument that the Fe-rich phase found in meteorites is a LM phase akin to γ-Fe which has a different electronic structure than the HM ordinary taenites [Rancourt99]. Because of its similarities with other LM phases, it is assumed that it has predominantly antiferromagnetic couplings and is hence given the name antitaenite [Rancourt95, Rancourt97, Rancourt99].

The observation that antitaenite is indeed a new mineral which differs from taenite only by its electronic structure (they have the same crystallographic structure) has lead to much of the work presented in the following chapters regarding the existence of HM and LM phases of FCC Fe-Ni alloys from both a theoretical and experimental point of view.

4. Overview of Fe-Ni Alloys as Collinear Ferromagnets

Ni-rich FCC Fe-Ni alloys which exhibit collinear magnetism at 0 K has been extensively studied by Rancourt and Ping [Rancourt91b, Rancourt92, Ping92, Rancourt93, Rancourt96] and Dang *et al.* [Dang95, Dang96a, Dang96b, Dang96c], so we will simply present the most relevant information. The purpose of this recapitulation is to inform the reader of the properties of these alloys so one may better understand the basis of magnetism in Fe-Ni alloys and the complexities and difficulties involved in describing the Fe-rich alloys. We shall focus primarily on the concentration dependence of hyperfine parameters, magnetic properties, and the lattice parameter.

4.1 Bulk Magnetic Moment: The Slater-Pauling Relation

In the case of a binary alloy of two magnetic species, if both species of atoms have an electronic and magnetic structure that is independent of the composition of the alloy, then the average magnetic moment will follow a simple linear relation with respect to the composition, known as the Slater-Pauling relation [Slater37, Pauling38]. This relation is illustrated in fig. 32, which shows several experimental measurements of the average saturation magnetic moment per atom, measured at or extrapolated to 4.2 K. One clearly sees that in the Ni-rich region, the moment follows a linear relation, $<\mu> = 0.6 + (2.8-0.6)c$, for compositions below approximately 50 at. % Fe. This is thus consistent with the expected moment based on the Slater-Pauling relation, assuming that $\mu_{Ni} = 0.6\mu_B$ and $\mu_{Fe} = 2.8\mu_B$. The validity of the Slater-Pauling curve indicates that the moments are stable and independent of the composition and that the magnetic structure is collinear. In fact, upon closer examination, one finds that there may be a slight curvature in the relation (dashed curve) which can be attributed to a slight composition

dependence of the Fe magnetic moment, as elucidated by electronic structure calculations [see chapter 5]. Based on the compositional stability of the electronic structure of Fe and Ni atoms and the magnetic structure of the alloy, it is possible to construct a simple model to explain the Mössbauer results described in the following paragraphs.

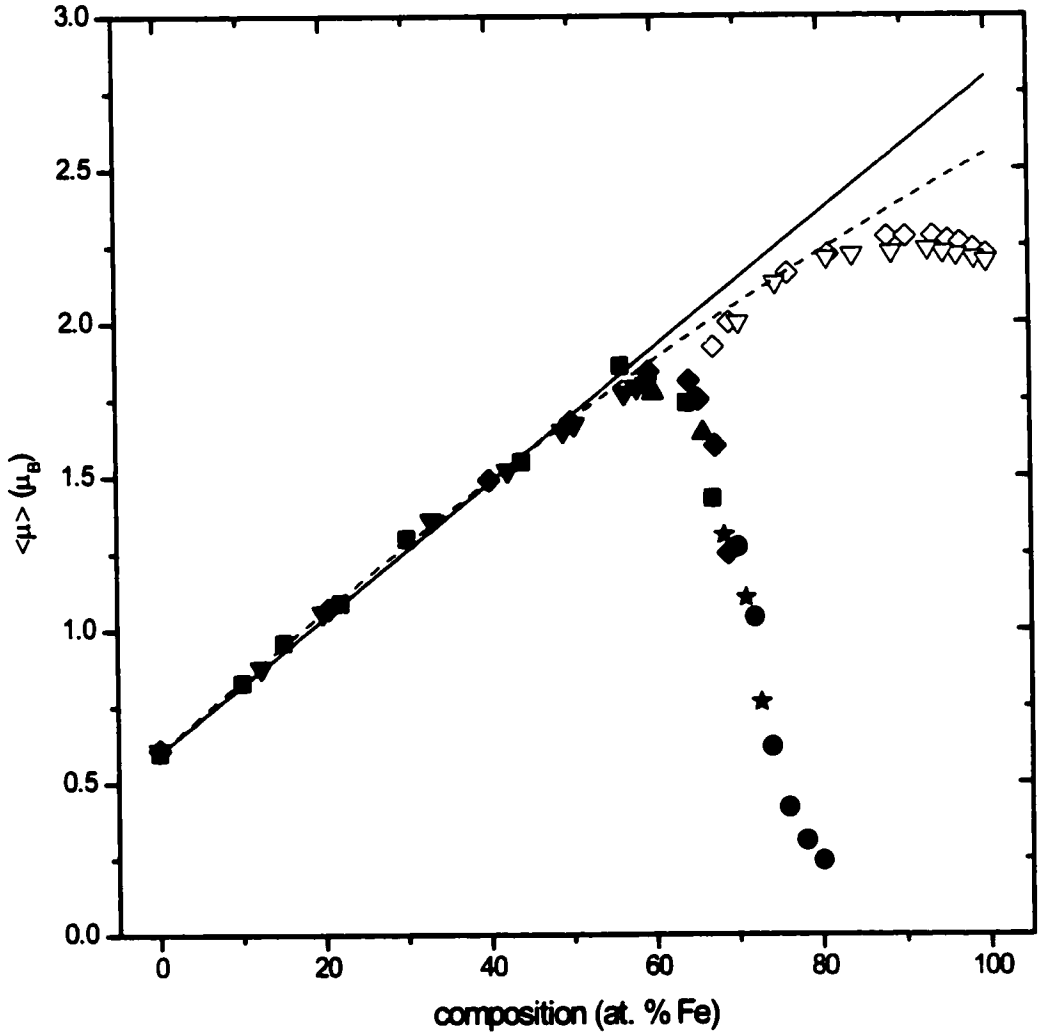

Figure 32 Experimental determinations of the average saturation magnetic moment in Fe-Ni alloys at 4.2 K and the Slater-Pauling relation. Filled symbols represent the FCC phase, whereas open symbols are for the BCC phase. Similar symbols (open and filled) correspond to the same reference: ■ Kondorskii and Fedotov [Kondorskii52], ◆ Crangle and Hallam [Crangle63], ▲ Cochrane and Graham [Cochrane70], ▼ Peschard [Peschard25], ● Brando [Brando64], ★ Asano [Asano69]. The solid line represents the Slater-Pauling relation, the dashed line represents a situation where the Fe moment is assumed to decrease linearly with the composition, as calculated in chapter 5.

4.2 Atomic Volume: Deviation from Vegard's law

In binary alloys where the electronic and magnetic structure of the atoms is not affected by composition and when there are no magneto-volume effects, the concentration dependence of the volume is expected to obey Vegard's law [Vegard28, Thorpe91] which states that the average atomic volume varies linearly with the concentration of either species. In fact, Vegard originally stated that the lattice parameter should depend linearly with the concentration [Vegard28] and later Zen [Zen56] suggested that it should be the volume that scales linearly with the composition. Because the Fe and Ni endpoints have similar volumes, there is not noticeable distinction between these two statements, and we hereafter use Vegard's name as he was the first to introduce the concept. In Fe-Ni, below ~50 at. %, where the Slater-Pauling relation is respected, one should thus expect Vegard's law to hold. Fig. 33 shows many experimental measurements of the concentration dependence of the mean atomic volume at RT, in the FCC and BCC phases, including new measurements which are described later in chapter 6.

In addition to the data, we have plotted a linear relation based on the data in the Ni-rich region (< 20 at. % Fe) where there are no anomalies in the thermal expansion curves. Although in general Vegard's law is seemingly obeyed up to ~60 at. %, there is a clear deviation towards *larger* volumes. Based on the results presented here and based on what is known about Fe-Ni alloys below 50 at. %, this deviation from Vegard's law does not come from a change in electronic structure (the slight drop in the Fe moment would be associated with a decrease in volume) or magnetic structure (these alloys exhibit collinear ferromagnetism at T = 0 K). It must be due to a magneto-volume effect. These deviations from Vegard's law may only occur at non-zero temperatures, so one should investigate this behaviour at T = 0 K. Based on the composition dependence of the thermal expansion of these alloys [Hayase73], it is in fact possible to extrapolate these measurements to T = 0 K, where one actually sees no change below ~30 at. % and an *increase* in the deviation above ~40 at. %, indicating that this positive deviation is not due to thermal effects but is inherent to the T = 0 K properties of the alloys. In fact, ESC calculations [chapter 5] also show a deviation from linearity in the FM HM alloys. This deviation is of extreme relevance to the Invar problem and will correspondingly be discussed later in more detail [chapters 6 and 7]. Above ~60 at. %, a very large deviation to smaller volumes is inexplicable in terms of HM alloys. This feature will also be discussed later, in chapters 5 and 6.

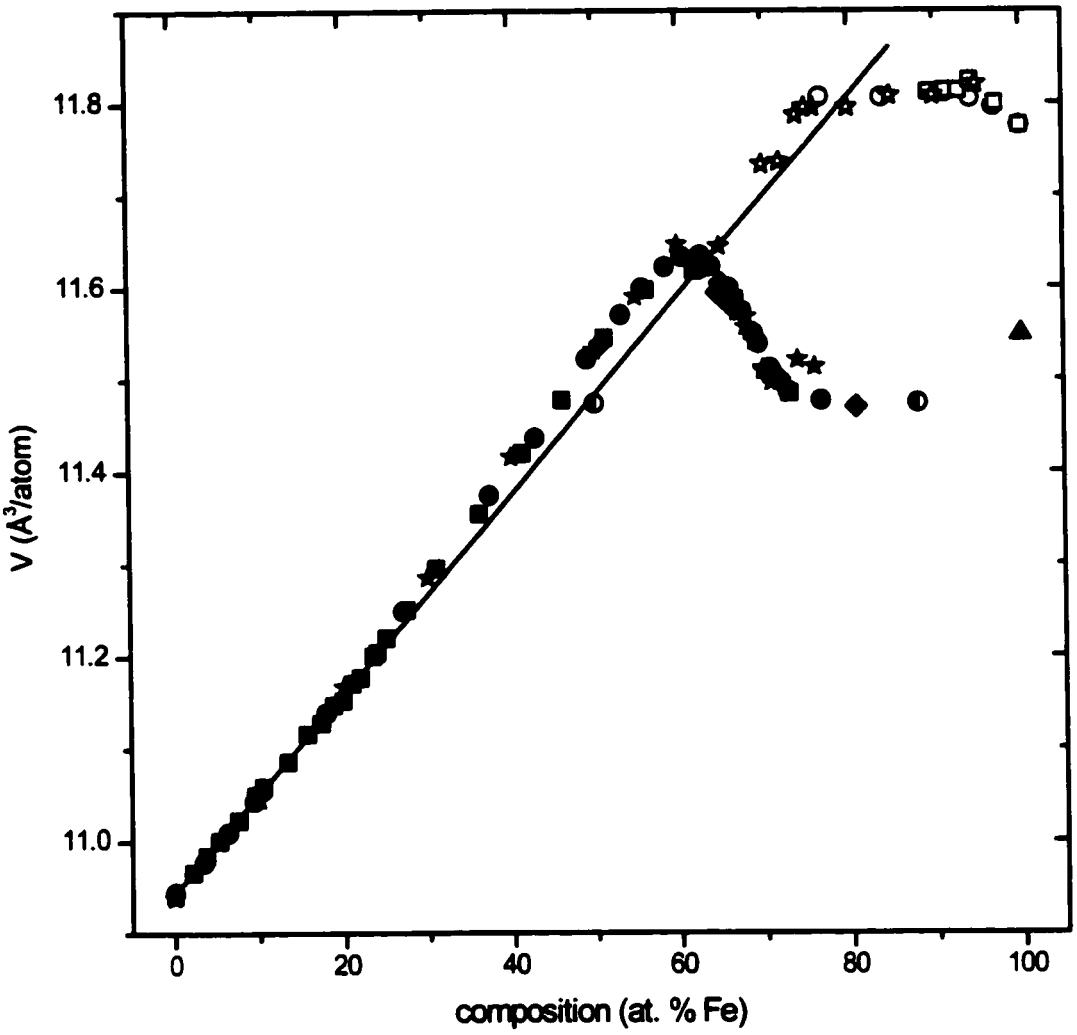

Figure 33 Composition dependence of the atomic volume in Fe-Ni alloys at RT. Solid symbols represent measurements of the FCC phase, open symbols are for the BCC phase. The straight line corresponds to Vegard's law, extrapolated from the Ni-rich (< 20 at. % Fe) data. Symbols are: ■ Bradley *et al.* [Bradley37], ◆ Phragmén [Phragmen31], ● Owen *et al.* [Owen37d], ▲ Newkirk [Newkirk57], ★ Dang [Dang96a] and Lagarec [see chapter 6].

4.3 Hyperfine Parameters: Analysis of Mössbauer Spectra

4.3.1 Analysis Methodology

Most of the Mössbauer spectra of FCC Fe-Ni alloy series taken in the lab of Dr. Rancourt have been consistently analysed using the xVBF method (see appendix A), to provide a consistent set of hyperfine parameters. The sample preparation, data acquisition and spectral folding for these samples have been described elsewhere [Dang96a]. The limits of the VBF method of fitting the spectra of FCC Fe-Ni alloys have been extensively described by Ping *et al.* [Ping92a]. I have found that the xVBF model could consistently produce better fits (lower χ^2) than other methods such as the VBF method, so we decided to re-analyse all spectra using this method. In cases where the VBF method yielded a similar quality of fit, it was also used to provide results based on a different model.

For spectra with fewer than 60 at. % Fe, a model which includes an arbitrarily shaped HFD (usually described by two or three Gaussian components) correlated to a Gaussian shaped QSD was found to produce the best fit. In this scenario, the *CS* is not distributed or correlated to the other hyperfine parameters. For alloys with more than 60 at. % Fe, a correlation between the *CS* and the HF is needed and is in fact the correlation which produces the largest effect on the spectra. In these cases, the VBF model was also applied, as it yields similar fits as the xVBF model. In addition, for these alloys (> 60 at. % Fe), it was found that some parameters are strongly dependent on the analysis model, so the use of two different models provides a complementary set of data. Even though these alloys have an average cubic symmetry, the site of each Fe atom does not necessarily have a cubic symmetry because of the alloying of Fe and Ni atoms. It is thus normal that there be a local EFG on each site, with a finite (but small) magnitude and a random orientation with respect to crystal axes and the hyperfine field. The average quadrupole shift (ε) was thus always forced to be 0 mm/s in order to avoid systematic effects on the centre shift (δ). However, in the xVBF model, the width of the QSD was allowed to be non-zero. A description of the specific problems encountered in fitting such spectra to extract accurate hyperfine parameters explains the choices made in fitting these spectra [chapter 2] . Some additional hyperfine parameters, such as the average centre shift $<\delta>$, the widths of the CSD (σ_δ) and QSD (σ_ε), three parameters describing the Zeeman splitting distribution (the

average of its magnitude $|z|$, its standard deviation σ_z and its skewness κ_z) have also been calculated from the parameters of the analysis model.

4.3.2 Results and Discussion

Tables 9 through 17 lists all the fitting parameters for compositions up to 70 at. %, at RT and LN_2T along with a concise list of calculated parameters used to describe the distributions of hyperfine parameters. For all alloys, it is found that the width of the QSD (σ_ε) increases slightly with Fe concentration up to ~40 at. % Fe. It is not known whether this composition dependence is real or whether it is an artefact of the fitting model because of increasing thickness effects (which were not corrected for). In any case, the magnitude of the width is reasonable when compared to ε in tetrataenite, which is ~0.2 mm/s [see chapter 3] and which could be taken as an extreme value. These results show that the fitting method produces physically realistic parameters. We will now examine in more detail the data relating to the HF and the *IS*.

Table 9 Parameters of the xVBF fit of the RT Mössbauer spectra of a series of splat quenched alloys (SQ #1). 2-σ (95 %) fitting uncertainties are given in the second column of the parameter. Parameters with an uncertainty of 0 were not refined during the fit.

15	0.68	1321400	114	0.099	0.006	118872	1603	3.08	0.08	2.32	0.06
25	0.55	353652	71	0.112	0.015	26325.5	905	3.01	0.16	2.38	0.14
30	0.43	183451	43	0.107	0.012	27154.7	650	3.11	0.11	2.34	0.09
35	0.72	602098	63	0.097	0.004	81750.5	798	3.01	0.06	2.29	0.04
40	0.93	613749	64	0.097	0.001	111892	787	2.99	0.07	2.40	0.05
45	1.08	1427100	274	0.125	0.018	121161	4128	2.97	0.10	2.23	0.07
50	0.82	697257	57	0.097	0.001	134567	755	2.88	0.05	2.12	0.04
55	0.83	1621510	128	0.097	0.003	280098	1992	2.89	0.04	2.14	0.03
60	0.99	1617620	192	0.129	0.009	323863	2634	2.77	0.04	2.17	0.04
65	0.46	354780	66	0.098	0.009	102806	924	2.99	0.10	2.17	0.07
68	0.98	2395310	166	0.098	0.002	495605	1974	2.88	0.11	2.03	0.11
70	0.45	131357	78	0.154	0.082	63089.6	1503	3	0	2	0

15	0	0	0	0	-0.14	0.06	0.007	0.002	0	0
25	0	0	0	0	-0.26	0.19	0.012	0.005	0	0
30	0	0	0	0	-0.40	0.13	0.019	0.003	0	0
35	0	0	0	0	-0.44	0.04	0.028	0.003	0	0
40	0	0	0	0	-0.39	0.03	0.030	0.002	0	0
45	0	0	0	0	-0.40	0.12	0.030	0.003	0	0
50	0	0	0	0	-0.34	0.03	0.033	0.002	0	0
55	0	0	0	0	-0.27	0.02	0.031	0.001	0	0
60	0	0	0	0	-0.51	0.12	0.028	0.002	0	0
65	-0.95	0.58	0.17	0.10	-0.46	0.09	0.023	0.002	0.034	0.013
68	0.66	0.38	0.70	0.23	-0.07	0.05	0.004	0.004	0.031	0.015
70	0	0	1.00	2.74	0	0	-0.038	0.011	0.040	0.140

15	0	0	0.052	0.010	0.343	0	1.826	0.005	0.040	0.007
25	0	0	0.064	0.025	0.266	0	1.891	0.024	0.054	0.019
30	0	0	0.068	0.020	0.225	0	1.926	0.014	0.064	0.016
35	0	0	0.082	0.006	0.277	0	1.953	0.005	0.076	0.005
40	0	0	0.090	0.006	0.874	0	2.060	0.008	0.116	0.004
45	0	0	0.076	0.019	1.000	0	2.119	0.003	0.135	0.004
50	0	0	0.090	0.004	0.969	0	2.114	0.002	0.118	0.002
55	0	0	0.098	0.004	0.986	0	2.104	0.001	0.118	0.001
60	0	0	0.062	0.015	0.735	0	2.032	0.015	0.111	0.005
65	0	0	0.041	0.010	0.383	0	1.910	0.005	0.146	0.004
68	0	0	0.111	0.028	0.186	0	1.647	0.006	0.183	0.010
70	0	0	0	0	0.875	0	0.007	0.279	0.701	0.022

(Table 9 continued)

15	0.657	0.077	1.910	0.010	0.083	0.004
25	0.734	0.166	2.012	0.024	0.105	0.015
30	0.775	0.084	2.055	0.012	0.121	0.006
35	0.723	0.025	2.087	0.004	0.120	0.003
40	0.126	0.049	2.240	0.014	0.074	0.011
45						
50	0.031	0.011	1.955	0.012	0.021	0.021
55	0.014	0.003	1.092	0.046	0.001	0.048
60	0.108	0.040	1.773	0.062	0.168	0.030
65	0.202	0.023	0.866	0.050	0.343	0.025
68	0.257	0.010	0.441	0.015	0.265	0.009
70	0.125	0.042	0.061	0.034	0.087	0.050

15						
25						
30						
35						
40						
45						
50						
55						
60	0.157	0.083	2.161	0.019	0.071	0.022
65	0.415	0.034	1.611	0.024	0.247	0.014
68	0.557	0.010	1.150	0.014	0.377	0.007
70						

Table 10 Compiled parameters of the fits of SQ #1.

15	0.007	0	0	0.052	1.881	0.082	0.48
25	0.012	0	0	0.064	1.980	0.108	0.33
30	0.019	0	0	0.068	2.026	0.123	0.27
35	0.028	0	0	0.082	2.050	0.125	0.25
40	0.030	0	0	0.090	2.083	0.127	0.00
45	0.030	0	0	0.076	2.119	0.135	0.00
50	0.033	0	0	0.090	2.109	0.119	0.05
55	0.031	0	0	0.098	2.090	0.166	-2.85
60	0.028	0	0	0.062	2.024	0.151	-0.90
65	0.023	0.034	0	0.041	1.575	0.449	-1.05
68	0.004	0.031	0	0.111	1.063	0.514	-0.12
70	-0.038	0.040	0	0	0.497	0.429	1.06

Table 11 Parameters of the xVBF fit of a second series of SQ alloys (SQ #2).

5	0.70	5647410	259	0.112	0.009	151193	3662	2.94	0.13	2.32	0.11
10	0.80	6558020	269	0.111	0.005	262696	3599	2.91	0.09	2.30	0.07
15	1.09	3494340	220	0.109	0.006	289573	3558	2.89	0.07	2.42	0.05
20	0.98	1615360	137	0.112	0.007	202937	2357	2.91	0.06	2.16	0.05
25	1.24	3751020	298	0.108	0.006	406714	4997	2.85	0.04	2.26	0.04
30	1.36	3308810	241	0.102	0.004	520576	3872	2.95	0.05	2.15	0.04
35	0.84	1605240	317	0.108	0.012	198264	4488	2.81	0.07	2.26	0.05
40	0.82	1357740	311	0.109	0.012	207235	4689	2.79	0.06	2.23	0.05
45	1.21	1632030	314	0.116	0.010	307266	4466	2.78	0.06	2.13	0.05
50	1.96	1863910	131	0.108	0.003	443299	1792	2.82	0.03	2.12	0.02
55	1.54	2032700	279	0.121	0.006	382622	4185	2.77	0.06	2.06	0.04
60	1.08	3979940	129	0.097	0.000	636066	2017	3.10	0.02	2.34	0.01
65	1.20	4133060	207	0.097	0.001	1078120	3107	3.09	0.03	2.18	0.03
68	0.71	4591120	279	0.138	0.017	835050	4234	2.48	0.16	1.66	0.09
68	0.71	4591100	293	0.136	0.017	834482	5367	2.50	0.13	1.65	0.07

5	0	0	0	0	-0.16	0.28	-0.004	0.003	0	0
10	0	0	0	0	-0.10	0.89	-0.002	0.003	0	0
15	0	0	0	0	-0.23	0.12	0.004	0.002	0	0
20	0	0	0	0	-0.37	0.13	0.008	0.002	0	0
25	0	0	0	0	-0.32	0.05	0.014	0.002	0	0
30	0	0	0	0	-0.35	0.04	0.020	0.002	0	0
35	0	0	0	0	-0.39	0.07	0.025	0.002	0	0
40	0	0	0	0	-0.38	0.07	0.028	0.002	0	0
45	0	0	0	0	-0.38	0.07	0.030	0.002	0	0
50	-0.72	0.10	-0.34	0.13	-0.40	0.04	0.031	0.002	0.011	0.002
55	-0.78	0.57	-0.10	0.11	-0.55	0.09	0.028	0.002	0.015	0.009
60	-0.89	0.03	0.00	0.06	-0.46	0.03	0.028	0.001	0.023	0.001
65	-0.97	0.01	0.22	0.03	-0.47	0.03	0.017	0.002	0.042	0.003
68	0	0	0.62	0.38	0	0	-0.001	0.004	0.038	0.028
68	0.97	0.83	0.40	0.27	0.19	0.48	0.000	0.003	0.065	0.035

5	0	0	0.030	0.017	0.597	0	1.800	0.003	0.016	0.011
10	0	0	0.015	0.022	0.385	0	1.799	0.003	0.019	0.008
15	0	0	0.037	0.012	0.319	0	1.813	0.006	0.031	0.008
20	0	0	0.043	0.014	0.323	0	1.841	0.006	0.049	0.007
25	0	0	0.081	0.008	0.269	0	1.869	0.009	0.052	0.018
30	0	0	0.088	0.006	0.285	0	1.920	0.007	0.067	0.008
35	0	0	0.091	0.012	0.146	0	1.936	0.011	0.052	0.022
40	0	0	0.094	0.014	0.099	0	1.949	0.008	0.047	0.017
45	0	0	0.088	0.013	0.915	0	2.134	0.036	0.116	0.017
50	0	0	0.073	0.004	0.984	0	2.123	0.001	0.119	0.001
55	0	0	0.058	0.011	0.882	0	2.102	0.005	0.109	0.003
60	0	0	0.059	0.002	0.770	0	2.064	0.001	0.125	0.001
65	0	0	0.043	0.002	0.306	0	1.932	0.003	0.133	0.002
68	0	0	0	0	0.122	0	1.714	0.027	0.152	0.017
68	0	0	0.023	0.044	0.122	0	1.715	0.023	0.149	0.015

(Table 11 continued)

5	0.403	0.136	1.840	0.021	0.068	0.012
10	0.615	0.093	1.865	0.010	0.066	0.006
15	0.681	0.086	1.903	0.010	0.075	0.005
20	0.677	0.058	1.942	0.008	0.090	0.004
25	0.731	0.074	1.980	0.010	0.103	0.004
30	0.715	0.057	2.042	0.009	0.118	0.003
35	0.854	0.063	2.070	0.010	0.117	0.005
40	0.901	0.046	2.092	0.008	0.120	0.004
45	0.085	0.243	1.976	0.041	0.063	0.022
50	0.016	0.007	1.946	0.055	0.039	0.032
55	0.118	0.035	2.228	0.010	0.062	0.022
60	0.176	0.003	1.845	0.006	0.200	0.006
65	0.352	0.002	1.116	0.006	0.477	0.009
68	0.650	0.042	0.809	0.040	0.433	0.017
68	0.651	0.033	0.808	0.033	0.431	0.013

5						
10						
15						
20						
25						
30						
35						
40						
45						
50						
55						
60	0.054	0.002	0.904	0.032	0.593	0.064
65	0.341	0.004	1.691	0.004	0.222	0.003
68	0.227	0.034	1.457	0.047	0.235	0.022
68	0.226	0.032	1.457	0.036	0.232	0.021

Table 12 Compiled parameters of the fits of SQ #2.

5	-0.004	0	0	0.030	1.816	0.049	1.10
10	-0.002	0	0	0.015	1.839	0.062	0.71
15	0.004	0	0	0.037	1.875	0.077	0.47
20	0.008	0	0	0.043	1.909	0.092	0.38
25	0.014	0	0	0.081	1.950	0.104	0.35
30	0.020	0	0	0.088	2.008	0.119	0.31
35	0.025	0	0	0.091	2.050	0.120	0.20
40	0.028	0	0	0.094	2.078	0.123	0.14
45	0.030	0	0	0.088	2.121	0.121	0.06
50	0.031	0.011	0	0.073	2.120	0.120	0.01
55	0.028	0.015	0	0.058	2.117	0.112	-0.11
60	0.028	0.023	0	0.059	1.964	0.319	-3.14
65	0.017	0.042	0	0.043	1.563	0.466	-1.02
68	-0.001	0.038	0	0	1.074	0.502	-0.16
68	0.000	0.065	0	0.023	1.072	0.501	-0.16

Table 13 Parameters of the xVBF fit of a third SQ series (SQ #3) and a series of three roller quenched alloys (RQ #1 - 50, 55 and 60 at. % Fe).

5	0.41	2235010	110	0.112	0.008	51995.2	1588	2.85	0.18	2.53	0.16
5	0.39	3110140	136	0.116	0.006	70211.7	1550	2.89	0.17	2.59	0.14
10	0.45	261182	18	0.115	0.006	11966.4	201	2.77	0.11	2.83	0.13
15	0.45	9884180	296	0.100	0.008	188309	3602	2.96	0.12	3.08	0.11
45	0.74	1855770	194	0.104	0.007	273751	2929	2.83	0.08	2.94	0.08
65	0.76	1520420	98	0.097	0.001	464265	1578	3.18	0.03	2.23	0.02
65	1.09	1520480	89	0.097	0.001	465131	1363	3.20	0.04	2.23	0.03
70	0.91	255960	66	0.144	0.030	101635	944	3	0	2	0
50	0.70	961414	189	0.117	0.008	203918	2868	2.85	0.05	2.11	0.03
55	0.85	1012610	171	0.107	0.007	274269	2596	3.00	0.06	2.20	0.04
60	0.67	923523	105	0.100	0.004	240595	1879	3.11	0.05	2.19	0.03

5	0	0	0	0	-0.74	0.48	-0.007	0.002	0	0
5	0	0	0	0	0	0	-0.003	0.003	0	0
10	0	0	0	0	0	0	-0.003	0.002	0	0
15	0	0	0	0	-0.20	0.31	0.005	0.003	0	0
45	0	0	0	0	-0.36	0.05	0.029	0.002	0	0
65	-0.98	0.03	0.27	0.06	-0.47	0.04	0.013	0.002	0.031	0.003
65	0	0	0.22	0.05	0	0	0.013	0.002	0.069	0.006
70	0	0	1.00	0.03	0	0	-0.027	0.007	0.101	0.021
50	0	0	0	0	-0.52	0.08	0.031	0.002	0	0
55	0	0	0	0	-0.42	0.05	0.028	0.001	0	0
60	-0.89	0.20	0.04	0.07	-0.49	0.04	0.024	0.001	0.017	0.003

5	0	0	0.025	0.018	0.460	0	1.803	0.004	0.000	0.005
5	0	0	0	0	0.446	0	1.803	0.003	0.004	0.015
10	0	0	0	0	0.764	0	1.877	0.018	0.063	0.009
15	0	0	0.043	0.020	0.385	0	1.836	0.012	0.046	0.012
45	0	0	0.101	0.011	0.849	0	2.088	0.019	0.113	0.007
65	0	0	0.042	0.002	0.362	0	1.107	0.012	0.472	0.009
65	0	0	0	0	0.379	0	1.128	0.007	0.479	0.008
70	0	0	0	0	0.866	0	0.186	0.054	0.701	0.019
50	0	0	0.069	0.009	0.787	0	2.105	0.011	0.105	0.004
55	0	0	0.067	0.008	0.443	0	2.097	0.004	0.117	0.004
60	0	0	0.051	0.004	0.772	0	2.054	0.002	0.125	0.002

(Table 13 continued)

5	0.540	0.118	1.858	0.014	0.050	0.011
5	0.554	0.121	1.848	0.015	0.060	0.008
10	0.236	0.159	1.802	0.012	0.000	0.022
15	0.615	0.106	1.932	0.014	0.086	0.008
45	0.151	0.139	2.229	0.023	0.072	0.047
65	0.308	0.002	1.931	0.003	0.133	0.002
65	0.289	0.003	1.933	0.003	0.128	0.003
70	0.134	0.017	0.035	0.011	0.129	0.034
50	0.213	0.090	2.245	0.020	0.081	0.013
55	0.542	0.047	2.124	0.004	0.118	0.004
60	0.069	0.013	1.224	0.136	0.581	0.082

5						
5						
10						
15						
45						
65	0.331	0.005	1.684	0.003	0.218	0.004
65	0.333	0.002	1.697	0.003	0.215	0.004
70						
50						
55	0.016	0.009	0.812	0.415	0.726	0.507
60	0.159	0.011	1.819	0.024	0.201	0.012

Table 14 Compiled parameters for the fits of SQ #3 and RQ #1.

5	-0.007	0	0	0.025	1.833	0.046	1.03
5	-0.003	0	0	0	1.828	0.050	0.94
10	-0.003	0	0	0	1.859	0.063	0.47
15	0.005	0	0	0.043	1.895	0.087	0.48
45	0.029	0	0	0.101	2.109	0.119	-0.09
65	0.013	0.031	0	0.042	1.552	0.469	-0.99
65	0.013	0.069	0	0	1.551	0.469	-0.98
70	-0.027	0.101	0	0	0.516	0.438	1.11
50	0.031	0	0	0.069	2.135	0.116	-0.03
55	0.028	0	0	0.067	2.093	0.205	-5.06
60	0.024	0.017	0	0.051	1.960	0.296	-2.79

Table 15 Parameters of the VBF fits to the RT Mössbauer spectra of alloys from the SQ #1, #2, #3 and RQ #1 series. 2-σ (95 %) fitting uncertainties are given in the second column of the parameter. Parameters with an uncertainty of 0 were kept fixed during the fit.

65	0.47	354903	52	0.145	0.010	105201	775	2.65	0.14	1.94	0.08
68	0.86	2395540	243	0.137	0.016	501203	3855	2.56	0.22	1.90	0.15
70	0.46	131330	35	0.144	0.040	62630.2	738	3	0	2	0
50	1.96	1865500	280	0.146	0.004	469339	4566	2.73	0.04	2.07	0.03
55	1.61	2033830	353	0.149	0.005	400627	6403	2.71	0.08	2.02	0.06
60	1.53	3981050	371	0.151	0.004	657104	5561	2.71	0.06	2.09	0.03
65	1.59	4134410	287	0.156	0.007	1105200	5369	2.65	0.11	1.90	0.08
68	0.65	4590710	247	0.105	0.004	826277	3308	3	0	1.99	0.05
68	0.64	4590890	267	0.123	0.012	830394	4087	2.73	0.16	1.83	0.10
68	0.64	4590900	243	0.123	0.012	830459	3944	2.73	0.14	1.83	0.10
65	0.98	1520840	154	0.138	0.009	472654	2726	2.88	0.14	2.05	0.10
70	0.91	255950	88	0.127	0.034	101328	1167	3	0	2	0
60	0.94	923655	123	0.145	0.005	243885	2138	2.73	0.05	2.02	0.03

65	-0.067	0.018	0.045	0.010	0.048	0	-0.030	0	0.226	0
68	-0.046	0.008	0.035	0.004	0.016	0	-0.015	0	0.181	0
70	-0.043	0.003	0.085	0.033	0	0	0	0	0.871	0
50	0.114	0.028	-0.039	0.013	0.552	0	-0.260	0	0.493	0
55	0.062	0.022	-0.016	0.010	0.548	0	-0.259	0	0.214	0
60	0.028	0.015	-0.002	0.007	0.414	0	-0.206	0	0.520	0
65	-0.070	0.013	0.044	0.007	0.061	0	-0.038	0	0.337	0
68	-0.043	0.008	0.035	0.005	-0.003	0	0.003	0	0.182	0
68	-0.042	0.006	0.034	0.004	0	0	0	0	0.181	0
68	-0.043	0.006	0.035	0.003	-0.002	0	0.002	0	0.180	0
65	-0.072	0.016	0.044	0.008	0.042	0	-0.027	0	0.333	0
70	-0.052	0.005	0.172	0.046	0	0	0	0	0.874	0
60	0.009	0.019	0.006	0.009	0.363	0	-0.181	0	0.230	0

(Table 15 continued.)

65	1.004	0.063	0.326	0.052	0.420	0.048	1.914	0.010	0.134	0.006
68	1.684	0.032	0.170	0.019	0.462	0.074	0.639	0.080	0.351	0.033
70	0.346	0.080	0.601	0.044	0.129	0.020	0.052	0.043	0.107	0.036
50	2.045	0.032	0.085	0.012	0.507	0.204	2.192	0.028	0.081	0.012
55	2.223	0.012	0.061	0.009	0.786	0.070	2.088	0.009	0.097	0.004
60	2.099	0.015	0.094	0.007	0.425	0.065	1.966	0.016	0.124	0.015
65	1.939	0.006	0.117	0.005	0.330	0.024	1.154	0.032	0.386	0.038
68	1.681	0.013	0.183	0.010	0.324	0.040	1.311	0.041	0.279	0.017
68	1.687	0.018	0.175	0.010	0.270	0.030	1.349	0.047	0.256	0.017
68	1.688	0.013	0.174	0.012	0.266	0.024	1.352	0.038	0.255	0.015
65	1.934	0.008	0.123	0.008	0.351	0.021	1.138	0.040	0.425	0.027
70	0.175	0.070	0.711	0.025	0.126	0.015	0.097	0.046	0.110	0.044
60	2.138	0.013	0.075	0.007	0.646	0.042	2.009	0.010	0.110	0.005

65	0.355	0.052	1.622	0.038	0.204	0.018
68	0.356	0.046	1.326	0.087	0.273	0.027
70						
50						
55						
60	0.055	0.022	1.522	0.188	0.344	0.122
65	0.333	0.027	1.698	0.021	0.184	0.010
68	0.494	0.039	0.628	0.036	0.375	0.018
68	0.549	0.033	0.699	0.032	0.397	0.013
68	0.554	0.031	0.703	0.034	0.399	0.013
65	0.316	0.024	1.684	0.022	0.193	0.012
70						
60	0.124	0.026	1.748	0.057	0.221	0.035

Table 16 Compiled parameters of the VBF fits of SQ #1, #2, #3 and RQ #1 series.

65	0.005	0	1.605	0.410	-1.05
68	-0.009	0	1.078	0.507	-0.18
70	-0.016	0	0.497	0.416	1.03
50	0.031	0	2.120	0.111	-0.05
55	0.028	0	2.117	0.106	-0.13
60	0.025	0	2.010	0.189	-2.27
65	0.001	0	1.600	0.415	-1.02
68	-0.006	0	1.048	0.518	-0.12
68	-0.006	0	1.060	0.511	-0.14
68	-0.006	0	1.060	0.510	-0.14
65	-0.003	0	1.576	0.439	-1.01
70	-0.024	0	0.526	0.441	1.11
60	0.022	0	2.007	0.166	-1.26

Table 17 Parameters of the xVBF fits of the LN_2T Mössbauer spectra of the alloys of the SQ #1 series. 2-σ (95 %) fitting uncertainties are given in the second column of each parameter. Parameters with 0 uncertainty were kept fixed during the fit.

15	0.64	1179820	111	0.098	0.004	131797	1499	3.11	0.07	2.55	0.07
25	0.67	1142070	159	0.099	0.010	114555	2389	3.02	0.10	2.11	0.07
30	0.85	1002620	145	0.108	0.007	175613	2393	2.95	0.06	1.74	0.04
35	0.65	658357	133	0.103	0.014	84091	2027	2.87	0.08	1.65	0.05
40	1.01	1100640	231	0.103	0.012	219775	3591	2.88	0.07	1.64	0.04
45	0.88	1866860	304	0.119	0.014	226104	4670	2.87	0.07	1.75	0.04
50	1.10	1067600	267	0.106	0.011	239587	3996	2.79	0.06	1.91	0.04
55	1.23	1438860	428	0.113	0.018	262051	6787	2.70	0.06	1.37	0.03
60	1.45	1853710	446	0.109	0.014	365463	6838	2.71	0.06	1.23	0.03
65	1.02	1022810	0	0.116	0.003	338898	1022	2.69	0.03	2.00	0.02
68	0.94	3570700	338	0.097	0.004	705761	4349	3.00	0.05	1.85	0.03

15	0	0	0	0	-0.15	0.04	0.124	0.002	0	0
25	0	0	0	0	-0.31	0.08	0.135	0.003	0	0
30	0	0	0	0	-0.38	0.05	0.140	0.002	0	0
35	0	0	0	0	-0.37	0.09	0.143	0.003	0	0
40	0	0	0	0	-0.39	0.08	0.151	0.003	0	0
45	0	0	0	0	-0.41	0.11	0.150	0.003	0	0
50	0	0	0	0	-0.32	0.05	0.157	0.003	0	0
55	0	0	0	0	-0.36	0.09	0.151	0.003	0	0
60	0	0	0	0	-0.32	0.07	0.151	0.003	0	0
65	-0.92	0.02	-0.03	0.05	-0.36	0.02	0.153	0.001	0.029	0.004
68	-0.96	0.15	0.13	0.06	-0.41	0.05	0.145	0.002	0.041	0.003

15	0	0	0.058	0.009	0.269	0	1.911	0.007	0.042	0.009
25	0	0	0.078	0.017	0.770	0	2.100	0.010	0.121	0.004
30	0	0	0.080	0.010	0.794	0	2.142	0.008	0.126	0.003
35	0	0	0.099	0.016	0.910	0	2.156	0.010	0.134	0.005
40	0	0	0.095	0.015	0.862	0	2.227	0.009	0.137	0.004
45	0	0	0.085	0.016	0.804	0	2.296	0.076	0.142	0.022
50	0	0	0.098	0.013	0.211	0	2.387	0.024	0.114	0.010
55	0	0	0.088	0.018	0.973	0	2.333	0.030	0.130	0.013
60	0	0	0.089	0.017	0.988	0	2.332	0.003	0.125	0.003
65	0	0	0.075	0.004	0.716	0	2.302	0.001	0.126	0.002
68	0	0	0.060	0.005	0.321	0	1.016	0.055	0.656	0.035

(Table 17 continued)

15	0.731	0.066	2.011	0.009	0.092	0.004
25	0.230	0.073	1.969	0.011	0.068	0.015
30	0.206	0.050	1.996	0.009	0.067	0.010
35	0.090	0.059	1.996	0.016	0.044	0.038
40	0.138	0.056	2.073	0.016	0.082	0.016
45	0.196	0.421	2.162	0.062	0.111	0.028
50	0.789	0.057	2.262	0.007	0.133	0.004
55	0.027	0.221	2.133	0.051	0.045	0.046
60	0.012	0.042	2.013	0.111	0.075	0.075
65	0.224	0.005	2.012	0.011	0.240	0.007
68	0.379	0.013	2.242	0.003	0.136	0.003

15						
25						
30						
35						
40						
45						
50						
55						
60						
65	0.060	0.002	0.813	0.019	0.140	0.0153
68	0.300	0.016	1.955	0.012	0.254	0.0094

4.3.2.1 Modelling the Hyperfine Field Distribution Using a Binomial Distribution of Nearest Neighbours

Figures 34a through c illustrate the average, standard deviation and skewness of the HFD at RT. The composition dependence of these parameters can be explained by a simple model for the local hyperfine field and a binomial distribution of nearest neighbours. In the saturated magnetic collinear regime (at low temperature), if we assume that the moments on the Fe and Ni atoms are composition independent, a simplified version of the model proposed by Rancourt and Ping [Rancourt91b] and by Dang [Dang96a] can be used to calculate the hyperfine field at an Fe nucleus, as a function of the number n (which can be from 0 to 12) of Fe nearest neighbours:

$$\begin{aligned} H(n) &= A\mu_{Fe} + B\left[n\,\mu_{Fe} + (12-n)\mu_{Ni}\right] \\ &= A\mu_{Fe} + 12\,B\,\mu_{Ni} + B(\mu_{Fe} - \mu_{Ni})\,n \end{aligned} \tag{39}$$

where A and B are (nearly) composition independent parameters. Because $H(n)$ depends linearly on n, the distribution $P(H)$ of H will have the same shape as the distribution $P(n)$ of n:

$$P(H) = P(n)\frac{dn}{dH} = P(n) / B(\mu_{Fe} - \mu_{Ni}) \tag{40}$$

In fact, this will also hold if the moments on Fe and Ni vary slowly and linearly with composition, as seems to be the case for Fe, based on electronic structure calculations [chapter 5].

If we assume that the nearest neighbours are distributed according to a binomial distribution, we can thus evaluate the characteristics of the HFD. Let $b(n, c)$ be the probability of finding n Fe nearest neighbours around the atom, when the bulk concentration of Fe atoms is c:

$$b(n,c) = \binom{n}{12} c^n (1-c)^{12-n} = \frac{n!}{12!\,(12-n)!}\, c^n (1-c)^{12-n} \tag{41}$$

The first three moments of this distribution result in:

$$\begin{aligned} <n>(c) &= 12\,c \\ \sigma_n(c) &= 2\sqrt{3}\sqrt{c(1-c)} \\ \kappa(c) &= \frac{1-2c}{\sigma_n} \end{aligned} \tag{42}$$

If we choose $B(\mu_{Fe} - \mu_{Ni}) = 15$ mm/s, we calculate the three curves also shown in figures 34a through c for the properties of the HFD. The concordance between these calculations and the observations indicates that the phenomenological model of the hyperfine field proposed by

Rancourt *et al.* and the binomial distribution of nearest neighbours seem valid for concentrations up to 50 at. % Fe. A more detailed model, as shown by Dang [Dang96a] is capable of explaining even more subtleties regarding the properties of the HFD (e.g. the average is not exactly a linear function of composition), but this simple model is sufficient to understand that these assumptions are generally respected in Ni rich Fe-Ni alloys.

Based on these results, we expect that if the magnetic structure remains ferromagnetic and collinear and if the moments do not change much with composition, the observed trend would continue at higher Fe concentrations. The breakdown of the agreement between the model and the observed HFD characteristics above 50 at. % Fe indicates that either the ground state magnetic structure shows deviation from collinear ferromagnetism or the moment magnitudes are changing, or both. This question has in part been resolved by several methods, including polarized Mössbauer spectroscopy which has shown that in $Fe_{65}Ni_{35}$, non-collinear, or at least anti-parallel, spin configurations occur in the ground state [Ullrich84, 85], resulting in the broadening of the HFD as the disordered magnetic structures produces a wide range of local magnetic environments. It is not yet clear, based on experimental evidence, if there is a distribution of moment magnitudes in Fe rich alloys. This will be discussed in greater detail when we explicitly analyse the results for Fe-rich alloys in chapter 6.

4.3.2.2 The Isomer Shift

Based on the *CS* (δ) measurements at various temperatures, it is possible to extract the *IS* and a Mössbauer effective Debye temperature Θ_D of the Fe sites as a function of composition, assuming that the *IS* is temperature independent:

$$CS(T) = IS + SOD(\Theta_D, T) \; . \tag{43}$$

The results for Θ_D are reported in fig. 35b. Given two *CS* measurements with an uncertainty of 0.003 mm/s, the uncertainty on Θ_D is about 20 K (assuming $\Theta_D \approx 380$ K and measurements are taken at RT and LN_2T). Based on this large uncertainty, it is reasonable to say that the extracted Θ_D for alloys in the collinear regime is approximately constant at 380 K. This figure is the same as had previously been calculated by Rancourt *et al.* [Rancourt92]. For alloys above 60 at. % Fe, the calculated Θ_D drops dramatically. It is not clear at this point whether this drop is real, or whether the assumption that the *IS* is temperature independent is incorrect and this will be

discussed in greater detail when specifically inspecting the *IS* of Fe-rich alloys in chapter 6. When considering only Ni-rich alloys, we can assume that Θ_D = 380 K and extract the *IS* for each spectrum using eq. 43 ($SOD(\Theta_D = 380\ K, RT)$ = -0.23309 mm/s). The resulting *IS*s are reported in fig. 35a.

It is very difficult to predict the composition dependence of the *IS* based on a simple model for several reasons. 1) The *IS* is related to the charge density at the nucleus, which can behave quite differently from the total *s*-electron density. 2) It is hard to predict if charge transfer occurs between the Fe and Ni atoms as they are alloyed, making it difficult to predict even changes in the total *s*-electron density. 3) One must take into account the change in lattice parameter due to the alloying, which also affects the charge density. The latter link can be naively modelled by assuming that the overall *s*-electron charge density scales with the inverse of the volume. Irrespective of the other factors, this would mean that an increase in volume (as the Fe concentration is increased) would cause a drop in the charge density and hence an increase in the *IS*. In fact, for alloys with less than 50 at. % Fe, the *IS* of the Fe atoms is seen to increase quasi-linearly, as shown in fig. 35, as is the atomic volume, shown in fig. 33.

At compositions above ~50 at. % Fe, deviations from the behaviour predicted from the models of collinear ferromagnetism start to appear. This is seen in the average moment, which starts dropping below the Slater-Pauling curve, before collapsing at around 70 at. % Fe (fig. 32). The RT HFD also exhibits an unusual behaviour, with a growing contribution at low field values which contributes to its increased width and abnormal skewness, until it also collapses around 70 at. % Fe. Even the *IS* departs from its Ni-rich composition dependence, although this might be also due to errors in calculating the *IS* due to changing Debye temperature. Taken together, these properties indicate a departure from the collinear ferromagnetism observed at lower Fe concentration.

In the following chapters, we explore the complex behaviours of Fe-rich Fe-Ni alloys and investigate its relations to the Invar effect and to moment-volume instabilities. Through this we will discover the intricacies of non-collinear magnetism, moment volume instability and how a complete and coherent picture of the T = 0 K and temperature dependent properties of the Fe-Ni alloys can be understood based on the results of ESCs, MC simulations and comparison with experiment.

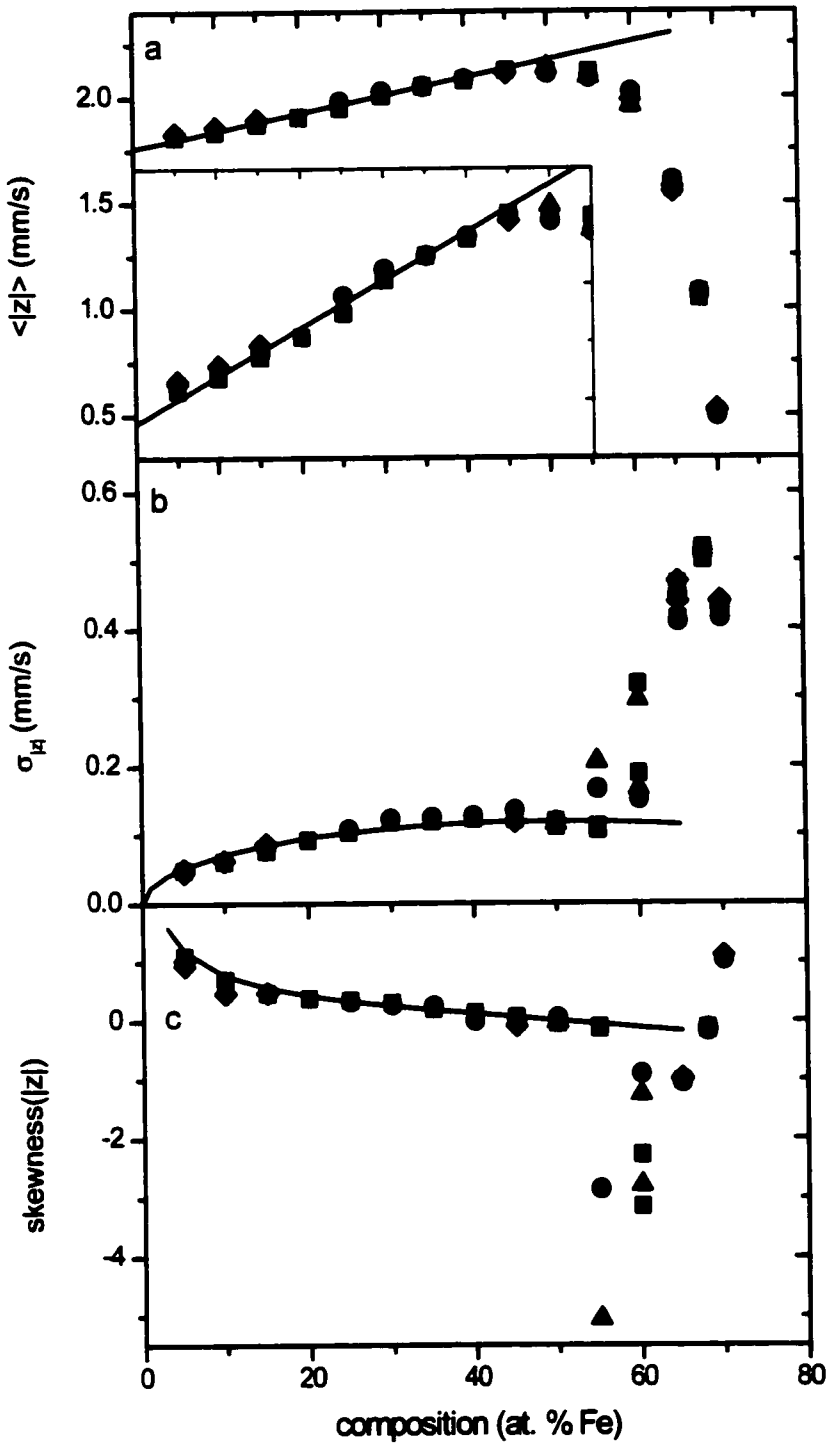

Figure 34 Properties of the HFD for RT SQ and RQ samples (the inset in (a) shows an expanded version). The solid line corresponds to the model described in the text. The deviation from the model line becomes apparent above ~50 at. % Fe and is at first mainly due to a deviation from collinear ferromagnetism. Symbols are for different series of synthetic alloys: ● SQ series #1, ■ SQ series #2, ◆ SQ series #3, ▲ RQ series #1.

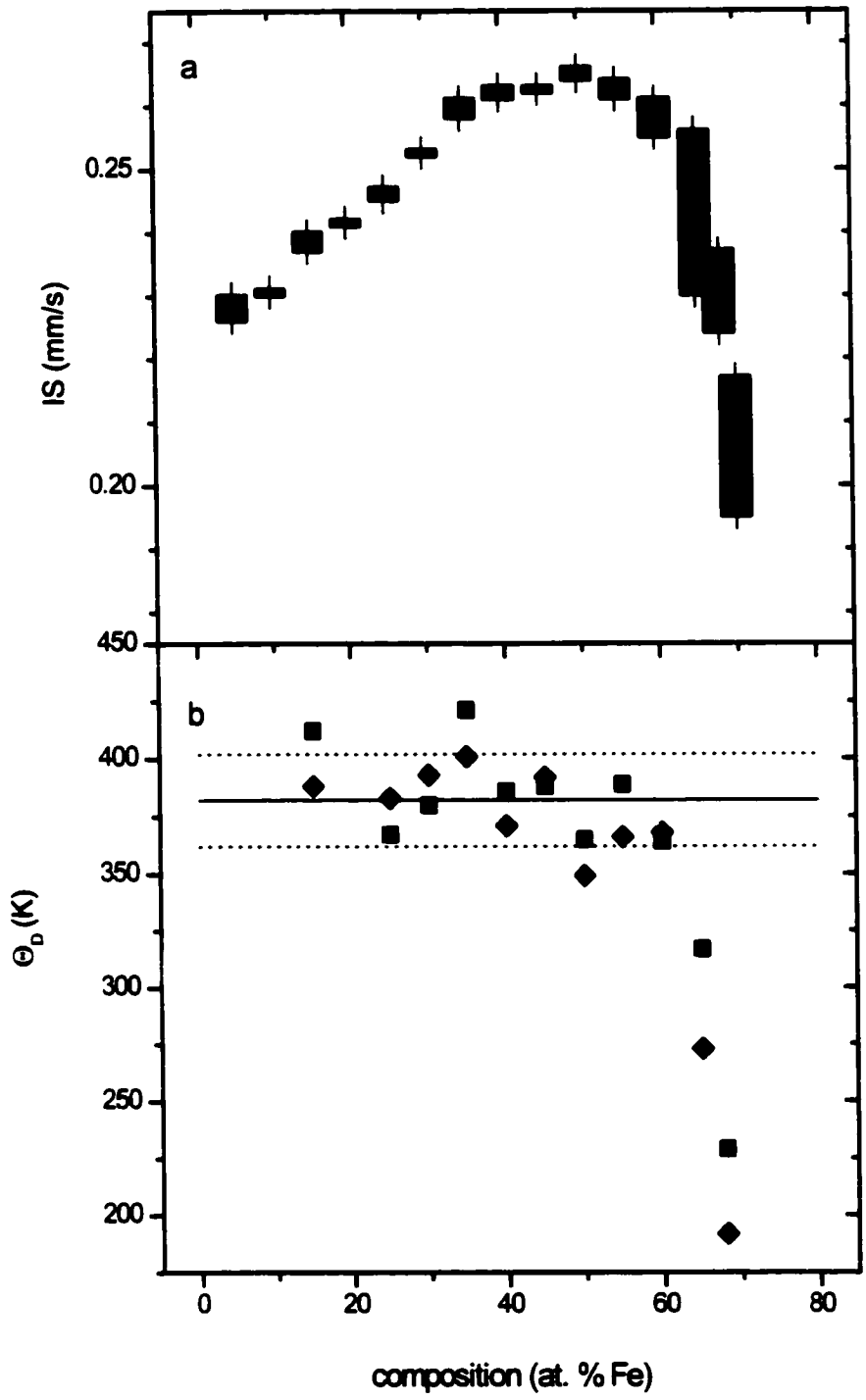

Figure 35 Calculated *IS* and Θ_D in FCC Fe-Ni alloys, assuming *IS* and Θ_D are temperature independent. The solid and dashed lines in (b) corresponds to Θ_D = 380 ± 20 K. The square and diamond symbols indicate different evaluations of Θ_D from two different pairs of *CS* data.

5. Electronic Structure Calculations of Fe-Ni Alloys

5.1 Introduction

Electronic structure calculations (ESCs) have been used more and more since the late 1970's to try to provide a theoretical understanding of the Invar and anti-Invar properties of FCC Fe-Ni alloys [Wasserman90 and references therein]. Most work has been focussed on finding the ground state properties of chemically ordered γ-Fe and Fe-Ni alloys [Wang85, Moruzzi86a, 86b, 88, Krasko87, Moroni89] and, more recently, in chemically disordered alloys [Akai89a, 89b, Abrikosov95], primarily in terms of the volume and moment. More recently yet, several studies were performed where non FM magnetic or non-collinear structures were considered [Pinski86, Mryasov92, Akai93, Wang97, Wang98, vanShilfgaarde99]. In this study, we have performed ESCs to provide direct predictions of other experimentally accessible parameters such as the HF and the *IS*. In addition, we have decided to characterize trends that give us a better understanding of the complex nature of these materials. We do not presume to be able to calculate the true properties of these alloys because of the limitations of ESC methods but we are confident that these calculations provide a strong foundation for understanding most of the perplexing properties of these alloys.

5.2 ESCs Using the LMTO Method

The linear muffin-tin orbitals (LMTO) method [Andersen75, Andersen77] is a first-principles method of calculating the electronic structure based on the density functional theory (DFT). It is applied here in the local spin-density approximation (LSDA) using the exchange potential of von Barth and Hedin [vonBarth72]. Using such a method, it is possible to calculate

the map of the spin and charge densities in a given periodic lattice. Also, by calculating the energy as a function of the lattice parameter, it is possible to obtain predictions on many experimentally accessible ground-state (T = 0 K) properties of the material.

This section is composed of three parts. The first describes how these properties can be calculated once the total energy as well as spin and charge densities are known as a function of volume. The second and third parts present and discuss the results of various calculations on Fe-Ni alloys in chemically ordered and chemically disordered phases. These calculations will be used in a subsequent section to understand the relevance of experimental observations with regards to the Invar effect.

5.2.1 Calculating T = 0 K Equilibrium Properties

5.2.1.1 The Lattice Parameter and Volume

The T = 0 K equilibrium volume for a material is the one at which the total energy is minimized. At this value, the internal pressure $P = -\partial E/\partial V$ is nil. In our application, all materials have cubic symmetry, so it is sufficient to minimize the energy with respect to a single lattice parameter. Because the precision of an ESC is about 0.1 mRy, it is not sufficient to find the lattice parameter which results in the lowest energy. A high precision of the equilibrium lattice parameter is obtained by performing several calculations around the equilibrium lattice parameter, spanning about 0.5 a_0, and fitting the resulting energy curve to a fourth-order polynomial which is used to calculate precisely the equilibrium lattice parameter. Using this method, a precision of about 0.001 a_0 can be obtained, based on the 0.1 mRy precision on the energy.

The lattice parameter calculated by a local density approximation (LDA) method is usually smaller than the experimentally observed lattice parameter. Also, this calculation does not include the volume expansion (~ 1%) which arises from the zero-point motion in, for example, the Debye model of lattice vibration. In the Debye model, the free energy due to phonons has a T = 0 K contribution should be taken into account for a more rigorous comparison between the experimental and theoretical results [Moruzzi88, Herper99], but we have decided not to include it here because there are more important problems which hinder an

exact comparison between experiment and calculations, such as the use of the LSDA, as opposed to a non-local generalized gradient method.

5.2.1.2 The Bulk Modulus

The $T = 0$ K bulk modulus, B, is related to the volume dependence of the internal pressure of the system:

$$B = -V\frac{\partial P}{\partial V} = V\frac{\partial^2 E}{\partial V^2}. \tag{44}$$

This parameter, which is also the inverse of the isothermal compressibility κ_T, is readily available experimentally and can be easily be calculated from the curvature of the energy curve. It characterizes the ability of a material to resist compression under the application of an isotropic hydrostatic pressure, and is thus partially related to the rigidity of the lattice.

5.2.1.3 The Magnetic Moment

The magnetic moment is automatically calculated in the program by integrating the net spin density inside the Wigner-Seitz radius (WSR) for all energies up to the Fermi energy:

$$\mu = \int_{-\infty}^{\epsilon_f} d\epsilon \left[n_+(\epsilon) - n_-(\epsilon) \right], \tag{45}$$

where $n_\pm(\epsilon)$ is the energy density of the number of majority (+) and minority (-) electrons of energy ϵ found inside the WSR of a specific atom. The Fermi energy ϵ_f is calculated such that the unit cell is charge neutral when all levels below the ϵ_f are occupied.

5.2.1.4 The Contact Hyperfine Field

There are several contributions to the HF at the nucleus of an atom: the Fermi contact term, which is due to the polarization of the electrons inside the nucleus; the spin-orbit term, which is due to the atomic angular momentum of the electrons; and the magnetic dipole term, which is due to the dipole interaction with all the electrons' spins (including those from

neighbouring atoms). The contact term is the dominant one in our case and is generally the only one that can be simply calculated in an ESC. Whenever we mention the calculated HF, we only take into account the contact term. Other terms most often account for only 10-20% of the total HF.

In a non-relativistic calculation, the contact HF is simply proportional to the spin density at the nucleus ($r = 0$) [Fermi30]:

$$H_{contact} = \frac{8\pi}{3}\mu_B [\rho_\uparrow(0) - \rho_\downarrow(0)] , \quad (46)$$

where $\rho_{\uparrow\downarrow}(0)$ are the majority and minority spin charge volume densities at the nucleus. When expressed in e^-/a_0^3, the conversion factor between the spin-density and the contact HF in T is 52.4303 T a_0^3/e^-.

When performing a relativistic (or scalar-relativistic) calculation, the contact term is no longer limited to the spin-density at the nucleus. Blügel *et al.* [Blugel87] have shown that the contact term can be calculated by integrating the spin density within the Thompson radius of the atom, $r_T = Z e^2 / (4\pi\varepsilon_0)^2 m c^2$, or $r_T = Z \alpha a_0 \approx 2.817 Z$ fm:

$$H_{contact}^{SRA} = \frac{8\pi}{3}\mu_B \int_0^{r_T} 4\pi r^2 dr [\rho_\uparrow(r) - \rho_\downarrow(r)] . \quad (47)$$

Because the Thompson radius is typically much larger than the nuclear radius (for Fe, $r_T/r_N \approx 18$), the error due to the use of a point-like nucleus in the calculation is relatively small [Battocletti96].

5.2.1.5 The Isomer Shift

As in the case of the contact HF, the method for calculating the *IS* in the non-relativistic and relativistic cases are different. In the non-relativistic case, the charge density is approximately constant inside the nuclear volume, so the *IS* is simply proportional to the calculated charge density at the nucleus:

$$IS = \alpha \rho(0) + IS_{ref} \quad (48)$$

where $\alpha = -0.24\ a_0^3/e^-$ mm/s for the 14.4 keV transition in ^{57}Fe, according to comparisons between calculated non-relativistic charge densities and experimental data [Akai86].

In the relativistic case, if a point nucleus is used, the charge density diverges at the nucleus, so eq. **(48)** cannot be used explicitly. It can be shown [see chapter 2] that the diverging relativistic charge density $\rho(r)$ can be associated with a non-divergent charge density $\rho_{nd}(r)$ equivalent to the non-relativistic one. We can then use eq. **(48)** using $\rho_{nd}(0)$ instead of $\rho(0)$, using the same value for α. The typical difference in charge density at the nucleus found between various compounds is of the order of 0.1 e^-/a_0^3, whereas the charge density itself is of the order of 10^4 e^-/a_0^3. This means a very high precision is needed in the calculation to notice minute changes in the *IS*, and also that ways of performing the calculations (exchange potential parametrization, relativistic corrections, etc.) will produce slightly different results. The use of additional approximations, such as the CPA can also lead to less accurate results than LMTO on ordered structures.

Because all experimental *IS*s are given relative to the CS of α-Fe at RT, we also calculated $\rho_{\alpha\text{-Fe}}(0)$ at its calculated equilibrium position in order to compare the calculated and the experimental *IS*s. We thus used

$$\begin{aligned} IS_{ref} &= -\alpha\,\rho_{\alpha\text{-Fe}}(0) - SOD(\Theta_{D,\alpha\text{-Fe}}=432\text{ K}, T=295\text{ K}) \\ &= 0.24\,\rho_{\alpha\text{-Fe}}(0) + 0.23809\text{ mm/s}. \end{aligned} \qquad (49)$$

The Debye temperature for α-Fe is taken as 432 K [Rancourt99]. Because the type of calculation (NRA or SRA) affects the equilibrium volume and thus the charge density at equilibrium, for each type of calculation, $\rho_{\alpha\text{-Fe}}(0)$ was recalculated using the same method. This means that even though the magnitudes of the charge densities might be very different in NRA and SRA calculations, the *IS* can generally be compared because it is a measure of the difference with respect to another material, not a measure of the absolute density as is the HF.

5.3 ESC of Chemically Ordered Phases

5.3.1 Description of the Crystallographic Structure

To calculate the properties of chemically ordered phases of the Fe-Ni system, we have used the LMTO code written by the group of O. Andersen at the Max-Planck Institute in Stuttgart. This code was provided to us by Dr. Bose, with permission from the Stuttgart group. This program allows us to calculate the electronic structure of chemically ordered structures

without magnetic moment or with collinear magnetic moments. It is also possible to impose collinear antiferromagnetic structures where the atoms have the same potential parameters, but opposite moments. We have performed calculations in both the NRA and the SRA. In the case of the SRA, a fully relativistic treatment (including the wavefunction) was used, instead of simply adding the relativistic Hamiltonian terms (mass-velocity, Darwin, etc.) to the non-relativistic Schrödinger equation. As previously stated, the von Barth and Hedin local exchange potential was used. Combined corrections for errors in the ASA were turned on. The same Wigner-Seitz radius (WSR) was used for both Fe and Ni atoms, and it was chosen such that the volume of all the atomic spheres was equal to the volume of the unit cell. 4*s*, 4*p* and 3*d* orbitals were taken into account in the calculation as valence orbitals. All lower orbitals are considered as core orbitals and do not contribute to the formation of a moment. Around 1000 *k*-points per irreducible Brillouin zone were used to ensure convergence of the energy (to ≤0.1 mRy) and of the moment (to ≤0.01 μ_B).

Five FCC phases (illustrated in fig. 36) with simple stoichiometries were investigated. Pure Ni and pure γ-Fe, of space group *F*m-3m (n° 225) are the end members. $FeNi_3$ and Fe_3Ni have 4 atoms per primitive unit cell in the $AuCu_3$ structure (space group *P*m-3m, n° 221, or L1_2). FeNi has a tetragonal AuCu structure (space group *P*4/mmm, n° 123, or L1_0) with 2 atoms per unit cell. Though FeNi is experimentally found to have a slight tetragonal distortion compared to the cubic structure (c/a =1.0036, [Albertsen81]), we have only performed calculations on purely cubic phases. α-Fe, which was used as the reference material for the calculation of the *IS* has a BCC structure (space group *I*m-3m, n°229).

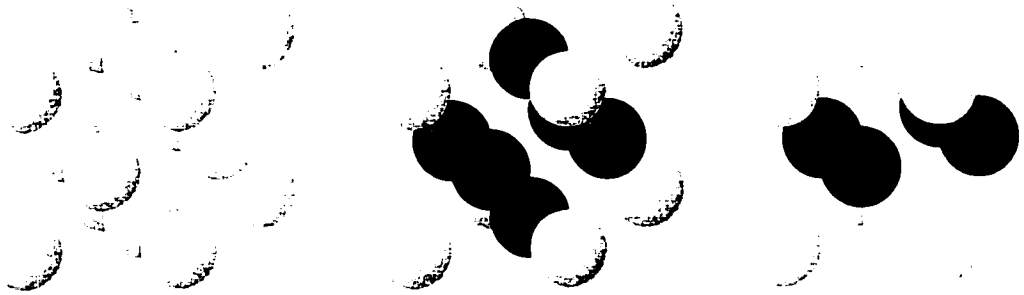

γ-Fe or Ni
Fm-3m

$FeNi_3$ or Fe_3Ni
Pm-3m
$L1_2$ structure

FeNi
*P*4/mmm
$L1_0$ structure

Figure 36 Chemically ordered structures in FCC Fe-Ni alloys with simple stoichiometries. The black and white atoms represent the two different species.

5.3.2 Calculated ESC in Ferromagnetic and Non-Magnetic Configurations

Since much of the recent work on Fe-Ni alloys has been focussed on the HM/LM (or HM/NM) transition, we have performed calculations for a wide range of lattice parameters for which we have a stable HM phase in all alloys at the high-end, and a NM phase at the low end. This permits us to follow the evolution of key parameters through the transition. It also allows us to investigate how the parameters vary with the lattice parameter within a stable (HM or NM) region to possibly predict their behaviour with temperature. This is possible because at the temperatures of interest (below 1000 K), we are far from the Fermi energy of these materials, and the main changes in their electronic structures are expected to come from the changes in lattice parameter due to thermal expansion. We have also performed calculations by imposing a non-magnetic electronic structure even when the ferromagnetic phase is more stable in order to compare the properties of the material at the equilibrium lattice parameter in the FM and NM phases. Many similar calculations have been performed on ordered phases of the Fe-Ni system [Moruzzi90, Mohn91, Entel93], so we will present our important results without describing the specifics of the ESC and the density of states (DOS) in detail. Our results agree with previously published calculations which used the same methods. In previous calculations, some parameters such as the charge density at the nucleus or the hyperfine field had not necessarily been calculated, so it was necessary to repeat them in this study.

5.3.2.1 Ground States and Magnetic Moments

Figures 37 through 41 show (a) the energy, (b) the magnetic moments, and (c) the charge density at the nucleus for the five ordered structures of the Fe-Ni system in the FM and NM states. When the HM FM state is not stable, the figures also show its properties based on extrapolations from the volume range where it is stable. The extrapolated energy curve is obtained from fourth-order polynomial approximation to E(V) where the HM state is stable. Other extrapolated properties are the result of second-order approximations. In γ-Fe, an antiferromagnetic (AF) configuration in the (001) direction was also explored.

All figures show a transition from a HM FM state at high volume to a NM state at lower volumes. In the case of Fe and FeNi (figs. 37 and 39 respectively), an intermediate moment (IM) state is also found to be stable (or metastable) close to the HM/NM transition volume. In the case of Fe_3Ni, no distinct IM state is observed, but rather there is a continuous decrease of the magnetic moments of the Fe and Ni atoms (fig. 38). In fact, in this case, the ground state is observed in the region where the moments are collapsing. In $FeNi_3$ and pure Ni (figs. 40 and 41), the moment collapse is sudden but continuous, indicating there are no distinct metastable states with different moment values. This situation is different from the one in γ-Fe where for a given volume, the AF, IM FM and HM FM states are all stable (or metastable), or in FeNi, where the IM and HM states can also both be stable at the same volume.

One must remember that when a mention is made of a HM "state", it is in the context of an extended and uniform phase. These calculations cannot simply be made to show there are distinct *ionic* states for the Fe (and Ni) atoms, because the phase must be uniform. An *ionic* state of an atom should exist independently (or nearly independently) of the other atoms or the magnetic structure. Anytime the word *state* is used, it is understood that it is in the context of a *phase* and cannot necessarily be separated from that context.

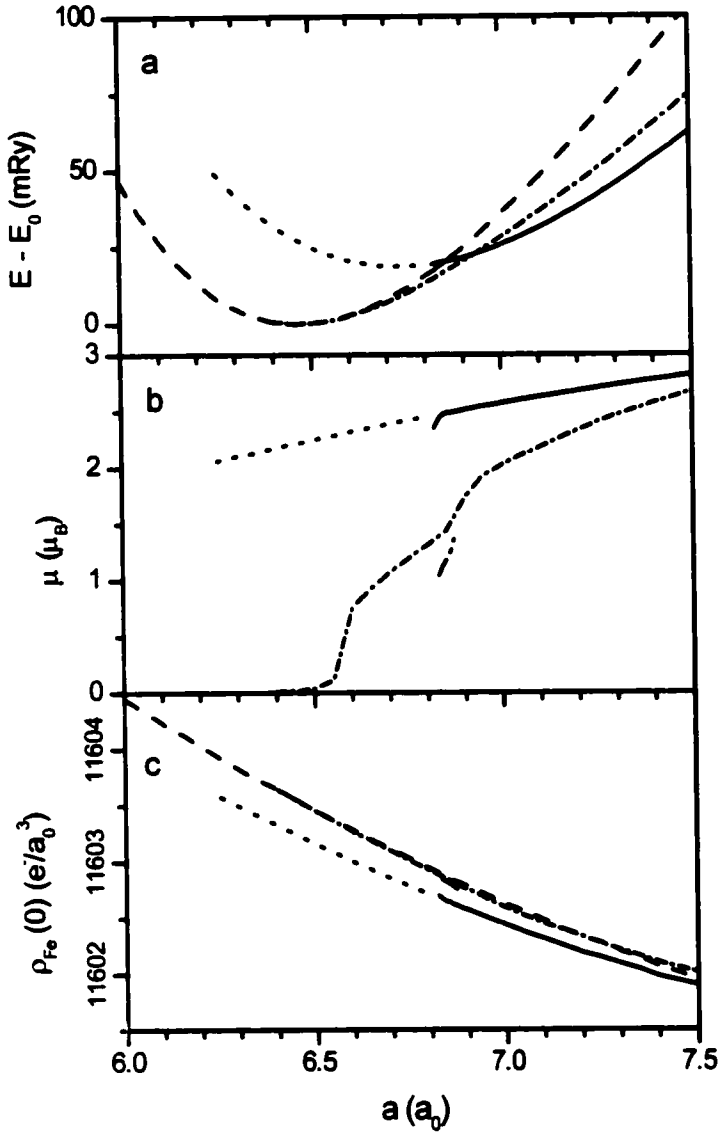

Figure 37 ESC results for γ-Fe. The solid line represents the HM FM state, the dash-doted line the IM FM state, the dashed line the NM state, the sort-dash-dotted line is the AF state and the dotted line the extrapolated HM FM state.

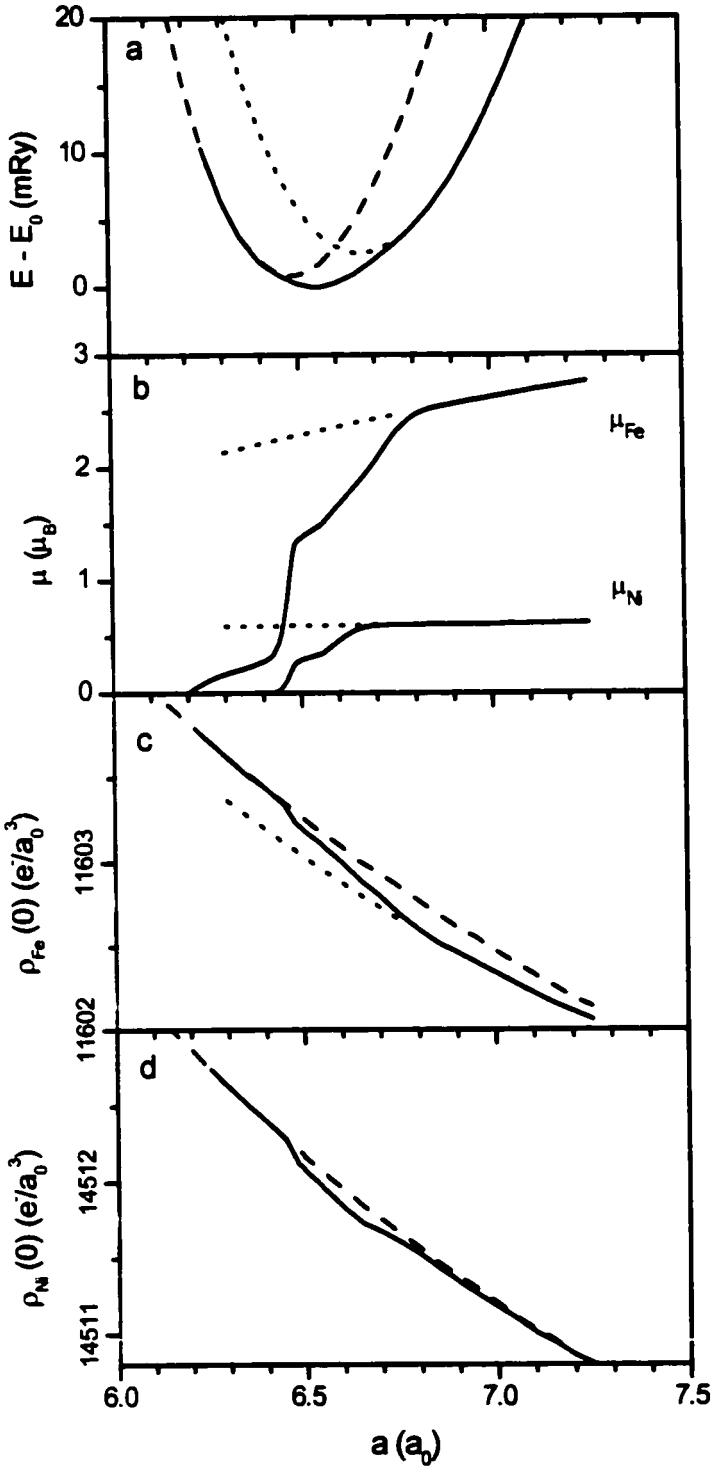

Figure 38 ESC results for Fe_3Ni. The solid line represents the FM state, the dashed line the NM state and the dotted line the extrapolated HM FM state.

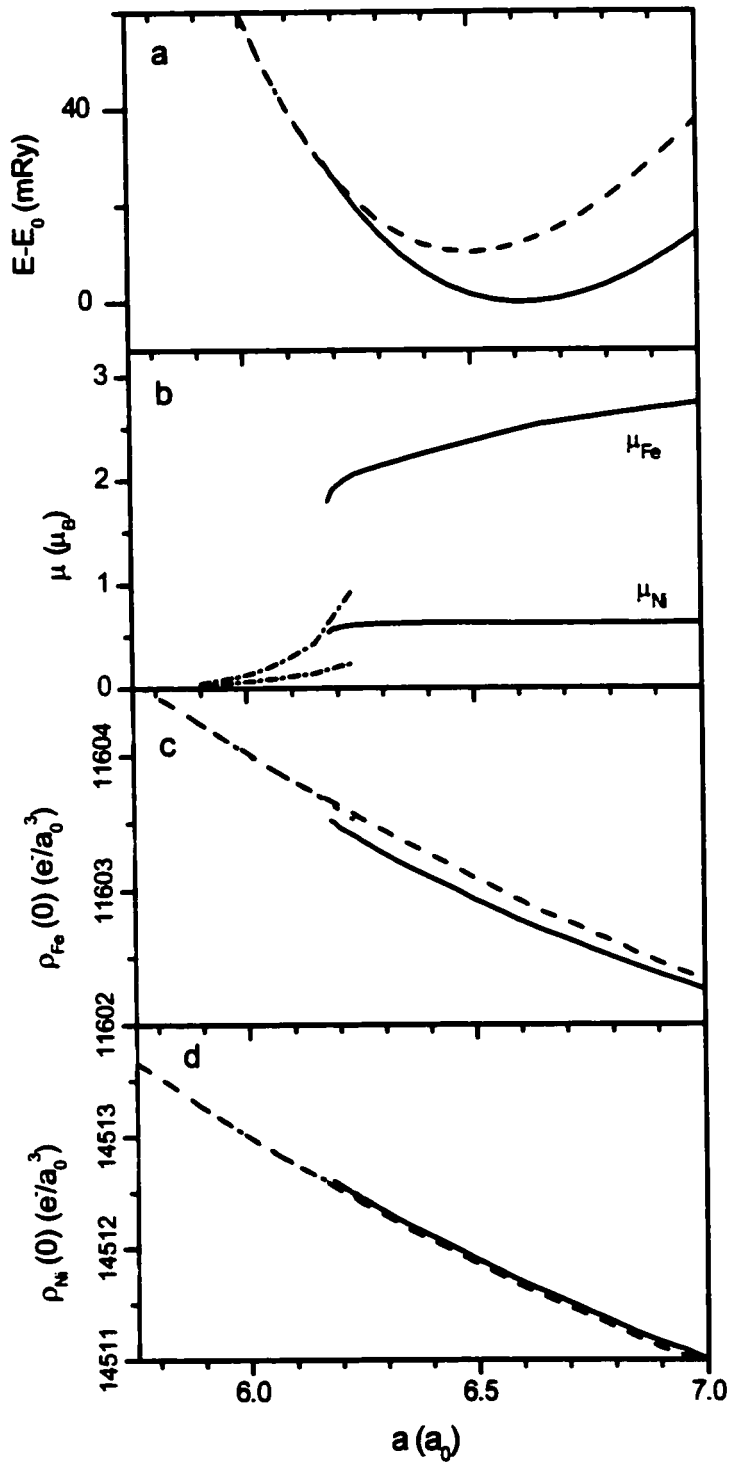

Figure 39 ESC results for cubic FeNi. The line styles represent the same states as in fig. 37.

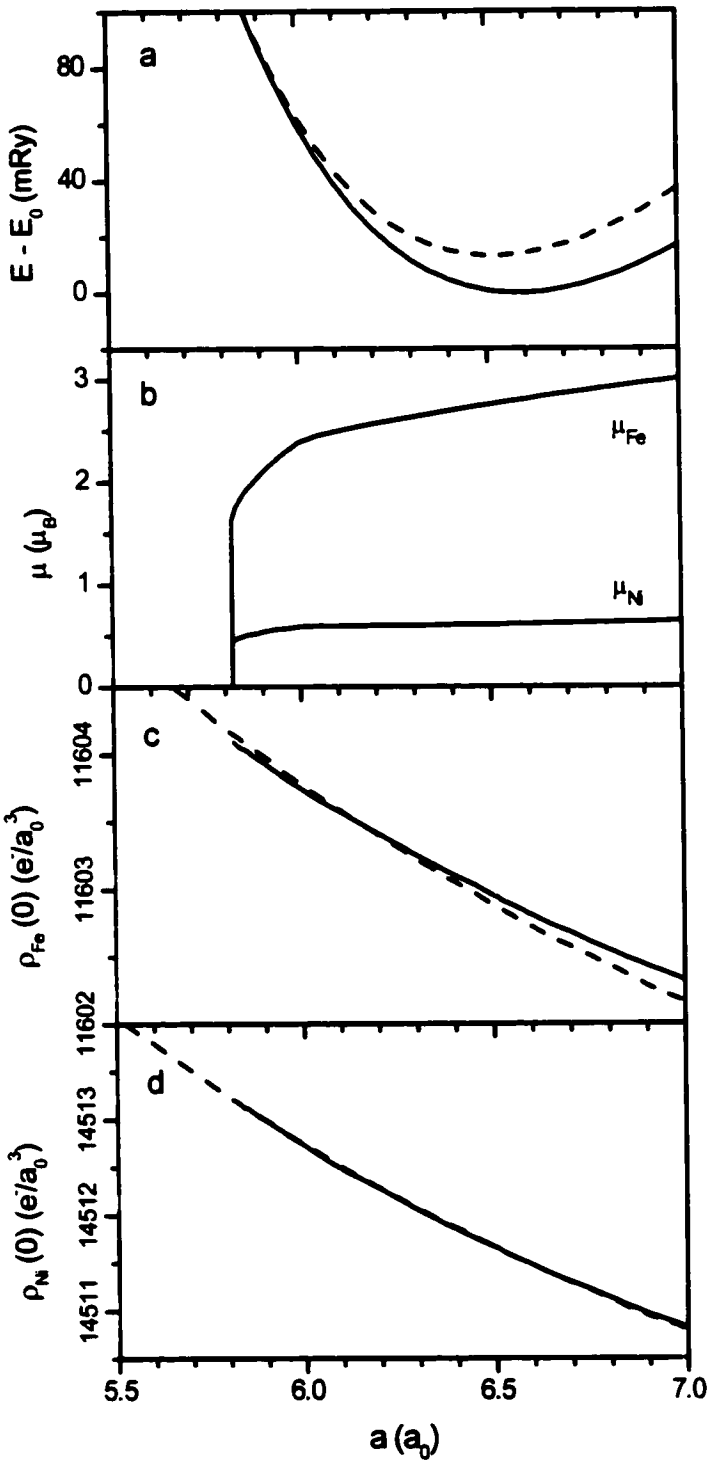

Figure 40 ESC results for $FeNi_3$. The line styles are the same as in fig. 37.

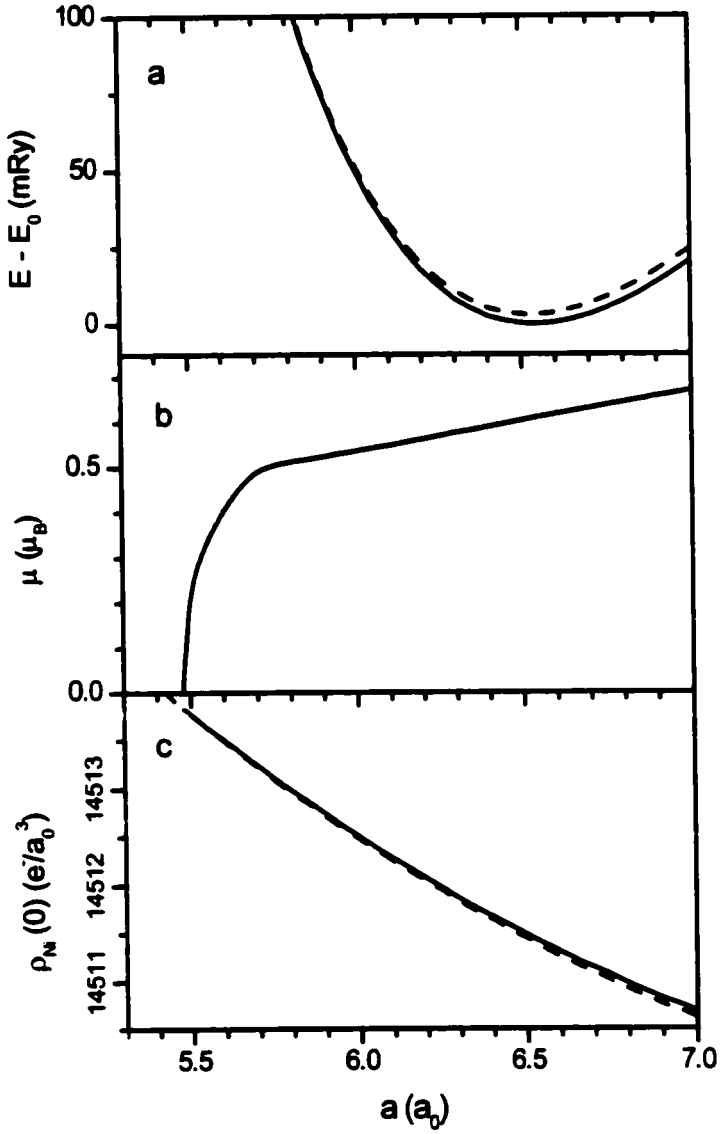

Figure 41 ESC results for Ni. The line styles represent the same states as in fig. 37.

5.3.2.2 Systematics of the Charge Density at the Nucleus

As seen in figures 37c/d through 41c/d, the charge density at the Fe and Ni nuclei normally decreases regularly with the volume. However, the exact volume dependence is quite different in the HM FM and NM cases, which leads to a discontinuity of the charge density through the HM/NM transition. In the case of $\rho_{Fe}(0)$, there is an increase of ~0.2-0.3 e^-/a_0^3 between the FM and NM states in γ-Fe, Fe_3Ni and FeNi, but it becomes less noticeable in $FeNi_3$. The same can also be said of $\rho_{Ni}(0)$, but the magnitude of the jump is much smaller and practically negligible given the precision of the calculation. When comparing $\rho_{Fe}(0)$ at the equilibrium positions of the NM and FM states, an additional increase when going from the FM state to the NM state is due to the lower volume of the NM ground state. This difference in volume accounts for an additional ~0.4-0.5 e^-/a_0^3 in γ-Fe, and lower values for decreasing Fe content, since the volume difference between the NM and FM ground states decreases.

If we assume that the charge density at the nucleus is independent of the magnetic order, but only depends on the spin state (HM or NM), and that thermal effects only affect the lattice parameter, it is possible to estimate the temperature dependence of the charge density. In the NM or FM states, we have $\partial\rho_{Fe}(0) / \partial a \sim -1\, e^-/a_0^4$. If we use $\alpha = -0.24$ mm/s a_0^3/e^- [Akai86] to convert to an *IS*, and assume that the thermal expansion is ~ $10^{-5}\,K^{-1}$, we get

$$\frac{\partial IS}{\partial T} \sim +1.5 \times 10^{-5} \text{ mm/s/K} \qquad (50)$$

for the Fe nuclei. Any measured rate of change $\partial IS / \partial T$ which is noticeably larger than 10^{-5} mm/s/K must then be associated with a separate phenomenon, such as thermal evolution from a NM to a HM state (or vice-versa), since it cannot be entirely accounted for by changes due directly to thermal expansion.

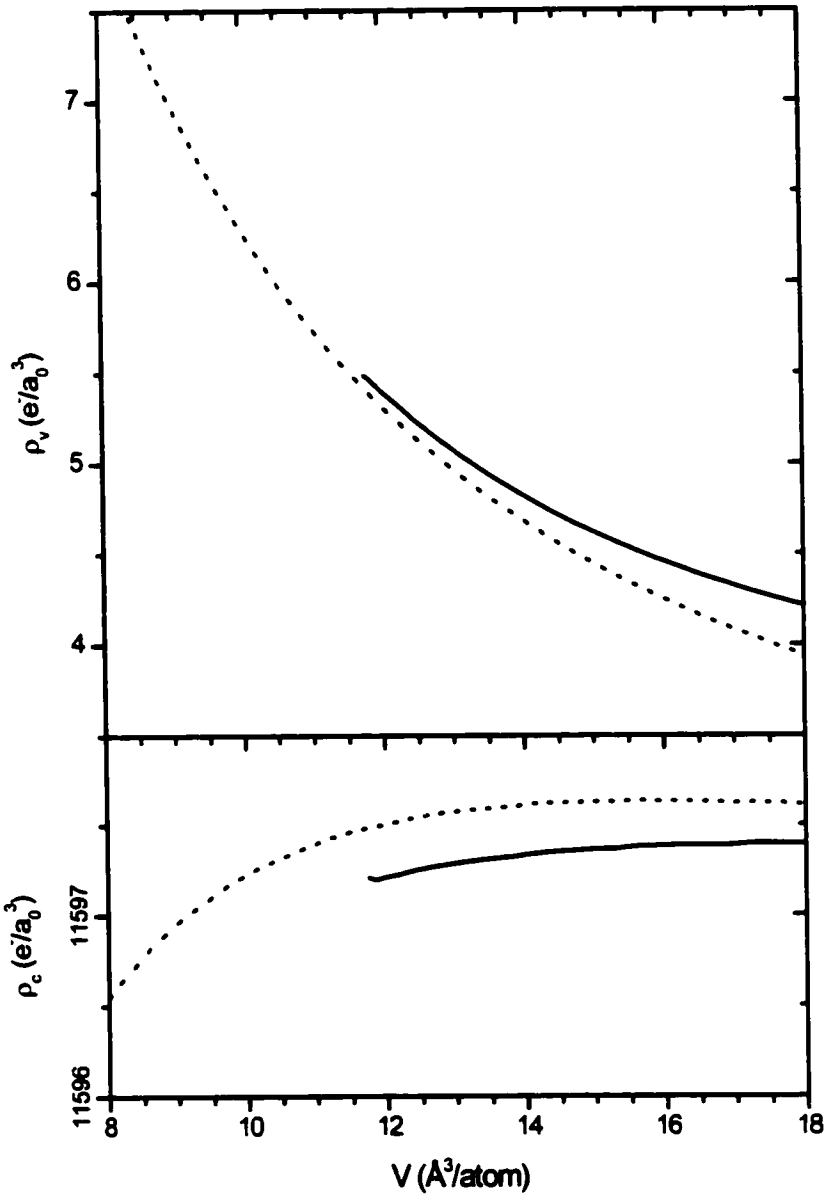

Figure 42 Valence ($\rho_v(0)$) and core ($\rho_c(0)$) charge densities at the Fe nucleus in NM (dotted line) and HM FM (solid line) γ-Fe.

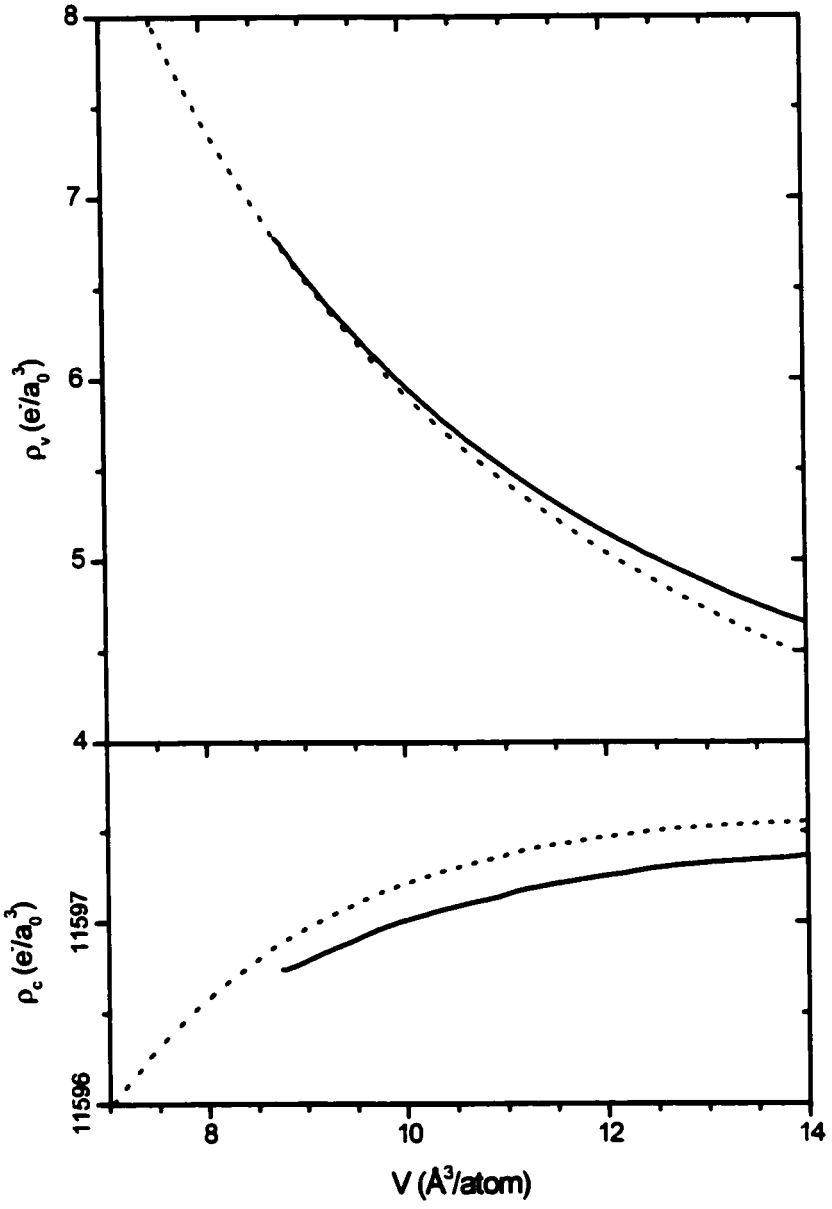

Figure 43 Valence ($\rho_v(0)$) and core ($\rho_c(0)$) charge densities at the Fe nucleus in NM (dotted line) and HM FM (solid line) FeNi.

Figures 42 and 43 also show the explicit volume dependence of the core and valence charge densities at the Fe nucleus in γ-Fe and FeNi. One clearly sees that i) the main volume dependence of the total charge density at the nucleus comes from the valence contribution, and ii) the discontinuity seen at the HM/NM transition volume is mainly due to the core contribution. This illustrates the necessity of using a fully relaxed (core+valence) charge density in order to see the full effects related to the HM/NM transition. In many calculations, the core contribution is assumed to be frozen, and only the valence charge density is calculated. In such cases, the discontinuity at the HM/NM transition would not be seen. It is also interesting to see that the valence charge density at the nucleus does approximately follow an inverse volume law, as if the shape of the distribution of total valence charge was volume independent. In γ-Fe, the total valence charge on the atom is always constant (8 electrons), so it would seem the shape of the charge distribution is approximately volume independent. For the case of FeNi, this is also true for the NM phase, where the valence charges on the Fe and Ni atoms remain constant. In the FM case however, the valence charge on the Fe atoms decreases with increasing volume, indicating that there is a charge transfer to the Ni. This leads to a stronger deviation from an inverse volume law in the FM case.

5.3.2.3 Systematics of the Hyperfine Field

In her thesis regarding magnetism in Fe-Ni alloys, Dr. Dang used a phenomenological model to describe the HF [Dang96a, Dang96b], which in the case of collinear magnetism at 0K, reduces (in its simplest form) to:

$$H_i = A\mu_i + B\sum_{NN}\mu_j, \tag{51}$$

where H_i is the HF at site i and the sum is on nearest-neighbours (NNs) of site i. It is worthwhile to investigate if this relation holds for the HFs and moments calculated in this study.

First of all, we consider the HF due to core electrons, H_c. Based on figs 45 and 46, we find that in both Fe and Ni atoms, it is generally proportional to the local magnetic moment: $H_c = (-11\ \mathrm{T}/\mu_B)\,\mu$. This result is well established [Freeman64], and is also seen to be independent of the magnetic structure, as it applies to FM Fe as well as AF Fe. On the other hand, the dependence of the HF due to valence electrons, H_v, is not as straightforward. This is due

primarily to the presence of a transferred term, in which the HF is related to the moments of the atoms in nearest-neighbour shells. It is important to recall here that the HF we calculate is only the Fermi contact term, which does not include the field due to dipolar interactions or due to spin-orbit interactions [Blügel87]. Although there is no clear dependency of H_v to the local magnetic moment, fig. 44 shows that there is a good general linear relation between the total HF, H, and $<\mu>$, the average magnetic moment in the structure:

$$H = (-15.5\ \mathrm{T}/\mu_B) <\mu> \ . \qquad (52)$$

It is also interesting to note that both these relations seem universal as they apply to HFs at the Fe and Ni nuclei.

It is possible to reconcile this model of Dang and Rancourt with eq. 52. Assuming parameters A and B in the model are independent of the concentration, we can write equations relating the HF to the individual moments on the Fe and Ni atoms for all the calculated structures (we use C = -15.5 T/μ_B):

in FM Fe	$H_{Fe} = (A + 12B)\,\mu_{Fe} = C\,\mu_{Fe}$
in AF Fe	$H_{Fe} = (A - 4B)\,\mu_{Fe} = 0$
in FM Fe_3Ni	$H_{Fe} = (A + 8B)\,\mu_{Fe} + 4B\,\mu_{Ni} = C\,(0.75\,\mu_{Fe} + 0.25\,\mu_{Ni})$
	$H_{Ni} = A\,\mu_{Ni} + 12B\,\mu_{Fe} = C\,(0.75\,\mu_{Fe} + 0.25\,\mu_{Ni})$
in FM FeNi	$H_{Fe} = (A + 4B)\,\mu_{Fe} + 8B\,\mu_{Ni} = C\,(0.5\,\mu_{Fe} + 0.5\,\mu_{Ni})$
	$H_{Ni} = (A + 4B)\,\mu_{Ni} + 8B\,\mu_{Fe} = C\,(0.5\,\mu_{Fe} + 0.5\,\mu_{Ni})$
in FM $FeNi_3$	$H_{Fe} = A\,\mu_{Fe} + 12B\,\mu_{Ni} = C\,(0.25\,\mu_{Fe} + 0.75\,\mu_{Ni})$
	$H_{Ni} = (A + 8B)\,\mu_{Ni} + 4B\,\mu_{Fe} = C\,(0.25\,\mu_{Fe} + 0.75\,\mu_{Ni})$
in FM Ni	$H_{Ni} = (A + 12B)\,\mu_{Ni} = C\,\mu_{Ni}$

Whatever the values of μ_{Fe} and μ_{Ni} , all these equations are solved simultaneously by $A = 4B$ and $A = C/4$, or numerically $A \approx$ -4 T/μ_B and $B \approx$ -1 T/μ_B. This must be compared with $|A| \approx$ 9 T/μ_B and $|B| \approx$ 0.4 T/μ_B, as obtained by Dang by fitting experimental results. Although these parameters are significantly different, it does not invalidate the model. The calculated HF is only the contact term, and even this term is very sensitive to the details of calculations [Battocletti96], but these results do show that there are inherent systematics which can be exploited by

phenomenological models. We should also note the slight problem for the case of AF Fe. Since the average moment is 0 in AF Fe, this model would also lead to a nil HF. Though this is not the case, the calculated values of the HF in this case are small (the magnitudes of the total HF are found to be less than 5 T) as the core and valence contributions almost cancel out (fig. 45a and b), indicating that the model should be fairly good for any magnetic structure.

Even though accurate calculations of the HF in transition metal alloys are difficult [Blügel87, Battocletti96], these calculations do seem to validate, in addition to the direct comparison with the experiments, the phenomenological model proposed by Dang to describe the HF values obtained in Fe-Ni alloys.

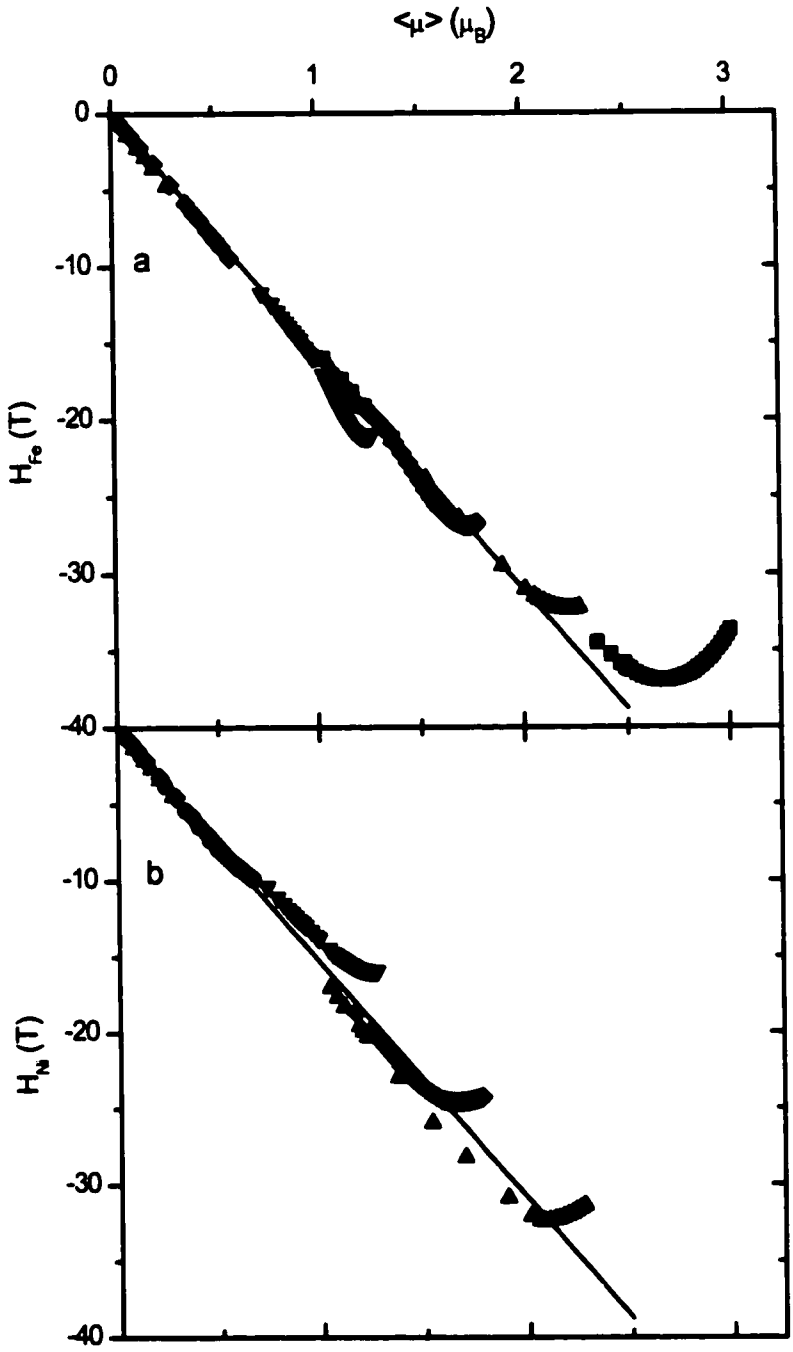

Figure 44 Calculated total hyperfine field at the Fe (a) and Ni (b) nuclei, as a function of the average magnetic moment per atom in the structure. ■ FM γ-Fe, ▲ Fe_3Ni, ◆ FeNi, ▼ $FeNi_3$, ● Ni. The solid line is H = -15.5 μ.

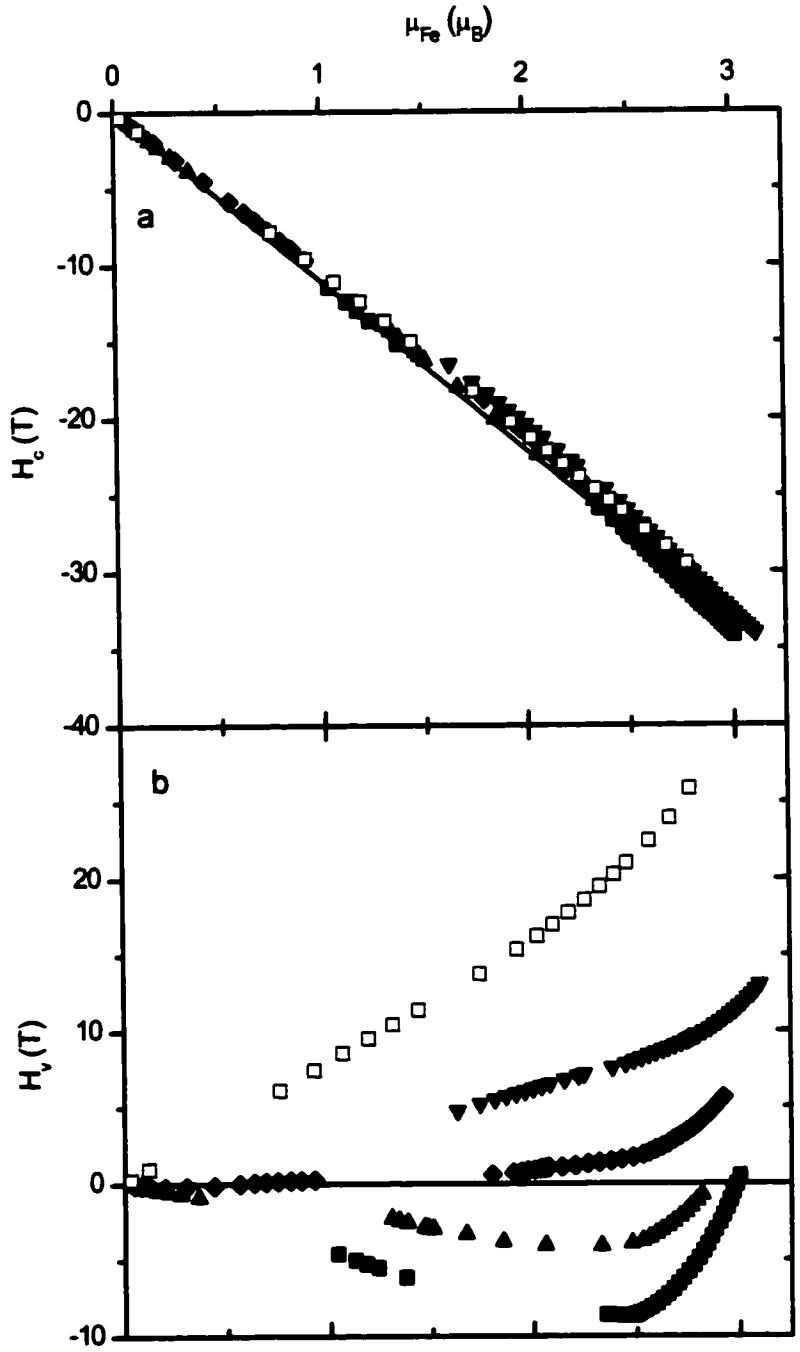

Figure 45 Calculated core (a, H_c) and valence (b, H_v) hyperfine fields at the nuclei as a function of the moment on the Fe atoms. ■ FM γ-Fe, □ AF γ-Fe, ▲ Fe_3Ni, ◆ FeNi, ▼ $FeNi_3$. The solid line in (a) is H_c = -11 μ.

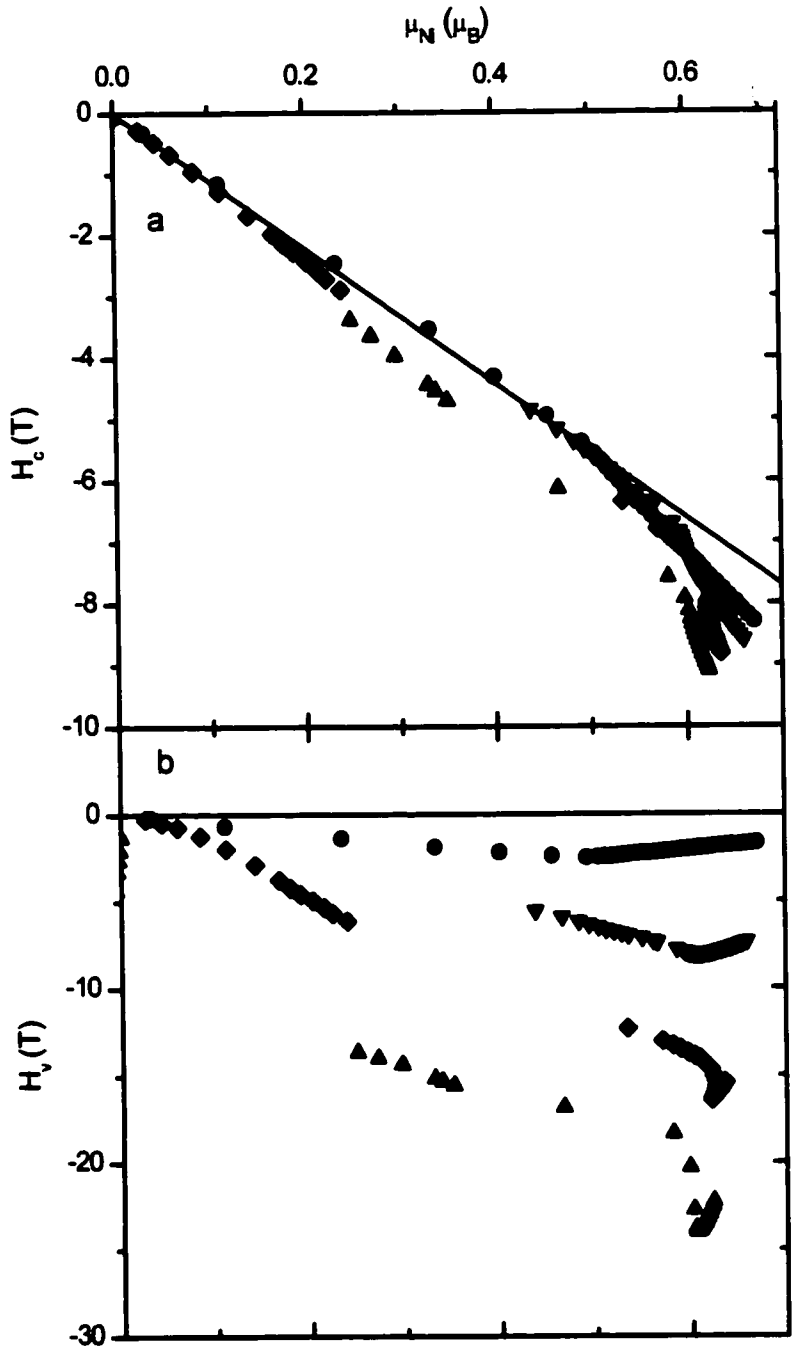

Figure 46 Calculated core (a, H_c) and valence (b, H_v) hyperfine fields at the Ni nuclei as a function of the moment on the Ni atoms. ● Ni, ▼ $FeNi_3$, ◆ FeNi, ▲ Fe_3Ni. The solid line in a. is H_c = -11 μ.

5.3.2.4 Site to Site Variations in Fe-Rich Alloys

In every structure considered up to now, all Fe atoms are equivalent, as are all Ni atoms. This means that while we can establish relations between parameters at different concentrations and volumes, we cannot identify correlations between parameters that can occur in a true alloy of a given composition at a given volume. In an alloy, all atoms are in different local environments which lead to possibly different local hyperfine parameters such as the HF and the *IS*. To identify how these parameters are distributed and correlated in Fe-rich alloys, we have also performed calculations in an $Fe_{11}Ni_5$ (68.75 at. % Fe) supercell where there are 11 distinct sites for Fe atoms (listed in Table 18). This enables us to study possible links between parameters.

Because of the time required for the calculation, the ESC of this structure was only calculated at one lattice parameter ($a = 6.66\ a_0$), as opposed to other calculations where the energy was minimized with respect to the lattice parameter. The lattice parameter in question is approximately the one expected for the HM FM phase based on the calculations at other concentrations. At this lattice parameter, we find that the site to site moment magnitudes are quite diverse, with one Fe moment actually opposite to the bulk magnetization (negative moment). We should note that while such collinear antiferromagnetism is characteristic of the true alloy at $T = 0$ K, we also expect moment non-collinearity to occur in such Fe-rich alloys [vanSchilfgaarde99, Wang95]. However, we could not take non-collinearity into account in our calculation.

Based on this calculation, the single most important local environment parameter that affects all parameters of the Fe atoms is the number of Fe atoms in the NN shell. The data given in table 19 and illustrated in fig. 47 shows that the moment magnitudes of both Fe and Ni atoms are directly related to it (the more NN Fe atoms, the lower the moment magnitude) and that anti-parallel alignment of Fe moments can actually occur in a sufficiently rich Fe environment. In fact, it also seems that the anti-parallel alignment of the moment actually stabilizes its large magnitude, compared to other moments in an Fe-rich environment (9 Fe NNs). One might expect that, in more Fe-rich alloys, there would simply be more anti-parallel moments but that their magnitude would remain that of the HM alloys. This calculation clearly suggests that the observed deviation from the Slater-Pauling curve is due to both a slight decrease of the moments in more Fe-rich environments which leads to a small and slow deviation and the appearance of

anti-parallel Fe moments which is the main cause of the dramatic decrease of the average bulk moment (see fig. 32, in chapter 4). Also, in such a structure, the existence of anti-parallel Fe moments in sufficiently Fe-rich environments is a clear indication of the negative (antiferromagnetic) magnetic exchange between Fe moments in Fe-Ni alloys.

Upon further inspection of fig. 47, we also find that the number of valence electrons (integration of the valence charge density within an atom, defined by the WSR) is directly linked to the local chemical environment. In previous calculations, because the WSR of Fe and Ni atoms changed with concentration (at the equilibrium volume), it was difficult to establish when charge transfer occurs, as the "true" radii of the atoms are not known. However, because all Fe atoms in this calculation have different local environments but the same WSR, it is possible to say that electrons are transferred from the Fe atoms to the Ni atoms, since Fe atoms with more Ni NNs have less valence electrons than Fe atoms in an Fe-rich environment (fig. 47a). There also seems to be a clear correlation between the number of valence electrons and the charge density at the nucleus and we find in fact that the valence contribution to the charge density at the nucleus is directly proportional to the number of *s*-valence electrons (fig. 49), as if the total *s*-electrons charge density was simply scaled uniformly by the number of *s*-electrons, independently of the charge transferred. There doesn't seem to be any simple correlation between the local environment (number of Fe NNs, charge transfer, etc.) and the core contribution to the charge density at the nucleus, as is expected since these electrons are less sensitive to the environment outside of the atom. Because both the moment and the number of valence electrons are closely linked to the local chemical environment, it is obvious they should also be linked together. Figure 48 shows the relation between the number of valence electrons and the local moment. The moment seems to drop and become unstable when the number of valence electrons becomes too large, indicating that the local density of valence electrons may be a key to understanding the instability of the Fe moment, as opposed to the average density of valence electrons. For a given material, the moment is rendered unstable by decreasing the volume, yet in Ni-rich alloys, where the mean atomic volume is much lower than in Fe-rich alloys, a large moment is stable. This could be due to the fact that charge is transferred to the Ni atoms, so that the local valence charge density is actually lower in these alloys, even though the average number of valence electrons is larger and the volume in smaller.

The local HF also seems very dependent on the local environment. As previously stated,

the core contribution to the contact HF is proportional to the moment and since the moment magnitude is strongly correlated with the number of Fe NNs, so is the core HF. The valence contribution to the HF is not as clearly linked, though there is evidence of some dependence with the local environment. Most importantly though, is the local magnetic environment. As seen in table 19, the HF of the moment which is aligned opposite to the bulk has a very large contribution from the valence electrons, compared with this contribution for other Fe moments. Based on this examination, it thus seems that the valence HF has a component proportional (or dependent) to the local moment and a component proportional (or dependent) to the NN moments. In a FM material, both these components nearly cancel each other out but in the case where the NN moments are aligned opposite to the local moment, the contributions add up to a large valence contribution which is opposite in sign relative to the core contribution, resulting in a low effective contact HF. This is also compatible with the model of Dang and Rancourt presented previously. At this specific composition, we find that the model can be applied locally to each atomic site. In fact, as shown in table 20, we also obtain nearly identical parameters, since a fit to the data of the $Fe_{11}Ni_5$ alloy results in A = -5 T/μ_B and B = -0.9 T/μ_B. If the total HF is linearly dependent on the local and NN moments and the core HF is proportional to the local moment (with A' = -10.8 T/μ_B), then, as stated, the valence HF will also depend linearly on the local and NN moments (with $A'' \approx A - A'$ = 5.5 T/μ_B and $B'' \approx B$ = -0.85 T/μ_B). It is thus evident that in a material which has moments aligned opposite to the bulk magnetization, the HF distribution will contain a low-field component (as shown in fig. 50) because the transferred field from the NN almost cancels out the field due to the local moment. This has been described in great detail by Ping and Rancourt [Ping92] based on experimental measurements of HFDs in Fe-Ni alloys. The resulting link between the local environment and the HF also results in a strong correlation between the HF and the charge density at the nucleus (or the *IS*). The correlation parameter between the two is 0.004 mm/s/T (fig. 51) and the implications of this will be discussed in greater detail in the next chapter when we will analyse Mössbauer spectra of Fe-rich alloys in which this correlation can be seen experimentally.

This single calculation for this small supercell has clearly shown the influence of the local chemical (number of Fe NNs) and magnetic (orientation of magnetic moments) environments on several parameters in these alloys and has established grounds for understanding experimental observations.

Table 18 Atomic positions (in units of $a = 6.66\ a_0$) of the Fe and Ni atoms in the $Fe_{11}Ni_5$ supercell. The NNs are also given, as well as the total number of Fe NNs.

Fe	0.5	0.5	0		2	2	2						1	1			2	1	1	*8*
Fe1	0	0.5	0.5	2		1		1				1	2	2	2		1			*9*
Fe2	0.5	0	0.5	2	1		1		2		1		2			1		2		*9*
Fe3	1	0.5	0.5	2		1		1				1			2		1	2	2	*5*
Fe4	1.5	0	0.5		1		1			2	1		2		2	1		2		*7*
Fe5	0.5	1.5	0			2					2		1	1		2	2	1	1	*6*
Fe6	1.5	1.5	0					2			2	2	1	1		2		1	1	*8*
Fe7	1	1.5	0.5			1		1	2	2		1					1	2	2	*7*
Fe8	1.5	1	0.5		1		1			2	1			2	2	1			2	*7*
Fe9	0	0	0	1	2	2		2	1	1					1	2				*9*
Fe10	0	1	0	1	2				1	1		2			1	2	2			*7*
Ni	1.5	0.5	0		2		2	2				2	1	1				1	1	*10*
Ni1	0	1.5	0.5			1		1	2	2		1	2	2			1			*11*
Ni2	0.5	1	0.5	2	1		1		2		1			2		1			2	*9*
Ni3	1	0	0	1		2	2	2	1	1	2				1					*11*
Ni4	1	1	0	1			2		1	1	2	2			1		2			*9*

Table 19 Calculated properties of the Fe and Ni atoms in an $Fe_{11}Ni_5$ supercell with $a = 6.66\ a_0$.

Fe	8	0.627	0.764	6.556	7.946	1.807	-19.43	-0.27	-19.70	11597.24	5.68	11602.92	0.2419
Fe1	9	0.631	0.777	6.576	7.984	1.482	-15.95	-0.49	-16.44	11597.25	5.72	11602.98	0.2279
Fe2	9	0.630	0.770	6.597	7.996	0.990	-10.75	-4.17	-14.93	11597.29	5.71	11602.99	0.2241
Fe3	5	0.610	0.742	6.498	7.850	2.306	-24.84	1.70	-23.14	11597.24	5.52	11602.75	0.2817
Fe4	7	0.621	0.757	6.537	7.915	1.948	-20.88	3.49	-17.38	11597.25	5.63	11602.87	0.2530
Fe5	6	0.616	0.752	6.511	7.879	2.100	-22.55	3.88	-18.67	11597.26	5.57	11602.83	0.2624
Fe6	8	0.626	0.765	6.570	7.961	1.704	-18.40	-3.19	-21.59	11597.23	5.67	11602.90	0.2463
Fe7	7	0.621	0.758	6.539	7.918	2.057	-22.20	-1.98	-24.18	11597.22	5.63	11602.84	0.2601
Fe8	7	0.622	0.759	6.534	7.915	2.133	-23.01	-0.55	-23.57	11597.20	5.64	11602.84	0.2606
Fe9	9	0.639	0.796	6.499	7.934	-1.886	19.39	-24.14	-4.75	11597.32	5.83	11603.14	0.1882
Fe10	7	0.619	0.759	6.543	7.921	1.980	-21.44	-2.13	-23.57	11597.22	5.59	11602.82	0.2665
Ni	10	0.701	0.852	8.602	10.155	0.480	-6.14	-11.58	-17.72	14505.38	6.31	14511.69	
Ni1	11	0.707	0.860	8.610	10.177	0.430	-5.47	-9.39	-14.85	14505.37	6.37	14511.74	
Ni2	9	0.695	0.838	8.597	10.130	0.537	-6.87	-13.13	-19.99	14505.39	6.24	14511.63	
Ni3	11	0.707	0.865	8.609	10.182	0.535	-6.98	-14.80	-21.78	14505.37	6.36	14511.73	
Ni4	9	0.697	0.840	8.600	10.137	0.596	-7.60	-13.05	-20.65	14505.38	6.26	14511.65	

Table 20 Core and valence hyperfine fields on local sites in $Fe_{11}Ni_5$. The model of Dang and Rancourt is used to calculate the HF contributions based on the local and NN moments, according to $H_i = A\mu_i + B\sum_{NN}\mu_j$ where the A and B best fit parameters are listed at the bottom.

Fe	1.807	11.856	-19.43	-0.27	-19.70	-19.51	-0.08	-19.63
Fe1	1.482	10.371	-15.95	-0.49	-16.44	-16.01	-0.61	-16.69
Fe2	0.990	11.387	-10.75	-4.17	-14.93	-10.69	-4.18	-15.16
Fe3	2.306	12.444	-24.84	1.70	-23.14	-24.91	2.17	-22.64
Fe4	1.948	7.943	-20.88	3.49	-17.38	-21.04	4.01	-16.81
Fe5	2.100	9.254	-22.55	3.88	-18.67	-22.68	3.73	-18.75
Fe6	1.704	14.361	-18.40	-3.19	-21.59	-18.40	-2.77	-21.38
Fe7	2.057	15.477	-22.20	-1.98	-24.18	-22.22	-1.77	-24.13
Fe8	2.133	15.796	-23.01	-0.55	-23.57	-23.03	-1.62	-24.80
Fe9	-1.886	15.792	19.39	-24.14	-4.75	20.36	-23.74	-4.86
Fe10	1.980	15.255	-21.44	-2.13	-23.57	-21.38	-2.01	-23.55
Ni	0.480	16.963	-6.14	-11.58	-17.72	-5.19	-11.71	-17.65
Ni1	0.430	13.404	-5.47	-9.39	-14.85	-4.65	-8.97	-14.20
Ni2	0.537	19.240	-6.87	-13.13	-19.99	-5.80	-13.32	-19.98
Ni3	0.535	20.694	-6.98	-14.80	-21.78	-5.77	-14.56	-21.28
Ni4	0.596	20.157	-7.60	-13.05	-20.65	-6.44	-13.77	-21.10
					A =	-10.8	5.5	-5.0
					B =	0.0	-0.85	-0.9

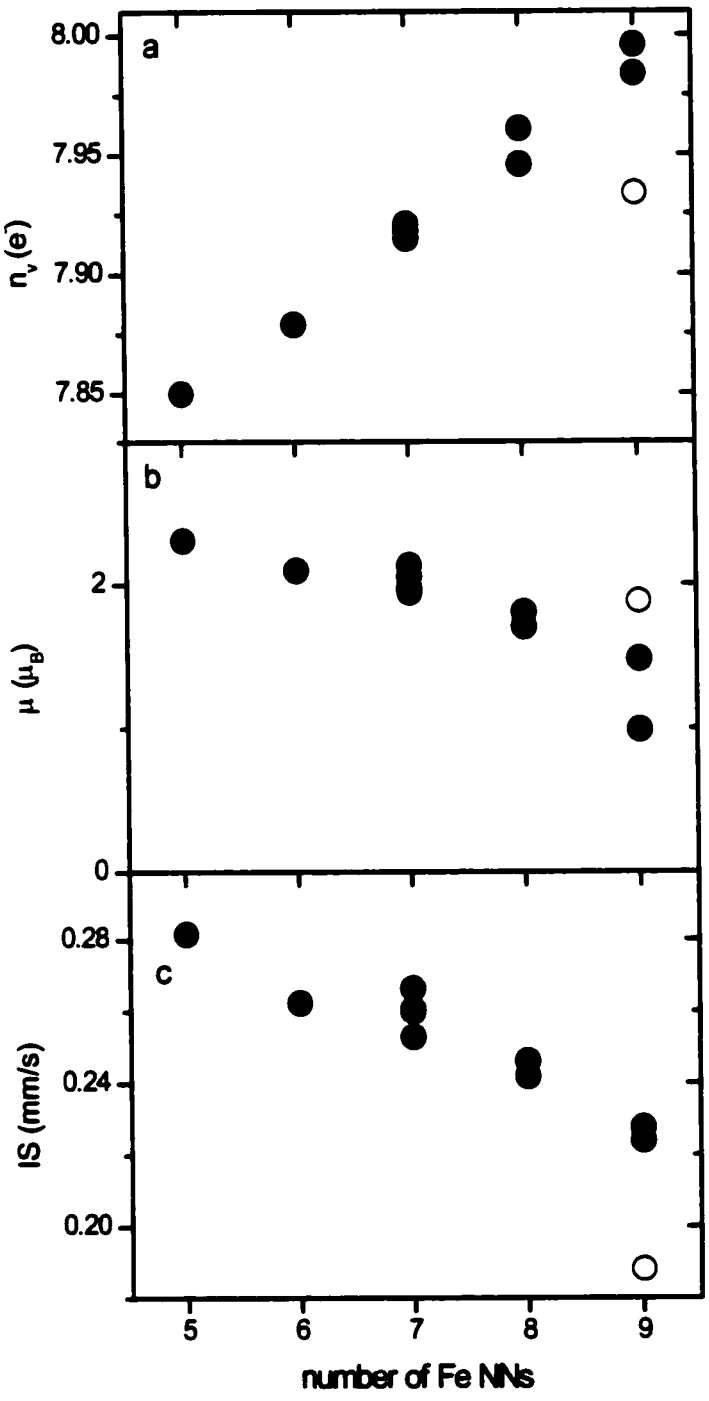

Figure 47 Effect of the local chemical environment on (a) the number of valence electrons, (b) the Fe moment and (c) the isomer shift. The open symbol represents the atom whose moment is aligned opposite to the others.

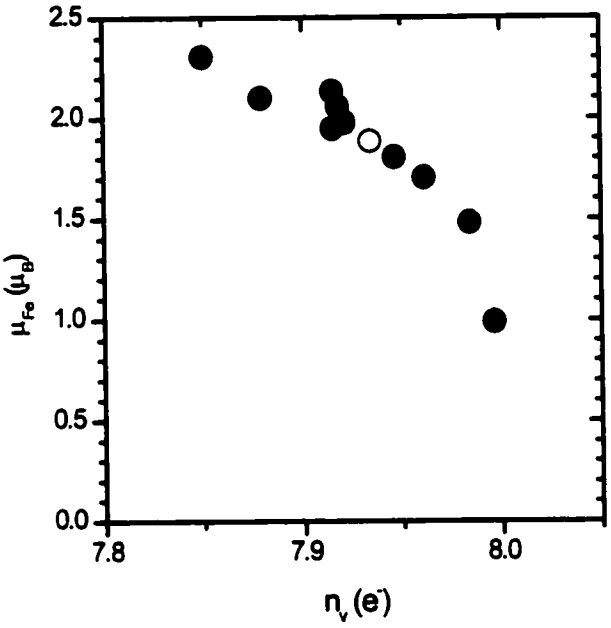

Figure 48 Effect of the local number of valence electrons on the moment of the Fe atoms.

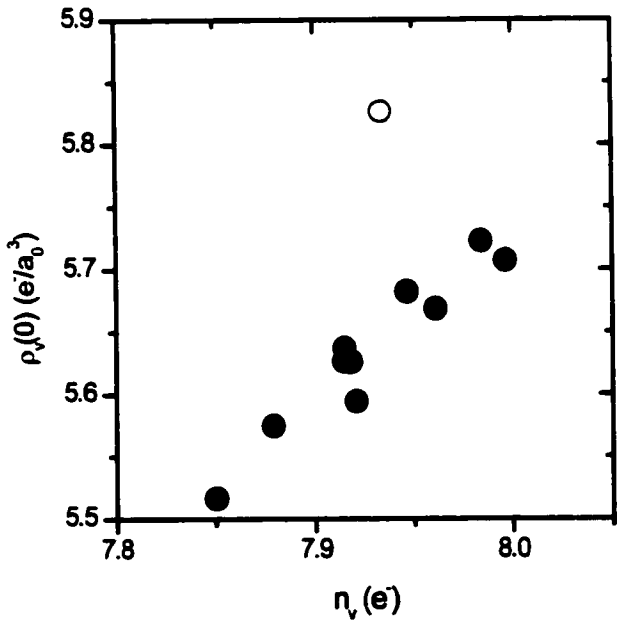

Figure 49 Correlation between the valence contribution to the charge density at the nucleus and the total number of valence electrons at the Fe atoms.

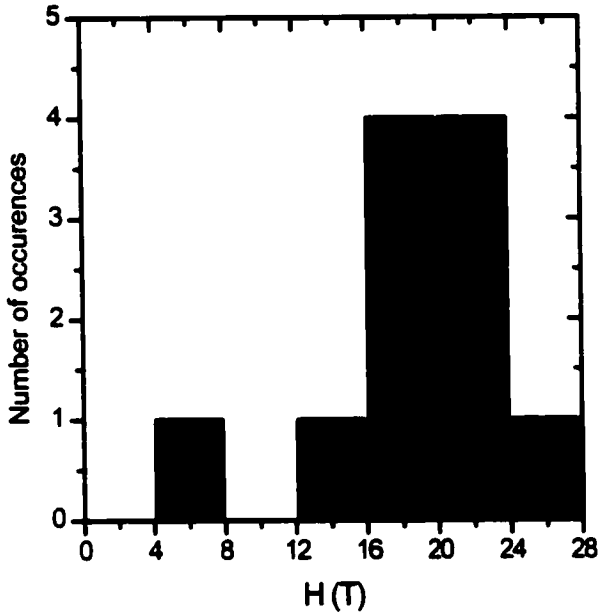

Figure 50 Hyperfine field distribution on the Fe atoms in $Fe_{11}Ni_5$. The low field component is due to the atom whose moment is aligned opposite to the others.

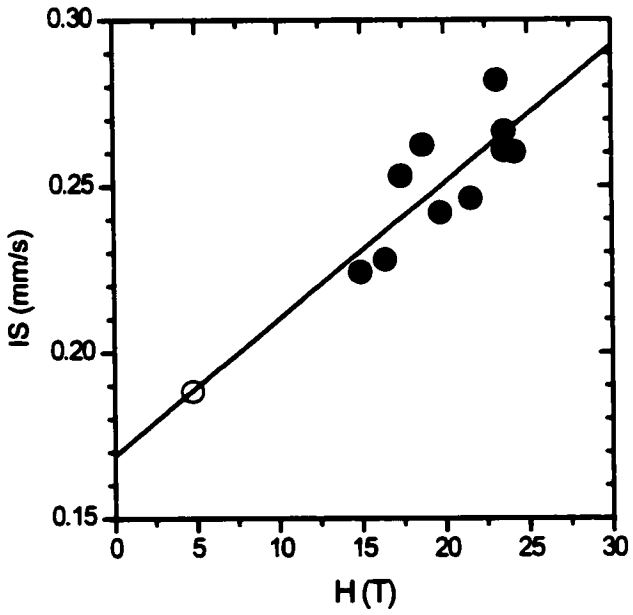

Figure 51 Correlation between the hyperfine field and the isomer shift of Fe atoms in $Fe_{11}Ni_5$.

5.3.2.5 Composition Dependence of the Ground State Properties

Figs. 52 and 53 plot several key properties as a function of composition, as calculated from the plots in figs. 37 through 46. Fig 52a shows the mixing energy for the various structures, which is relative to the energies of the FM Ni and NM Fe endpoints. The mixing energy for a structure with composition Fe_xNi_{1-x} is defined as $E_{mix}(x) = E(x) - [xE_{Fe} + (1-x)E_{Ni}]$. This mixing energy indicates the relative stabilities of the phases and indicates the true ground states in the Fe-Ni binary phase diagram (at $T = 0$ and $P = 0$). Within the LSDA, γ-Fe is found to be more stable than α-Fe, even though experimentally this is not the case. We thus limit our discussion to the FCC phases but, in fact, α-Fe is the stable Fe end-member phase. $FeNi_3$ and FeNi both lie below the $E = 0$ line, indicating that they are more stable than equivalent amounts of pure Ni and Fe. However, FeNi lies above the line joining $FeNi_3$ and Fe, indicating that an alloy with more than 25 at. % Fe should separate into distinct phases of $FeNi_3$ and Fe. An alloy with less than 25 at. % Fe should separate into Ni and $FeNi_3$. Of course, we have not yet included the results for the disordered alloy, so we can only describe the relative stability of the ordered phases. The CPA calculations described later will provide the mixing energies of the disordered phases, enabling us to get a complete picture. It does however suggest that FeNi is only a metastable phase in the Fe-Ni phase diagram. This plot also shows how the difference in energy between the FM and NM phases varies with composition.

Fig. 52b shows the composition dependence of the equilibrium volumes of each of the phases. As previously stated, the HM values for Fe_3Ni and Fe are extrapolated, so they are not necessarily as precise as for the other phases. For both the HM FM and NM phases, we observe a linear behaviour of the volume reminiscent of Vegard's law [Vegard28]. Also, the accuracy of the calculation is off, as the calculated volumes are lower than the experimentally observed volumes because primarily of the LSDA. Finally, fig 52c shows that the NM phase is less compressible than the HM FM phase, primarily because of the lower volumes. It is interesting to note that the true ground state of Fe_3Ni has a lower bulk modulus than the HM FM and NM phases. This softening of the lattice is due to the added degrees of freedom stemming from the instability of the magnetic moment around the equilibrium volume. As in the case of the volume, this calculation produces inaccurate results when compared to experimental values [James92] (B_{Ni}^{exp} = 180 GPa, B_{Ni}^{calc} = 254 GPa, $B_{\alpha\text{-}Fe}^{exp}$ = 170 GPa, $B_{\alpha\text{-}Fe}^{calc}$ = 251 GPa). This discrepancy can be due to

the smaller calculated volume, as the bulk modulus tends to increase as the volume decreases (a material becomes less compressible as its density increases).

Fig. 53a, which represents the *IS* on the Fe atoms, is interesting because it shows the large difference between the HM and NM at large Fe content, which could serve to identify a HM/LM transition. In particular, one sees that the equilibrium point for Fe_3Ni, which occurs at an Fe moment of 1.5 μ_B, deviates strongly from the HM values and tends to the NM ones. This indicates that the *IS* might be used to gauge the degree of HM or NM character of an alloy. This feature of the *IS*s will be discussed in more detail in chapter 6 based on experimental results. Fig. 53b shows that in both Fe and Ni, in the HM FM phase, the HF's magnitude increases linearly with composition, as is seen experimentally within the collinear magnetism domain of Fe-Ni alloys [chapter 4]. Departure from this linear trend must thus come from i) a reduced moment, as in the equilibrium case of Fe_3Ni, or ii) non-collinearity or anti-parallel alignment, as seen in AF Fe. Finally, fig. 53c shows the actual moment magnitudes on the Fe and Ni atoms, as well as their average. Though not exactly a straight line, the average is consistent with the Slater-Pauling relation. Deviation from linearity comes from the fact that the Fe moment does in fact change with the composition, as has been established by James *et al.* [James99]. This also shows that any dramatic deviation from the Slater-Pauling curve at high Fe-content must come from a reduced moment, or non-collinearity.

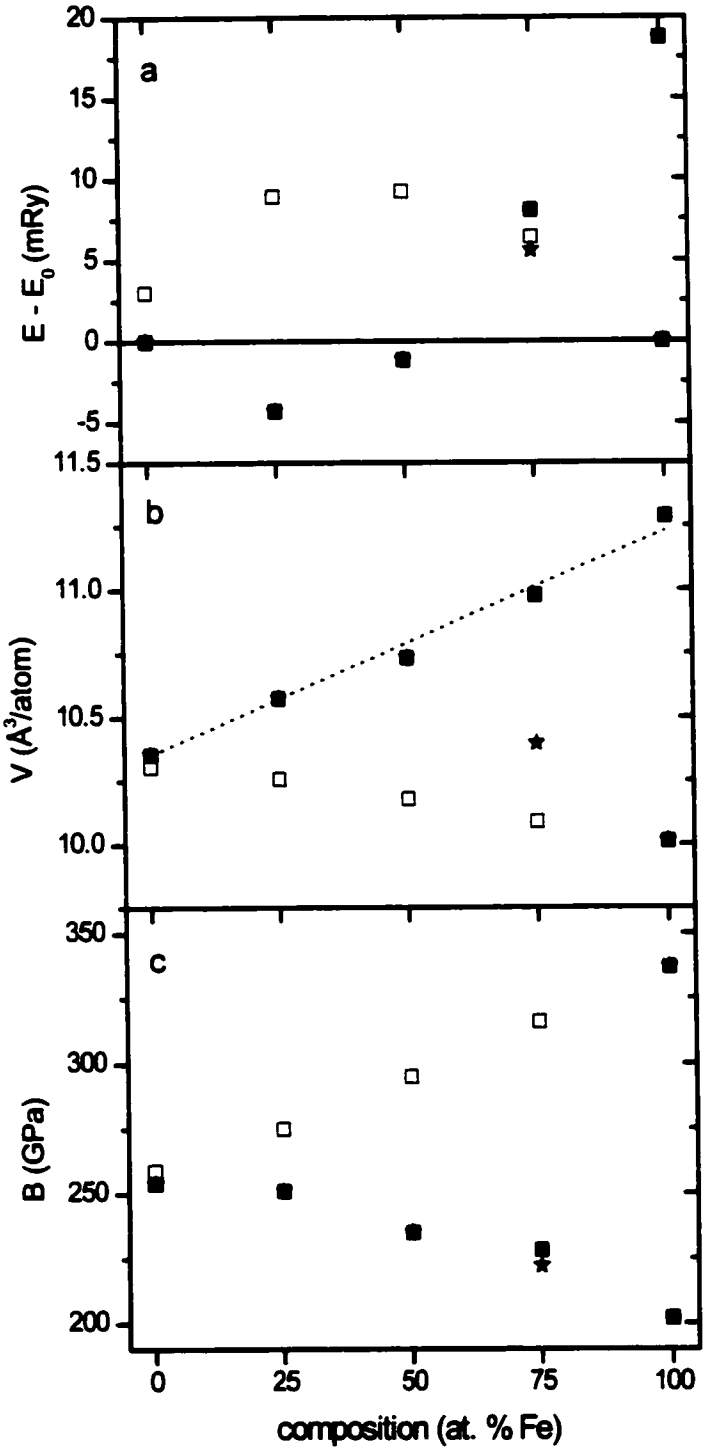

Figure 52 Calculated composition dependencies of the energy (a), atomic volume (b) and bulk modulus (c) of the ordered phases. ■ FM HM, □ NM, ★ equilibrium. In (a), at each composition, E_0 is the linear interpolation between the energies of pure Ni and pure Fe.

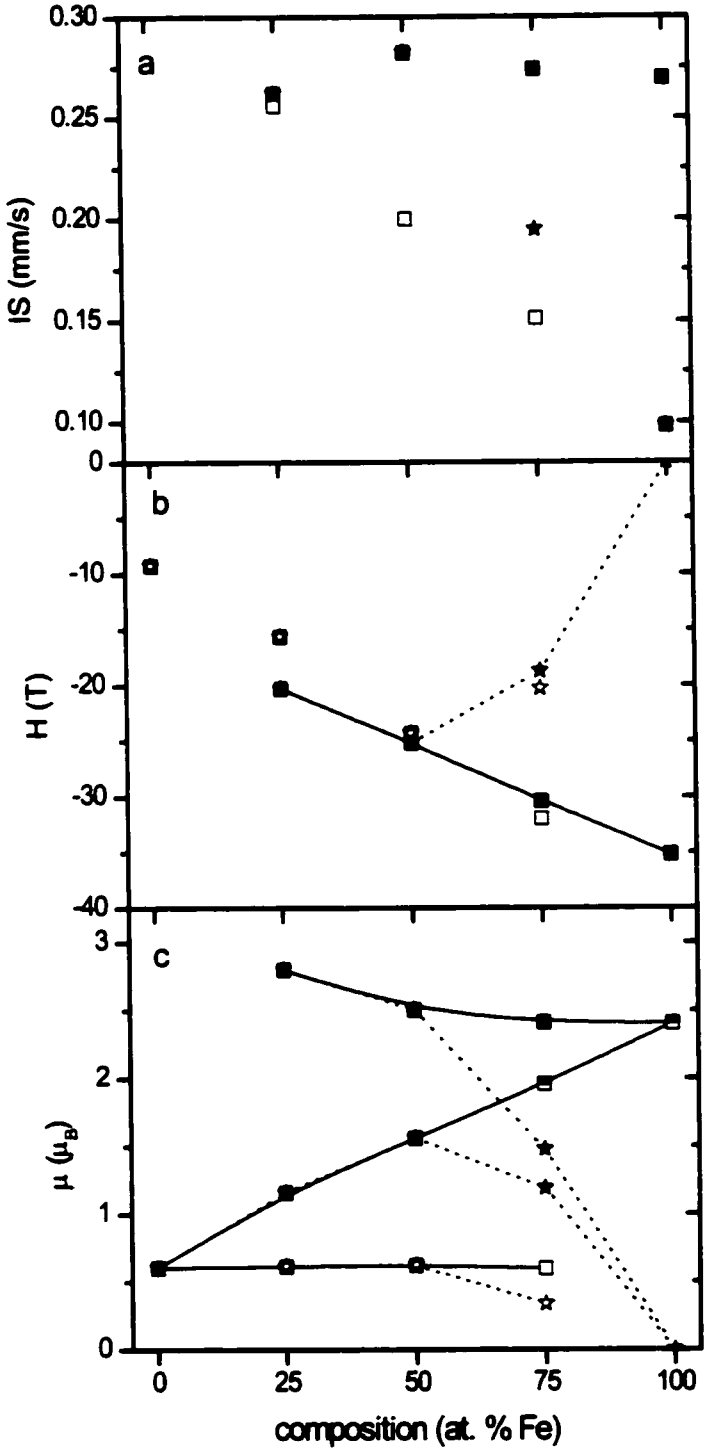

Figure 53 Calculated composition dependencies of (a) the isomer shifts, (b) the hyperfine fields and (c) the magnetic moments of the ordered phases. In (a) ■ HM FM, □ NM, ★ equilibrium. In (b) and (c) ■/□ HM FM, ★/☆ equilibrium. Filled symbols are for Fe atoms, open symbols for Ni atoms and half filled for the average.

5.4 ESC of Chemically Disordered Phases Using the CPA

5.4.1 Constrained Collinear Magnetic Structure Calculations

To treat chemically disordered systems such as Fe-Ni alloys, the coherent potential approximation (CPA) is used to perform electronic structure calculations on small sized systems [Kudrnovský94]. In this approximation, instead of having distinct Fe and Ni atoms at various crystal positions, each crystal position is occupied by an "average" atom. This is thus a mean field approximation that is calculated in the following manor:

i) Assuming a starting electronic structure for the Fe and Ni atoms, the compositional average of the transfer matrix is used to calculate an CPA average atom.

ii) The calculation of the transfer matrix of an Fe or an Ni atom embedded in the structure containing only CPA average atoms is performed

iii) The new transfer matrices of the Fe and Ni atoms are used to recalculate the CPA atom.

iv) The calculation is repeated until the ESC has converged, i.e. the CPA average results in individual Fe and Ni atoms that, when averaged, reproduce the CPA average.

This approximation thus treats all Fe (or Ni) atoms identically such that only average parameters of the Fe or Ni atoms can be obtained. This is different from a supercell calculations in which the alloy is treated as a regular crystal with a large (32 atoms or more) unit cell. In a supercell calculation, each atom has a (possibly) distinct environment and thus different properties, resulting in a true alloy-like distribution of parameters. Such a calculation is unfortunately computationally very time consuming when dealing with large supercells. We have thus used the CPA calculation to treat Fe-Ni alloys.

It is important to understand the implications of the CPA. In a real alloy, each atom has a distinct environment with leads to distinct parameters (moment, HF, etc.) which, when dealing with the alloy as a whole, must be dealt with as distributions. It is often useful to use the average of the distribution to characterize the alloy. In the CPA approximation, an average electronic structure (characterized by its transfer matrix) is calculated, resulting in the CPA averages of

parameters such as the moment and HF. However, the CPA averages of the parameters might not be the same as the averages of the true alloy, even if the LMTO calculation was exact. This is because of the non-linear correspondence between the electronic structure and the resulting parameters. We must thus always be careful when dealing with CPA averaged parameters. Despite the possibility of error from using a mean field approximation, the CPA has been proven to be a reliable means of treating alloyed systems [Faulkner82, Ducastelle91]. In the case of Fe-Ni alloys, a direct comparison between supercell and CPA calculations has shown that the CPA reproduces the average moment magnitudes of the supercell calculation [James99].

The CPA calculations were all performed by our collaborators Dr. Bose and Dr. Sanyal of Brock University. In order to deal with the Madelung term which results from the charge transfer from one species to the next, the atomic radii of both species were systematically optimized to guarantee charge neutrality of the spheres (to better than 0.001 e^-). The sphere overlap was checked and remained within the limit of validity of the ASA (no overlap correction was used in these calculations). Although the calculation was non-relativistic, first order relativistic corrections (mass-velocity and Darwin terms) were included in the energy values.

5.4.2 Disordered Local Moment Calculations

The disordered local moment model was introduced to investigate the properties of magnetic materials above their critical temperatures, when no magnetic order is thought to be present but where local moments are still present [Pindor83]. The concept is simple. In the case of a single species material such as γ-Fe, one performs a CPA calculation of $Fe_\uparrow Fe_\downarrow$ where the spin ↑ and ↓ atoms are assumed to be identical (same potential parameters) but with opposite moments, as would be the case at high temperature. Unfortunately, the analogy with high-temperature materials is limited because the calculation doesn't take into account the entropy of the phase which takes on a critical importance at high temperature. Another use of the DLM calculation is to investigate the stability of the magnetic moment, irrespective of the magnetic

Table 21 Calculated equilibrium properties of $Fe_{65}Ni_{35}$ in various phases

FM	11.050	0.0	2.543	0.631	11861.14	0.304
DLM	10.653	4.8	1.968	0.000	11861.43	0.234
NM	10.177	7.7	0.000	0.000	11861.66	0.178

structure. In a true local moment material the moment magnitude is independent of the magnetic configuration but in the case of itinerant magnetism, the magnetic order is of great importance to stabilize the moment. Ni is a good example of this. In the absence of magnetic order at 0 K (in a DLM calculation), the Ni moment vanishes [Pindor83]. When a FM order is imposed, a moment of ~0.6 μ_B is found. In γ-Fe, a moment persist in the DLM state, even though it is slightly different from the one in the FM case [Pinski86]. The inherent stability of the magnetic moment can thus be evaluated by a DLM calculation and the distinction between the energy of stabilization of the moment (internal to each atom) and the energy of interaction with the other atoms (external, or between atoms) can be made [Rosengaard97].

In the case of an Fe-Ni alloy with concentration c of Fe, this is treated by a four-component CPA calculation $(Fe_\uparrow Fe_\downarrow)_c(Ni_\uparrow Ni_\downarrow)_{1-c}$. In fact, as in the case for pure Ni, in the DLM model, Ni atoms always have vanishing moments, so the DLM can be treated as a three component system $(Fe_\uparrow Fe_\downarrow)_c Ni_{1-c}$, where the Ni is non-magnetic. Akai and coworkers have also pushed this type of analysis further by allowing different concentrations of up and down atoms, such as $Fe_{\uparrow,x}Fe_{\downarrow,c-x}Ni_{\uparrow,y}Ni_{\downarrow,1-c-y}$ [Akai93] to deal with partial antiferromagnetic alignment. This treatment should not, however, be considered as a replacement (or an analogue) to a large-scale supercell calculation with anti-parallel moments, since it does not distinguish between various local environments: all Fe atoms have the same mean-field environment and simply have a finite probability of being in a parallel or anti-parallel configuration.

5.4.3 CPA Calculations of $Fe_{65}Ni_{35}$

Before presenting the ground state properties for the complete series of alloys, we will illustrate the differences between FM, NM and DLM calculations in the case of $Fe_{65}Ni_{35}$. Such calculations have already been performed by Akai [Akai93] using the Korringa-Kohn-Rostoker (KKR) method. The results can be slightly different in these LMTO calculations because of the different methods. Fig. 54 shows the energy, magnetic moments and charge density at the nucleus in $Fe_{65}Ni_{35}$ as a function of volume. As in the ordered compound, there is a transition from a HM FM state at large volume to a NM state at low volume. The drop in the moment at the transition volume is sudden in both Fe and Ni atoms. As in the ordered structures, a discontinuity in the charge density at the nucleus is observed at the transition volume. The DLM

phase has an equilibrium energy which is lower than the NM phase but higher than the FM phase, indicating that this alloy favours the presence of a moment on the Fe atom (compared to the NM phase) but is even more stabilized by ferromagnetic interactions between large Fe and Ni moments. In fact, supercell calculations that admit non-collinearity (or at least anti-parallel alignment) find that the lowest energy phase has large Fe and Ni moments but that some Fe moments are antiparallel to the bulk magnetization when they are in an Fe-rich local environment [YangWang97, vanSchilfgaarde99]. Of course, such configurations are not attainable in the CPA calculations we have performed, or in the CPA treatment for partial antiferromagnetic proposed by Akai *et al.* [Akai93].

In table 21, we see that even though the FM and DLM equilibrium moments are suggestive of a HM state, $\rho_{Fe}(0)$ and the *IS* are quite different. Part of this is due to the difference in equilibrium volumes of the two phases but fig. 54c shows that, at the same volume, $\rho_{Fe}(0)$ is quite different in the DLM and FM phases.

Another important note is regarding the equilibrium volumes. The DLM equilibrium volume is found to be quite smaller than the FM equilibrium volume. In a local-moment material where the exchange interactions are volume independent, the DLM phase should have the same moment and a similar energy curve as the FM phase, with a volume-independent offset corresponding to the magnetic interaction energy, $\Delta E_m = \sum_{<ij>} J_{ij} \mu_i \mu_j$ (assuming a Heisenberg Hamiltonian). In our case, we find that although the moments in the DLM and FM phases are of similar magnitude, the energy curve is clearly shifted towards lower volumes, indicating that the difference ΔE_m in magnetic interaction energy between the FM and DLM changes with the volume. Since the moments are similar, this suggests that the exchange interaction parameters J_{ij} are strongly volume dependent.

We can also discuss the difference between the NM and DLM phases. The increase in the volume from the NM to the DLM ground state gives an idea of the difference in volume that results from creating a large moment, as is postulated in the 2-γ-state model of Weiss [Weiss63]. In this respect, it is interesting to compare our LMTO result to the KKR result of Akai *et al.* [Akai93]. In their work, Akai and coworkers found that the DLM state actually had the lowest energy of all three states considered but that its equilibrium volume was very close to the NM equilibrium volume, indicating that the creation of a large moment is accomplished without a change in volume, thereby breaking the Weiss hypothesis. In any case, both calculations show a

large volume difference between the FM and DLM solutions, which we interpret as being due to a dramatic volume dependence of the magnetic exchange interaction parameters. The implications of such a volume dependence of the exchange parameters on the Invar problem are discussed in chapter 7.

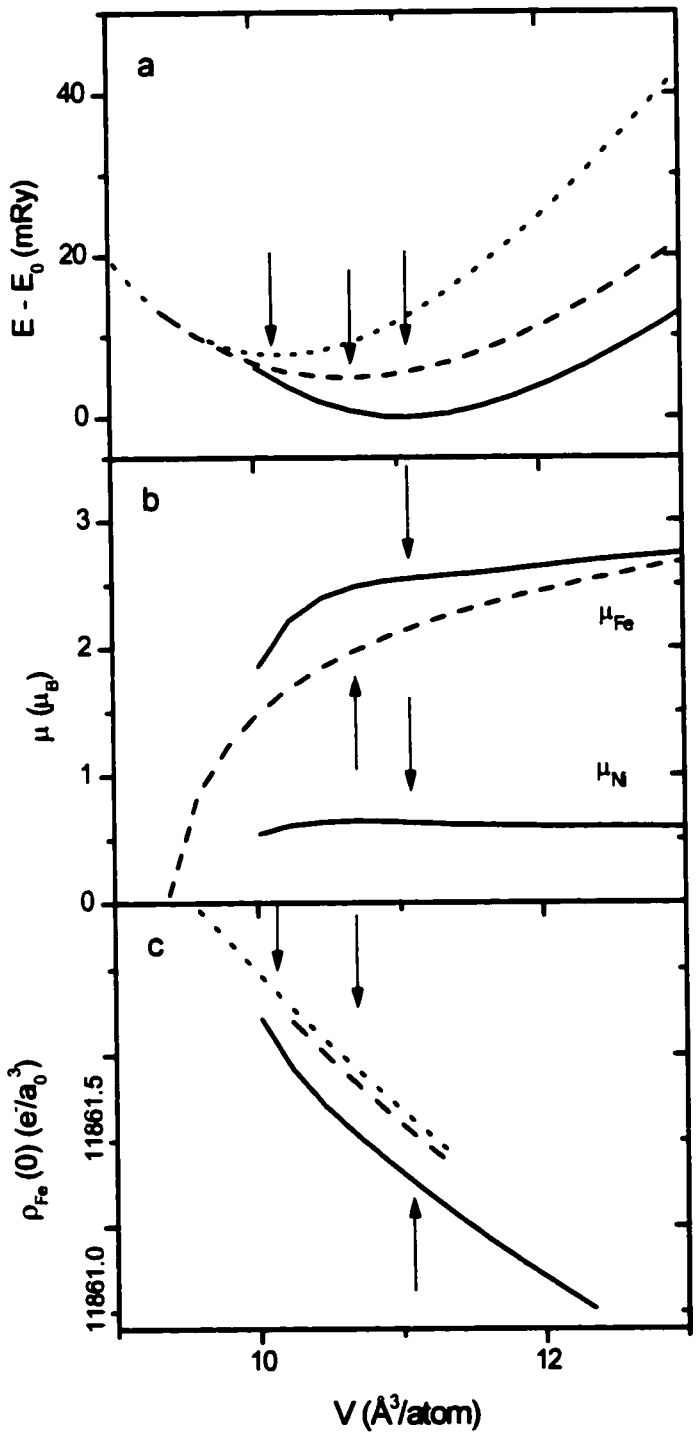

Figure 54 CPA results for $Fe_{65}Ni_{35}$ in the FM (solid line), DLM (dashed line) and NM (dotted line) phases. The arrows indicate the equilibrium volumes for each phase (a). In (b) the Ni moment in the DLM phase is 0.

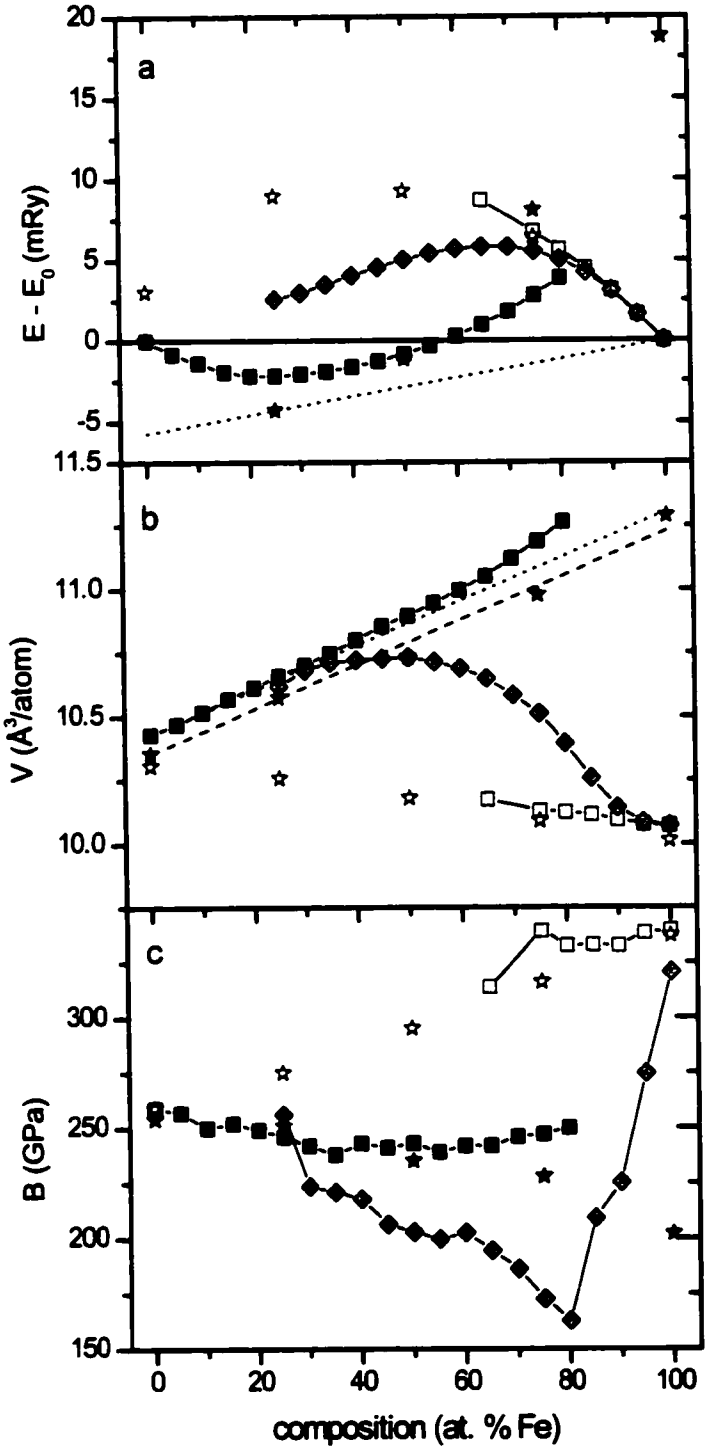

Figure 55 Calculated composition dependence of the energy (a), the atomic volume (b) and the bulk modulus (c) of the chemically disordered phases (■ FM, □ NM, ◆ DLM) and the chemically ordered phases (★ HM FM, ☆ NM).

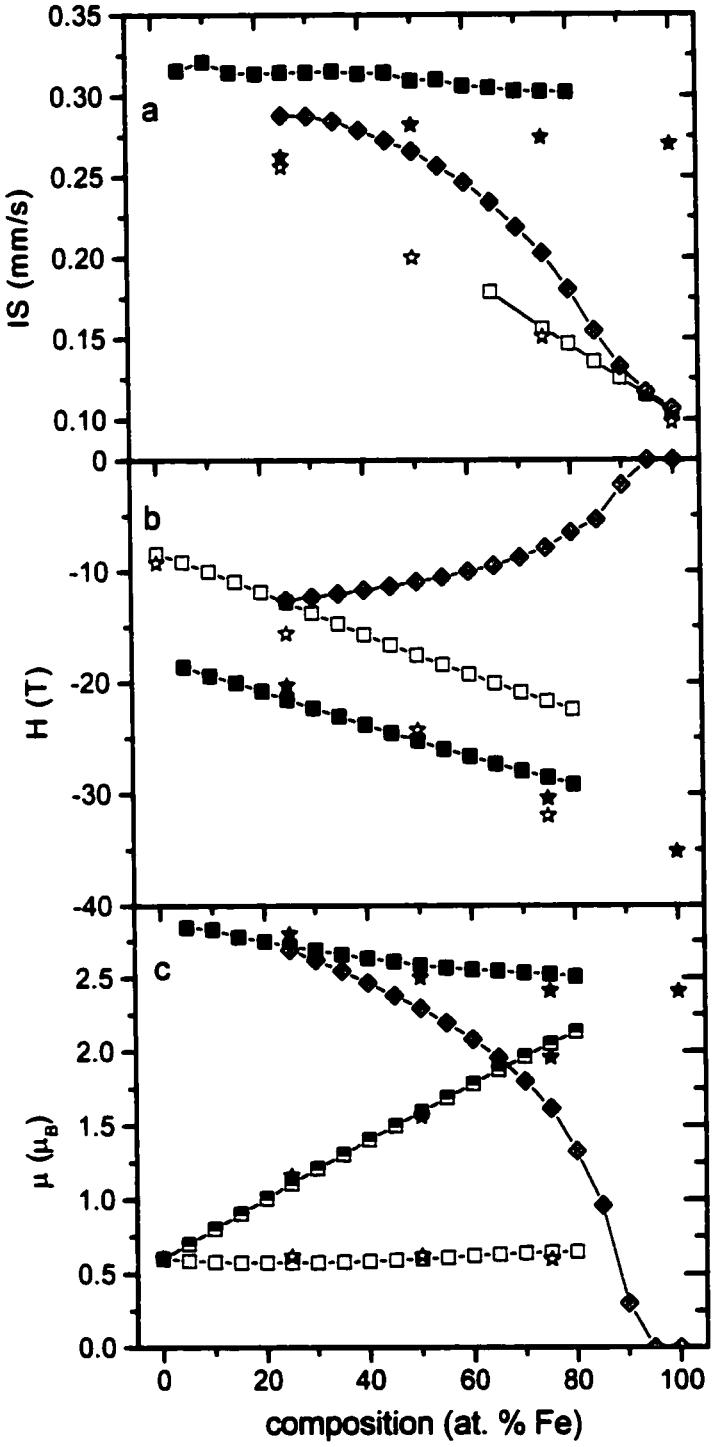

Figure 56 Calculated composition dependence of the isomer shift (a), hyperfine field (b) and magnetic moment (c). In (a), ■ FM, □ NM, ◆ DLM, ★ HM FM-ordered, ☆ NM-ordered. In (b) and (c), ■ FM Fe, □ FM Ni, ◆ DLM Fe (in the DLM case, Ni is non-magnetic), ★ Fe HM FM-ordered, ☆ Ni HM FM-ordered. Half-filled symbols represent the averages.

5.4.4 Composition Dependence of the CPA FM, DLM and NM Equilibrium Properties

Figs 55 and 56 highlight several of the properties resulting from the CPA FM and DLM calculations as a function of composition. As in fig. 52a for the ordered compounds, fig. 55a shows the energy of the chemically ordered and disordered alloy, relative to an idealized mix of pure Ni and pure γ-Fe, thereby indicating the stability of the homogeneous alloy relative to segregation into separate phases. This figure shows that at no composition is the chemically disordered alloy stable with respect to segregation into $FeNi_3$ and γ-Fe, as their energies all fall above the dotted line. One can also see that the chemically ordered phase FeNi has a slightly lower energy than its disordered alloy, $Fe_{50}Ni_{50}$, indicating that it is metastable and may form if the mobility of the atoms is insufficient for them to segregate into $FeNi_3$ and γ-Fe.

We should be careful in ascribing too much value to these comparisons between chemically ordered and disordered compounds, as the calculations were not performed in the exact same context. As previously mentioned, the CPA calculations included relativistic corrections in a non-relativistic treatment, whereas the calculations for the ordered compounds were fully scalar-relativistic. Small differences in energies might be due to the treatment used rather than to real differences between the compounds. It is however possible to compare all CPA calculations with each other.

We find that the FM state is more stable than the NM or DLM state up to 83.5 at. % Fe. Above this composition, the DLM state is more stable, until it converges with the NM state as the moment drops continuously to 0 μ_B at ~91 at. % Fe. Based on these results, calculations which include non-collinear magnetism and partial anti-parallel spin arrangements (which require a supercell treatment) can potentially produce lower energies at compositions in the Fe rich region. This has in fact been shown for $Fe_{65.6}Ni_{34.4}$ [vanSchilfgaarde99], where a non-collinear ground state is found, having a non-collinear ground state less than 1 mRy lower than the FM ground state. When considering only the collinear magnetic structures, we find that the FM state becomes less stable than the NM state at 84.5 at. % Fe. This is similar to the value of 74 at. % obtained by Abrikosov *et al.* [Abrikosov95] who performed similar calculations, but using a Green's method instead of the LMTO method. Because of the very small energy difference between the two phases around these compositions, it is not unexpected that different methods

produce different results.

In the disordered alloy, the concentration dependence of the equilibrium volume (fig. 55b) is similar to the one obtained in the ordered phases: the HM FM phase has a volume which increases quasi linearly with concentration, whereas the volume of the NM phase decreases linearly with the concentration, as would be expected from Vegard's law [Vegard28]. It is worthwhile to point out that the ordered phase calculations and disordered phase calculations (CPA) do not give the same result for the end-members (Fe and Ni), since different approximations were used (fully scalar-relativistic *vs.* non-relativistic with relativistic corrections). However, the behaviour of both ordered and disordered phases are similar and in fact $\partial V/\partial c$ is the same at c = 0 at. % Fe (dashed and dotted lines in fig. 55b). Experimentally, chemically ordered $FeNi_3$ has nearly the same volume as chemically disordered $Fe_{25}Ni_{75}$ (11.205 ± 0.007 Å^3 *vs.* 11.226 ± 0.002 Å^3, [Wakelin52], $\Delta V/V$ = -0.2 %) but FeNi has a more significantly lower volume than its disordered alloy (11.475 ± 0.005 Å^3 [Albertsen81] *vs.* 11.531 ± 0.003 Å^3 [Owen37], $\Delta V/V$ = -0.5 %,), as is predicted by the ESCs. Comparisons for Fe_3Ni and HM γ-Fe are not possible as these phases are not observed experimentally. Compared to the HM FM phase, the DLM phase results in a concentration dependence of the volume which is quite unusual, linking the HM FM volume at low Fe concentration to the NM volume at high Fe concentration, as the DLM's phase's moment drops continuously from the HM value to 0 (fig. 56c). It is also interesting to note that, as is experimentally observed and reported in the previous section, there is, for Fe-rich alloys, a deviation from Vegard's law towards *larger* volumes. This feature is disturbing since one would expect that as the Fe moment drops (albeit slightly) with increasing Fe content, the volume would also drop because of the moment *vs.* volume relation. The fact that there is a positive deviation can only be understood in terms of a magneto-volume effect due to the Fe-Fe magnetic exchange parameter. This very important point and its relation to the Invar effect will be discussed in greater detail in the next chapter.

The calculated bulk moduli B of the chemically ordered and disordered alloys agree well with each other in the FM and NM phases (fig. 55c). As seen in the ordered phase, B drops very slightly as Fe content is increased in the FM phase and tends to rise in the NM phase. A large difference between the FM and NM phases is clear and is mainly attributed to the difference in equilibrium volume between the two phases (the drop in volume is associated with an increase in compressibility). Even though the volume of the DLM phase is lower than that of the HM phase,

B has a tendency to decrease, especially as the Fe content is increased and as the Fe moment deviates more strongly from the HM value. At 80 at. % Fe, the value is lowest and then starts rising up to the NM value at larger Fe content. This clearly shows that the magnetic disorder generally increases the compressibility of the lattice (lowers *B*) compared to constrained FM and NM situations, as was calculated by van Schilfgaarde *et al.* [vanSchilfgaarde99]. Experimentally, the decrease in *B* between 40 and 65 at. % Fe is substantially larger than expected from data below 40 at. % Fe indicating it is most likely due to the onset of non-collinear magnetism.

It is also interesting to note that, although other parameters vary continuously from the HM value to the NM value as Fe content is increased (volume, moment, etc.), *B* exhibits a strange behaviour and suddenly the concentration of 80 at. % Fe is physically associated with some form of discontinuity. One should note that the calculation of the bulk modulus requires the second derivative of the $E(V)$ curve, so it is sensitive to round-off errors in the energy. We took all precautions to correctly evaluate the curvature of the energy curve in order to get a value of the *B* which is precise to about 5-10 GPa for the HM/NM calculations and 10-15 GPa for the DLM calculation.

Following Moruzzi [Moruzzi88] and Herper *et al.* [Herper99a], the Debye temperature can be calculated from the ESC according to:

$$\Theta_D = 41.63\left(\frac{r_0 B}{M}\right)^{1/2}, \tag{53}$$

where r_0 is the WSR in a.u., *B* is in kbar (1 kbar = 0.1 GPa) and *M* is the atomic mass. When using this formula, we find (fig. 57) that the Θ_D = 350 K and varies very little with the composition (~10 K over the entire range), as is experimentally observed based on the Mössbauer measurements from the previous section. We also find that Θ_D in the NM phase is also composition independent and higher than in the FM phase (Θ_D = 405 K).

The calculated *IS* (fig. 56a) in the HM chemically disordered phase does show a systematic discrepancy with the chemically ordered phase, possibly due to the CPA. In any case, it also shows a large drop at the HM/NM transition. The drop is due both to the decrease in volume and the difference between the charge densities at the nucleus in both phases. The DLM result is interesting as it shows the *IS* drops continuously away from the HM value as the Fe content is increased. Even when the moment is still large (around 65 at. %), the *IS* in the DLM phase is closer to that of the NM phase than the HM phase. This seems to indicate that magnetic

ordering substantially affects the *IS* in Fe-Ni alloys, contrary to what is expected in a pure local moment material. As in the case of the HM/NM drop, part of the HM/DLM drop is due to the decrease in volume but another part is due to the difference between the DLM and HM charge densities at the nucleus, as shown in fig. 54 for $Fe_{65}Ni_{35}$. Temperature-induced magnetic disordering effects can thus possibly be seen in these alloys, as is investigated experimentally in chapter 6.

The contact hyperfine field (fig. 56b) in both Fe and Ni vary linearly with Fe content in the HM FM phase, though their behaviour is quite different than that calculated for the ordered compounds. This is most likely due to the use of a full-relativistic treatment in the ordered phases' calculations. The effect of the ESC parameters on the HF has been extensively studied by Blügel [Blugel87] and Battocletti [Battocletti96]. As in the case of the *IS*, the HF is always smaller (in magnitude) in the DLM phase compared to the HF in the HM FM phase. The HF on the Ni atoms is always zero in the DLM phase and the HF on the Fe atoms drops monotonously to 0 as the moment drop to 0. Previously, we showed that the HF could be calculated based on the local and NN moments as $H = A\mu + B\Sigma\mu_i$. When using the SRA calculations on the ordered

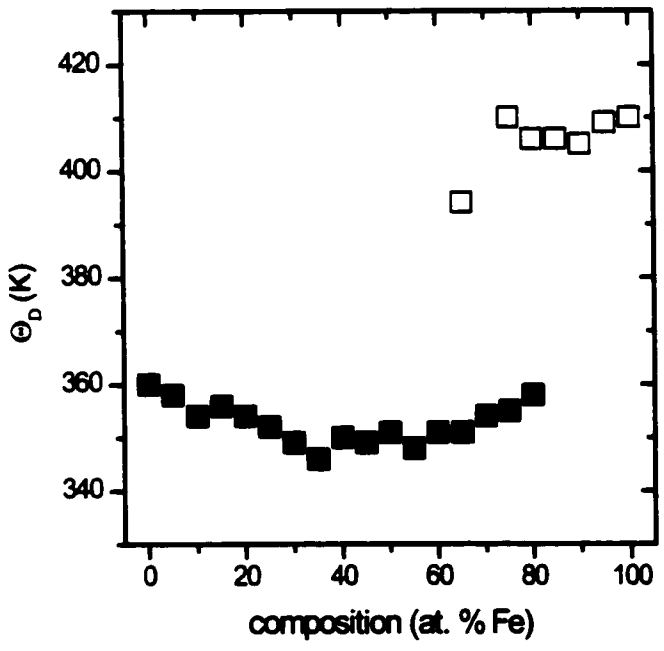

Figure 57 Calculated Θ_D for Fe-Ni alloys based on the CPA calculations in the FM (■) and NM (□) phases.

phases, we found A = -4 T/μ_B and B = -1 T/μ_B. In these non-relativistic calculations, we have already seen that the HF is different from the HF in the SRA calculations, so we can expect the coefficients A and B to be different. In the case of a disordered alloy, the NN moments should be taken as the average moment and we find that the model still holds but with A = -4.5 T/μ_B and B = -0.7 T/μ_B. In the DLM case, the NN moment should be taken as nil and we find that we still have $H = A\mu$ with A = -4.8 T/μ_B, a value very similar to that obtained in the FM configuration. As in the case for the calculations of ordered phases, these results all tend to support the use of the phenomenological model proposed by Dang and Rancourt [Dang96a, Dang96b] to explain the HFD in Fe-Ni alloys.

The final and very important properties we have represented are the magnetic moments on the Fe and Ni atoms (fig 56c). The HM FM results compare well with those in the chemically ordered phases, both in terms of the individual moments on the Fe and Ni atoms and the average moment of the bulk material. We find that although the Ni moment remains nearly constant over the range of stability of the HM phase, the Fe moment drops slightly as the Fe concentration is increased. This results in an average moment which is nearly linear, as predicted by the Slater-Pauling relation but has a slight curvature resulting is a sub-linear relation with Fe concentration. The drop in the Fe moment can be associated with a drop in the Fe moment based on the NN environment, as shown by James *et al.* [James99]. If the moment of an Fe atom varies linearly with n, the number of Fe NNs, as $\mu_{Fe}(n) = \mu_{Fe}^0 + \alpha n$, then the average Fe moment in a random binary alloy of Fe concentration c will be $\mu_{Fe}(c) = \mu_{Fe}^0 + 12\alpha c$, a linear dependence with the Fe concentration. In fact, the concentration dependence of μ_{Fe} is not quite linear but the idea has been shown to be valid. In the DLM case, the Ni moment is always 0. This is because the energy of formation of a moment (internal, or intra-atomic, energy) is always positive, meaning that the Ni atom on its own will not develop a moment at 0 K (since we do not take entropy into account at 0 K). When the magnetic ordering (external or inter-atomic) energy of the FM phase is taken into account, a moment occurs, of magnitude around ~0.6 μ_B. In the DLM case, no magnetic ordering energy is present, so the moment always collapses. The Fe moment, however, behaves quite differently. At low Fe content a high moment is found, similar to the one found in the HM FM phase. This clearly shows that the internal energy of formation of the moment is negative. The FM magnetic ordering only slightly stabilizes the moment close to the DLM value (fig. 56c). As the Fe content is increased, the moment drops

monotonously but only substantially above 70-75 at. % Fe. Below this concentration, the DLM moment should still be considered a HM. The collapse of the moment as the concentration increases is akin to its collapse as the volume is reduced (when considering a fixed concentration). Based on both the FM and DLM calculations, one can argue that, in a phase with partially non-collinear moments, the Fe moment is expected to remain high but slightly less than in the FM phase.

There are very interesting yet puzzling relations between the various calculated parameters presented in this section. For example, the volume increase in the DLM phase relative to the HM phase, $(V_{DLM} - V_{NM})/(V_{HM} - V_{NM})$, is found to be directly proportional to the square of the Fe moment in the DLM phase, μ_{Fe}^2 (fig. 58). This type of relation is unexplained though an attempt can be made. We assume Vegard's law holds for the HM FM and NM phases and that the volume of the Ni atom is independent of its state ($V_{NM}^{Ni} = V_{HM}^{Ni}$). If the equilibrium volume of any alloy of concentration c is semi-universal, i.e. $V(c) = V_{NM}^{Fe}(c) + f(\mu(c))$, then we would have

$$\frac{V(c) - V_{NM}(c)}{V_{HM}(c) - V_{NM}(c)} = \frac{\left[V^{Ni} + (V_{NM}^{Fe} + f(\mu) - V^{Ni})c\right] - \left[V_{Ni} + (V_{NM}^{Fe} - V^{Ni})c\right]}{(V_{HM}^{Fe} - V_{NM}^{Fe})c} = \frac{f(\mu)}{V_{HM}^{Fe} - V_{NM}^{Fe}} \quad (54)$$

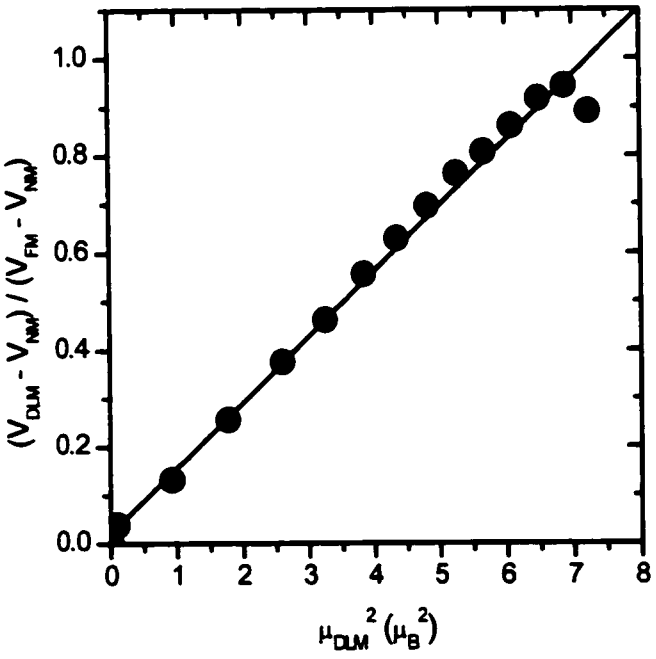

Figure 58 Relation between the DLM moment squared and the relative volume between the DLM and NM phases in Fe-Ni alloys.

If $f(\mu) = \alpha \mu^2$, then we would have the relation we have described. However, the volume-moment relation observed in the DLM phases of $Fe_{65}Ni_{35}$ and γ-Fe do not behave this way (we actually have $f(\mu, 0.65) \propto \mu^{4.0}$ and $f(\mu, 1.0) \propto \mu^{3.2}$, indicating that $f(\mu, c)$ does in fact depend on both μ and c, not just μ. Such relations can thus only be elucidated when a complete analysis of the volume dependence of the internal and external energies related to the moment are known.

The CPA calculations of HM FM alloys indicate that Fe-Ni alloys can to some degree be considered as simple binary alloys which obey Vegard's law and the Slater-Pauling relation but upon closer inspection, deviations from these relations are at the heart of the complexities involving these alloys. The DLM calculations shed new light on the nature of the magnetic moment and the electronic structure (through the *IS*) when the magnetic order is changed. The dramatic differences between magnetically ordered (HM FM) and disordered (DLM) phases clearly indicate that the alloys are quite complex and that many of their properties will be intrinsically linked to the magnetic order of the alloys. Though extensions to finite temperatures are uncertain, these calculations seem to show that the loss of (long-range) magnetic order at T_C will certainly be accompanied with unusual changes in properties, like the *IS* or *B*, which are usually very well behaved and understood. Further inspection of experimental results in light of these calculations can reveal new and very important information regarding the Invar and anti-Invar effects, as will be manifested in the following chapter.

5.5 Magnetism of γ-Fe: FM, AF and DLM Calculations

The magnetism of γ-Fe has long been discussed in terms of constrained equilibrium states which are obtained from ESCs [Anderson77, Kubler81, Wang85]. In particular, the initial calculations which imposed FM magnetic coupling found that three states were obtained as a function of the lattice volume. At low volumes, the NM phase is found to be more stable than any FM phase but upon increasing the volume, one would find an IM FM phase with a moment ~1 μ_B and at higher volumes, a HM FM phase with a moment ≥2.5 μ_B. Based on these calculations, many others concluded that γ-Fe could occur in one of two states, as earlier

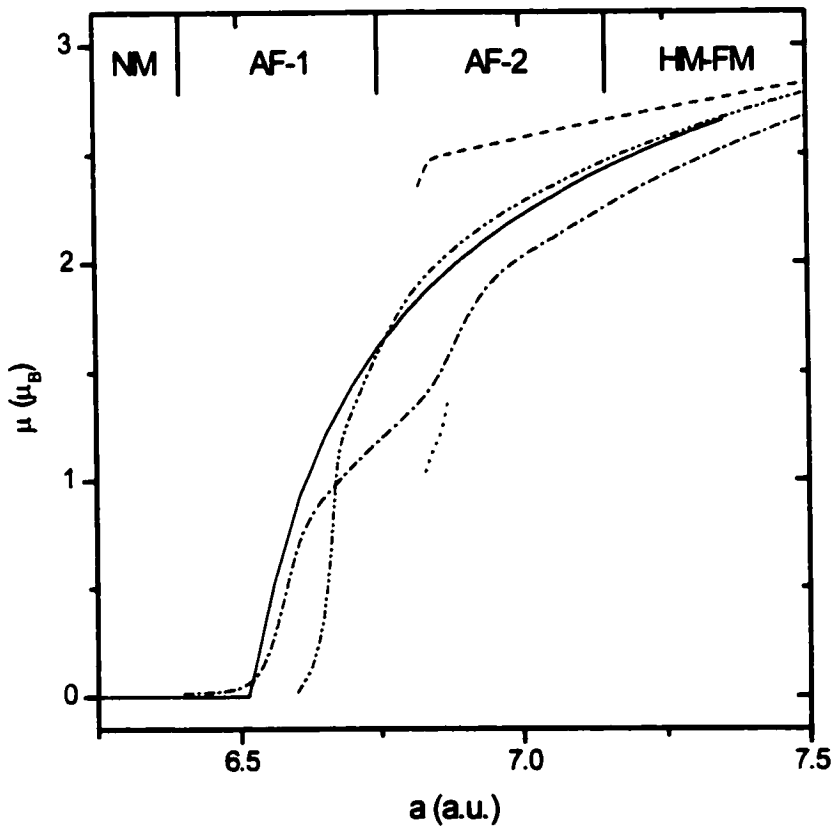

Figure 59 Calculated moments in γ-Fe for different magnetic structures: — DLM phase, - - HM FM phase, ··· IM FM phase, - ·- AF-1 phase, - ··- AF-2 phase. The DLM calculation was non-relativistic, with some relativistic corrections while the other calculations were fully scalar-relativistic. The phase which is most stable at the given lattice parameter is indicated at the top (this excludes the DLM phase because the energies cannot be directly compared).

proposed by Weiss [Weiss63] and that many of its finite temperature properties could be explained by thermal excitation between the states.

More refined calculations, which for example treated AF order, also found an AF constrained minimum with a small moment ~1 μ_B. Spin-spiral and more complex AF structures [James99 and references therein] found even more possible states for γ-Fe with moments which range from 0 to the HM value. Finally, as shown in fig. 59, DLM calculations of γ-Fe show that the stable DLM moment shows a continuous increase from the NM value at low volume, to a HM value at large volume [these calculations, Pinski86]. Several other solutions are also plotted in fig. 59, showing that the stable moments in each structure are usually close to the DLM moment but they may be stabilized to slightly higher or lower values, depending on the magnetic structure (as illustrated in fig. 60). This tends to indicate that, as a function of the volume, γ-Fe stabilizes a finite moment which varies continuously from 0 to a HM value and which is partially affected by the imposed magnetic order. As commented by James *et al.* [James99], one should also note that the equilibrium volumes for each of the considered phases also increases with volume, indicating that there are not only two equilibrium phases (in the sense of energy minima) but a large number of phases associated with various magnetic configurations. The continuity of the magnetic moment from the NM phase to the HM FM phase thus tends to indicate that the transition from a HM to a NM atom is of second-order as a function of volume, as opposed to the first-order transition presented in the 2-γ-state model.

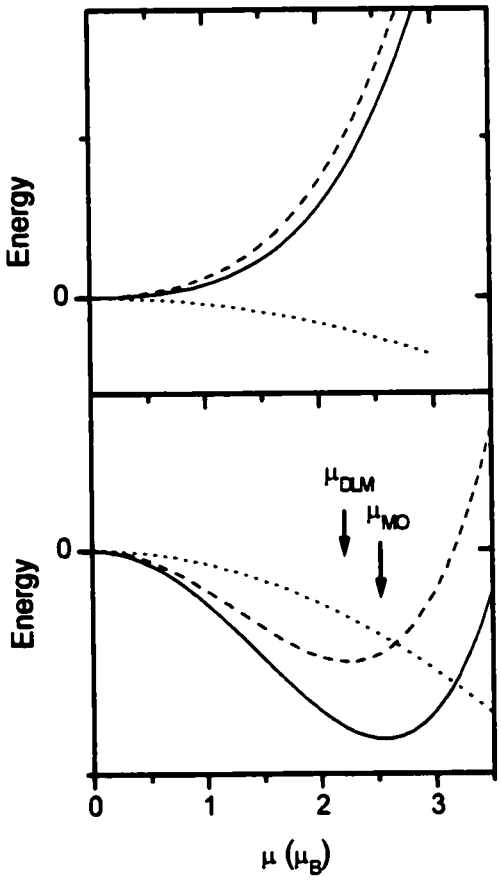

Figure 60 Illustrations of (a) NM and (b) HM states. – – internal energy (of formation of the moment), ··· magnetic ordering energy (= $-J\mu^2$ in a NN Heisenberg model), — total energy. In the HM case, the moments in the DLM case (μ_{DLM}) and with magnetic order (μ_{MO}) are indicated.

Table 22 Effective Heisenberg magnetic exchange interactions with the first 3 NN shells, for the various magnetic structures considered (the total exchange interaction should be maximum when the structure is stable)

NN	$+12J_{01}$	$-4J_{01}$	$+4J_{01}$	0
NNN	$+6J_{02}$	$+6J_{02}$	$+2J_{02}$	0
$N^{(3)}$	$+24J_{03}$	$-8J_{03}$	$-8J_{03}$	0

Also shown in fig. 60 are the volume ranges where the various phases have the lowest energy. Since the HM FM phase is stable at large volume, the magnetic exchange interaction (J_0) parameter must be positive. At lower volume, the AF-1 structure (which corresponds to individual planes in the (001) direction with up and down moments) is more stable, indicating that the at least the NN exchange interaction parameter (J_{01}) must be negative, according to table 22. For intermediate volumes, the AF-2 structure (which corresponds to individual planes in the (001) direction with up and down moments) is more stable, indicating that there might be negative long-range magnetic exchange interaction constants. The fact that different magnetic structures are stable at slightly different volumes indicates that the magnetic exchange interaction parameter is changing dramatically with the volume, as has been calculated by Sabiryanov *et al.* [Sabiryanov95]. This also explains the collapse of the moment in the FM calculation: because J_0 is negative and too large, the magnetic ordering energy in the constrained FM phase exceeds the internal energy of formation of the moment, so the moment vanishes. In the AF-2 structure, the same collapse is seen but at lower volume. In the AF-1 structure, at small enough volume, the magnetic ordering energy seems relatively small, such that the stable moment is simply given by the minimum in the internal energy (calculated by the DLM method).

When alloyed with another species, the state of the Fe atoms (the magnitude of its moment) that will be stable will be dependent on the atomic volume of the other species but also on the magnetic interaction between the Fe moments and the other species. For example, in Fe-Pt alloys, the large atomic volume of Pt will result in a large average Fe-Fe distance and the large volume HM FM state is stabilized. Of course, because of charge transfer, the alloying will also affect the moment-volume relation shown in fig. 59. As previously stated, in Fe-Ni alloys the HM state is also stabilized because of charge transfer, even though the atomic volume is smaller than where the HM is stable in γ-Fe.

The complex magnetism of γ-Fe is thus due to two distinct phenomena: the instability of

the moment at low volume (or large valence electron density) which causes a collapse of the DLM moment and a change in the magnetic exchange parameter with volume, which results in the stabilisation of various magnetic configurations as a function of volume. In this view, the concept of two states disappears as there is a continuous evolution from a NM phase at low volume (which, if there was a moment would be AF) to a HM FM phase at larger volume.

5.6 Conclusion

The study of Fe-Ni alloys has always been supported by many different types of experimental observations. Since the end of the 1970's the use of ESCs in providing a theoretical explanation to the Invar effect has rapidly grown to be the major source of insight on Fe-Ni alloys. We have decided to take advantage of the enormous predictive capabilities of current ESCs to investigate in more detail than ever before certain aspects and properties related to the magnetism of Fe-Ni alloys. These calculations are proven to be reliable in explaining some known aspects of Fe-Ni magnetism, most notably within the context of Ni-rich collinear magnetism. A careful study of alloys in the Fe-rich region illustrates the extremely complex nature of the magnetism of FCC Fe. Even though these calculations only give information on idealized systems at $T = 0$ K, they provide insight on how various parameters are linked and how one might expect to characterize finite temperature properties.

The precision of the calculation of the charge density at the nucleus is now good enough to predict what can be observed experimentally through the *IS*, measured by Mössbauer spectroscopy. We have found that the *IS* can be used as a sensitive probe of the nature of the magnetic moment in Fe-Ni alloys. The analysis of HFs in these calculations also shows that the HFDs measured experimentally can be conclusively linked to various intrinsic features of the alloys which are otherwise hard to grasp.

It is on the basis of these calculations that we will present in the next chapter a review of experimental data pertaining to Fe-Ni alloys in the collinear magnetic regime and advance new experimental data which will be used to shed light on the problems of Invar and anti-Invar properties of alloys.

6. Experimental Observation of a HM/LM Transition in Fe-Rich FCC Fe-Ni Alloys. Implications Regarding the Invar and Anti-Invar Effects

6.1 Introduction

In order to better understand the anomalous properties of FCC Fe-Ni alloys in the range of 60 to 80 at. % Fe, we have performed a detailed MS study of rapidly quenched samples. Unlike bulk measurements such as magnetisation or dilatometry, with this experimental method it is possible to distinguish the FCC and BCC phases that might coexist in a sample, therefore enabling us to study the properties of the FCC phase up to 78 at. % Fe. There were two main purposes to this study:

1) To examine the RT *IS* (and other hyperfine parameters) and possibly relate them to the composition-driven HM/LM transition predicted by ESC calculations;

2) To examine the thermal evolution of the *IS* in FCC Fe-Ni alloys and its implications regarding the Invar and anti-Invar phenomena.

This chapter comprises three main parts which deal with the sample preparation and experimental methods, the RT measurements (MS and XRD) and their analysis, and the high temperature MS measurements and their analysis. The analysis of the *IS* of the RT measurements unambiguously identifies a composition-driven HM/LM transition occurring around 70 at. % Fe. On the other hand, the higher temperature measurements show two distinct effects: the

reduction of the HM magnitude with loss of magnetic order in Invar alloys, and the increase of the moment magnitude with temperature in anti-Invar alloys. Discussions relating these observations to the thermal expansion properties of such alloys are given, leading to an explanation of the anti-Invar effect. On the other hand, the questions relating to the Invar effect will be resolved in the next chapter.

6.2 Experimental Procedures

6.2.1 Sample Preparation

The samples were prepared by Prof. R. A. Dunlap from Dalhousie University. They were prepared by melting stoichiometric mixtures of Fe and Ni then quenching them by the twin roller quench method. The estimated quench rate from the melt is 10^5-10^6 K/s. This allowed samples that had enough retained FCC phase at RT to be produced up to 78 at.% Fe. The resulting flakes, which have thicknesses which varied between 50 and 200 μm, show some signs of oxidation on the surface but none of our measurements revealed any oxides, indicating that the bulk of the flakes were pure Fe-Ni. For MS, we chose flakes in order to produce a sample with an approximately uniform thickness of ~100 μm. The same flakes were also used for the XRD. The samples were not analysed to determine their composition. The nominal composition of the Fe-Ni melt was used. Actual compositions should vary by at most 0.5 at.% Fe, as can be inferred from the correlations between measurements at various compositions, and the comparison between our measurements and other published measurements.

6.2.2 X-ray Diffraction

Because of the proximity of the martensitic transition in these Fe-rich samples, the FCC phase is often unstable when the sample is filled or polished. For this reason, we had to use the flakes in their original state to do "powder" XRD measurements. For these measurements, we chose flat flakes which could be fixed onto a low-background holder using double-sided tape. As this inevitably leads to an error in the reference position of the absorber, some fine Si powder (SRM 604b) was sprinkled on the flakes to provide a calibrated reference height. We performed

the measurements on a Philips X'Pert PW3710 system θ-2θ powder diffractometer equipped with a Kevex® solid state Si(Li) detector. A copper target was used for the source, and Cu Kα radiation was used by electronic filtering using a single channel analyser (SCA). Both $K\alpha_1$ and $K\alpha_2$ were present and accounted for in the analysis, using $\lambda_{K\alpha_1}$ = 1.540585 Å and $\lambda_{K\alpha_2}$ = 1.544413 Å, with an intensity ratio $I_{K\alpha_2} / I_{K\alpha_1}$ = 0.509 [Lide93]. All measurements were performed at RT using a spinning absorber to attenuate preferred orientation effects. The data was typically acquired in 2θ steps of 0.02° from 30° to 110°.

Each diffractogram was analysed by the full pattern Rietveld method to obtain accurate lattice parameters. For this purpose, the program DBWS-9411 produced by R.A. Young [Young95] was used. In all cases, only a minimal number of parameters were used to fit the diffractogram. In all Rietveld analyses, the known lattice parameter of the Si powder were fixed, and the sample displacement parameter was allowed to vary.

6.2.3 Mössbauer Spectroscopy

The details regarding the setup for Mössbauer spectroscopy are described in chapter 2. RT measurements were performed on all samples (67 at. % to 78 at. %) in the normal transmission geometry. High-temperature measurements were only performed on some of the samples, using the oven described in chapter 2. In addition, we performed measurements on three splat quenched samples (30, 50 and 60 at. % Fe) that had been used in the work of M.-Z. Dang [Dang96a]. Various models were consistently used to determine the *CS*.

Because the spectra show a wide range of characteristics such as broad HFDs, *CS*-*z* or ε-*z* coupling, dynamic spin flipping effects near T_C, several models were used to obtain *CS*s so that we get the range of plausible *CS*s, independent of the model used. This is an important point since using a specific model can usually yield a different *CS* than another model because of couplings between parameters, distribution shapes, or other characteristics. Here is a list of all the models considered in the case of spectra showing magnetic splitting (see description of Recoil at http://www.physics.uottawa.ca/~recoil and appendix A for details on the analysis models):

1. HFD (VBF analysis). ε, δ, and Lorentzian HWHM are free parameters.
   a. No coupling

b. ε-z coupling

c. δ-z coupling

d. ε-z and δ-z couplings

2. HFD and other distributions (xVBF analysis). $<\varepsilon>$, $<\delta>$, and Lorentzian HWHM are free parameters.

   a. ε distribution (1 Gaussian), with ε-z correlation

   b. δ distribution (1 gaussian), with δ-z correlation

   c. ε and δ distributions, with ε-z, δ-z and ε-δ correlations

3. When close to T_C. Dynamic lineshape analysis, using the model of Blume and Tjon. ε, δ, and Lorentzian HWHM are free parameters. $\rho = 0$ is fixed but f is free.

4. Above T_C, QSD (VBF analysis). δ, Δ, and Lorentzian HWHM are free parameters

   a. No coupling

   b. δ-Δ coupling

5. When close to and above T_C. Fit to a single Voigt peak with variable Lorentzian and Gaussian widths and area. This is equivalent to a CSD of Voigt shape.

When the spectrum was a singlet, above T_C, the spectrum was fit using a single Voigt peak, or using a VBF model with a QSD. Only fits that lead to physically acceptable parameters were considered. Situations which lead to unphysical parameters, such as large ε or δ distributions, or a poor quality fit were discarded.

6.3 Description of the RT Mössbauer Spectra

Figs. 61 and 62 show the RT Mössbauer spectra of the RQ samples. As revealed by these spectra, pure FCC samples were produced up to 72 at. % Fe, whereas the BCC phase is present and dominant for more Fe-rich samples. The spectrum of the 78 at. % Fe alloy shows that the FCC phase has practically totally disappeared and in fact no meaningful analysis of the FCC phase could be performed on this spectrum. In addition to the passage through the martensitic start boundary which causes this FCC/BCC behaviour, we also see that as the Fe concentration increases, we are gradually going past the magnetic ordering temperature (T_C) in the FCC phase.

This results in the collapse of the sextet and the narrowing of the peak as we go past T_C. Though several analyses have shown that the broad lines in spectra like the one for 67 at. % are due to inhomogeneous broadening (static broadening caused by a distribution of hyperfine parameters) [Ullrich84, 85, Dang96a, 96b], homogenous broadening (due to dynamic effects) is also present for alloys close to T_C [Rancourt85, 91b, Ping92]. Homogenous broadening is the result of fluctuations of hyperfine parameters during the lifetime of the excited state of the Mössbauer transition. In this case, the predominant fluctuation is that of the HF which changes direction as the local magnetic moment changes direction near and above T_C. Far above T_C, fluctuations are so fast that an effectively static (nil) HF is observed.

Because of the complexity of the spectra which exhibit such homogeneous and inhomogeneous broadening, we have found it necessary to use many plausible fitting models in order to determine the range of possible values for the hyperfine parameters. This is required because of the intrinsic degeneracy of valid solutions of the fitting, which arises because similar spectral features can be produced by various parameters or combinations of parameters. In particular, from a single spectrum, it is impossible to distinguish between homogeneous and inhomogeneous broadening. We must therefore consider both possibilities, within physical limits that we set ourselves. Tables 23 through 28 give the results from fitting the spectra shown above using the models described in the previous section. It becomes clear that a single precise value of the *CS* cannot be obtained for spectra below but close to T_C (all samples with less than 72 at. % Fe). As an example, consider the analyses of the spectrum of $Fe_{67}Ni_{33}$. Fits which do not include a coupling of the *CS* to the Zeeman splitting yield a value around 0.015 mm/s, whereas those that include such a coupling yield a value around -0.012 mm/s. On inspection of the χ^2 we should favour the values around -0.012 mm/s, but the other group of results also have a statistically significant χ^2. Within the context of these analyses, we can only conclude that the "true" average *CS* is within this range of values. The same can be said of other spectra, which yield widely varying CSs, though they are not always grouped according to simple systematics. In producing figs. 66, we have therefore indicated the range of plausible values by a solid bar, to which we add the statistical fitting uncertainty. For $Fe_{67}Ni_{33}$, the range of values is large even though the fitting uncertainty is small, but for $Fe_{77}Ni_{23}$, all fits give approximately the same result, but the fitting uncertainty is large.

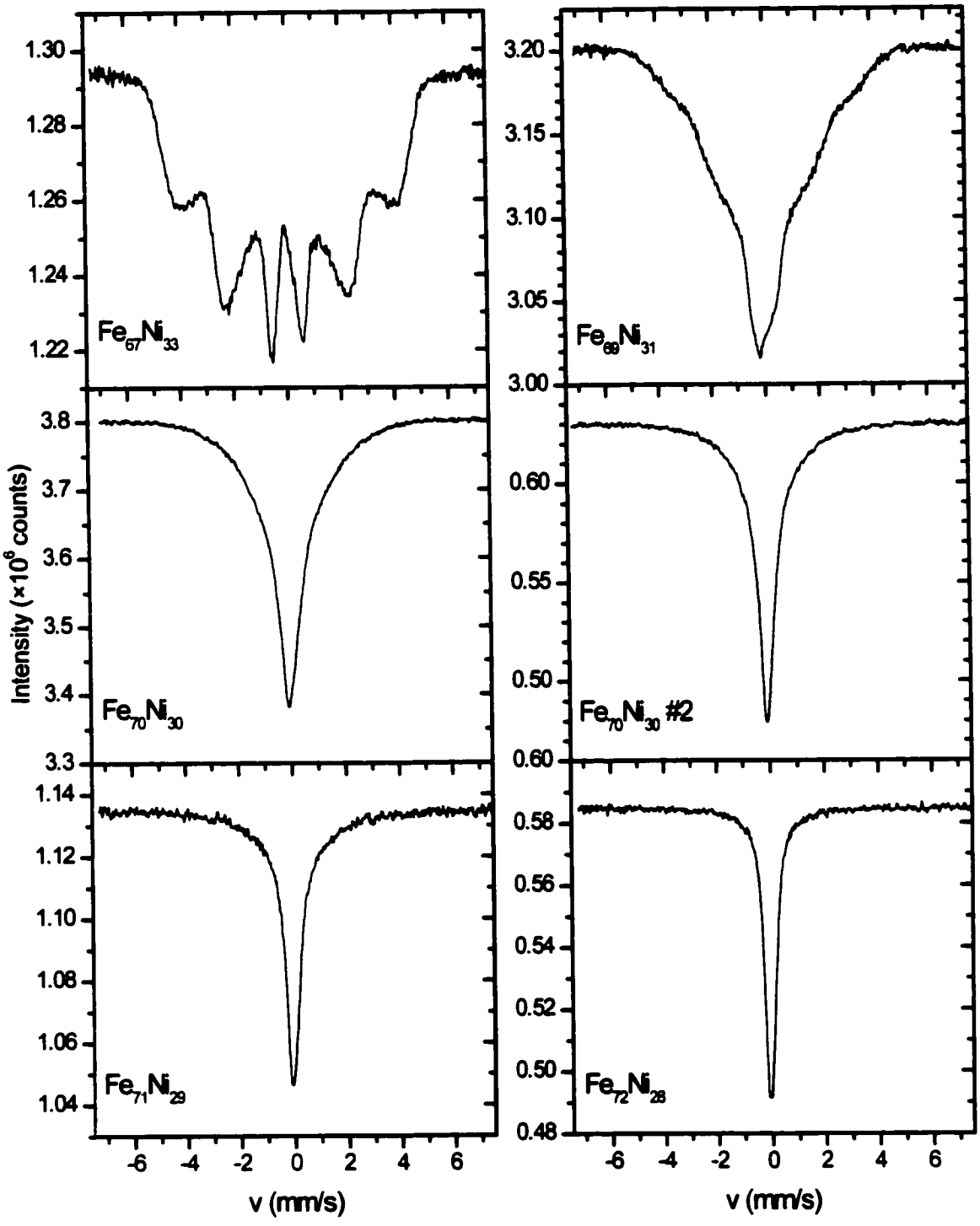

Figure 61 RT Mössbauer spectra of RQ Fe-Ni alloys with compositions from 67 to 72 at. % Fe.

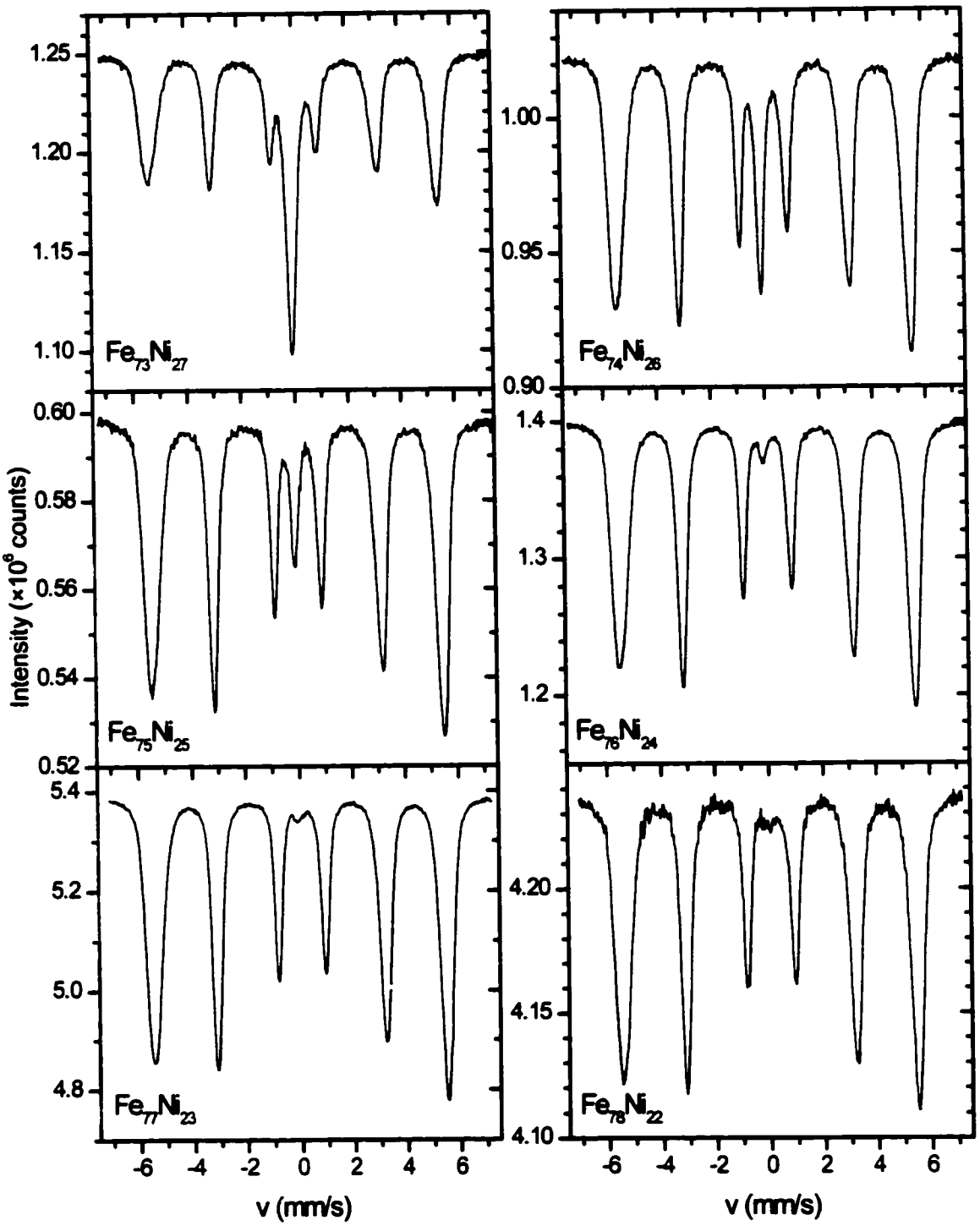

Figure 62 RT Mössbauer spectra of RQ Fe-Ni alloys with compositions from 73 to 78 at. % Fe.

6.4 Observation of a HM/LM Transition Occurring Around 70 at. % Fe

6.4.1 The Hyperfine Field

Fig. 63 illustrates the range of the average HF for the complete composition series of FCC alloys, including the ones analysed in the previous chapter. One can clearly see a continuous drop of the HF, indicating that the nominal compositions of the prepared Fe-rich alloys are quite accurate. The only exception is alloy $Fe_{70}Ni_{30}$ #2, which, according to its spectrum and average HF, seems to have a true composition of ~70.5 at. % Fe. However, without a more precise characterization, we will still represent it in figures as having 70 at. %. The drop in the average HF comes primarily from two factors: 1) the presence, above ~50 at. %, of antiparallel spin configurations in the ground state, and 2) the fact that these measurements are taken at RT, and that the T_C of Fe-rich alloys drops dramatically with increasing Fe content such that, at RT, as we increase the Fe content, we get closer to T_C and indeed are above it, above ~70.5 at. % Fe (fig. 64). Broadening due to dynamic effects occurs for compositions where the measurement temperature is close to T_C, resulting in a non-vanishing average HF (up to ~73 at. % Fe) when an analysis assuming a static HF is used. This effect may also be seen in fig. 65 where the FWHM of the FCC signal is illustrated. Apart from the dramatic decrease when passing above 70 at. % Fe, the width remains larger than its true paramagnetic value up to 73 at. % where dynamic effects due to spin fluctuations are still present. Incidentally, this figure also illustrates the difference between the two alloys which have a nominal composition of 70 at. % Fe. Again, the #2 alloy seems to have a true composition around 70.5 at. % Fe.

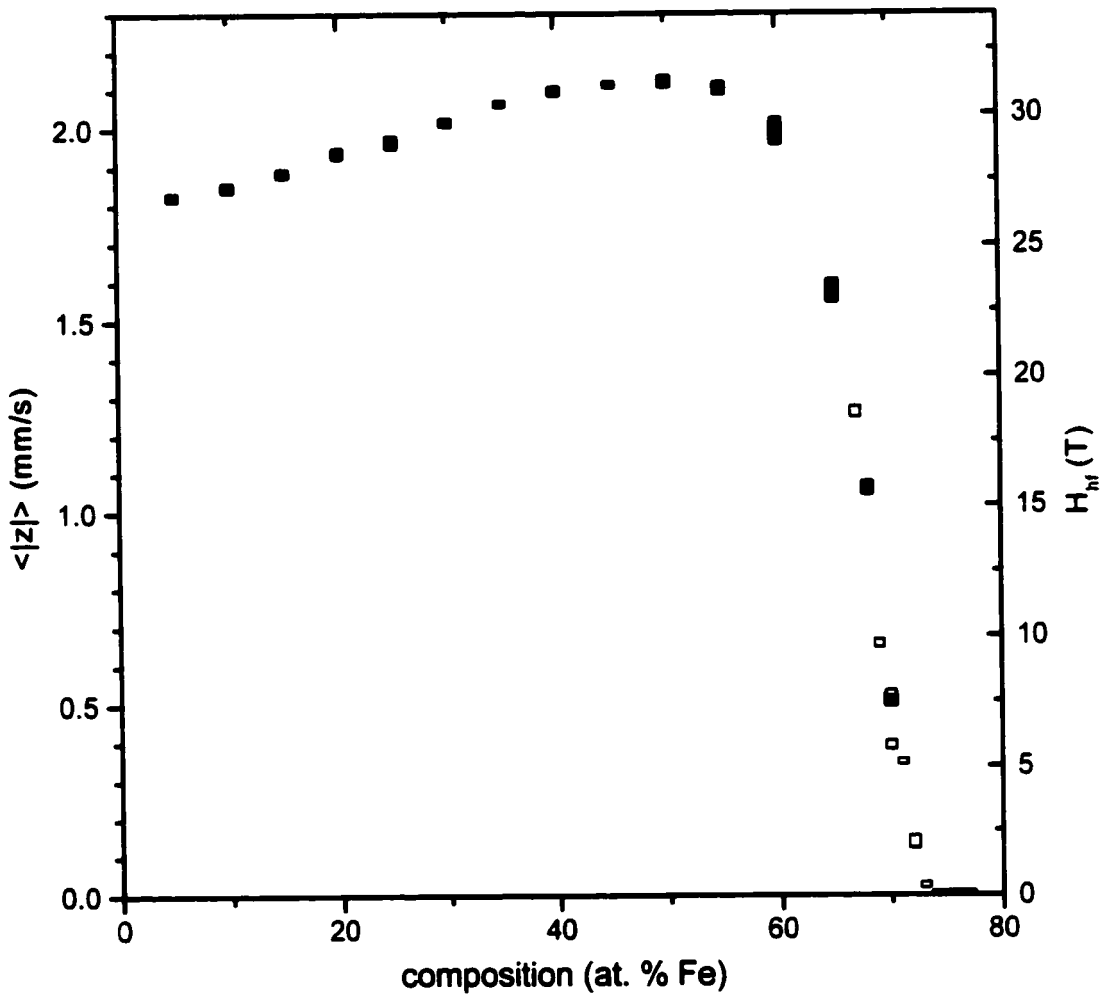

Figure 63 Range of values of the average Zeeman splitting as a function of composition, for different analysis models. The dark symbols represent data presented in the previous chapter, whereas the light columns represent data for Fe-rich alloys presented in this chapter.

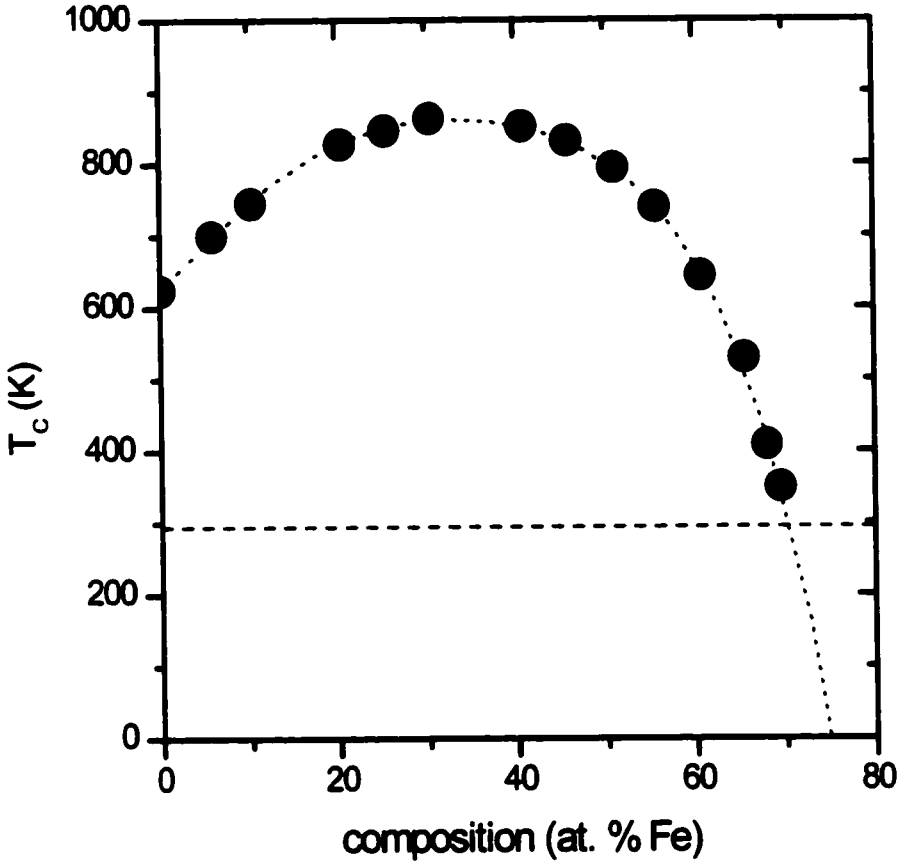

Figure 64 Variation of the Curie temperature of Fe-Ni alloys as a function of composition. The data are from [Wassermann90]. The horizontal dashed line represents RT. Alloys with compositions below 70.5 at. % Fe are magnetic at RT, while alloys with an Fe content above this composition are paramagnetic.

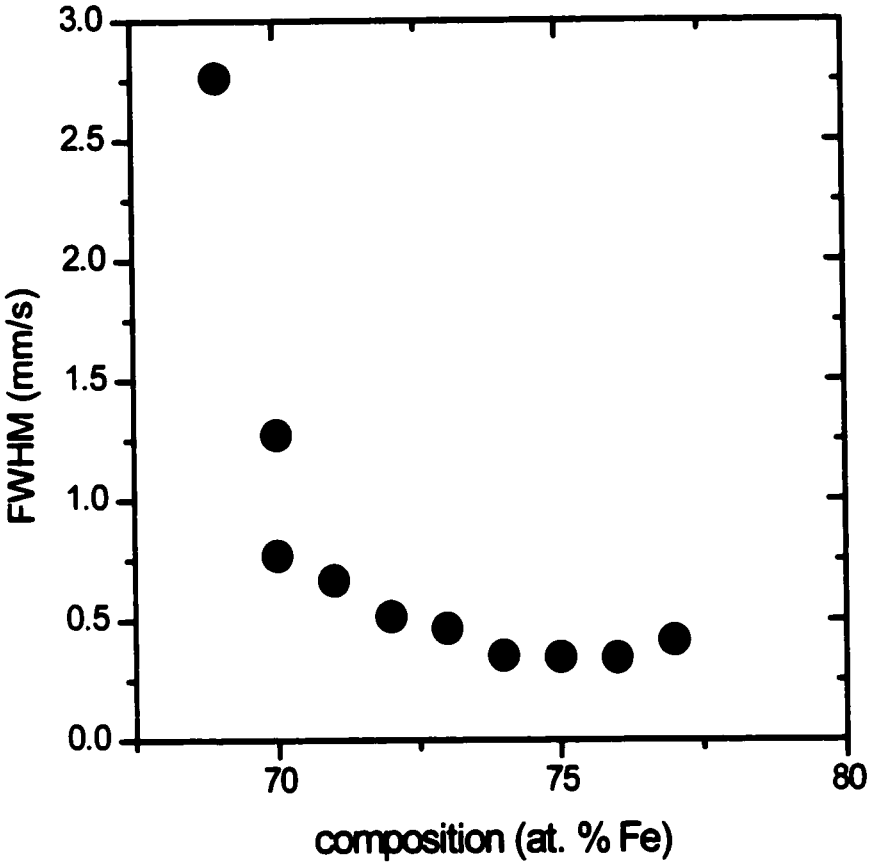

Figure 65 Variation of the FWHM of the FCC signal as a function of composition. In the absence of thickness effects in the absorber or the source and hyperfine parameter distributions, the theoretical FWHM would be 0.2 mm/s.

6.4.2 The Isomer Shift

Upon examination of the parameters in tables 23 through 28, in addition to the Zeeman splitting, the *CS* seems to be dramatically affected by the change in compostion above 60 at. % Fe. As found in the case of collinear Fe-Ni alloys [chapter 4], the Debye temperature of these alloys is fairly independent of the composition at Θ_D = 380 K, which permits us to extract the *IS* from the *CS* by subtracting the *SOD*. Without the *SOD*, the *IS* is a more characteristic property of the alloy since it is related to the electron density at the nucleus, and hence is a direct measure of the electronic structure of the material.

As seen in chapter 4, the *IS* of alloys which exhibit collinear magnetism tends to increase linearly with Fe content in the Ni-rich region, but reach a plateau at a value of 0.265 mm/s for alloys with compositions around 50 at. % Fe. Fig. 66 shows that upon further increasing the Fe concentration, the *IS* undergoes a dramatic drop over a small composition range with a midpoint around 70 at. % Fe. The total magnitude of the drop (~0.1 mm/s) can only be associated with a substantial increase in the charge density at the nucleus in the Fe atoms which must be associated with some reorganisation of the electronic structure. Because the *IS* is calculated by subtracting the *SOD* contribution from the measured *CS*, we must be sure that this drop can't be due to a change in the Debye temperature of the alloy. Given that Θ_D = 380 K for alloys below ~50 at. % Fe, even if Θ_D dropped to an unphysical value of 0 K in more Fe-rich alloys, this would only lead to a drop of 0.023 in the *CS*. In light of the known properties of these materials at RT, the maximum amplitude of change in Θ_D (if there is one) could be around 100 K, resulting in a drop of the *CS* of only 0.01 mm/s. The observed drop in the *CS* can thus entirely be attributed to a drop in the *IS*, as we have assumed in the previous sections.

We can also clearly associate this drop in the *IS* as being due to a transition from a HM alloy to a LM alloy as Fe content is increased above ~70 at. %. In chapter 5, ESCs which assumed a collinear FM ground state predict a first-order transition from a HM phase to a NM phase at 74.5 at. % Fe and also predict that this transition can be observed through three key parameters: a drop in the moment magnitude (hence the name HM/LM transition), a drop in the lattice parameter, and a drop in the charge density at the nucleus or, equivalently, the *IS*. Because of antiparallel spin configurations (and possibly some amount of non-collinearity), a direct measure of the moment magnitude in these alloys is not feasible. However, we do in fact observe the drop

in *IS*, as predicted by the ESCs. Fig. 67 illustrates more clearly the comparison between the measured *IS* in FCC and BCC Fe-Ni alloys and the results of the ESCs. In addition, we have also plotted the extracted *IS* of γ-Fe which is known to be a LM material ($\mu_{Fe} \approx 0.7\ \mu_B$, [Abrahams62]), the *IS* of antitaenite (c = 0.88 at. % Fe), also a known LM material [see chapter 3] and measured *IS* of nanophase Fe-Ni produced by mechanical alloying [Rancourt99].

First of all, the observed drop in the *IS* is the same order of magnitude as the drop predicted by the ESCs, and we can thus unambiguously identify this drop as a transition from a HM phase to a LM phase, because only such a dramatic change in the electronic structure can account for this drop in *IS*. The said transition is predicted to be of first-order when treating only collinear ferromagnetic phases, whereas the observed transition is clearly continuous and thus second-order in nature. This discrepancy can be attributed to the limited applicability of the ESC prediction because of the constraint to collinear ferromagnetism. When considering the DLM phase or a phase with anti-parallel spin configurations, the *IS* is seen to be reduced relative to a purely FM phase. A second-order transition from a HM FM phase to a NM phase driven by both non-collinearity (or antiparallel spin configurations) and moment magnitude reduction would thus produce the observed smooth composition dependence of the drop in the *IS*. In fact, both ESCs which use supercells and allow for non-collinearity [Wang97, vanSchlifgaarde99] and experimental evidence [Ullrich85, Dang96a] indicate that deviations from collinear ferromagnetism do occur, and that this is the mechanism for smoothing out the transition.

We can also compare the *IS* of the FCC alloys to other *IS*s extracted from measurements performed on BCC and known LM alloys. As in the case of HM FCC alloys, the BCC alloys, which exhibit a Fe moment of ~2.2 μ_B (making it a HM alloy), have an *IS* which is always around 0.25 mm/s and tends to increase with the Ni content. On the other hand, measurements of the *IS* in γ-Fe give a value of ~0.15 mm/s. This same value is found in antitaenite, an Fe-rich meteoritic Fe-Ni alloy which exhibits LM properties. The fact that the observed *IS* in our synthetic FCC Fe-Ni alloys drops from 0.25 mm/s at ~60 at. % to 0.17 mm/s at ~72 at. % seems to show a clear transition from a HM phase to a LM phase. We can also compare these values to those obtained in nanophase Fe-Ni obtained by mechanical alloying [Rancourt99]. All alloys produced by mechanical alloying consisted of two phases: the HM FCC or BCC phase which is magnetically split, and a paramagnetic phase (usually less than ~5 % fraction) whose *IS* is reported in fig. 67. We do not know what the composition of the paramagnetic phase is, so it is

reported in this figure as the bulk composition of the alloy. Nonetheless, the extracted *IS*s also appear around ~0.14 mm/s, as is characteristic of the LM alloys.

We have thus unambiguously determined that in FCC Fe-Ni alloys at RT, there is a second-order composition-driven transition from a HM phase to a LM phase, with a mid-point around 70 at. %. Also, it is clear from these results that this transition is due to a change in the electronic structure which leads to the reduction of the moment magnitudes on both the Fe and Ni atoms and the increase in the charge density at the nucleus (or drop in the *IS*). This is the first unequivocal observation of this transition that was first predicted by Moruzzi [Moruzzi86b] and whose supposed presence is a corner stone of 2-γ-state like models of Invar. The moment magnitudes in the LM phase are not known, except in the case of pure γ-Fe, because the disordered magnetic structure and chemical alloying, in addition to the coexistence with the BCC phase, make its experimental determination very difficult, if not impossible.

In regards to the composition variation of the Curie temperature, this transition may also explain, to some extent, the sharpness of the decrease of T_C in Fe-rich alloys, as MC simulations have shown that while it is possible to explain it to some extent based on a negative Fe-Fe magnetic exchange, it is difficult to properly reproduce the steepness of the drop. If the moment magnitude was collapsing around 70 at. %, then the effective exchange would also be weakened, leading to an accentuated drop in T_C.

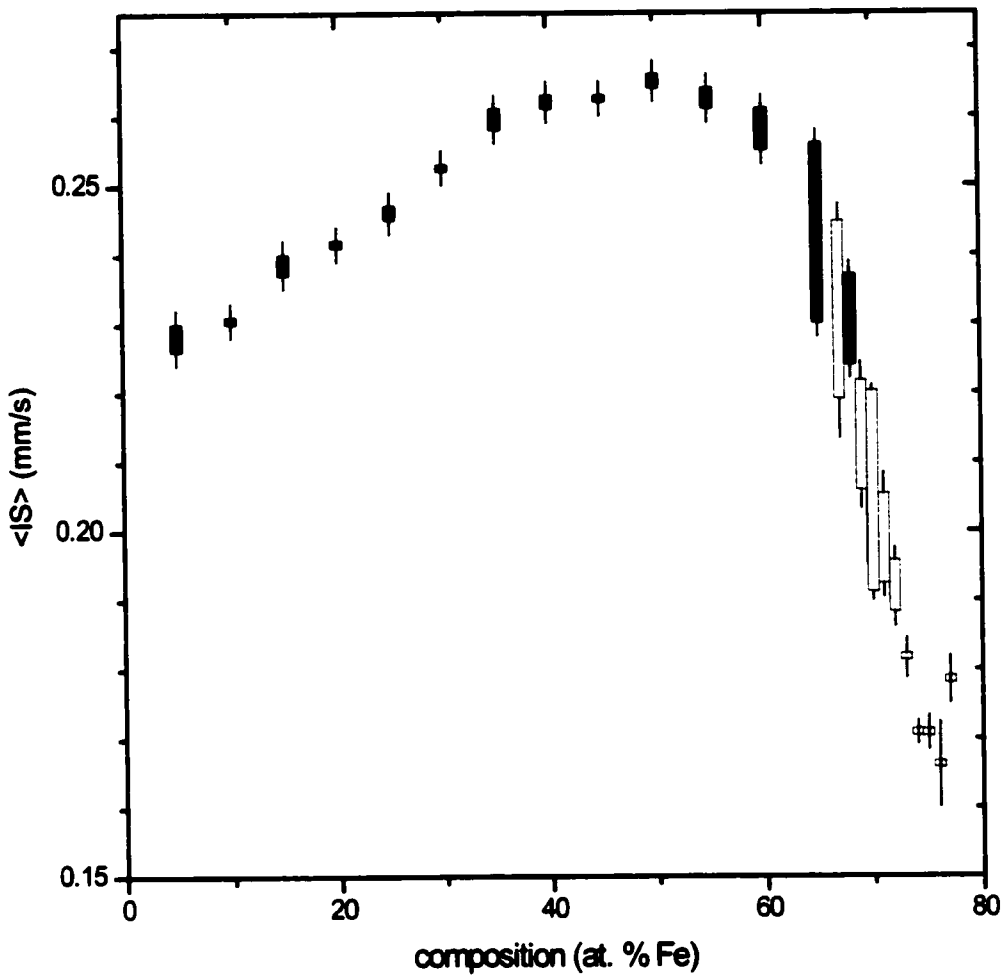

Figure 66 Average RT *IS* of FCC Fe-Ni alloys as a function of composition. The column represents the range of possible values obtained from satisfactory fits using different models, and the error bars represent the 1-σ statistical uncertainty due to the fitting. Again, the dark columns represents previously reported data, and the light columns the results of analysis of new Fe-rich alloys.

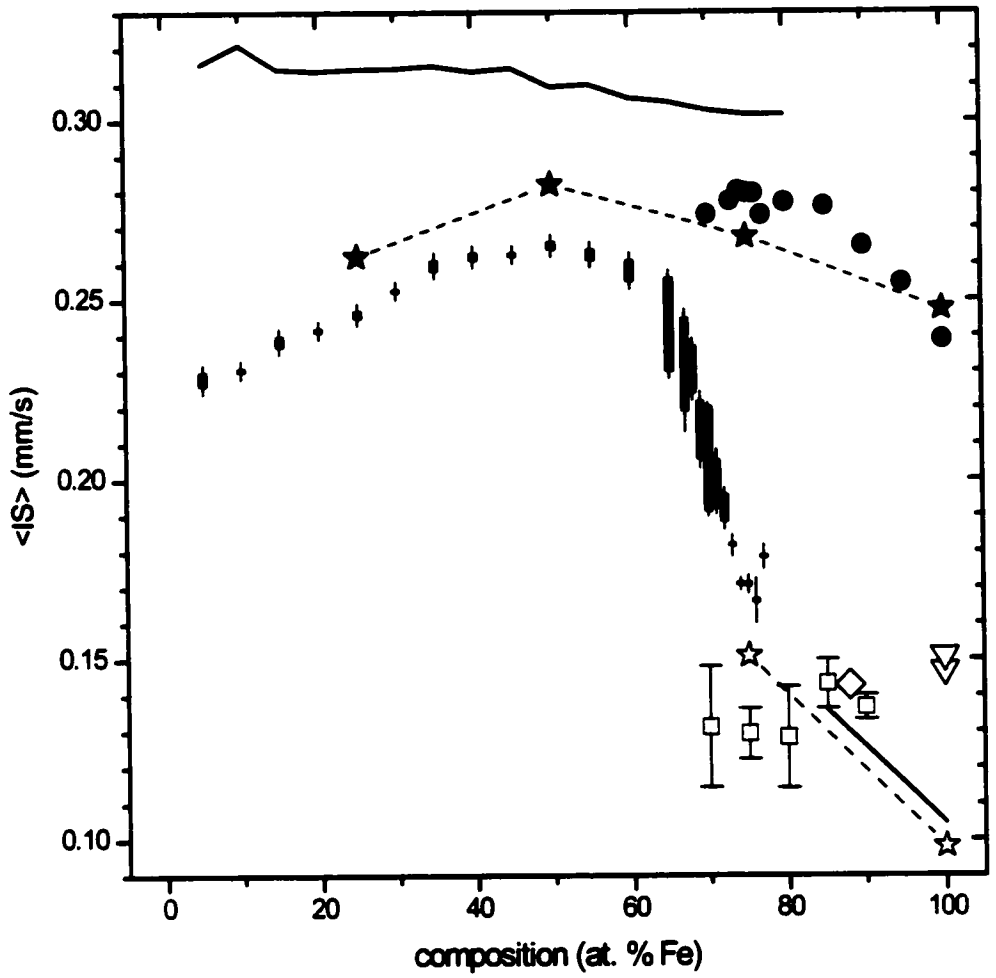

Figure 67 Experimental and calculated *IS* in various HM and LM Fe-Ni alloys. Vertical columns with error bars represent the synthetic FCC Fe-Ni alloys described in this chapter. Other symbols for experimental RT data are: (●) BCC Fe-Ni alloys [Dang96a and this work], (▽) LM γ-Fe [Keune77, Halbauer83], (◇) meteoritic antitaenite [chapter 3], (□) nanophase FCC material [Rancourt99]. Theoretical results based on ESCs using the CPA are represented by solid lines, ESC results on ordered structures are given by (★) and (☆), where the solid symbols represent the HM solution, and the open symbol the NM solution. The dashed lines are for presentation clarity only as they link the values calculated for chemically ordered alloys in the HM and NM phases.

6.4.3 The Lattice Parameter

Having established the existence and the nature of a HM/LM transition in the FCC Fe-Ni alloys around 70 at. % Fe, it is possible to understand one of the most puzzling anomalies in the alloys' properties: its lattice parameter. As in MS, the BCC and FCC phases can be separately analyzed in XRD, making it a useful tool for exploring the Fe-rich region of FCC alloys where there is coexistence with the BCC phase. Many investigations of the composition dependence of the lattice parameter have been performed in the past, so, contrarily to the novelty of our *CS* measurements, our XRD measurements are simply a complement to a vast collection.

6.4.3.1 Identifying the HM/LM Transition

Fig. 68, which was already given in chapter 4, provides a compilation of the average RT atomic volume as a function of concentration, for both FCC and BCC alloys. Before analysing it in detail, it is necessary to understand what a "normal" plot would look like. In the case of a binary alloy, if the two atomic species have comparable atomic volumes, it is possible to get a wide range of composition over which a single phase may be stable. In the absence of large magneto-volume effects or phase transitions, the composition dependence of the volume will obey Vegard's law which states that there should be a linear dependence of the average atomic volume on composition [Vegard28, Thorpe91]. Upon inspection of fig. 68, we see that for compositions up to 60 at. % Fe, this is *approximately* respected but above 60 at. % Fe there is a significant deviation to lower volumes with a transition midpoint at ~70 at. %. In the previous paragraphs, we have shown that at these compositions, there is a HM to LM transition, as predicted by ESCs and observed by MS. In fact, the ESCs also show that the volume of the LM phase should have a smaller volume than that of the HM phase, as is observed in fig. 55 [chapter 5]. This is clear evidence that drops in both *IS* and atomic volume around 70 at. % are due to an electronic transition from a HM phase to a LM phase.

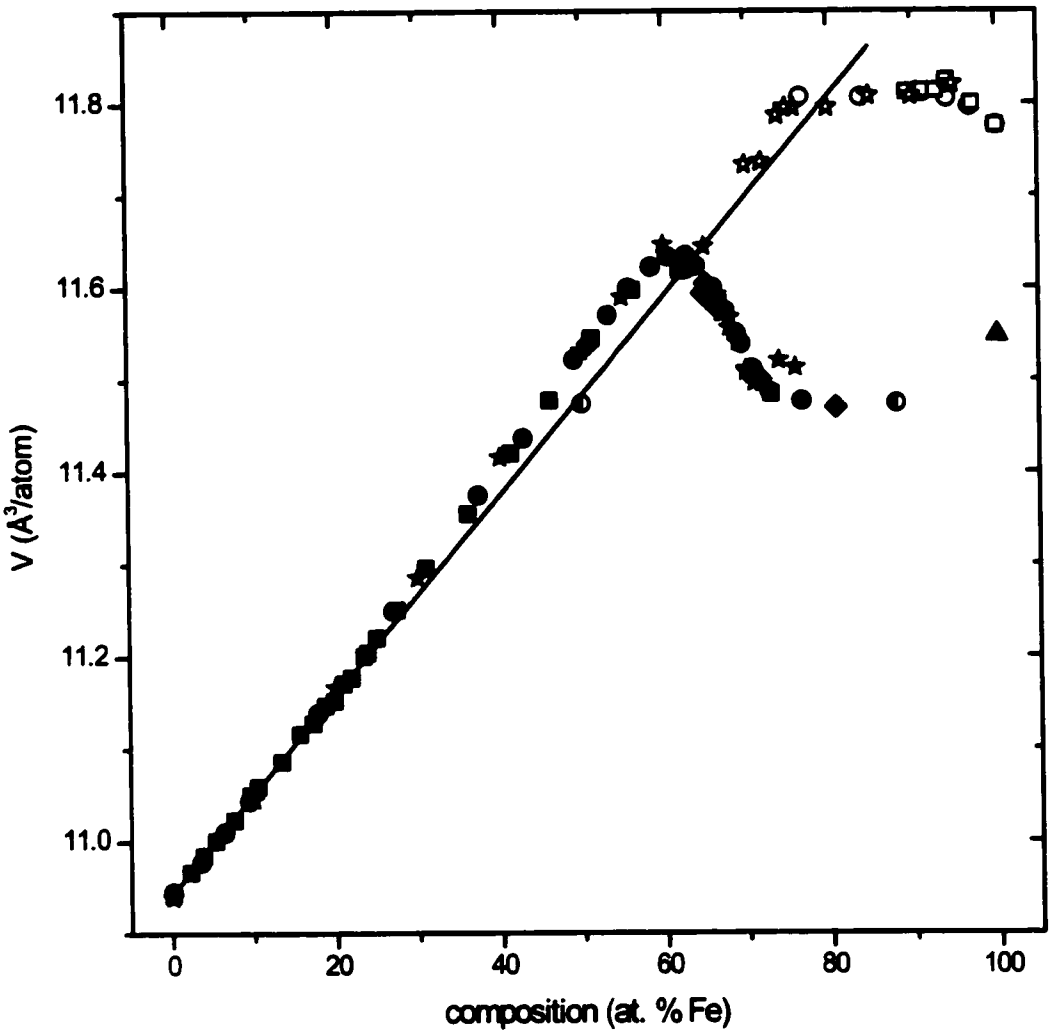

Figure 68 Composition dependence of the RT volume in FCC (solid symbols) and BCC (open symbols) Fe-Ni alloys. The straight line represents Vegard's law, as obtained by extrapolating from volumes of alloys with compositions less than 20 at. % Fe. See chapter 4 for the references regarding all the data points.

6.4.3.2 Distinction Between the HM/LM Transition and the Invar Effect

The reason for the *reduction* in the atomic volume relative to the expected Vegard's law behaviour has been one of the most puzzling aspects of the Fe-Ni system's properties, as it could not be reconciled with the *expansion* observed in alloys which exhibit the Invar effect. The HM/LM transition causes the $T = 0$ K ground state volume to be *contracted* compared to expected behaviour, while the magneto-volume *expansion* which is the Invar effect is an *expansion* relative to normal behaviour at high temperature, where the effect disappears. Clearly these two phenomena, the HM/LM transition and the Invar effect, must be distinct, even though they might occur simultaneously over some range of compositions.

To better accept that the two effects are distinct, one simply has to inspect alloys whose Fe content is such that they are unaffected by the HM/LM transition, yet still exhibit an Invar effect. Fig. 69 shows ω_{s0}, the spontaneous volume expansion at $T = 0$ K, and α_{RT}, the RT thermal expansion coefficient, of fcc Fe-Ni alloys. ω_{s0} is the relative expansion between the

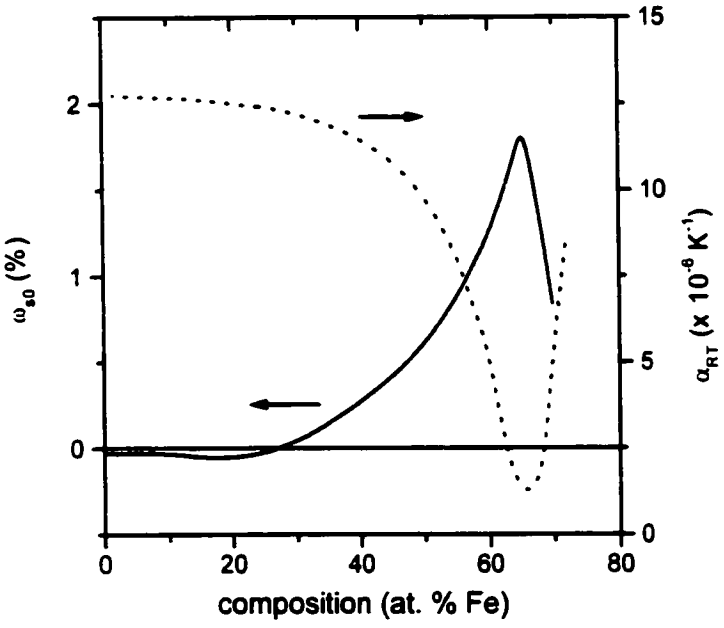

Figure 69 Spontaneous volume expansion ω_{s0} at $T = 0$ K (solid line) and RT thermal expansion coefficient α_{RT} (dotted line) of FCC Fe-Ni alloys (data taken from [Wassermann90]).

observed T = 0 K volume and the T = 0 K volume extrapolated from high-temperatures, where there are no more magneto-volume effects and where a "normal" Grüneisen-type behaviour is observed. One clearly sees that ω_{s0} and α_{RT} are strongly correlated, and are such that, at ~65 at. % Fe, they result in a near zero thermal expansion over a wide range of temperatures, known as the Invar effect. Although the spectacular effect is observed only close to 65 at. % Fe, the microscopic process which leads to it at 65 at. % Fe is present and active in alloys with as little as 30 at. % Fe. This fact is clear since the deviation from normal behaviour (ω_{s0} = 0 and $\alpha_{RT} \approx 13 \cdot 10^{-6} K^{-1}$) is continuous from ~30 at. % Fe up to ~65 at. % Fe.

Upon closer inspection of fig. 68 in the 0-60 at. % Fe range, we do in fact find that there is a deviation from linearity, as had once been pointed out by Bradley *et al.* [Bradley37], but was since neglected. Considering that Ni-rich alloys with compositions below 25 at. % Fe do not exhibit significant magneto-volume effects, we calculated the Vagard's law reference for non magneto-volume active Fe-Ni alloys by extrapolating from the data below 25 at. % Fe. When this reference volume is subtracted, one finds that there is an *expansion*, relative to non magneto-volume active alloys which increases with Fe content and which is of the same order of magnitude as ω_{s0}, as seen in fig. 70. Above ~50 at. % Fe, ω_{s0} is found to be larger than the

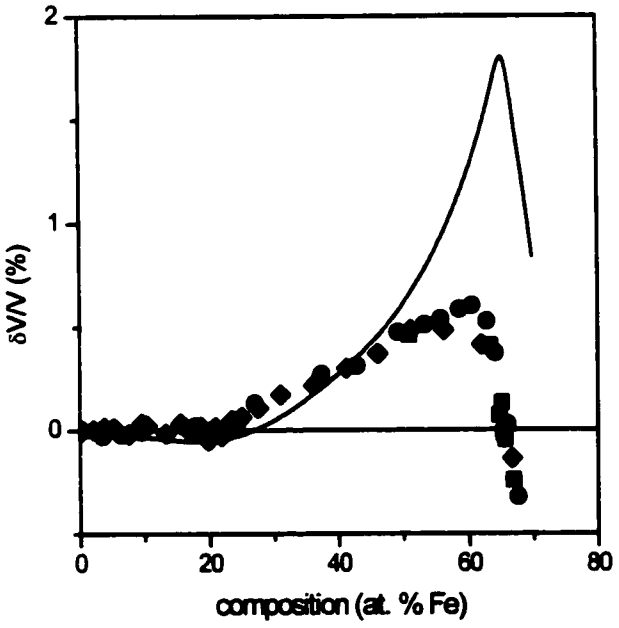

Figure 70 T = 0 deviation from Vegard's law and comparison with ω_{s0}.

deviation from our Vegard's law reference, but this is to be expected, as the reference volume starts decreasing as the HM/LM transition starts. There is thus a clear distinction between the volume reduction, seen in Fe-rich alloys, which is due to the HM/LM transition, and the volume expansion, seen in less Fe-rich alloys, which is the main cause of the Invar effect. These concepts are illustrated in fig. 71 which distinguishes the two effects.

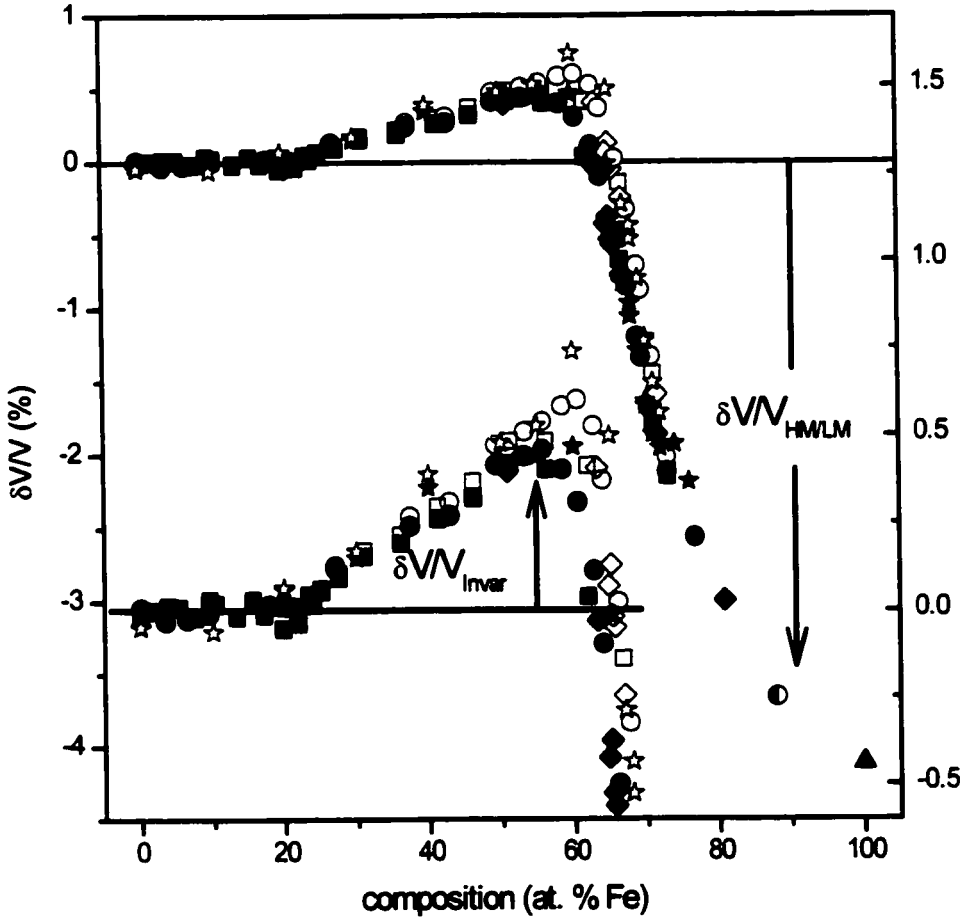

Figure 71 Illustration of the difference between the Invar expansion and HM/LM transition contraction of the atomic volume in FCC Fe-Ni alloys, relative to Vegard's law. Symbols are the same as used in fig. 68. Solid Symbols represent RT measurements, and open symbols represent extrapolation to $T = 0$ K based on thermal expansion curves between 0 K and RT (from [Hayase73]). As seen, the HM/LM contraction (left scale), which has a midpoint around 70 at. % Fe is an order of magnitude larger than the Invar expansion seen in alloys of lower Fe content (right scale).

6.4.4 Differentiating the Observation of the HM/LM Transition from the Normal *IS* and Volume Correlation

Because the *IS* is related to the charge density at the nucleus, a change in the volume will result in a change in the *IS*. It is therefore important to further investigate the relation between the drop in *IS* and the drop in the atomic volume. As seen in chapter 5, the average slope of the *IS* with a change in volume is $\partial IS/\partial V = -0.1$ mm/s/Å^3. At 70 at. %, the drop in volume is ~ 0.2 Å^3, which results in a drop in *IS* of ~0.02 mm/s, or less than half of the observed drop. It is thus clear that the observed drop in the *IS* must be due to a change in the electronic structure, and that the observed drop in the volume cannot explain it entirely. It is difficult to prove that the drop in the volume is due to the HM/LM transition but the observed drop in the *IS* is conclusively attributed to the change in electronic structure which constitutes the HM/LM transition.

Table 23 Parameters of the magnetic phase of the xVBF fits of RT Mössbauer spectra of Fe-rich RQ Fe-Ni alloys. 2-σ (95 %) fitting uncertainties are given in the second column for each parameter. For alloys with $c > 73$ at. %, the parameters of the BCC phase are given.

67	1.15	1294190	209	0.106	0.013	448919	3251	3	0	2	0
67	1.15	1294190	226	0.107	0.013	448926	3546	3	0	2	0
69	0.92	3202230	235	0.134	0.008	658139	3079	3	0	2	0
69	0.81	3202220	196	0.130	0.007	657855	2875	3	0	2	0
69	0.81	3202200	205	0.126	0.011	657178	3034	3	0	2	0
70	0.72	3801790	152	0.140	0	873525	1940	3	0	2	0
70	0.71	3801810	115	0.140	0	873750	1409	3	0	2	0
70 #2	0.70	629935	110	0.140	0	207485	1417	3	0	2	0
70 #2	0.68	629997	84	0.140	0	208419	1128	3	0	2	0
70 #2	0.67	630068	110	0.140	0	209512	1494	3	0	2	0
71	0.71	1134580	323	0.152	0.028	109122	6135	3	0	2	0
71	0.71	1134600	102	0.155	0.020	109461	1009	3	0	2	0
71	0.70	1134580	124	0.153	0.042	109263	1728	3	0	2	0
72	0.71	584740	47	0.156	0.003	74089	495	3	0	2	0
72	0.67	584746	81	0.167	0.008	74256	776	3	0	2	0
73	2.41	1249360	382	0.145	0.012	94409	2191	3	0	2	0
74	3.18	1022380	315	0.112	0.008	330704	4670	2.542	0.081	1.790	0.058
75	2.41	598095	170	0.112	0.006	214863	2728	2.533	0.065	1.807	0.043
76	7.46	1399260	636	0.118	0.010	635958	10121	2.555	0.074	1.890	0.057
77	19.37	5387510	1026	0.106	0.006	1830780	16626	2.558	0.024	1.818	0.015

67	0	0	0.239	0.090	0	0	0.0044	0.0054	0.087	0.019
67	0.57	0.19	0.223	0.081	-0.028	0.057	0.0048	0.0047	0.091	0.025
69	0	0	0	0	-1.000	0.182	-0.0273	0.0051	0	0
69	0.92	0.10	0.336	0.083	-0.062	0.067	-0.0131	0.0053	0.066	0.022
69	0	0	1.000	0.285	0	0	-0.0113	0.0051	0.026	0.017
70	0	0	1	0	0	0	-0.0171	0.0021	0.041	0.003
70	0.90	0.01	0.265	0.017	-0.171	0.027	-0.0210	0.0012	0.108	0.006
70 #2	0	0	0	0	-0.991	0.021	-0.0419	0.0018	0	0
70 #2	0	0	0.837	0.084	0	0	-0.0310	0.0044	0.131	0.027
70 #2	0.77	0.11	0.576	0.092	0.046	0.140	-0.0291	0.0041	0.115	0.020
71	0	0	0	0	0.982	0.109	-0.0315	0.0052	0	0
71	-0.08	0.52	0.910	0.291	0.338	0.622	-0.0346	0.0026	0.069	0.020
71	0	0	1.000	0.299	0	0	-0.0341	0.0036	0.096	0.032
72	0	0	0	0	1	0	-0.0375	0.0013	0	0
72	0	0	0.934	0.157	0	0	-0.0374	0.0026	0.062	0.015
73	0	0	0	0	0	0	-0.0517	0.0047	0	0
74	0	0	0	0	-0.420	0.059	0.0425	0.0021	0	0
75	0	0	0	0	-0.397	0.046	0.0419	0.0022	0	0
76	-0.27	0.50	0	0	-0.478	0.095	0.0419	0.0026	0.027	0.012
77	0	0	0	0	-0.333	0.074	0.0358	0.0010	0	0

(Table 23 continued)

67	0	0	0	0	0.523	0	0.878	0.050	0.429	0.029
67	0	0	0.106	0.018	0.479	0	0.833	0.069	0.405	0.037
69	0	0	0.025	0.008	0.803	0	0.576	0.022	0.481	0.026
69	0	0	0.064	0.041	0.784	0	0.565	0.011	0.464	0.012
69	0	0	0	0	0.780	0	0.563	0.016	0.462	0.018
70	0	0	0	0	0.054	0	0.087	0.003	0.049	0.008
70	0	0	0.098	0.009	0.072	0	0.102	0.002	0.033	0.007
70 #2	0	0	0.126	0.025	0.404	0	0.036	0.003	0.132	0.009
70 #2	0	0	0	0	0.231	0	0.041	0.005	0.041	0.008
70 #2	0	0	0.115	0.020	0.392	0	0.066	0.012	0.067	0.018
71	0	0	0.129	0.041	0.404	0	0.046	0.005	0.041	0.027
71	0	0	0.073	0.022	0.373	0	0.045	0.009	0.020	0.015
71	0	0	0	0	0.368	0	0.054	0.010	0.016	0.014
72	0	0	0.090	0.007	0.815	0	0.046	0.002	0.017	0.004
72	0	0	0	0	0.833	0	0.050	0.003	0.013	0.004
73	0	0	0	0	1	0	0	0	0.070	0.008
74	0	0	0.087	0.011	0.235	0	2.356	0.007	0.029	0.013
75	0	0	0.088	0.010	0.233	0	2.354	0.004	0.023	0.007
76	0	0	0.065	0.014	0.141	0	2.373	0.009	0.013	0.013
77	0	0	0.090	0.006	0.105	0	2.416	0.007	0.000	0.010

67	0.116	0.026	1.833	0.015	0.132	0.013
67	0.137	0.033	1.821	0.015	0.126	0.012
69	0.197	0.031	1.417	0.019	0.279	0.015
69	0.216	0.015	1.406	0.015	0.283	0.009
69	0.220	0.024	1.406	0.019	0.289	0.012
70	0.789	0.004	0.272	0.008	0.458	0.007
70	0.776	0.002	0.288	0.003	0.464	0.002
70 #2	0.437	0.038	0.316	0.074	0.727	0.057
70 #2	0.481	0.037	0	0	0.798	0.036
70 #2	0.389	0.045	0	0	0.889	0.053
71	0.563	0.044	0	0	0.623	0.101
71	0.560	0.019	0	0	0.543	0.022
71	0.560	0.047	0	0	0.533	0.038
72	0.185	0.012	0.029	0.151	0.607	0.061
72	0.167	0.024	0.267	0.260	0.546	0.132
73						
74	0.765	0.072	2.273	0.008	0.084	0.004
75	0.767	0.049	2.270	0.006	0.082	0.004
76	0.825	0.146	2.294	0.013	0.078	0.012
77	0.593	0.101	2.317	0.003	0.059	0.009

(Table 23 continued)

67	0.361	0.037	1.588	0.032	0.247	0.016
67	0.384	0.043	1.554	0.052	0.253	0.017
69						
69						
69						
70	0.156	0.001	1.166	0.009	0.338	0.013
70	0.152	0.002	1.145	0.008	0.363	0.008
70 #2	0.159	0.033	0.364	0.058	0.327	0.040
70 #2	0.288	0.029	0.099	0.030	0.292	0.035
70 #2	0.219	0.049	0.396	0.053	0.239	0.034
71	0.033	0.050	1.513	0.654	0.239	0.401
71	0.067	0.011	1.398	0.097	0.252	0.063
71	0.072	0.025	1.355	0.109	0.279	0.068
72						
72						
73						
74						
75						
76	0.034	0.129	2.126	0.066	0.054	0.039
77	0.302	0.058	2.243	0.004	0.093	0.008

Table 24 Parameters of the VBF fits to the RT Mössbauer spectra of Fe-rich RQ Fe-Ni alloys. 2-σ (95 %) fitting uncertainties are given in the second column of each parameter.

67	1.34	1294440	169	0.133	0.007	453776	2850	3	0	2	0
67	1.28	1294440	238	0.151	0.018	454650	3856	2.75	0.22	1.99	0.15
67	0.86	1294420	208	0.133	0.004	453526	2843	3	0	2	0
67	0.86	1294420	171	0.133	0.005	453530	2622	3	0	2	0
67	0.79	1294520	196	0.164	0.012	456468	3163	2.59	0.15	1.85	0.10
67	0.79	1294520	214	0.164	0.015	456409	3576	2.60	0.17	1.86	0.12
69	0.84	3202140	245	0.123	0.010	656127	3427	3	0	2	0
69	0.74	3202150	217	0.122	0.008	656304	3047	3	0	2	0
69	0.73	3202120	243	0.116	0.008	655464	3009	3	0	2	0
70	0.78	3801770	266	0.120	0	871693	3451	3	0	2	0
70	0.78	3801660	248	0.120	0	869972	2876	3	0	2	0
70	0.74	3801620	283	0.120	0	869473	3343	3	0	2	0
70 #2	0.80	629800	109	0.120	0	205085	1464	3	0	2	0
70 #2	0.79	629942	114	0.127	0	207338	1675	3	0	2	0
70 #2	0.72	631063	155	0.120	0	227907	2641	3	0	2	0
71	0.85	1134570	130	0.120	0	108689	1570	3	0	2	0
71	0.71	1134650	163	0.120	0	109873	2326	3	0	2	0
71	0.69	1134580	133	0.120	0	108892	1557	3	0	2	0
72	0.99	584650	57	0.120	0	72521	662	3	0	2	0
72	0.70	584660	66	0.120	0	72657	785	3	0	2	0
73	2.37	1249920	243	0.162	0.005	96647	1752	3	0	2	0

67	0.0109	0.0042	0	0	0.0044	0	-0.0035	0.0016
67	0.0117	0.0050	0	0	0.0040	0	-0.0031	0.0027
67	-0.0803	0.0115	0	0	-0.0001	0	0.0002	0.0023
67	-0.0803	0.0100	0.053	0.006	0	0	0	0
67	-0.0871	0.0106	0.058	0.006	0.0010	0	-0.0007	0.0020
67	-0.0876	0.0097	0	0	0	0	0	0
69	-0.0271	0.0033	0	0	0.0284	0	-0.0376	0.0046
69	-0.0357	0.0034	0	0	0.0140	0	-0.0186	0.0046
69	-0.0422	0.0030	0.038	0.004	0	0	0	0
70	-0.0403	0.0018	0.054	0.008	0	0	0	0
70	-0.0328	0.0015	0	0	0.0179	0	-0.0371	0.0050
70	-0.0355	0.0015	0.030	0.009	0.0096	0	-0.0202	0.0064
70 #2	-0.0414	0.0026	0	0	0.0220	0	-0.0664	0.0202
70 #2	-0.0565	0.0038	0	0	0	0	0	0
70 #2	-0.0691	0.0027	0.908	0.040	-0.0340	0	0.6957	0.0362
71	-0.0430	0.0061	0	0	0	0	0	0
71	-0.0503	0.0051	0	0	0	0	0	0
71	-0.0320	0.0027	0	0	0.0248	0	-0.0758	0.0324
72	-0.0448	0.0043	0	0	0	0	0	0
72	-0.0662	0.0062	0	0	0	0	0	0
73	-0.0516	0.0053	0	0	0	0	0	0

(Table 24 contibued)

67	0.165	0	1.824	0.015	0.145	0.012	0.514	0.042	0.869	0.044
67	0.196	0	1.816	0.012	0.144	0.010	0.463	0.046	0.840	0.071
67	0.169	0	1.824	0.022	0.145	0.032	0.509	0.036	0.862	0.036
67	0.169	0	1.824	0.011	0.145	0.008	0.509	0.028	0.862	0.028
67	0.192	0	1.822	0.009	0.137	0.008	0.492	0.027	0.889	0.035
67	0.188	0	1.823	0.008	0.136	0.008	0.490	0.026	0.886	0.040
69	0.738	0	0.533	0.024	0.431	0.025	0.262	0.037	1.378	0.030
69	0.730	0	0.529	0.022	0.426	0.021	0.270	0.032	1.372	0.026
69	0.715	0	0.521	0.017	0.416	0.015	0.285	0.027	1.362	0.024
70	0.499	0	0.289	0.045	0.274	0.020	0.086	0.046	0.096	0.012
70	0.541	0	0.212	0.029	0.308	0.039	0.025	0.007	0.069	0.007
70	0.536	0	0.202	0.038	0.312	0.031	0.022	0.020	0.071	0.010
70 #2	0.169	0	0.067	0.005	0.041	0.021	0.434	0.090	0.147	0.068
70 #2	0.257	0	0.088	0.005	0.060	0.012	0.240	0.045	0.205	0.055
70 #2	0.152	0	0.084	0.007	0.053	0.006	0.303	0.027	0.083	0.017
71	0.308	0	0.069	0.005	0.041	0.015	0.592	0.062	0.213	0.193
71	0.291	0	0.076	0.004	0.037	0.016	0.213	0.085	0.196	0.085
71	0.306	0	0.069	0.002	0.038	0.013	0.568	0.039	0.260	0.063
72	0.721	0	0.065	0.002	0.040	0.007	0.279	0.018	0.018	0.182
72	0.716	0	0.067	0.002	0.037	0.003	0.284	0.019	0.042	0.121
73	1.000	0	0.000	0.000	0.059	0.005				

67	0.423	0.024	0.321	0.046	1.552	0.034	0.235	0.019
67	0.401	0.025	0.342	0.039	1.521	0.039	0.233	0.018
67	0.418	0.018	0.322	0.169	1.548	0.109	0.234	0.059
67	0.418	0.016	0.322	0.022	1.548	0.025	0.234	0.011
67	0.402	0.017	0.315	0.027	1.539	0.021	0.217	0.012
67	0.401	0.013	0.323	0.028	1.541	0.021	0.219	0.014
69	0.301	0.016						
69	0.303	0.014						
69	0.310	0.014						
70	0.082	0.036	0.415	0.046	0.867	0.052	0.447	0.026
70	0.005	0.020	0.435	0.057	0.840	0.060	0.445	0.024
70	0.005	0.033	0.441	0.056	0.831	0.062	0.448	0.025
70 #2	0.252	0.061	0.397	0.116	0.650	0.168	0.507	0.036
70 #2	0.255	0.052	0.503	0.055	0.273	0.089	0.732	0.055
70 #2	0.337	0.022	0.546	0.023	0.020	0.034	1.201	0.066
71	0.437	0.086	0.101	0.053	1.331	0.168	0.301	0.099
71	0.185	0.072	0.496	0.096	0.353	0.232	0.764	0.128
71	0.368	0.053	0.126	0.040	1.267	0.106	0.332	0.086
72	0.474	0.036						
72	0.469	0.046						
73								

Table 25 Parameters of the DLS fit of the RT spectra of Fe-rich RQ Fe-Ni alloys with T_C close to RT.

70	2.20	3806045	395	0.2734	0.0032	953141	5764	1 0
70 #2	2.51	630584	101	0.1784	0.0077	221574	2104	1 0
71	1.50	1134561	133	0.1573	0.0151	110742	2394	1 0

70	-0.0450	0.0014	0	0	0.918	0.018	1.90	0.07
70 #2	-0.0540	0.0043	0	0	1.267	0.068	6.10	0.60
71	-0.0449	0.0079	0	0	1.317	0.098	8.18	1.16

Table 26 Parameters of the xVBF fit of the paramagnetic FCC phase of the RT spectra of Fe-rich RQ Fe-Ni alloys.

73	2.2	1249240	349	0.142	0.010	93150	1786	1 0
74	3.2	1022380	315	0.112	0.008	40662	1007	1 0
75	2.4	598095	170	0.112	0.006	14419	474	1 0
76	7.5	1399260	636	0.118	0.010	9717	777	1 0
77	19.4	5387510	1026	0.106	0.006	13824	529	1 0

73	0	0	-0.0508	0.0045	0	0	0	0	0.241	0.019
74	0	0	-0.0616	0.0043	0	0	0	0	0.175	0.016
75	0	0	-0.0617	0.0060	0	0	0	0	0.163	0.022
76	0	0	-0.0663	0.0134	0	0	0	0	0.116	0.053
77	0	0	-0.0540	0.0077	0	0	0	0	0.185	0.016

Table 27 Compiled results (FCC phase) of the xVBF fits of the RT spectra of Fe-rich RQ Fe-Ni alloys.

67	0.0044	0.087	0	0	1.249	0.515
67	0.0048	0.091	0	0.106	1.248	0.511
69	-0.0273	0	0	0.025	0.785	0.496
69	-0.0131	0.066	0	0.064	0.786	0.495
69	-0.0113	0.026	0	0	0.788	0.497
70	-0.0171	0.041	0	0	0.343	0.581
70	-0.0210	0.108	0	0.098	0.348	0.575
70 #2	-0.0419	0	0	0.126	0.386	0.414
70 #2	-0.0310	0.131	0	0	0.317	0.483
70 #2	-0.0291	0.115	0	0.115	0.306	0.514
71	-0.0315	0	0	0.129	0.351	0.418
71	-0.0346	0.069	0	0.073	0.353	0.420
71	-0.0341	0.096	0	0	0.356	0.415
72	-0.0375	0	0	0.090	0.127	0.233
72	-0.0374	0.062	0	0	0.123	0.221
73	-0.0517	0	0	0	0.056	0.042
73	-0.0508	0			0	0
74	-0.0616	0			0	0
75	-0.0617	0			0	0
76	-0.0663	0			0	0
77	-0.0540	0			0	0

Table 28 Compiled results of the VBF fits of the RT spectra of Fe-rich RQ Fe-Ni alloys.

67	0.0109	1.249	0.513	-0.409
67	0.0117	1.266	0.506	-0.462
67	-0.0139	1.248	0.513	-0.406
67	-0.0140	1.248	0.513	-0.406
67	-0.0133	1.275	0.496	-0.463
67	-0.0133	1.275	0.496	-0.463
69	-0.0271	0.788	0.498	0.377
69	-0.0184	0.788	0.498	0.376
69	-0.0130	0.790	0.499	0.380
70	-0.0128	0.537	0.432	0.956
70	-0.0328	0.534	0.428	0.936
70	-0.0213	0.534	0.427	0.936
70 #2	-0.0414	0.390	0.394	1.440
70 #2	-0.0032	0.401	0.418	1.642
70 #2	-0.0246	0.620	0.664	1.609
71	-0.0430	0.386	0.424	1.505
71	0.0152	0.404	0.454	1.706
71	-0.0320	0.388	0.428	1.512
72	-0.0448	0.154	0.208	2.695
72	-0.0386	0.155	0.208	2.681
73	-0.0516	0.047	0.036	0.995

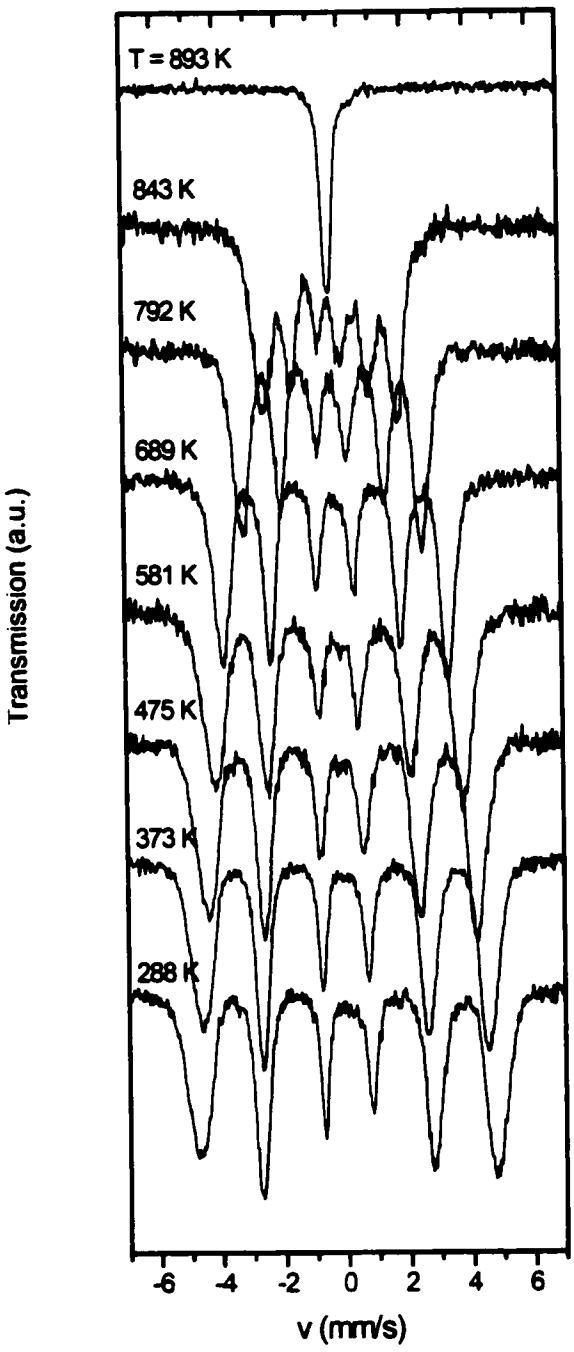

Figure 72 High-temperature Mössbauer spectra of $Fe_{30}Ni_{70}$ ($T_C \approx 860$ K).

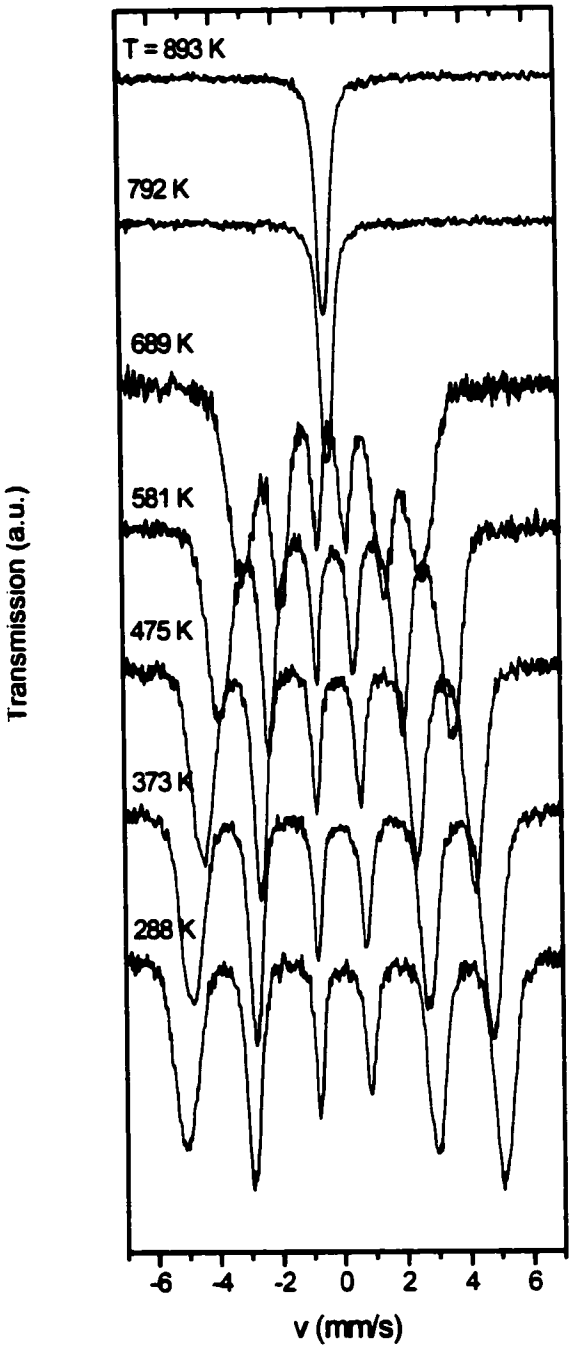

Figure 73 High-temperature Mössbauer spectra of $Fe_{50}Ni_{50}$ ($T_C \approx 790$ K).

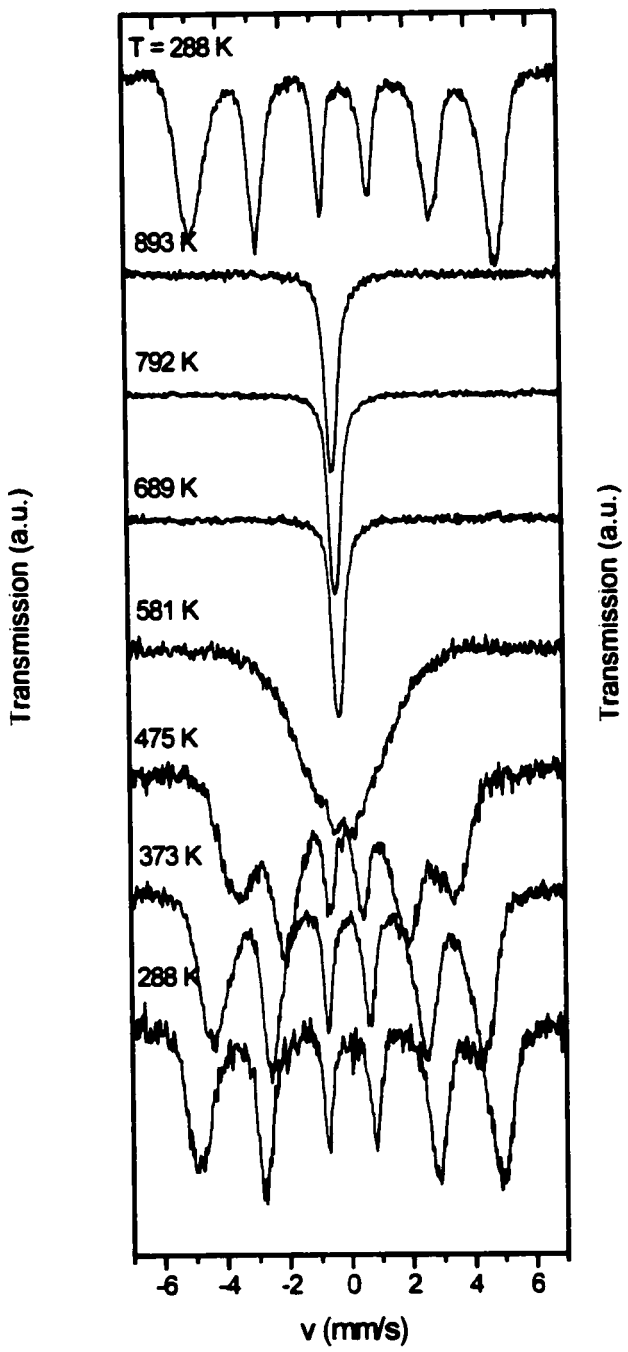

Figure 74 High-temperature Mössbauer spectra of $Fe_{60}Ni_{40}$ (T_C ≈ 665 K).

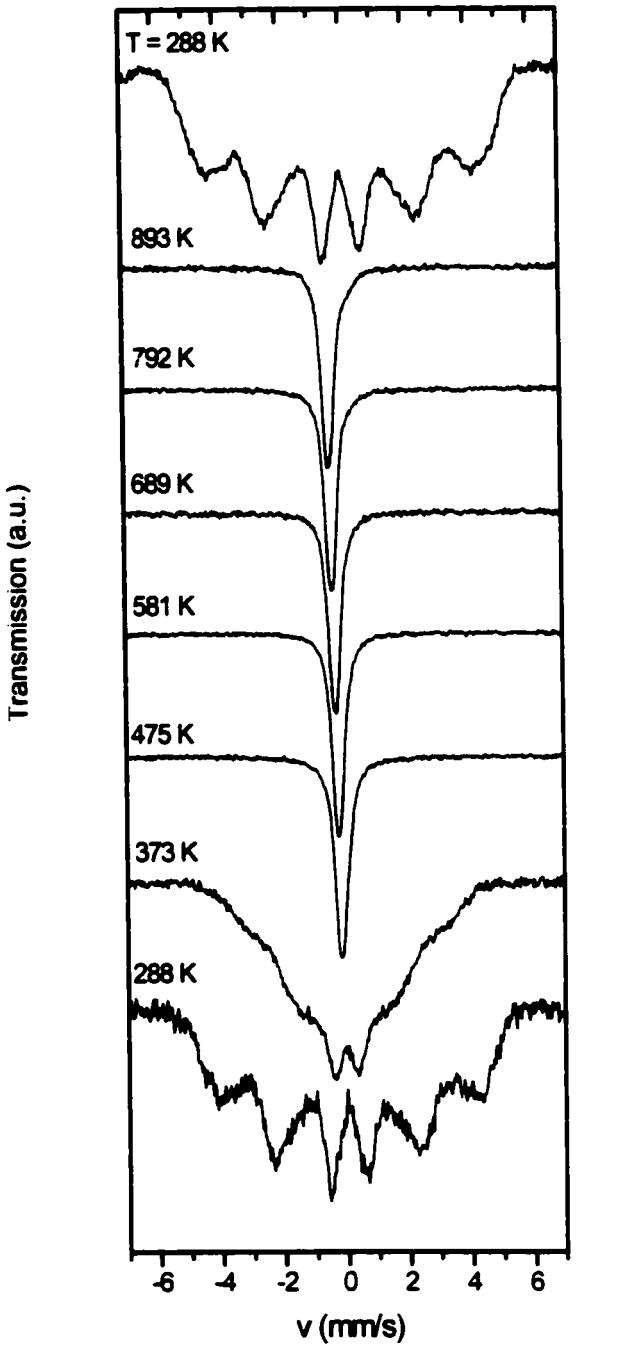

Figure 75 High-temperature Mössbauer spectra of $Fe_{67}Ni_{33}$ (T_C = 460 K).

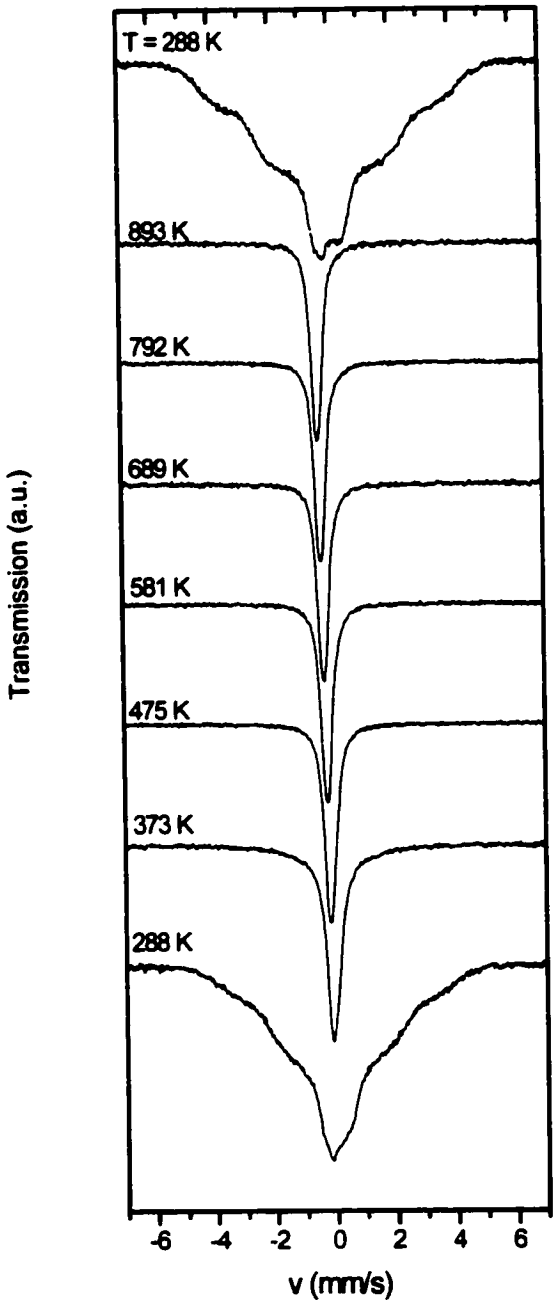

Figure 76 High-temperature Mössbauer spectra of $Fe_{69}Ni_{31}$ (T_C = 370 K). The cooled RT spectrum (top) shows that the sample has undergone a spinodal decomposition into phases of slightly different compositions, as is evidenced by the increase in the Zeeman splitting.

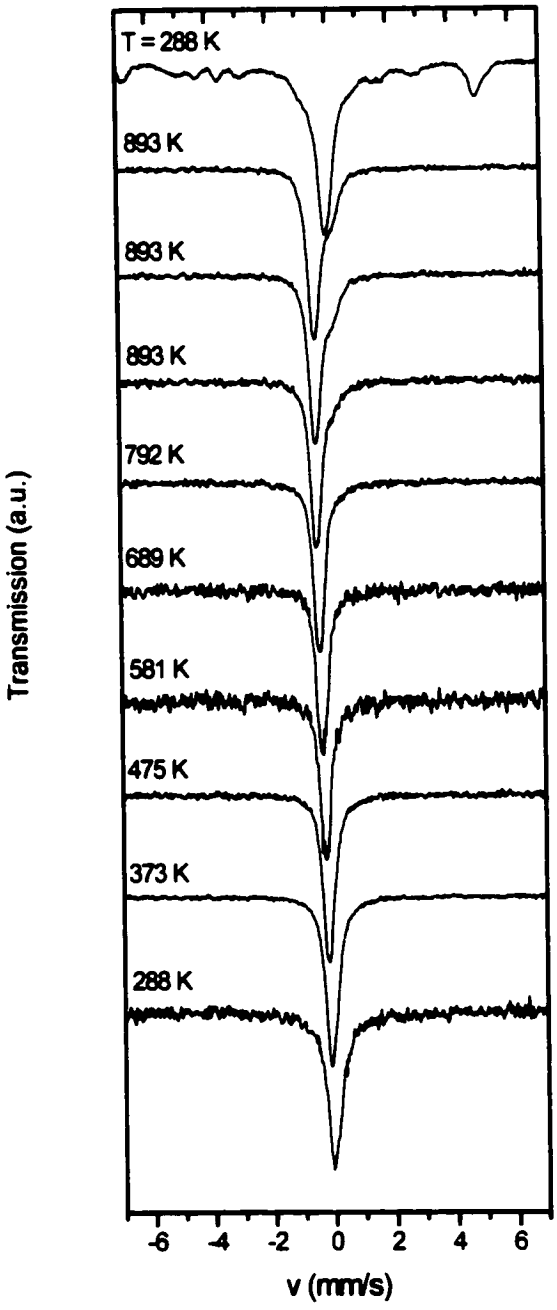

Figure 77 High-temperature Mössbauer spectra of $Fe_{71}Ni_{29}$ (T_C = 270 K). The high temperature and cooled RT (top) spectra show important signs of oxidation (this was the first series taken, before the leak in the oven was discovered and fixed).

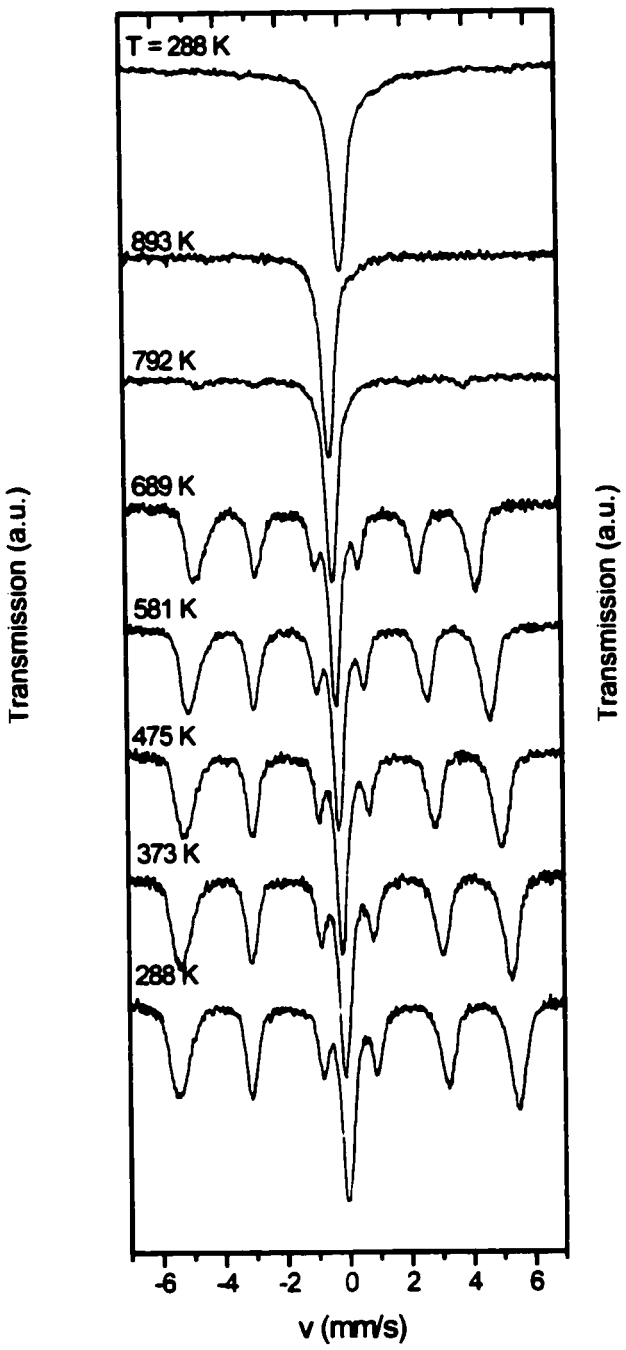

Figure 78 High-temperature Mössbauer spectra of $Fe_{73}Ni_{27}$ (T_C < RT). The BCC phase disappears at the austenitic end temperature (~800 K). The cooled sample is nearly pure FCC.

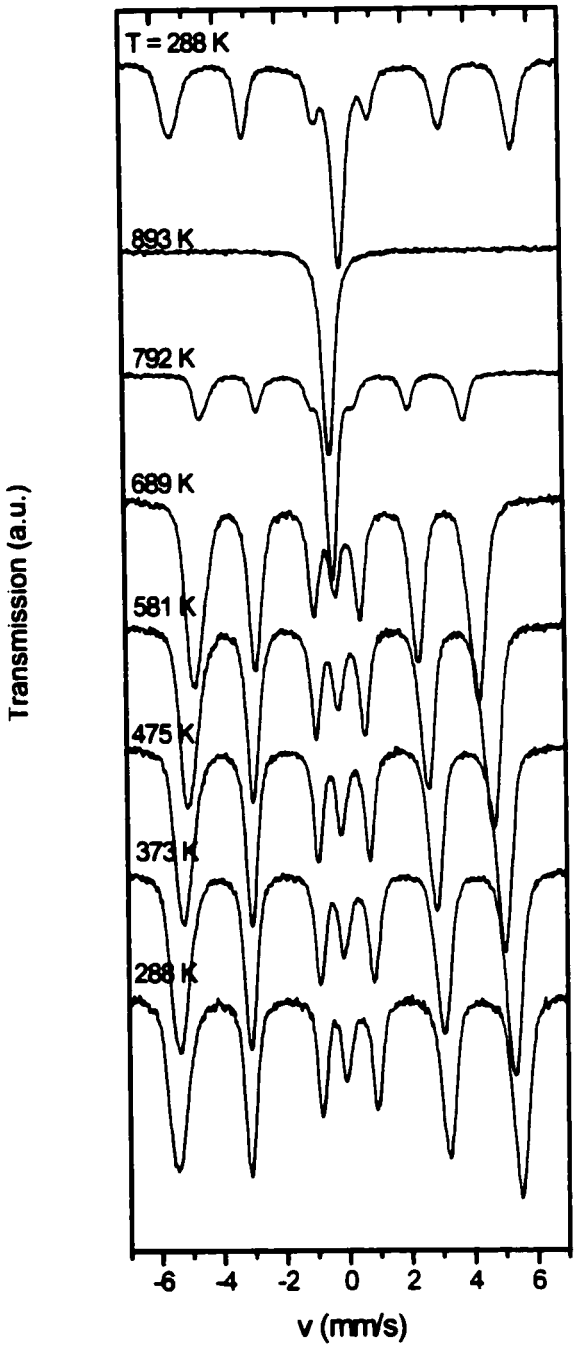

Figure 79 High-temperature Mössbauer spectra of $Fe_{75}Ni_{25}$ (T_C < RT). Again we see a disappearance of the BCC phase above 800 K, and a recovered sample which has a higher proportion of the FCC phase.

6.5 High-Temperature Measurements

Using the *IS*, it is possible to characterize the ground state electronic structure of FCC Fe-Ni alloys and to follow the composition-driven HM/LM transition. In the interest of better understanding these alloys, it is also necessary to investigate if and how changes in the electronic structure occur at temperatures above RT. We have thus measured the Mössbauer spectra of several Fe-Ni samples, ranging in composition from 30 at % Fe to 75 at. % Fe, which span the region of the stable HM phase through the transition to the LM phase, including compositions where the Invar effect is maximum. Similar measurement have already been performed for an alloy with 65 at. % Fe by Rancourt *et al.* [Rancourt85] as well as Willgeroth *et al.* [Willgeroth84] in the case of more Fe rich materials in the paramagnetic phase. The data of Kobeissi [Kobeissi81] and Kovats and Walker [Kovats69] were also used for γ-Fe. Our oven could not reach the temperatures where the latter phase is stable. Because of their size, all the parameters from the analyses are listed in tables in appendix D.

6.5.1 Analysis Method

As in the case of RT spectra, the xVBF and VBF models were used to obtain the *CS*, in addition to a simple Voigt line when appropriate. The *IS* could then be obtained by removing the SOD contribution by using the Debye model, with Θ_D = 380 K for FCC alloys and Θ_D = 430 K for BCC alloys [Rancourt99]. At the temperatures of interest (300-900 K), the temperature dependence of the SOD is nearly linear and is not very sensitive to Θ_D, especially at the higher temperatures. For this reason, our choice of Θ_D does not significantly affect the results. The largest source of error was the calibration of the sample temperature, as the thermocouple in the oven is not in direct contact with the sample. The uncertainty from the sample temperature is included in the uncertainty displayed in the figures, whereas the uncertainty given in the tables is strictly due to the fitting statistics.

6.5.2 Observation of a Correlation Between the *IS* and *z* in Invar Alloys

The analysis of the spectra of the sample with 30 at. % Fe shows that the *IS* is not

temperature dependent, as would be expected in a material where the electronic structure does not change with temperature, as we are well below the Fermi temperatures in these alloys. The slight variations that are observed in the extracted *IS* [Appendix D] can be due to errors in the estimated temperature which are underestimated. It is clear, however, that we cannot ascribe a systematic temperature dependence to the *IS*.

However, for other Invar alloys with compositions 50, 60 and 67 at. %, fig. 80 shows there is a systematic temperature variation of the *IS*, as it is seen to drop moderately but concurrently with the Zeeman splitting *z*, which is related to the magnetization. Above T_C, the *IS* seems relatively stable. The magnitude of the drop is very small at 50 at. % Fe compared to the uncertainties involved, but increases with the Fe concentration.

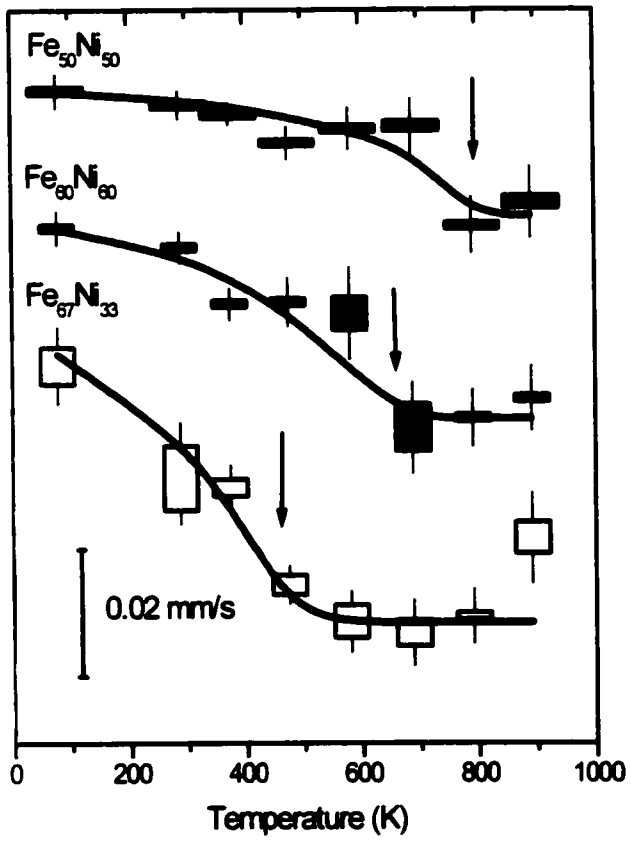

Figure 80 Illustration of the correlation between the *IS* (columns) and $< |z| >$ (solid lines) in Invar alloys. The given scale is for the *IS* and is the same for all alloys. The *IS* of each alloy is vertically offset for more clarity. The $< |z| >$ data is rescaled for each alloy to match the range of the *IS* and is displayed as a continuous curve for comparative purposes. The arrows indicate T_C for each of the alloys.

In light of the ESCs presented in the previous chapter, this correlation can be well understood. ESCs of Fe rich Fe-Ni alloys in the DLM phase have shown that the ground state moment and *IS* were lower than in the FM phase, indicating that the HM state is partially stabilized by the ferromagnetic interactions. The observed drop in the *IS* which is correlated with the magnetization simply illustrates this small drop in the moment as the system goes from a ferromagnetic phase below T_C to a paramagnetic (magnetically disordered) phase above T_C. As seen from the values of the *IS*, the magnitude of this drop is quite small, much smaller in fact than the difference between the HM and LM values of the *IS*. In Invar alloys, there thus seems to be a small reduction of the magnetic moment magnitude as the system loses long-range ferromagnetic correlations. It is nevertheless important to note that the DLM phase does not correctly describe the high-temperature phase of the Fe-Ni alloys, as it neglects entropic contributions to the free energy, as well as short-range magnetic correlations. Both the entropic contributions and the short-range correlations will tend to stabilize the moment magnitude, thus limiting its reduction. Based on the value of the *IS*, it seems clear that these alloys remain within the scope of HM alloys, even in the paramagnetic regime, and that the observed effects are simply mild corrections due to the growing instability of the magnetic moment with increasing temperature, which results in the HM/LM transition at higher Fe concentrations.

6.5.3 Thermal Stabilization of a HM Phase in Anti-Invar Alloys

6.5.3.1 Description of the Experimental Data

Compared to Invar alloys, alloys which exhibit primarily LM qualities and which are paramagnetic anywhere above RT are seen to have a different yet equally systematic temperature dependence of the *IS*. As seen in fig. 81, alloys with compositions above 70 at. % Fe show an increasing *IS* with increasing temperature, which would be consistent with the stabilization of a larger moment magnitude (correlated to a larger *IS*) at high temperatures. This analysis is also compatible with experimental measurements of the magnetic moment in the paramagnetic and pure FCC phases of the alloys by Acet *et al.* [Acet2000].

This systematic behaviour is clearly observed in Fe-rich alloys such as the one with 75 at. % Fe, where the *IS* is seen to vary linearly with the temperature with a slope of 6-10 $\times$ 10^{-5}

mm/s/K. According to the ESC calculations of the previous chapter, the increase in *IS* due to thermal expansion (and the correlated drop in $\rho_e(0)$) could *at most* account for a change of 5×10^{-5} mm/s/K. Once again, this clearly indicates that the observed change is due to a more substantial change in the electronic structure, such as the evolution towards a phase with larger moment magnitudes. This behaviour is also observed in antitaenite, as measured but not recognized by De Grave *et al.* [DeGrave92, see chapter 3], and in the thermally stable high-temperature γ phase of Fe. In fact, if the *IS* of γ-Fe within its high-temperature region of stability is back-extrapolated to RT, one obtains the measured *IS* of epitaxially or structurally stabilized low-temperature γ-Fe (fig. 82). This would explain why, although they are the same phase, high-temperature neutron measurements indicate a large moment magnitude [Boni85], whereas the low-temperature phase is known to be a low moment ($\mu \approx 0.7\ \mu_B$ [Abrahams62]) material.

In alloys which exhibit residual effects of magnetic order, we find that the *IS* does not immediately increase with temperature. This is again consistent with the stabilization of a larger moment magnitude (associated with a larger *IS*) by the ferromagnetism, compared to a magnetically disordered alloy of the same composition. With the disappearance of magnetic correlations, the moment would tend to drop, but the opposite effect of thermal stabilization of the moment seen in higher Fe-concentration alloys results in a moment (and *IS*) which is unchanged around RT. Once the short-range magnetic order has vanished, the *IS* is seen to increase again, with a similar slope as found in $Fe_{75}Ni_{25}$.

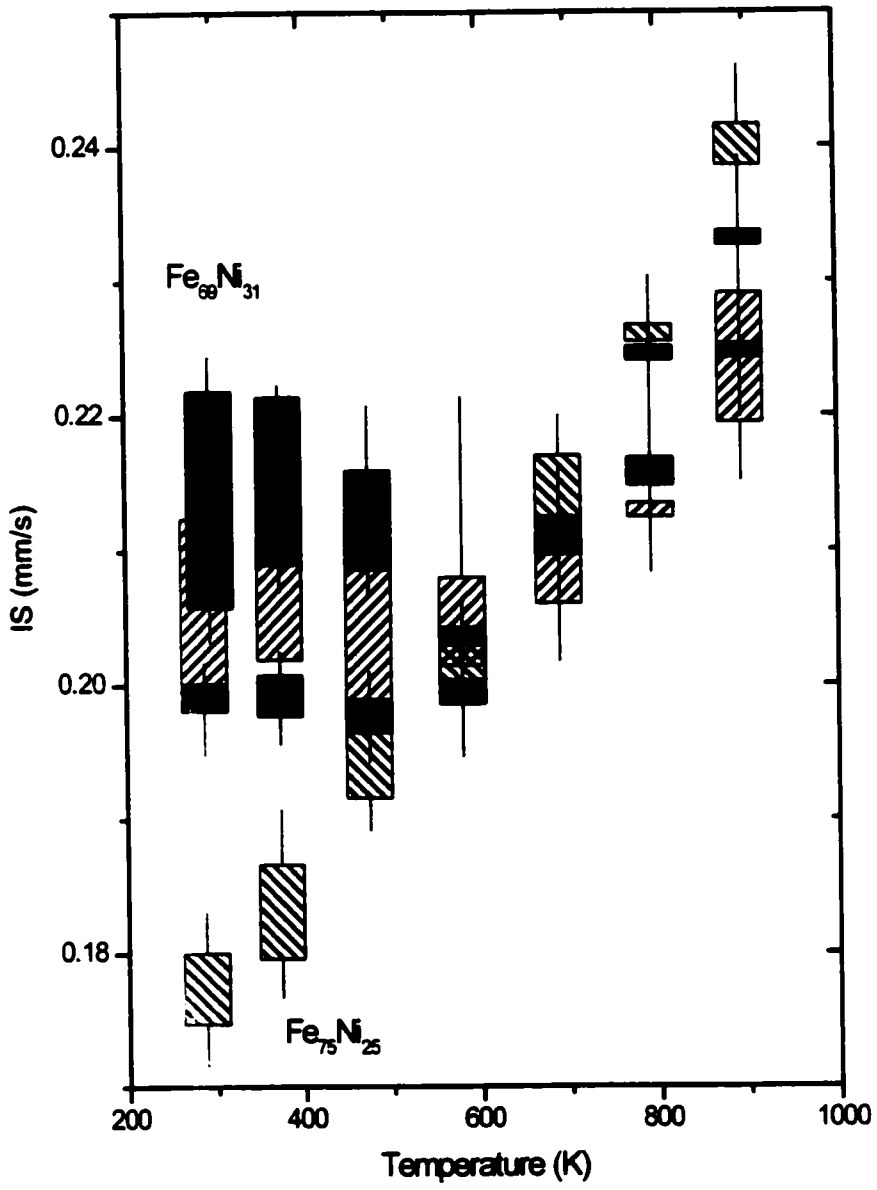

Figure 81 Thermal evolution of the *IS* in anti-Invar alloys (from top to bottom at RT: 69 - dark and solid, 71 - ///, 73 - light and solid and 75 at. % Fe - \\\).

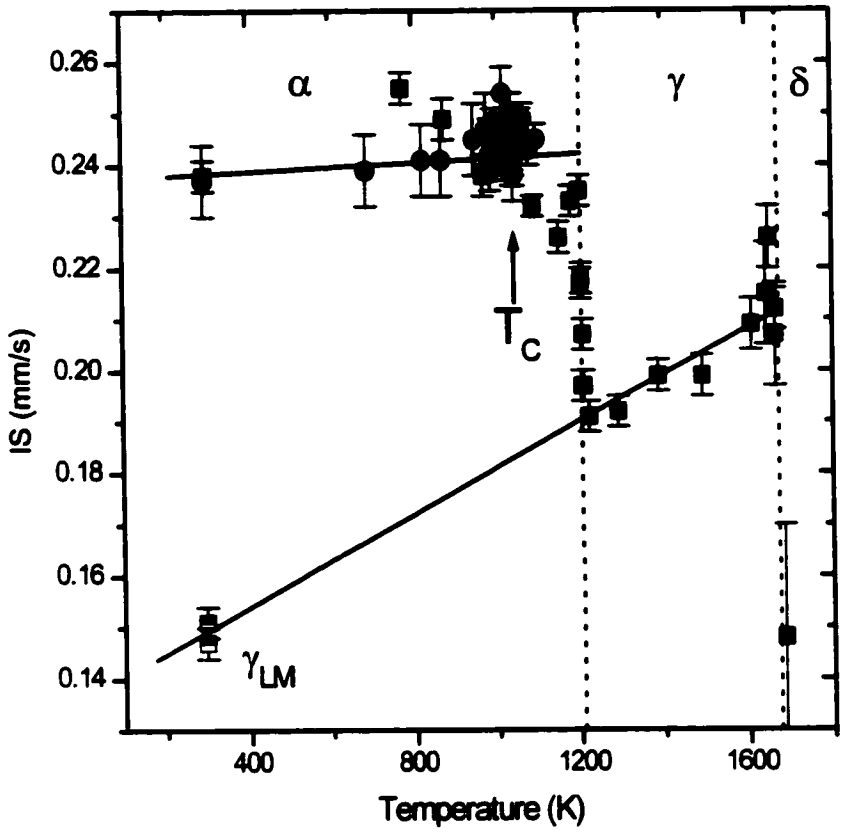

Figure 82 *IS* in the various phases of pure Fe. The Curie point of α-Fe is shown by an arrow. The equilibrium α (BCC), γ (FCC), and δ (reentrant BCC) phase regions are separated by vertical dotted lines. The original *CS* data is from Kobeissi [Kobeissi81] (filled circles), Kovats *et al.* [Kovats69] (filled squares), and Keune *et al.* [Keune77] and Halbauer *et al.* [Halbauer83] (half-filled squares). The solid lines are guides to the eye.

6.5.3.2 Entropic Drive Towards a Larger Moment Magnitude and the Anti-Invar Effect

Though it is clear from the above experimental measurements that there is thermal evolution towards a phase with larger moments, we have not yet given any physical explanation for this phenomenon. Proponents of a 2-γ-state model of Invar and anti-Invar explain it as a thermal excitation of a HM state of the Fe atoms from the LM ground state. The high temperature phase would thus consist of a mixture of atoms in a HM or LM state in thermal equilibrium. This picture originates in part from ESC of γ-Fe in constrained FM configurations which show two minima corresponding to LM and HM phases [Moruzzi86]. More complex calculations find that many more phases can be stabilized when various magnetic configurations are imposed [Schröter95] , invalidating the idea of distinct ground states which will be thermally populated. Instead, it seems possible to have a continuum of states between the LM and HM extremes. It is with this perspective that we shall explain our observations.

Since the relevant observations all pertain to the paramagnetic phase, it is more realistic to investigate ground states in a DLM configuration, rather than a magnetically ordered phase. As seen in the previous chapter, the ground state of DLM phases of $Fe_{65}Ni_{35}$ and γ-Fe as a function of lattice parameter yield a continuous range of Fe magnetic moments which increases with lattice parameter, as shown in fig. 83. Although the DLM is limited in its representation of the true paramagnetic phase, it does give an idea of the internal energy minima as a function of lattice parameter in a phase which resembles the paramagnetic phase. Based on this model of the energy curve, we shall show that is it possible to explain the observed stabilization of an increasingly large moment, and that it is directly responsible for the anti-Invar effect.

Consider the entropic contribution due only to the magnetic moment magnitude. For simplicity, we shall consider a classical model to describe magnetic moments: the moments can take any orientation and any magnitude. This model is not necessarily realistic, but it will show the effect of entropy and moment magnitudes. We shall also consider that each moment is uncorrelated to the others such that they can be treated as independent, as is approximately the case in the paramagnetic regime. In this classical model, the phase space $\Omega(\mu)$ accessible to a moment of magnitude μ is proportional to the surface of the sphere of radius μ in phase-space, hence $\Omega(\mu) \sim 4\pi\mu^2$. The entropy contribution of these states, $S(\mu) = k \ln \Omega(\mu)$, is thus

proportional to ln μ, which increases with the moment magnitude. The one-particle free energy (at 0 pressure) of a system composed of non-interacting moments can be written

$$\begin{aligned} F &= E - TS \\ &= E_{lattice}(V) - TS_{lattice}(V) + E_{mom}(\mu, V) - \zeta T \ln \mu \,, \end{aligned} \tag{55}$$

where the first two terms represent the lattice contribution. The other terms include the energy of the moment and its entropy, and ζ is simply a constant. The distinction between the $E_{lattice}$ and E_{mom} is arbitrary, as only the total binding energy is calculated, but we assume it can be separated into a component which has no dependence on the moment, and one that includes the difference with the total energy. We shall now concentrate on the last two terms of eq. 55, knowing that the lattice contributions lead to a "normal" thermal expansion. The average moment $\mu_0(T)$ and volume $V_0(T)$ of the system are obtained by minimizing the free energy, as in

$$\left(\frac{\partial F}{\partial V}\right)_{V=V_0} = 0 \text{ and } \left(\frac{\partial F}{\partial \mu}\right)_{\mu=\mu_0} = 0 . \tag{56}$$

These equations are minimized when there is a balance between the minimization of the internal energy E, and a maximization of the entropy S. Based on ESCs, we already know that the T = 0 K minimization of the energy leads to a *positive* correlation between the volume and the moment, that is, energy is minimized such that a larger moment corresponds to a larger volume (fig. 83). As temperature increases, the entropic contribution to the free energy becomes more and more important, and since the entropy increases with the moment magnitude, it will favour a larger moment, which in turn leads to a larger volume. The positive correlation between the moment magnitude and the volume, combined with the entropic contribution of the moment will thus lead to a thermal expansion, in addition to the normal lattice thermal expansion. This additional thermal expansion causes (is) the anti-Invar effect.

In order to evaluate it quantitatively, a more rigorous evaluation of the entropy is necessary, yet within the scope of this model, it is possible to get an order of magnitude estimate and show this moment-induced thermal expansion is of the correct magnitude. At 500 K, a material with a normal thermal expansion shows a volume increase of ~2 % over the T = 0 K value. What would it take to have an additional expansion of 5 %? Based on the ESC calculations, this corresponds roughly to 2 mRy/atom, or ~300 K. Consider a moment which has a value of ~0.7 μ_B at T = 0 K. Based on fig. 83, normal thermal expansion would, by

increasing the volume, also increase the moment to ~0.9 μ_B. An additional 5% increase in volume would increase the moment to ~1.5 μ_B, which correspond to an increase in entropy of $\Delta S = 2k\ln(1.5/0.9) \approx k$. The increase in internal energy $\Delta E \approx 300$ K is thus entirely compensated by an increase in entropy of $T\Delta S \approx 500$ K. This simple model thus predicts a larger thermal expansion and it shows that the order of magnitude of the expected volume increase is in line with what is measured as the anti-Invar effect. Experimentally, we know the increase in the moment is not as large (roughly 0.3-0.5 μ_B), and we don't have an exact formulation for the entropy due to the moment magnitude but this shows that at temperatures around 500-1000 K, it is entirely reasonable that the entropy of the moment causes its increase, which in turn leads to a volume expansion comparable to that measured in anti-Invar systems.

Within this model, it is necessary to consider two possible scenarios, depending on the magnitude of the low temperature moment.

i) For a system where the moment at $T = 0$ K is small, because $\partial\mu/\partial V$ and $\partial S/\partial\mu$ are large for small μ, it is easier for those moments to increase to a medium or large magnitude moment, because the chemical bonding (lattice) energy associated with the resulting small volume increase is easily overcome by the large gain in entropy.

ii) For a system where the $T = 0$ K moment is fairly large, as $\partial\mu/\partial V$ and $\partial S/\partial\mu$ are smaller for larger moments, they will not tend to increase much, since the gain in entropy is limited. Even a small increase in μ must be accompanied with a substantially larger increase in V, which would incur a large increase in bonding energy which is not balanced by the gain in entropy.

These two situations clearly indicate why a substantial thermal increase of the moment magnitude would only occur in materials which are LM at $T = 0$ K. The anti-Invar effect, which is closely linked to this increase in moment magnitude will thus also occur only in materials which are LM at low temperatures. In addition, because this process is entropy driven, it will only occur at high enough temperatures and in the paramagnetic regime, when entropic effects (maximization of entropy) become dominant, compared to low temperature, where energetics (minimization of energy) play the dominant role.

Although we have used a classical moment to model the observed behaviour, the basic results are compatible with more realistic theories such as spin-fluctuation theories in itinerant systems, which also point to an increase of the magnetic moment magnitude with temperature in

initially weak itinerant magnetic materials such as the LM Fe-Ni alloys [Moriya85]. The Mössbauer measurements have thus shown how we can follow the thermal evolution of the magnitudes of the moments, as they are intricately linked to the *IS* through the general electronic structure. These measurements make it possible to distinguish between materials where the large moment is partially stabilized by ferromagnetic interactions and materials where a larger moment magnitude can be thermally stabilized. This last observation, in conjunction with results from ESCs, provides a simple yet conclusive model for the anti-Invar behaviour in these materials.

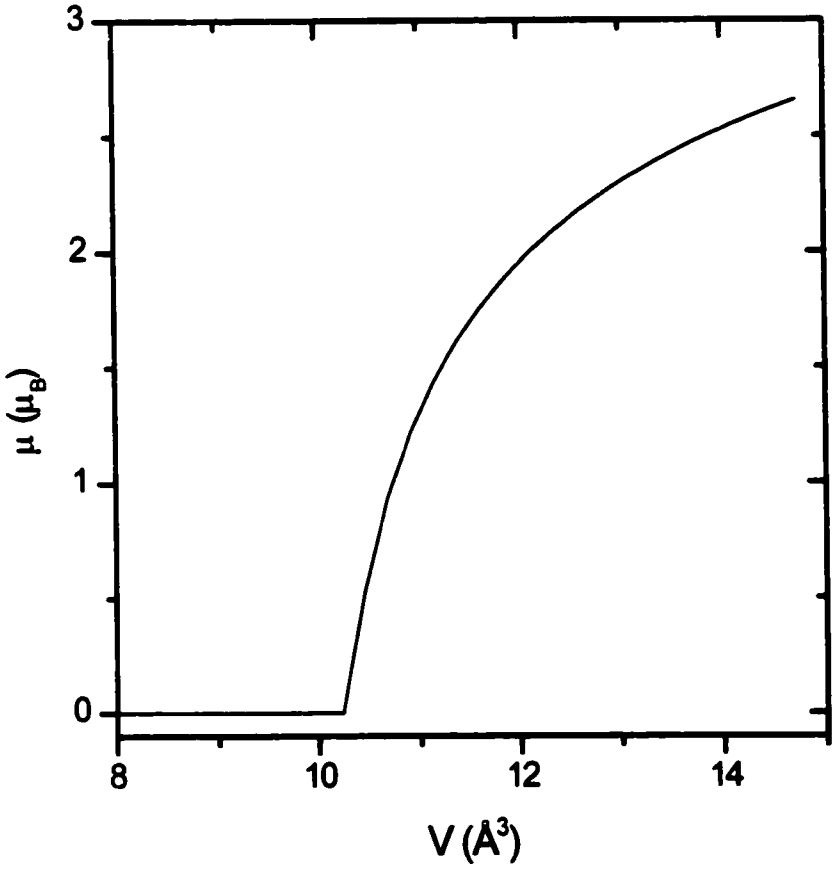

Figure 83 Calculated magnetic moment in the DLM state in γ-Fe as a function of volume [see chapter 5 for details].

6.5.3.3 Analysis of Peak Widths for Evidence of Thermal Excitations

In the event of dynamic fluctuations of a hyperfine parameter, the resulting effect on the Mössbauer spectrum can be quite varied. We shall now investigate if it is possible to obtain information on fluctuations of hyperfine parameters in the paramagnetic phase, based on the width of the signal. Specifically, we shall investigate the model of excitations between two states, as in the Weiss hypothesis, and see if it is or isn't compatible with observations. In the Weiss hypothesis, the high-temperature phase consists of a thermal population of Fe atoms in either the LM state (which is assigned an *IS* of 0.16 mm/s) and a HM state (assigned an *IS* of 0.26 mm/s). Consider separate cases: 1) The fluctuations from one state to the other are quick compared to the lifetime τ_{MS} of the excited state of the Mössbauer transition. In such a case, the signal would consist of an effectively static signal with average parameters (*IS* ≈ 0.21 mm/s, if the populations are equal) and no dynamic broadening. 2) The fluctuations between the states are slow compared to τ_{MS}. In this case, one would see a superposition of the two signals, as if they were each static. 3) Fluctuation times are of the same order of magnitude as τ_{MS}. In such a case, the spectrum would exhibit dynamic broadening, with as limiting possibilities, the spectra of cases 1) and 2). Can differences between these scenarios be seen?

To investigate this, we have simulated spectra consisting of two subspectra of equal areas as in case 2), with identical parameters, except for different *IS*s. The FWHM of the resulting peak is then compared to the FWHM of the peaks of each phase (fig. 85). Experimentally, we have measured the FWHM of the signals of the paramagnetic phases, as shown in fig. 84. Unfortunately, because of the broadening due to the chemical alloying (which results in a QSD), the reference FWHM is quite large and the increase, if any, cannot be observed given the existing thermal broadening and the limited precision of the measurement. Because of the strong dependence of the *IS* with composition for these compositions, any spinodal decomposition would also increase the broadening through a static distribution of *IS* as a result of the composition gradient. In the end, these measurements of the widths cannot be used to prove or disprove models of thermal excitations of states such as the Weiss hypothesis.

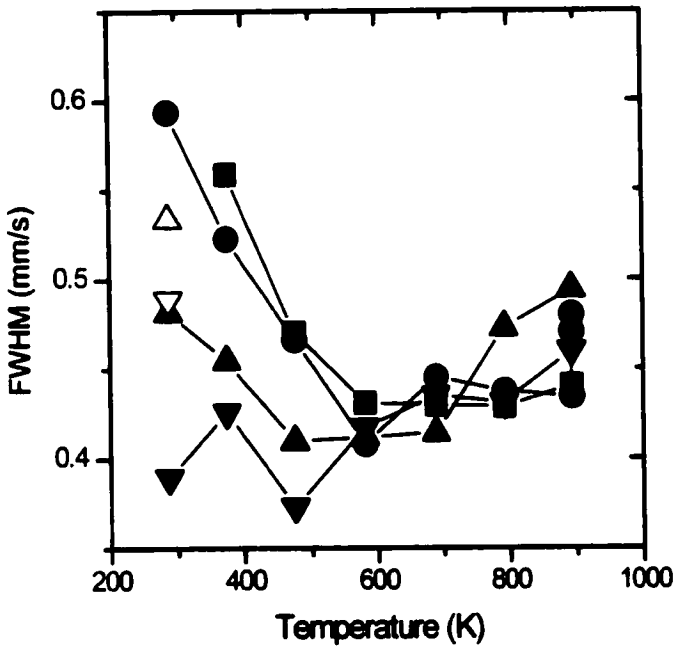

Figure 84 Thermal evolution of the FCC signal's FWHM in paramagnetic alloys. (■) 69 at. % Fe, (●) 71 at. % Fe, (▲) 73 at. % Fe, (▼) 75 at. % Fe. The hollow symbols at RT correspond to measurements taken on the sample after cooling from the highest temperature. The theoretical FWHM in the absence of thickness effects, hyperfine parameter distributions or thermal gradients is 0.2 mm/s.

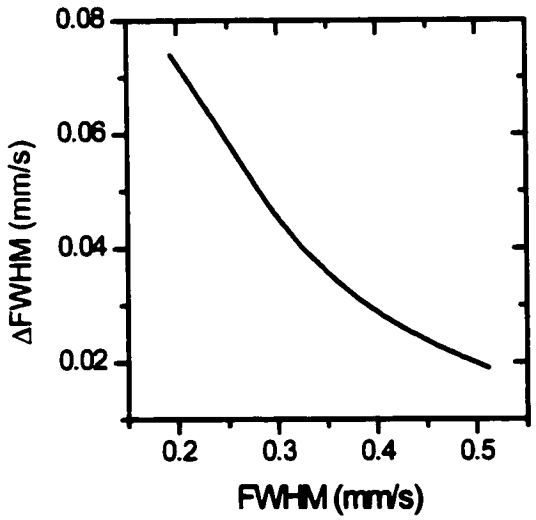

Figure 85 Increased linewidth (ΔFWHM) of a peak resulting from the superposition of two overlapping peaks of a given FWHM and separated by an *IS* of 0.1 mm/s.

6.5.3.4 Austenitic Transformation

Fe-Ni alloys with compositions above 68 at. % Fe are known as martensitic alloys, because under normal cooling they undergo a martensitic transition from the FCC phase to the BCC phase as they are cooled from high temperatures. This transition occurs in a range of temperatures below the martensitic start temperature, as shown in fig. 88. On the other hand, when these materials are heated from RT, they will undergo the reverse transition, known as the austenitic transition, as they revert to an FCC phase. Again the process occurs within a range of temperatures known as the austenitic start and stop temperatures.

When measuring Mössbauer spectra of "thin" absorbers, the spectral area of each phase is proportional to its relative content of ^{57}Fe atoms multiplied by its recoilless fraction or f-factor f_a. Within the context of the Debye model, f_a can be calculated as a function of the temperature, so we can determine if the proportions of each phase are changing. Only samples with 73 and 75 at. % had some BCC phase, so they were compared to see if there were any differences between the two. In figs. 86 and 87, we have plotted the ratio between the spectral area and the background, and compared them with calculated thermal variations due solely to f_a. Even though these samples are not thin in the Mössbauer sense (t_a = 25), their areas do follow the theoretical Debye-model behaviour, with Debye temperatures of 370-380 K for the both the FCC and BCC phases. These numbers agree well with the values established for the FCC phase based on *CS* variations and reported in chapter 4, but are slightly lower than the value of ~430 K expected for the BCC phase. We start seeing an increase in the FCC proportion at temperatures as low as 600 K in $Fe_{73}Ni_{27}$, and 700 K in $Fe_{75}Ni_{25}$ but the BCC→FCC transition effect becomes obvious around 800 K, where it is nearly complete in $Fe_{73}Ni_{27}$, but only halfway in $Fe_{75}Ni_{25}$ (fig. 87). The transition is complete at 900 K in both alloys. Without more data points, it is impossible to determine precisely the austenitic start and stop temperatures for these alloys, but we can say that they are slightly lower in $Fe_{73}Ni_{27}$ than in $Fe_{75}Ni_{25}$, as expected from other measurements (fig. 88). We should also note that precise start and stop temperatures depend strongly on the sample's thermal history and microstructure, so variations between different studies are to be expected. We also notice similar effects in the reverse martensitic transition. For example, the amount of retained austenite (FCC phase) in both the 73 and 75 at. % samples is greater after the sample has been heated and cooled compared to when it was originally quenched. There is no

evidence that these heated samples are homogeneous in composition, so it is better to deal with the quenched samples for detailed studies.

6.6 Conclusion

Based on the prediction of a HM/LM transition in Fe-Ni alloys from ESCs, we have measured the Mössbauer spectra of Fe-rich FCC alloys and extracted the *IS* at RT. A drop in the *IS* measured as the composition ranged from ~60 to 80 at. % showed conclusively that a transition from a HM phase to a LM phase was taking place as Fe content was increased. This validates the existence of distinct phases, as had been required for 2-γ-state models of Invar. On the other hand, analysis of the RT atomic volume shows a positive deviation from Vegard's law, of the same magnitude as the spontaneous magneto-volume expansion which leads to the Invar effect. This also showed that the Invar effect was an expansion relative to normal behaviour (Vegard's law), while the HM/LM transition caused a contraction of the volume. High-temperature measurements of the *IS* in Invar alloys also showed that, although the HM phase was slightly destabilized by the disappearance of magnetic order, Invar alloys remained HM alloys and as such, thermal excitation of the LM phase (or a similar phenomenon) was not the cause of the Invar effect. In anti-Invar alloys with higher Fe content, it was shown that the *IS* increases with temperature, indicating the stabilization of higher moment phases with increased temperature. It was demonstrated that based on the entropy of the larger moments, such a stabilization would happen because of the moment-volume instability and that it would result in the abnormal volume expansion known as the anti-Invar effect.

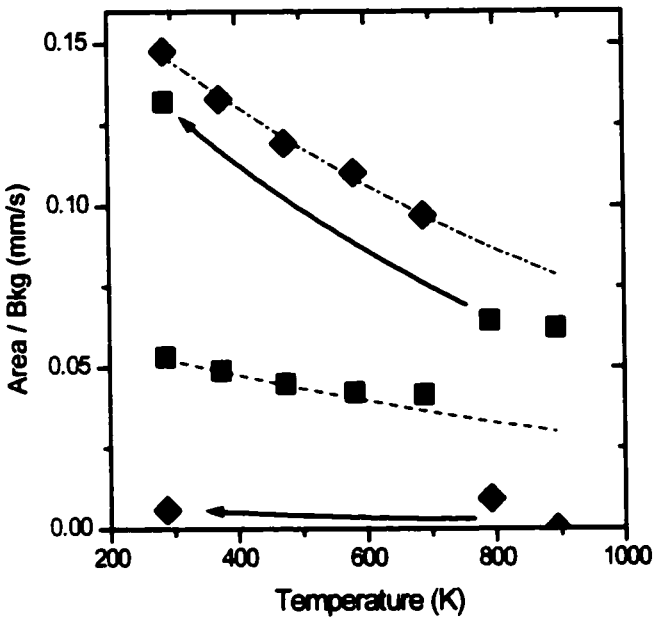

Figure 86 Variation of the normalized areas of the FCC (■) and BCC (◆) phases of $Fe_{73}Ni_{27}$. The lines are fits to a Debye model. The arrows indicate how the proportions of the phases at high temperature evolved as they were cooled back to RT.

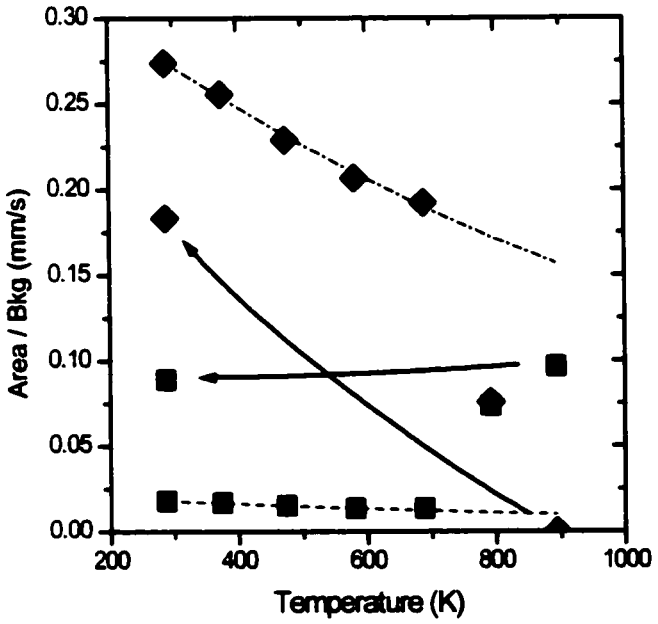

Figure 87 Variation of the normalized areas of the FCC (■) and BCC (◆) phases of $Fe_{75}Ni_{25}$. The lines are fits to a Debye model. The arrows indicate how the proportions of the phases at high-temperature evolved as they were cooled back to RT.

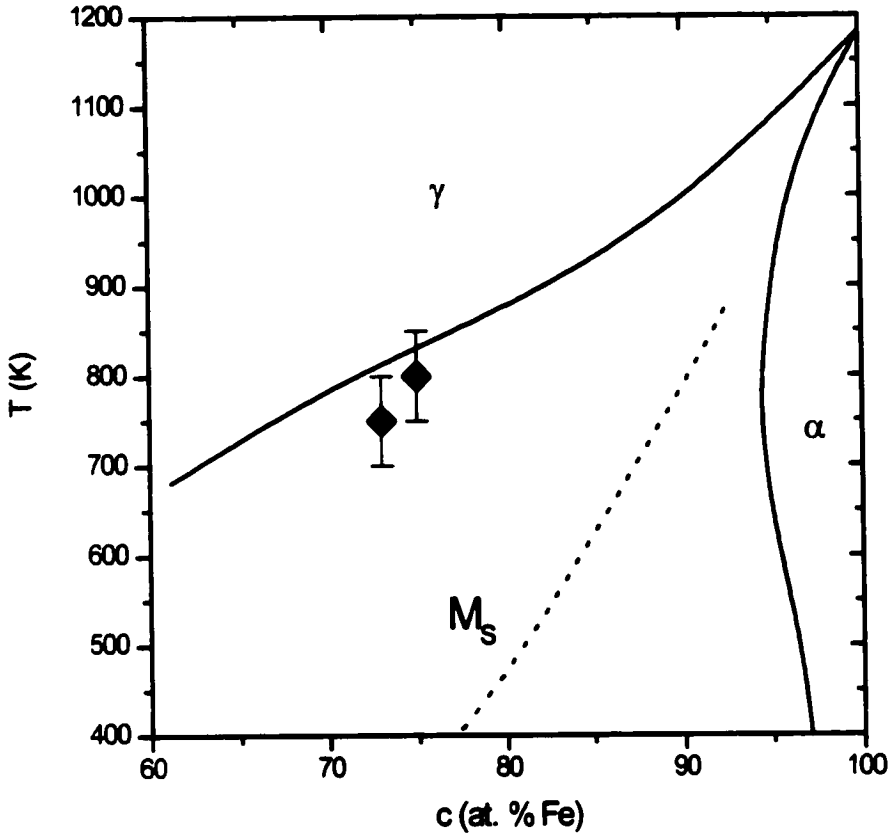

Figure 88 High-temperature phase diagram of the Fe-Ni systems. The ranges of stability of the γ (FCC) and α (BCC) phase are indicated, as well as the martensitic start temperature (M_S, dotted line) [data from Reuter88]. The diamonds indicate the approximate temperatures at which the austenitic transition was half complete.

7. Monte Carlo Simulation of Magneto-Volume Effects in Fe-Ni Alloys

We have investigated the effects of a large volume dependence of the Fe-Fe magnetic exchange parameter on several key structural and magnetic parameters as a function of temperature and applied pressure over the entire field of Fe-Ni alloys. In order to combine magnetic and atomic degrees of freedom, we have developed a code to perform isothermal-isobaric Monte Carlo (MC) simulations of alloys whose chemical energy is described by Lennard-Jones pair-wise interactions and where the magnetic energy is described by an Ising Hamiltonian. Only NN interactions are taken into account in both the chemical and magnetic Hamiltonians.

7.1 Model Hamiltonian of the System

We assume that the atomic and magnetic degrees of freedom can be treated separately and that all interactions are between pairs of NN atoms and spins only. The general Hamiltonian used in this study is:

$$H = \sum_{<i,j>} U_{ij}(|\vec{r}_i - \vec{r}_j|) - \sum_{<i,j>} J_{ij}(|\vec{r}_i - \vec{r}_j|)\,\sigma_i\sigma_j . \qquad (57)$$

In this expression, the i and j indices represent Fe or Ni atoms located at positions $\vec{r}_i$ and $\vec{r}_j$, and the sums are on NN pairs only. For simplicity, $U_{FeFe}(r)$, $U_{FeNi}(r)$ and $U_{NiNi}(r)$ are chosen to be Lennard-Jones potentials. The magnetic exchange parameter $J_{ij}(r)$ is allowed to be dependent on the interatomic distance and, in this formalism, it includes the magnitudes of the spins, so that we have $\sigma_i = \pm 1$.

Lennard-Jones potentials are characterized by two parameters each, the equilibrium

position r^0 and the dissociation energy U^0:

$$U_{ij}(r) = -U_{ij}^0\left[2\left(\frac{r_{ij}^0}{r}\right)^6 - \left(\frac{r_{ij}^0}{r}\right)^{12}\right]. \quad (58)$$

The values of $r_{NiNi}^0 = 2.482$ Å and $U_{NiNi}^0 = 5000$ K (431 meV) are chosen so that the simulated volume and thermal expansion of pure Ni at 300 K coincide with the known experimental values ($\alpha_{Ni}^{RT} = 13.4 \times 10^{-6}$ K^{-1}, [Lide93]). We have chosen to reproduce the values at RT since this semi-classical simulation does not correctly reproduce the thermal expansion at low temperature (below ~100 K). We have also chosen that the dissociation energy U^0 be the same for all types of pairs to minimize the number of variables in the model. This means that, in the absence of magnetism, there would be no preferred chemical ordering and the thermal expansion coefficients of pure Ni and pure γ-Fe would be similar. This is partially justified by the fact that the melting and boiling temperatures of both Fe (1811 K and 3134 K, respectively [Lide93]) and Ni (1728 K and 3186 K, respectively [Lide93]) are similar, indicating that the dissociation energy is similar. $r_{FeFe}^0 = 2.561$ Å is chosen such that the simulated volume of pure γ-Fe at 300 K coincides with the linearly extrapolated volume (following Vegard's law) of Fe from the experimental volumes of alloys with less than 20 at. % Fe, since these alloys are known to exhibit no magneto-volume anomalies. Finally, $r_{FeNi}^0 = 2.5187$ Å is determined by the requirement that, at $T = 100$ K and in the absence of magnetism and magneto-volume effects, the equilibrium volumes of the alloys follow Vegard's law, that is, their volumes depend linearly on the concentrations of either species.

In the case of the magnetic interaction, J_{NiNi} and J_{FeNi} are assumed to be independent of the interatomic distance. Though this is clearly not true for Ni which has a known magneto-volume effect around T_C, the magnitude of the effect is approximately 100 times smaller than the Invar effect, so we can safely neglect magneto-volume effects due to the interatomic distance dependence of J_{NiNi}, compared to those seen in Invar alloys. The assumption that J_{FeNi} is volume independent can also be made from the fact that Ni-rich (less than 20 at. % Fe) Fe-Ni alloys do not show significant magneto-volume effects. A more rigorous substantiation will be given later when we investigate the exchange parameters obtained from ESCs of Fe-Ni alloys. It is also assumed that J_{NiNi} and J_{FeNi} are independent of the concentration of the alloy. This assumption is unfounded but represents a first approximation to this problem. In these circumstances, the

value of J_{NiNi} = 65 K (5.6 meV) is used to reproduce the measured Curie point in Ni, which is 631 K [Lide93]. The value of J_{FeNi} can similarly be obtained by equating the measured and simulated Curie points of chemically ordered $FeNi_3$ (T_C = 954 K, [Lagarec00]), since only Ni-Ni and Fe-Ni interactions exist in the chemically ordered structure, when taking into account only NN interactions. Using J_{NiNi} = 65 K (5.6 meV), these constraints result in J_{FeNi} = 127 K (10.9 meV). If these parameters were expressed independently of the moment magnitudes ($J_{ij} = \bar{J}_{ij}\mu_i\mu_j/(4\mu_B^2)$), and using μ_{Ni} = 0.6 μ_B and μ_{Fe} = 2.8 μ_B , then we would have $\bar{J}_{NiNi}$ = 722 K and $\bar{J}_{FeNi}$ = 302 K. These values are quite similar to the ones used by Dang and Rancourt when they studied the magnetism of Fe-Ni alloys by MC simulation ($\bar{J}_{NiNi}$ = 700 K and $\bar{J}_{FeNi}$ = 355 K) [Dang95, Dang96a, Dang96b]. We will discuss the choice of the Fe-Fe magnetic exchange parameter in more detail later.

7.2 Simulation Method

Combined molecular dynamics and Monte Carlo have already been used to study a single species system with ferromagnetic interactions only [Grossmann96]. We have, however, decided to determine average thermal properties by Monte Carlo simulation only, but one which includes freedom of the atomic positions and of the volume. This has the advantage of removing the assumptions about different time scales in the magnetic and structural dynamics because MC simulations are not based on dynamics but only on the sampling of the phase space.

In MC simulations, average parameters of the system are obtained by efficiently sampling the phase space of the system and performing the average at a given temperature and pressure. In an isothermal-isobaric ensemble with atomic and spin degrees of freedom, averages are calculated as

$$< A> \; = \frac{1}{Z}\int_0^{\infty} dV \int_{\Omega} d\vec{r} \sum_{\Omega_\sigma} A(\vec{r},\{\sigma\}) \exp\{-[PV + E(\vec{r},\{\sigma\})]/k_B T\}, \qquad (59)$$

where Ω is the accessible space of all atomic coordinates (given a volume V), Ω_σ is the space of all magnetic coordinates (spin states), and $E(\vec{r},\{\sigma\})$ is the total internal energy of the system in a specific configuration. If we express the particle coordinates in reduced units ($\vec{p}_i = \vec{r}_i / V^{1/3}$), then the average $<A>$ can be written as

$$< A> = \frac{1}{Z''} \sum_{\Omega_\sigma} \int_0^\infty dV \int_\omega d\vec{\rho}\, A(V^{1/3}\vec{\rho}, \{\sigma\})\, V^N \exp(-PV/k_B T) \exp\left[-E(V^{1/3}\vec{\rho}, \{\sigma\})/k_B T\right], \quad (60)$$

where ω is now the unit cube (if a cubic volume is used), N is the number of atoms in the system and Z'' is the partition function in reduced coordinates (which reduces to a normalization constant at a given temperature). We can then apply a Metropolis algorithm to accept or reject the moves to new configurations, where the change from configuration w to configuration w' is accepted depending on

$$\Delta\mathcal{H}(w \to w') = NP(V_{w'} - V_w)/k_B T - N\ln(V_{w'}/V_w) + \Delta E(w \to w')/k_B T, \quad (61)$$

where $\Delta E(w \to w')$ is the change in internal energy. In the standard Metropolis algorithm, the change is accepted if $\Delta\mathcal{H} \le 0$ or $\exp(-\Delta\mathcal{H})$ is larger than a random number uniformly sampled between 0 and 1. In the simulation, instead of uniformly sampling the volume V, we sampled the length $L = V^{1/3}$ of the box, which causes a biassed sampling of the volume. This is corrected by using

$$\Delta\mathcal{H}(w \to w') = NP(V_{w'} - V_w)/k_B T - (N+2/3)\ln(V_{w'}/V_w) + \Delta E(w \to w')/k_B T \quad (62)$$

instead of the expression given in eq. 61. The additional term of 2/3 comes from the change of variable from V to L in the integrand of eq. 60: $V^N dV = 3L^{3N+2} dL = 3V^{N+2/3} dL$.

The system must first be equilibrated, that is, a certain number $n_{\text{warm-up}}$ of MC loops must be performed until the system has reached its thermal equilibrium. Once equilibrated, a number n_{sampling} of MC loops are performed to sample the phase space in order to calculate the averages of selected parameters. Because configurations from subsequent loops are strongly correlated to each other, only every n_{step}'s configuration is used in the average. One MC loop is performed as follows:

- repeat N_{volume} times
  - randomly select a box length change from $[-\Delta L, \Delta L]$ (uniform sampling)
  - calculate $\Delta\mathcal{H}$ corresponding to the change in volume
  - accept or reject the new volume using the Metropolis selection criterion

- repeat N_{atomic} times
  - repeat N times (so that each atom is selected, on average, at random)

- randomly select an atom
- calculate a new displacement $\Delta\vec{r}$ by randomly sampling a cube of length $L_{displacement}$ (centred on (0,0,0))
- calculate $\Delta\mathcal{H}$ corresponding to the change in displacement from its current position
- accept or reject the new atomic position using the Metropolis selection criterion

- repeat $N_{magnetic}$ times
  - repeat N times (so that each atom is selected, on average, at random)
    - randomly select an atom
    - calculate $\Delta\mathcal{H}$ corresponding to a change of its spin (*spin flip*)
    - accept or reject the new spin direction using the Metropolis selection criterion

The parameters N_{volume}, N_{atomic} and $N_{magnetic}$ have been chosen such that the equilibration time is optimized. They each permit the volume, atomic positions and magnetic configuration to stabilize independently. In the limit where atomic motion is quick relative to transverse spin fluctuations, the calculation should, as it does, permit the volume and atomic positions to reach equilibrium for each new magnetic configuration. Of course, since this is a MC simulation, true dynamics are not included in the calculation and the MC loops are simply meant to provide a method for sampling phase space. The MC simulation is most precise when the sampling is expansive so it requires efficient sampling. The efficiency of the sampling has also been optimized by the choice of ΔL (the change in the box length) and $L_{displacement}$. Both these parameters were chosen such that approximately half the new volumes and atomic positions are accepted. To ensure that this is true at all temperatures, the parameters are scaled by $T^{1/2}$.

It is important to note that the statistical averages described above are semi-classical. The magnetic formalism (Ising model) is truly based on quantum mechanics since the sampled configurations are actually eigenvectors of the magnetic Hamiltonian. On the other hand, the lattice contribution is treated as a classical system, since the eigenstates of the quantum lattice Hamiltonian are not known. For this reason, the simulated lattice properties at low temperature

($T \leq 100$ K) are not expected to reproduce experimental results. The most important feature missing will thus be the drop in thermal expansion at low temperature which is observed experimentally and which is due to quantization of lattice excitations (phonons). We have chosen to use an Ising system because, since we can treat it in a true quantum formalism, it is better suited to reproduce experimentally observed magnetisation curves than a classically treated Heisenberg system, which, at low temperature, exhibits a substantial drop in magnetization that is linear with temperature. The Ising model, on the other hand produces no drop in magnetization ($\partial M / \partial T = 0$) at $T = 0$ K in a (single specied) ferromagnetic system. This more closely resembles the slow $T^{3/2}$ dependence experimentally observed in most alloys (the $T^{3/2}$ dependence is due to spin-waves, which are the primary form of magnetic excitation in the quantum Heisenberg system).

7.3 Details of the Simulations

Simulations were performed on systems with 1372 atoms (7^3 unit cells of 4 atoms) with periodic boundary conditions in three dimensions. Population samples were taken every n_{step} = 20 MC loops to minimize the auto-correlation of the configurations (fig. 71). Typically, $n_{warm\text{-}up}$ = 10000 MC loops are performed to reach equilibrium and $n_{sampling}$ = 30000-100000 MC loops to calculate averages. In all cases, the simulation was started at low temperature from an ideal FCC lattice of the approximate volume, in a magnetic configuration where the Ni spins are aligned ferromagnetically, and the Fe spins are randomly oriented (up or down). In most cases, we checked that the results obtained by raising the temperature are the same as those obtained by reducing the temperature.

7.3.1 Sample Averages Calculated in the Simulation

The averages for the following parameters were obtained from the simulation: the volume V of the system, the total energy E, the specific heat c_p, the reduced magnetization of the Fe and Ni spins, the bulk magnetization (assuming $\mu_{Fe} = 2.8\ \mu_B$ and $\mu_{Ni} = 0.6\ \mu_B$), the reduced magnetic zero-field susceptibilities of the Fe and Ni spins, the bulk magnetic zero-field susceptibility χ_M, the average NN distance, the average Ni-Ni, Fe-Ni and Fe-Fe NN distances,

the average Fe-Fe NN distances for parallel and anti-parallel spin configurations (Fe↑-Fe↑ and Fe↑-Fe↓). The thermal expansion coefficient α_T and the bulk modulus B_m were also calculated directly from the simulation.

By virtue of its definition, $c_p \equiv (\partial E/\partial T)_{N,P}$, the specific heat could be calculated as

$$c_p = N(< E(E+PV) > - < E > < E+PV >)/k_B T^2 \tag{63}$$

from a single simulation, or as

$$c_p = \Delta < E > /\Delta T \tag{64}$$

from two simulations performed at different temperatures. The zero-field susceptibility $\chi_M \equiv (\partial M/\partial H)_{N,P,H=0}$ can also be calculated from a single simulation as

$$\chi_M = (< M^2 > - < M > ^2)/k_B T. \tag{65}$$

We could also have calculated it from $\chi_M = \Delta < M > /\Delta H$ from simulations at $H = 0$ and $H = \Delta H$. The thermal expansion can also be calculated directly from a single simulation, since $\alpha_T = (\partial V/\partial T)_{N,P}/3V$ can be expressed as

$$\alpha_T = N(< V(E+PV) > - < V > < E+PV >)/3k_B T^2 < V > , \tag{66}$$

but we preferred to calculate it as

$$\alpha_T = (\Delta V/\Delta T)/3V \tag{67}$$

from the volume thermal expansion curve obtained at various temperatures. It was found that the first expression (which uses the variance of the volume fluctuations) converged very slowly to the correct value and thus required a large number of MC loops. The average volume, on the other hand converges quite rapidly. The same can be said about the bulk modulus, $B = -V(\partial P/\partial V)_{N,T}$, which can be calculated as

$$B = k_B T < V > /N(< V^2 > - < V > ^2), \tag{68}$$

is more readily calculated as

$$B = - < V > (\Delta P/\Delta < V >) \tag{69}$$

after performing simulations at $P = 0$ and $P = \Delta P$. All the averages used above are averages per atom, for example, $< V >$ is considered to be the average volume per atom. The average NN distances are calculated as the sample averaged distances (over the N sample atoms or $6N$ sample NN bonds) between MC averaged atomic positions (over many MC loops), as is understood experimentally.

7.3.2 Avoiding Sampling Autocorrelation Effects

In most MC methods, because the new configuration at each step is derived from the previous one, there is usually a strong correlation between successive parameters. Because MC is based on finite sampling of the phase space, it is necessary to perform averages using uncorrelated, or weakly correlated, configurations to avoid biases. We have thus calculated the autocorrelation function of various parameters, as a function of the "distance" (number of MC loops performed) between successive samples. For a parameter p evaluated at each of the n samples, the autocorrelation function $S(l)$ is calculated as:

$$S(l) = \frac{< (p(n+l) - \bar{p})(p(n) - \bar{p}) >_n}{\sigma_p^2}, \qquad (70)$$

where the average is performed over all sampled configurations and $\sigma_p^2 = < (p - \bar{p})^2 >$ is the variance of p. $S(0)$ is always 1 (self-correlation) and $S(l)$ typically decays to 0 as l increases. This functions has been calculated for three important parameters of the simulation: the energy (E), the volume (V) and the magnetization (M_{Fe} and M_{Ni}). Fig. 89 shows the results, for a simulation of $Fe_{50}Ni_{50}$ at 700 K. Based on these types of results, we have chosen to sample new configurations every 20 MC loops to avoid correlations ($S(l) < 10$ %).

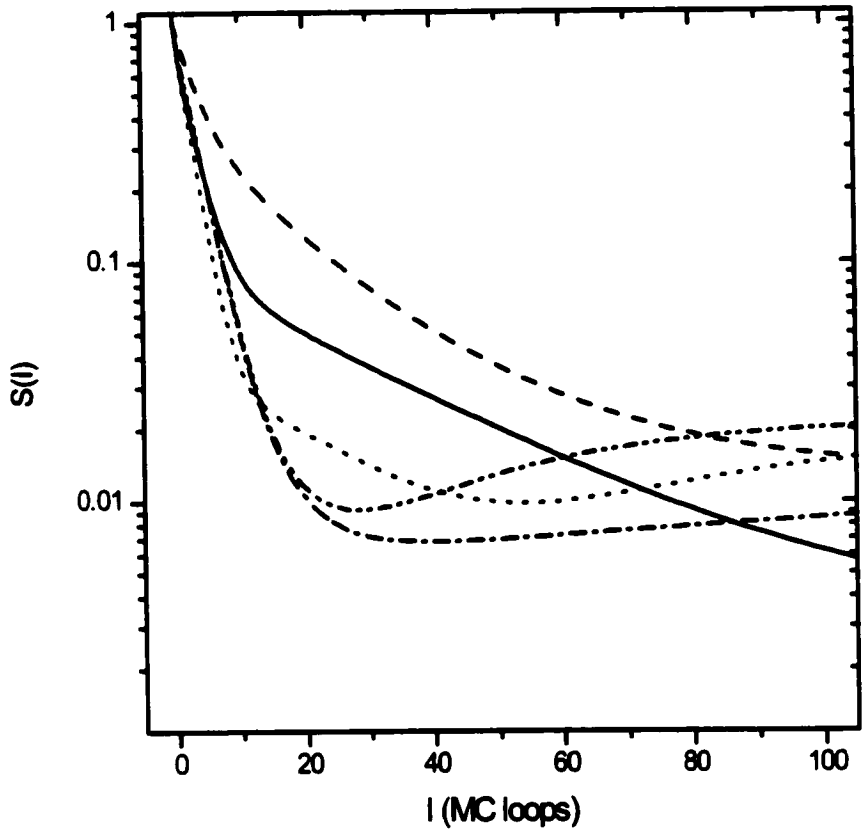

Figure 89 Autocorrelation functions of V (solid line), E (dashed line), $E \times V$ (dotted line), M_{Fe} (dash-dotted line) and M_{Ni} (dash-double dotted line).

7.4 Choice of the Fe-Fe Magnetic Exchange Parameter

7.4.1 Theoretical Calculations of $J_{FeFe}(r)$

Until recently, there was no way of determining the interatomic distance dependence of the magnetic exchange interaction in magnetic materials. With the development of ESCs which include magnetism, two separate methods have been applied to determine the magnetic exchange parameters between local moments. The first is to calculate a map of the energy as a function of relative angles between moments which are ordered as spin spirals and to fit the exchange

parameters according to a given model (for example, a Heisenberg model with NN interactions only) [Rosengaarde97]. The second is to directly calculate the effective Heisenberg parameters from the scattering matrices obtained during the ESC. This method, which is based directly on the LSDA was developed by Liechtenstein *et al.* [Liechtenstein84] and was recently reviewed by Gubanov *et al.* [Gubanov92].

It is using this method that Sabiryanov *et al.* [Sabiryanov95] have calculated the total effective exchange interaction parameter J_0 in pure γ-Fe as a function of the interatomic distance. This J_0 represents the sum of all the magnetic interactions (it includes the moment magnitudes) for a given atom. Fig. 90 shows their result, converted into units of Kelvins and divided by 12 (assuming only the 12 NN interactions contribute to the total interaction). In γ-Fe, a HM to NM transition occurs as the volume is reduced, so only the data from the region where the HM phase

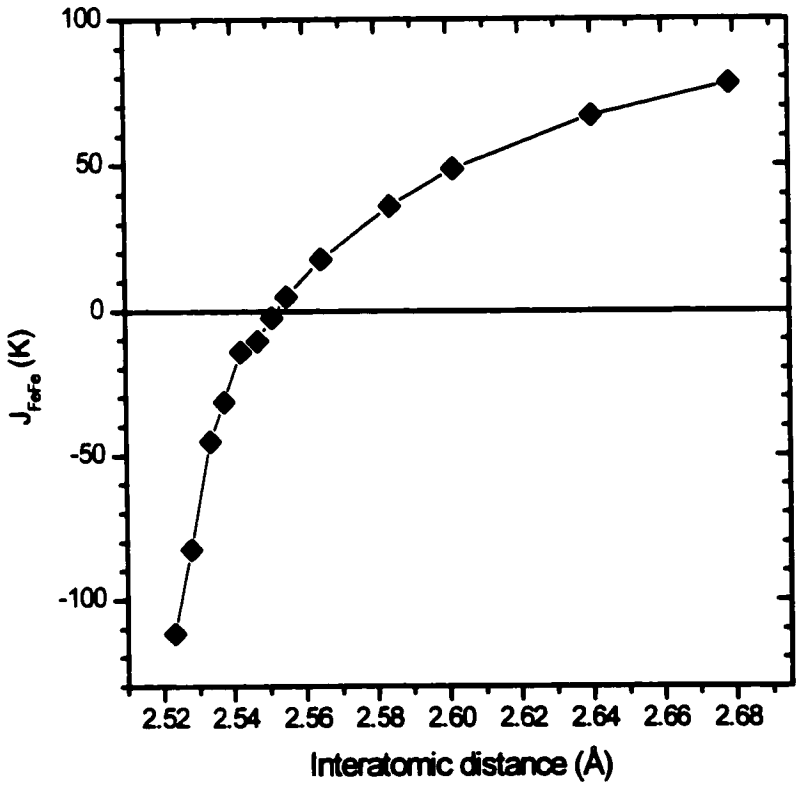

Figure 90 Effective Fe-Fe NN magnetic exchange parameter, based on the calculation by Sabiryanov *et al.* [Sabiryanov95].

is stable is shown in fig. 90. One clearly finds that there is a large drop from a positive value at large volumes to a negative value at lower volumes, even before the HM/NM transition which occurs at 2.52 Å.

The same type of calculation was performed for us by Dr. Bose (one of the co-authors of Sabiryanov95) for Fe_3Ni. There are several interesting results of these calculations that should be given. Here again, the calculation was performed in the region where the HM phase is stable. Fig. 91 illustrates the resulting moments, total exchange parameter ($J_{0,Ni}$ and $J_{0,Fe}$) and interatomic exchange parameters J_{ij}. The calculated exchange parameters already include the product of the moment magnitudes, but since the moment changes, it is difficult to distinguish between changes in the exchange constants (moment independent) and changes in the moment magnitudes. We have thus renormalized the exchange constants by dividing them by the products of the calculated moment, and multiplying them by the products of fixed HM moment magnitudes (arbitrarily chosen as 0.61 for Ni and 2.63 for Fe, which are the moment magnitudes at the largest volume considered). This results in fig. 92, in which we have also illustrated the renormalized $J_{0,Ni}/12$. In Fe_3Ni, all NNs of the Ni atom are Fe, so, if there are only NN interactions between Fe and Ni, we should have $J_{0,Ni} = 12\, J_{FeNi}$. This is indeed the case and in fact we find that J_{FeNi} is also nearly independent of the interatomic distance. The situation is more complicated for Fe-Fe interactions, as both NN (J_{FeFe}) and next-NN ($J^{(2)}_{FeFe}$) are large. We can say, however, that the main contribution to the dependence with interatomic distance comes from the NN term, and from fig. 91b ($J_{0,Fe}$), it is justified again to use ± 100 K as bounds for a "generalized" NN exchange parameter for Fe. The fact that the next-NN (and indeed higher order) exchange parameter is non-negligible illustrates a breakdown of local moment magnetism (characterized by interactions between strongly localized points in space though $J(\vec{r},\vec{r}')$) and a transition to itinerant magnetism (characterized by interactions at strongly localized wavevectors in reciprocal space through $J(\vec{q},\vec{q}')$). To keep the model simple, we will use only NN interactions, even though this means we will not correctly reproduce the magnetism. Because the NN interaction is the dominant contribution to the dependence with the interatomic distance, this should not greatly affect the results due to the magneto-volume coupling.

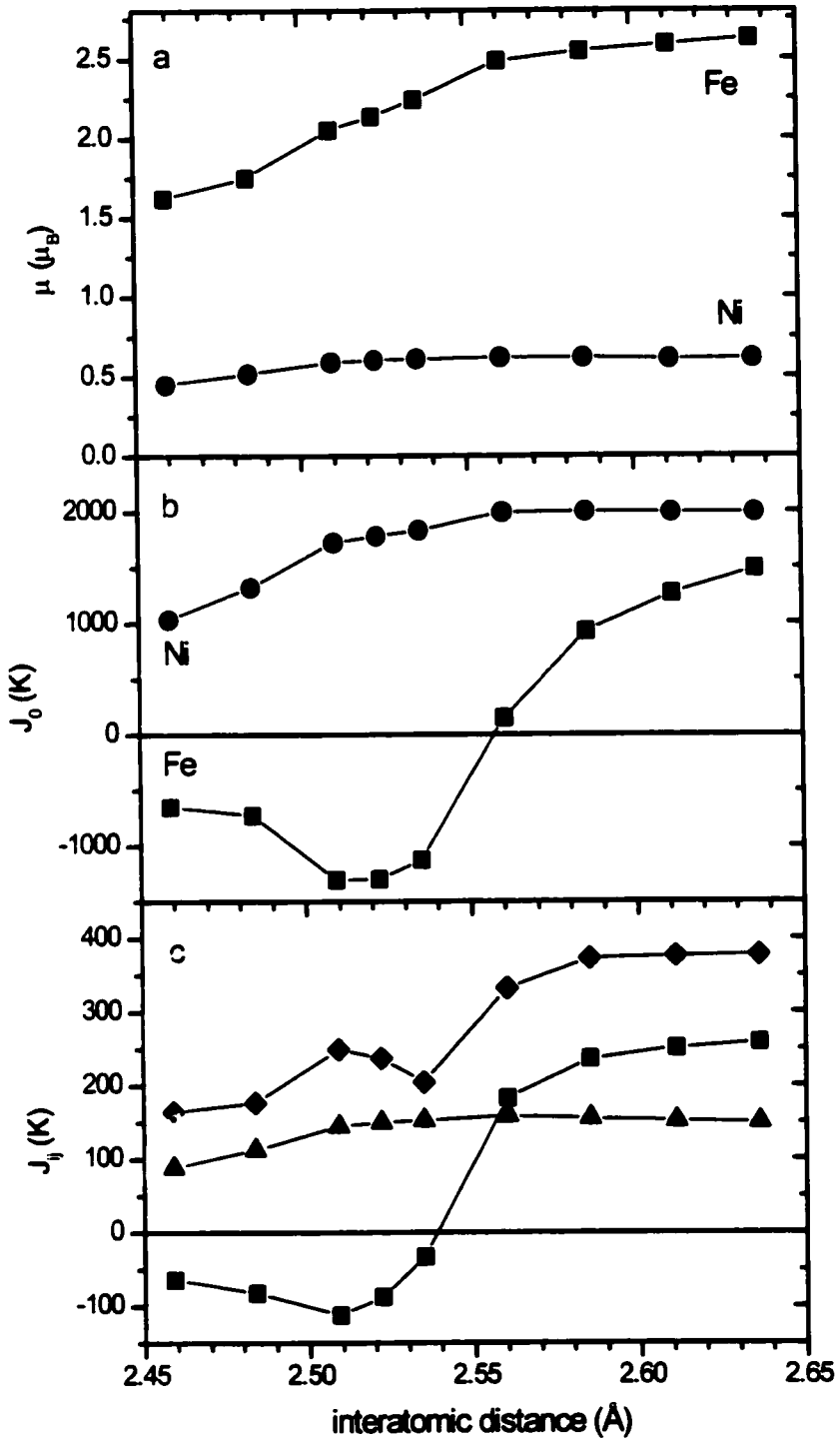

Figure 91 Calculated magnetic moment and magnetic exchange parameters in Fe_3Ni. In (c), the symbols are: ■ J_{FeFe}, ▲ $J^{(2)}_{FeFe}$ and ◆ J_{FeNi}.

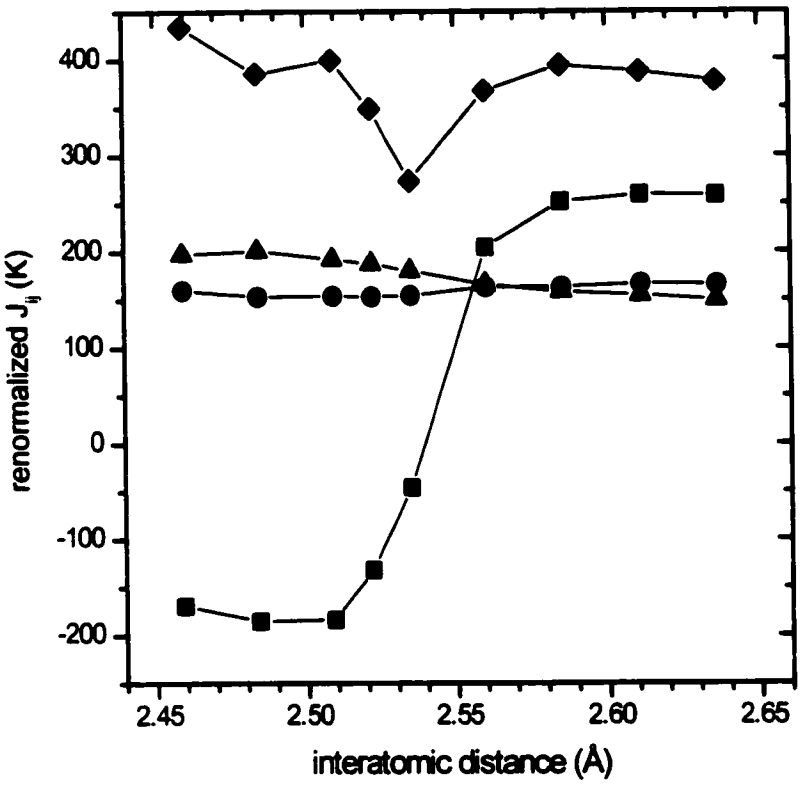

Figure 92 Renormalized (see text) magnetic exchange parameters in Fe_3Ni. ■ J_{FeFe}, ◆ $J^{(2)}_{FeFe}$, ▲ J_{FeNi} and ● $J_{0,Ni}/12$.

7.4.2 Model $J_{FeFe}(r)$ Used in the Simulations

7.4.2.1 Interatomic Distance and Composition dependence of $J_{FeFe}(r)$

To perform the simulations, we made several simplifying choices regarding the volume and concentration dependence of J_{FeFe}:

① $J_{FeFe}(r)$ is simplified and broken into 3 parts, as shown in fig. 93. Upon setting the upper and lower limits to ±100 K, $J_{FeFe}(r)$ is characterized by two parameters, the distance d_0 and the slope $J'_{FeFe} = \partial J_{FeFe}/\partial r$ with which is rises from -100 to +100 K. This

simplification is due to our inexact knowledge of the interaction, apart from its basic shape. Also, because of its simplicity, it permits us to understand more clearly how and why magneto-volume effects arise.

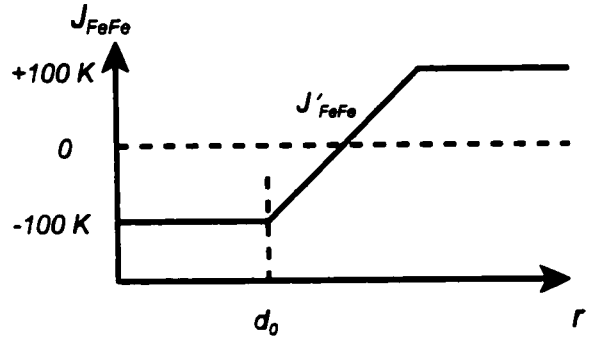

Figure 93 Effect of the NN distance on J_{FeFe} as used in the simulation.

② $J_{FeFe}(r)$ is assumed to vary with the composition. Without an exact calculation, we can only guess how it is affected by the composition, which changes the number of valence electrons and thus most likely changes the exchange. We have chosen $J_{FeFe}(r)$ to vary with composition only by changing d_0 and in such a manner that the crossover volume ($\propto d_0^3$) scales with the average simulated volume of the paramagnetic and non magneto-volume active alloy ($V_{para}(c)$):

$$\frac{d_0^3(c)}{d_0^3(c=1)} = \frac{V_{para}(c)}{V_{para}(c=1)} \tag{71}$$

Within this assumption, the interaction between Fe atoms, in the absence of magneto-volume effects is approximately the same at each composition. As we shall see later, the Fe-Fe distance does not scale exactly with the average NN distance, so the average exchange will be slightly different for different compositions. A discussion regarding the implications of this choice of scaling with concentration will be given once the results of the simulation are analysed.

③ Even though NNN (and longer range) interactions are important in γ-Fe, there is reason to believe only the NN interaction has a large volume dependence. We have chosen to

assume the complete interaction is due to NN interactions. The neglected longer range interactions should contribute with respect to the magnetic solution but, because they lack a volume dependence, they should not significantly affect the magneto-volume properties that we are trying to simulate.

7.4.2.2 Choice of J'_{FeFe} and $d_0(c=0.65)$

We have shown that our model Fe-Fe exchange parameter (fig. 93) does in fact roughly describe the calculated parameter based on ESCs (fig. 90). However, the calculated J_{FeFe} is more rounded than our model exchange parameter and there is no precise way of determining what slope we should use. In fact, the exchange parameter calculated for pure Fe has a range of slopes from ~9000 K/Å to ~500 K/Å depending on the interatomic distance. We have investigated the effect of various combinations of J'_{FeFe} and $d_0(c=0.65)$ on the thermal expansion and magnetization at T = 300 K.

Fig. 94 shows the contour plots of the thermal expansion and reduced magnetization (with respect to the Slater-Pauling value at 0 K) at 300 K as a function of J'_{FeFe} and $d_0(c=0.65)$. Experimentally, the values for Invar are 2×10^{-6} K^{-1} and ~0.65. Although it is not possible with this model to get exactly those values, there is a wide range of values of J'_{FeFe} and $d_0(c=0.65)$ which can produce results similar to the experimental measurements. One very interesting feature seen in fig. 94 is that the magnetization and the thermal expansion are very strongly correlated, making it difficult to choose. For example, if we were to decide to have $0.80 < M < 0.85$ and $4 \times 10^{-6} < \alpha_T < 6 \times 10^{-6}$, we find that we can choose any value of J'_{FeFe} between 4000 and 20000 K/Å, with $d_0(c=0.65)$ ranging (not independently) from 2.54 to 2.56 Å. It is thus clear that the value of J'_{FeFe} is not required to be specific, but that a wide range of values can produce effects such as a reduced thermal expansion.

Somewhat arbitrarily, we have chosen the values J'_{FeFe} = 5000 K/Å and $d_0(c=0.65)$ = 2.545 Å. This value of J'_{FeFe} is well within the range of values as calculated by ESCs and results in a sufficiently large range of interatomic distances where J_{FeFe} is not constant ($\Delta r = 200/J'_{FeFe}$ = 0.04 Å or $\Delta r/r$ = 1.6 %).

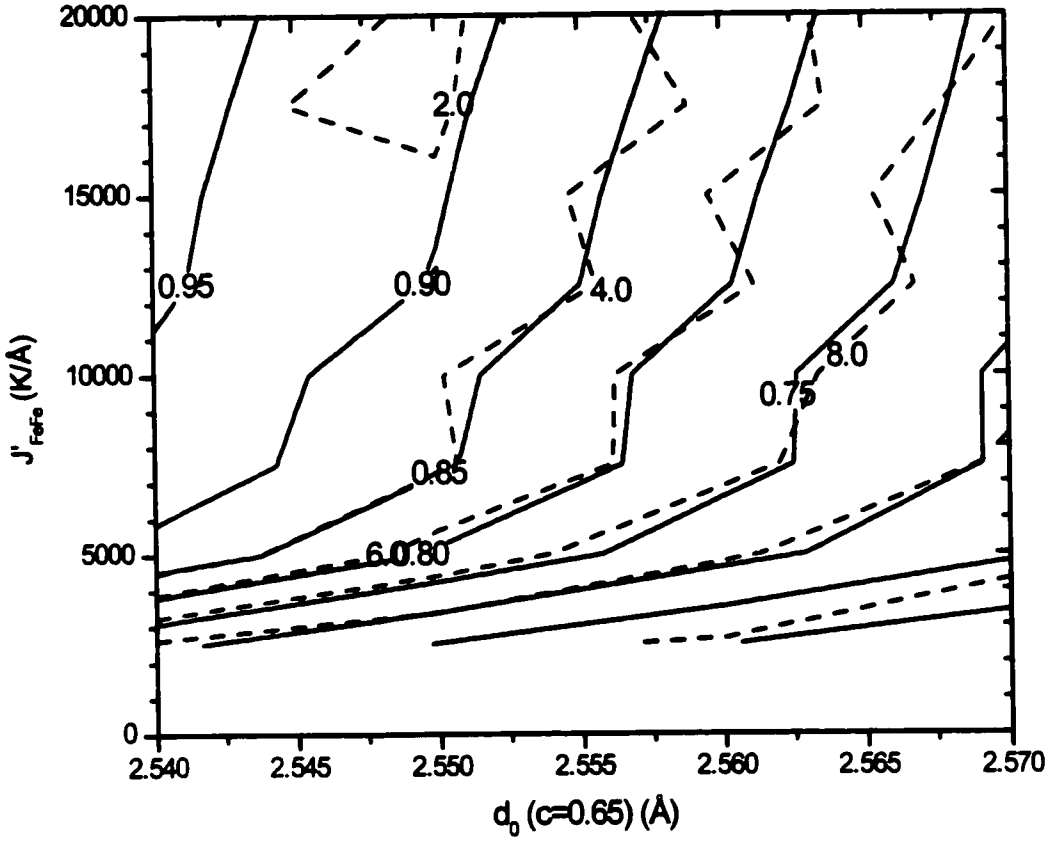

Figure 94 Simulated reduced magnetization (relative to the Slater-Pauling value, solid line) and linear thermal expansion coefficient ($\times 10^{-6}$ K^{-1}, dashed line) at T = 300 K in $Fe_{65}Ni_{35}$ as a function of J'_{FeFe} and $d_0(c=0.65)$.

7.5 Simulation Results

7.5.1 Simulated Properties as a Function of Composition

7.5.1.1 Pure Ni

MC simulations were initially performed on pure Ni to determine a reference point, as Ni is, within the parameters of this simulation, non-magnetovolume active. Also, as it is not an alloy but a single species crystal, some T = 0 K properties can be calculated exactly and

compared with the simulations' results. Fig. 95 shows the variation of the volume V with temperature and the resulting linear thermal expansion α_T. At $T = 0$ K, because this is not an alloy, we know that the equilibrium volume is $V_0 = (r^0_{NiNi})^3/\sqrt{2} = 10.812$ Å^3/atom. Indeed, the simulated volume does tend towards this value as the temperature goes to 0. We observe that the thermal expansion increases slightly with temperature, as is the case experimentally. Finally, the simulated thermal expansion is ~13.6 × 10^{-6} K^{-1}, close to the experimental value of 13.4 × 10^{-6} K^{-1} we were targeting. In fig. 95b, we can compare the values obtained by differentiating the thermal dependence of the volume (eq. 67) and by direct calculation in the simulation (eq. 66). Clearly, the differentiation method is better suited when temperature series are performed.

In fig. 96, we have reported the bulk modulus B and the lattice contribution to the specific heat c_p, as calculated by differentiation (eqs. 69 and 64) and directly (eqs. 68 and 63). Again, the differentiation method is more precise. In both cases, it is also possible to calculate the expected $T = 0$ K result analytically. In the case of a Lennard-Jones potential with 6 NN interactions per atom, in the equilibrium configuration ($r = r^0_{NiNi}$), the bulk modulus is

$$B = V\frac{\partial^2 E}{\partial V^2} = 48\sqrt{2}\,\frac{U^0_{NiNi}}{(r^0_{NiNi})^3}. \qquad (72)$$

Using the parameters listed above, this results in $B(0) = 22198$ K/Å^3 = 306.5 GPa, which is where the simulated values converge as T goes to 0. It is interesting to note that this comparison between theoretical value and simulated value is what lead to the choice of $N_{volume} = N_{atomic} = 1$ in the simulations. When using a larger value for N_{volume}, the volume at $T > 0$ was found to be larger than with $N_{volume} = 1$. At finite temperature, we do not know what the theoretical volume should be and there was no way of favouring one result over another. The bulk modulus, on the other hand, was found to be lower than the theoretical value for N_{volume}, even at $T = 0$, thus enabling us to chose $N_{volume} = 1$ so that the simulated result be compatible with the theoretical value. Like the thermal expansion coefficient, the specific heat shows little variation with temperature, and converges to the value 3/2 k_B, at $T = 0$ K, as expected based on the equipartition theorem, which states that each degree of freedom contributes 1/2 k_B to the specific heat. Because the simulation allows 3 degrees of freedom (x, y and z), the simulated value of 3/2 k_B is correct.

Figs. 97 and 98 show several properties related to the magnetism of Ni. The average

magnetization shows that the long-range magnetic order vanishes at $T_C \approx 630$ K, with some finite size effects (due to the finite size of the lattice and the periodic boundary conditions). The magnetic susceptibility also follows the expected Curie-Weiss law above T_C [Ashcroft76]. In fig. 98, the magnetic contribution to the specific heat is given, also showing the expected "lambda"-type discontinuity at T_C [Ashcroft76].

We can also note that in general, the magnetic contribution to c_p is smaller than the lattice contribution, except close to T_C. Because there is no simulated magneto-volume coupling ($\partial J_{\mathrm{NiNi}} / \partial r = 0$) in this system, it is possible to distinguish the magnetic and lattice contributions. In general, however, the internal energy is dependent on both the magnetic state and lattice state of the system and they cannot be separated, so only the total c_p will be given.

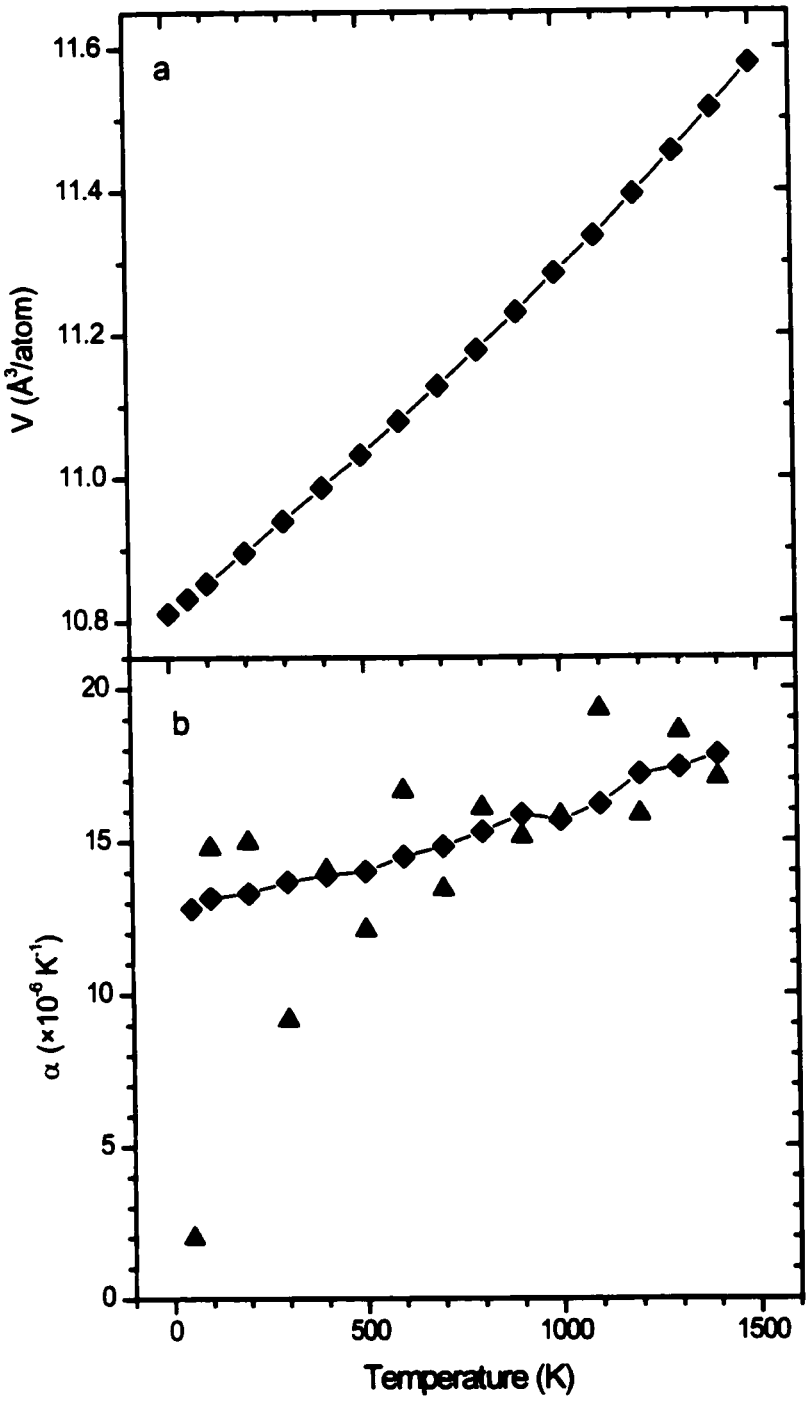

Figure 95 Simulated atomic volume (a, V) and linear thermal expansion (b, α_T) of Ni as a function of temperature. In (a), the volume at $T = 0$ K is the volume calculated from r^0_{NiNi}. In (b), ◆ are calculated by numerically differentiating data in (a) and ▲ are calculated in the simulation at each temperature.

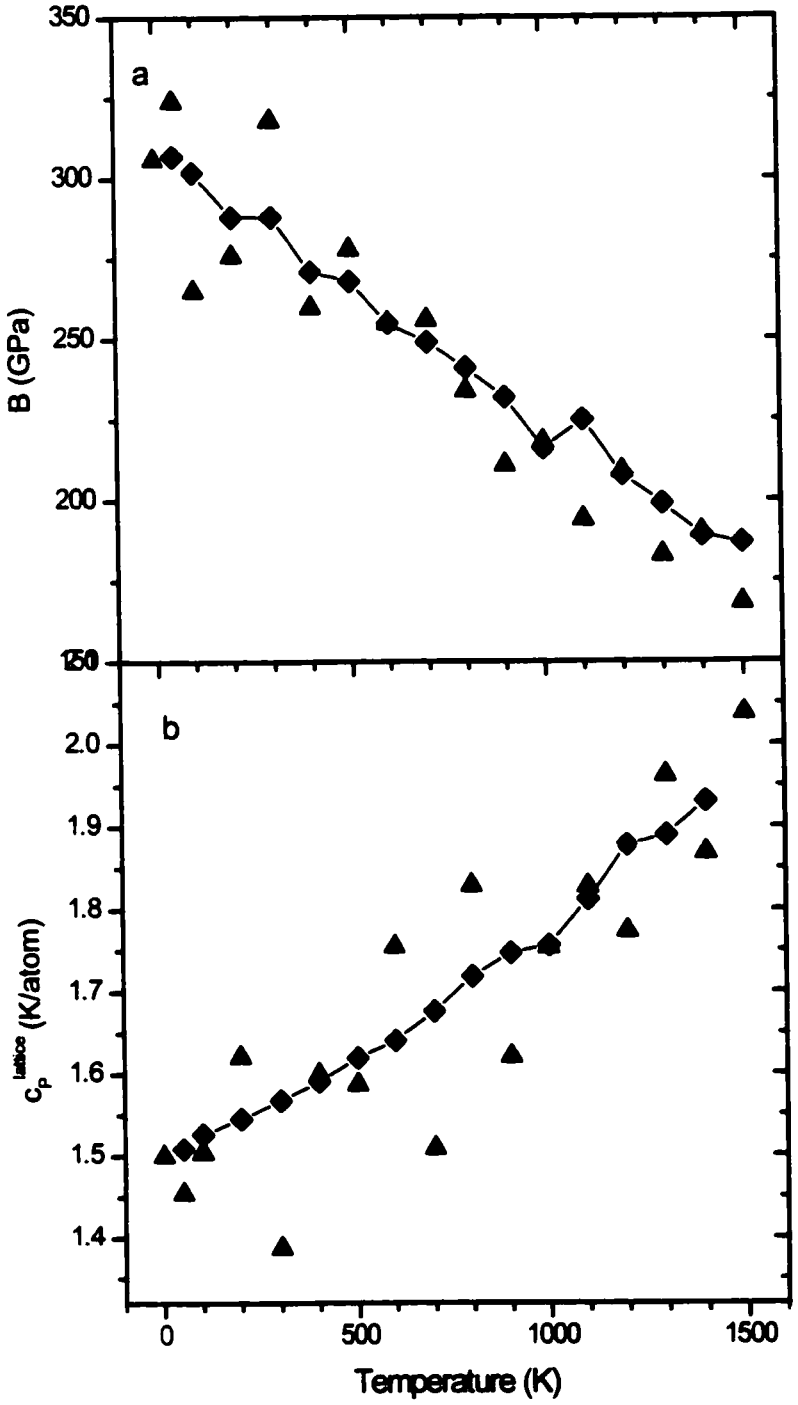

Figure 96 Simulated bulk modulus (a, *B*) and specific heat (b, c_p lattice contribution only) of pure Ni as a function of temperature. Again ◆ are calculated by differentiation whereas ▲ are obtained directly from the simulation.

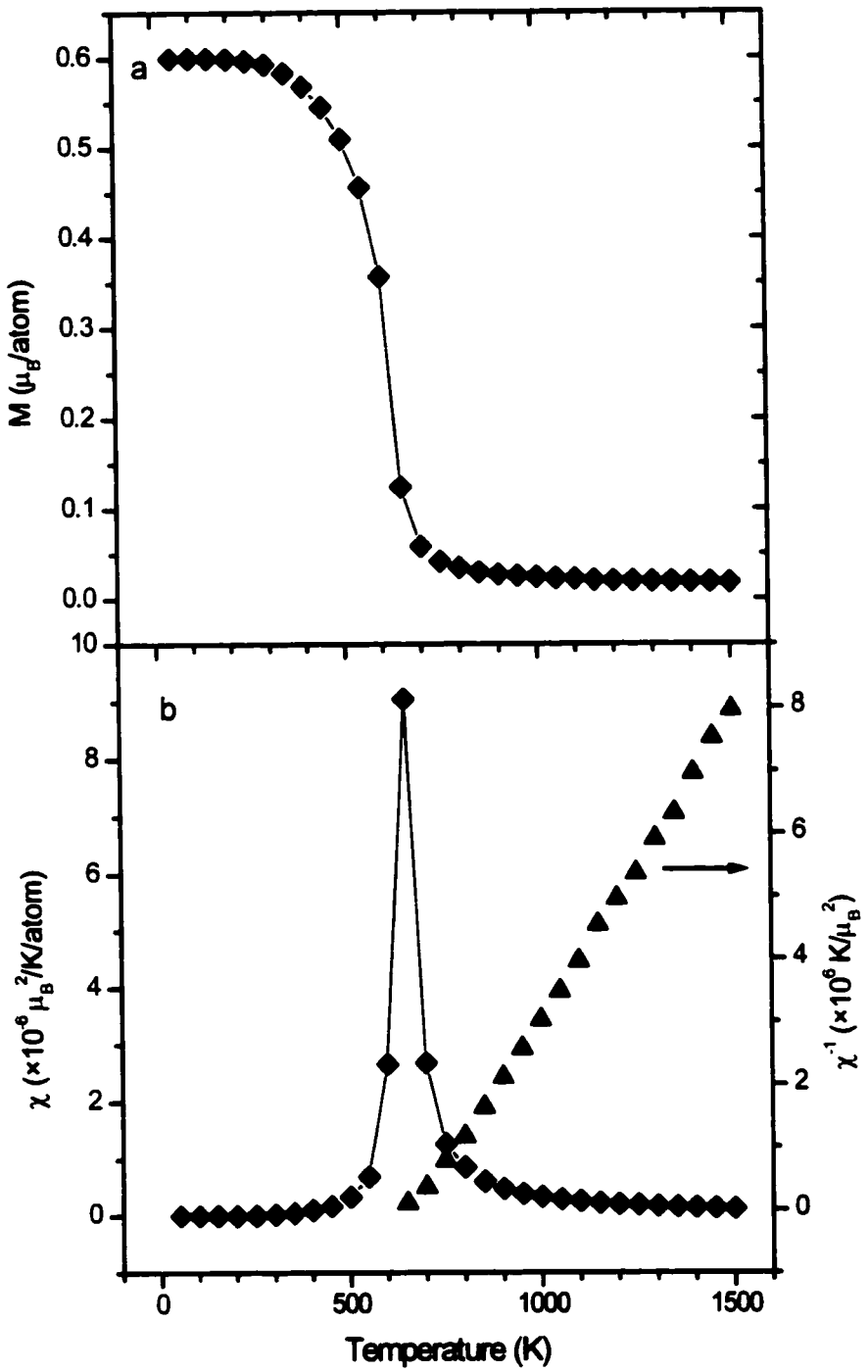

Figure 97 Simulated average moment per atom (a, M) and magnetic susceptibility (b, χ_M) of pure Ni. In (b), the inverse susceptibility (▲, χ_M^{-1}) shows a standard Curie-Weiss law above T_C, with a Curie-Weiss temperature just below 650 K.

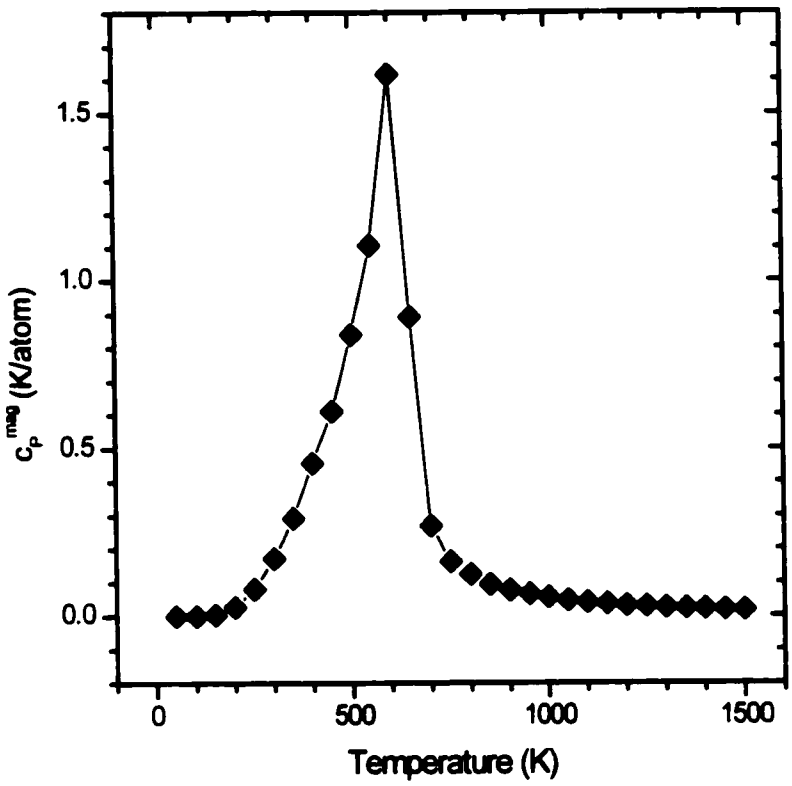

Figure 98 Simulated magnetic contribution to the specific heat (c_p^{mag}) which shows a standard "lambda" divergence at the critical temperature that is estimated to be between 600 K and 650 K.

7.5.1.2 Alloy Properties in the Absence of Magneto-Volume Coupling

Before simulating the properties of Fe-Ni alloys when a large magneto-volume coupling is present, we have determined the baseline, or reference, properties of these alloys when no magneto-volume coupling is present. Specifically, we have performed simulations, as a function of concentration, for T = 275 and T = 325 K, *without any form of magnetism*. This way, we can extract the "normal" composition dependence of specific parameters at T = 300 K (near RT). When necessary, the average of the parameter at T = 275 and 300 K is taken and in other cases (to compute α_T and c_p), a numerical differentiation with respect to temperature is performed by a discrete numerical derivative.

Fig. 99 shows that the average atomic volume does indeed follow Vegard's law, that is, it has a linear relation with the composition [Vegard28, Zen56, Thorpe91]. In fig. 99b, we see that the deviation from perfect linearity is very small, less than 0.015 % throughout the composition range. When the simulation will include magneto-volume coupling, we will be able to investigate the differences with respect to this plot.

Fig. 100a shows the variation of the chemical potential energy as a function of composition, relative to $6\,U_0$ = 30000 K, the ground state chemical energy of both pure Ni and pure γ-Fe. The offset of ~450 K is due to the thermal expansion which is such that the average interatomic distances are (at least for pure Fe and pure Ni) larger than the equilibrium distances, thus increasing the potential energy. The specific shape, on the other hand, is related to the different expansions or contractions of the different types of bonds relative to their equilibrium values. The change in the interatomic distances with composition shown in fig. 102 is consistent with what is expected. That is, the lengths of each type of bond increases linearly as the average volume increases, even though the Ni-Ni bonds remain slightly shorter than the Fe-Fe bonds.

Figs. 100b and 101 on the other hand show that the bulk modulus, the thermal expansion and the specific heat show little variation with composition, at least none that can be identified within the precision we have obtained. This is expected since the chemical potentials are the same for all types of bonds, except for slightly different equilibrium distances. We thus consider that the scatter observed in figs. 100 and 101 are representative of the precision we obtain from the MC simulation. Also, we note that the bulk modulus is approximately 50% larger than experimentally determined (B_{sim} (Ni) = 262 GPa, B_{exp} (Ni) = 180 GPa [James92]). This is in part

due to the use of the Lennard-Jones potential, as the repulsive term ($O(r^{-12})$) is too strong to correctly reproduce the bulk modulus in metallic systems.

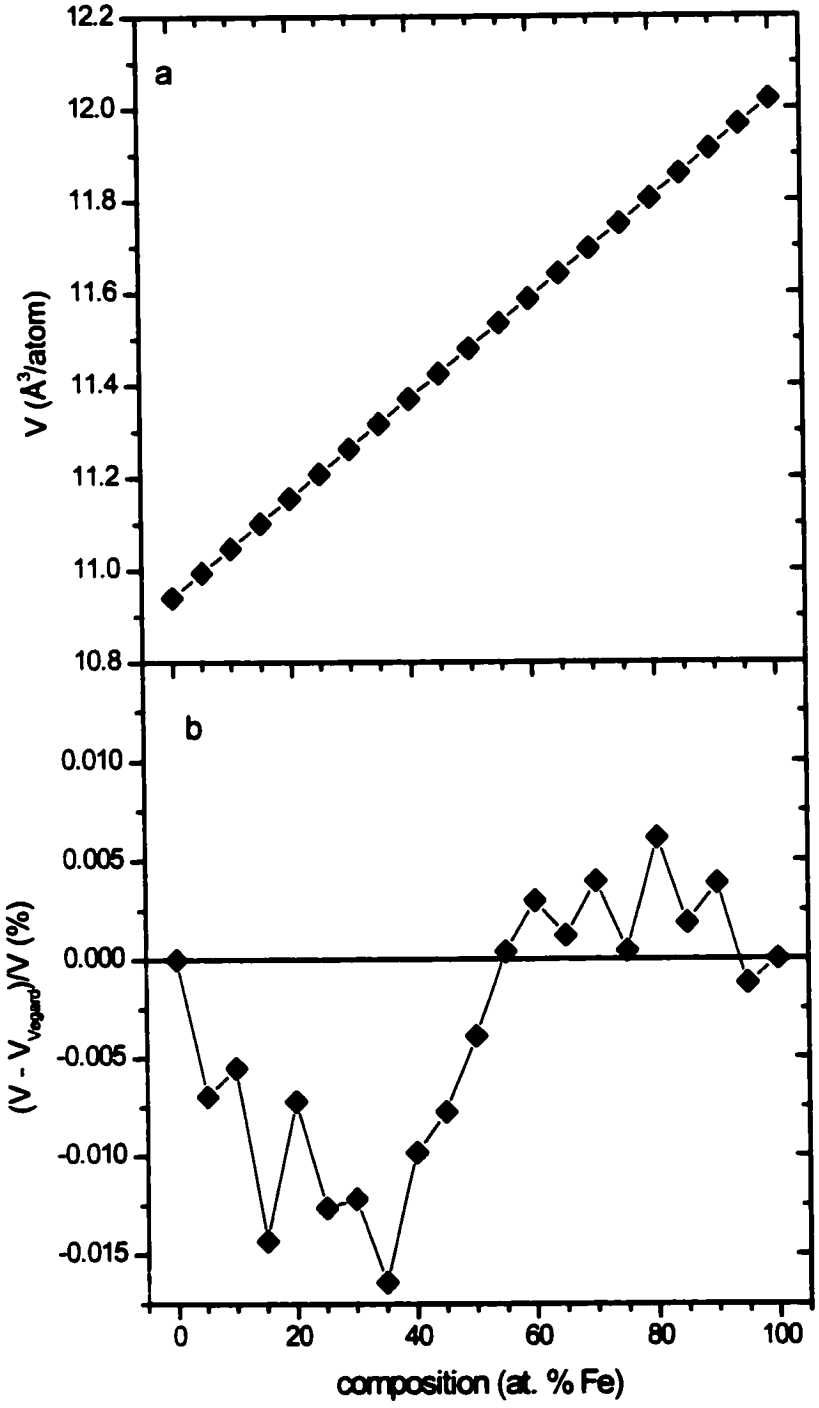

Figure 99 Simulated atomic volume (a) and deviation from Vegard's law (b) at T = 300 K in the absence of magneto-volume effects. In (b), we see that the deviation is at most ±0.015 % throughout the composition range.

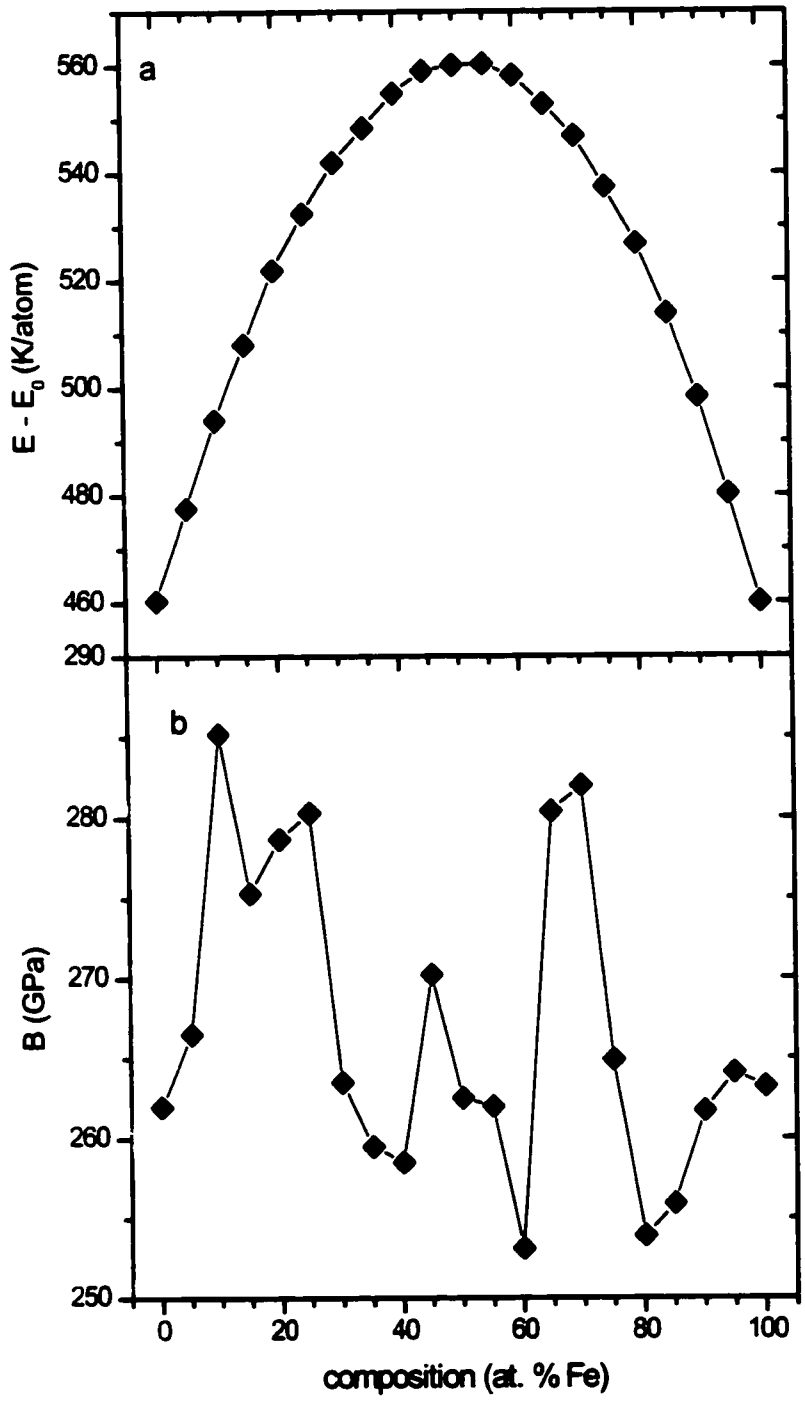

Figure 100 Average chemical potential energy per atom relative to E_0 (see text) (a) and bulk modulus (b) at T = 300 K in the absence of magneto-volume effects.

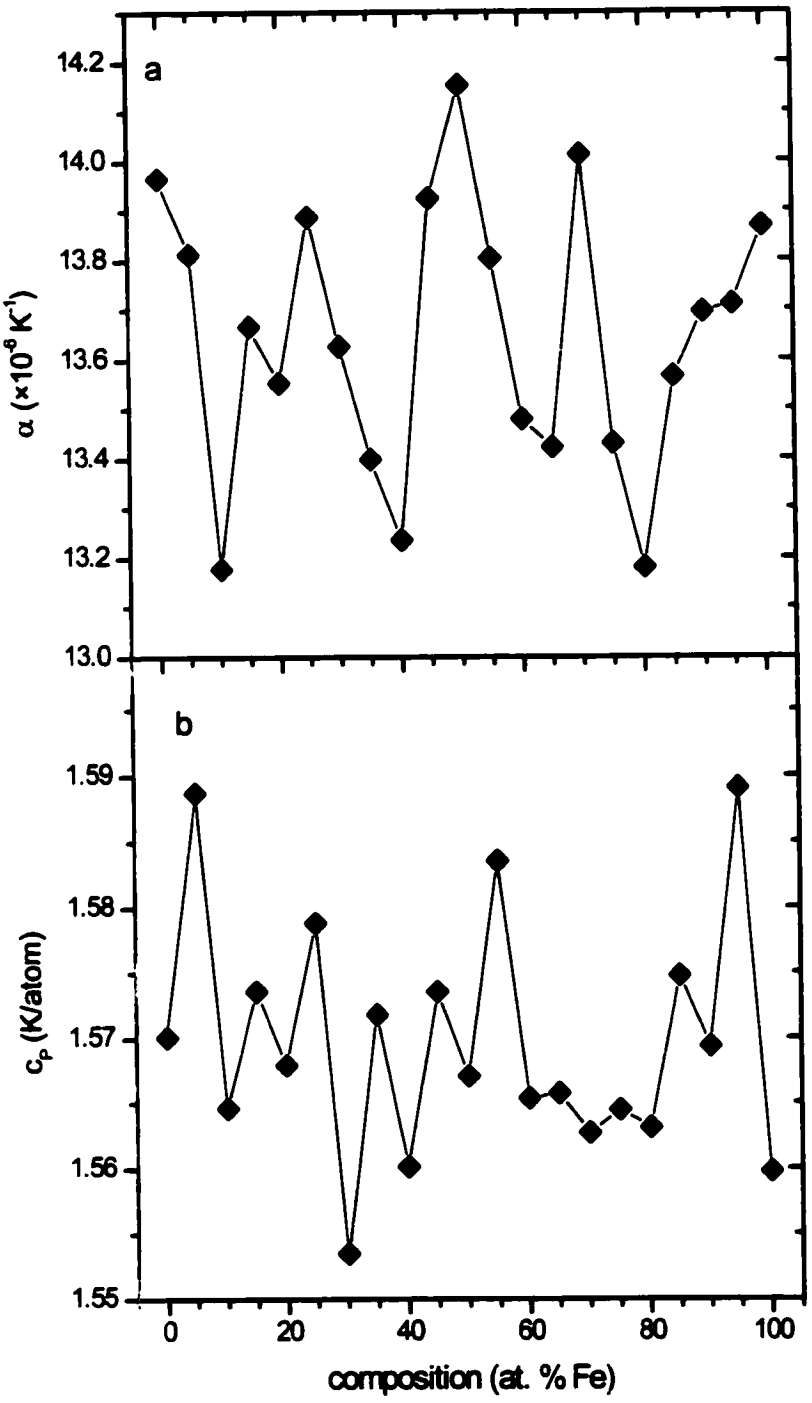

Figure 101 Composition dependence of the linear thermal expansion (a) and specific heat (b, lattice only) at $T = 300$ K in the absence of magneto-volume effects.

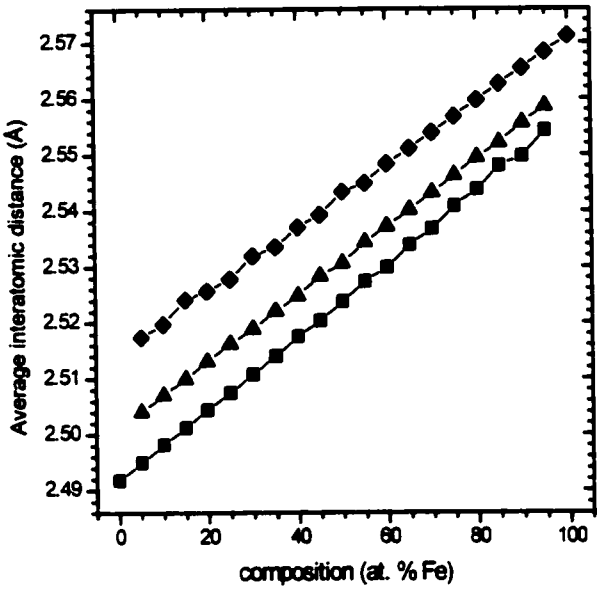

Figure 102 Composition dependence of the average interatomic distance at T = 300 K, separated by the type of bond (◆ d_{FeFe}, ▲ d_{FeNi} and ■ d_{NiNi}). The equilibrium positions for the pair-wise interactions are 2.561 Å, 2.519 Å and 2.482 Å respectively.

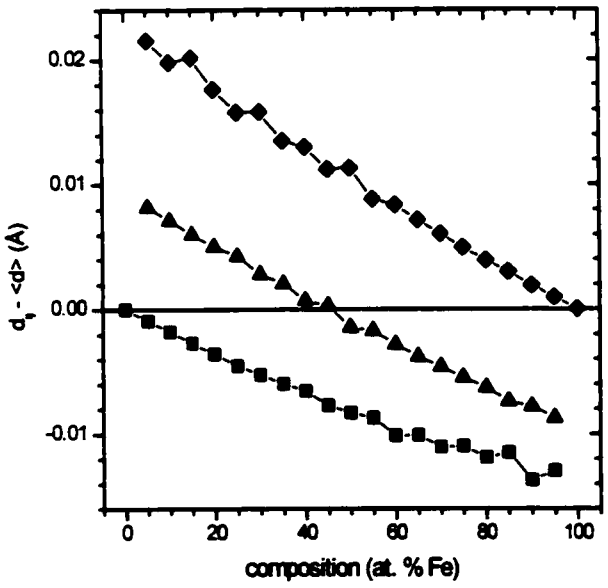

Figure 103 Difference between the average interatomic distances illustrated in fig. 102 and the average interatomic distance (◆ d_{FeFe}, ▲ d_{FeNi} and ■ d_{NiNi}).

7.5.2 Properties with Magneto-Volume Coupling

7.5.2.1 Simulating the Invar Effect in $Fe_{65}Ni_{35}$

One of the main purposes of this study was to see if a simple model such as the one described is capable of reproducing the main structural and magnetic properties that occur in $Fe_{65}Ni_{35}$ (*the* Invar alloy) as a function of temperature and pressure.

The main effect we investigated was the anomalous near-zero volume expansion at low temperatures, which quickly returns to normal above the Curie temperature. As seen in fig. 105, the simulation does indeed produce a flattening out of the volume expansion at low temperatures. Because the simulated expansion at low temperature (below 100-200 K) is incorrect, it is better to compare the difference between the non-magneto-volume active simulation and the simulation with magneto-volume coupling. This is shown in fig. 105b for the atomic volume and is compared to experimental data. Because the simulated T_C (= 700 K) is somewhat larger than the real T_C (= 500 K [Wassermann90]), we have plotted all graphs as a function of T / T_C for comparison with experimental results. In this way it is also easy to see if an effect is related to T_C or not. As seen in fig. 105b, the comparison between experiment and simulation is quite good, indicating that the magneto-volume coupling through a volume dependent Fe-Fe exchange parameter is capable of reproducing the Invar volume anomaly.

More specific properties can also be investigated to determine if the model correctly reproduces them. The linear thermal expansion coefficient is seen in fig. 104 and compared to experiment in fig. 104b. As seen experimentally, the anomalous thermal expansion which leads to the Invar effect disappears above T_C as in the simulation. Though the exact shape of the curve is not retained, the order of magnitude and general reduced temperature dependence are reproduced.

The same is found for the specific heat (fig. 106) which exhibits a peak at T_C and remains slightly above the value simulated in the absence of magnetism of magneto-volume effects above T_C. The bulk modulus (fig. 107) also shows an Invar related anomaly which exists only below T_C. In this case however, the concordance between the simulated result and the experimental result is less than perfect, showing a larger drop at low temperature. Nonetheless, the order of magnitude is correct, except at very low temperatures.

Finally, it is interesting to see the average magnetization as a function of temperature (fig. 108). Not only is the saturation value less than the Slater-Pauling value (μ_{S-P} = 2.03 μ_B) but the reduced temperature dependence is noticeably different from what is observed in Ni. Both these features are also observed experimentally but are due to the presence of mixed exchange (positive J_{NiNi} and J_{FeNi}, negative average J_{FeFe} - at least below T_C) and are not related to magneto-volume coupling.

Within the simulation, it is also possible to calculate the average bond lengths based on chemical species (Fe-Fe, Fe-Ni or Ni-Ni), but also based on spin pair orientations (parallel - ↑↑ or ↓↓, or antiparallel - ↑↓ or ↓↑). Because the magnetic exchange coupling for the Fe-Fe bond is distance-dependent, the spin-pairs whose orientations are due to their inter-spin bond and to their bonds to other atoms will have different bond-lengths whether they are parallel or anti-parallel. The average (spin-independent) bond length is shown in fig. 109 along with the spin-dependent distances for Fe-Fe. Overall, the anomalous expansion due to the magneto-volume coupling affects all types of bonds, but the Fe-Fe bonds are obviously more affected. The effect on other types of bonds is secondary and occurs because of the Fe-Fe bond expansion (Fe-Fe bonds represent 42.25 % of all bonds). To minimize strain in the lattice, the other bonds also expand slightly compared to their "normal" length.

It is also very interesting to investigate the effect of spin-pair orientations on the bond-length. In fig. 109, the average bond length is assigned to either group (parallel or antiparallel) based on the average spin orientations. Note that this is different from calculating the average of the bond lengths grouped by the instantaneous spin orientations (in the specific sampled configuration). In this simulation, J'_{FeFe} = 5000 K/Å and d_0 = 2.545 Å, so at d = 2.565 Å, J_{FeFe} = 0 K. At low temperature, antiparallel Fe-Fe spin pairs have a distance which corresponds to $J_{FeFe} < 0$ and they actually contract more than their "normal"(in the absence of magneto-volume coupling) length to minimize the bond energy ($U_{ij} = -J_{FeFe}\,\sigma_i\sigma_j = +J_{FeFe}$ so $\partial U_{ij}/\partial d > 0$ and $\Delta U_{ij} < 0$ if $\Delta d < 0$). On the other hand, parallel Fe-Fe spin pairs are expanded, and even to the point where J_{FeFe} becomes positive ($U_{ij} = -J_{FeFe}\,\sigma_i\sigma_j = -J_{FeFe}$ so $\partial U_{ij}/\partial d < 0$ and $\Delta U_{ij} < 0$ if $\Delta d > 0$). Because of the string ferromagnetic interaction with Ni spins, the majority of Fe-Fe bonds are parallel which results in a net volume expansion relative to the volume in the absence of magneto-volume coupling. It is more difficult to understand the behaviour of the bonds lengths at higher temperatures (but below T_C), since we see the bond length of the pairs with

antiparallel spin orientations actually expand more than the for pairs with parallel spin orientations. We have yet no clear explanation of this behaviour which might, in fact, be an artefact due to the way the averages are performed (calculate the averages, then group the pairs as opposed to grouping and taking the averages in each group). Above T_C, the average spin directions are completely random and there is no difference between the two cases. It is also interesting to note that for temperatures of interest to the Invar problem, the interatomic Fe-Fe distances are such that we never reach the plateau of ± 100 K in J_{FeFe}. This means that the choice of ± 100 K as bounds to J_{FeFe} is not very important to this model (it does however become important if a larger J'_{FeFe} is chosen).

This model, as simple as it is, is thus capable of reproducing to some degree all of the anomalous structural and magnetic properties associated with Invar at the composition of 65 at. % Fe. In the following section, we shall see how it also reproduces similar anomalous properties which are observed as a function of composition, such as deviation from Vegard's law and the Slater-Pauling curve.

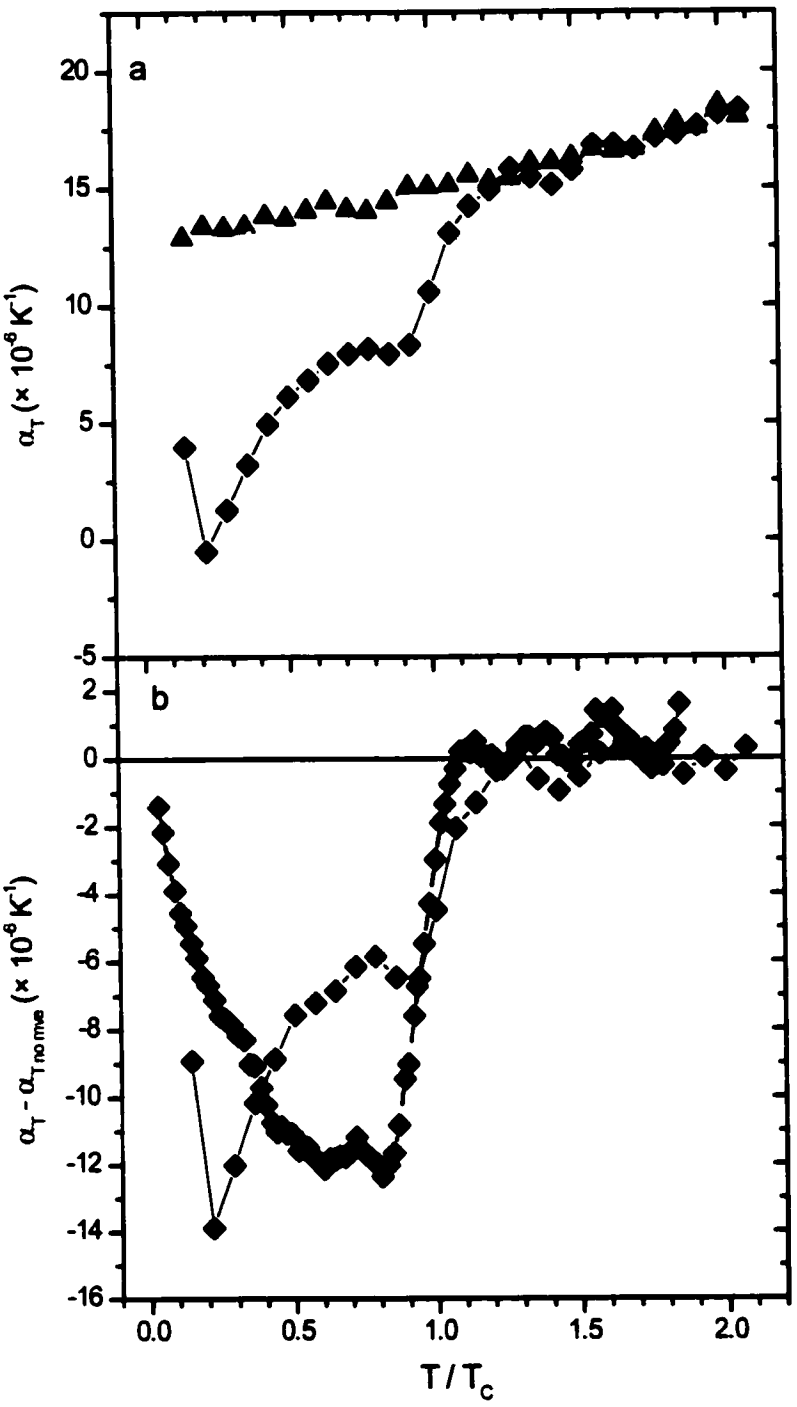

Figure 104 Simulated linear thermal expansion in $Fe_{65}Ni_{35}$ in the presence (a, ◆) and in the absence (a, ▲) of magneto-volume coupling. In (b), the difference is shown (◆), as well as the experimentally observed difference (dashed line) [after data from Hayase73].

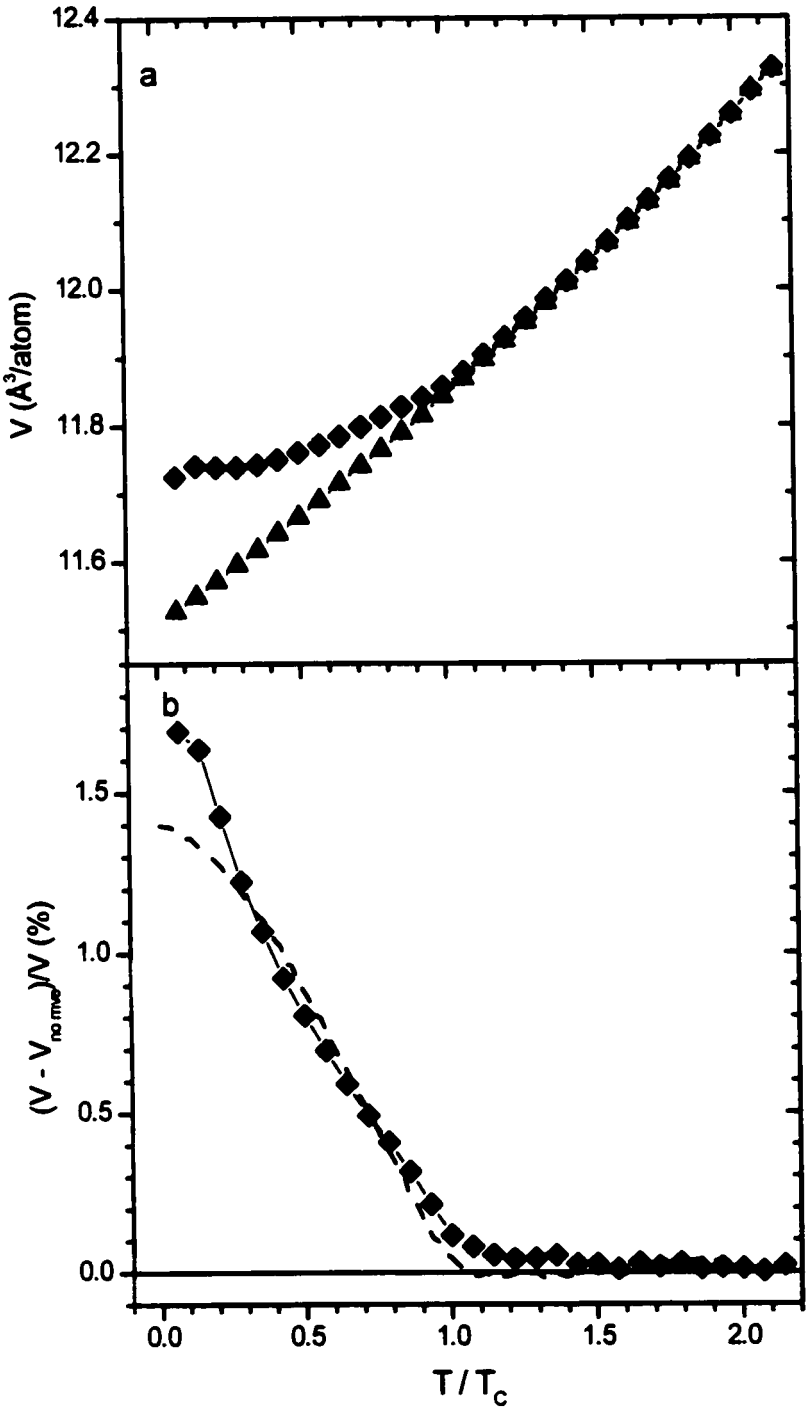

Figure 105 Simulated atomic volume in $Fe_{65}Ni_{35}$ in the presence (a, ◆) and in the absence (a, ▲) of magneto-volume coupling. In (b), the difference between the two volumes (◆) is shown to disappear at T_C, as is observed experimentally (dashed line) [data from Hayase73].

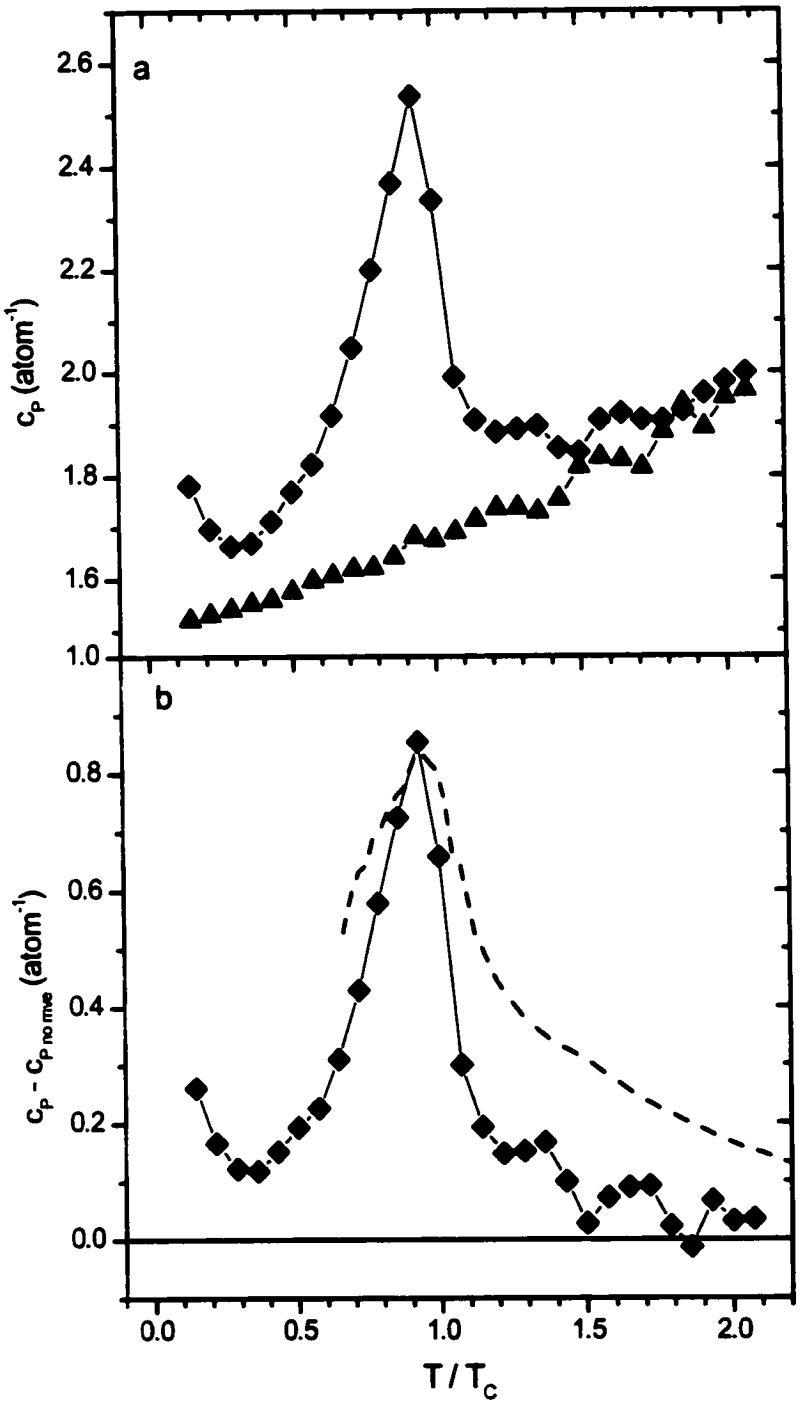

Figure 106 Simulated specific heat per atom in $Fe_{65}Ni_{35}$ in the presence (a, ◆) and in the absence (b, ▲) of magneto-volume coupling. In (b), the difference is shown (◆), as well as the experimentally determined difference (dashed line) [data from Wassermann90].

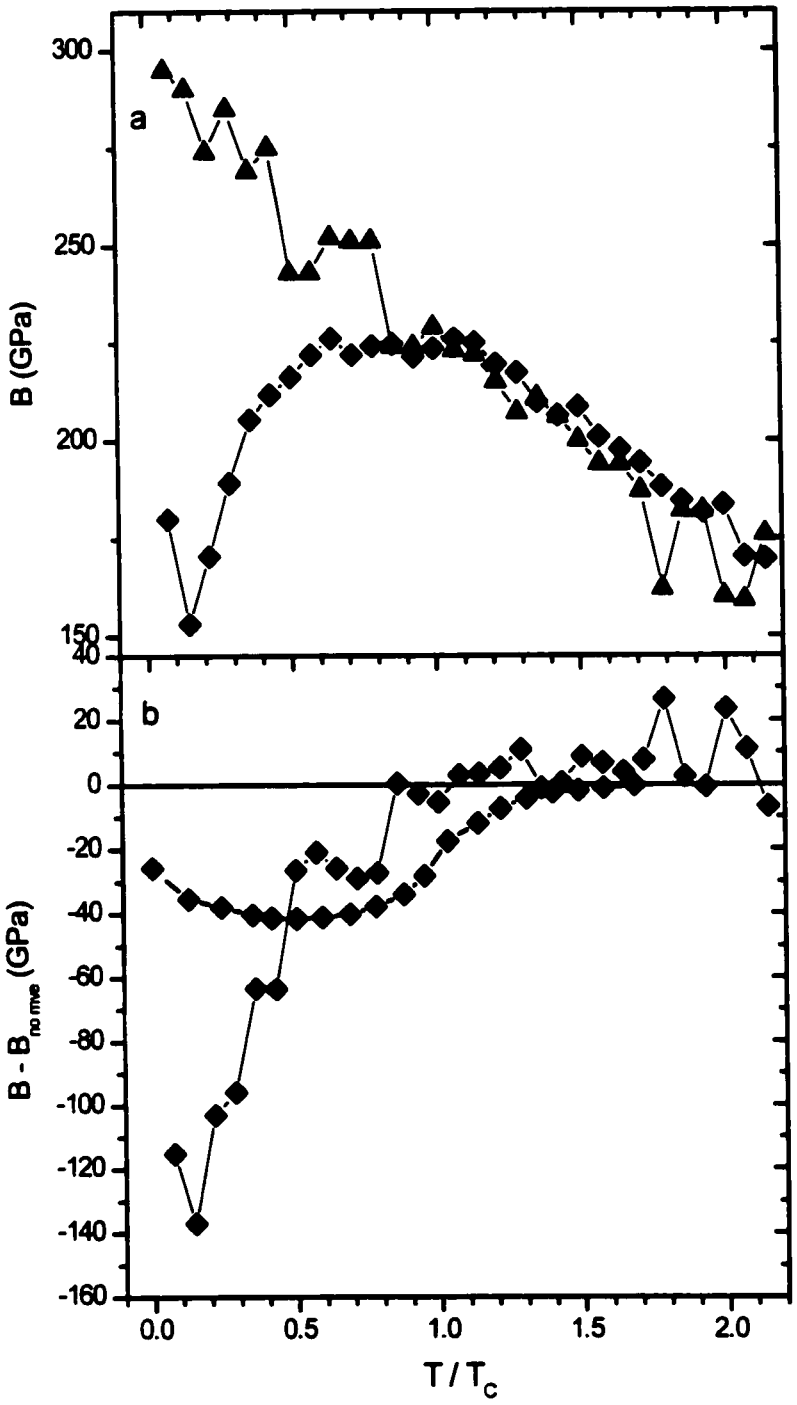

Figure 107 Simulated bulk modulus in $Fe_{65}Ni_{35}$ in the presence (a, ◆) and in the absence (a, ▲) of magneto-volume coupling. In (b), the difference is shown (◆), as well as the experimentally determined difference (dashed line) [data from Wassermann90].

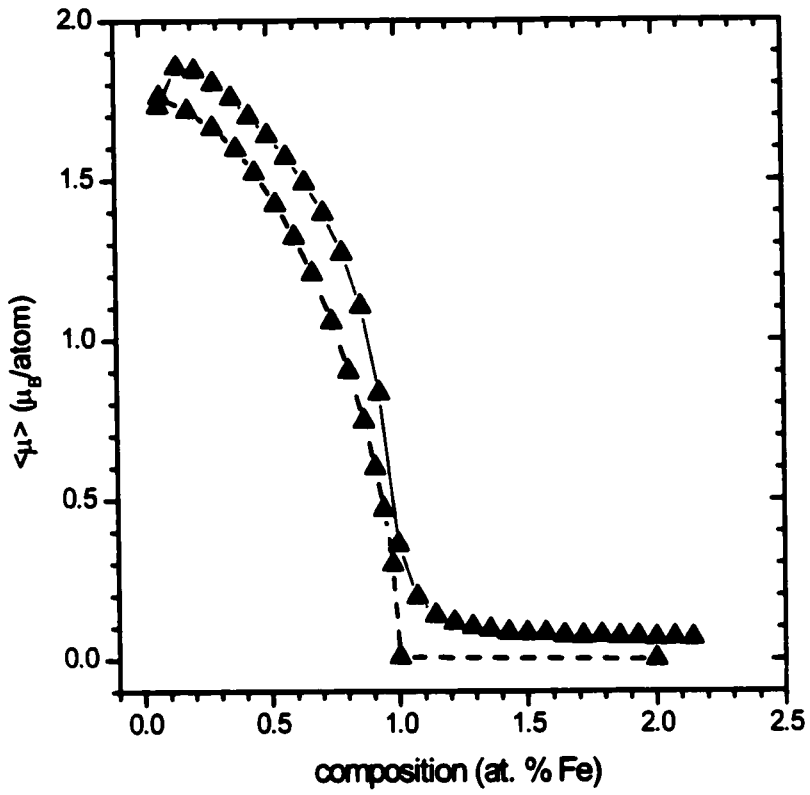

Figure 108 Simulated average magnetization in $Fe_{65}Ni_{35}$ in the presence of magneto-volume coupling. The experimental data for $Fe_{65.8}Ni_{34.2}$ are shown as a dotted line [Crangle63]. T_C is found to be ~700 K. The slight increase at very low temperature is due to the mixed interactions (some positive and some negative exchange constants) and the use of the Ising model. It does not occur in the measured data.

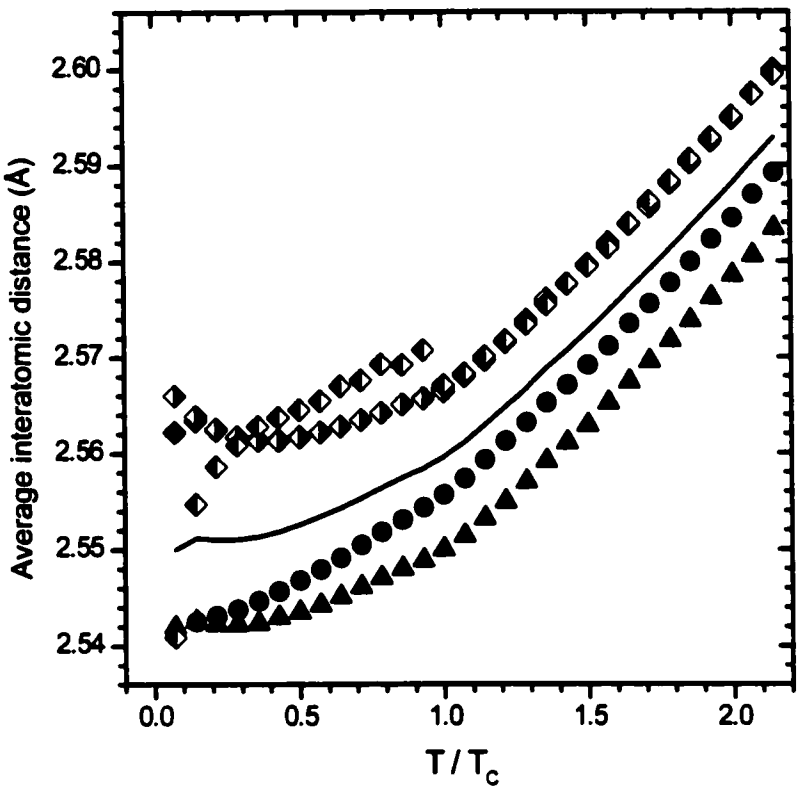

Figure 109 Simulated average interatomic distances in $Fe_{65}Ni_{35}$ grouped by the type of bond (◆ Fe-Fe, ● Fe-Ni and ▲ Ni-Ni, the solid line is the average bond length). In addition, the Fe-Fe bonds are distinguished based on the average spin pair orientations (half-filled symbols, solid on the right for parallel bonds, solid on the left for anti-parallel bonds).

7.5.2.2 Invar Effect at Other Compositions

In the previous section, we have shown that a simple model which uses an interatomic distance dependent Fe-Fe exchange parameter is capable of reproducing the main magnetic and structural properties of $Fe_{65}Ni_{35}$ Invar. We shall now show that the same model is also capable of explaining the magnetic and structural Invar related anomalies found at other compositions.

Simulations were performed at T = 300 K throughout the entire composition range for chemically disordered alloys. Fig. 110a shows the average energy per atom (chemical + magnetic) in the presence of magnetic interactions. When compared to the energy when neglecting magnetic interactions, one realizes that the difference resides primarily in the magnetic energy (the change in chemical energy due to the magneto-volume coupling is less important), especially in the Ni-rich composition range where the moments are ferromagnetically aligned and the dominant interactions are Ni-Ni (J_{NiNi} = 65 K) and Fe-Ni (J_{FeNi} = 127 K). The drop in the bulk magnetization above 60 at. % (fig. 110b) and the reduction of the exchange interaction (J_{FeFe} is relatively small) as the number of Fe-Fe pairs increases cause the energy to increase back towards its non-magnetic value at higher Fe concentration.

Fig. 110b also shows how this model reproduces some of the deviation from the Slater-Pauling curve. Again, this is not linked to the magneto-volume coupling, but has only to do with the negative average Fe-Fe exchange interaction which causes antiparallel Fe spin orientations. In addition, since we are at T = 300 K, the drop in the T_C in very Fe-rich alloys can contribute to the reduction of the average magnetization. When compared to the experimental measurements at 4.2 K, we find that the drop at high Fe content is much quicker than the simulated drop, even though the simulated data is taken at 300 K and is systematically lower than the saturated (T = 0 K) data would be. This is most likely due to the reduction of the magnetic moment magnitude, in addition to antiparallel spin orientations (or spin canting). In our model, we assume that $\mu_{Fe} = 2.8\mu_B$ and $\mu_{Ni} = 0.6\mu_B$ throughout the composition range, thereby avoiding any effects to to the HM/LM transition in Fe-rich alloys.

One of the most intriguing features of the Fe-Ni system is the atomic volume. As shown in chapters 4 and 6, before the HM/LM transition occurs beyond ~70 at. %, there is a small positive deviation from Vegard's law which is not properly understood. Within the context of this model of magneto-volume coupling, such a deviation is natural since the Fe-Fe bond length

enhancement which occurs at 65 at. % to produce the Invar effect is also present in more Ni-rich alloys. Because of the low number of Fe-Fe bonds in Ni-rich alloys, this effect is not as significant as at 65 at. %, but it is still present, as shown in fig. 111. In fig. 111b, the difference between the volume in the presence and absence of magneto-volume coupling is compared to 1) the positive deviation from linearity observed in experimental measurements of the atomic volume at RT and 2) the spontaneous volume enhancement at $T = 0$ K, calculated as the difference between the measured $T = 0$ K volume and the $T = 0$ K volume extrapolated from high temperature data where there are no magneto-volume effects [Wassermann90]. In our model, because the composition dependence of the volume without magneto-volume coupling is linear and the high temperature volumes with and without magneto-volume coupling are the same, the two quantities are identical, except for the difference in temperatures (one should use the spontaneous volume enhancement at RT). In the real alloy, effects of the HM/LM transition appear from ~60 at. %, so they will not be identical, but one does find there is a strong correlation between the simulated and the measured expansions below ~60 at. %. Our model successfully explains this anomalous behaviour of the volume even though it overestimates the effect at low Fe content. This can be due to the fact that J'_{FeFe} might not be identical throughout the composition range. If J'_{FeFe} was half as small at 30 at. % than it is at 65 at. % Fe, then the agreement would be much better.

Similar conclusions can be made regarding the RT linear thermal expansion coefficient (fig. 112) and the bulk modulus (fig. 113). In each case, the simulated composition dependence is consistent with what is observed experimentally, except that the effect is overestimated at low Fe content. The general tendency is correct, illustrating the validity of this model for understanding the Invar effect in Fe-Ni alloys. The experimentally measured thermal expansion coefficient (fig. 111) is another perfect example that shows that the Invar effect is not specific to the composition of 65 at. % but that the effect is present at all compositions, though maximal at 65 at. % as simulated by this model.

In all cases, the effect is related to the expansion of Fe-Fe bonds with parallel spins and as such will increase with the number of Fe-Fe pairs, as long as the material is ferromagnetic. At compositions above 65 at. %, because of the negative J_{FeFe}, the number of pairs of anti-parallel Fe-Fe moments increases, thus reducing the effect. It is important to note that in Fe-Ni alloys, J_{FeFe} must be negative to explain the deviation from the Slater-Pauling curve in chemically

disordered alloys. However, in other FCC Fe-based alloys, it is possible that J_{FeFe} be positive, in which case an Invar effect could also occur at higher Fe content than in Fe-Ni. This, for example, is the case in Fe-Pt and Fe-Pd alloys. In both these systems, the atomic volume is larger than in Fe-Ni, resulting in $J_{FeFe} > 0$ (but J'_{FeFe} is still large!) and no deviation from the Slater-Pauling curve. When discussing the properties Fe-Ni Invar alloy, Rancourt and Dang [Rancourt96a] showed that the frustration of magnetic Fe-Fe bonds was a key to understanding the Invar effect. In general, however, one must simply consider the magnetic order (difference between the number of aligned and anti-aligned Fe-Fe bonds) and the sign of J'_{FeFe} rather than specifically at bond frustration (the sign of J_{FeFe} is not really important). As $J'_{FeFe} > 0$ based on ESCs, expansion will occur for pairs of spins with parallel alignment. In the case of Fe-Ni alloys, because at the volumes of interest $J_{FeFe} < 0$, it is necessary that the bonds be frustrated to have an Invar effect. In cases where $J_{FeFe} > 0$, no frustration is necessary.

The model presented in this chapter and these concepts have also been applied to explain why an Invar effect also occurs in $Fe_{65}Ni_{35}$ films which exhibit Fe_3Ni-type chemical ordering [Lagarec00], even though there is no deviation from the Slater-Pauling curve in these films. Again, the cause of the expansion is due to a majority of pairs of Fe spins with parallel alignment and is otherwise not directly related to the magnetic or chemical structure of the material. In this paper, we show that MC simulation of chemical ordering in Fe-Ni alloys using the method of Dang and Rancourt [Dang96a, 96c] produces an alloy which would show no deviation from the Slater-Pauling curve and a higher T_C, as is observed experimentally in films grown by evaporation at RT [Dumpich87, 88, 92, Wassermann92]. In addition, MC simulations of magneto-volume effects show that an Invar effect would arise in both the chemically ordered films and the chemically disordered films, as is observed experimentally.

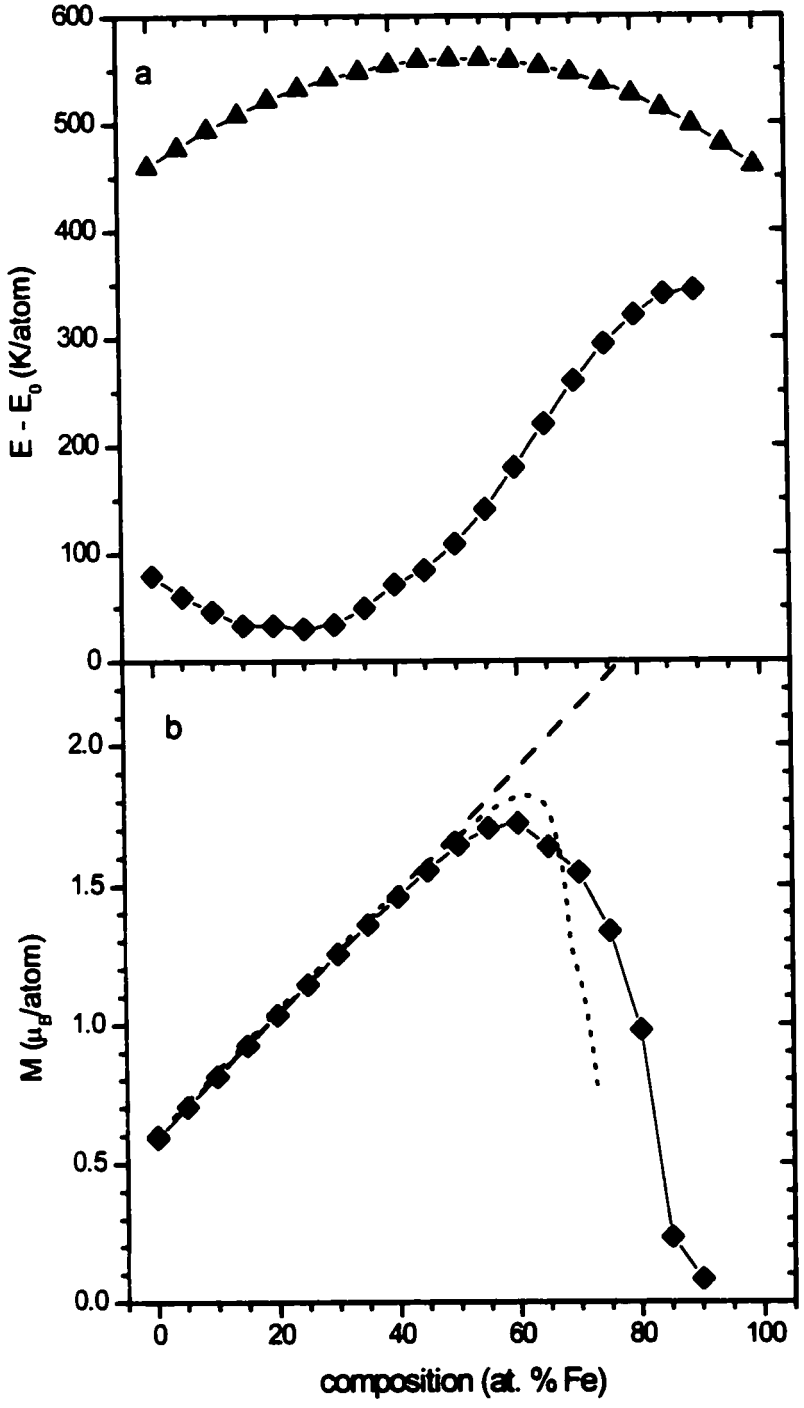

Figure 110 Average energy per atom (potential+magnetic) at T = 300 K in the presence (a, ◆) and in the absence (a, ▲) of magnetism and magneto-volume coupling. Average moment per atom at T = 300 K (b, ◆) with the Slater-Pauling relation (dashed line) and the T = 4.2 K measured magnetic moments (b, dotted line [Crangle63, Brando64]).

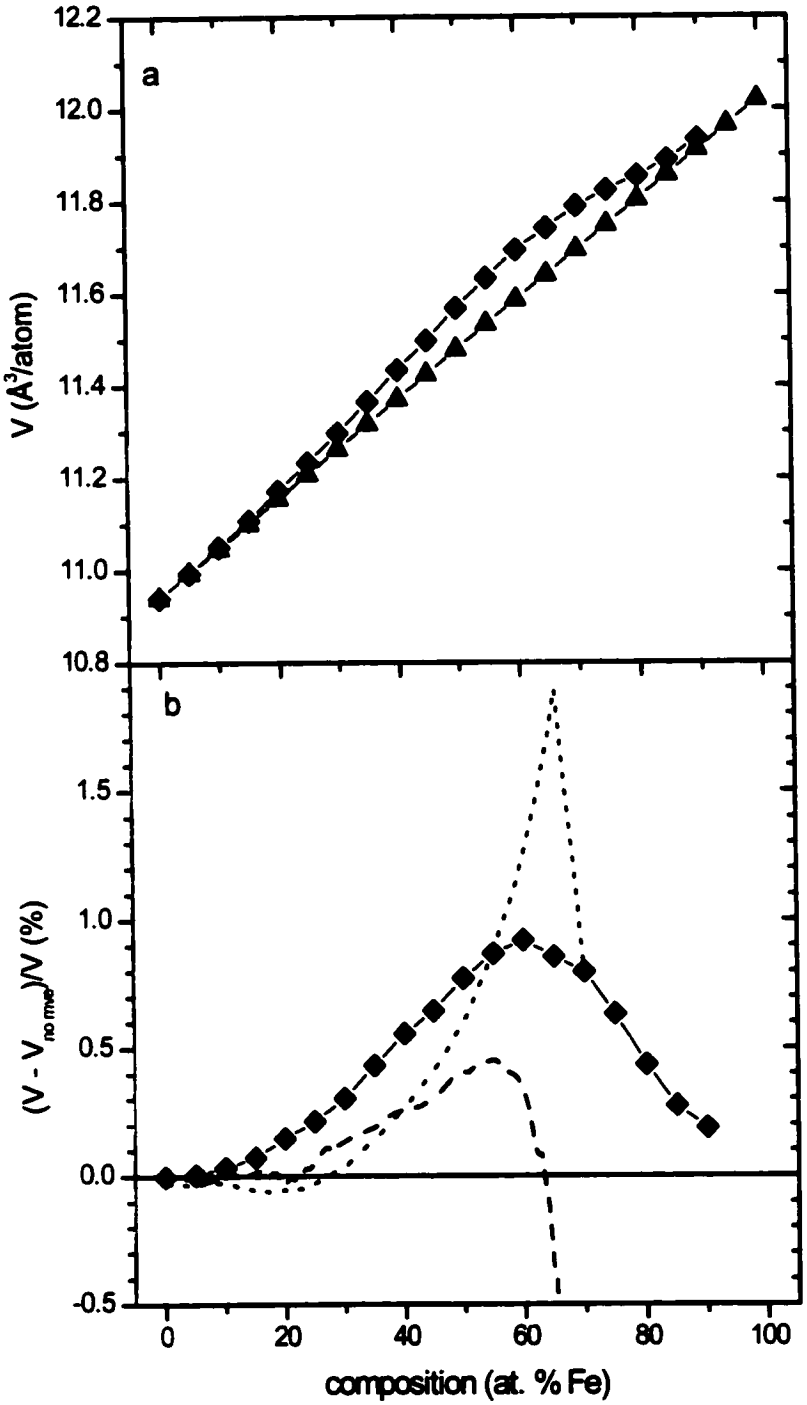

Figure 111 Simulated atomic volume at T = 300 K in the presence (a, ◆) and in the absence (a, ▲) of magneto-volume coupling. The relative difference between the two is plotted in (b), as well as the experimental deviation from the linear composition dependence of the volume which occurs below 20 at. % Fe (dashed line, data from [Bradley37]) and the T = 0 K volume enhancement relative to the volume extrapolated from high temperatures (dotted line, data from [Wassermann90]).

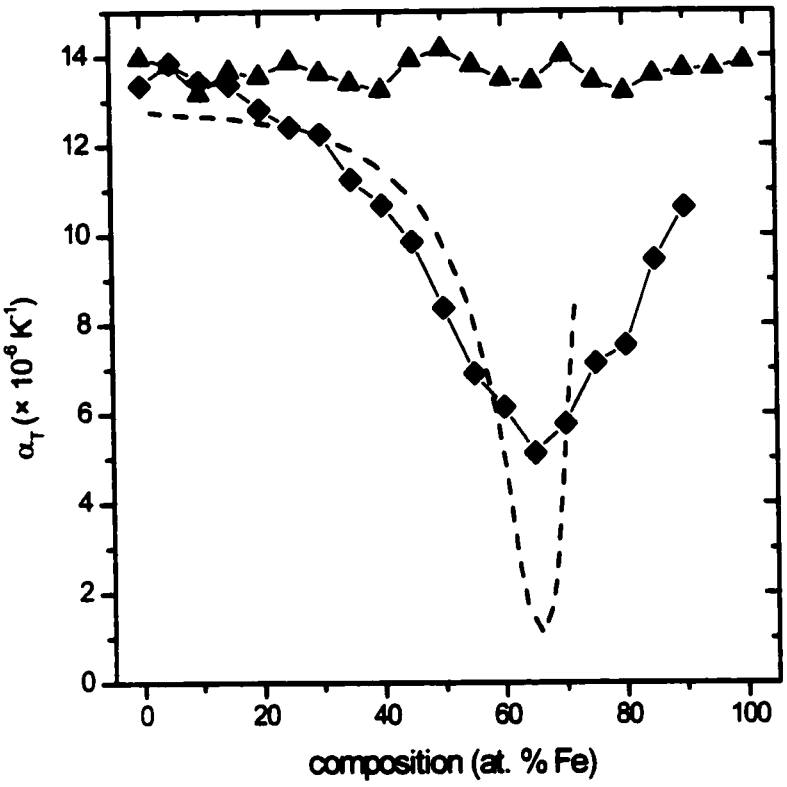

Figure 112 Simulated linear thermal expansion coefficient at T = 300 K in the presence (◆) and in the absence (▲) of magneto-volume coupling. The dashed line represents experimental results at RT (295 K) [Wassermann90].

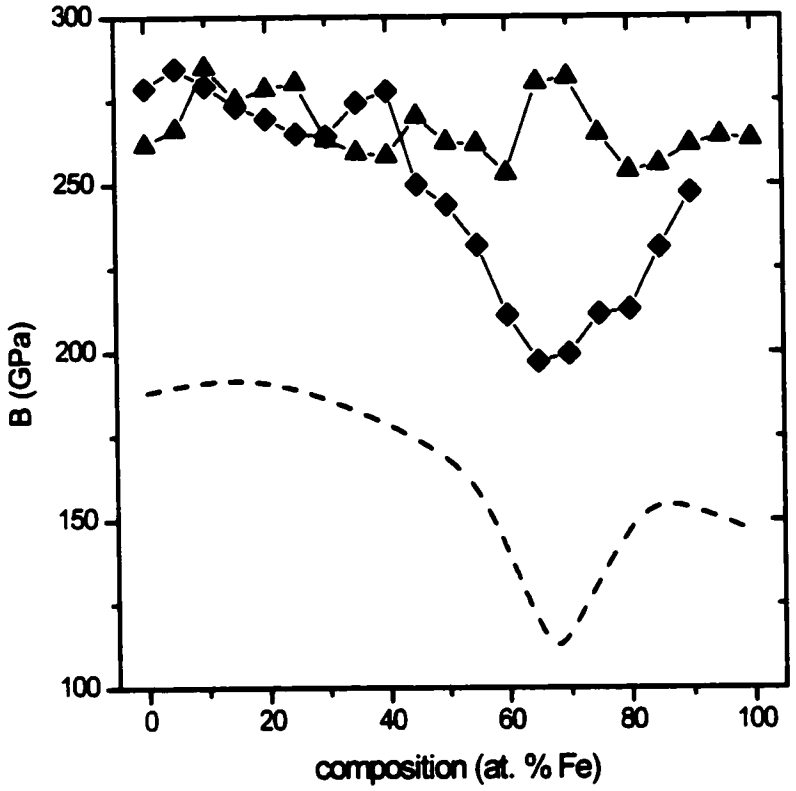

Figure 113 Simulated bulk modulus at T = 300 K in the presence (◆) and in the absence (▲) of magneto-volume coupling. The dashed line represents the experimental results at RT [Tanji83].

7.5.3 Effect of the choice of $J_{FeFe}(c)$

We should also briefly discuss the effect of the concentration dependence of J_{FeFe}. As stated initially, we chose J_{FeFe} to vary with the alloy's composition such that, at the T = 0 K volume in the absence of magneto-volume coupling and assuming an undistorted lattice, J_{FeFe} would be the same for all alloys ($d_0^3(c)$ scales with $V_{no\ mve}(c)$). We will now see how other choices would have affected the results, considering that they should be the same at c = 65 at. %:

① If J_{FeFe} was not composition dependent. Based on fig. 102, at T = 300 K, for all concentrations below ~60 at. % the average Fe-Fe interatomic distance would be smaller than d_0 = 2.545 Å and there would be no Invar effect (in the plateau, J'_{FeFe} = 0). Alloys with compositions of less than 50 at. % would likely show no Invar effect at all, then the effects would increase rapidly and give the same result at ~65 at. % as already calculated. All more Fe-rich alloys would exhibit the same effects since saturation (J_{FeFe} = +100 K) is never reached around T = 300 K.

② If $d_0^3(c)$ scaled with the volume at which the HM/LM transition occurs (see chapter 5). The transition volume also varies approximately linearly with composition, but in pure Ni, it is much lower than $V_{no\ mve}(c)$. In this case, at T = 300 K, in alloys with less than some Fe content, J_{FeFe} would be saturated (J_{FeFe} = +100 K and J'_{FeFe} = 0) resulting in no effect. As the Fe content increased, J_{FeFe} at $V_{no\ mve}(c)$ would slowly drop from +100 K to -100 K within some range (which includes 65 at. % Fe). Possibly, in very Fe-rich alloys, J_{FeFe} could saturate in the lower value of -100 K. Again, in such a situation, the effect would only occur within a certain concentration range around 65 at. %, rising from no effect (when J_{FeFe} is saturated) to the calculated value at 65 at. % Fe.

In any case, in the scenario we chose, at each composition, the Fe-Fe non-magneto-volume active interatomic distance $d_{no\ mve}$ is such that $J'_{FeFe}(d_{no\ mve})$ is non-zero ($J_{FeFe}(d_{no\ mve})$ is not on the ±100 K plateaus) so the Invar effect will take place at all compositions and its magnitude will depend on the number and state of the Fe-Fe bonds. In the other scenarios, there are ranges of composition where the Fe-Fe distance is such that J'_{FeFe} = 0 so no Invar effect can occur. The composition range over which the large magneto-volume effect occurs would thus be reduced if $d_0(c)$ behaved differently. Also, since the effect is directly related to J'_{FeFe}, a change in J'_{FeFe} with composition would reduce or enhance the effect we have already calculated. It thus

seems clear that although this model is a rough approximation of the true situation, it provides the grounds for understanding and reproducing the magneto-volume anomalies related to the Invar effect.

7.6 Conclusion

The idea of a J_{FeFe} that is dependent on interatomic distance has long been thought as a possible cause of the Invar effect [Kondorskii60]. However, two main hurdles prevented this idea from being widely accepted: (1) the magnitude of the slope J'_{FeFe} was much larger than what would be expected and (2) the expected positive J'_{FeFe} should lead to a contraction if J_{FeFe} was negative, not the expansion that is observed. The first point was only recently resolved by a calculation of J_{FeFe} based on ESCs [Sabiryanov95], though its relation to the Invar problem was not immediately recognized. The second point was also recently resolved by Rancourt and Dang [Rancourt96a] who showed that the frustration due to the strong ferromagnetic interaction with Ni would in fact cause the desired expansion. By using MC simulations which combined magnetic and atomic degrees of freedom, we have illustrated for the first time how such a simple model could explain the magnetic and structural anomalies associated with the Invar effect in Fe-Ni alloys. This model is also applicable to other Invar alloys such as Fe-Pt or Fe-Pd and, contrary to other models, naturally provides the direct relationship between the Invar effect and the magnetic order which is well established.

8. Conclusion

When I started working on this project, my intent was to study the antitaenite and other unusual Fe-Ni minerals found in meteorites. After the first MS experiments, it became clear that antitaenite was no ordinary alloy and that the *IS* could be a reliable criterion to differentiate HM and LM alloys. With this information, we would perform new and meaningful experiments which enabled us to collect more information on Invar and anti-Invar alloys, at RT as well as at high temperatures where the effects take place (anti-Invar) or disappear (Invar). In order to understand and fully exploit this wealth of information, we established a collaboration with Dr. Bose to perform ESCs of Fe-Ni alloys in various chemical and magnetic configurations. Though this theoretical and experimental work on the HM/LM transition helped us understand many features of Fe-rich alloys, including the anti-Invar effect, it was clear that the Invar effect was not directly related to this transition but caused by something else. In light of recent calculations of the magnetic exchange parameter, we performed simple yet convincing finite temperature MC simulations based on the local moment model of Rancourt and Dang [Rancourt96a] and found it to successfully explain the Invar effect.

8.1 Summary of Results

The study of the Santa Catharina meteorite resulted in two important yet very different points. First of all, it provided us with detailed information about an Fe-rich FCC material, antitaenite, which is found to be stabilized by an epitaxial relation with a stable FCC phase, tetrataenite. Tetrataenite is also an extraordinary alloy in that it is a chemically ordered phase that cannot be synthesised by traditional methods. A detailed MS study and state-of-the-art electron microprobe imaging and analysis led us to determine the chemical composition of antitaenite which had previously been a source of debate. The Néel temperature of antitaenite

was determined by MS, and a simulation of the magnetic interplay between tetrataenite and antitaenite has lead to a simple explanation of the unusual temperature dependence of the width of the Mössbauer signal of antitaenite. On a note more related to the rest of the work in this thesis, on the basis of MS, antitaenite was shown to have a distinct electronic structure from traditional HM alloys. This use of MS in differentiating HM and LM alloys would prove to be invaluable and represents the main experimental contribution of this thesis.

The rest of the work dealt with understanding, from a more general point of view, the properties of FCC Fe-Ni alloys as a whole. After reviewing the known and well understood properties of FCC Fe-Ni alloys, we have performed several types of ESCs to gather information on HM-FM and NM phases of the alloys as well as investigate the stability of the magnetic moment in these alloys using the DLM model. We used the ESCs to calculate precisely and accurately the *IS* observed in MS as well as to determine systematics of the HF in FM alloys. The composition-driven HM/LM transition, which is predicted on the basis of ESCs, was then indisputably observed for the first time in Fe-rich alloys. The use of the *IS* as a marker made it possible to clarify when the transition was occurring and how it affected the lattice parameter of Fe-Ni alloys, a feature that for a long time had not been understood. High temperature MS measurements provided first-hand evidence for thermally induced moments in anti-Invar alloys, whereas Invar alloys were found to remain HM above T_C. Further evidence that the Invar effect was unrelated to the HM/LM transition was found from the deviation from Vegard's law which was interpreted to show that the volume of Invar alloys is in fact, at low temperature, expanded relative to "normal" non-magneto-volume active alloys. While the anti-Invar effect could be understood on the basis of the moment-volume instability in Fe-rich alloys, the Invar effect needed a different interpretation. Using a simple local moment model with magneto-volume coupling, we simulated the magnetic and structural properties of Invar alloys within the context of a HM local moment model. We showed that all properties could be satisfactorily explained by this model and that the assumptions of the model were actually justified on the basis of the previously published and new results of the volume dependence of the Fe-Fe magnetic exchange parameter. This work has thus enabled us to answer the two major questions regarding FCC Fe-Ni alloys: What causes the Invar effect? and What causes the anti-Invar effect?

8.2 What Causes the Invar Effect?

Based on the evidence presented in chapters 5, 6 and 7, it is now clear that the Invar effect is mainly due to the disappearance, as temperature increases, of a volume expansion caused in HM alloys by a strong volume dependence of the Fe-Fe magnetic exchange parameter J_{FeFe}. In alloys with concentrations far from where the HM/LM transition occurs, the HM phase is stable throughout the temperature range and one finds that the Invar effect is a true local moment magneto-volume effect. This volume expansion, relative to the non-magneto-volume active alloys is clearly seen as a deviation from Vegard's law that is of the same order of magnitude as the spontaneous volume magneto-expansion relative to the high temperature phase. The existence of a large volume dependence of J_{FeFe}, which is required to produce this effect, is obtained from ESCs and occurs within the stability range of the HM phase. MC simulations using a very simple model of this volume dependence of J_{FeFe} are quite capable of reproducing the anomalous magnetic and structural properties. The magnetism itself is correctly explained by the simple local moment model that was originally put forth as the latent antiferromagnetism model.

In alloys with compositions closer to the HM/LM transition composition, the HM phase remains stable at low temperature by the presence of ferromagnetic order, but the moment magnitudes are seen to be slightly dependent on the magnetic configuration. This behaviour is consistent with calculations given in chapter 5 and experimental evidence in chapter 6 that shows a minor drop of the *IS* as the temperature exceeds T_C. In these conditions, the high temperature phase (above T_C) is not, in terms of magnetic moment magnitudes the same as the low temperature phase. Even though Invar alloys should generally be considered as HM alloys, there is some effect of moment instability with temperature which can contribute to the anomalous thermal expansion of the alloys. Because these alloys are already experiencing effects of the HM/LM transition, the reference volume of their high temperature phases do fall below Vegard's law, as extrapolated from the volumes of Ni-rich alloys. We should note, however, that if this thermal instability of the moment has an effect on the thermal expansion of the alloy, it is not of great importance compared to the true Invar effect, which is due solely to the volume dependence of J_{FeFe}.

In short, the Invar effect is due to the large volume dependence of J_{FeFe} and is directly mediated by the magnetic order of the alloy, thus disappearing around T_C. The anomalously

large volume dependence of J_{FeFe} most likely arises as a precursor sign of the moment-volume instability in FCC Fe which occurs at reduced volumes. The Invar effect is not due to thermal excitation of a low moment phase or state or thermal fluctuations of the moment, as the accumulated evidence shows that a large moment is stable above T_C.

8.3 What Causes the Anti-Invar Effect?

Whereas the Invar effect is a low temperature effect driven primarily by energetics of the alloy as a magnetic and structural ensemble, the anti-Invar effect is a high temperature effect driven primarily by entropy.

The anti-Invar effect occurs in alloys whose ground state is a LM phase and at a volume where there is a moment-volume instability and for which there is a positive correlation between the moment magnitude and the volume where the system with such a moment is most stable. In these conditions, at high temperature, the entropic drive towards increasing the moment magnitude and hence the moments contribution to entropy also results in an increased volume compared to the volume expected in the absence of this entropic-driven effect. This leads to an anomalously high thermal expansion which subsides as the energy increase from the enlarged moment magnitude becomes harder to compensate with a gain in entropy.

8.4 What Can We Learn From This Work?

Because of the complexity of the system and the large number of different effects which arise within a short range of compositions, it has been difficult to associate experimentally observed effects to a specific cause. Within the range of ~50 to ~75 at. % Fe, there is:

- a drop in the magnetic moment due to anti-ferromagnetic Fe-Fe magnetic exchange,
- a peak in the magneto-volume anomalies below T_C related to the Invar effect (due to a large magneto-volume coupling),
- an instability with respect to a martensitic transition because of competition between two lattice structures which have very similar energies,
- a drop in the atomic volume due to a transition from a HM material to a LM material
- and the appearance of the anti-Invar effect at high-temperatures due to the a moment

volume instability.

Fortunately, by combining various theoretical and experimental methods, we have been able to discriminate these effects and find their intrinsic causes. This represents a conclusive step in the evolution of the problem. Unlike many researchers in the past, we have not only attempted to understand a specific measurement or a specific feature but rather to get a global picture which is compatible with all known experimental results. It is still necessary to investigate how this understanding can be transferred to other materials that exhibit Invar or anti-Invar behaviour. As stated in the introduction, the term "Invar effect" has now become a general way of saying "low thermal expansion", and the causes of the anomalies in various materials need not be the same. It is for this reason we have decided to focus primarily on Fe-Ni alloys, the original and most studies Invar alloys. As a result we now provide a comprehensive understanding of the magnetic and structural properties of FCC Fe-Ni alloys. We can also state with confidence that in similar materials such as Fe-Pt or Fe-Pd alloys, which also exhibit Invar-like properties in the FCC phase, the causes are most likely the same as in Fe-Ni alloys. In other cases, such as in laves phases, it is more tenuous to expect that the cause be the same.

From an application standpoint, an understanding of the microscopic processes that cause anomalous properties is of great value, because it becomes possible to predict the properties of new alloys and new materials on physical grounds, rather than through trial-and-error. Because Invar and Elinvar alloys are still widely used in precision time pieces and industrial and technological applications, this knowledge can help material scientist tailor-make new materials with targeted properties by using a combination of ESCs and MC simulations, in light of our results.

More than ever before, more than a century after the discovery of the Invar effect, with the help of decades of experimental data and decades of sifting through various theoretical hypotheses, we can finally say that we not only know how FCC Fe-Ni alloys behave but more importantly fundamentally understand why they behave the way they do.

Appendix A

The Extended Voigt-Based Fitting Method

A new model [Lagarec97] for distributions of hyperfine parameters in Mössbauer spectroscopy is presented and is applied to the spectrum of a synthetic taenite. The method is based on the Voigt-based fitting (VBF) method introduced by Rancourt and Ping [Rancourt91a] and generalizes VBF to handle the more realistic cases of correlated distributions of several hyperfine parameters. For this reason, it is named the extended Voigt-based fitting method (xVBF). The degree of correlation can be nil, giving simultaneous independent distributions, or it can be varied, up to a perfect linear correlation or anti-correlation. The proposed multidimensional probability density distribution of xVBF produces a Mössbauer spectrum which can be expressed analytically as a sum of Voigt lines, making it amenable to non-linear fitting. The paramagnetic and magnetic cases are treated, along with an example of a magnetic alloy with a comparison to the linear coupling model used in VBF.

A.1 Introduction

It is very common when analysing Mössbauer spectra of complex phases such as those found in clays, soils or sediments, to make use of distributions of hyperfine parameters. In these materials, distributions of hyperfine parameters arise from subtle variations in the local environments of the probe nuclei, including but not restricted to structural variations or modulations (e.g. in bond lengths), chemical environment variations (e.g. due to alloying) and differences in the local spin structure. Even though such variations are present, the probe nuclei

can still be conceptually considered to be in the same "site", characterized by a set of similar parameters which may or may not be distributed. Most of the models used to describe these complex materials use this concept of a "site" to analyse and interpret their Mössbauer spectra.

In particular, Rancourt [Rancourt94a] has shown that the usual approach using Lorentzian doublets to fit the room temperature spectra of paramagnetic minerals such as layer silicates is incorrect and that distributions of quadrupole splittings must be taken into account [Rancourt94c]. Here the VBF method with linear coupling between the quadrupole splitting and the centre shift seems adequate but the present xVBF approach will allow one to test the extent to which simultaneous correlated distributions of both quadrupole splitting and centre shift are required.

It should be noted that such analyses — with distributions of hyperfine parameters — are only easily applicable in the *static* or *effectively static* case, when time-dependent fluctuations in the local environment occur outside the time frame of the measurement (lifetime of the excited level in Mössbauer spectroscopy). When this is not true, as is often the case near a phase transition, a more comprehensive and complicated analysis must be performed [Rancourt96]. The analysis of spectra in the presence of time-dependent fluctuations in these situations is beyond the scope of this discussion.

We shall thus consider methods used to determine static distributions of the hyperfine parameters involved in Mössbauer spectroscopy. The numerous methods which have been developed to obtain such distributions have recently been reviewed [Rancourt96, Vandenberghe94] and can be loosely categorized as follows: (i) direct extraction methods by deconvolution (Fourier methods, combined partial deconvolution), (ii) direct extraction by matrix methods (step functions — direct or with refinements, using Bayesian inference theory), (iii) fitting to an analytical model of the distribution (simple Gaussian or binomial distribution, more general VBF method for arbitrary distribution shapes [Rancourt91a]. In general, these methods are all used to model the spectrum with a single *primary* parameter whose distribution is desired and other parameters which aren't distributed or are linearly coupled with the primary parameter, thus being *slave* parameters.

The model we present in this article is of the third type, and actually extends the VBF method. For this reason, it has been named the xVBF model, or the extended Voigt-based fitting model. Instead of extracting the distribution of a single hyperfine parameter, with which slave

parameters can be linearly correlated, this model admits simultaneous independent distributions of several parameters. Additionally, they can be partially or completely linearly correlated with each other. This model provides a more "realistic" representation of the hyperfine parameter distributions, since it has long been known that the correlations between distributed parameters are often not perfect couplings [Lines83]. This is the first model to provide an analytical solution to the modelling of this general case.

A brief mathematical description of the model is followed by an example where the model is used to analyse a spectrum of a synthetic taenite which exhibits magnetic splitting.

A.2 Mathematical Description

In the rest of this article, we will only treat spectra which exhibit no experimental artifacts such as thickness effects, and no dynamic effects. In such a case, the elemental multiplet associated with a discrete set of hyperfine parameters $\vec{p}$ is a sum of Lorentzian lines of area A_l, centred at positions $\omega_l(\vec{p})$ and whose full width at half maximum (FWHM) is the intrinsic line width W_0. At velocity v, it is given by

$$E(\mathrm{v},\vec{p}) = \sum_l A_l L(\mathrm{v}-\omega_l(\vec{p}),W_0). \tag{73}$$

Inhomogeneous broadening occurs when a distribution of sites is probed at the same time, and the resulting signal is the convolution of the elemental multiplet of each site with the distribution of hyperfine parameters:

$$S(\mathrm{v}) = \int_{\Omega_p} E(\mathrm{v},\vec{p})\, P(\vec{p})\, d\vec{p} \tag{74}$$

where $P(\vec{p})$ is the total distribution of hyperfine parameters. We propose a model for extracting a true multidimensional distribution in both the paramagnetic and the magnetic case.

A.2.1 Paramagnetic Case

In the paramagnetic case, the only relevant hyperfine parameters are the quadrupole splitting Δ and the centre shift δ. The combined probability density distribution (PDD) is modelled by the following expression:

$$P(\delta,\Delta) = \sum_{i=1}^{n_\delta}\sum_{j=1}^{n_\Delta} \frac{p_{\delta_i} p_{\Delta_j}}{2\pi\sigma_{\delta_i}\sigma_{\Delta_j}\sqrt{1-\rho^2}} \times \exp\left(-\frac{1}{2(1-\rho^2)}\left(\frac{(\delta-\delta_{0_i})^2}{\sigma_{\delta_i}^2} + \frac{(\Delta-\Delta_{0_j})^2}{\sigma_{\Delta_j}^2} - 2\rho\frac{(\delta-\delta_{0_i})(\Delta-\Delta_{0_j})}{\sigma_{\delta_i}\sigma_{\Delta_j}} \right) \right) \quad (75)$$

where ρ is a correlation parameter between the centre shift and the quadrupole splitting. The partially integrated probability densities (PIPD) of the centre shift $P_\delta(\delta)$ and of the quadrupole splitting $P_\Delta(\Delta)$ are obtained by integrating out the other variable. This results in:

$$P_\delta(\delta) = \sum_{i=1}^{n_\delta} \frac{p_{\delta_i}}{\sqrt{2\pi}\sigma_{\delta_i}} \exp\left(-\frac{(\delta-\delta_{0_i})^2}{2\sigma_{\delta_i}^2} \right) \quad (4a)$$

$$P_\Delta(\Delta) = \sum_{j=1}^{n_\Delta} \frac{p_{\Delta_j}}{\sqrt{2\pi}\sigma_{\Delta_j}} \exp\left(-\frac{(\Delta-\Delta_{0_j})^2}{2\sigma_{\Delta_j}^2} \right) \quad (4b)$$

These PIPDs do not depend on the correlation parameter ρ which is removed by the partial integration. As in the VBF method they are expressed as sums of Gaussians. In addition, in the total distribution, they are independent or correlated via the parameter ρ. This can result in linear coupling when $\rho = \pm 1$.

When using the proposed PDD, the convolution with the elemental doublet of ^{57}Fe (or any Mössbauer isotope with a 3/2−1/2 transition) results in a sum of Voigt lines which, though they have no analytical expression, can be effectively approximated by several analytical functions [Rancourt89]. The final lineshape is given by:

$$S(\nu) = \sum_{l=1}^{2}\sum_{i=1}^{n_\delta}\sum_{j=1}^{n_\Delta} A_l p_{\delta_i} p_{\Delta_j} V(\nu-\delta_{0_i}-\alpha_l\Delta_{0_j}, \sigma_{ij,l}, W_0) \quad (77)$$

where $\alpha_l = \pm 1/2$ and

$$\sigma_{ij,l}^2 = \sigma_{\delta_i}^2 + \alpha_l^2\sigma_{\Delta_j}^2 + 2\rho\alpha_l\sigma_{\delta_i}\sigma_{\Delta_j} \quad (78)$$

Figs. 114 and 115 (a) through (c) illustrate the effect of the correlation on the spectrum and the probability density distribution.

The paramagnetic case is of great importance in the analysis of spectra of clay minerals, whose Mössbauer "signatures" reside not only in the average values of the hyperfine parameters but also in the shapes of their multi-parameter distributions. Since these distributions contain a

great deal of information regarding a mineral's structure and crystal chemistry [Rancourt94a, 94b, 94c], a method such as the one presented must be used to obtain reliable and, if possible, accurate distributions. The proposed PDD used is versatile enough to model a broader range of physical solutions and it can be used to explore the domain of solutions obtained from a Mössbauer spectrum in more detail than most other practical methods.

A.2.2 Magnetic Case

Within the perturbation limit, three hyperfine parameters suffice to describe the elemental sextet of ^{57}Fe. The centre shift δ, the quadrupole shift ε and the Zeeman splitting z produce a sextet whose lines are centred at $\omega_l(\delta,\varepsilon,z) = \delta + \alpha_l\varepsilon + \beta_l z$, where α_l and β_l are constants. The general PDD we propose in this case is a natural extension to the previous 2-dimensional case:

$$P(\delta,\varepsilon,z) = \sum_{i=1}^{n_\delta}\sum_{j=1}^{n_\varepsilon}\sum_{k=1}^{n_z} \frac{p_{\delta_i} p_{\varepsilon_j} p_{z_k}}{(2\pi)^{3/2}\sigma_{\delta_i}\sigma_{\varepsilon_j}\sigma_{z_k}\sqrt{1-\rho_0}} \times$$
$$\exp\left[-\frac{1}{2(1-\rho_0)}\left((1-\rho_{\varepsilon z}^2)\frac{(\delta-\delta_{0_i})^2}{\sigma_{\delta_i}^2} + (1-\rho_{\delta z}^2)\frac{(\varepsilon-\varepsilon_{0_j})^2}{\sigma_{\varepsilon_j}^2} + (1-\rho_{\delta\varepsilon}^2)\frac{(z-z_{0_k})^2}{\sigma_{z_k}^2}\right.\right.$$
$$-2(\rho_{\delta\varepsilon}-\rho_{\delta z}\rho_{\varepsilon z})\frac{(\delta-\delta_{0_i})(\varepsilon-\varepsilon_{0_j})}{\sigma_{\delta_i}\sigma_{\varepsilon_j}} - 2(\rho_{\delta z}-\rho_{\delta\varepsilon}\rho_{\varepsilon z})\frac{(\delta-\delta_{0_i})(z-z_{0_k})}{\sigma_{\delta_i}\sigma_{z_k}}$$
$$\left.\left.-2(\rho_{\varepsilon z}-\rho_{\delta\varepsilon}\rho_{\delta z})\frac{(\varepsilon-\varepsilon_{0_j})(z-z_{0_k})}{\sigma_{\varepsilon_j}\sigma_{z_k}}\right)\right], \tag{79}$$

with $\rho_0 = \rho_{\delta\varepsilon}^2+\rho_{\delta z}^2+\rho_{\varepsilon z}^2-2\rho_{\delta\varepsilon}\rho_{\delta z}\rho_{\varepsilon z}$. Here, when a single component is used for each distributed parameter, the 2D surface of equiprobability is an ellipsoid in 3D parameter space.

Once again, the PIPDs for each parameter is simply the sum of their Gaussian components, irrespective of the correlation parameters. Also, the convolution with the elemental sextet can be expressed as a sum of Voigt functions where only the Gaussian width is affected by the correlations:

$$S(v) = \sum_{l=1}^{6} A_l \sum_{i=1}^{n_\delta}\sum_{j=1}^{n_\varepsilon}\sum_{k=1}^{n_z} p_{\delta_i} p_{\varepsilon_j} p_{z_k}\, V(v-\delta_{0_i}-\alpha_l\varepsilon_{0_j}-\beta_l z_{0_k}, \sigma_{ijk,l}, W_0) \tag{80}$$

with

$$\sigma_{ijkl}^{2} = \sigma_{\delta_i}^{2} + \alpha_l^2\sigma_{\varepsilon_j}^{2} + \beta_l^2\sigma_{\zeta_k}^{2} + 2\rho_{\delta\varepsilon}\alpha_l\sigma_{\delta_i}\sigma_{\varepsilon_j} + 2\rho_{\delta\zeta}\beta_l\sigma_{\delta_i}\sigma_{\zeta_k} + 2\rho_{\varepsilon\zeta}\alpha_l\beta_l\sigma_{\varepsilon_j}\sigma_{\zeta_k} \quad (81)$$

The effect of each correlation is more complicated than in the paramagnetic case, because the six lines are affected differently, depending on the type of correlation. Figs. 116 (a) through (c) provide a description of the effect of the correlations and thus how to identify which ones are present from a visual inspection. It should also be noted that the effect of a correlation depends not only on the magnitude of the correlation parameter ρ_{ij}, but also on the widths of the parameter distributions.

A.3 Application to a Synthetic Taenite

To illustrate the power of this new model, we have chosen a spectrum of an $Fe_{65}Ni_{35}$ alloy (Invar) at 77 K. This is a simulated thin-limit spectrum obtained by correcting the measured spectrum for thickness effects by the method described by Rancourt [Rancourt95]. For comparison, results using the linear coupling VBF method are presented. Based on a visual inspection of the spectrum (fig. 117), it can be seen that the correlation between the quadrupole shift and the Zeeman splitting ($\rho_{\varepsilon\zeta}$) is dominant, so both these parameters will be distributed and correlated to measure the importance of each effect. We also assume the Zeeman splitting distribution will be the one with the most structure: in the xVBF model, only one Gaussian component will be used for the quadrupole shift distribution. In every case, the Lorentzian FWHM is frozen at W_0 but the background is allowed to vary for each fit. The centre shift is fitted but is not-distributed. Whatever the fitting model, the average quadrupole splitting was found to be 0 mm/s, as expected from the cubic symmetry of the crystal.

Table 29 shows the evolution of the fit with various fitting conditions, giving the parameters used, the number of fitted parameters and the resulting reduced χ^2. Table 30 gives a comparison of the parameters obtained from each method's best fit. It should be noted that when no correlations or couplings are present and only the Zeeman splitting is distributed, both models are identical. From Table 29, we see that a pure distribution of Zeeman splittings (HFD) is not adequate, but both a coupling or correlation and an independent QSD significantly improve the fit. The VBF fit cannot be further improved. Adding a correlation between the distributions in the xVBF model provides a statistically significant fit, and converges to a

physically sound distribution of parameters.

Fig. 117 also gives the residuals obtained from the best fit of each method, clearly showing that the linear coupling fails to provide accurate width for all the peaks. The xVBF method fits them more adequately because the distributions are only partially correlated.

In addition, the PIPDs of the Zeeman splitting and quadrupole shift from each method's best fit are given (figs. 118 and 119), along with the contour plot for the total PDD, as obtained from the xVBF method (fig. 120). One notes that whereas the HFD-PIPDs are essentially identical, the QSD-PIPDs for xVBF and VBF are significantly different.

A.4 Conclusion

It is obvious from the example presented that linear coupling is not in general adequate to model multidimensional distributions of hyperfine parameters. We propose an analytical model to deal with such cases. This model is also useful to explore distributions with varying degrees of complexity by changing the number of Gaussian components. An elementary assessment might use only pure Gaussian distributions, while a more detailed study can, in a controlled way, admit more and more complexity to any of the distributions. This versatility also allows it to better explore the often extremely degenerate solution to the problem of extracting hyperfine parameter distributions from Mössbauer spectra.

Table 29 Evolution of the fit quality with the complexity of the xVBF and VBF models.

xVBF	1HFD	9.5	7
	1HFD+1QSD	7.9	8
	1HFD+1QSD+$\rho_{\varepsilon z}$	5.7	9
	2HFD	5.7	10
	2HFD+1QSD	4	11
	2HFD+1QSD+$\rho_{\varepsilon z}$	1.9	12
	3HFD+1QSD+$\rho_{\varepsilon z}$	1.2	15
VBF	2HFD	5.7	10
	2HFD+coupling	4.1	11
	3HFD	5.1	13
	3HFD+coupling	3.4	14

Table 30 Comparison of the fitted parameters from the best fits using the xVBF and VBF models.

bkg (counts)	328740	100	328260	250
A_3 **(counts mm**	12910	140	12170	180
A_2/A_3	2.207	23	2.232	40
$\langle\delta\rangle$ **(mm/s)**	0.0249	15	0.0252	34
$\langle\varepsilon\rangle$ **(mm/s)**	-0.0002	17	N/A	
$\sigma_{\varepsilon 1}$ **(mm/s)**	0.088	38	N/A	
p_1 **(%)**	74.1		77.7	
z_1 **(mm/s)**	2.3475	23	2.3469	36
σ_{z1} **(mm/s)**	0.1286	42	0.1341	30
p_2 **(%)**	15.6	47	12.6	18
z_2 **(mm/s)**	2.092	91	2.047	53
σ_{z2} **(mm/s)**	0.267	33	0.239	28
p_3 **(%)**	10.2	16	9.6	19
z_3 **(mm/s)**	1.13	12	1.13	18
σ_{z3} **(mm/s)**	0.64	78	0.653	71
$\rho_{\varepsilon z}$	-0.341	22	N/A	
ε_0 **(mm/s)**	N/A		0.34	91
ε_1	N/A		-145	38

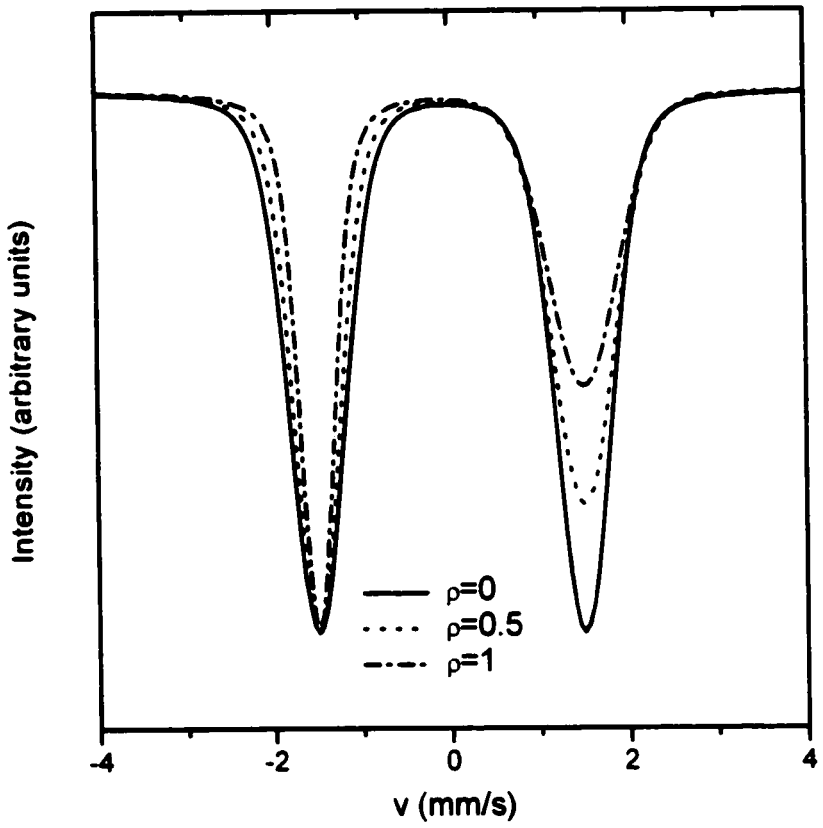

Figure 114 Effect of the δ-Δ correlation on the Mössbauer spectrum. All spectra use a single Gaussian distribution for the quadrupole splitting ($<\Delta>$ = 3 mm/s, σ_Δ = 0.8 mm/s) and the centre shift ($<\delta>$ = 0 mm/s, σ_δ = 0.2 mm/s).

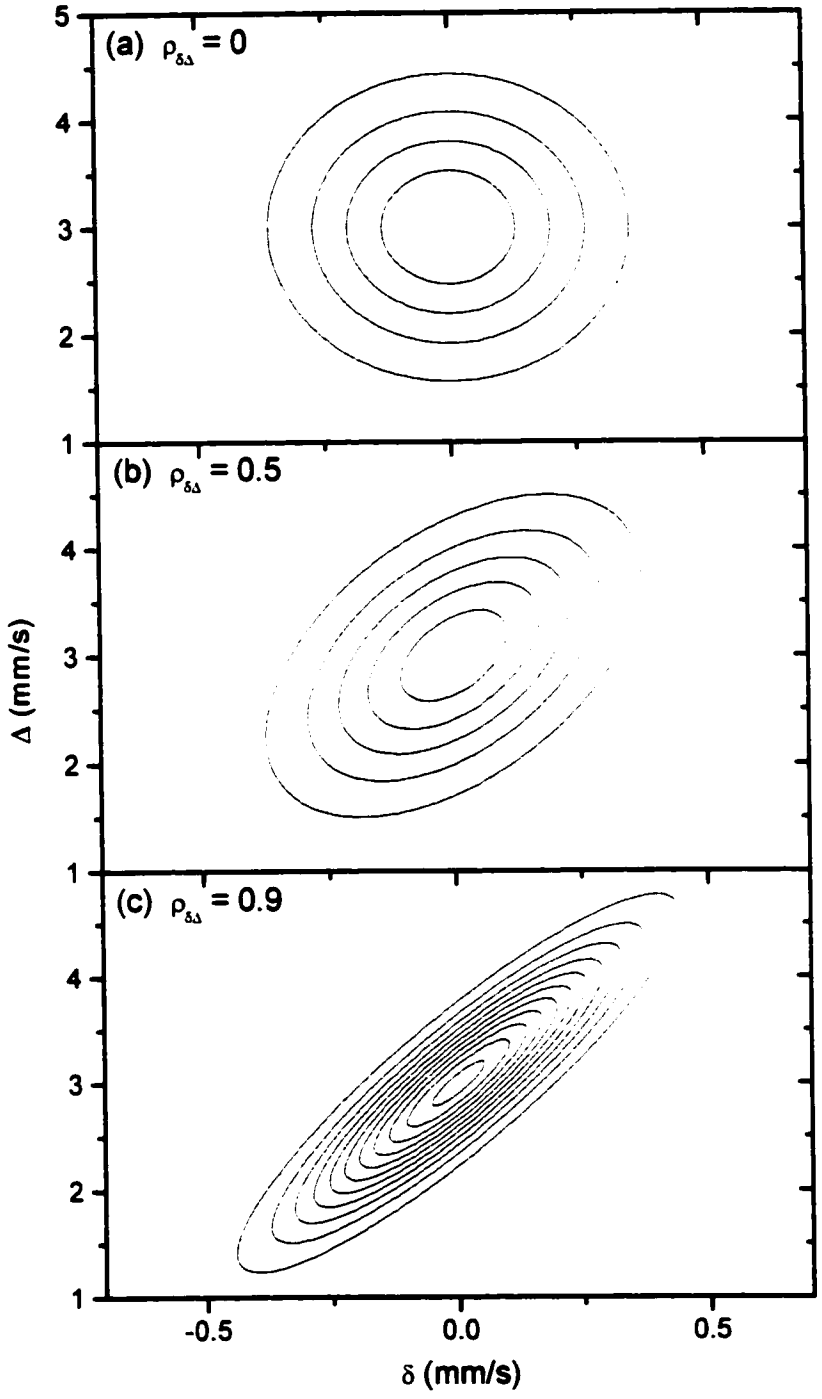

Figure 115 xVBF probability density contour plots corresponding to the spectra in fig. 114. (a) $\rho_{\delta\Delta} = 0$, (b) $\rho_{\delta\Delta} = 0.5$ and (c) $\rho_{\delta\Delta} = 0.9$ (instead of 1). In the case where $\rho_{\delta\Delta} = 1$, the contour plot would simply yield a straight line.

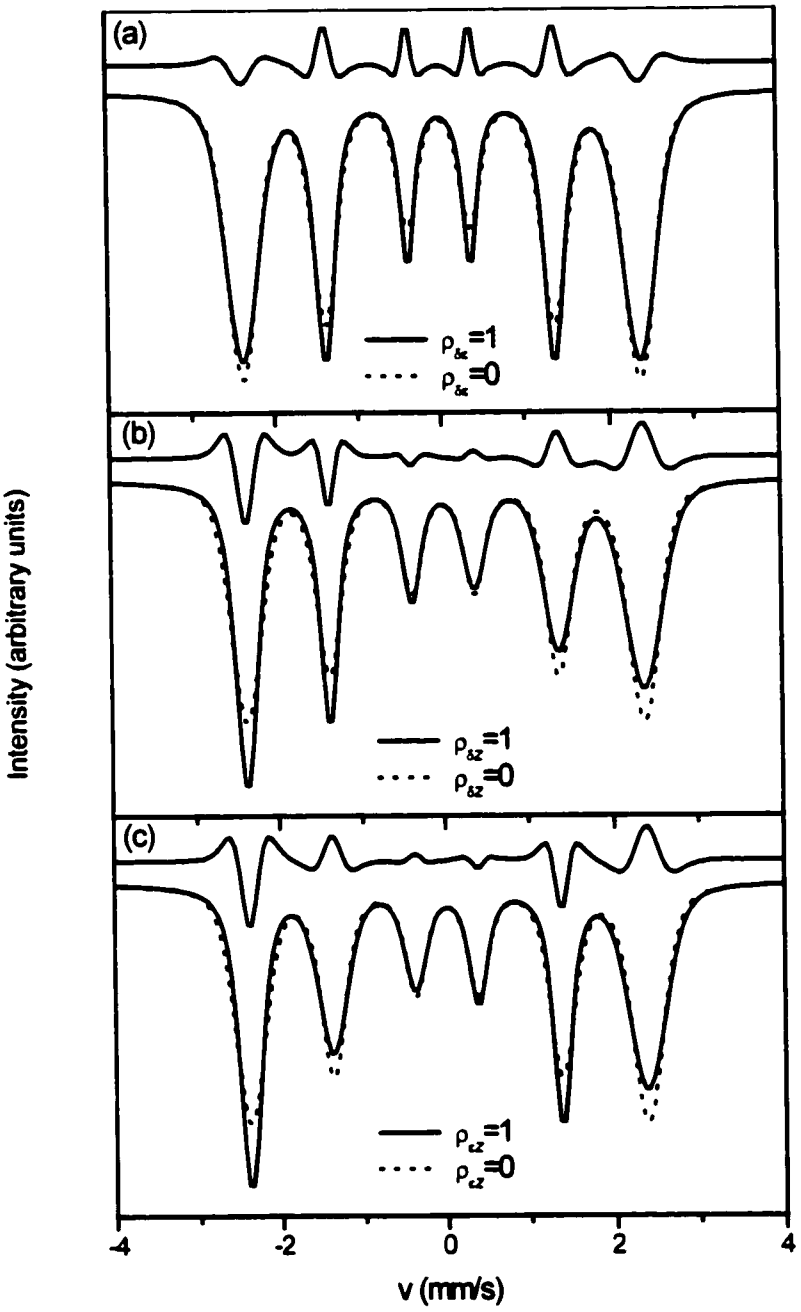

Figure 116 Effect of the various correlations on magnetically split Mössbauer spectra, compared to the spectra in the absence of correlations ($\rho = 0$). All spectra were generated using PIPDs with only a single Gaussian component for the Zeeman splitting ($<\delta> = 0$ mm/s and $\sigma_\delta = 0.05$ mm/s), the quadrupole shift ($<\varepsilon> = 0$ mm/s and $\sigma_\varepsilon = 0.05$ mm/s) and the centre shift ($<\delta> = 0$ mm/s and $\sigma_\delta = 0.05$ mm/s) with the following correlation parameters: (a) $\rho_{\delta\varepsilon} = 0$ and 1, (b) $\rho_{\delta z} = 0$ and 1 and (c) $\rho_{\varepsilon z} = 0$ and 1. The difference spectra between the spectra with uncorrelated and correlated distributions are also plotted on the same scale.

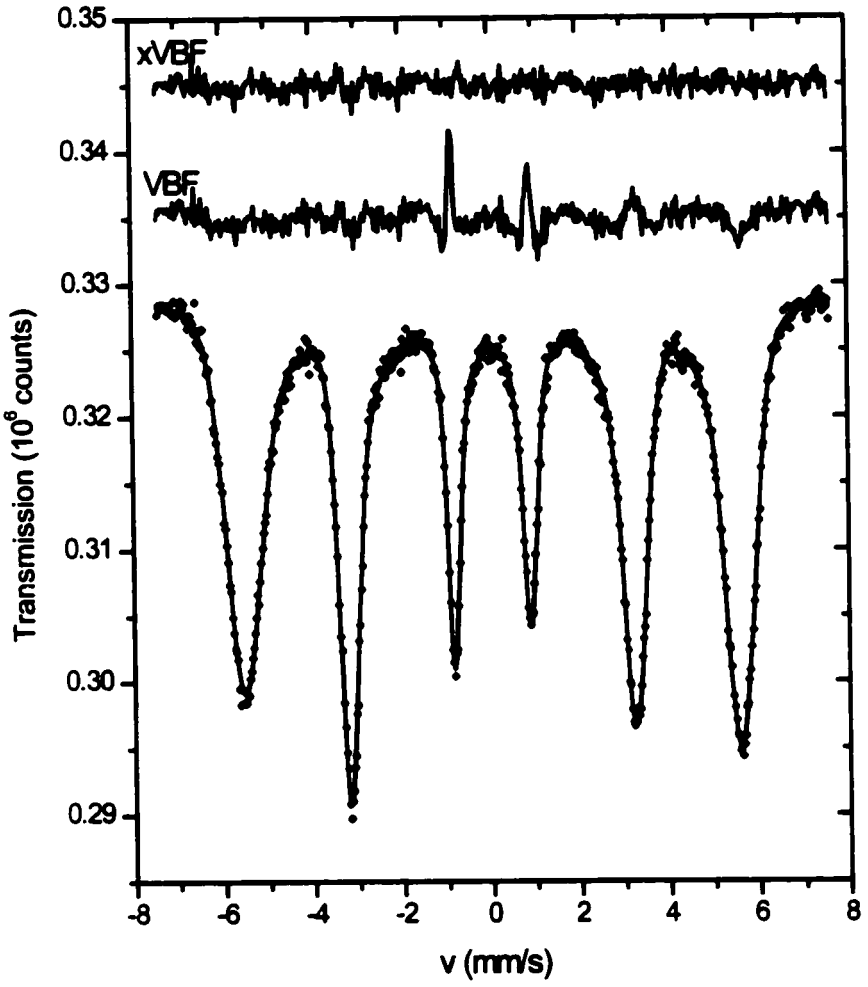

Figure 117 Thickness corrected Mössbauer spectrum of $Fe_{65}Ni_{35}$ at 77 K. The residuals spectra correspond to the best fits of the xVBF and VBF models, as explained in the text. Notice how the VBF model, which uses linear coupling, cannot correctly model all the peaks' widths, whereas the xVBF model does so correctly.

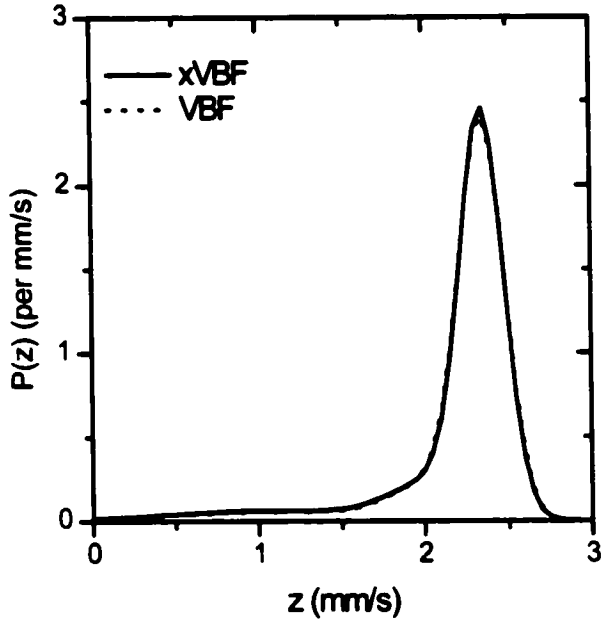

Figure 118 Partially integrated probability density (PIPD) of the Zeeman splitting z of the spectrum in fig. 117, as obtained by the xVBF (solid line) and VBF (dashed line) models.

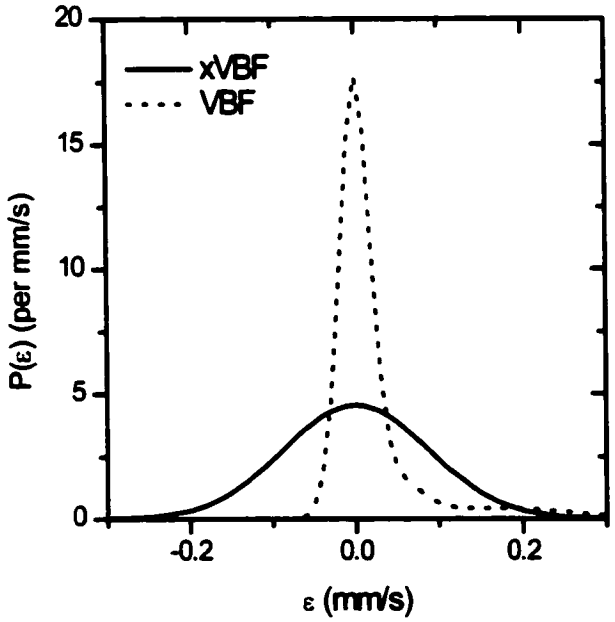

Figure 119 Partially integrated probability density (PIPD) of the quadrupole shift ε of the spectrum in fig. 117, as obtained by the xVBF (solid line) and VBF (dashed line) models. Notice the artificial "tail" in the distribution obtained by the VBF model, which is due to the coupling with the Zeeman splitting distribution.

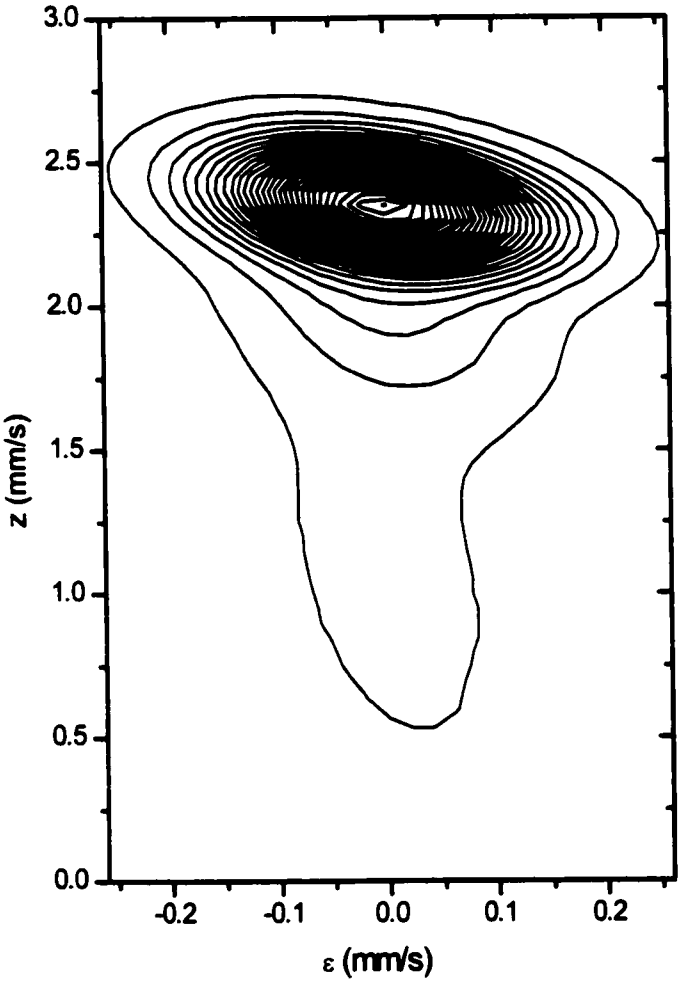

Figure 120 Contour plot of the total probability density distribution (PDD) of Zeeman splitting and quadrupole shift, obtained by the xVBF method.

Appendix B

A General Method for Removing Non-Uniform Thickness Effects in Mössbauer Spectra

In this section, we present a novel method for correcting spectra which were taken with absorber that have non-uniform thicknesses. The basic principles are the same as in the method of Rancourt and Ping [Rancourt96] which corrects for uniform thickness effects.

B.1 The Transmission Integral Formulation

If a source with recoilless fraction f_s emits γ-rays with a spectral distribution $L(E)$ onto a sample characterized by:

- a thickness t (in cm)
- n_a Mössbauer active nuclei per volume (in cm^{-3})
- a recoilless fraction f_a
- a resonant cross-section $\sigma_M(E)$ (in cm^2)
- a non-resonant mass absorption coefficient μ_e (in $cm^2 \cdot g^{-1}$)
- a density ρ (in $g \cdot cm^{-3}$)

then the transmission spectrum is

$$S(v) = e^{-\mu_e \rho t} \left[\eta_0 + (1 - f_s)\eta_M + \eta_M f_s \int_{-\infty}^{\infty} dE L(E - v)\, e^{-n_a f_a \sigma_M(E) t} \right] \quad (82)$$

where η_M and η_0 are the number of γ-rays from the Mössbauer transition (14.4 keV for ^{57}Fe spectroscopy) and from other (non 14.4 keV) transitions that impinge on the absorber. These numbers include any correction due to detector response and absorption in air.

B.2 Assumptions and Limitations

Before proceeding, here is a list of the assumptions that are made in deriving the following expressions and the limits of applicability:

1) Absence of geometrical or other experimental artefacts (cosine smearing, detector saturation, etc...).
2) Each granule of the absorber is non-polarizing (it is not too large to cause problems).
3) The absorber is thin enough so that multiple-absorption effects are not present.

Most of these conditions can be satisfied by correctly preparing the absorber. In some cases, however, it is not possible, and it will be impossible to correct for thickness effects.

B.3 Dealing with Non-Uniform Thickness

The absorber is modelled as a series of cylinders along the direction of the γ-ray. In each cylinder, the γ-ray must pass through a certain amount of material.
We will distinguish two physical situations:

① There is only resonantly absorbing material (any non-resonantly absorbing material must have a uniform thickness over the area of the absorber)

② The absorber is made of resonantly absorbing material (particles) in a non-resonantly absorbing matrix. The thickness of the absorber is considered uniform over its area.

In both cases, $P(t)$, the probability distribution of the thickness is sufficient to characterize the sample's non-uniformity. The transmission integral becomes, in each case:

$$① \quad S(v) = \int_0^\infty dt\, P(t)\, e^{-\mu_a \rho t} \left[\eta_0 + (1-f_s)\,\eta_M + \eta_M f_s \int_{-\infty}^{\infty} dE\, L(E-v)\, e^{-n f_a \sigma_M(E) t} \right] \tag{83}$$

$$\textcircled{2}\quad S(\nu) = \int_0^T dt\, P(t)\, e^{-\mu_{nr}\rho_{nr}(T-t)} e^{-\mu_e\rho t} \left[\eta_0 + (1-f_s)\eta_M + \eta_M f_s \int_{-\infty}^{\infty} dE\, L(E-\nu)\, e^{-n f_a \sigma_M(E) t} \right] \tag{84}$$

where the *nr* subscript refers to the non-resonantly absorbing matrix. T is the uniform absorber thickness. By making use of the Laplace transform of the thickness distribution,

$$F(s) = \int_0^{\infty} dt\, P(t)\, e^{-st}, \tag{85}$$

we can simplify these equations as

$$\textcircled{1}\quad S(\nu) = F(\mu_e\rho)\left[\eta_0 + (1-f_s)\eta_M\right] + \eta_M f_s \int_{-\infty}^{\infty} dE\, L(E-\nu)\, F(\mu_e\rho + n f_a \sigma_M(E)) \tag{86}$$

$$\textcircled{2}\quad S(\nu) = e^{-\mu_{nr}\rho_{nr}T}\Big[F(\mu_e\rho - \mu_{nr}\rho_{nr})\left[\eta_0 + (1-f_s)\eta_M\right] + \eta_M f_s \int_{-\infty}^{\infty} dE\, L(E-\nu)\, F(\mu_e\rho - \mu_{nr}\rho_{nr} + n f_a \sigma_M(E)) \Big] \tag{87}$$

In both cases, the first term of the RHS is a constant (the background), and all the spectral information is contained in the second term. These fundamental equations can now be used to treat many true physical scenarios

B.3.1 Some Physical Examples

- Absorber with holes (otherwise uniform thickness)

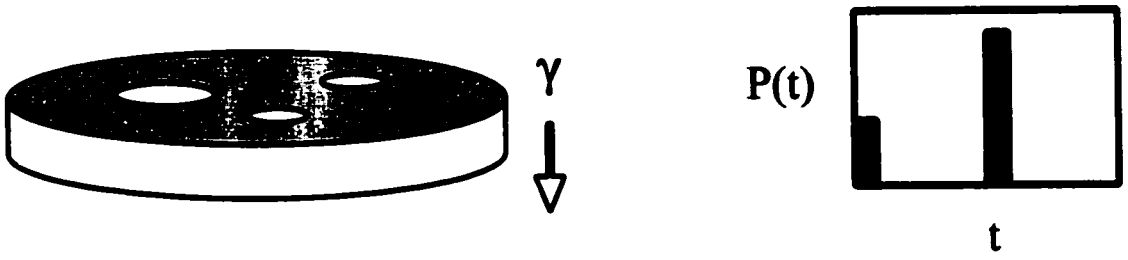

- Wedge-like absorber

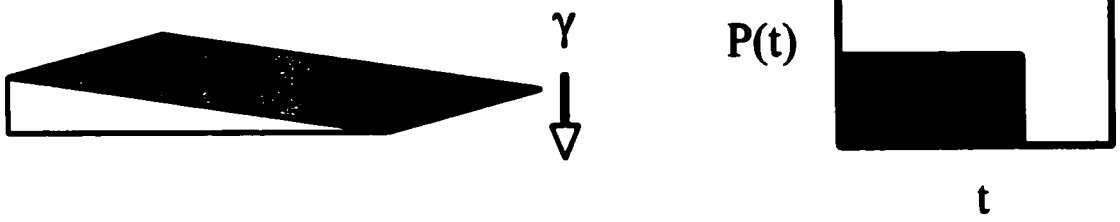

- Randomly distributed uniform sized particles (Poisson distribution)

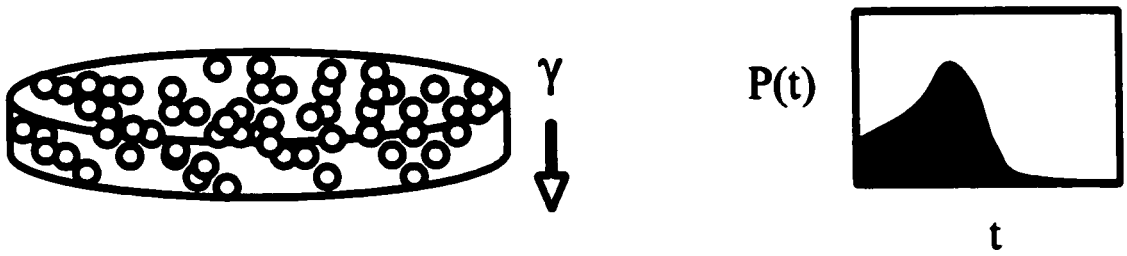

- Randomly distributed random sized particles (Normal distribution)

In each of the cases shown here, the Laplace transform can be calculated analytically. Otherwise, it might need to be evaluated numerically.

B.3.2 General Method to Correct for Non-Uniform Thickness Effects

B.3.2.1 Prior Knowledge About the Absorber

In order to apply the following method to correct for thickness effects, it is necessary to know:

- The thickness distribution $P(t)$ of the absorber. This might be inferred from knowledge of the absorber or it may be necessary to measure it experimentally.
- Some physical characteristics about the absorber and the matrix (if applicable): the density ρ, the mass absorption coefficient μ_e,

Since the total spectral area is known experimentally, and the total cross-section $\int dE\,\sigma_M(E)$ is also known, a normalisation condition can be applied to determine either

- $n_a f_a$, the Mössbauer properties of the absorber (which otherwise can be determined by the stoichiometry and a reasonable guess of f_a), or
- $\eta_M f_s$, the number of recoilless γ-rays that can be resonantly absorbed (which can otherwise be determined experimentally separately)

One of these parameters must be known in advance.

B.3.2.2 Pattern Smoothing using the Voigt Lineshape

Before trying to extract the intrinsic cross-section of the absorber, it is necessary to obtain a smooth spectrum, free of noise. A natural way of smoothing the spectrum is to fit it to an arbitrary number of Voigt lines, until one gets a statistically perfect fit, as is done in the method for correction of uniform thickness effects. Since the source spectral shape is a Lorentzian function with half-width at half maximum γ_0, it can be deconvoluted analytically from a sum of Voigt lines.

B.3.2.3 Self-Consistent Solution to the Problem

In both cases presented above, the calculated spectrum is of the form:

$$S(v) = A + B\int_{-\infty}^{\infty} dE\, L(E-v, \gamma_0)\, F(g(E)) \qquad (88)$$

and we wish to determine g(E). If the spectrum is expressed as a sum of Voigt lines,

$$S(v) = A + \sum_i V(v - v_i, \gamma_i, \sigma_i) \tag{89}$$

and we directly get

$$F(g(v)) = \frac{1}{B} \sum_i V(v - v_i, \gamma_i - \gamma_0, \sigma_i) \tag{90}$$

by using the fact that the convolution of a Voigt line with the source Lorentzian simply increases its Lorentzian γ parameter by γ_0.

- If B is known, we can determine $F(g(v))$ at any velocity, and hence solve for $g(v)$ (and thus $\sigma M(v)$). If $F(s)$ is an analytic function, this is very quick. The normalization condition on $\sigma M(v)$ will determine $n_a f_a$.

- If B is not known, using an estimate, we solve for $\sigma M(v)$, and use the normalization condition to improve the estimate of B. This is done iteratively until B and $\sigma M(v)$ are determined.

B.3.2.4 Generating a Thickness-Effect Free Spectrum

Once the cross-section $\sigma_M(v)$ of a material is known, it can be used to generate a spectrum which has no thickness effects, usually referred to as a thin-limit spectrum. A thin-limit spectrum is one where the first-order Taylor expansion of the exponential is valid, i.e.

$$e^{-n_a f_a \sigma_M(E) t} \approx 1 - n_a f_a \sigma_M(E) t . \tag{91}$$

If we chose to generate a spectrum with the same background as the original spectrum, we can simply use

$$S(v) = bkg - e^{-\mu_s \rho \bar{t}} \eta_M f_s n_a f_a \bar{t} \int_{-\infty}^{\infty} dE\, L(E - v)\, \sigma_M(E) \tag{92}$$

Now, if we add noise with the correct statistics, this spectrum can be analysed to get precise hyperfine parameters distributions and spectral areas with whatever model or program we want to use.

Appendix C

Correcting for Geometrical Artifacts in Mössbauer Spectra

C.1 Introduction

Geometrical effects are those which are due to the lateral dimensions of the source and absorber, as opposed to their thickness. They come from the fact that the Doppler shifting of the source does not shift the energy of the γ-ray independently from its direction, but rather by a factor $v \cos\theta$, where v is the velocity of the source and θ is the angle between the source direction and the direction of the emitted γ-ray. If the source and the absorber have large lateral dimensions or are put too close to each other, the measured signal actually results from an

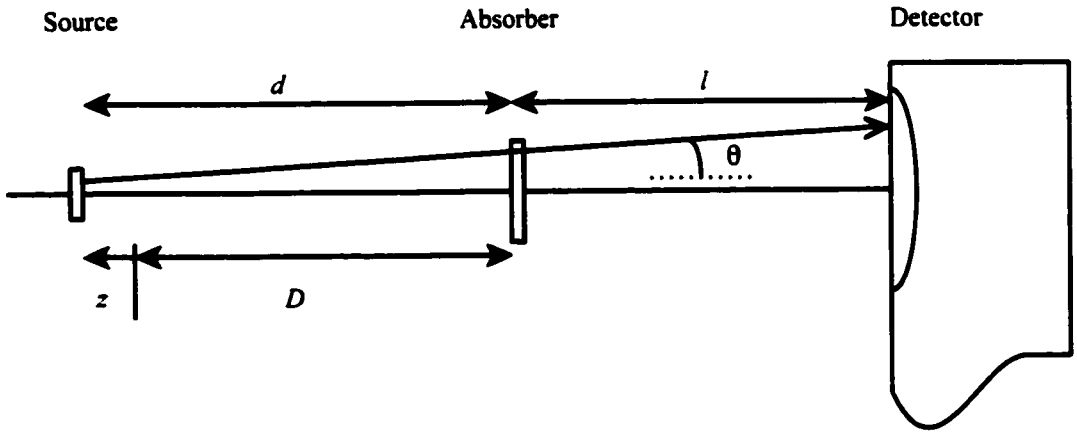

Figure 121 Schematic drawing of the MS geometrical specifications.

intrinsic signal modulated by many different velocities corresponding to all the possible angles linking points on the source to points on the absorber and on the detector. Assuming that the source and absorber are positioned as described in fig. 121, this is expressed mathematically as follows:

$$S(d,v) = \frac{I_0}{A_s}\int_{source} d\vec{a}_s \int_{absorber} d\vec{a}_a \frac{1}{[(d+l)/\cos\theta]^2}\tau(1/\cos\theta)\, S^0(v\cos\theta) \ . \qquad (93)$$

Both integrations are performed on the areas of the source and absorber. $S^0(v)$ is the true signal that would be obtained in the absence of geometrical artefacts (if both the source and the absorber were points along the direction of motion of the source). $\tau(x)$ is a function which describes the amount of signal generated by a relative thickness x of the absorber as compared to the signal along the direction of motion of the source. For a thin sample in transmission geometry, $\tau(x) = x$, that is the signal is proportional to the thickness of the material. The explicit separation of $\tau(x)$ and $S^0(v)$ in eq. 93 assumes that there are no thickness effects or distributions of thickness which would otherwise link the signal to thickness of the absorber in a non-linear way. θ is the angle between the direction of motion of the source and the line joining two positions on the source and absorber:

$$\cos\theta = \frac{\vec{v}\cdot(\vec{r}_a - \vec{r}_s)}{v\ ||\vec{r}_a - \vec{r}_s||} \ . \qquad (94)$$

The factor $1/[(d+l)/\cos\theta]^2$ takes into account the decrease of the intensity of the source with distance from the source to the detector (l is the distance between the sample and the detector). I_0 is the total intensity of the source, emitted isotropically from every point on an area A_s.

Based on this formalism, we can see that the integrand is linear in the intrinsic signal, which means that is we could decompose the intrinsic signal into a sum of peaks, then the resulting signal is a sum of the independently integrated modified peaks:

$$\begin{aligned} \text{if } S^0(v) &= \sum_i A_i P_i(v, \{m_i\}) \\ \text{then } S(d,v) &= \sum_i A_i \frac{I_0}{A_s}\int_{source} d\vec{a}_s \int_{absorber} d\vec{a}_a \frac{1}{[(d+l)/\cos\theta]^2}\tau(1/\cos\theta)\, P_i(v\cos\theta, \{m_i\}) \\ &= \sum_i A_i P_i'(v,d,\{m_i\}) \ . \end{aligned} \qquad (95)$$

If we fit the signal to a sum of modified peaks $P_i'(v,d,\{m_i\})$, then we can recover the intrinsic signal $S^0(v)$ and analyse it by whichever method we want. We shall now give an example to

show what geometrical effects can be in simple situations.

Consider a point source, such that there is no need to integrate over the source area., and a cylindrical absorber, such that integration over its area can be reduced to integration over its radius. $\cos\theta$ can be expressed as

$$\cos\theta = \frac{d}{\sqrt{d^2+r^2}} = \frac{1}{\sqrt{1+(r/d)^2}}, \tag{96}$$

such that the observed signal is:

$$S(d,v) = \frac{2\pi I_0}{(d+l)^2}\int_0^{R_a} dr\, r\, \frac{1}{1+(r/d)^2}\,\tau\left(\sqrt{1+(r/d)^2}\right) S^0\left(\frac{v}{\sqrt{1+(r/d)^2}}\right). \tag{97}$$

If we assume that $\tau(x) = x$ (the situations where this assumption is valid will be discussed later), then

$$S(d,v) = \frac{2\pi I_0}{(d+l)^2}\int_0^{R_a} dr\, r\, \frac{1}{\sqrt{1+(r/d)^2}}\, S^0\left(\frac{v}{\sqrt{1+(r/d)^2}}\right). \tag{98}$$

A change of variable $x = 1/\sqrt{1+(r/d)^2}$ further clarifies this expression:

$$S(d,v) = \frac{2\pi I_0 d^2}{(d+l)^2}\int_{1/\sqrt{1+(R_a/d)^2}}^{1} dx \frac{1}{x^2} S^0(v\,x). \tag{99}$$

If we take the limit of infinitely small or infinitely distant absorber ($R_a \ll d$), we retrieve $S(d \gg R_a, v) = \pi R_a^2 I_0 S^0(v)/(d+l)^2$ as expected. Eq. 99 shows that it is the ratio R_a/d which determines how much the spectrum will be distorted by geometrical effects.

C.2 Geometrical Effects on a Folded Spectrum

When a spectrum is accumulated in real time, the transmitted or emitted intensity is recorded as a function of time. Depending on the driving waveform, the velocity of the source can be expressed as a linear function of time (constant acceleration mode) or a sinusoidal function of time (sinusoidal mode). Because of the back-and-forth motion of the source, there are two points in space where the source has the same velocity, as seen in fig. 122 for a constant acceleration mode. In order to generate an intensity versus velocity spectrum, the velocity versus

time function is determined via calibration and the raw spectrum is "folded" such that channels corresponding to the same velocity are binned together. The folded spectrum will thus be expressed as

$$S^{folded}(v) = S(D+z, v) + S(D-z, v) \tag{100}$$

since the equal velocity positions correspond to opposite positions around the average source position. D is the distance from the average source position to the absorber along the source direction of motion (taken as the z axis).

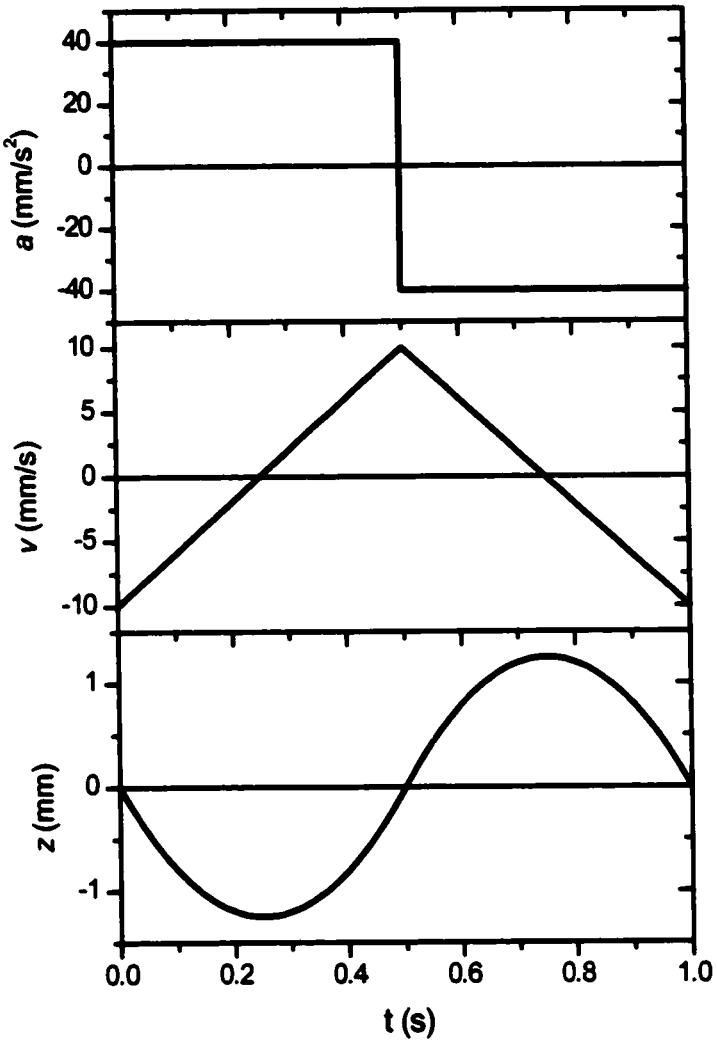

Figure 122 Illustration of the time dependence of the acceleration, velocity and source position in a "constant acceleration" mode.

C.2.1 Effect on the Background

If we assume there is no resonant absorption or emission (no Mössbauer active nuclei in the sample), then we can set $S^0(v)$ to a constant and calculate the observed background after folding for an identical setup with a Mössbauer active sample:

$$\begin{aligned} S^{folded}(v) &= 2\pi I_0 \left[\frac{(D+z)^2}{(D+l+z)^2} \int_{1/\sqrt{1+(R_a/(D+z))^2}}^{1} \frac{dx}{x^2} + \frac{(D-z)^2}{(D+l-z)^2} \int_{1/\sqrt{1+(R_a/(D-z))^2}}^{1} \frac{dx}{x^2} \right] \\ &= 2\pi I_0 \left[\frac{(D+z)^2}{(D+l+z)^2} \left(\sqrt{1+(R_a/(D+z))^2} - 1 \right) + \frac{(D-z)^2}{(D+l-z)^2} \left(\sqrt{1+(R_a/(D-z))^2} - 1 \right) \right]. \end{aligned} \tag{101}$$

A series expansion in R_a/D gives:

$$\begin{aligned} \frac{S^{folded}(v)}{2\pi I_0} &= \left[\frac{1}{(D+l+z)^2} + \frac{1}{(D+l-z)^2} \right] \frac{R_a^2}{2} \\ &\quad - \left[\frac{1}{(D+z)^2 (D+l+z)^2} + \frac{1}{(D-z)^2 (D+l-z)^2} \right] \frac{R_a^4}{8} + O\left(\frac{R_a}{D} \right)^6. \end{aligned} \tag{102}$$

Even if we keep only the leading term, we find that the background is not necessarily flat but does depend on the velocity (since z depends on the velocity):

$$\begin{aligned} \frac{S^{folded}(v)}{2\pi I_0} &= \left[\frac{1}{(D+l+z)^2} + \frac{1}{(D+l-z)^2} \right] \frac{R_a^2}{2} \\ &= \left[1 + 3\left(\frac{z}{D+l} \right)^2 + O\left(\frac{z}{D+l} \right)^4 \right] \frac{R_a^2}{(D+l)^2} \end{aligned} \tag{103}$$

The exact form of the background depends on $z(v)$, but the following conclusions can be drawn: $z = 0$ occurs at the maximum (positive and negative) velocities, whereas z is maximum when $v = 0$. The background thus has a bell-shaped curve with a maximum at the zero-velocity point, as shown in fig. 123. The amount of curvature depends on the extent of the motion of the source relative to the source-detector distance, $z_{max}/(D+l)$. This type of background is rarely encountered in transmission geometries where the users usually set conditions to avoid geometrical artefacts, but it is more common in CEMS where the source can be positioned and moving very close to the absorber. It is interesting to note that the background shape depends

more on the extent of the motion of the source, rather than the actual size of the absorber. Even for a small absorber, if the source motion is large, there will be this effect. The reason this effect should be taken into account, is that when spectral areas are compared, features that occur at different velocities are modulated by a different amount, so precise area ratios might be affected (only when dealing with precisions of better than 1%).

C.2.2 Effect on the Peak Shape

To show how a peak can be distorted, we will use a simplified version of eqs. 99 and 100. We first assume that the source motion is infinitely small compared to the source-sample distance ($z_{max} \ll D, d = D$) and that the detector is directly located behind the absorber ($l = 0$). In this case, the folded spectrum becomes

$$S(v) = 4\pi I_0 \int_{1/\sqrt{1+(R_d/D)^2}}^{1} dx \frac{S^0(v\,x)}{x^2} \tag{104}$$

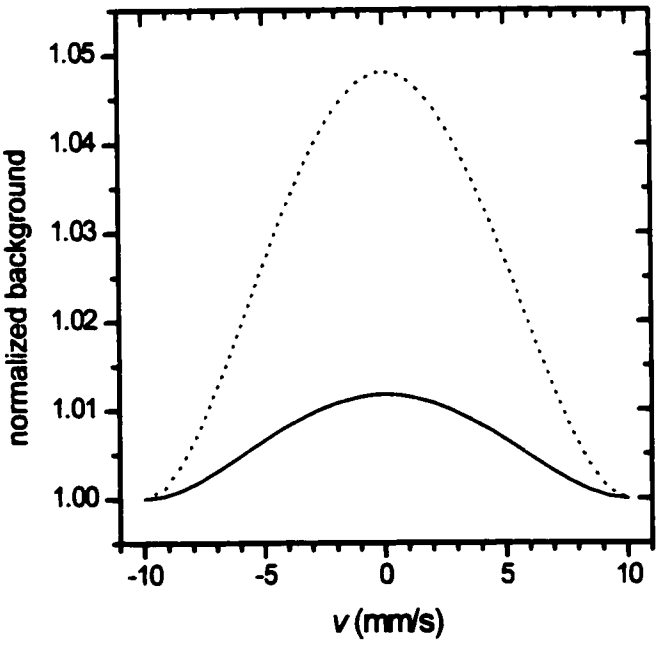

Figure 123 Effect of source motion on the background in a folded spectrum. The solid and dashed lines represent cases where $z_{max}/(D+l) = 1/20$ and $z_{max}/(D+l) = 1/10$, respectively, for a constant acceleration waveform with a frequency of 1 Hz, and a range of ± 10 mm/s.

Neglecting the source-sample distance simply avoids the artifact described in the previous section. Setting $l = 0$ simply changes the pre-factor, and doesn't affect the shape of the spectrum. Let us now consider the effect of the relative absorber radius (R_a/D) on a Lorentzian peak centred on $\nu_0 = 5$ mm/s, with a HWHM $\gamma = 0.1$ mm/s:

$$S^0(\nu) = \frac{\gamma}{\pi} \frac{1}{(\nu-\nu_0)^2 + \gamma^2} \tag{105}$$

The folded spectrum can be evaluated analytically as

$$\begin{aligned} S(\nu) = & \left[\nu (\nu_0^2 - \gamma^2) \left[\tan^{-1}\left(\frac{\nu - \nu_0}{\gamma} \right) - \tan^{-1}\left(\frac{\nu/\alpha - \nu_0}{\gamma} \right) \right] \right. \\ & \left. - \gamma \nu \nu_0 \ln \left[\frac{(\nu - \nu_0)^2 + \gamma^2}{\alpha^2 [(\nu/\alpha - \nu_0)^2 + \gamma^2]} \right] + \gamma (\nu_0^2 + \gamma^2)(\alpha - 1) \right] / \left[\pi (\nu_0^2 + \gamma^2)^2 \right] \end{aligned} \tag{106}$$

where $\alpha = \sqrt{1 + (R_a/D)^2}$. Figs. 124 through 126 show the effect of the ratio of finite size of the absorber to the distance from the sample. In fig. 126, we see that an increase absorber size causes a shifting to higher velocities (because the effective velocity seen at the edge of the absorber is lower, where resonant absorption does occur), and also a broadening of the peak. The actual shift in position and broadening of the peak is shown in fig. 125. We see that the position has an approximately quadratic dependence on R_a/D, whereas the FWHM has a quartic dependence. However, to get accurate peak positions and widths, it is necessary to use small absorbers, or to correct for this effect. Finally, from fig. 124, we also see that the effect becomes more pronounced for peaks at larger velocities, so all the peaks of a spectrum will be affected differently.

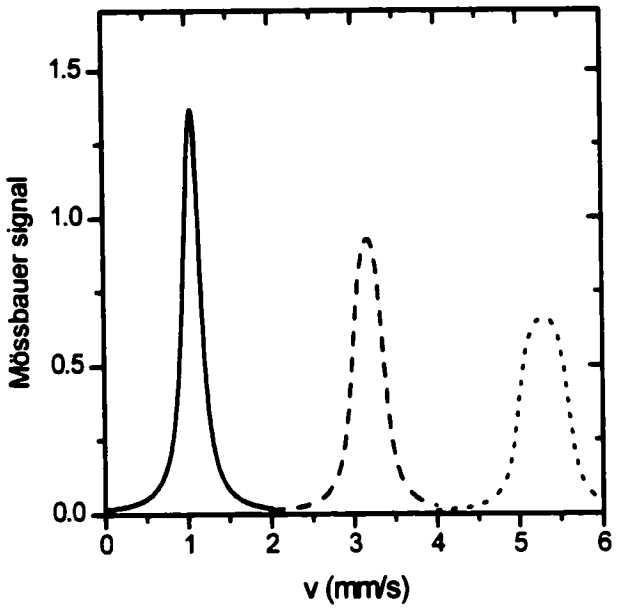

Figure 124 Effect of cosine smearing at different peak positions. All peaks are calculated with $R_a/D = 1/2$.

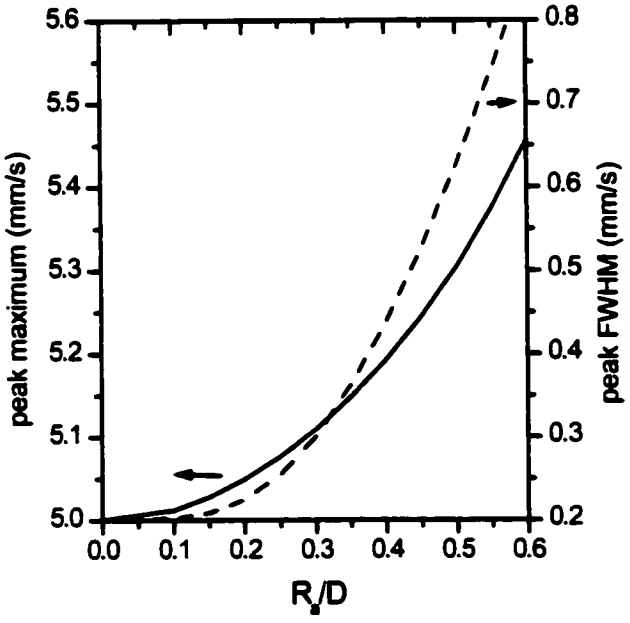

Figure 125 Effect of R_a/D on the position of the maximum (—) and on the FWHM (···) of a peak located at $v_0 = 5$ mm/s.

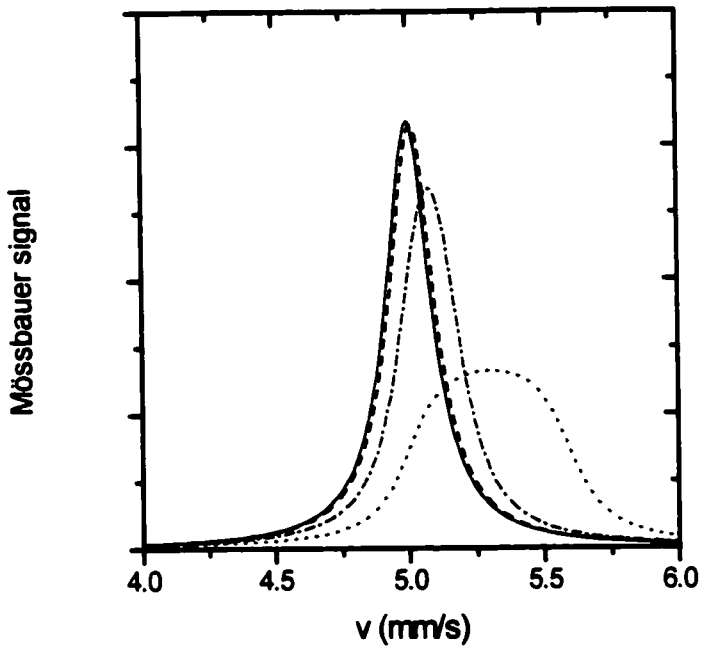

Figure 126 Effect of R_a/D on a peak located at v_0 = 5 mm/s. R_a/D ratios are (—) 1/100, (- -) 1/10, (- ·-) 1/4, (···) 1/2.

C.3 Correcting for Geometrical Artifacts

Now that we have established the potential for errors from fitting a spectrum which exhibits geometrical artifacts, we will show how it is possible to correct the effects and generate a "clean" spectrum which can be analysed by any suitable method.

First of all, as previously stated, the Mössbauer signal must be proportional to the cross-section, so only spectra of thin absorbers can be treated. This, fortunately, includes CEMS spectra, since the short escape depth of electrons results in an effectively thin sample. It is also necessary to have a calibration 1) relative to the *source velocity*, as opposed to a calibration relative to a standard material (a simple offset of the velocities can be applied) and 2) that is free of geometrical effects. This second point means that the calibration spectrum couldn't be taken in the same condition as the distorted spectrum. This is important because if the calibration spectrum includes geometrical effects, the peak positions won't be correct, and the calibration will artificially (and incorrectly) "correct" for erroneous peak positions. It is, however, also

possible to treat an unfolded calibration spectrum to get the "true" calibration. But if a spectrum is already folded, it must be folded from the true velocity of the source.

So assume we have such a folded spectrum of a thin sample but which was taken in a non-ideal geometry. Eq. 100 shows that the folded signal is comprised of two terms which depend on the motion of the source. Either we assume the motion is negligible ($z_{max} \ll D$) or we must use the function $d(v)$ giving the position of the source as a function of velocity, which is given from the calibration $v(t)$, as

$$d(v_0) = \int_0^{t_0} dt' \, v(t') , \tag{107}$$

where $v(t_0) = v_0$. Now if the true Mössbauer signal is given by a sum of some function, as expressed in eq. 95, then we can calculate, using eqs. 95 and 100 the resulting distorted signal, assuming the geometry of the source and sample are known. The solution is thus to simply fit the observed signal with an arbitrary number of distorted peaks, such that the fit is statistically significant ($\chi^2 \approx 1$). The original Mössbauer signal is simply the sum of the undistorted peaks, it is merely necessary to add noise according to its statistical distribution, and we have a distortion free spectrum which can be analysed by whatever means we want.

There is, of course, the problem of the function $\tau(x)$, which related the amount of signal to the thickness x of the sample (in the direction of the γ-ray). As previously stated, for a thin transmission absorber, $\tau(x) = x$. For a CEMS signal, it is necessary to know the relation between the intensity and the depth at which the emitting site was located. Although this problem can be complicated, it is in general tractable, so we could still calculate the integral in eq. 95 and correct the spectrum.

Appendix D

Tables of Results of Analyses of High Temperature MS Spectra

The following tables list the parameters which result from various analyses of the high-temperature MS spectra dealt with in chapter 6. Table 46 lists the resulting extracted average *IS* and *z* from these various analyses. In all cases, a 2-σ (95 %) fitting uncertainty is given in the second column for each parameter, except for the average *IS* (table 46) where the 1-σ (67 %) uncertainty includes the uncertainty due to the fitting and the uncertainty due to the temperature calibration. The temperatures for each spectrum are given in table 46. In some cases, the parameters for magnetically split and paramagnetic spectra are listed in the same table. In those cases, the quadrupole shift and quadrupole splitting, as well as the widths of their distributions, are given in the same column but should not be considered equivalent.

Table 31 Parameters of the xVBF fits of Mössbauer spectra of $Fe_{30}Ni_{70}$.

Hfe3000	0.98	1025930	162	0.109	0.011	120715	2538	2.87	0.07	2.18	0.05	0	0
Hfe3001	0.96	1914320	240	0.113	0.008	206946	3224	2.81	0.07	2.16	0.05	0	0
Hfe3002	0.86	1392900	176	0.116	0.012	134473	2545	2.82	0.07	2.11	0.05	0	0
Hfe3003	0.66	1436190	181	0.178	0.015	119815	2339	2.97	0.11	2.15	0.07	0	0
Hfe3004	0.68	1395200	156	0.115	0.009	108088	1659	2.77	0.11	1.94	0.07	0	0
Hfe3005	1.07	1580600	181	0.127	0.014	111443	2198	2.57	0.08	1.68	0.06	0	0
Hfe3007	0.84	1201010	129	0.186	0.024	89619	1799	2.71	0.21	1.84	0.13	0	0
Hfe3006	0.69	429935	52	0.117	0.007	22583	387	1	0			0	0

Hfe3000	0	0	-0.402	0.102	0.0237	0.0026	0	0	0	0	0.073	0.016
Hfe3001	0	0	-0.394	0.056	-0.0359	0.0020	0	0	0	0	0.081	0.010
Hfe3002	0	0	-0.243	0.034	-0.1119	0.0031	0	0	0	0	0.107	0.011
Hfe3003	0	0	-0.288	0.198	-0.1838	0.0032	0	0	0	0	0.082	0.031
Hfe3004	0	0	-0.237	0.054	-0.2496	0.0027	0	0	0	0	0.080	0.016
Hfe3005	0	0	-0.112	0.047	-0.3157	0.0033	0	0	0	0	0.111	0.017
Hfe3007	-0.072	0.068	0	0	-0.3533	0.0050	0.090	0.032	0	0	0	0
Hfe3006					-0.3959	0.0020	0	0	0.165	0.004	0.088	0.026

Hfe3000	0.219	0	1.912	0.013	0.064	0.014	0.781	0.078	2.040	0.011	0.115	0.007
Hfe3001	0.258	0	1.855	0.008	0.058	0.011	0.742	0.084	1.967	0.011	0.105	0.004
Hfe3002	0.877	0	1.799	0.014	0.084	0.012	0.123	0.205	1.998	0.065	0.051	0.041
Hfe3003	0.147	0	1.596	0.020	0.021	0.032	0.853	0.141	1.687	0.015	0.098	0.008
Hfe3004	0.769	0	1.500	0.008	0.059	0.007	0.231	0.128	1.610	0.060	0.083	0.031
Hfe3005	1	0	1.211	0.002	0.067	0.004						
Hfe3007	1	0	0.901	0.003	0.072	0.008						
Hfe3006												

Table 32 Parameters of the xVBF fits of Mössbauer spectra of $Fe_{50}Ni_{50}$.

Hfe5010	0.98	361577	146	0.131	0.014	78456	2168	2.70	0.07	2.05	0.05	0	0
Hfe5010 (2)	0.97	361546	92	0.127	0.010	77965	1505	2.72	0.08	2.07	0.05	-0.69	0.68
Hfe5011	1.12	657568	75	0.122	0.005	131159	810	2.72	0.03	2.06	0.02	0	0
Hfe5011 (2)	1.09	657606	121	0.125	0.007	131765	1731	2.72	0.04	2.05	0.03	0.18	0.24
Hfe5012	0.92	495401	99	0.108	0.009	87887	1399	2.83	0.09	2.12	0.06	0	0
Hfe5012 (2)	0.92	495379	118	0.106	0.009	87545	1470	2.84	0.08	2.15	0.06	-0.92	0.54
Hfe5013	0.74	481212	65	0.140	0.010	79885	979	2.71	0.07	2.05	0.05	0	0
Hfe5013 (2)	0.74	481213	87	0.140	0.012	79898	1165	2.72	0.06	2.05	0.05	0.06	1.00
Hfe5014	0.71	455202	86	0.153	0.021	68955	1083	2.53	0.08	1.99	0.05	0	0
Hfe5014 (2)	0.70	455202	64	0.152	0.016	68952	1059	2.54	0.08	1.98	0.07	0.18	1.01
Hfe5015	0.70	354378	44	0.157	0.005	33062	300	1	0			0	0
Hfe5015 (2)	0.71	354378	37	0.157	0.006	33053	297	1	0			0.09	0.12
Hfe5016	0.73	417332	53	0.160	0.008	35702	506	1	0			0	0
Hfe5016 (2)	0.72	417329	51	0.159	0.008	35660	427	1	0			0.21	0.23

Hfe5010	0	0	-0.43	0.09	0.0371	0.0029	0	0	0	0	0.083	0.016
Hfe5010 (2)	-0.25	0.15	-0.53	0.11	0.0374	0.0032	0.020	0.006	0	0	0.066	0.015
Hfe5011	0	0	-0.36	0.03	-0.0226	0.0012	0	0	0	0	0.091	0.005
Hfe5011 (2)	-0.13	0.12	-0.39	0.02	-0.0223	0.0023	0.030	0.019	0	0	0.088	0.006
Hfe5012	0	0	-0.33	0.05	-0.0980	0.0021	0	0	0	0	0.090	0.012
Hfe5012 (2)	0.03	0.12	-0.41	0.07	-0.0981	0.0030	0.022	0.005	0	0	0.068	0.019
Hfe5013	0	0	-0.48	0.32	-0.1716	0.0033	0	0	-0.007	0.003	0.049	0.023
Hfe5013 (2)	-0.11	0.38	-0.58	0.17	-0.1715	0.0025	0.025	0.032	-0.007	0.003	0.042	0.010
Hfe5014	0	0	-0.19	0.09	-0.2478	0.0036	0	0	0	0	0.078	0.029
Hfe5014 (2)	0.22	0.24	-0.17	0.10	-0.2493	0.0039	0.047	0.038	0	0	0.075	0.036
Hfe5015					-0.3381	0.0013	0	0	0.189	0.004	0.095	0.017
Hfe5015 (2)					-0.3376	0.0021	0.036	0.008	0.189	0.005	0.065	0.018
Hfe5016					-0.4080	0.0024	0	0	0.190	0.013	0.114	0.040
Hfe5016 (2)					-0.4062	0.0019	0.038	0.014	0.190	0.009	0.092	0.027

Hfe5010	0.898	0	2.121	0.007	0.106	0.005	0.102	0.048	2.276	0.014	0.038	0.030
Hfe5010 (2)	0.897	0	2.121	0.006	0.110	0.006	0.103	0.047	2.274	0.019	0.049	0.029
Hfe5011	0.944	0	2.013	0.003	0.104	0.002	0.056	0.020	2.152	0.004	0.000	0.016
Hfe5011 (2)	0.915	0	2.009	0.003	0.101	0.005	0.085	0.020	2.148	0.008	0.001	0.018
Hfe5012	0.938	0	1.822	0.004	0.100	0.005	0.062	0.031	1.999	0.023	0.029	0.045
Hfe5012 (2)	0.941	0	1.823	0.005	0.105	0.005	0.059	0.030	2.000	0.018	0.042	0.031
Hfe5013	0.312	0	1.458	0.045	0.107	0.017	0.688	0.184	1.598	0.018	0.092	0.010
Hfe5013 (2)	0.281	0	1.448	0.028	0.104	0.015	0.719	0.082	1.596	0.009	0.093	0.007
Hfe5014	0.241	0	1.319	0.033	0.082	0.029	0.759	0.128	1.158	0.023	0.130	0.013
Hfe5014 (2)	0.247	0	1.316	0.025	0.080	0.023	0.753	0.122	1.157	0.024	0.129	0.014
Hfe5015												
Hfe5015 (2)												
Hfe5016												
Hfe5016 (2)												

Table 33 Parameters of the xVBF fits of Mössbauer spectra of $Fe_{60}Ni_{40}$.

Hfe6000	0.76	221816	95	0.155	0.022	34913	1271	2.57	0.12	1.99	0.08	0	0
Hfe6000 (2)	0.74	221771	75	0.104	0.009	34020	1113	3	0	2.23	0.05	0	0
Hfe6001	0.85	1221590	199	0.130	0.018	176601	2680	3	0	2.16	0.04	0	0
Hfe6002	0.79	1329760	140	0.153	0.023	156114	2117	3	0	2.44	0.09	-0.97	0.50
Hfe6003	0.66	1279550	90	0.098	0.014	120400	968	3	0	2.86	0.55	0	0
Hfe6003 (2)	0.66	1279550	83	0.097	0.016	120536	886	3	0	2.86	0.41	0	0
Hfe6004	0.81	698887	59	0.155	0.009	38282	785	1	0	0	0	0	0
Hfe6004 (2)	0.68	698854	67	0.123	0.016	34429	2503	1	0	0	0	0	0
Hfe6005	0.79	2035260	108	0.129	0.012	97327	4396	1	0	0	0	0	0
Hfe6006	0.68	773409	71	0.131	0.012	36052	950	1	0	0	0	0	0
Hfe6007	0.88	1352260	110	0.097	0.002	187505	1527	3	0	1.88	0.03	-0.89	0.10

Hfe6000	0	0	-0.47	0.38	0.0311	0.0036	0	0	0	0	0.050	0.029
Hfe6000 (2)	0	0	-0.25	0.06	0.0310	0.0037	0	0	0	0	0.087	0.012
Hfe6001	0	0	-0.33	0.13	-0.0357	0.0037	0	0	0	0	0.078	0.029
Hfe6002	0.11	0.21	-0.33	0.19	-0.1068	0.0057	0.038	0.029	0	0	0.042	0.022
Hfe6003	-0.08	0.17	0	0	-0.1867	0.0078	0.090	0.045	0	0	0	0
Hfe6003 (2)	0	0	0.11	0.23	-0.1817	0.0080	0	0	0	0	0.088	0.038
Hfe6004	0	0	0	0	-0.2752	0.0035	0	0	0	0	0.219	0.018
Hfe6004 (2)	0	0	0	0	-0.2823	0.0037	0	0	0	0	0.252	0.018
Hfe6005	0	0	0	0	-0.3516	0.0029	0	0	0	0	0.256	0.015
Hfe6006	0	0	0	0	-0.4216	0.0022	0	0	0	0	0.267	0.017
Hfe6007	-0.01	0.09	-0.45	0.04	0.0318	0.0018	0.032	0.003	0	0	0.072	0.005

Hfe6000	0.806	0	2.066	0.017	0.109	0.012	0.194	0.136	1.862	0.073	0.183	0.051
Hfe6000 (2)	0.757	0	2.065	0.006	0.119	0.005	0.210	0.043	1.839	0.066	0.230	0.039
Hfe6001	0.556	0	1.877	0.010	0.123	0.006	0.340	0.063	1.668	0.039	0.195	0.018
Hfe6002	0.155	0	0.675	0.140	0.288	0.066	0.507	0.091	1.536	0.019	0.149	0.015
Hfe6003	0.626	0	0.756	0.047	0.341	0.022	0.374	0.075	0.342	0.023	0.210	0.023
Hfe6003 (2)	0.629	0	0.753	0.055	0.345	0.014	0.371	0.097	0.344	0.018	0.211	0.053
Hfe6004												
Hfe6004 (2)												
Hfe6005												
Hfe6006												
Hfe6007	0.675	0	2.086	0.003	0.119	0.002	0.275	0.020	1.930	0.012	0.188	0.009

Table 34 Parameters of the xVBF fits to Mössbauer spectra of $Fe_{67}Ni_{33}$.

Hfe6700	0.82	461872	73	0.098	0.003	96625	993	3	0	1.883	0.063	0	0
Hfe6701	0.63	1550560	68	0.097	0.001	281767	930	3	0	1.958	0.061	0	0
Hfe6702 (2)	0.76	2127180	142	0.158	0.008	186257	1835	3	0	2	0	0	0
Hfe6702	0.87	2127010	125	0.191	0.005	184257	1654	1	0			0.96	0.06
Hfe6703	0.87	2169960	149	0.172	0.004	168454	1154	1	0			1.0	1.0
Hfe6703 (2)	0.68	2169910	94	0.160	0.004	162571	1445	1	0			0.77	0.17
Hfe6704	0.76	993687	68	0.175	0.005	71309	811	1	0			0.96	1.70
Hfe6704 (2)	0.66	993638	87	0.158	0.005	68419	822	1	0			-1.00	0.32
Hfe6705	0.63	1969820	80	0.162	0.004	128182	1056	1	0			0.11	0.65
Hfe6706	0.62	1479390	97	0.162	0.007	91718	1331	1	0			1.00	0.19
Hfe6706 (2)	0.64	1479370	96	0.156	0.006	89764	1518	1	0			0	0
Hfe6707	0.83	3093040	299	0.098	0.006	632072	3712	3	0	1.661	0.050	0	0

Hfe6700	0.164	0.073	0	0	0.0163	0.0071	0.101	0.015	0	0	0	0
Hfe6701	0.125	0.043	0	0	-0.0471	0.0042	0.086	0.008	0	0	0	0
Hfe6702 (2)	1.000	0.101	0	0	-0.1330	0.0016	0.099	0.013	0	0	0	0
Hfe6702					-0.1358	0.0015	0.063	0.016	0.152	0.019	0.061	0.016
Hfe6703					-0.2130	0.0012	0.014	0.020	0.154	0.009	0.113	0.050
Hfe6703 (2)					-0.2179	0.0015	0.009	0.002	0.163	0.008	0.113	0.021
Hfe6704					-0.2928	0.0019	0.001	0.005	0.163	0.007	0.035	0.046
Hfe6704 (2)					-0.2967	0.0021	0.004	0.003	0.168	0.007	0.092	0.025
Hfe6705					-0.3665	0.0011	0.024	0.011	0.168	0.006	0.034	0.023
Hfe6706					-0.4251	0.0021	0.008	0.004	0.155	0.029	0.141	0.035
Hfe6706 (2)					-0.4299	0.0026	0.027	0.027	0.151	0.035	0.146	0.021
Hfe6707	0.082	0.027	0	0	0.0210	0.0036	0.154	0.009	0	0	0	0

Hfe6700	0.666	0	1.048	0.024	0.519	0.016	0.334	0.024	1.743	0.007	0.205	0.010
Hfe6701	0.483	0	1.174	0.016	0.319	0.008	0.517	0.020	0.485	0.011	0.273	0.007
Hfe6702 (2)	0.893	0	0.041	0.006	0.013	0.004	0.107	0.021	0.159	0.201	0.535	0.090
Hfe6702												
Hfe6703												
Hfe6703 (2)												
Hfe6704												
Hfe6704 (2)												
Hfe6705												
Hfe6706												
Hfe6706 (2)												
Hfe6707	0.573	0	1.027	0.022	0.498	0.013	0.395	0.109	1.839	0.054	0.217	0.021

Hfe6707	0.032	0.1	1.434	0.130	0.110	0.061

Table 35 Parameters of the VBF fits of the Mössbauer spectra of $Fe_{67}Ni_{33}$.

Hife6700	0.822	461946	118	0.129	0.008	98041	1504	3	0	1.87	0.11
Hife6701	0.614	1550660	136	0.125	0.009	283976	1668	3	0	2.08	0.11
Hife6707	0.978	3094600	492	0.167	0.005	657587	5809	3	0	1.62	0.06

Hife6700	-0.042	0.023	0.038	0.012	0	0	0	0
Hife6701	-0.070	0.008	0.024	0.007	0	0	0	0
Hife6707	-0.032	0.013	0.031	0.007	0	0	0	0

Hife6700	0.320	0	1.746	0.008	0.196	0.016	0.680	0.049	1.062	0.052	0.523	0.034
Hife6701	0.463	0	1.193	0.025	0.305	0.014	0.537	0.034	0.490	0.020	0.281	0.010
Hife6707	0.391	0	1.830	0.005	0.224	0.007	0.609	0.024	1.069	0.025	0.511	0.016

Table 36 Parameters of the xVBF fits of Mössbauer spectra of $Fe_{69}Ni_{31}$.

Hfe6901	0.756	1214360	104	0.173	0.002	171083	1048	3	0	2	0	0	0
Hfe6902	0.681	1819660	83	0.160	0.006	187446	8458	1	0			0.72	0.12
Hfe6902	1.312	1819610	99	0.152	0.006	184280	1926	1	0			0	0
Hfe6903	0.698	1328470	115	0.154	0.004	123639	1241	1	0			0.02	1.00
Hfe6904	0.722	1188810	93	0.148	0.006	101028	3283	1	0			0	0
Hfe6905	0.62	1871020	97	0.149	0.003	152677	1365	1	0			0	0
Hfe6906	0.727	1216720	81	0.156	0.005	93198	834	1	0			0	0
Hfe6907	0.691	2947730	259	0.103	0.014	699772	3805	3	0	1.68	0.10	0	0

Hfe6901	1.00	0.02	0	0	-0.0655	0.0015	0.0552	#####	0	0	0	0
Hfe6902					-0.1424	0.0093	0.0270	#####	0.149	0.014	0.140	0.035
Hfe6902					-0.1496	0.0028	0	0	0.145	0.051	0.165	0.053
Hfe6903					-0.2301	0.0013	0.0245	#####	0.153	0.004	0.049	0.050
Hfe6904					-0.2993	0.0020	0	0	0.157	0.004	0.082	0.020
Hfe6905					-0.3610	0.0013	0	0	0.160	0.003	0.078	0.017
Hfe6906					-0.4252	0.0016	0	0	0.151	0.007	0.107	0.029
Hfe6907	0.28	0.10	0	0	0.0035	0.0031	0.094	0.024	0	0	0	0

Hfe6901	0.677	0	0.053	0.001	0.021	0.004	0.323	0.009	0.172	0.096	0.642	0.030
Hfe6902												
Hfe6902												
Hfe6903												
Hfe6904												
Hfe6905												
Hfe6906												
Hfe6907	0.190	0	1.567	0.010	0.257	0.010	0.793	0.019	0.733	0.019	0.528	0.024

Table 37 Parameters of the VBF fits of the Mössbauer spectra of $Fe_{69}Ni_{31}$.

Hfe6901	0.793	1214370	162	0.134	0.009	170646	1877	3	0	2	0
Hfe6907	0.727	2947990	245	0.132	0.010	705692	3658	3	0	1.75	0.08

Hfe6901	-0.113	0.007	0.806	0.164	0	0	0	0
Hfe6907	-0.033	0.005	0.035	0.004	0	0	0	0

Hfe6901	0.585	0	0.063	0.002	0.037	0.004	0.415	0.020	0.015	0.051	0.625	0.037
Hfe6907	0.226	0	1.553	0.013	0.267	0.012	0.774	0.026	0.693	0.020	0.504	0.020

Table 38 Parameters of the xVBF fits of spectra of $Fe_{71}Ni_{29}$.

Hife7101	0.62	166773	30	0.213	0.019	12366	284	3	0	2	0	0	0
Hife7102	0.69	2990090	148	0.187	0.003	175450	1083	1	0			0.97	0.15
Hife7103	0.62	886017	69	0.143	0.012	45243	668	1	0			0.81	0.09
Hife7104	0.69	109256	21	0.145	0	4983	203	1	0			0.99	0.19
Hife7105	0.53	166093	31	0.147	0.014	7583	205	1	0			1.00	0.25
Hife7106	0.57	1088610	81	0.158	0.007	47076	590	1	0			-0.22	0.86
Hife7107	0.67	1132850	80	0.158	0.008	42155	733	1	0			1.00	0.15
Hife7108	0.62	2738400	132	0.161	0.007	99959	1875	1	0			0.93	0.27
Hife7109	0.66	4242770	165	0.148	0.010	157608	4676	1	0			0.66	0.11
htfe7110	0.78	2986320	317	0.13	0	142270	1598	3	0	2	0	0	0
htfe7111	1.04	6507260	102	0.168	0.001	421246	1730	3	0	2	0	0	0

Hife7101	1.00	0.06	0	0	-0.0162	0.0075	0.064	0.015	0	0	0	0
Hife7102					-0.0760	0.0017	0.048	0.005	0.178	0.008	0.097	0.011
Hife7103					-0.1458	0.0040	0.071	0.021	0.101	0.029	0.230	0.025
Hife7104					-0.2258	0.0134	0.108	0.015	0.048	0.057	0.100	0.071
Hife7105					-0.3000	0.0051	0.017	0.012	0.169	0.034	0.105	0.056
Hife7106					-0.3726	0.0030	0.005	0.008	0.160	0.006	0.068	0.034
Hife7107					-0.4362	0.0035	0.012	0.005	0.148	0.016	0.110	0.044
Hife7108					-0.4389	0.0043	0.010	0.007	0.149	0.032	0.149	0.043
Hife7109					-0.4293	0.0102	0.065	0.035	0.073	0.041	0.249	0.036
htfe7110	0.75	0.13	0	0	-0.0674	0.0026	0.126	0.007	0	0	0	0
htfe7111	0.89	0.08	0	0	-0.0133	0.0019	0.108	0.004	0	0	0	0

Hife7101	0.81634	0	0.0498	0.00656	0.02786	0.00887	0.18366	0.04284	0.53489	0.17925	0.43607	0.13627
Hife7102												
Hife7103												
Hife7104												
Hife7105												
Hife7106												
Hife7107												
Hife7108												
Hife7109												
htfe7110	0.82545	0	0.04553	0.00428	0.02799	0.00936	0.17455	0.02044	0.00083	0.1152	0.49596	0.10703
htfe7111	0.53228	0	0.04592	0.00303	0.02132	0.00271	0.46773	0.00411	0.01384	0.04794	0.65312	0.00968

Table 39 Parameters of the fit of the spectra of $Fe_{71}Ni_{29}$ using a single Voigt line.

Hife7101	288	-0.0304	0.0066	0.283	0.052	0.594
Hife7102	374	-0.0850	0.0046	0.192	0.111	0.523
Hife7103	475	-0.1597	0.0050	0.188	0.085	0.467
Hife7104	581	-0.2323	0.0078	0.204	0.000	0.408
Hife7105	689	-0.3052	0.0064	0.141	0.112	0.445
Hife7106	792	-0.3727	0.0039	0.146	0.105	0.437
Hife7107	893	-0.4424	0.0030	0.133	0.113	0.435
Hife7108	893	-0.4413	0.0026	0.138	0.126	0.471
Hife7109	893	-0.4472	0.0024	0.154	0.120	0.480

Table 40 Parameters of the xVBF fits of the FCC phase of $Fe_{73}Ni_{27}$.

Hfe7300	1.00	543288	127	0.138	0.009	29007	438	1	0	0	0
Hfe7301	1.01	446007	144	0.119	0.017	21849	637	1	0	0	0
Hfe7302	0.88	526912	106	0.148	0.009	23685	456	1	0	0	0
Hfe7303	1.02	1151430	200	0.130	0.011	48617	1021	1	0	0	0
Hfe7304	0.82	558460	96	0.158	0.008	23275	397	1	0	0	0
Hfe7305	0.68	900101	89	0.157	0.010	58007	2552	1	0	0	0
Hfe7306	0.75	731869	74	0.175	0.009	45512	779	1	0	0	0

Hfe7300	-0.0285	0.0030	0.131	0.008	0	0	0	0
Hfe7301	-0.0862	0.0035	0.132	0.014	0	0	0	0
Hfe7302	-0.1593	0.0034	0.091	0.010	0	0	0	0
Hfe7303	-0.2334	0.0016	0.104	0.008	0	0	0	0
Hfe7304	-0.3002	0.0024	0.080	0.008	0	0	0	0
Hfe7305	-0.3708	0.0027	0.113	0.006	0	0	0	0
Hfe7306	-0.4337	0.0022	0.110	0.009	0	0	0	0

Table 41 Parameters of the fits of spectra of $Fe_{73}Ni_{27}$ using a single Voigt line.

Hfe7300	288	-0.0305	0.0030	0.155	0.120	0.482
Hfe7301	374	-0.0892	0.0041	0.148	0.111	0.455
Hfe7302	475	-0.1618	0.0037	0.186	0.052	0.410
Hfe7303	581	-0.2352	0.0019	0.163	0.078	0.412
Hfe7304	689	-0.3016	0.0016	0.188	0.052	0.414
Hfe7305	792	-0.3688	0.0023	0.191	0.086	0.473
Hfe7306	893	-0.4335	0.0023	0.176	0.110	0.494
Hfe7307	288	-0.0316	0.0039	0.126	0.162	0.534

Table 42 Parameters of the xVBF fits of the BCC phase in $Fe_{73}Ni_{27}$.

Hife7300	1.001	543288	127	0.138	0.009	80273	1600	2.32	0.05	1.62	0.04	0 0
Hife7301	1.013	446007	144	0.119	0.017	59315	1636	2.53	0.10	1.70	0.06	0 0
Hife7302	0.88	526912	106	0.148	0.009	62876	1332	2.67	0.08	1.83	0.05	0 0
Hife7303	1.023	1151430	200	0.130	0.011	126897	2148	2.57	0.07	1.72	0.04	0 0
Hife7304	0.821	558460	96	0.158	0.008	54255	1285	2.46	0.09	1.68	0.07	0 0
Hife7305	0.682	900089	72	0.154	0.008	8391	844	2.52	2.42	1.57	1.45	0 0
Hife7307	0.853	1334570	108	0.209	0.004	7945	1385	3	0	2	0	0 0

Hife7300	0	0	-0.42	0.07	0.0432	0.0022	0	0	0	0	0.089	0.010
Hife7301	0	0	-0.34	0.09	-0.0144	0.0041	0	0	0	0	0.097	0.017
Hife7302	0	0	-0.82	0.35	-0.0884	0.0030	0	0	0	0	0.036	0.018
Hife7303	0	0	-0.42	0.09	-0.1696	0.0025	0	0	0	0	0.081	0.014
Hife7304	0	0	-0.96	0.23	-0.2547	0.0038	0	0	0	0	0.045	0.021
Hife7305	0	0	0	0	-0.3458	0.0212	0	0	0	0	0	0
Hife7307	0	0	0	0	-0.0611	0.0610	0	0	0	0	0	0

Hife7300	0.195	0	2.371	0.007	0.000	0.018	0.805	0.052	2.276	0.006	0.080	0.004
Hife7301	0.453	0	2.275	0.021	0.049	0.031	0.547	0.225	2.192	0.024	0.092	0.015
Hife7302	0.230	0	2.215	0.010	0.028	0.017	0.770	0.080	2.115	0.009	0.078	0.006
Hife7303	0.318	0	2.085	0.006	0.000	0.006	0.682	0.042	1.987	0.007	0.083	0.006
Hife7304	0.296	0	1.959	0.011	0.002	0.007	0.228	0.068	1.767	0.034	0.095	0.024
Hife7305	1	0	1.787	0.009	0.038	0.013						
Hife7307	1	0	2.266	0.028	0.095	0.060						

Table 43 Parameters of the xVBF fits of the FCC phase of $Fe_{75}Ni_{25}$.

Hife7500	2.30	595565	267	0.119	0.012	10627	372	1	0	0	0
Hife7501	2.51	1477290	397	0.121	0.009	25010	814	1	0	0	0
Hife7502	1.88	1259130	288	0.116	0.008	19105	603	1	0	0	0
Hife7503	1.59	1562790	280	0.112	0.008	21168	382	1	0	0	0
Hife7504	2.88	2227430	208	0.153	0.005	30439	686	1	0	0	0
Hife7505	1.11	1541940	164	0.114	0.006	113701	1472	1	0	0	0
Hife7506	0.67	929057	63	0.166	0.004	89756	683	1	0	1.00	0.13
Hife7507	2.09	943487	229	0.173	0.007	83973	957	1	0	0	0

Hife7500	-0.0485	0.0062	0.100	0.013	0	0	0	0
Hife7501	-0.1003	0.0082	0.113	0.013	0	0	0	0
Hife7502	-0.1606	0.0058	0.096	0.010	0	0	0	0
Hife7503	-0.2309	0.0036	0.115	0.008	0	0	0	0
Hife7504	-0.2943	0.0023	0.086	0.006	0	0	0	0
Hife7505	-0.3590	0.0017	0.124	0.005	0	0	0	0
Hife7506	-0.4168	0.0016	0.060	0.015	0.150	0.022	0.022	0.012
Hife7507	-0.0362	0.0013	0.111	0.006	0	0	0	0

Table 44 Parameters of the fits of spectra of $Fe_{75}Ni_{25}$ using a single Voigt line.

Hife7500	288	-0.0538	0.0062	0.175	0.051	0.390
Hife7501	374	-0.1072	0.0057	0.200	0.043	0.426
Hife7502	475	-0.1666	0.0040	0.173	0.042	0.373
Hife7503	581	-0.2350	0.0050	0.173	0.072	0.418
Hife7504	689	-0.2995	0.0043	0.218	0.003	0.435
Hife7505	792	-0.3601	0.0024	0.100	0.132	0.431
Hife7506	893	-0.4198	0.0016	0.161	0.105	0.461
Hife7507	288	-0.0378	0.0039	0.186	0.099	0.489

Table 45 Parameters of the xVBF fits of the BCC phase of $Fe_{75}Ni_{25}$.

Hife7500	2.302	595565	267	0.119	0.012	163150	4124	2.568	0.058	1.824	0.042	0	0
Hife7501	2.513	1477290	397	0.121	0.009	377683	6520	2.578	0.058	1.850	0.040	0	0
Hife7502	1.884	1259130	288	0.116	0.008	288296	4125	2.669	0.056	1.894	0.042	0	0
Hife7503	1.585	1562790	280	0.112	0.008	323048	3987	2.750	0.056	1.914	0.043	0	0
Hife7504	2.883	2227430	208	0.153	0.005	428243	2274	2.497	0.046	1.733	0.035	0	0
Hife7505	1.111	1541940	164	0.114	0.006	116602	1511	2.309	0.106	1.528	0.069	0	0
Hife7507	2.09	943487	229	0.173	0.007	172841	2525	2.157	0.043	1.583	0.031	0	0

Hife7500	0	0	-0.275	0.043	0.0389	0.0029	0	0	0	0	0.088	0.012
Hife7501	0	0	-0.348	0.041	-0.0201	0.0023	0	0	0	0	0.114	0.009
Hife7502	0	0	-0.345	0.045	-0.0877	0.0020	0	0	0	0	0.095	0.008
Hife7503	0	0	-0.250	0.038	-0.1669	0.0017	0	0	0	0	0.106	0.009
Hife7504	0	0	-0.311	0.043	-0.2486	0.0018	0	0	0	0	0.093	0.010
Hife7505	0	0	-0.331	0.113	-0.3313	0.0026	0	0	0	0	0.091	0.011
Hife7507	0	0	-0.454	0.077	0.0343	0.0017	0	0	0	0	0.068	0.012

Hife7500	1	0	2.304	0.002	0.084	0.002						
Hife7501	0.249	0	2.305	0.007	0.004	0.015	0.751	0.073	2.218	0.009	0.078	0.005
Hife7502	0.196	0	2.215	0.006	0.003	0.016	0.804	0.053	2.126	0.007	0.080	0.004
Hife7503	0.261	0	2.092	0.007	0.000	0.016	0.739	0.064	2.003	0.008	0.085	0.004
Hife7504	0.321	0	1.954	0.004	0.000	0.008	0.679	0.038	1.858	0.006	0.075	0.004
Hife7505	0.551	0	1.788	0.005	0.005	0.008	0.449	0.092	1.711	0.014	0.055	0.009
Hife7507	1	0	2.285	0.001	0.065	0.002						

Table 46 Compiled parameters of the fits of the high temperature Mössbauer spectra of Fe-Ni alloys.

Hife3000	xVBF	288	0.2523	0.0026	2.012	0.1186
Hife3001	xVBF	374	0.2509	0.0020	1.938	0.1070
Hife3002	xVBF	475	0.2464	0.0031	1.823	0.1041
Hife3003	xVBF	581	0.2500	0.0032	1.674	0.0964
Hife3004	xVBF	689	0.2617	0.0027	1.525	0.0800
Hife3005	xVBF	792	0.2700	0.0033	1.211	0.0672
Hife3007	xVBF	843	0.2688	0.0050	0.901	0.0719
Hife3006	xVBF	893	0.2625	0.0020	0	

Hife5010	xVBF	288	0.2657	0.0015	2.137	0.111
Hife5010 (2)	xVBF	288	0.2660	0.0016	2.137	0.115
Hife5011	xVBF	374	0.2643	0.0007	2.021	0.106
Hife5011 (2)	xVBF	374	0.2645	0.0012	2.021	0.104
Hife5012	xVBF	475	0.2602	0.0016	1.833	0.106
Hife5012 (2)	xVBF	475	0.2602	0.0020	1.833	0.111
Hife5013	xVBF	581	0.2623	0.0026	1.554	0.117
Hife5013 (2)	xVBF	581	0.2623	0.0024	1.554	0.117
Hife5014	xVBF	689	0.2634	0.0033	1.197	0.138
Hife5014 (2)	xVBF	689	0.2619	0.0034	1.196	0.137
Hife5015	xVBF	792	0.2475	0.0036	0	
Hife5015 (2)	xVBF	792	0.2480	0.0037	0	
Hife5016	xVBF	893	0.2504	0.0045	0	
Hife5016 (2)	xVBF	893	0.2522	0.0044	0	

Hife6000	xVBF	288	0.2596	0.0018	2.027	0.150
Hife6000 (2)	xVBF	288	0.2595	0.0018	1.966	0.328
Hife6001	xVBF	374	0.2511	0.0019	1.718	0.331
Hife6002	xVBF	475	0.2514	0.0031	1.301	0.350
Hife6003	xVBF	581	0.2472	0.0044	0.606	0.351
Hife6003 (2)	xVBF	581	0.2521	0.0045	0.607	0.351
Hife6004	xVBF	689	0.2361	0.0033	0	
Hife6004 (2)	xVBF	689	0.2290	0.0034	0	
Hife6005	xVBF	792	0.2340	0.0038	0	
Hife6006	xVBF	893	0.2369	0.0044	0	
Hife6007	xVBF	288	0.2604	0.0009	1.979	0.331

(Table 46 continued)

Hfe6700	xVBF	288	0.2448	0.0036	1.286	0.535
Hfe6701	xVBF	374	0.2398	0.0021	0.822	0.446
Hfe6702 (2)	xVBF	475	0.2253	0.0015	0.084	0.167
Hfe6702	xVBF	475	0.2224	0.0014	0	
Hfe6703	xVBF	581	0.2208	0.0021	0	
Hfe6703 (2)	xVBF	581	0.2159	0.0022	0	
Hfe6704	xVBF	689	0.2185	0.0030	0	
Hfe6704 (2)	xVBF	689	0.2146	0.0030	0	
Hfe6705	xVBF	792	0.2191	0.0036	0	
Hfe6706	xVBF	893	0.2333	0.0044	0	
Hfe6706 (2)	xVBF	893	0.2285	0.0045	0	
Hfe6707	xVBF	288	0.2496	0.0018	1.365	0.552
Hfe6700	VBF	288	0.2351	0.0020	1.287	0.534
Hfe6701	VBF	374	0.2372	0.0020	0.820	0.447
Hfe6707	VBF	288	0.2386	0.0020	1.370	0.552
Hfe6901	xVBF	374	0.2214	0.0009	0.208	0.319
Hfe6902	xVBF	475	0.2159	0.0048	0	
Hfe6902	xVBF	475	0.2086	0.0019	0	
Hfe6903	xVBF	581	0.2038	0.0021	0	
Hfe6904	xVBF	689	0.2120	0.0030	0	
Hfe6905	xVBF	792	0.2246	0.0036	0	
Hfe6906	xVBF	893	0.2332	0.0044	0	
Hfe6907	xVBF	288	0.2320	0.0015	0.911	0.550
Hfe6901	VBF	374	0.2090	0.0020	0.245	0.325
Hfe6907	VBF	288	0.2275	0.0020	0.917	0.536
Hfe7101	xVBF	288	0.2124	0.0075	0.148	0.261
Hfe7102	xVBF	374	0.2109	0.0017	0	
Hfe7103	xVBF	475	0.2125	0.0040	0	
Hfe7104	xVBF	581	0.2080	0.0134	0	
Hfe7105	xVBF	689	0.2113	0.0051	0	
Hfe7106	xVBF	792	0.2130	0.0030	0	
Hfe7107	xVBF	893	0.2223	0.0035	0	
Hfe7108	xVBF	893	0.2195	0.0043	0	
Hfe7109	xVBF	893	0.2291	0.0102	0	
htfe7110	xVBF	374	0.2194	0.0026	0.038	0.209
htfe7111	xVBF	288	0.2152	0.0019	0.024	0.448
Hfe7101	Voigt	288	0.1981	0.0033		
Hfe7102	Voigt	374	0.2019	0.0023		
Hfe7103	Voigt	475	0.1986	0.0028		
Hfe7104	Voigt	581	0.2015	0.0044		
Hfe7105	Voigt	689	0.2061	0.0043		
Hfe7106	Voigt	792	0.2129	0.0041		
Hfe7107	Voigt	893	0.2160	0.0046		
Hfe7108	Voigt	893	0.2171	0.0045		
Hfe7109	Voigt	893	0.2112	0.0045		

(Table 46 continued)

Hfe7300	xVBF	288	0.2001	0.0015
Hfe7301	xVBF	374	0.2007	0.0018
Hfe7302	xVBF	475	0.1989	0.0021
Hfe7303	xVBF	581	0.2004	0.0022
Hfe7304	xVBF	689	0.2111	0.0030
Hfe7305	xVBF	792	0.2148	0.0038
Hfe7306	xVBF	893	0.2247	0.0044
Hfe7300	Voigt	288	0.1981	0.0015
Hfe7301	Voigt	374	0.1977	0.0021
Hfe7302	Voigt	475	0.1965	0.0022
Hfe7303	Voigt	581	0.1986	0.0022
Hfe7304	Voigt	689	0.2097	0.0029
Hfe7305	Voigt	792	0.2168	0.0037
Hfe7306	Voigt	893	0.2250	0.0045
Hfe7307	Voigt	288	0.1969	0.0020

Hfe7500	xVBF	288	0.1800	0.0031
Hfe7501	xVBF	374	0.1866	0.0041
Hfe7502	xVBF	475	0.1976	0.0032
Hfe7503	xVBF	581	0.2030	0.0027
Hfe7504	xVBF	689	0.2170	0.0030
Hfe7505	xVBF	792	0.2267	0.0037
Hfe7506	xVBF	893	0.2416	0.0044
Hfe7507	xVBF	288	0.1924	0.0007

Appendix E

Source Code for MC Simulations

The following C++ code was used to perform the MC simulations in chapter 3 and 7. It is written to be portable and efficient yet simple enough to modify.

```
File:         mc_ntp.cpp
Author:       Ken Lagarec
Purpose:      isothermal-isobaric MC simulation on a FCC lattice with magnetic and
              atomic degrees of freedom

#define USE_STD_METROPOLIS
// Borland compiler has __int8 type but GNU compiler doesn't
#if !defined(__BORLANDC__)
  #define __int8 char
#endif

// do chemical MC (volume changes) unless otherwise specified
#if !defined(NO_VOLUMEMC)
  #define DO_VOLUMEMC
#endif

// do atomic MC (atomic position changes) unless otherwise specified
#if !defined(NO_ATOMICMC)
  #define DO_ATOMICMC
#endif

// applied H can only be used if doing magnetic MC
#if defined(DO_APPLIEDH)
  #if !defined(DO_MAG)
    #error DO_MAG must be set to use DO_APPLIEDH
  #endif
#endif

#include <stdio.h>
#include <stdlib.h>
#include <fstream.h>
#include <math.h>
#include <values.h>
#include <time.h>
#if defined(__WIN32__)
  #include <windows.h>
  #define GetTime() ((double)GetTickCount()/1000.)
  #define time_t double
#else
  #define GetTime() (time(0))
```

```
#endif

#include "random.h"
#include "mcprob.h"
#include "mcspin.h"

#if defined(DO_TRACE)
  #define TRACE(x) cout << x << endl;
#else
  #define TRACE(x)
#endif

#if defined(DO_MAG)
  #if defined(DO_VOLUMEMC) || defined(DO_ATOMICMC)
const char fnprefix[] = "mc NTP";
  #else
const char fnprefix[] = "mc";
  #endif
#else
const char fnprefix[] = "mc NTP no mag";
#endif
typedef unsigned __int8 species_t;


ofstream os_main;
const unsigned NUMSITESPERCELL = 4;
const int NUMNNPERSITE = 12;
const int NUMNNPERSITE_2 = 6;
const int NUM2NNPERSITE = 6;
const int NUM2NNPERSITE_2 = 3;
const int NUM3NNPERSITE = 24;
const int NUM3NNPERSITE_2 = 12;
const unsigned NUMSPECIES = 2;

#if defined(DO_MAG)
const unsigned NUM_MCMAGSTEPS = 1;  // number of steps of magnetic annealing
between steps of volume adjustments
#else
const unsigned NUM_MCMAGSTEPS = 0;  // number of steps of magnetic annealing
between steps of volume adjustments
#endif
const unsigned NUM_MCVOLSTEPS = 1;
const double SCALE_DNN = 7.0e-5;
const double SCALE_NNDEV = 3.5e-4;

#if defined(DO_HDISTRIBUTION)
// <H> = A*<mu> + B*SumNN(<mu>)
const double Hhf_A = 20;
const double Hhf_B = 0.3;
#endif
const double MU[NUMSPECIES] = {2.8, 0.6};

struct position_t {
  __int8 i;
  __int8 j;
  __int8 k;
  __int8 l;
};
inline position_t
operator + (const position_t& p, const position_t& dp) {
  position_t ppdp;
  ppdp.i = p.i + dp.i;
  ppdp.j = p.j + dp.j;
  ppdp.k = p.k + dp.k;
  ppdp.l = dp.l;
```

```
  return ppdp;
}

// Nearest-neighbour positions
position_t nn[NUMSITESPERCELL][NUMNNPERSITE] = {
// l = 0
 {{0, 0, 0, 1}, {-1, 0, 0, 1}, {0, 0, 0, 2}, {-1, 0, 0, 2}, {0, 0, 0, 3}, {0, -1,
0, 3},
  {0, -1, 0, 1}, {-1, -1, 0, 1}, {0, 0, -1, 2}, {-1, 0, -1, 2}, {0, 0, -1, 3},
{0, -1, -1, 3}},
// l = 1
 {{1, 1, 0, 0}, {0, 1, 0, 0}, {0, 0, 0, 2}, {0, 1, 0, 2}, {0, 0, 0, 3}, {1, 0, 0,
3},
  {0, 0, 0, 0}, {1, 0, 0, 0}, {0, 0, -1, 2}, {0, 1, -1, 2}, {0, 0, -1, 3}, {1, 0,
-1, 3}},
// l = 2
 {{1, 0, 1, 0}, {0, 0, 1, 0}, {0, 0, 1, 1}, {0, -1, 1, 1}, {0, 0, 0, 3}, {1, 0,
0, 3},
  {0, 0, 0, 0}, {1, 0, 0, 0}, {0, 0, 0, 1}, {0, -1, 0, 1}, {0, -1, 0, 3}, {1, -1,
0, 3}},
// l = 3
 {{0, 0, 1, 0}, {0, 1, 1, 0}, {0, 0, 1, 1}, {-1, 0, 1, 1}, {0, 1, 0, 2}, {-1, 1,
0, 2},
  {0, 0, 0, 0}, {0, 1, 0, 0}, {0, 0, 0, 1}, {-1, 0, 0, 1}, {0, 0, 0, 2}, {-1, 0,
0, 2}}
};

// Next nearest-neighbour positions
position_t nnn[NUMSITESPERCELL][NUM2NNPERSITE] = {
// l = 0
 {{1, 0, 0, 0}, {0, 1, 0, 0}, {0, 0, 1, 0}, {-1, 0, 0, 0}, {0, -1, 0, 0}, {0, 0,
-1, 0}},
// l = 1
 {{1, 0, 0, 1}, {0, 1, 0, 1}, {0, 0, 1, 1}, {-1, 0, 0, 1}, {0, -1, 0, 1}, {0, 0,
-1, 1}},
// l = 2
 {{1, 0, 0, 2}, {0, 1, 0, 2}, {0, 0, 1, 2}, {-1, 0, 0, 2}, {0, -1, 0, 2}, {0, 0,
-1, 2}},
// l = 3
 {{1, 0, 0, 3}, {0, 1, 0, 3}, {0, 0, 1, 3}, {-1, 0, 0, 3}, {0, -1, 0, 3}, {0, 0,
-1, 3}},
};

struct atom {
  spin_t s;          // spin
  species_t el;      // type of atom (0 = Fe, 1 = Ni)
  float dr[3];      // displacement relative to true fcc position
  float avgdr[3];    // sum of displacements (eventually stores the average)
  spinf_t avgs;        // sum of spin state (eventually stores the average)
  static unsigned nsum;
  atom() {
    s = 0;
    el = 0;
    dr[0] = dr[1] = dr[2] = 0;
    avgdr[0] = avgdr[1] = avgdr[2] = 0;
    avgs = 0;
  }
  atom& operator = (const atom& a) {
    s = a.s;
    el = a.el;
    dr[0] = a.dr[0];
    dr[1] = a.dr[1];
    dr[2] = a.dr[2];
    avgdr[0] = a.avgdr[0];
    avgdr[1] = a.avgdr[1];
```

```
    avgdr[2] = a.avgdr[2];
    avgs = a.avgs;
    return *this;
  }
  void calc_avg() {
    avgdr[0] /= nsum;
    avgdr[1] /= nsum;
    avgdr[2] /= nsum;
    avgs = avgs/nsum;
  }
  void sample_avg(double a) {
    avgdr[0] += a*dr[0];
    avgdr[1] += a*dr[1];
    avgdr[2] += a*dr[2];
    avgs += s;
  }
  void reset_avg() {
    avgdr[0] = 0;
    avgdr[1] = 0;
    avgdr[2] = 0;
    avgs = 0;
  }
};
unsigned atom::nsum = 0;

inline ostream&
operator << (ostream& os, const atom& a) {
#if defined(HEISENBERG)
  os << (int)a.el << '\t' << a.s << '\t' << a.dr[0] << '\t' << a.dr[1] << '\t' <<
a.dr[2] << '\t' << a.avgdr[0] << '\t' << a.avgdr[1] << '\t' << a.avgdr[2] << '\t'
<< a.avgs;
#else
  os << (int)a.el << '\t' << (int)a.s << '\t' << a.dr[0] << '\t' << a.dr[1] <<
'\t' << a.dr[2] << '\t' << a.avgdr[0] << '\t' << a.avgdr[1] << '\t' << a.avgdr[2]
<< '\t' << a.avgs;
#endif
  return os;
}
inline istream&
operator >> (istream& is, atom& a) {
  double t3;
#if defined(HEISENBERG)
  int t1;
  is >> t1 >> a.s >> a.dr[0] >> a.dr[1] >> a.dr[2] >> a.avgdr[0] >> a.avgdr[1] >>
a.avgdr[2] >> a.avgs;
  a.el = (species_t)t1;
#else
  int t1, t2;
  is >> t1 >> t2 >> a.dr[0] >> a.dr[1] >> a.dr[2] >> a.avgdr[0] >> a.avgdr[1] >>
a.avgdr[2] >> a.avgs;
  a.el = (species_t)t1;
  a.s = (spin_t)t2;
#endif
  return is;
}

// chemical potential parameters for a Lennard-Jones potential
//   U(d) = U0*((d0/d)^12-2*(d0/d)^6)
//   U(d0) = -U0
//   U'(d0) = 0
double U0[NUMSPECIES][NUMSPECIES];  // U[0][0] = UFeFe, U[1][1] = UNiNi, U[0][1]
= U[1][0] = UFeNi
double d0[NUMSPECIES][NUMSPECIES];  // equilibrium positions for Fe-Fe, Fe-Ni and
Ni-Ni bonds
double d02[NUMSPECIES][NUMSPECIES];  // squared equilibrium positions for Fe-Fe,
```

```
Fe-Ni and Ni-Ni bonds
// Lennard-Jones potential using d as the argument (interatomic distance)
inline double
U(species_t a1, species_t a2, double d) {
  double rho6 = d0[a1][a2]/d;
  rho6 *= rho6*rho6;
  rho6 *= rho6;
  return U0[a1][a2]*rho6*(rho6-2);
}
// Lennard-Jones potential using d^2 as the argument (instead of d)
//   more efficient since d2 is calculated when getting r. Eliminiates the call
to sqrt()
//   and two multiplies
inline double
U2(species_t a1, species_t a2, double d2) {
  double rho6 = d02[a1][a2]/d2;
  rho6 *= rho6*rho6;
  return U0[a1][a2]*rho6*(rho6-2);
}

// magnetic exchange parameters
double J0[NUMSPECIES][NUMSPECIES];  // [0][0] = JFeFe, [1][1] = JNiNi, [0][1] =
[1][0] = JFeNi
double dJ_dr[NUMSPECIES][NUMSPECIES];  // [0][0] = dJFeFe/dr, [1][1] = dJNiNi/dr,
[0][1] = [1][0] = dJFeNi/dr
double dJ_dr2[NUMSPECIES][NUMSPECIES];  // [0][0] = dJFeFe/dr, [1][1] =
dJNiNi/dr, [0][1] = [1][0] = dJFeNi/dr
double dnn0, dnn02, dnn12;                    // linear Taylor expansion around
dnn0 (up to dnn1 if JFEFE_MINMAX)
double dFeFe_dnn02;
#if defined(DO_VOLUMEMC) || defined(DO_ATOMICMC)
inline double
JFeFe(double d2) {
#if defined(JFEFE_BOSE)
  d2 *= dFeFe_dnn02;
  return d2<6.909 ? -16379*d2+86651*sqrt(d2)-114555 : 49;
#elif defined(JFEFE_MINMAX)
  return d2 < dnn02 ? -100 : d2 < dnn12 ? -100+dJ_dr2[0][0]*(d2-dnn02) : 100;
#else
  return J0[0][0]+dJ_dr2[0][0]*(d2-dnn02);
#endif
}
#else
inline double
JFeFe(double d2) {
  return J0[0][0];
}
#endif

struct dnnInfo {
  double avg[3];
  double stdev[3];
  float pup;
  unsigned n;
};

class lattice
{
  public:
    enum spinorder {ferro, antiferro, para, Niferro};
    enum chemorder {Fe3Ni, FeNi, FeNi3, disordered};
    atom**** atoms;    // array of atoms in the system
    double dnn, dnn2x2, avgdnn;        // near neighbour distance and 2*dnn^2
    unsigned Nx, Ny, Nz;      // size of box (number of unit cells)
    unsigned N, N0;           // total # of atoms + # of atoms of species 0
```

```
    double c;                    // concentration of species 0
    chemorder chemlro;
    double T, P, H;     // P is in units of K/A^3 (1 K/A^3 = 0.0138 GPa)
    mutable double Energy;

    lattice(unsigned Nx_, unsigned Ny_, unsigned Nz_, double c_);
    ~lattice();

    void setup();
    void reset_atomavg();
    void setTemp(double T_);
    void setPressure(double P_);
    void setH(double H_);
    void setdnn(double dnn_);
    void resetE(double E_);
    void initialize(spinorder state);
    void initialize(chemorder state);
    bool saveSystem(char* fn);
    bool readSystem(char* fn);

    double calcE() const;
    double calcMagE() const;
    double calcChemE() const;
    spinsum_t calcM(species_t el) const;
    spinsum_t calcMaf() const;
    double calcSROP_AF(double* sig=0) const;
#if defined(DO_HDISTRIBUTION)
    double calcHhf(unsigned i, unsigned j, unsigned k, unsigned l) const;
    double calcHhfDistribution(double** PHhf, unsigned n, double dHhf);
#endif

    double calcd(int i1, int j1, int k1, int l1, int i2, int j2, int k2, int l2)
const;
    double calcd2(int i1, int j1, int k1, int l1, int i2, int j2, int k2, int l2)
const;
    double calcavgd(int i1, int j1, int k1, int l1, int i2, int j2, int k2, int
l2, double avga) const;
    double calcJ(int i1, int j1, int k1, int l1, int i2, int j2, int k2, int l2)
const;
    spinf_t calcJs2(int i1, int j1, int k1, int l1, int i2, int j2, int k2, int
l2) const;
    double calcChemE(unsigned i, unsigned j, unsigned k, unsigned l) const;
    double calcMagE(unsigned i, unsigned j, unsigned k, unsigned l) const;
    unsigned calcFrustratedFeBonds(unsigned& nFeFe) const;
    double calcChemSROP(species_t el, double* sig=0) const;
    double calcChemLROP(double* sig=0) const;
    double calcMagSROP(species_t el, double* sig=0) const;
    double calcMagLROP(double* sig=0) const;

    double calcAvgdnn(double avga, species_t a1, species_t a2, dnnInfo*
dnninfo=0) const;

    unsigned getNumAtoms() const;
    unsigned getNumAtoms(species_t el) const;
    double getdnn() const;
    spin_t& getSpin(int i, int j, int k, int l);
    const spin_t getSpin(int i, int j, int k, int l) const;
    species_t& getSpecies(int i, int j, int k, int l);
    const species_t getSpecies(int i, int j, int k, int l) const;
    atom& getAtom(int i, int j, int k, int l);
    const atom& getAtom(int i, int j, int k, int l) const;

    void sumNNSpins(unsigned i, unsigned j, unsigned k, unsigned l, spinsum_t
sumSpins[NUMSPECIES]) const;
    void sumNNAtoms(unsigned i, unsigned j, unsigned k, unsigned l, species_t
```

```
sumSpecies[NUMSPECIES]) const;

    float calcVolProb(double d, double& dE);
    float calcMoveProb(unsigned i, unsigned j, unsigned k, unsigned l, float
dr[3], double& dE);
    float calcFlipProb(unsigned i, unsigned j, unsigned k, unsigned l, const
spin_t& news, double& dE) const;
    void run(unsigned nsteps, unsigned startsampling, unsigned samplingstep,
const char* fn);

    static bool areNN(unsigned i1, unsigned j1, unsigned k1, unsigned l1,
unsigned i2, unsigned j2, unsigned k2, unsigned l2);
};

template <class TR, class TF> TR
doNNCalc(lattice& lat, unsigned i, unsigned j, unsigned k, unsigned l, TF F);
template <class TR, class TF> TR
doNNCalc(const lattice& lat, unsigned i, unsigned j, unsigned k, unsigned l, TF
F);

lattice::lattice(unsigned Nx_, unsigned Ny_, unsigned Nz_, double c_):
  Nx(Nx_), Ny(Ny_), Nz(Nz_), c(c_)
{
  setup();
  dnn = 0;
  dnn2x2 = 0;
  P = 0;
  H = 0;
}

void
lattice::setup()
{
  N = NUMSITESPERCELL*Nx*Ny*Nz;
  N0 = 0;
  atoms = new atom***[Nx+2];     // use periodic boundary conditions in x and y
(using only nn or nnn)
  atoms += 1;                    // if 0 .. N-1 are valid, then -1 maps to N-1
and N maps to 0
  for (unsigned i=0; i<Nx; i++) {
    atoms[i] = new atom**[Ny+2];
    atoms[i] += 1;
    for (unsigned j=0; j<Ny; j++) {
      atoms[i][j] = new atom*[Nz+2];
      atoms[i][j] += 1;
      for (unsigned k=0; k<Nz; k++)
        atoms[i][j][k] = new atom[NUMSITESPERCELL];
      atoms[i][j][-1] = atoms[i][j][Nz-1];
      atoms[i][j][Nz] = atoms[i][j][0];
    }
    atoms[i][-1] = atoms[i][Ny-1];
    atoms[i][Ny] = atoms[i][0];
  }
  atoms[-1] = atoms[Nx-1];
  atoms[Nx] = atoms[0];
}

lattice::~lattice()
{
  for (unsigned i=0; i<Nx; i++) {
    for (unsigned j=0; j<Ny; j++) {
      for (unsigned k=0; k<Nz; k++)
        delete[] atoms[i][j][k];
      delete[] (atoms[i][j]-1);
    }
```

```
    delete[] (atoms[i]-1);
  }
  delete[] (atoms-1);
}

void
lattice::reset_atomavg()
{
  for (unsigned i=0, j, k, l; i<Nx; i++)
    for (j=0; j<Ny; j++)
      for (k=0; k<Nz; k++)
        for (l=0; l<NUMSITESPERCELL; l++)
          getAtom(i, j, k, l).reset_avg();
}

inline unsigned
lattice::getNumAtoms() const {
  return N;
}

inline unsigned
lattice::getNumAtoms(species_t el) const {
  return (el == 0 ? N0 : N-N0);
}

inline double
lattice::getdnn() const {
  return dnn;
}

inline spin_t&
lattice::getSpin(int i, int j, int k, int l) {
  return atoms[i][j][k][l].s;
}

inline const spin_t
lattice::getSpin(int i, int j, int k, int l) const {
  return atoms[i][j][k][l].s;
}

inline species_t&
lattice::getSpecies(int i, int j, int k, int l) {
  return atoms[i][j][k][l].el;
}

inline const species_t
lattice::getSpecies(int i, int j, int k, int l) const {
  return atoms[i][j][k][l].el;
}

inline atom&
lattice::getAtom(int i, int j, int k, int l) {
  return atoms[i][j][k][l];
}

inline const atom&
lattice::getAtom(int i, int j, int k, int l) const {
  return atoms[i][j][k][l];
}

inline double
lattice::calcE() const
{
#if defined(DO_MAG)
  Energy = calcMagE()+calcChemE();
```

```
#else
  Energy = calcChemE();
#endif
  return Energy;
}

double
lattice::calcMagE() const
{
#if !defined(DO_ATOMICMC)
  double E = 0;
  species_t a;
  spinsum_t sumSpins[NUMSPECIES];
  double Jr[2][2];
  Jr[0][0] = JFeFe(dnn*dnn);
  Jr[0][1] = Jr[1][0] = J0[0][1];//(0, 1, dnn*dnn);
  Jr[1][1] = J0[1][1];//J2(1, 1, dnn*dnn);
  for (unsigned i=0, j, k, l; i<Nx; i++)
    for (j=0; j<Ny; j++)
      for (k=0; k<Nz; k++)
        for (l=0; l<NUMSITESPERCELL; l++) {
          a = getSpecies(i,j,k,l);
          sumNNSpins(i,j,k,l,sumSpins);
#if defined(DO_APPLIEDH)
          E -= getSpin(i,j,k,l)*(Jr[a][0]*sumSpins[0]+Jr[a][1]*sumSpins[1]+H);
#else
          E -= getSpin(i,j,k,l)*(Jr[a][0]*sumSpins[0]+Jr[a][1]*sumSpins[1]);
#endif
        }
  return E/2.;
#else
  double E = 0;
  spinf_t Ei;
  for (unsigned i=0, j, k, l; i<Nx; i++)
    for (j=0; j<Ny; j++)
      for (k=0; k<Nz; k++) {
      // only count nn pairs once if swept through completely
        l = 0;
        Ei = calcJs2(i,j,k,l,i,j,k,l)
            + calcJs2(i,j,k,l,i-1,j,k,l)
            + calcJs2(i,j,k,l,i,j,k,2)
            + calcJs2(i,j,k,l,i-1,j,k,2)
            + calcJs2(i,j,k,l,i,j,k,3)
            + calcJs2(i,j,k,l,i,j-1,k,3);
#if defined(DO_APPLIEDH)
        E -= (Ei+H)*getSpin(i,j,k,l);
#else
        E -= Ei*getSpin(i,j,k,l);
#endif
        l = 1;
        Ei = calcJs2(i,j,k,l,i+1,j+1,k,0)
            + calcJs2(i,j,k,l,i,j+1,k,0)
            + calcJs2(i,j,k,l,i,j,k,2)
            + calcJs2(i,j,k,l,i,j+1,k,2)
            + calcJs2(i,j,k,l,i,j,k,3)
            + calcJs2(i,j,k,l,i+1,j,k,3);
#if defined(DO_APPLIEDH)
        E -= (Ei+H)*getSpin(i,j,k,l);
#else
        E -= Ei*getSpin(i,j,k,l);
#endif
        l = 2;
        Ei = calcJs2(i,j,k,l,i+1,j,k+1,0)
            + calcJs2(i,j,k,l,i,j,k+1,0)
            + calcJs2(i,j,k,l,i,j,k+1,1)
```

```
            + calcJs2(i,j,k,l,i,j-1,k+1,1)
            + calcJs2(i,j,k,l,i,j,k,3)
            + calcJs2(i,j,k,l,i+1,j,k,3);
#if defined(DO_APPLIEDH)
        E -= (Ei+H)*getSpin(i,j,k,l);
#else
        E -= Ei*getSpin(i,j,k,l);
#endif
        l = 3;
        Ei = calcJs2(i,j,k,l,i,j,k+1,0)
            + calcJs2(i,j,k,l,i,j+1,k+1,0)
            + calcJs2(i,j,k,l,i,j,k+1,1)
            + calcJs2(i,j,k,l,i-1,j,k+1,1)
            + calcJs2(i,j,k,l,i,j+1,k,2)
            + calcJs2(i,j,k,l,i-1,j+1,k,2);
#if defined(DO_APPLIEDH)
        E -= (Ei+H)*getSpin(i,j,k,l);
#else
        E -= Ei*getSpin(i,j,k,l);
#endif
      }
  return E;
#endif
}

double
lattice::calcChemE() const
{
#if !defined(DO_ATOMICMC)
// In this case, all bond lengths are equal, so we only need to know
// how many near-neighbours of each type there are
/*  species_t a;
  int sumSpecies[NUMSPECIES];
  int N[2][2] = {{0,0},{0,0}};
  for (unsigned i=0, j, k, l; i<Nx; i++)
    for (j=0; j<Ny; j++)
      for (k=0; k<Nz; k++)
        for (l=0; l<NUMSITESPERCELL; l++) {
          a = getSpecies(i,j,k,l);
          sumNNAtoms(i,j,k,l,sumSpecies);
          N[a][0] += sumSpecies[0];
          N[a][1] += sumSpecies[1];
        }
  double E = U(0,0,dnn)*N[0][0];
  E += U(0,1,dnn)*(N[0][1]+N[1][0]);
  E += U(1,1,dnn)*N[1][1];
  return E/2.;*/
  return 0;
#else
  long double E = 0;
  species_t el;
  for (unsigned i=0, j, k, l; i<Nx; i++)
    for (j=0; j<Ny; j++)
      for (k=0; k<Nz; k++) {
      // only count nn pairs once if swept through completely
        l = 0;
        el = getSpecies(i,j,k,l);
        E +=  U2(el, getSpecies(i,j,k,l),    calcd2(i,j,k,l,i,j,k,l))
            + U2(el, getSpecies(i-1,j,k,l),  calcd2(i,j,k,l,i-1,j,k,l))
            + U2(el, getSpecies(i,j,k,2),    calcd2(i,j,k,l,i,j,k,2))
            + U2(el, getSpecies(i-1,j,k,2),  calcd2(i,j,k,l,i-1,j,k,2))
            + U2(el, getSpecies(i,j,k,3),    calcd2(i,j,k,l,i,j,k,3))
            + U2(el, getSpecies(i,j-1,k,3),  calcd2(i,j,k,l,i,j-1,k,3));

        l = 1;
```

```
        el = getSpecies(i,j,k,l);
        E +=  U2(el, getSpecies(i+1,j+1,k,0), calcd2(i,j,k,l,i+1,j+1,k,0))
            + U2(el, getSpecies(i,j+1,k,0),   calcd2(i,j,k,l,i,j+1,k,0))
            + U2(el, getSpecies(i,j,k,2),     calcd2(i,j,k,l,i,j,k,2))
            + U2(el, getSpecies(i,j+1,k,2),   calcd2(i,j,k,l,i,j+1,k,2))
            + U2(el, getSpecies(i,j,k,3),     calcd2(i,j,k,l,i,j,k,3))
            + U2(el, getSpecies(i+1,j,k,3),   calcd2(i,j,k,l,i+1,j,k,3));

        l = 2;
        el = getSpecies(i,j,k,l);
        E +=  U2(el, getSpecies(i+1,j,k+1,0), calcd2(i,j,k,l,i+1,j,k+1,0))
            + U2(el, getSpecies(i,j,k+1,0),   calcd2(i,j,k,l,i,j,k+1,0))
            + U2(el, getSpecies(i,j,k+1,1),   calcd2(i,j,k,l,i,j,k+1,1))
            + U2(el, getSpecies(i,j-1,k+1,1), calcd2(i,j,k,l,i,j-1,k+1,1))
            + U2(el, getSpecies(i,j,k,3),     calcd2(i,j,k,l,i,j,k,3))
            + U2(el, getSpecies(i+1,j,k,3),   calcd2(i,j,k,l,i+1,j,k,3));

        l = 3;
        el = getSpecies(i,j,k,l);
        E +=  U2(el, getSpecies(i,j+1,k+1,0), calcd2(i,j,k,l,i,j+1,k+1,0))
            + U2(el, getSpecies(i,j,k+1,0),   calcd2(i,j,k,l,i,j,k+1,0))
            + U2(el, getSpecies(i,j,k+1,1),   calcd2(i,j,k,l,i,j,k+1,1))
            + U2(el, getSpecies(i-1,j,k+1,1), calcd2(i,j,k,l,i-1,j,k+1,1))
            + U2(el, getSpecies(i,j+1,k,2),   calcd2(i,j,k,l,i,j+1,k,2))
            + U2(el, getSpecies(i-1,j+1,k,2), calcd2(i,j,k,l,i-1,j+1,k,2));
      }
/*  for (unsigned i=0, j, k, l, m; i<Nx; i++)
    for (j=0; j<Ny; j++)
      for (k=0; k<Nz; k++)
        for (l=0; l<NUMSITESPERCELL; l++) {
          el = getSpecies(i,j,k,l);
          for (m=0; m<NUMNNPERSITE_2; m++) {
            e2 = getSpecies(i+nn[l][m].i,j+nn[l][m].j,k+nn[l][m].k,nn[l][m].l);
            r2 =
calcd2(i,j,k,l,i+nn[l][m].i,j+nn[l][m].j,k+nn[l][m].k,nn[l][m].l);
            E += U2(el, e2, r2);
          }
/*          for (m=0; m<NUM2NNPERSITE_2; m++) {
            e2 =
getSpecies(i+nnn[l][m].i,j+nnn[l][m].j,k+nnn[l][m].k,nnn[l][m].l);
            r2 =
calcd2(i,j,k,l,i+nnn[l][m].i,j+nnn[l][m].j,k+nnn[l][m].k,nnn[l][m].l);
            E += U2(el, e2, r2);
          }*/
//        }
  return E;
#endif
}

spinsum_t
lattice::calcM(species_t el) const
{
  spinsum_t M = 0;
  for (unsigned i=0, j, k, l; i<Nx; i++)
    for (j=0; j<Ny; j++)
      for (k=0; k<Nz; k++)
        for (l=0; l<NUMSITESPERCELL; l++)
          if (getSpecies(i,j,k,l) == el)
            M += getSpin(i,j,k,l);
  return M;
}

// Calculated staggered (along 001 direction) magnetization
spinsum_t
lattice::calcMaf() const
```

```
{
  spinsum_t M = 0;
  for (unsigned i=0, j, k, l; i<Nx; i++)
    for (j=0; j<Ny; j++)
      for (k=0; k<Nz; k++) {
        for (l=0; l<2; l++)
          M += getSpin(i,j,k,l);
        for (l=2; l<4; l++)
          M -= getSpin(i,j,k,l);
      }
  return M;
}

template <class TR, class TF> TR
doNNCalc(lattice& lat, unsigned i, unsigned j, unsigned k, unsigned l, TF F)
{
  TR retval = 0;
  for (unsigned m; m<NUMNNPERSITE; m++)
    retval += F(lat.getAtom(i+nn[l][m].i,j+nn[l][m].j,k+nn[l][m].k,nn[l][m].l));
  return retval;
}

template <class TR, class TF> TR
doNNCalc(const lattice& lat, unsigned i, unsigned j, unsigned k, unsigned l, TF
F)
{
  TR retval = 0;
  for (unsigned m=0; m<NUMNNPERSITE; m++)
    retval += F(lat.getAtom(i+nn[l][m].i,j+nn[l][m].j,k+nn[l][m].k,nn[l][m].l));
  return retval;
}

bool
lattice::areNN(unsigned i1, unsigned j1, unsigned k1, unsigned l1, unsigned i2,
unsigned j2, unsigned k2, unsigned l2)
{
  double p[3];
  p[0] = i1 - i2;
  p[1] = j1 - j2;
  p[2] = k1 - k2;
  if (l1 == 1) {
    p[0] += 0.5;
    p[1] += 0.5;
  } else if (l1 == 2) {
    p[0] += 0.5;
    p[2] += 0.5;
  } else if (l1 == 3) {
    p[1] += 0.5;
    p[2] += 0.5;
  }
  if (l2 == 1) {
    p[0] -= 0.5;
    p[1] -= 0.5;
  } else if (l2 == 2) {
    p[0] -= 0.5;
    p[2] -= 0.5;
  } else if (l2 == 3) {
    p[1] -= 0.5;
    p[2] -= 0.5;
  }
  double d2 = p[0]*p[0] + p[1]*p[1] + p[2]*p[2];
  return (d2 < 0.501 && d2 > 0.499);
}

inline double
```

```
lattice::calcd2(int i1, int j1, int k1, int l1, int i2, int j2, int k2, int l2)
const
{
  double p[3];
  const atom& a1 = getAtom(i1,j1,k1,l1);
  const atom& a2 = getAtom(i2,j2,k2,l2);
  p[0] = i1 + a1.dr[0] - (i2 + a2.dr[0]);
  p[1] = j1 + a1.dr[1] - (j2 + a2.dr[1]);
  p[2] = k1 + a1.dr[2] - (k2 + a2.dr[2]);
  if (l1 == 1) {
    p[0] += 0.5;
    p[1] += 0.5;
  } else if (l1 == 2) {
    p[0] += 0.5;
    p[2] += 0.5;
  } else if (l1 == 3) {
    p[1] += 0.5;
    p[2] += 0.5;
  }
  if (l2 == 1) {
    p[0] -= 0.5;
    p[1] -= 0.5;
  } else if (l2 == 2) {
    p[0] -= 0.5;
    p[2] -= 0.5;
  } else if (l2 == 3) {
    p[1] -= 0.5;
    p[2] -= 0.5;
  }
// no need to check for periodic boundary condition since spin after N is
referred
// to as N+1, and i2-i1, etc are used in this calculation

  return dnn2x2*(p[0]*p[0] + p[1]*p[1] + p[2]*p[2]);
}

inline double
lattice::calcd(int i1, int j1, int k1, int l1, int i2, int j2, int k2, int l2)
const
{
  return sqrt(calcd2(i1,j1,k1,l1,i2,j2,k2,l2));
}

inline double
lattice::calcavgd(int i1, int j1, int k1, int l1, int i2, int j2, int k2, int l2,
double avga) const
{
  double p[3];
  const atom& a1 = getAtom(i1,j1,k1,l1);
  const atom& a2 = getAtom(i2,j2,k2,l2);
  p[0] = i1 - i2 + (a1.avgdr[0] - a2.avgdr[0])/avga;
  p[1] = j1 - j2 + (a1.avgdr[1] - a2.avgdr[1])/avga;
  p[2] = k1 - k2 + (a1.avgdr[2] - a2.avgdr[2])/avga;
  if (l1 == 1) {
    p[0] += 0.5;
    p[1] += 0.5;
  } else if (l1 == 2) {
    p[0] += 0.5;
    p[2] += 0.5;
  } else if (l1 == 3) {
    p[1] += 0.5;
    p[2] += 0.5;
  }
  if (l2 == 1) {
    p[0] -= 0.5;
```

```
    p[1] -= 0.5;
  } else if (l2 == 2) {
    p[0] -= 0.5;
    p[2] -= 0.5;
  } else if (l2 == 3) {
    p[1] -= 0.5;
    p[2] -= 0.5;
  }
// no need to check for periodic boundary condition since spin after N is
referred
// to as N+1, and i2-i1, etc are used in this calculation

  return avga*sqrt(p[0]*p[0] + p[1]*p[1] + p[2]*p[2]);
}

inline double
lattice::calcJ(int i1, int j1, int k1, int l1, int i2, int j2, int k2, int l2)
const
{
  species_t a1 = getSpecies(i1,j1,k1,l1);
  species_t a2 = getSpecies(i2,j2,k2,l2);
  if (a1 | a2)
    return J0[a1][a2];
  double d2 = calcd2(i1,j1,k1,l1,i2,j2,k2,l2);
  return JFeFe(d2);
}

inline spinf_t
lattice::calcJs2(int i1, int j1, int k1, int l1, int i2, int j2, int k2, int l2)
const
{
  return calcJ(i1,j1,k1,l1,i2,j2,k2,l2)*getSpin(i2,j2,k2,l2);
}

double
lattice::calcChemSROP(species_t el, double* sig) const
{
// simple SROP for FeNi ordering
// simply returns the average number of Fe nn's
  int s = 0;
  int s2 = 0;
  species_t sum[NUMSPECIES];
  for (unsigned i=0, j, k, l; i<Nx; i++)
    for (j=0; j<Ny; j++)
      for (k=0; k<Nz; k++)
        for (l=0; l<NUMSITESPERCELL; l++) {
          if (getSpecies(i,j,k,l) == el) {
            sumNNAtoms(i,j,k,l,sum);
            s += sum[0];
            s2 += sum[0]*sum[0];
          }
        }
  if (sig)
    *sig = sqrt(fabs(s2*(double)getNumAtoms(el)-s*s))/getNumAtoms(el);
  return s/(double)getNumAtoms(el);
}

double
lattice::calcChemLROP(double* /*sig*/) const
{
  int s = 0;
  switch (chemlro) {
    case FeNi3:  {
                  for (unsigned i=0, j, k; i<Nx; i++)
                    for (j=0; j<Ny; j++)
```

```
                    for (k=0; k<Nz; k++) {
                      s += (getSpecies(i,j,k,0) == 0 ? 1 : -1);
                      s += (getSpecies(i,j,k,1) == 1 ? 1 : -1);
                      s += (getSpecies(i,j,k,2) == 1 ? 1 : -1);
                      s += (getSpecies(i,j,k,3) == 1 ? 1 : -1);
                    }
                  return (s/(double)getNumAtoms());
                }
    case FeNi:  {
                  for (unsigned i=0, j, k; i<Nx; i++)
                    for (j=0; j<Ny; j++)
                      for (k=0; k<Nz; k++) {
                        s += (getSpecies(i,j,k,0) == 0 ? 1 : -1);
                        s += (getSpecies(i,j,k,1) == 0 ? 1 : -1);
                        s += (getSpecies(i,j,k,2) == 1 ? 1 : -1);
                        s += (getSpecies(i,j,k,3) == 1 ? 1 : -1);
                      }
                  return (s/(double)getNumAtoms());
                }
    case Fe3Ni:  {
                  for (unsigned i=0, j, k; i<Nx; i++)
                    for (j=0; j<Ny; j++)
                      for (k=0; k<Nz; k++) {
                        s += (getSpecies(i,j,k,0) == 1 ? 1 : -1);
                        s += (getSpecies(i,j,k,1) == 0 ? 1 : -1);
                        s += (getSpecies(i,j,k,2) == 0 ? 1 : -1);
                        s += (getSpecies(i,j,k,3) == 0 ? 1 : -1);
                      }
                  return (s/(double)getNumAtoms());
                }
  }
  return 0;
//  Fe3Ni ordering
//
/*  int s = 0;
  for (unsigned i=0, j, k; i<Nx; i++)
    for (j=0; j<Ny; j++)
      for (k=0; k<Nz; k++)
          if (getSpecies(i,j,k,0) == 1)
            s++;
  return (4*s/(double)getNumAtoms() - (1-c))/c;*/
}

double
lattice::calcSROP_AF(double* /*sig*/) const
{
  double s = 0;
  spinsum_t sumSpins[NUMSPECIES];
  for (unsigned i=0, j, k, l; i<Nx; i++)
    for (j=0; j<Ny; j++) {
      for (k=0; k<Nz; k++)
        for (l=0; l<NUMSITESPERCELL; l++) {
          sumNNSpins(i,j,k,l,sumSpins);
          s += getSpin(i,j,k,l)*(sumSpins[0]+sumSpins[1])/(double)NUMNNPERSITE;
        }
    }
  return -3*s/(4*Nx*Ny*Nz);
}

unsigned
lattice::calcFrustratedFeBonds(unsigned& nFeFe) const
{
  unsigned nf = 0;
  nFeFe = 0;
  spin_t s;
```

```
  atom a;
  double Jr;
  position_t p, pnn;
  for (p.i=0; p.i<Nx; p.i++)
    for (p.j=0; p.j<Ny; p.j++)
      for (p.k=0; p.k<Nz; p.k++)
        for (p.l=0; p.l<NUMSITESPERCELL; p.l++)
          if (getSpecies(p.i,p.j,p.k,p.l) == 0) {
             s = getSpin(p.i,p.j,p.k,p.l);
            for (unsigned m=0; m<NUMNNPERSITE_2; m++) {
              pnn = p + nn[p.l][m];
              a = getAtom(pnn.i, pnn.j, pnn.k, pnn.l);
              if (a.el == 0) {
                nFeFe++;
                Jr = calcJ(p.i, p.j, p.k, p.l, pnn.i, pnn.j, pnn.k, pnn.l);
                if (Jr*(a.s*s) < 0)
                  nf++;
              }
            }
          }
  return nf;
}

double
lattice::calcAvgdnn(double avga, species_t a1, species_t a2, dnnInfo* dnninfo)
const
{
  species_t a, ann;
  double d = 0, d2 = 0, di;
  double sd[2] = {0, 0};
  double sd2[2] = {0, 0};
  unsigned n = 0, sn0 = 0;
  position_t p, pnn;
  for (p.i=0; p.i<Nx; p.i++)
    for (p.j=0; p.j<Ny; p.j++)
      for (p.k=0; p.k<Nz; p.k++)
        for (p.l=0; p.l<NUMSITESPERCELL; p.l++) {
          a = getSpecies(p.i,p.j,p.k,p.l);
          for (unsigned m=0; m<NUMNNPERSITE_2; m++) {
            pnn = p + nn[p.l][m];
            ann = getSpecies(pnn.i, pnn.j, pnn.k, pnn.l);
            if ((a == a1 && ann == a2) || (a == a2 && ann == a1)) {
              di = calcavgd(p.i, p.j, p.k, p.l, pnn.i, pnn.j, pnn.k, pnn.l,
avga);
              if (getAtom(p.i, p.j, p.k, p.l).avgs*getAtom(pnn.i, pnn.j, pnn.k,
pnn.l).avgs > 0) {
                sd[0] += di;
                sd2[0] += di*di;
                sn0++;
              } else {
                sd[1] += di;
                sd2[1] += di*di;
              }
              d += di;
              d2 += di*di;
              n++;
            }
          }
        }
  if (n == 0)
    n = 1;
  d /= n;
  if (dnninfo) {
    dnninfo->avg[0] = d;
    dnninfo->avg[1] = sn0 ? sd[0]/sn0 : 0;
```

```
    dnninfo->avg[2] = n-sn0 ? sd[1]/(n-sn0) : 0;
    dnninfo->stdev[0] = sqrt(fabs(d2/n - d*d));
    dnninfo->stdev[1] = sn0 ? sqrt(fabs(sd2[0]/sn0 -
dnninfo->avg[1]*dnninfo->avg[1])) : 0;
    dnninfo->stdev[2] = n-sn0 ? sqrt(fabs(sd2[1]/(n-sn0) -
dnninfo->avg[2]*dnninfo->avg[2])) : 0;
    dnninfo->pup = (float)sn0/(float)n;
    dnninfo->n = n;
  }
  return d;
}

#if defined(DO_HDISTRIBUTION)
double
lattice::calcHhf(unsigned i, unsigned j, unsigned k, unsigned l) const
{
  double Hhf = Hhf_A*MU[0]*getSpinSum(i,j,k,l)/(double)atom::nsums;
  int sum = 0;
  switch(l) {
    case 0:  sum += MU[getSpecies(i,j,k,l)]*getSpinSum(i,j,k,l);
             sum += MU[getSpecies(i-1,j,k,l)]*getSpinSum(i-1,j,k,l);
             sum += MU[getSpecies(i,j-1,k,l)]*getSpinSum(i,j-1,k,l);
             sum += MU[getSpecies(i-1,j-1,k,l)]*getSpinSum(i-1,j-1,k,l);
             sum += MU[getSpecies(i,j,k,2)]*getSpinSum(i,j,k,2);
             sum += MU[getSpecies(i-1,j,k,2)]*getSpinSum(i-1,j,k,2);
             sum += MU[getSpecies(i,j,k-1,2)]*getSpinSum(i,j,k-1,2);
             sum += MU[getSpecies(i-1,j,k-1,2)]*getSpinSum(i-1,j,k-1,2);
             sum += MU[getSpecies(i,j,k,3)]*getSpinSum(i,j,k,3);
             sum += MU[getSpecies(i,j-1,k,3)]*getSpinSum(i,j-1,k,3);
             sum += MU[getSpecies(i,j,k-1,3)]*getSpinSum(i,j,k-1,3);
             sum += MU[getSpecies(i,j-1,k-1,3)]*getSpinSum(i,j-1,k-1,3);
             break;
    case 1:  sum += MU[getSpecies(i,j,k,0)]*getSpinSum(i,j,k,0);
             sum += MU[getSpecies(i+1,j,k,0)]*getSpinSum(i+1,j,k,0);
             sum += MU[getSpecies(i,j+1,k,0)]*getSpinSum(i,j+1,k,0);
             sum += MU[getSpecies(i+1,j+1,k,0)]*getSpinSum(i+1,j+1,k,0);
             sum += MU[getSpecies(i,j,k,2)]*getSpinSum(i,j,k,2);
             sum += MU[getSpecies(i,j+1,k,2)]*getSpinSum(i,j+1,k,2);
             sum += MU[getSpecies(i,j,k-1,2)]*getSpinSum(i,j,k-1,2);
             sum += MU[getSpecies(i,j+1,k-1,2)]*getSpinSum(i,j+1,k-1,2);
             sum += MU[getSpecies(i,j,k,3)]*getSpinSum(i,j,k,3);
             sum += MU[getSpecies(i+1,j,k,3)]*getSpinSum(i+1,j,k,3);
             sum += MU[getSpecies(i,j,k-1,3)]*getSpinSum(i,j,k-1,3);
             sum += MU[getSpecies(i+1,j,k-1,3)]*getSpinSum(i+1,j,k-1,3);
             break;
    case 2:  sum += MU[getSpecies(i,j,k,0)]*getSpinSum(i,j,k,0);
             sum += MU[getSpecies(i+1,j,k,0)]*getSpinSum(i+1,j,k,0);
             sum += MU[getSpecies(i,j,k+1,0)]*getSpinSum(i,j,k+1,0);
             sum += MU[getSpecies(i+1,j,k+1,0)]*getSpinSum(i+1,j,k+1,0);
             sum += MU[getSpecies(i,j,k,1)]*getSpinSum(i,j,k,1);
             sum += MU[getSpecies(i,j-1,k,1)]*getSpinSum(i,j-1,k,1);
             sum += MU[getSpecies(i,j,k+1,1)]*getSpinSum(i,j,k+1,1);
             sum += MU[getSpecies(i,j-1,k+1,1)]*getSpinSum(i,j-1,k+1,1);
             sum += MU[getSpecies(i,j,k,3)]*getSpinSum(i,j,k,3);
             sum += MU[getSpecies(i+1,j,k,3)]*getSpinSum(i+1,j,k,3);
             sum += MU[getSpecies(i,j-1,k,3)]*getSpinSum(i,j-1,k,3);
             sum += MU[getSpecies(i+1,j-1,k,3)]*getSpinSum(i+1,j-1,k,3);
             break;
    case 3:  sum += MU[getSpecies(i,j,k,0)]*getSpinSum(i,j,k,0);
             sum += MU[getSpecies(i,j+1,k,0)]*getSpinSum(i,j+1,k,0);
             sum += MU[getSpecies(i,j,k+1,0)]*getSpinSum(i,j,k+1,0);
             sum += MU[getSpecies(i,j+1,k+1,0)]*getSpinSum(i,j+1,k+1,0);
             sum += MU[getSpecies(i,j,k,1)]*getSpinSum(i,j,k,1);
             sum += MU[getSpecies(i-1,j,k,1)]*getSpinSum(i-1,j,k,1);
             sum += MU[getSpecies(i,j,k+1,1)]*getSpinSum(i,j,k+1,1);
```

```
            sum += MU[getSpecies(i-1,j,k+1,1)]*getSpinSum(i-1,j,k+1,1);
            sum += MU[getSpecies(i,j,k,2)]*getSpinSum(i,j,k,2);
            sum += MU[getSpecies(i-1,j,k,2)]*getSpinSum(i-1,j,k,2);
            sum += MU[getSpecies(i,j+1,k,2)]*getSpinSum(i,j+1,k,2);
            sum += MU[getSpecies(i-1,j+1,k,2)]*getSpinSum(i-1,j+1,k,2);
            break;
  }
  Hhf += Hhf_B*sum/(double)atom::nsums;
  return fabs(Hhf);
}

double
lattice::calcHhfDistribution(double** PHhf, unsigned n, double dHhf)
{
  if (getNumAtoms(0) == 0)
    return 0;
  double Hhfavg = 0;
  unsigned ni;
  for (unsigned j=0; j<13; j++)
    for (unsigned i=0; i<n; i++)
      PHhf[j][i] = 0;
  double Hhf;
  int sum[NUMSPECIES];
  for (unsigned i=0, j, k, l; i<Nx; i++)
    for (j=0; j<Ny; j++)
      for (k=0; k<Nz; k++)
        for (l=0; l<4; l++)
          if (getSpecies(i,j,k,l) == 0) {
            Hhf = calcHhf(i,j,k,l);
            Hhfavg += Hhf;
            ni = floor(Hhf/dHhf);
            if (ni < n) {
              sumNNAtoms(i,j,k,l,sum);
              PHhf[sum[0]][ni]++;
            }
          }
   for (unsigned j=0; j<13; j++)
     for (unsigned i=0; i<n; i++)
       PHhf[j][i] /= getNumAtoms(0);
   return Hhfavg/getNumAtoms(0);
}
#endif

inline void
lattice::setTemp(double T_)
{
  T = T_;
  reset_atomavg();
}

inline void
lattice::setPressure(double P_)
{
  P = P_;
  reset_atomavg();
}

inline void
lattice::setdnn(double dnn_) {
  dnn = dnn_;
  dnn2x2 = 2*dnn*dnn;
}

inline void
lattice::resetE(double E_) {
```

```
  Energy = E_;
}

inline float
lattice::calcVolProb(double d, double& dE) {
// remember current values
  double prevE = Energy;
  double prevd = dnn;
  double prev2d2 = dnn2x2;
// set new values
  dnn = d;
  dnn2x2 = 2*dnn*dnn;
  dE = calcE() - prevE;
  float p;
  if (P != 0) {
    double prevd3 = prevd*prevd*prevd;
    double d3 = dnn*dnn*dnn;
    double dV = N*(d3-prevd3)*M_SQRT_2;
  // we use N+2/3 because we are uniformly sampling the length (biased sampling)
  // as opposed to the volume, in which case we would use N
    p = metropolisProb(-(dE+P*dV)/T + (N+0.6666666666666666667)*log(d3/prevd3));
  } else
    p = metropolisProb(-dE/T + (3*N+2)*log(d/prevd));
// return to initial values
  dnn = prevd;
  dnn2x2 = prev2d2;
  Energy = prevE;
  return p;
}

inline float
lattice::calcMoveProb(unsigned i, unsigned j, unsigned k, unsigned l, float
dr[3], double& dE)
{
  atom& at = getAtom(i,j,k,l);
#if defined(DO_MAG)
  double Eprev = calcChemE(i,j,k,l)+calcMagE(i,j,k,l);
#else
  double Eprev = calcChemE(i,j,k,l);
#endif
/*  float prevdr[3];
  prevdr[0] = at.dr[0];
  prevdr[1] = at.dr[1];
  prevdr[2] = at.dr[2];*/
  at.dr[0] += dr[0];
  at.dr[1] += dr[1];
  at.dr[2] += dr[2];
#if defined(DO_MAG)
  dE = calcChemE(i,j,k,l)+calcMagE(i,j,k,l)-Eprev;
#else
  dE = calcChemE(i,j,k,l)-Eprev;
#endif
/*  at.dr[0] = prevdr[0];
  at.dr[1] = prevdr[1];
  at.dr[2] = prevdr[2];*/
  return metropolisProb(-dE/T);
}

inline float
lattice::calcFlipProb(unsigned i, unsigned j, unsigned k, unsigned l, const
spin_t& news, double& dE) const
{
#if defined(HEISENBERG)
  spin_t olds = getSpin(i,j,k,l);
  getSpin(i,j,k,l) = news-olds;
```

```
  dE = calcMagE(i,j,k,l);
  getSpin(i,j,k,l) = olds;
#else
  dE = -2*calcMagE(i,j,k,l);
#endif
  return metropolisProb(-dE/T);
}

void
lattice::initialize(spinorder state)
{
  switch(state) {
    case ferro:       {
                       for (unsigned i=0, j, k, l; i<Nx; i++)
                         for (j=0; j<Ny; j++)
                           for (k=0; k<Nz; k++)
                             for (l=0; l<NUMSITESPERCELL; l++)
                               getSpin(i,j,k,l) = 1;
                      }
                      break;
    case Niferro:     {
                       for (unsigned i=0, j, k, l; i<Nx; i++)
                         for (j=0; j<Ny; j++)
                           for (k=0; k<Nz; k++)
                             for (l=0; l<NUMSITESPERCELL; l++) {
                               if (getSpecies(i,j,k,l) == 1)
                                 getSpin(i,j,k,l) = 1;
                               else {
#if defined(HEISENBERG)
                                 float ct = 2*ranf()-1;
                                 float phi = 2*M_PI*ranf();
                                 getSpin(i,j,k,l).x = cos(phi)*sqrt(1-ct*ct);
                                 getSpin(i,j,k,l).y = sin(phi)*sqrt(1-ct*ct);
                                 getSpin(i,j,k,l).z = ct;
#else
                                 getSpin(i,j,k,l) = ranf() < 0.5 ? 1 : -1;
#endif
                               }
                             }
                      }
                      break;
    case antiferro:   {
                       for (unsigned i=0, j, k; i<Nx; i++)
                         for (j=0; j<Ny; j++)
                           for (k=0; k<Nz; k++) {
                             getSpin(i,j,k,0) = 1;
                             getSpin(i,j,k,1) = 1;
                             getSpin(i,j,k,2) = -1;
                             getSpin(i,j,k,3) = -1;
                           }
                      }
                      break;
    default:          {
                       for (unsigned i=0, j, k, l; i<Nx; i++)
                         for (j=0; j<Ny; j++)
                           for (k=0; k<Nz; k++)
                             for (l=0; l<NUMSITESPERCELL; l++) {
#if defined(HEISENBERG)
                               float ct = 2*ranf()-1;
                               float phi = 2*M_PI*ranf();
                               getSpin(i,j,k,l).x = cos(phi)*sqrt(1-ct*ct);
                               getSpin(i,j,k,l).y = sin(phi)*sqrt(1-ct*ct);
                               getSpin(i,j,k,l).z = ct;
#else
                               getSpin(i,j,k,l) = (ranf() < 0.5 ? -1 : 1);
```

```
#endif
                                }
                        }
                        break;
  }
}

void
lattice::initialize(chemorder state)
{
  chemlro = state;
  switch(state) {
    case Fe3Ni:     {
                      N0 = 0;
                      if (c <= 0.75) {
                        for (unsigned i=0, j, k; i<Nx; i++)
                          for (j=0; j<Ny; j++)
                            for (k=0; k<Nz; k++) {
                              getSpecies(i,j,k,0) = 1;
                              if (ranf() < c/0.75) {
                                getSpecies(i,j,k,1) = 0;
                                N0++;
                              } else
                                getSpecies(i,j,k,1) = 1;
                              if (ranf() < c/0.75) {
                                getSpecies(i,j,k,2) = 0;
                                N0++;
                              } else
                                getSpecies(i,j,k,2) = 1;
                              if (ranf() < c/0.75) {
                                getSpecies(i,j,k,3) = 0;
                                N0++;
                              } else
                                getSpecies(i,j,k,3) = 1;
                            }
                      } else {
                        for (unsigned i=0, j, k; i<Nx; i++)
                          for (j=0; j<Ny; j++)
                            for (k=0; k<Nz; k++) {
                              if (ranf() < (c-0.75)/0.25) {
                                getSpecies(i,j,k,0) = 0;
                                N0++;
                              } else
                                getSpecies(i,j,k,0) = 1;
                              getSpecies(i,j,k,1) = 0;
                              getSpecies(i,j,k,2) = 0;
                              getSpecies(i,j,k,3) = 0;
                              N0 += 3;
                            }
                      }
                    }
                    break;
    case FeNi:      {
                      N0 = 0;
                      if (c >= 0.5) {
                        for (unsigned i=0, j, k; i<Nx; i++)
                          for (j=0; j<Ny; j++)
                            for (k=0; k<Nz; k++) {
                              getSpecies(i,j,k,0) = 0;
                              getSpecies(i,j,k,1) = 0;
                              N0 += 2;
                              if (ranf() < (c-0.5)/0.5) {
                                getSpecies(i,j,k,2) = 0;
                                N0++;
                              } else
```

```
                        getSpecies(i,j,k,2) = 1;
                      if (ranf() < (c-0.5)/0.5) {
                        getSpecies(i,j,k,3) = 0;
                        N0++;
                      } else
                        getSpecies(i,j,k,3) = 1;
                    }
                  } else {
                    for (unsigned i=0, j, k; i<Nx; i++)
                      for (j=0; j<Ny; j++)
                        for (k=0; k<Nz; k++) {
                          getSpecies(i,j,k,0) = 0;
                          getSpecies(i,j,k,1) = 0;
                          N0 += 2;
                          if (ranf() < (0.5-c)/0.5) {
                            getSpecies(i,j,k,2) = 0;
                            N0++;
                          } else
                            getSpecies(i,j,k,2) = 1;
                          if (ranf() < (0.5-c)/0.5) {
                            getSpecies(i,j,k,3) = 0;
                            N0++;
                          } else
                            getSpecies(i,j,k,3) = 1;
                        }
                  }
                }
                break;
case FeNi3:     {
                  N0 = 0;
                  if (c >= 0.25) {
                    for (unsigned i=0, j, k; i<Nx; i++)
                      for (j=0; j<Ny; j++)
                        for (k=0; k<Nz; k++) {
                          getSpecies(i,j,k,0) = 0;
                          N0++;
                          if (ranf() < (c-0.25)/0.75) {
                            getSpecies(i,j,k,1) = 0;
                            N0++;
                          } else
                            getSpecies(i,j,k,1) = 1;
                          if (ranf() < (c-0.25)/0.75) {
                            getSpecies(i,j,k,2) = 0;
                            N0++;
                          } else
                            getSpecies(i,j,k,2) = 1;
                          if (ranf() < (c-0.25)/0.75) {
                            getSpecies(i,j,k,3) = 0;
                            N0++;
                          } else
                            getSpecies(i,j,k,3) = 1;
                        }
                  } else {
                    for (unsigned i=0, j, k; i<Nx; i++)
                      for (j=0; j<Ny; j++)
                        for (k=0; k<Nz; k++) {
                          if (ranf() < (0.25-c)/0.25)
                            getSpecies(i,j,k,0) = 1;
                          else {
                            getSpecies(i,j,k,0) = 0;
                            N0++;
                          }
                          getSpecies(i,j,k,1) = 1;
                          getSpecies(i,j,k,2) = 1;
                          getSpecies(i,j,k,3) = 1;
```

```
                        }
                    }
                }
                break;
    default:    {
                    N0 = 0;
                    for (unsigned i=0, j, k, l; i<Nx; i++)
                      for (j=0; j<Ny; j++)
                        for (k=0; k<Nz; k++)
                          for (l=0; l<NUMSITESPERCELL; l++)
                            if (ranf() < c) {
                              getSpecies(i,j,k,l) = 0;
                              N0++;
                            } else
                              getSpecies(i,j,k,l) = 1;
                }
                break;
  }
  unsigned N0c = floor(getNumAtoms()*c+0.5);
  unsigned i, j, k, l;
  while (N0 > N0c && N0 > 0) {
    i = Nx*ranf();
    j = Ny*ranf();
    k = Nz*ranf();
    l = NUMSITESPERCELL*ranf();
    if (getSpecies(i,j,k,l) == 0) {
      getSpecies(i,j,k,l) = 1;
      N0--;
    }
  }
  while (N0 < N0c && N0 < N) {
    i = Nx*ranf();
    j = Ny*ranf();
    k = Nz*ranf();
    l = NUMSITESPERCELL*ranf();
    if (getSpecies(i,j,k,l) == 1) {
      getSpecies(i,j,k,l) = 0;
      N0++;
    }
  }
  c = N0/(double)N;
// expected volume from Vegaard's law
  double d =
pow(c*(d0[0][0]*d0[0][0]*d0[0][0])+(1-c)*(d0[1][1]*d0[1][1]*d0[1][1]),
0.333333333333333333);
  double d65 =
pow(0.65*(d0[0][0]*d0[0][0]*d0[0][0])+0.35*(d0[1][1]*d0[1][1]*d0[1][1]),
0.333333333333333333);
// set dnn0 to the paramagnetic volume at T=0
  dnn0 = dnn0*d/d65;
#if defined(DO_MAG)
#if defined(JFEFE_BOSE)
  dFeFe_dnn02 = d0[0][0]*d0[0][0]/(d*d);

#else
  dnn02 = dnn0*dnn0;
  dJ_dr2[0][0] = dJ_dr[0][0]/(2*dnn0);
  dJ_dr2[1][0] = dJ_dr[1][0]/(2*dnn0);
  dJ_dr2[0][1] = dJ_dr[0][1]/(2*dnn0);
  dJ_dr2[1][1] = dJ_dr[1][1]/(2*dnn0);
  #if defined(JFEFE_MINMAX)
  dnn12 = dJ_dr2[0][0] != 0 ? dnn02 + 200/dJ_dr2[0][0] : 1000*dnn02;
  TRACE("dnn0 = " << dnn0 << ", dnn1 = " << sqrt(dnn12));
  #endif
#endif  // JFEFE_BOSE
```

```
#endif  // DO_MAG
}

bool
lattice::saveSystem(char* fn)
{
  ofstream os(fn);
  if (!os)
    return false;
  os << "constant pressure, constant temperature MC system" << endl;
  os << Nx << '\t' << Ny << '\t' << Nz << '\n';
  os << "N = " << getNumAtoms() << "\tc = " <<
getNumAtoms(0)/(double)getNumAtoms() << endl;
  os << "magnetic exchange parameters:\t" << J0[0][0] << '\t' << J0[0][1] << '\t'
<< J0[1][1] << '\t' << dJ_dr[0][0] << '\t' << dJ_dr[0][1] << '\t' << dJ_dr[1][1]
<< '\t' << dnn0 << endl;
//  os << "magnetic exchange parameters:\t" << J0[0][0] << '\t' << J0[0][1] <<
'\t' << J0[1][1] << '\t' << alphaJ << '\t' << betaJ << '\t' << dnn0J2 << '\t' <<
r0J2 << endl;
//  os_main << "chemical exchange parameters:\t" << U0[0][0] << '\t' << d0[0][0]
<< '\t' << U0[0][1] << '\t' << d0[0][1] << '\t' << U0[1][1] << '\t' << d0[1][1]
<< endl;
  os << dnn << '\t' << avgdnn << endl;
  for (unsigned i=0, j, k, l; i<Nx; i++)
    for (j=0; j<Ny; j++)
      for (k=0; k<Nz; k++)
        for (l=0; l<NUMSITESPERCELL; l++)
          os << getAtom(i,j,k,l) << '\n';
  return !os.fail();
}

bool
lattice::readSystem(char* fn)
{
  ifstream is(fn);
  if (!is)
    return false;
  char buf[255];
  is.getline(buf, sizeof(buf));
  int format = 0;
  TRACE("loading system from " << fn);
  if (strcmp(buf, "constant pressure, constant temperature MC system") == 0)
    format = 1;
  else
    is.seekg(0, ios::beg);
  for (unsigned i=0; i<Nx; i++) {
    for (unsigned j=0; j<Ny; j++) {
      for (unsigned k=0; k<Nz; k++)
        delete[] atoms[i][j][k];
      delete[] (atoms[i][j]-1);
    }
    delete[] (atoms[i]-1);
  }
  delete[] (atoms-1);
  is >> Nx >> Ny >> Nz;
  is.ignore();
  if (format == 1) {
    is.getline(buf, sizeof(buf));
    is.getline(buf, sizeof(buf));
    is >> dnn >> avgdnn;
    is.ignore(255, '\n');
    dnn2x2 = 2*dnn*dnn;
  }
  setup();
  N0 = 0;
```

```
  int t1, t2;
  for (unsigned i=0, j, k, l; i<Nx; i++)
    for (j=0; j<Ny; j++)
      for (k=0; k<Nz; k++)
        for (l=0; l<NUMSITESPERCELL; l++) {
          if (format == 1) {
            is >> getAtom(i,j,k,l);
            is.ignore(255, '\n');
          } else {
            is >> t1 >> t2;
            getSpecies(i,j,k,l) = (species_t)t1;
            getSpin(i,j,k,l) = (spin_t)t2;
          }
          if (getSpecies(i,j,k,l) == 0)
            N0++;
        }
  c = N0/(double)N;
  double d =
pow(c*(d0[0][0]*d0[0][0]*d0[0][0])+(1-c)*(d0[1][1]*d0[1][1]*d0[1][1]),
0.333333333333333333);
  double d65 =
pow(0.65*(d0[0][0]*d0[0][0]*d0[0][0])+0.35*(d0[1][1]*d0[1][1]*d0[1][1]),
0.333333333333333333);
// set dnn0 to the paramagnetic volume at T=0
  dnn0 = dnn0*d/d65;
#if defined(JFEFE_BOSE)
  dFeFe_dnn02 = d0[0][0]*d0[0][0]/(d*d);
#else
  dnn02 = dnn0*dnn0;
  dJ_dr2[0][0] = dJ_dr[0][0]/(2*dnn0);
  dJ_dr2[1][0] = dJ_dr[1][0]/(2*dnn0);
  dJ_dr2[0][1] = dJ_dr[0][1]/(2*dnn0);
  dJ_dr2[1][1] = dJ_dr[1][1]/(2*dnn0);
#if defined(JFEFE_MINMAX)
  dnn12 = dJ_dr2[0][0] != 0 ? dnn02 + 200/dJ_dr2[0][0] : 1000*dnn02;
#endif
#endif
  return !is.fail();
}

void
lattice::sumNNSpins(unsigned i, unsigned j, unsigned k, unsigned l, spinsum_t
sumSpins[NUMSPECIES]) const
{
  sumSpins[0] = 0;
  sumSpins[1] = 0;
  switch(l) {
    case 0:  sumSpins[getSpecies(i,j,k,1)] += getSpin(i,j,k,1);
             sumSpins[getSpecies(i-1,j,k,1)] += getSpin(i-1,j,k,1);
             sumSpins[getSpecies(i,j-1,k,1)] += getSpin(i,j-1,k,1);
             sumSpins[getSpecies(i-1,j-1,k,1)] += getSpin(i-1,j-1,k,1);
             sumSpins[getSpecies(i,j,k,2)] += getSpin(i,j,k,2);
             sumSpins[getSpecies(i-1,j,k,2)] += getSpin(i-1,j,k,2);
             sumSpins[getSpecies(i,j,k-1,2)] += getSpin(i,j,k-1,2);
             sumSpins[getSpecies(i-1,j,k-1,2)] += getSpin(i-1,j,k-1,2);
             sumSpins[getSpecies(i,j,k,3)] += getSpin(i,j,k,3);
             sumSpins[getSpecies(i,j-1,k,3)] += getSpin(i,j-1,k,3);
             sumSpins[getSpecies(i,j,k-1,3)] += getSpin(i,j,k-1,3);
             sumSpins[getSpecies(i,j-1,k-1,3)] += getSpin(i,j-1,k-1,3);
             break;
    case 1:  sumSpins[getSpecies(i,j,k,0)] += getSpin(i,j,k,0);
             sumSpins[getSpecies(i+1,j,k,0)] += getSpin(i+1,j,k,0);
             sumSpins[getSpecies(i,j+1,k,0)] += getSpin(i,j+1,k,0);
             sumSpins[getSpecies(i+1,j+1,k,0)] += getSpin(i+1,j+1,k,0);
             sumSpins[getSpecies(i,j,k,2)] += getSpin(i,j,k,2);
```

```
            sumSpins[getSpecies(i,j+1,k,2)] += getSpin(i,j+1,k,2);
            sumSpins[getSpecies(i,j,k-1,2)] += getSpin(i,j,k-1,2);
            sumSpins[getSpecies(i,j+1,k-1,2)] += getSpin(i,j+1,k-1,2);
            sumSpins[getSpecies(i,j,k,3)] += getSpin(i,j,k,3);
            sumSpins[getSpecies(i+1,j,k,3)] += getSpin(i+1,j,k,3);
            sumSpins[getSpecies(i,j,k-1,3)] += getSpin(i,j,k-1,3);
            sumSpins[getSpecies(i+1,j,k-1,3)] += getSpin(i+1,j,k-1,3);
            break;
    case 2:  sumSpins[getSpecies(i,j,k,0)] += getSpin(i,j,k,0);
            sumSpins[getSpecies(i+1,j,k,0)] += getSpin(i+1,j,k,0);
            sumSpins[getSpecies(i,j,k+1,0)] += getSpin(i,j,k+1,0);
            sumSpins[getSpecies(i+1,j,k+1,0)] += getSpin(i+1,j,k+1,0);
            sumSpins[getSpecies(i,j,k,1)] += getSpin(i,j,k,1);
            sumSpins[getSpecies(i,j-1,k,1)] += getSpin(i,j-1,k,1);
            sumSpins[getSpecies(i,j,k+1,1)] += getSpin(i,j,k+1,1);
            sumSpins[getSpecies(i,j-1,k+1,1)] += getSpin(i,j-1,k+1,1);
            sumSpins[getSpecies(i,j,k,3)] += getSpin(i,j,k,3);
            sumSpins[getSpecies(i+1,j,k,3)] += getSpin(i+1,j,k,3);
            sumSpins[getSpecies(i,j-1,k,3)] += getSpin(i,j-1,k,3);
            sumSpins[getSpecies(i+1,j-1,k,3)] += getSpin(i+1,j-1,k,3);
            break;
    case 3:  sumSpins[getSpecies(i,j,k,0)] += getSpin(i,j,k,0);
            sumSpins[getSpecies(i,j+1,k,0)] += getSpin(i,j+1,k,0);
            sumSpins[getSpecies(i,j,k+1,0)] += getSpin(i,j,k+1,0);
            sumSpins[getSpecies(i,j+1,k+1,0)] += getSpin(i,j+1,k+1,0);
            sumSpins[getSpecies(i,j,k,1)] += getSpin(i,j,k,1);
            sumSpins[getSpecies(i-1,j,k,1)] += getSpin(i-1,j,k,1);
            sumSpins[getSpecies(i,j,k+1,1)] += getSpin(i,j,k+1,1);
            sumSpins[getSpecies(i-1,j,k+1,1)] += getSpin(i-1,j,k+1,1);
            sumSpins[getSpecies(i,j,k,2)] += getSpin(i,j,k,2);
            sumSpins[getSpecies(i-1,j,k,2)] += getSpin(i-1,j,k,2);
            sumSpins[getSpecies(i,j+1,k,2)] += getSpin(i,j+1,k,2);
            sumSpins[getSpecies(i-1,j+1,k,2)] += getSpin(i-1,j+1,k,2);
            break;
  }
}

void
lattice::sumNNAtoms(unsigned i, unsigned j, unsigned k, unsigned l, species_t
sumSpecies[NUMSPECIES]) const
{
  sumSpecies[0] = 0;
  sumSpecies[1] = 0;
  switch(l) {
    case 0:  sumSpecies[getSpecies(i,j,k,1)]++;
            sumSpecies[getSpecies(i-1,j,k,1)]++;
            sumSpecies[getSpecies(i,j-1,k,1)]++;
            sumSpecies[getSpecies(i-1,j-1,k,1)]++;
            sumSpecies[getSpecies(i,j,k,2)]++;
            sumSpecies[getSpecies(i-1,j,k,2)]++;
            sumSpecies[getSpecies(i,j,k-1,2)]++;
            sumSpecies[getSpecies(i-1,j,k-1,2)]++;
            sumSpecies[getSpecies(i,j,k,3)]++;
            sumSpecies[getSpecies(i,j-1,k,3)]++;
            sumSpecies[getSpecies(i,j,k-1,3)]++;
            sumSpecies[getSpecies(i,j-1,k-1,3)]++;
            break;
    case 1:  sumSpecies[getSpecies(i,j,k,0)]++;
            sumSpecies[getSpecies(i+1,j,k,0)]++;
            sumSpecies[getSpecies(i,j+1,k,0)]++;
            sumSpecies[getSpecies(i+1,j+1,k,0)]++;
            sumSpecies[getSpecies(i,j,k,2)]++;
            sumSpecies[getSpecies(i,j+1,k,2)]++;
            sumSpecies[getSpecies(i,j,k-1,2)]++;
            sumSpecies[getSpecies(i,j+1,k-1,2)]++;
```

```
            sumSpecies[getSpecies(i,j,k,3)]++;
            sumSpecies[getSpecies(i+1,j,k,3)]++;
            sumSpecies[getSpecies(i,j,k-1,3)]++;
            sumSpecies[getSpecies(i+1,j,k-1,3)]++;
            break;
    case 2:  sumSpecies[getSpecies(i,j,k,0)]++;
            sumSpecies[getSpecies(i+1,j,k,0)]++;
            sumSpecies[getSpecies(i,j,k+1,0)]++;
            sumSpecies[getSpecies(i+1,j,k+1,0)]++;
            sumSpecies[getSpecies(i,j,k,1)]++;
            sumSpecies[getSpecies(i,j-1,k,1)]++;
            sumSpecies[getSpecies(i,j,k+1,1)]++;
            sumSpecies[getSpecies(i,j-1,k+1,1)]++;
            sumSpecies[getSpecies(i,j,k,3)]++;
            sumSpecies[getSpecies(i+1,j,k,3)]++;
            sumSpecies[getSpecies(i,j-1,k,3)]++;
            sumSpecies[getSpecies(i+1,j-1,k,3)]++;
            break;
    case 3:  sumSpecies[getSpecies(i,j,k,0)]++;
            sumSpecies[getSpecies(i,j+1,k,0)]++;
            sumSpecies[getSpecies(i,j,k+1,0)]++;
            sumSpecies[getSpecies(i,j+1,k+1,0)]++;
            sumSpecies[getSpecies(i,j,k,1)]++;
            sumSpecies[getSpecies(i-1,j,k,1)]++;
            sumSpecies[getSpecies(i,j,k+1,1)]++;
            sumSpecies[getSpecies(i-1,j,k+1,1)]++;
            sumSpecies[getSpecies(i,j,k,2)]++;
            sumSpecies[getSpecies(i-1,j,k,2)]++;
            sumSpecies[getSpecies(i,j+1,k,2)]++;
            sumSpecies[getSpecies(i-1,j+1,k,2)]++;
            break;
  }
}

double
lattice::calcChemE(unsigned i, unsigned j, unsigned k, unsigned l) const
{
  const species_t e1 = getSpecies(i,j,k,l);
  double E = 0;
  switch(l) {
    case 0: E += U2(e1, getSpecies(i,j,k,1),       calcd2(i,j,k,l,i,j,k,1))
              + U2(e1, getSpecies(i-1,j,k,1),     calcd2(i,j,k,l,i-1,j,k,1))
              + U2(e1, getSpecies(i,j-1,k,1),     calcd2(i,j,k,l,i,j-1,k,1))
              + U2(e1, getSpecies(i-1,j-1,k,1),   calcd2(i,j,k,l,i-1,j-1,k,1))
              + U2(e1, getSpecies(i,j,k,2),       calcd2(i,j,k,l,i,j,k,2))
              + U2(e1, getSpecies(i-1,j,k,2),     calcd2(i,j,k,l,i-1,j,k,2))
              + U2(e1, getSpecies(i,j,k-1,2),     calcd2(i,j,k,l,i,j,k-1,2))
              + U2(e1, getSpecies(i-1,j,k-1,2),   calcd2(i,j,k,l,i-1,j,k-1,2))
              + U2(e1, getSpecies(i,j,k,3),       calcd2(i,j,k,l,i,j,k,3))
              + U2(e1, getSpecies(i,j-1,k,3),     calcd2(i,j,k,l,i,j-1,k,3))
              + U2(e1, getSpecies(i,j,k-1,3),     calcd2(i,j,k,l,i,j,k-1,3))
              + U2(e1, getSpecies(i,j-1,k-1,3),   calcd2(i,j,k,l,i,j-1,k-1,3));
             break;
    case 1:  E += U2(e1, getSpecies(i+1,j+1,k,0),   calcd2(i,j,k,l,i+1,j+1,k,0))
              + U2(e1, getSpecies(i,j,k,0),       calcd2(i,j,k,l,i,j,k,0))
              + U2(e1, getSpecies(i+1,j,k,0),     calcd2(i,j,k,l,i+1,j,k,0))
              + U2(e1, getSpecies(i,j+1,k,0),     calcd2(i,j,k,l,i,j+1,k,0))
              + U2(e1, getSpecies(i,j+1,k,2),     calcd2(i,j,k,l,i,j+1,k,2))
              + U2(e1, getSpecies(i,j,k,2),       calcd2(i,j,k,l,i,j,k,2))
              + U2(e1, getSpecies(i,j,k-1,2),     calcd2(i,j,k,l,i,j,k-1,2))
              + U2(e1, getSpecies(i,j+1,k-1,2),   calcd2(i,j,k,l,i,j+1,k-1,2))
              + U2(e1, getSpecies(i+1,j,k,3),     calcd2(i,j,k,l,i+1,j,k,3))
              + U2(e1, getSpecies(i+1,j,k-1,3),   calcd2(i,j,k,l,i+1,j,k-1,3))
              + U2(e1, getSpecies(i,j,k,3),       calcd2(i,j,k,l,i,j,k,3))
              + U2(e1, getSpecies(i,j,k-1,3),     calcd2(i,j,k,l,i,j,k-1,3));
```

```
            break;
    case 2:  E += U2(e1, getSpecies(i+1,j,k+1,0),   calcd2(i,j,k,l,i+1,j,k+1,0))
              + U2(e1, getSpecies(i,j,k,0),        calcd2(i,j,k,l,i,j,k,0))
              + U2(e1, getSpecies(i+1,j,k,0),      calcd2(i,j,k,l,i+1,j,k,0))
              + U2(e1, getSpecies(i,j,k+1,0),      calcd2(i,j,k,l,i,j,k+1,0))
              + U2(e1, getSpecies(i,j,k+1,1),      calcd2(i,j,k,l,i,j,k+1,1))
              + U2(e1, getSpecies(i,j-1,k+1,1),    calcd2(i,j,k,l,i,j-1,k+1,1))
              + U2(e1, getSpecies(i,j-1,k,1),      calcd2(i,j,k,l,i,j-1,k,1))
              + U2(e1, getSpecies(i,j,k,1),        calcd2(i,j,k,l,i,j,k,1))
              + U2(e1, getSpecies(i+1,j,k,3),      calcd2(i,j,k,l,i+1,j,k,3))
              + U2(e1, getSpecies(i+1,j-1,k,3),    calcd2(i,j,k,l,i+1,j-1,k,3))
              + U2(e1, getSpecies(i,j-1,k,3),      calcd2(i,j,k,l,i,j-1,k,3))
              + U2(e1, getSpecies(i,j,k,3),        calcd2(i,j,k,l,i,j,k,3));
            break;
    case 3:  E += U2(e1, getSpecies(i,j+1,k+1,0),   calcd2(i,j,k,l,i,j+1,k+1,0))
              + U2(e1, getSpecies(i,j,k,0),        calcd2(i,j,k,l,i,j,k,0))
              + U2(e1, getSpecies(i,j,k+1,0),      calcd2(i,j,k,l,i,j,k+1,0))
              + U2(e1, getSpecies(i,j+1,k,0),      calcd2(i,j,k,l,i,j+1,k,0))
              + U2(e1, getSpecies(i,j,k+1,1),      calcd2(i,j,k,l,i,j,k+1,1))
              + U2(e1, getSpecies(i-1,j,k+1,1),    calcd2(i,j,k,l,i-1,j,k+1,1))
              + U2(e1, getSpecies(i-1,j,k,1),      calcd2(i,j,k,l,i-1,j,k,1))
              + U2(e1, getSpecies(i,j,k,1),        calcd2(i,j,k,l,i,j,k,1))
              + U2(e1, getSpecies(i,j+1,k,2),      calcd2(i,j,k,l,i,j+1,k,2))
              + U2(e1, getSpecies(i-1,j+1,k,2),    calcd2(i,j,k,l,i-1,j+1,k,2))
              + U2(e1, getSpecies(i-1,j,k,2),      calcd2(i,j,k,l,i-1,j,k,2))
              + U2(e1, getSpecies(i,j,k,2),        calcd2(i,j,k,l,i,j,k,2));
            break;
  }
// much slower code
/*  double E2 = 0;
  for (unsigned m=0; m<NUMNNPERSITE; m++) {
    e2 = getSpecies(i+nn[l][m].di,j+nn[l][m].dj,k+nn[l][m].dk,nn[l][m].l);
    r2 = calcd2(i,j,k,l,i+nn[l][m].di,j+nn[l][m].dj,k+nn[l][m].dk,nn[l][m].l);
    E += U2(e1, e2, r2);
  }*/
/*  for (unsigned m=0; m<NUM2NNPERSITE; m++) {
//    e2 = getSpecies(i+nn[l][m].i,j+nn[l][m].j,k+nn[l][m].k,nn[l][m].l);
    r2 =
calcd2(i,j,k,l,i+nnn[l][m].di,j+nnn[l][m].dj,k+nnn[l][m].dk,nnn[l][m].l);
    E += U2(e1, e2, r2);
  }*/
  return E;
}

double
lattice::calcMagE(unsigned i, unsigned j, unsigned k, unsigned l) const
{
  spinf_t E;
  switch(l) {
    case 0: E = calcJs2(i,j,k,l,i,j,k,l)
              + calcJs2(i,j,k,l,i-1,j,k,l)
              + calcJs2(i,j,k,l,i,j-1,k,l)
              + calcJs2(i,j,k,l,i-1,j-1,k,l)
              + calcJs2(i,j,k,l,i,j,k,2)
              + calcJs2(i,j,k,l,i-1,j,k,2)
              + calcJs2(i,j,k,l,i,j,k-1,2)
              + calcJs2(i,j,k,l,i-1,j,k-1,2)
              + calcJs2(i,j,k,l,i,j,k,3)
              + calcJs2(i,j,k,l,i,j-1,k,3)
              + calcJs2(i,j,k,l,i,j,k-1,3)
              + calcJs2(i,j,k,l,i,j-1,k-1,3);
            break;
    case 1:  E = calcJs2(i,j,k,l,i+1,j+1,k,0)
              + calcJs2(i,j,k,l,i,j,k,0)
              + calcJs2(i,j,k,l,i+1,j,k,0)
```

```
              + calcJs2(i,j,k,l,i,j+1,k,0)
              + calcJs2(i,j,k,l,i,j+1,k,2)
              + calcJs2(i,j,k,l,i,j,k,2)
              + calcJs2(i,j,k,l,i,j,k-1,2)
              + calcJs2(i,j,k,l,i,j+1,k-1,2)
              + calcJs2(i,j,k,l,i+1,j,k,3)
              + calcJs2(i,j,k,l,i+1,j,k-1,3)
              + calcJs2(i,j,k,l,i,j,k,3)
              + calcJs2(i,j,k,l,i,j,k-1,3);
            break;
    case 2:  E = calcJs2(i,j,k,l,i+1,j,k+1,0)
              + calcJs2(i,j,k,l,i,j,k,0)
              + calcJs2(i,j,k,l,i+1,j,k,0)
              + calcJs2(i,j,k,l,i,j,k+1,0)
              + calcJs2(i,j,k,l,i,j,k+1,1)
              + calcJs2(i,j,k,l,i,j-1,k+1,1)
              + calcJs2(i,j,k,l,i,j-1,k,1)
              + calcJs2(i,j,k,l,i,j,k,1)
              + calcJs2(i,j,k,l,i+1,j,k,3)
              + calcJs2(i,j,k,l,i+1,j-1,k,3)
              + calcJs2(i,j,k,l,i,j-1,k,3)
              + calcJs2(i,j,k,l,i,j,k,3);
            break;
    case 3:  E = calcJs2(i,j,k,l,i,j+1,k+1,0)
              + calcJs2(i,j,k,l,i,j,k,0)
              + calcJs2(i,j,k,l,i,j,k+1,0)
              + calcJs2(i,j,k,l,i,j+1,k,0)
              + calcJs2(i,j,k,l,i,j,k+1,1)
              + calcJs2(i,j,k,l,i-1,j,k+1,1)
              + calcJs2(i,j,k,l,i-1,j,k,1)
              + calcJs2(i,j,k,l,i,j,k,1)
              + calcJs2(i,j,k,l,i,j+1,k,2)
              + calcJs2(i,j,k,l,i-1,j+1,k,2)
              + calcJs2(i,j,k,l,i-1,j,k,2)
              + calcJs2(i,j,k,l,i,j,k,2);
            break;
  }
// much slower code
/*  position_t p, pnn;
  p.i = i;
  p.j = j;
  p.k = k;
  p.l = l;
  for (unsigned m=0; m<NUMNNPERSITE; m++) {
    pnn = p+nn[p.l][m];
    E -= getSpin(pnn.i, pnn.j, pnn.k, pnn.l) * calcJ(p.i, p.j, p.k, p.l, pnn.i,
pnn.j, pnn.k, pnn.l));
  }*/
#if defined(DO_APPLIEDH)
  return -((E+H)*getSpin(i,j,k,l));
#else
  return -(E*getSpin(i,j,k,l));
#endif
}

void
lattice::run(unsigned nsteps, unsigned startsampling, unsigned samplingstep,
const char* fn)
{
  char buf[255];
#if defined(DO_HDISTRIBUTION)
  sprintf(buf, "%s.Hhf", fn);
  ofstream os_H(buf);
#endif  // DO_HDISTRIBUTION
#if defined(DO_DETAILS)
```

```
  sprintf(buf, "%s.mc", fn);
  ofstream os_mc(buf);
#endif  // DO_DETAILS
  double Etot = calcE();
#if defined(DO_MAG)
  spinsum_t MFe = calcM(0);
  spinsum_t MNi = calcM(1);
  spin_t news;
#endif
#if defined(DO_DETAILS)
  os_mc.precision(10);
  os_mc << "initial configuration" << '\t' << Etot/getNumAtoms() << '\t' << dnn
<< '\t';
#if defined(DO_MAG)
  if (getNumAtoms(0))
    os_mc << MFe/(double)getNumAtoms(0) << '\t';
  else
    os_mc << "N/A\t";
  if (getNumAtoms(1))
    os_mc << MNi/(double)getNumAtoms(1) << endl;
  else
    os_mc << "N/A\n";
#else
  os_mc << '\n';
#endif
  int details = 0;
#endif  // DO_DETAILS
  const unsigned atommc = getNumAtoms();
  unsigned mc, magmc;
  unsigned m;
  unsigned i, j, k, l;
  double p;
  double dd, dE;
  float dr[3];
  double sigdnn = dnn*SCALE_DNN*sqrt(T);
  double signnpos = dnn*SCALE_NNDEV*sqrt(T);
//  First, reach thermal equilibrium for the volume+magnetic system
//
  unsigned successVol = 0;
  unsigned successMove = 0;
  for (mc=0; mc<startsampling; mc++) {
#if defined(DO_VOLUMEMC)
    for (m=0; m<NUM_MCVOLSTEPS; m++) {
      dd = sigdnn*symranf();    // trial dnn change (gaussian deviate propto
sqrt(T)*dnn)
      if (testProb(calcVolProb(dnn+dd, dE))) {
        dnn += dd;
        dnn2x2 = 2*dnn*dnn;
        Etot += dE;
      }
    }
#if defined(DO_ATOMICMC)
    for (m=0; m<atommc; m++) {
    // select an atom at random
      i = Nx*ranf();
      j = Ny*ranf();
      k = Nz*ranf();
      l = NUMSITESPERCELL*ranf();
    // select random gaussian displacements
      dr[0] = signnpos*symranf();
      dr[1] = signnpos*symranf();
      dr[2] = signnpos*symranf();
      if (!testProb(calcMoveProb(i,j,k,l,dr,dE))) {
        atom& at = getAtom(i,j,k,l);
        at.dr[0] -= dr[0];
```

```
        at.dr[1] -= dr[1];
        at.dr[2] -= dr[2];
      }
    }
#endif  // DO_ATOMICMC
    for (magmc=0; magmc<NUM_MCMAGSTEPS; magmc++) {
#endif  // DO_VOLUMEMC
#if defined(DO_MAG)
      for (m=0; m<getNumAtoms(); m++) {
        i = Nx*ranf();
        j = Ny*ranf();
        k = Nz*ranf();
        l = NUMSITESPERCELL*ranf();
        spin_t& s = getSpin(i,j,k,l);
#if defined(HEISENBERG)
        float ct = 2*ranf()-1;
        float st = sqrt(1-ct*ct);
        float phi = 2*M_PI*ranf();
        float cp = cos(phi);
        news.x = cp*st;
        news.y = phi > M_PI ? -sqrt(1-cp*cp)*st : sqrt(1-cp*cp)*st;
        news.z = ct;
#else
        news = -s;
#endif
        p = calcFlipProb(i,j,k,l,news,dE);
        if (testProb(p)) {
          if (getSpecies(i,j,k,l) == 0)
            MFe += news-s;
          else
            MNi += news-s;
          s = news;
        }
      }
#endif
#if defined(DO_VOLUMEMC)
    }
#endif  // DO_VOLUMEMC
    Etot = calcE();
#if defined(DO_DETAILS)
    os_mc << (mc+1) << '\t' << Etot/getNumAtoms() << '\t' << dnn << '\t';
#if defined(DO_MAG)
    if (getNumAtoms(0))
      os_mc << MFe/(double)getNumAtoms(0) << '\t';
    else
      os_mc << "N/A\t";
    if (getNumAtoms(1))
      os_mc << MNi/(double)getNumAtoms(1) << endl;
    else
      os_mc << "N/A\n";
#else
    os_mc << '\n';
#endif  // DO_MAG
#endif  // DO_DETAILS
  }
  unsigned sampl = samplingstep;
  double t1, t2;
  long double Eavg = 0, E2 = 0;
  long double EpV = 0, EpV2 = 0;
  long double Vavg = 0, V2 = 0;
  long double VEpV = 0;
  long double davg = 0, d2 = 0;
#if defined(DO_MAG)
  long double MFeavg = 0, MFe2 = 0, MFe3 = 0, MFe4 = 0;
  long double MNiavg = 0, MNi2 = 0, MNi3 = 0, MNi4 = 0;
```

```
  long double M = 0, M2 = 0, M3 = 0, M4 = 0;
  long double nf = 0, nf2 = 0;
#endif
  atom::nsum = 0;
  unsigned n = 0;
  for (i=0, j, k, l; i<Nx; i++)
    for (j=0; j<Ny; j++)
      for (k=0; k<Nz; k++)
        for (l=0; l<NUMSITESPERCELL; l++)
          getAtom(i,j,k,l).reset_avg();
  sigdnn = dnn*SCALE_DNN*sqrt(T);
  signnpos = dnn*SCALE_NNDEV*sqrt(T);
  for (; mc<nsteps; mc++, sampl++) {
#if defined(DO_VOLUMEMC)
    resetE(Etot);
    for (m=0; m<NUM_MCVOLSTEPS; m++) {
      dd = sigdnn*symranf();    // trial volume change
      if (testProb(calcVolProb(dnn+dd, dE))) {
        dnn += dd;
        dnn2x2 = 2*dnn*dnn;
        Etot += dE;
        successVol++;
      }
    }
#if defined(DO_ATOMICMC)
    for (m=0; m<atommc; m++) {
    // select an atom at random
      i = Nx*ranf();
      j = Ny*ranf();
      k = Nz*ranf();
      l = NUMSITESPERCELL*ranf();
    // select random gaussian displacements
      dr[0] = signnpos*symranf();
      dr[1] = signnpos*symranf();
      dr[2] = signnpos*symranf();
      if (!testProb(calcMoveProb(i,j,k,l,dr,dE))) {
        atom& at = getAtom(i,j,k,l);
        at.dr[0] -= dr[0];
        at.dr[1] -= dr[1];
        at.dr[2] -= dr[2];
      } else
        successMove++;
    }
#endif  // DO_ATOMICMC
    for (magmc=0; magmc<NUM_MCMAGSTEPS; magmc++) {
#endif  // DO_VOLUMEMC
#if defined(DO_MAG)
      for (m=0; m<getNumAtoms(); m++) {
        i = Nx*ranf();
        j = Ny*ranf();
        k = Nz*ranf();
        l = NUMSITESPERCELL*ranf();
        spin_t& s = getSpin(i,j,k,l);
#if defined(HEISENBERG)
        float ct = 2*ranf()-1;
        float st = sqrt(1-ct*ct);
        float phi = 2*M_PI*ranf();
        float cp = cos(phi);
        news.x = cp*st;
        news.y = phi > M_PI ? -sqrt(1-cp*cp)*st : sqrt(1-cp*cp)*st;
        news.z = ct;
#else
        news = -s;
#endif
        if (testProb(calcFlipProb(i,j,k,l,news,dE))) {
```

```
          if (getSpecies(i,j,k,l) == 0)
            MFe += news-s;
          else
            MNi += news-s;
          s = news;
        }
      }
#endif
#if defined(DO_VOLUMEMC)
    }
#endif  // DO_VOLUMEMC
    Etot = calcE();
//
// sample the desired properties
//
    if (sampl == samplingstep) {
      davg += dnn;
      d2 += dnn*dnn;
      t1 = Etot/getNumAtoms();
      Eavg += t1;
      E2 += t1*t1;
      double V = dnn*dnn*dnn*M_SQRT_2;
      t1 += P*V;
      EpV += t1;
      EpV2 += t1*t1;
      Vavg += V;
      V2 += V*V;
      VEpV += V*t1;
#if defined(DO_MAG)
       spinf_t atomM = (MU[0]*MFe+MU[1]*MNi)/getNumAtoms();
#if defined(HEISENBERG)
      t1 = atomM.norm();
#else
      t1 = fabs(atomM);
#endif
      M += t1;
      t2 = t1*t1;
      M2 += t2;
      M3 += t1*t2;
      M4 += t2*t2;
#if defined(HEISENBERG)
      atomM.normalize();
#else
      atomM = atomM > 0 ? 1 : -1;
#endif
      if (getNumAtoms(0)) {
        t1 = (atomM*MFe)/getNumAtoms(0);
        MFeavg += t1;
        t2 = t1*t1;
        MFe2 += t2;
        MFe3 += t2*t1;
        MFe4 += t2*t2;
      }
      if (getNumAtoms(1)) {
        t1 = (atomM*MNi)/getNumAtoms(1);
        MNiavg += t1;
        t2 = t1*t1;
        MNi2 += t2;
        MNi3 += t2*t1;
        MNi4 += t2*t2;
      }
      unsigned nFeFe;
      unsigned nfcalc = calcFrustratedFeBonds(nFeFe);
      nf += nfcalc;
      nf2 += nfcalc*nfcalc;
```

```
#endif
      double a = dnn*M_SQRT2;
      for (i=0; i<Nx; i++)
        for (j=0; j<Ny; j++)
          for (k=0; k<Nz; k++)
            for (l=0; l<NUMSITESPERCELL; l++) {
              getAtom(i,j,k,l).sample_avg(a);
#if defined(DO_SPINAVG)
              // count the "spin" as being the component along the average
magnetization for that species
              if (getSpecies(i,j,k,l) == 0)
                getSpinSum(i,j,k,l) += MFe > 0 ? getSpin(i,j,k,l) :
-getSpin(i,j,k,l);
              else
                getSpinSum(i,j,k,l) += MNi > 0 ? getSpin(i,j,k,l) :
-getSpin(i,j,k,l);
#endif
            }
      atom::nsum++;
      n++;
      sampl = 0;
    }
#if defined(DO_DETAILS)
    os_mc << (mc+1) << '\t' << Etot/getNumAtoms() << '\t' << dnn << '\t';
#if defined(DO_MAG)
    if (getNumAtoms(0))
      os_mc << MFe/(double)getNumAtoms(0) << '\t';
    else
      os_mc << "N/A\t";
    if (getNumAtoms(1))
      os_mc << MNi/(double)getNumAtoms(1) << endl;
    else
      os_mc << "N/A\n";
#else
    os_mc << '\n';
#endif  // DO_MAG
#endif  // DO_DETAILS
  }
//  cout << 100*successVol/(double)(NUM_MCVOLSTEPS*(nsteps-startsampling)) <<
endl;
//  cout << 100*successMove/(double)(atommc*(nsteps-startsampling)) << endl;
//
// results are in. calculate averages and output them to file
//
  if (n == 0)
    n = 1;
  davg /= n;
  avgdnn = davg;
  d2 /= n;
  Eavg /= n;
  E2 /= n;
  EpV /= n;
  EpV2 /= n;
  Vavg /=n;
  V2 /= n;
  VEpV /= n;
#if defined(DO_MAG)
  nf /= n;
  nf2 /= n;
  M /= n;
  M2 /= n;
  M3 /= n;
  M4 /= n;
  if (getNumAtoms(0)) {
    MFeavg /= n;
```

```
    MFe2 /= n;
    MFe3 /= n;
    MFe4 /= n;
//    MFeAFavg /= (n*getNumAtoms(0));
//    MFeAF2 /= (n*getNumAtoms(0)*getNumAtoms(0));
  }
  if (getNumAtoms(1)) {
    MNiavg /= n;
    MNi2 /= n;
    MNi3 /= n;
    MNi4 /= n;
//    MNiAFavg /= (n*getNumAtoms(1));
//    MNiAF2 /= (n*getNumAtoms(1)*getNumAtoms(1));
  }
#endif
  if (atom::nsum)
    for (i=0, j, k, l; i<Nx; i++)
      for (j=0; j<Ny; j++)
        for (k=0; k<Nz; k++)
          for (l=0; l<NUMSITESPERCELL; l++)
            getAtom(i,j,k,l).calc_avg();
  os_main.precision(10);
  os_main << T << '\t' << P << '\t' << davg*M_SQRT2 << '\t' <<
sqrt(fabs(d2-davg*davg))*M_SQRT2 << '\t' << Eavg << '\t' <<
sqrt(fabs(E2-Eavg*Eavg));
#if defined(DO_MAG)
  cout << T << '\t' << P << '\t' << davg*M_SQRT2 << '\t' <<
M/(c*MU[0]+(1-c)*MU[1]) << endl;
#else
  cout << T << '\t' << P << '\t' << davg*M_SQRT2 << endl;
#endif
  os_main << '\t' << EpV << '\t' << EpV2 << '\t' << Vavg << '\t' << V2 << '\t' <<
VEpV;
  os_main << '\t' << getNumAtoms()*(VEpV-Vavg*EpV)/(3*T*T*Vavg) << '\t' <<
getNumAtoms()*(EpV2 - EpV*EpV)/(T*T) << '\t' <<
T*Vavg/(getNumAtoms()*(V2-Vavg*Vavg));
//  os_main << '\t' << (E2-Eavg*Eavg)/(T*T) << '\t' <<
sqrt(fabs(E4+Eavg*(-4*E3+8*E2*Eavg-4*Eavg*Eavg*Eavg)-E2*E2))/(T*T);
#if defined(DO_MAG)
  os_main << '\t' << M << '\t' << M2 << '\t' << M3 << '\t' << M4;
  os_main << '\t' << (M2-M*M)/T;// << '\t' <<
sqrt(fabs(MFe4+MFeavg*(-4*MFe3+8*MFe2*MFeavg-4*MFeavg*MFeavg*MFeavg)-MFe2*MFe2))/
T;
  if (getNumAtoms(0)) {
    os_main << '\t' << MFeavg << '\t' << MFe2 << '\t' << MFe3 << '\t' << MFe4;
    os_main << '\t' << (MFe2-MFeavg*MFeavg)/T;// << '\t' <<
sqrt(fabs(MFe4+MFeavg*(-4*MFe3+8*MFe2*MFeavg-4*MFeavg*MFeavg*MFeavg)-MFe2*MFe2))/
T;
  } else
    os_main << "\tN/A\tN/A\tN/A\tN/A\tN/A";
  if (getNumAtoms(1)) {
    os_main << '\t' << MNiavg << '\t' << MNi2 << '\t' << MNi3 << '\t' << MNi4;
    os_main << '\t' << (MNi2-MNiavg*MNiavg)/T;// << '\t' <<
sqrt(fabs(MNi4+MNiavg*(-4*MNi3+8*MNi2*MNiavg-4*MNiavg*MNiavg*MNiavg)-MNi2*MNi2))/
T;
  } else
    os_main << "\tN/A\tN/A\tN/A\tN/A\tN/A";
  os_main << '\t' << nf << '\t' << sqrt(fabs(nf2-nf*nf));
#endif
  dnnInfo dnninfo[3];
  calcAvgdnn(davg*M_SQRT2, 0, 0, &dnninfo[0]);
  calcAvgdnn(davg*M_SQRT2, 1, 0, &dnninfo[1]);
  calcAvgdnn(davg*M_SQRT2, 1, 1, &dnninfo[2]);
  os_main << '\t' << dnninfo[0].avg[0] << '\t' << dnninfo[1].avg[0] << '\t' <<
dnninfo[2].avg[0];
```

```
  os_main << '\t' << dnninfo[0].stdev[0] << '\t' << dnninfo[1].stdev[0] << '\t'
<< dnninfo[2].stdev[0];
  os_main << '\t' << dnninfo[0].pup << '\t' << dnninfo[1].pup << '\t' <<
dnninfo[2].pup;
  os_main << '\t' << dnninfo[0].n << '\t' << dnninfo[1].n << '\t' <<
dnninfo[2].n;
  os_main << '\t' << dnninfo[0].avg[1] << '\t' << dnninfo[0].avg[2];
  os_main << '\t' << dnninfo[0].stdev[1] << '\t' << dnninfo[0].stdev[2];
#if defined(DO_HDISTRIBUTION)
  unsigned nHhf = floor((MU[0]*Hhf_A + 12*MU[0]*Hhf_B)/0.5+0.5)+1;
  double** PHhf = new double*[13];
  for (unsigned i=0; i<13; i++)
    PHhf[i] = new double[nHhf];
  double Hhfavg = calcHhfDistribution(PHhf, nHhf, 0.5);
  for (unsigned j=0; j<13; j++)
    os_H << '\t' << j;
  os_H << endl;
  for (unsigned i=0; i<nHhf; i++) {
    os_H << i*0.5;
    for (unsigned j=0; j<13; j++)
      os_H << '\t' << PHhf[j][i];
    os_H << endl;
  }
  delete[] PHhf;
  os_main << '\t' << Hhfavg;
#endif
  os_main << endl;
#if defined(DO_SPINAVG)
  sprintf(buf, "%s.mom", fn);
  ofstream os_mom(buf);
  for (unsigned i=0, j, k, l; i<Nx; i++)
    for (j=0; j<Ny; j++)
      for (k=0; k<Nz; k++)
        for (l=0; l<NUMSITESPERCELL; l++) {
          double m = getSpinSum(i,j,k,l)/(double)atom::nsums;
          os_mom << i << '\t' << j << '\t' << k << '\t' << l << '\t' << m << '\t'
<< sqrt(1-m*m) << '\n';
        }
#endif
#if defined(DO_FENNINFO)
  sprintf(buf, "%s.FeNN", fn);
  ofstream os_nn(buf);
  int sum[NUMSPECIES];
  for (unsigned i=0, j, k, l; i<Nx; i++)
    for (j=0; j<Ny; j++)
      for (k=0; k<Nz; k++)
        for (l=0; l<NUMSITESPERCELL; l++) {
           sumNNAtoms(i,j,k,l,sum);
          os_nn << i << '\t' << j << '\t' << k << '\t' << l << '\t' <<
(int)getSpecies(i,j,k,l) << '\t' << sum[0] << '\n';
        }
#endif
}

#if 1
int
main(int argc, char* argv[])
{
  // warm up the random number generator
#if defined(USE_RAN1)
  idum = -1;
#else
  seedMT(4357U);
#endif
  for (unsigned i=0; i<10000; i++)
```

```
    ranf();
  if (argc < 4) {
    cout << "Invalid number of parameters" << endl << endl;
    cout << "Usage: mc_NTP [at.% Fe] [f|a|p] [Fe3Ni|FeNi|FeNi3|d] (ini file)" <<
endl << endl;
    cout << "  where f initializes the lattice with a ferromagnetic structure" <<
endl;
    cout << "        a initializes the lattice with an antiferromagnetic(001)
structure" << endl;
    cout << "        p initializes the lattice with a random nonmagnetic
structure" << endl << endl;
    cout << "        Fe3Ni initializes the lattice with a chemically ordered
Fe3Ni structure" << endl;
    cout << "        FeNi initializes the lattice with a chemically ordered FeNi
structure" << endl;
    cout << "        FeNi3 initializes the lattice with a chemically ordered
FeNi3 structure" << endl;
    cout << "        d initializes the lattice with a chemically disordered
structure" << endl;
    return 1;
  }
  char inibuf[256];
  if (argc == 5)
    strcpy(inibuf, argv[4]);
  else
    strcpy(inibuf, "mc_NTP.ini");
  ifstream is(inibuf);
  unsigned N;
  double d, dnn0_65;
  char buf[255];
  is >> N >> d >> dnn0_65;
  dnn0 = dnn0_65;
  is >> J0[0][0] >> J0[1][0] >> J0[1][1];
  J0[0][1] = J0[1][0];
  is >> dJ_dr[0][0] >> dJ_dr[1][0] >> dJ_dr[1][1];
  dJ_dr[0][1] = dJ_dr[1][0];
  is.ignore();
  is >> U0[0][0] >> U0[1][0] >> U0[1][1];
  U0[0][1] = U0[1][0];
  is >> d0[0][0] >> d0[1][0] >> d0[1][1];
  d0[0][1] = d0[1][0];
  d02[0][0] = d0[0][0]*d0[0][0];
  d02[0][1] = d0[0][1]*d0[0][1];
  d02[1][0] = d0[1][0]*d0[1][0];
  d02[1][1] = d0[1][1]*d0[1][1];
  time_t timer = GetTime();
  lattice lat(N, N, N, atof(argv[1]));
  lat.setdnn(d);
  bool read = false;
  bool load_lattice = false;
  if (strcmp(argv[3], "Fe3Ni") == 0)
    lat.initialize(lattice::Fe3Ni);
  else if (strcmp(argv[3], "FeNi") == 0)
    lat.initialize(lattice::FeNi);
  else if (strcmp(argv[3], "FeNi3") == 0)
    lat.initialize(lattice::FeNi3);
  else if (strcmp(argv[3], "d") == 0)
    lat.initialize(lattice::disordered);
  else if (strcmp(argv[3], "load") == 0)
    load_lattice = true;
  else
    if (!lat.readSystem(argv[3])) {
      cerr << "unable to open file " << argv[3] << endl;
      return false;
    } else
```

```
      read = true;
  if (!read)
    switch(argv[2][0]) {
      case 'f':  lat.initialize(lattice::ferro); break;
      case 'a':  lat.initialize(lattice::antiferro); break;
      case 'n':  lat.initialize(lattice::Niferro); break;
      default:   lat.initialize(lattice::para);
    }
  double P;
  is >> P;
  lat.setPressure(P);
#if defined(DO_MAG)
  #if defined(JFEFE_BOSE)
  sprintf(buf, "%s c=%.3f %c %s Bose.P=%g.dat", fnprefix,
lat.getNumAtoms(0)/(double)lat.getNumAtoms(), argv[2][0], argv[3], lat.P, T);
  #else
  sprintf(buf, "%s c=%.3f %c %s %g %g.P=%g.dat", fnprefix,
lat.getNumAtoms(0)/(double)lat.getNumAtoms(), argv[2][0], argv[3], dJ_dr[0][0],
dnn0_65, lat.P);
  #endif
#else
  sprintf(buf, "%s c=%.3f %s.P=%g.dat", fnprefix,
lat.getNumAtoms(0)/(double)lat.getNumAtoms(), argv[3], lat.P);
#endif
  os_main.open(buf);
  if (!os_main) {
    cout << "unable to open " << buf << endl;
    return 1;
  }
  int nsteps;
  int startsampling;
  int samplingstep;
  is >> nsteps >> startsampling >> samplingstep;
  unsigned nFeFe;
  lat.calcFrustratedFeBonds(nFeFe);
  cout << "N = " << lat.getNumAtoms() << "\tc = " <<
lat.getNumAtoms(0)/(double)lat.getNumAtoms() << endl;
  os_main << "N = " << lat.getNumAtoms() << "\tc = " <<
lat.getNumAtoms(0)/(double)lat.getNumAtoms() << endl;
#if defined(DO_MAG)
  #if defined(JFEFE_BOSE)
  cout << "magnetic exchange parameters:\tFit to Bose JFeFe data" << endl;
  os_main << "magnetic exchange parameters:\tFit to Bose JFeFe data" << endl;
  #else
  cout << "magnetic exchange parameters:\t" << J0[0][0] << '\t' << J0[0][1] <<
'\t' << J0[1][1] << '\t' << dJ_dr[0][0] << '\t' << dJ_dr[0][1] << '\t' <<
dJ_dr[1][1] << '\t' << dnn0_65 << endl;
  os_main << "magnetic exchange parameters:\t" << J0[0][0] << '\t' << J0[0][1] <<
'\t' << J0[1][1] << '\t' << dJ_dr[0][0] << '\t' << dJ_dr[0][1] << '\t' <<
dJ_dr[1][1] << '\t' << dnn0_65 << endl;
  #endif
#else
  cout << "no magnetic interactions" << endl;
  os_main << "no magnetic interactions" << endl;
#endif
  cout << "chemical potential parameters:\t" << U0[0][0] << '\t' << d0[0][0] <<
'\t'<< U0[0][1] << '\t' << d0[0][1] << '\t' << U0[1][1] << '\t' << d0[1][1] <<
endl;
//  cout << "initial conditions:\t" << lat.calcE() << '\t' << lat.calcM(0) <<
'\t' << lat.calcM(1) << '\t' << nFeFe << endl;
  os_main << "chemical potential parameters:\t" << U0[0][0] << '\t' << d0[0][0]
<< '\t'<< U0[0][1] << '\t' << d0[0][1] << '\t' << U0[1][1] << '\t' << d0[1][1] <<
endl;
  os_main << "initial conditions:\t" << lat.calcE() << '\t' << lat.calcM(0) <<
'\t' << lat.calcM(1) << '\t' << nFeFe << '\t' << argv[2] << '\t' << argv[3] <<
```

```
endl;
  os_main << nsteps << " steps, start sampling at " << startsampling << ", sample
every " << samplingstep << endl;
  os_main << "T (K)\tP (K/Å3)\t" << "a (Å)\tsa\t" << "<E> (K)" << '\t' << "sE" <<
'\t';
  os_main << "<E+pV> (K)" << '\t' << "<(E+pV)^2>" << '\t';
  os_main << "<V> (Å3)" << '\t' << "<V^2>" << '\t';
  os_main << "<V(E+pV)> (KÅ3)" << '\t';
  os_main << "alpha (K-1)" << '\t' << "Cp" << '\t' << "B_T (K/Å3)" << '\t';
#if defined(DO_MAG)
  os_main << "<M>" << '\t' << "<M2>" << '\t' << "<M3>" << '\t' << "<M4>" << '\t'
<< "chi" << '\t';
  os_main << "<MFe>" << '\t' << "<MFe2>" << '\t' << "<MFe3>" << '\t' << "<MFe4>"
<< '\t' << "chiFe" << '\t';
  os_main << "<MNi>" << '\t' << "<MNi2>" << '\t' << "<MNi3>" << '\t' << "<MNi4>"
<< '\t' << "chiNi" << '\t';
  os_main << "nFefrust\t\t";
#endif
  os_main << "dFeFe (Å)\tdFeNi (Å)\tdNiNi (Å)";
#if defined(DO_HDISTRIBUTION)
  os_main << '\t' << "<Hhf>";
#endif
  os_main << endl;
  cout << lat.calcChemE()/lat.getNumAtoms() << endl;
#if defined(DO_MAG)
  cout << lat.calcMagE()/lat.getNumAtoms() << endl;
#endif

  long t = time(0);
  struct tm* tblock = localtime(&t);
  cout << "starting calculation on " << asctime(tblock);
  double T;
  double T0, T1, dT;
  is >> T0 >> T1 >> dT;
  if (dT < 0)
    for (T=T0; T>T1; T+=dT) {
      if (load_lattice) {
        dnn0 = dnn0_65;
        sprintf(buf, "%s c=%.3f %c %s %g %g.P=%g.T=%g.lattice", fnprefix,
lat.getNumAtoms(0)/(double)lat.getNumAtoms(), argv[2][0], argv[3], dJ_dr[0][0],
dnn0_65, lat.P, T);
        if (!lat.readSystem(buf)) {
          cerr << "unable to read " << buf << endl;
          continue;
        }
      }
#if defined(DO_MAG)
  #if defined(JFEFE_BOSE)
      sprintf(buf, "%s c=%.3f %c %s Bose.%g.%g", fnprefix,
lat.getNumAtoms(0)/(double)lat.getNumAtoms(), argv[2][0], argv[3], lat.P, T);
  #else
      sprintf(buf, "%s c=%.3f %c %s %g %g.%g.%g", fnprefix,
lat.getNumAtoms(0)/(double)lat.getNumAtoms(), argv[2][0], argv[3], dJ_dr[0][0],
dnn0_65, lat.P, T);
  #endif
#else
      sprintf(buf, "%s c=%.3f %s.%g.%g", fnprefix,
lat.getNumAtoms(0)/(double)lat.getNumAtoms(), argv[3], lat.P, T);
#endif
      lat.setTemp(T);
      lat.run(nsteps, startsampling, samplingstep, buf);
      t = time(0);
      tblock = localtime(&t);
      cout << (GetTime()-timer) << " seconds elapsed, " << asctime(tblock);
#if defined(DO_MAG)
```

```
  #if defined(JFEFE_BOSE)
      sprintf(buf, "%s c=%.3f %c %s Bose.P=%g.T=%g.lattice", fnprefix,
lat.getNumAtoms(0)/(double)lat.getNumAtoms(), argv[2][0], argv[3], lat.P, T);
  #else
      sprintf(buf, "%s c=%.3f %c %s %g %g.P=%g.T=%g.lattice", fnprefix,
lat.getNumAtoms(0)/(double)lat.getNumAtoms(), argv[2][0], argv[3], dJ_dr[0][0],
dnn0_65, lat.P, T);
  #endif
#else
      sprintf(buf, "%s c=%.3f %s.P=%g.T=%g.lattice", fnprefix,
lat.getNumAtoms(0)/(double)lat.getNumAtoms(), argv[3], lat.P, T);
#endif
      lat.saveSystem(buf);
    }
  else
    for (T=T0; T<T1; T+=dT) {
      if (load_lattice) {
        dnn0 = dnn0_65;
        sprintf(buf, "%s c=%.3f %c %s %g %g.P=%g.T=%g.lattice", fnprefix,
lat.getNumAtoms(0)/(double)lat.getNumAtoms(), argv[2][0], argv[3], dJ_dr[0][0],
dnn0_65, lat.P, T);
        if (!lat.readSystem(buf)) {
          cerr << "unable to read " << buf << endl;
          continue;
        }
      }
#if defined(DO_MAG)
  #if defined(JFEFE_BOSE)
      sprintf(buf, "%s c=%.3f %c %s Bose.%g.%g", fnprefix,
lat.getNumAtoms(0)/(double)lat.getNumAtoms(), argv[2][0], argv[3], lat.P, T);
  #else
      sprintf(buf, "%s c=%.3f %c %s %g %g.%g.%g", fnprefix,
lat.getNumAtoms(0)/(double)lat.getNumAtoms(), argv[2][0], argv[3], dJ_dr[0][0],
dnn0_65, lat.P, T);
  #endif
#else
      sprintf(buf, "%s c=%.3f %s.%g.%g", fnprefix,
lat.getNumAtoms(0)/(double)lat.getNumAtoms(), argv[3], lat.P, T);
#endif
      lat.setTemp(T);
      lat.run(nsteps, startsampling, samplingstep, buf);
      t = time(0);
      tblock = localtime(&t);
      cout << (GetTime()-timer) << " seconds elapsed, " << asctime(tblock);
#if defined(DO_MAG)
  #if defined(JFEFE_BOSE)
      sprintf(buf, "%s c=%.3f %c %s Bose.P=%g.T=%g.lattice", fnprefix,
lat.getNumAtoms(0)/(double)lat.getNumAtoms(), argv[2][0], argv[3], lat.P, T);
  #else
      sprintf(buf, "%s c=%.3f %c %s %g %g.P=%g.T=%g.lattice", fnprefix,
lat.getNumAtoms(0)/(double)lat.getNumAtoms(), argv[2][0], argv[3], dJ_dr[0][0],
dnn0_65, lat.P, T);
  #endif
#else
      sprintf(buf, "%s c=%.3f %s.P=%g.T=%g.lattice", fnprefix,
lat.getNumAtoms(0)/(double)lat.getNumAtoms(), argv[3], lat.P, T);
#endif
      lat.saveSystem(buf);
    }
  is >> T1 >> dT;
  while (is) {
    if (dT < 0)
      for (; T>T1; T+=dT) {
        if (load_lattice) {
          dnn0 = dnn0_65;
```

```
          sprintf(buf, "%s c=%.3f %c %s %g %g.P=%g.T=%g.lattice", fnprefix,
lat.getNumAtoms(0)/(double)lat.getNumAtoms(), argv[2][0], argv[3], dJ_dr[0][0],
dnn0_65, lat.P, T);
          if (!lat.readSystem(buf)) {
            cerr << "unable to read " << buf << endl;
            continue;
          }
        }
#if defined(DO_MAG)
  #if defined(JFEFE_BOSE)
        sprintf(buf, "%s c=%.3f %c %s Bose.%g.%g", fnprefix,
lat.getNumAtoms(0)/(double)lat.getNumAtoms(), argv[2][0], argv[3], lat.P, T);
  #else
        sprintf(buf, "%s c=%.3f %c %s %g %g.%g.%g", fnprefix,
lat.getNumAtoms(0)/(double)lat.getNumAtoms(), argv[2][0], argv[3], dJ_dr[0][0],
dnn0_65, lat.P, T);
  #endif
#else
        sprintf(buf, "%s c=%.3f %s.%g.%g", fnprefix,
lat.getNumAtoms(0)/(double)lat.getNumAtoms(), argv[3], lat.P, T);
#endif
        lat.setTemp(T);
        lat.run(nsteps, startsampling, samplingstep, buf);
        t = time(0);
        tblock = localtime(&t);
        cout << (GetTime()-timer) << " seconds elapsed, " << asctime(tblock);
#if defined(DO_MAG)
  #if defined(JFEFE_BOSE)
        sprintf(buf, "%s c=%.3f %c %s Bose.P=%g.T=%g.lattice", fnprefix,
lat.getNumAtoms(0)/(double)lat.getNumAtoms(), argv[2][0], argv[3], lat.P, T);
  #else
        sprintf(buf, "%s c=%.3f %c %s %g %g.P=%g.T=%g.lattice", fnprefix,
lat.getNumAtoms(0)/(double)lat.getNumAtoms(), argv[2][0], argv[3], dJ_dr[0][0],
dnn0_65, lat.P, T);
  #endif
#else
        sprintf(buf, "%s c=%.3f %s.P=%g.T=%g.lattice", fnprefix,
lat.getNumAtoms(0)/(double)lat.getNumAtoms(), argv[3], lat.P, T);
#endif
        lat.saveSystem(buf);
      }
    else
      for (; T<T1; T+=dT) {
        if (load_lattice) {
          dnn0 = dnn0_65;
          sprintf(buf, "%s c=%.3f %c %s %g %g.P=%g.T=%g.lattice", fnprefix,
lat.getNumAtoms(0)/(double)lat.getNumAtoms(), argv[2][0], argv[3], dJ_dr[0][0],
dnn0_65, lat.P, T);
          if (!lat.readSystem(buf)) {
            cerr << "unable to read " << buf << endl;
            continue;
          }
        }
#if defined(DO_MAG)
  #if defined(JFEFE_BOSE)
        sprintf(buf, "%s c=%.3f %c %s Bose.%g.%g", fnprefix,
lat.getNumAtoms(0)/(double)lat.getNumAtoms(), argv[2][0], argv[3], lat.P, T);
  #else
        sprintf(buf, "%s c=%.3f %c %s %g %g.%g.%g", fnprefix,
lat.getNumAtoms(0)/(double)lat.getNumAtoms(), argv[2][0], argv[3], dJ_dr[0][0],
dnn0_65, lat.P, T);
  #endif
#else
        sprintf(buf, "%s c=%.3f %s.%g.%g", fnprefix,
lat.getNumAtoms(0)/(double)lat.getNumAtoms(), argv[3], lat.P, T);
```

```
#endif
        lat.setTemp(T);
        lat.run(nsteps, startsampling, samplingstep, buf);
        t = time(0);
        tblock = localtime(&t);
        cout << (GetTime()-timer) << " seconds elapsed, " << asctime(tblock);
#if defined(DO_MAG)
  #if defined(JFEFE_BOSE)
        sprintf(buf, "%s c=%.3f %c %s Bose.P=%g.T=%g.lattice", fnprefix,
lat.getNumAtoms(0)/(double)lat.getNumAtoms(), argv[2][0], argv[3], lat.P, T);
  #else
        sprintf(buf, "%s c=%.3f %c %s %g %g.P=%g.T=%g.lattice", fnprefix,
lat.getNumAtoms(0)/(double)lat.getNumAtoms(), argv[2][0], argv[3], dJ_dr[0][0],
dnn0_65, lat.P, T);
  #endif
#else
        sprintf(buf, "%s c=%.3f %s.P=%g.T=%g.lattice", fnprefix,
lat.getNumAtoms(0)/(double)lat.getNumAtoms(), argv[3], lat.P, T);
#endif
        lat.saveSystem(buf);
      }
    is >> T1 >> dT;
  }
  return 0;
}
```

```
File:         mcprob.h, included in mc_ntp.cpp
Author:       Ken Lagarec

#if !defined(mcprob_h)
#define mcprob_h

inline bool
testProb(float p) {
  return (ranf() < p);
}

inline float
metropolisProb(double mdE_T) {
  return mdE_T < FMINEXP ? 0 : mdE_T > 0 ? 1 : exp(mdE_T);
}

#endif
```

```
File:         mcspin.h, included in mc_ntp.cpp
Author:       Ken Lagarec

#if !defined(mcspin_h)
#define mcspin_h

#if defined(HEISENBERG)
struct vector {
  float x, y, z;
  vector(): x(0), y(0), z(0) {}
  vector(float x_, float y_, float z_): x(x_), y(y_), z(z_) {}
  vector(float a) {
    x = 0;
    y = 0;
    z = (a != 0) ? a/fabs(a) : 0;
  }
  vector& operator = (float a) {
    x = 0;
    y = 0;
    z = (a != 0) ? a/fabs(a) : 0;
    return *this;
  }
  vector& operator += (const vector& v) {
    x += v.x;
    y += v.y;
    z += v.z;
    return *this;
  }
  vector& operator -= (const vector& v) {
    x -= v.x;
    y -= v.y;
    z -= v.z;
    return *this;
  }
  float norm() {
    return sqrt(x*x+y*y+z*z);
  }
  void normalize() {
    float n = norm();
    if (n == 0)
      return;
    x /= n;
    y /= n;
    z /= n;
  }
};
inline vector
operator + (const vector& v1, const vector& v2) {
  return vector(v1.x+v2.x, v1.y+v2.y, v1.z+v2.z);
}
inline vector
operator - (const vector& v1, const vector& v2) {
  return vector(v1.x-v2.x, v1.y-v2.y, v1.z-v2.z);
}
inline vector
operator * (const float a, const vector& v) {
  return vector(a*v.x, a*v.y, a*v.z);
}
inline vector
operator / (const vector& v, const float a) {
  return vector(v.x/a, v.y/a, v.z/a);
}
inline float
operator * (const vector& v1, const vector& v2) {
  return v1.x*v2.x + v1.y*v2.y + v1.z*v2.z;
```

```
}
inline ostream&
operator << (ostream& os, const vector& v) {
  os << v.x << '\t' << v.y << '\t' << v.z;
  return os;
}
inline istream&
operator >> (istream& is, const vector& v) {
  is >> v.x >> v.y >> v.z;
  return is;
}

typedef vector spin_t;
typedef vector spinsum_t;
typedef vector spinf_t;
#else
typedef signed __int8 spin_t;
typedef int spinsum_t;
typedef double spinf_t;
#endif

#endif // mcspin_h
```

References

Abrahams, S.C., Guttman, L., and Kasper, J.S., 1962, Phys. Rev. **127**, 2052.

Abrikosov, I.A., Eriksson, O., Söderlind, P., Skriver, H.L., and Johansson, B., 1995, Phys. Rev. B **51**, 1058.

Acet, M., Zähres, H., Wassermann, E.F., and Pepperhoff, W., 1994a, Phys. Rev. B **49**, 6012.

Acet, M., Schneider, T., Zähres, H., Wassermann, E.F., and Pepperhoff, W., 1994b, J. Appl. Phys. **75**, 7015.

Acet, M., Wassermann, E.F., Andersen, K., Murani, A., and Schärpff, O., 1997a, J. Appl. Phys. **81**, 3876.

Acet, M., Wassermann, E.F., Andersen, K., Murani, A., and Schärpff, O., 1997b, Europhys. Lett. **40**, 93.

Acet, M., Wassermann, E.F., and Pepperhoff, W., 2000, Philos. Mag. B **80**, 127.

Akai, H., Blügel, S., Zeller, R., and Dedrichs, P.H., 1986, Phys. Rev. Lett. **56**, 2407.

Akai, H., 1989a, Mater. Sci. **37** , 211.

Akai, H., 1989b, J. Phys. - Condens. Mat. **1**, 8045.

Akai, H. and Dederichs, P.H., 1993, Phys. Rev. B **47**, 8739.

Albertsen, J.F., Jensen, G.B., and Knudsen, J.M., 1978a, Nature **273**, 453.

Albertsen, J.F., Jensen, G.B., Knudsen, J.M., and Danon, J., 1978b, Meteorit. Planet. Sci. **13**, 379.

Albertsen, J.F., Roy-Poulsen, N.O., and Vistisen, L., 1980a, Meteorit. Planet. Sci. **15**, 258.

Albertsen, J.F., Knudsen, J.M., Roy-Poulsen, N.O., and Vistisen, L., 1980b, Phys. Scripta **22**, 171.

Albertsen, J.F., 1981, Phys. Scripta **23**, 301.

Albertsen, J.F., Nielsen, H.P., and Buchwald, V.F., 1983, Phys. Scripta **27**, 314.

Andersen, O.K., 1975, Phys. Rev. B **12**, 3060.

Andersen, O.K., Madsen, J., Poulsen, U.K., Jepsen, O., and Kollar, J., 1977, Physica B **86-88**, 249.

Aschroft, N.W. and Mermin, D., 1976, *Solid State Physics*, (Saunders College Publishing, Philadelphia)

Battocletti, M., Ebert, H., and Akai, H., 1996, Phys. Rev. B **53**, 9776.

Blügel, S., Akai, H., Zeller, R., and Dederichs, P.H., 1987, Phys. Rev. B **35**, 3271.

Böni, P., Shirane, G., Wicksted, J.P., and Stassis, C., 1985, Phys. Rev. B **31**, 4597.

Bradley, A.J., Jay, A.H., and Taylor, A., 1937, Philos. Mag. **23**, 545.

Brando, Y., 1964, J. Phys. Soc. Jpn. **19**, 237.

Carr Jr., W.J., 1952, Phys. Rev. **85**, 590.

Carr Jr., W.J., 1979, J. Magn. Magn. Mater. **10**, 197.

Chikazumi, S., Mizoguchi, T., and Yamaguchi, N., 1968, J. Appl. Phys. **39**, 939.

Chikazumi, S., 1979, J. Magn. Magn. Mater. **10**, 113.

Chikazumi, S., 1980, J. Magn. Magn. Mater. **15-18**, 1130.

Christiansen, A., Larsen, L., Roy-Poulsen, H., Roy-Poulsen, N.O., Vistinsen, L., and Knudsen, J.M., 1984, Phys. Scripta **29**, 94.

Clarke, R.S.Jr. and Scott E. R. D., 1980, Am. Mineral. **65**, 624.

Colling, D.A. and Carr Jr., W.J., 1970, J. Appl. Phys. **41**, 5125.

Crangle, J. and Hallam, G.C., 1963, Proc. R. Soc. Ser. A Sciences **272**, 119.

Cranshaw, T.E., 1987, J. Phys. F Met. Phys. **17**, 967.

Dang, M.Z., Dube, M., and Rancourt, D.G., 1995, J. Magn. Magn. Mater. **147**, 133.

Dang, M.Z., 1996a, *Interplay of Spin Structures, Hyperfine Magnetic Field Distributions and Chemical Order-Disorder Phenomena in Face Centered Cubic Fe-Ni Alloys Studied by Mössbauer Spectroscopy Measurements and Monte Carlo Simulations*, Ph. D. Thesis, University of Ottawa.

Dang, M.Z. and Rancourt, D.G., 1996b, in *Conference Proceedings «ICAME-95»*, edited by I. Ortalli, (SIF, Bologna), p. 367.

Dang, M.Z. and Rancourt, D.G., 1996c, Phys. Rev. B **53**, 2291.

Danon, J., Scorzelli, R., Souza Azevedo, I., Curvello, W., Albertsen, J.F., and Knudsen, J.M., 1978a, CR Acad. Sci. II B **287**, 199.

Danon, J., Scorzelli, R., Souza, A.I., Curvello, W., Albertsen, J.F., and Knudsen, J.M., 1979a, Nature **277**, 283.

Danon, J., Scorzelli, R., Souza Azevedo, I., and Christophe-Michel-Lévy, M., 1979b, Nature **281**, 469.

Danon, J., Scorzelli, R., and Souza Azevedo, I., 1979c, An. Acad. Bras. Cienc. **51**, 175.

Danon, J., Scorzelli, R., Souza Azevedo, I., Laugier, J., and Chamberod, A., 1980a, Nature **284**, 537.

Danon, J., Scorzelli, R.B., and Souza Azevedo I., 1980b, J. Phys. - Paris **41**, C1-364.

Danon, J. and Scorzelli, R.B., 1983, Meteorit. Planet. Sci. **20**, 631.

De Grave E., Vandenberghe, R.E., De Bakker, P.M.A., Van Alboom A., Vochten, R., and Van Tassel, R., 1992, Hyperfine Interact. **70**, 1009.

Ducastelle, F., 1991, chapter 7 in *Order and Phase Stability in Alloys* (North-Holland,

Amsterdam).

Dumpich, G., Wassermann, E.F., Manns, V., Murayama, S., and Miyako, Y., 1987, J. Magn. Magn. Mater. **67**, 55.

Dumpich, G., Becker, E., Schletz, K., Stamm, W., Keune, W., Kiauka, W., and Murayama, S., 1988, J. Magn. Magn. Mater. **74**, 237.

Dumpich, G., Kästner, J., Kirschbaum, U., Mühlbauer, H., Liang, J., Lübeck, Th., and Wassermann, E.F., 1992, Phys. Rev. B **46**, 9258.

Entel, P., Hoffmann, E., Mohn, P., Schwarz, K., and Moruzzi, V.L., 1993, Phys. Rev. B **47**, 8706.

Faulkner, J.S., 1982, *The Modern Theory of Alloys*, Progress in Materials Science, vol. 27, 187 p.

Fermi, E., 1930, Z. Phys. **60**, 320.

Goldstein, J.I., Williams, D.B., Zhang, J., and Clarke, R., 1990, in *Physical Metallurgy of Controlled Expansion Invar-Type Alloys*, edited by K.C. Russell and D.F. Smith (The Minerals, Metals and Material Society, Warrendale PA) p. 67.

Goldstein, J.I., Reisner, R.J., Rancourt, D.G., Lagarec, K., and Scorzelli, R.B., 1998, in *Proceedings of the 61st Meteoritical Society Meeting*, in Dublin, Ireland

Gonser, U., Meechan, C.J., Muir, A.H., and Wiedersich, H., 1963, J. Appl. Phys. **34**, 2373.

Gros, Y. and Péray-Peyroula, J.C., 1964, Phys. Lett. **13**, 5.

Gros, Y., Paulevé, J., Dautreppe, D., and Péray-Peyroula, J.C., 1968, CR Acad. Sci. **266**, 1199.

Gros, Y. and Paulevé, J., 1970, J. Phys. - Paris **31**, 459.

Grossmann, B. and Rancourt, D.G., 1996, Phys. Rev. B **54**, 12294.

Gubanov, V.A., Liechtenstein, A.I., and Postnikov, A.V., 1992, in *Magnetism and the Electronic Structure of Crystals*, edited by M. Cardona, P. Fulde, K. von Klitzing, and H.-J. Queisser

(Springer, Berlin)

Guillaume, C.E., 1897, CR Acad. Sci. **124**, 176.

Guillaume, C.E., 1920, P. Phys. Soc. Lond. **32**, 374.

Halbauer, R. and Gonser, U., 1983, J. Magn. Magn. Mater. **35**, 55.

Hayase, M., Shiga, M., and Nakamura, Y., 1973, J. Phys. Soc. Jpn. **34**, 925.

Hoffmann, E., Entel, P., Schwarz, K., and Mohn, P., 1995, J. Magn. Magn. Mater. **140-144**, 237.

Jago, R.A., Clark, P.E., and Rossiter, P.L., 1982, Physica Status Solidi **74**, 247.

James, A.M. and Lord, M.P., 1992, *Macmillan's Chemical and Physical Data*, (Macmillan, London)

James, P., Eriksson, O., Johansson, B., and Abrikosov, I.A., 1999, Phys. Rev. B **59**, 419.

Johanson, G.J., McGirr, M.B., and Wheeler, D.A., 1970, Phys. Rev. B **1**, 3208.

Keune, W., Halbauer, R., Gonser, U., Lauer, J., and Williamson, D.L., 1977, J. Appl. Phys. **48**, 2976.

Kobeissi, M.A., 1981, Phys. Rev. B **24**, 2380.

Kondorskii, E.I. and Fedotov, L.N., 1952, Invest. Akad. Nauk. SSSR **16**, 432.

Kondorskii, E.I. and Sedov, V.L., 1959, J. Exp. Theor. Phys. **35**, 586.

Kondorskii, E.I., 1960a, J. Exp. Theor. Phys. **10**, 1284.

Kondorskii, E.I. and Sedov, V.L., 1960b, J. Appl. Phys. **31**, 331.

Kovats, T.A. and Walker, J.C., 1969, Phys. Rev. **181**, 610.

Krasko, G.L., 1987, Phys. Rev. B **36**, 8565.

Kudrnovský, J., Turek, I., and Drchal, V., 1994, in *Lectures on Methods of Electronic Structure*

Calculations, edited by V. Kumar, O.K. Andersen, and A. Mookerjee (World Scientific), p. 231.

Lagarec, K. and Rancourt, D.G., 1997, Nucl. Instrum. Meth. B **129**, 266.

Lagarec, K. and Rancourt, D.G., 2000, Phys. Rev. B **62**, 978.

Larsen, L., Roy-Poulsen, H., Roy-Poulsen, N.O., Vistisen, L., and Knudsen, J.M., 1982, Phys. Rev. Lett. **48**, 1054.

Larsen, L., Roy-Poulsen, H., Roy-Poulsen, N.O., Vistinsen, L., Jensen, G.B., and Knudsen, J.M., 1984, Meteorit. Planet. Sci. **19**, 258.

Laugier, J. and Paulevé, J., 1965, CEA-N 540.

Lide, D.R., 1993, *CRC Handbook of Chemistry and Physics*, 74th ed. (CRC Press Inc., Boca Raton, USA)

Liechtenstein, A.I., Katsnelson, M.I., and Gubanov, V.A., 1984, J. Phys. F Met. Phys. **14**, L125.

Lines, M.E. and Eibschütz, M., 1983, Solid State Comm. **45**, 435.

Matsui, M. and Chikazumi, S., 1978, J. Phys. Soc. Jpn. **45**, 458.

Matsui, M. and Adachi, K., 1979, J. Magn. Magn. Mater. **10**, 152.

Matsui, M., Adachi, K., and Chikazumi, S., 1980, J. Appl. Phys. **51**, 6319.

Melosh, H.J., 1997, Nature **390**, 439.

Menshikov, A.Z., 1977, J. Magn. Magn. Mater. **5**, 188.

Menshikov, A.Z., 1979, J. Magn. Magn. Mater. **10**, 205.

Miller M. K. and Russell, K.F., 1990, in *Physical Metallurgy of Controlled Expansion Invar-Type Alloys*, edited by K.C. Russell and D.F. Smith (The Minerals, Metals and Material Society, Warrendale PA).

Mohn, P., Schwarz, K., and Wagner, D., 1989, Physica B **161**, 153.

Mohn, P., Schwarz, K., and Wagner, D., 1991, Phys. Rev. B **43**, 3318.

Moroni, E.G. and Jarlborg, T., 1989, Helv. Phys. Acta **62**, 195.

Moruzzi, V.L., Marcus, P.M., Schwarz, K., and Mohn, P., 1986a, Phys. Rev. B **34**, 1784.

Moruzzi, V.L., 1986b, Phys. Rev. Lett. **57**, 2211.

Moruzzi, V.L., Janak, J.F., and Schwarz, K., 1988, Phys. Rev. B **37**, 790.

Moruzzi, V.L., 1989a, Physica B **161**, 99.

Moruzzi, V.L., Marcus, P.M., and Kübler, J., 1989b, Phys. Rev. B **39**, 6957.

Moruzzi, V.L., 1990, Phys. Rev. B **41**, 6939.

Moruzzi, V.L., 1992, Solid State Comm. **83**, 739.

Mössbauer Effect Data Center, 1989, *Mössbauer Effect Data*, (University of North Carolina, Ashville, USA)

Mryasov, O.N., Gubanov, V.A., and Liechtenstein, A.I., 1992, Phys. Rev. B **45**, 12330.

Paulevé, J., Dautreppe, D., Laugier, J., and Néel, L., 1962a, CR Acad. Sci. **254**, 965.

Paulevé, J., Dautreppe, D., Laugier, J., and Néel, L., 1962b, J. Phys. - Paris **23**, 841.

Pauling, L., 1938, Phys. Rev. **54**, 899.

Petersen, J.F., Aydin, M., and Knudsen, J.M., 1977, Phys. Lett. **62A**, 192.

Pindor, A.J., Staunton, J., Stocks, G.M. and Winter, H, 1983, J. Phys. F Met. Phys. **13**, 979.

Ping, J.Y. and Rancourt, D.G., 1992, J. Magn. Magn. Mater. **103**, 285.

Pinski, F.J., Staunton, J.B., Gyorffy, B.L., Johnson, D.D., and Stocks, G.M., 1986, Phys. Rev. Lett. **56**, 2096.

Rancourt, D.G., Julian, S.R., and Daniels, J.M., 1985, J. Magn. Magn. Mater. **51**, 83.

Rancourt, D.G., 1989a, Physics in Canada **January**, 3.

Rancourt, D.G., 1989b, Nucl. Instrum. Meth. B **44**, 199.

Rancourt, D.G. and Ping, J.Y., 1991a, Nucl. Instrum. Meth. B **58**, 85.

Rancourt, D.G. and Ping, J.Y., 1991b, Hyperfine Interact. **69**, 497.

Rancourt, D.G., Ping, J.Y., and Dang, M.Z., 1992, Can. J. Phys. **70**, 1241.

Rancourt, D.G., 1994a, Phys. Chem. Minerals **21**, 244.

Rancourt, D.G., 1994b, Phys. Chem. Minerals **21**, 250.

Rancourt, D.G., Ping, J.Y., and Berman, R.G., 1994c, Phys. Chem. Miner. **21**, 258.

Rancourt, D.G. and Scorzelli, R.B., 1995, J. Magn. Magn. Mater. **150**, 30.

Rancourt, D.G. and Dang, M.Z., 1996a, Phys. Rev. B **54**, 12225.

Rancourt, D.G., 1996b, in *Mössbauer Spectroscopy Applied to Magnetism and Materials Science*, edited by G.J. Long and F. Grandjean (Plenum Press, New York) Vol. 2, p. 361 pp.

Rancourt, D.G. and Scorzelli, R.B., 1997, J. Magn. Magn. Mater. **174**, 324.

Rancourt, D.G., Lagarec, K., Densmore, A., Dunlap, R.A., Goldstein, J.I., Reisner, R.J., and Scorzelli, R.B., 1999, J. Magn. Magn. Mater. **191**, L255-L260.

Reuter, K.B., Williams, D.B., and Goldstein, J.I., 1988, Metall. Mater. Trans. A **20**, 719.

Rosengaard, N.M. and Johansson, B., 1997, Phys. Rev. B **55**, 14975.

Russell, K.C. and Smith, D.F., 1990, in *Physical Metallurgy of Controlled Expansion Invar-Type Alloys*, edited by K.C. Russell and D.F. Smith (The Minerals, Metals and Material Society, Warrendale PA).

Sabiryanov, R. F., Bose, S. K. and Mryasov, O. N., 1995, Phys. Rev. B **51**, 8958.

Sato, H., 1978, *Physics and Applications of Invar Alloys*, (Maruzen Company Ltd., Tokyo)

Schorscher, H.D., Wiedemann, C.M., Danon, J., Scorzelli, R.B., and Souza Azevedo, I., 1980, Meteorit. Planet. Sci. **15**, 363.

Schröter, M., Ebert, H., Akai, H., Entel, P., Hoffmann, E., and Reddy, G.G., 1995, Phys. Rev. B **52**, 188.

Scorzelli, R.B., 1982, *Étude des alliages fer-nickel de la météorite Santa-Catharina par spectrométrie Mössbauer et diffraction de rayons x*, Thèse de Doctorat, Université Pierre et Marie Curie.

Scorzelli, R.B. and Danon, J., 1990, in *Physical Metallurgy of Controlled Expansion Invar-Type Alloys*, edited by K.C. Russell and D.F. Smith (The Minerals, Metals and Material Society, Warrendale PA) p. 85.

Shiga, M., 1993, in *Electronic and Magnetic Properties of Metals and Ceramics*, edited by K.H.J. Buschow (VCH, Weinheim) p. 159.

Shirley, D.A., 1964, Rev. Mod. Phys. **36**, 336.

Slater, J.C., 1937, J. Appl. Phys. **8**, 385.

Tajima, K., Böni, P., Shirane, G., and Ishikawa, Y., 1987, Phys. Rev. B **35**, 274.

Tanji, Y., Nakagawa, Y., and Steinemann, S., 1983, Physica B **119**, 109114.

Thorpe, M.F., Jin, W., and Mahanti, S.D., 1991, in *Disorder in Condensed Matter Physics*, edited by J.A. Blackman and J. Taguera (Oxford University Press, New York) p. 22.

Ullrich, H. and Hesse, J., 1984, J. Magn. Magn. Mater. **45**, 315.

Ullrich, H., Huck, B., and Hesse, J., 1985, in *Proceedings of ICAME-83* (Gordon & Breach Science Publishers, New York), Vol. 2, p. 711.

van Schilfgaarde, M., Abrikosov, I.A., and Johansson, B., 1999, Nature **400**, 46.

Vandenberghe, R.E., De Grave E., and De Bakker, P.M.A., 1994, Hyperfine Interact. **83**, 29.

Vegard, L., 1928, Z. Kristallogr. **67**, 239.

von Barth, U. and Hedin, L., 1972, J. Phys. C - Solid **5**, 1629.

Wakelin, R.J. and Yates, E.L., 1953, P. Phys. Proc. Lond. B **66**, 221.

Wang, C.S., Klein, B.M., and Krakaner, H., 1985, Phys. Rev. Lett. **54**, 1852.

Wang, Y., Stocks, G.M., Nicholson, D.M.C., Shelton, W.A., Antropov, V.P., and Harmon, B.N., 1997, J. Appl. Phys. **81**, 3873.

Wassermann, E.F., 1987, Festkorperproblem **27**, 85.

Wassermann, E.F., 1990, in *Ferromagnetic Materials: A handbook on the properties of magnetically*

ordered materials, edited by K.H.J. Buschow and E.P. Wohlfarth (Elsevier Science Publishers B. V.) Vol. 5, p. 238.

Wassermann, E.F., 1991, J. Magn. Magn. Mater. **100**, 346.

Wassermann, E.F., Dumpich, G., Kirschbaum, U., and Liang, J., 1992, in *Proceedings of the International Conference on the Physics of Transition Metals 1992*, edited by P. M. Oppeneer, and J. Kübler, (World Scientific, London), Vol. 2.

Weiss, R.J., 1963, P. Phys. Proc. Lond. **82**, 281.

Willgeroth, S., Ullrich, H., and Hesse, J., 1984, J. Phys. F Met. Phys. **14**, 387.

Williams, A.R., Moruzzi, V.L., Gelatt, C.D.Jr., Kübler, J., and Schwarz, K., 1982, J. Appl. Phys. **53**, 2019.

Williams, A.R., Moruzzi, V.L., Gelatt, C.D.Jr., and Kübler, J., 1983, J. Magn. Magn. Mater. **31-34** , 88.

Window, B., 1973, J. Appl. Phys. **44**, 2853.

Window, B., 1974, J. Phys. F Met. Phys. **4**, 329.

Wittenauer, J., 1996, *The Invar Effect. A Centennial Symposium*, (The Minerals, Metals & Materials Society, Warrendale, Pennsylvania) 349 p.

Wohlfarth, E.P., 1975, IEEE Trans. Magn. **11**, 1638.

Wohlfarth, E.P., 1979, J. Magn. Magn. Mater. **10**, 120.

Wohlfarth, E.P., 1980, Solid State Comm. **35**, 797.

Young, R.A., 1995, *The Rietveld Method*, (Oxford University Press, Oxford).

Zen, E., 1956, Am. Mineral. **41**, 523.